Geotechnologies and the Environment

Nicola Masini
Francesco Soldovieri *Editors*

Sensing the Past

From artifact to historical site

Springer

Geotechnologies and the Environment

Volume 16

The *Geotechnologies and the Environment* series is intended to provide specialists in the geotechnologies and academics who utilize these technologies, with an opportunity to share novel approaches, present interesting (sometimes counter-intuitive) case studies, and, most importantly, to situate GIS, remote sensing, GPS, the internet, new technologies, and methodological advances in a real world context. In doing so, the books in the series will be inherently applied and reflect the rich variety of research performed by geographers and allied professionals.

Beyond the applied nature of many of the papers and individual contributions, the series interrogates the dynamic relationship between nature and society. For this reason, many contributors focus on human-environment interactions. The series is not limited to an interpretation of the environment as nature per se. Rather, the series "places" people and social forces in context and thus explores the many socio-spatial environments humans construct for themselves as they settle the landscape. Consequently, contributions will use geotechnologies to examine both urban and rural landscapes.

More information about this series at http://www.springer.com/series/8088

Nicola Masini • Francesco Soldovieri
Editors

Sensing the Past

From artifact to historical site

Springer

Editors
Nicola Masini
CNR-IBAM Institute of Archaeological and Monumental Heritage
Tito Scalo, PZ, Italy

Francesco Soldovieri
Institute for Electromagnetic Sensing of the Environment (CNR-IREA)
Napoli, Italy

ISSN 2365-0575 ISSN 2365-0583 (electronic)
Geotechnologies and the Environment
ISBN 978-3-319-50516-9 ISBN 978-3-319-50518-3 (eBook)
DOI 10.1007/978-3-319-50518-3

Library of Congress Control Number: 2017936470

Printed on acid-free paper

This Springer imprint is published by Springer Nature
The registered company is Springer International Publishing AG
The registered company address is: Gewerbestrasse 11, 6330 Cham, Switzerland

Foreword

"Social and Cultural Innovation" is a syntagma that has become current usage among researchers in recent years in response to the name chosen by the European Strategy Forum on Research Infrastructures (RIs) for the working group whose objective is the landmarks and projects that are primarily connected with the social sciences and humanities.[1] For itself, innovation means the creation of new products and services by bringing to the market a new idea. Although fundamental research is *curiosity driven*, it also has a translational impact, because the transfer of knowledge makes innovation possible, and innovation is *product driven*, insofar as it generates new products and production lines. Innovation is the affair of research councils all over the world, which are quite different from both universities and academies. Research councils were founded about a century ago, at the time of World War I, whereas universities date back to the Middle Ages and academies to the Renaissance. These differ because universities are devoted to teaching and professors are free to teach and investigate whatever they like and academies were funded by kings who wanted scholars to live at court, so that they might be able to pose questions of their own interest and receive answers; in contrast, governments funded research councils to achieve results of strategic relevance for the country.

The *Milan Declaration on Culture as an Instrument of Dialogue Among Peoples*, unanimously adopted by the Ministers of Culture of 80 countries at the international conference of 31 July to 4 August 2015 that was organized by the Italian Ministry of Cultural Heritage and Activities and Tourism at the Expo in Milan, states that:

> Cultural Heritage is the mirror of history, civilization and of the society, which is expected to protect it. Cultural Heritage, both tangible and intangible, is also the essence of identity, the memory of peoples and their past and present civilizations. It expresses, at the same time, universally recognized values of tolerance, dialogue, and mutual understanding . . . the work of man and his extraordinary talent must be protected and preserved for the benefit of future generations.

Knowledge conservation, protection, and use trigger integration policies; they also promote cultural, economic, and social growth. We are talking about areas such as knowledge and in situ protection of cultural contexts and artifacts, postwar archeology, virtual reality, and sustainable museography,[2] whose impact implies (a) making

cultural heritage instrumental for science and cultural diplomacy; (b) protecting and promoting cultural diversity; (c) documenting, conserving, monitoring, and using cultural diversity; and eventually (e) protecting it from environmental and anthropic threats in the Middle East and in North Africa. In Brussels, the strategic approach to cultural diplomacy points to cultural diversity as an integral part of the values of the European Union. The 2016 *Joint Communication to the European Parliament and the Council: Towards an EU Strategy for International Cultural Relations* of the High Representative of the Union for Foreign Affairs and Security Policy has outlined the following five guiding principles:

1. Promote cultural diversity and respect for human rights.
2. Foster mutual respect and intercultural dialogue.
3. Ensure respect for complementarity and subsidiarity.
4. Encourage a cross-cutting approach to culture.
5. Promote culture through existing frameworks for cooperation.

The current migrant and refugee crisis has made it clear how urgent it has become for local, regional, national, and international administrations to work out policies of social and cultural innovation to the advantage of new citizens that make them welcome in full dignity.

The great challenge is the passage from *data of science* to *data of humanities*. The European Union has recognized the need and urgency to provide advanced facilities for interdisciplinary, cutting-edge research in social and cultural innovations. The main goal is to address every aspect of science and technology related to the field, offering innovative solutions to the societal challenges of the new millennium. As a matter of fact, social and cultural innovation researchers also are confronted with huge amounts of data of increasing complexity in highly interdisciplinary settings. Let us only think of enabling technologies such as NFC (near-field communication), CRM (content rights management), contents-aware networks (fruition and enjoyment), low-latency networks (warning and security), and huge-bandwidth networks (augmented reality).

The object of *Sensing the Past* is to provide readers and users with top-rate solutions for data analysis in archeology and cultural heritage, in situ noninvasive technologies for monuments and artifacts, and generally ICT information and communication technology) and sensing technologies for cultural heritage. Currently, six research infrastructures for "Social and Cultural Innovation" are operational. Among them, the E-RIHS (European Research Infrastructure for Heritage Science) creates synergy for a multidisciplinary approach to heritage interpretation, preservation, documentation, and management. *Sensing the Past* is a substantial contribution toward the implementation of the grand Italian project of establishing the European Research Infrastructure for Heritage Science.

Rome, Italy Riccardo Pozzo

Notes

1. http://www.esfri.eu/working-groups/social-and-cultural-innovation: "The Social and Cultural Innovation SWG proposes possible solutions (related to RIs) that are able to help tackle the Grand Challenges facing society, such as health or demographic change, or the 'Inclusive, innovative and secure societies' challenge from the third pillar of Horizon 2020, called 'Tackling societal challenges.' It establishes possible methods through which social sciences and humanities could be used as an evaluation criterion for the activity of other RIs in the ESFRI roadmap (e.g., social impact). It also explores how RIs can contribute to social innovation or better knowledge transfer toward society."
2. For example, satellites and topographic techniques, drones and sensors for heritage protection in wide areas, advanced diagnostic systems, nanomaterials and nanotechnologies for conservation, 3D for the enhancement of cognitive access in historical and archaeological contexts, methodologies and protocols for 3D rendering in hazardous contexts, monitoring artifacts–context interaction, advanced exhibition systems, smart showcases.

Contents

Chapter 1
Cultural Heritage Sites and Sustainable Management Strategies

Nicola Masini and Francesco Soldovieri

Abstract This chapter first highlights the necessity of sustainable management and protection of cultural heritage (CH). This necessity is stated by pointing out the social and economic value of our cultural heritage, presenting the very challenging set of risk factors, and by briefly summarizing the recommendations of high-level policy makers. A possible answer to these necessities is the design and the implementation of a systematic approach, based on the integration of different concepts ranging from the sensing, to the information and communications technology (ICT) tools, to the materials design and implementation. In this framework, the present book describes the novel and state-of-the-art technologies in the field of diagnosis and monitoring and in ICT for the improved fruition of cultural heritages.

Keywords Sustainable management • Protection • Sensing technologies for diagnosis and monitoring • ICT

1.1 Introduction

The widespread presence of movable and immovable cultural assets, their high cultural value, and the accessibility of this patrimony by the different typologies of users make crucial the necessity of their sustainable management and protection. In fact, the cultural heritage (CH) is continuously under pressure because of its inherent fragility and the necessity to handle different risk factors having both environmental and anthropic causes. The necessity of adequate management and protection is amplified by the crucial significance of the cultural heritage in terms of social, cultural, and economic value. In fact, the cultural heritage is a crucial

N. Masini
CNR-IBAM Institute for Archaeological and Monumental Heritage,
C. da Santa Loja, 85050, Tito Scalo, Potenza, Italy

F. Soldovieri (✉)
Institute for Electromagnetic Sensing of the Environment (CNR-IREA),
Via Diocleziano 328, 80124, Napoli, Italy
e-mail: soldovieri.f@irea.cnr.it

N. Masini, F. Soldovieri (eds.), *Sensing the Past*, Geotechnologies and the Environment 16, DOI 10.1007/978-3-319-50518-3_1

element for the promotion of intercultural dialogue, the cultural and social growth, which concur with the definition and feeling of a territorial identity.

Therefore, cultural heritage has to be considered not only a proof of our memory but also a key component of our daily life and a driving force of inclusive regional and local development. In this context, the task of the different social actors (territorial planners, policy makers, schools, universities, economic actors, as well as citizens) to empower the collective awareness of their material and immaterial cultural heritage is important.

In addition, cultural heritage is an important factor of economic growth. For example, Europe, with its cultural diversity and exceptional ancient architectures and artifact collections, attracts millions of tourists every year with an annual revenue of €535.9 billion. Therefore, the sector is crucial for European economy and competitiveness and especially for the Mediterranean area, where the touristic exploitation of the cultural assets is one of the main factors of the social and economic progress of the territory.

Furthermore, the cultural heritage sector enables a significant economic contribution also in other markets as the one regarding renovation and maintenance. According to the European Construction Industry Federation, in 2014 renovation and maintenance represented 28.4% of the value of Europe's construction industry (Key Figures 2014).

In view of preserving the richness and diversity of "values" related to cultural heritage, the necessity is still more remarkable to take care of historical tangible and intangible artifacts with respect to the multiple risk scenario related to environmental and anthropic actions.

For example, looking at seismic risk, several earthquakes have occurred in past years and represented a serious threat for our cultural heritage. Recent examples are the seismic events such as the 1997 earthquake in central Italy, which severely affected the church of San Francesco in Assisi, as well as the cultural heritage damage caused by the 1999 Izmit earthquake in Turkey. More recently, the Nepal earthquake (2015) destroyed several monuments in the Kathmandu Valley World Heritage Site, among which is the famous Buddhist stupa in Kathmandu Durbar Square.

Earthquakes provide a wide spectrum of the challenges to be faced in preparing and responding to crisis events. Protection from earthquakes is mandatory, especially in a large area of the Mediterranean basin where the seismic risk is high, such as Greece, Turkey, and Italy, and where at the same time invaluable cultural and historical assets are located. In this framework, one lesson learned from the recent natural disasters is that cultural heritage is often more fragile with respect to the territory and, therefore, entails accurate preservation and mitigation of the natural hazards. This situation is worsened by the fact that our cultural heritage is a nonrenewable resource, unique, nonreplaceable, or noninterchangeable. In addition, cultural heritage protection also protects people, because the main cultural sites are crowded during the tourist season; in the case of a major earthquake occurring during a day of heavy crowds, the collapse of historical buildings would lead to a huge number of injuries.

Very recently, a pressing challenge is that regarding climate change and the related increasing occurrence of extreme climate events (IPCC 2014). The negative climate change impacts the cultural heritage assets in two main ways: (1) the direct physical effects on the buildings or structures and (2) the effects on social structures and habitats. The direct physical impacts on built heritage caused by climate change are summarized in WHC (2006), and general guidelines are indicated in Cultural Heritage Assets (2012). Climate change has also societal and cultural consequences related to the degradation of the property, which leads to changes affecting land-use planning, the economy of a territory, the human presence, and generally the territorial and societal conditions that currently concur to maintain the sites. Climate change could force a population to migrate (under the pressure of sea level rise, desertification, flooding, etc.), leading not only to the breakup of communities and to the abandonment of property, but also to the loss of the immaterial cultural heritage such as rituals and cultural memory. So far as the conservation of cultural heritage is concerned, this abandonment raises an important concern wherein traditional/local knowledge and skills are essential to ensure a proper maintenance of these properties. In conclusion, assessment and mitigation of the impacts of climate change on cultural heritage must account for the complex interactions among physical, natural, cultural, economic, and social aspects. The very significant proof of the effects of the extreme events are the collapses and landslides affecting the historical site of Pompeii, especially in recent years, as testified by the collapse of the 2000-year-old "House of the Gladiators" on 6 November 2010.

On the other hand, also the anthropic component represents a constant factor of damage and destruction. In particular, we refer to the urban pressure, to the archaeological looting linked to illicit trade antiquities, and the vandalism. The urban pressure has deleterious effects on monuments, as in the case of the Giza pyramid complex, which is a prominent example of this threat. The spread of urban land use produces a significant loss of the potential archaeological heritage conserved in the subsoil. This is the case of several regions all over the world, where the development policies are not accompanied by a sustainable vision of the society, including the protection of the cultural heritage. The archaeological heritage is systematically targeted for clandestine excavations that not only provoke the loss of precious artifacts, but also the loss of information about the civilizations or human settlements they represent. This loss is irreversible also in the case of recovery of archaeological artifacts. Finally, the vandalism in countries in war is probably the most dramatic phenomenon of the destruction of cultural heritage. Very recently there is an increasing occurrence of threats to the cultural heritage from terroristic actions because the CH are meaningful for their political and memory value; in this context, it is just necessary to recall the recent events in Tunisie, Syria (Palmira), and Iraq (Mosul).

It is worth noting that the capability of managing crisis events and the improvement of the resilience cannot be separately seen from the one regarding the mitigation of the deterioration/aging problems. In other words, it is necessary to avoid/mitigate a sort of cascading effect, where the cultural heritage that is not

effectively maintained represents structures more vulnerable in the presence of events other than an extreme crisis. For example, we stress how much part of Europe is affected by a middle seismic risk, which nonetheless can induce damages on the structures that are vulnerable.

In this frame, sustainable management should be well founded on a long-term (ordinary and extraordinary) maintenance, which should cover all the phases of the life cycle of the cultural heritage and be economically sustainable. This objective should be pursued by exploiting the support of the monitoring/diagnostic technologies for an improved situational awareness of the site during all its life cycle.

1.2 Political and High-Level Strategies and Recommendations

The scenario sketched in the foregoing section motivates the setup of high-level strategies defined by policy makers, with a focus on the sustainable management and protection of cultural heritage. A good proof of this effort is provided by CCE-EP (2015) and CEU (2014).

The report in CCE-EP (2015) describes the challenges that cultural heritage sector has to face:

- Public budgets are decreasing, as is participation in traditional cultural activities.
- High tourist influxes are a mixed blessing, because there are increasing revenues but also environmental and physical pressures.
- Trafficking of cultural artifacts remains a difficult issue requiring action at the European and international level.
- Global warming and climate change, in particular rising sea levels and the increased occurrence of extreme weather events, can put cultural heritage at risk.

To respond to these challenges:

- The heritage sector must identify new management and business models and develop novel professional skills, working with authorities in a coordinated way.
- The valorization and preservation of heritage should be part of a holistic approach regarding the long-term management and development plans.
- An integrated approach to heritage conservation, promotion, and valorization is necessary to have a beneficial impact on societal and economic aspects and on other public policies.
- Conservation should be considered as a tool for the development of the cultural landscape, by making the cultural heritage resources a key element for the social and economic life of the local community.

Cultural heritage should use profitably new scientific and technological opportunities in different domains (ICT, sensing and monitoring technologies, new materials,

structural and environmental assessment, etc.) organized under a synergic frame. In this context, to strengthen Europe's position in the field of cultural heritage preservation, restoration, and valorization, there is a need to do the following:

- Encourage the modernization of the heritage sector, raising awareness and engaging new audiences
- Apply a holistic approach to research and innovation, knowledge sharing, and smart specialization
- Exploit the opportunities offered by digitization; to reach out to new audiences
- Identify skills needs and improve the training of heritage professionals
- Continue developing more participative interpretation and governance models that are better suited to contemporary Europe, through greater involvement of the private sector and civil society

In CEU 2014, the Council of the European Union identifies a set of actions:

- Consider cultural heritage as a strategic resource for developing a society based on democratic, ethical, aesthetic, and ecological values, in particular in a moment of crisis
- Contribute to the mainstreaming of cultural heritage in national and continental policies
- Promote long-term heritage policy models and enhance the role of cultural heritage in sustainable development, focusing on urban and rural planning, redevelopment, and rehabilitation projects

To achieve these general aims, it is necessary to improve larger-scale networking and peer learning within different countries. Particular emphasis has to be placed on converging technologies and on multidisciplinary research and innovation for methodologies, products, and services in the cultural heritage sector. In the aforedescribed scenario, the necessity arises of research and innovation for the development of strategies, methodologies, and tools that can ensure dynamic and sustainable cultural heritage in Europe in response to the large set of environmental and anthropic hazards.

1.3 Necessities and Technological Solutions

Different necessities arise in the process of sustainable management and protection of cultural heritage, and we describe briefly them as well as a possible technological solution to these needs.

The first necessity regards sustainable and effective safeguarding and management of cultural heritage. In this context, it is necessary to implement reliable predictive and cost-effective maintenance, improved risk management, and diagnosis and treatment accompanied by thorough understanding of the historical and technological context of heritage materials and objects.

A possible strategy consists in setting up a systematic approach, wherein the sensing and observational technologies enable a context analysis and site health monitoring chain able to provide an always updated situational awareness, not only about the site but even of the territory as the cause of possible environmental and anthropogenic impacts. The key technological enabling factor is the integration of different sensing technologies from satellites, an airborne and ground-based platform for a multiscale vision of the site. This situational awareness is key information for the vulnerability assessment and is a crucial support to the identification and implementation of advanced solutions for remediation and restoration accounting, specifically in respect of integrity and reversibility. In this way, it is possible to define and implement reliable cost-effective long-term maintenance actions and operational procedures for risk management. This method allows us to do the following:

1. Prioritize, define, and optimize the maintenance interventions by establishing when, where, and in what way to make the interventions with a significant improvement of the economic sustainability and by accounting for the integrity of cultural heritage.
2. Improve risk management through a clear identification of risks and their magnitude and an always-updated knowledge of the site conditions. This step permits defining and realizing mitigation strategies and performing a thorough cost–benefit analysis.
3. Enable a reliable diagnosis and treatment and a better understanding of the historical and technological contexts of heritage materials and object. Monitoring and materials analysis as well as definition and realization of materials enable a positive feedback loop. In fact, the knowledge of the historical and technological contexts for material and objects accompanied by a multisensing diagnosis allows identifying and setting up a reliable treatment. Ultimately, the effectiveness of this treatment is verified through diagnosis/analysis tools and finally becomes a new piece of information for a better understanding of the historical and technological contexts of heritage materials and objects.

In the aforementioned context, a crucial task is that of ICT system architectures (SA) able to support the decisions and actions of the stakeholders. One of the functionalities of ICT SA is to integrate all the information, not only from monitoring/diagnosis, but even for the existing information (old images of the site, previous monitoring and condition archives, excavation reports, and all other relevant archived documents) to understand and identify any change over time. This method aids in building a knowledge base about materials and procedures for long-term maintenance and risks management. In conclusion, decision makers can be supported in the prioritization, planning, and cost–benefit analyses of the maintenance actions and risk mitigation strategies, even in view of the definition of future more sustainable actions.

The second main necessity regards an effective advice and input to long-term restoration and adaptation policies of government organizations and promotion of improved practices for the guardians of cultural heritage assets.

The adoption of sustainable management and protection procedures is possible only by the significant involvement of public and private expert end-users and stakeholders, including government organizations. The involvement of the end-users is crucial not only in the definition of the system/approach requirements but also to drive the scientific/technological development toward useful and timely solutions and to disseminate the results to a larger set of nonexpert end-users. Long-term maintenance and risk management methodologies, protocols, and open source tools become a crucial factor in the improvement of the management practices and policies related to maintenance, reinforcement, protection of cultural heritage sites and elements. Of course, for this aim a socioeconomic cost–benefit analysis mainly in terms of economic sustainability and respect of the integrity of the cultural heritage should be addressed.

The technological solution to the necessities above outlined can be stated as the definition and implementation of a systemic approach to ensure the protection and the preservation of the cultural heritage with respect to a multirisk scenario. This approach is founded on a multidisciplinary approach that bridges the gap between the two worlds of the cultural heritages stakeholders and the scientific/technological experts. This systematic approach should have the capabilities to do the following:

- Handle a wide spread of worldwide cultural heritages (historical towns, different ages/sites/elements, new architecture)
- Face risks factors related to environmental and anthropic hazards
- Achieve a multitemporal and spatial situational awareness of the site itself and as an element of a more general context, including also the territories in which the cultural heritage is located (wide and local monitoring, material diagnosis)
- Enable a sustainable long-term preservation and maintenance coupled with capabilities of risk reduction and crisis management
- Respect the historic and cultural integrity and valorize the socioeconomic value of the cultural heritage

The key elements of this systematic and interdisciplinary approach start from the identified needs (Fig. 1.1) and can be summarized as follows:

– An integrated dashboard populated by heterogeneous toolboxes based on sensing/environmental technologies (at wide and local scales) coupled with diagnosis/structural analysis methodologies for a multitemporal/multispatial monitoring of the cultural heritage asset
– An ICT platform able to provide a situational awareness about the cultural heritage status and support the decisions in both shorter term and longer term of the stakeholder involved in cultural heritage site management for risk reduction
– Innovative solutions and materials for the economically sustainable maintenance and remediation preserving the integrity and improving the social value of the cultural heritage
– Guidelines and protocols not only for the preservation of the cultural heritage site but also for overall risk cycle management

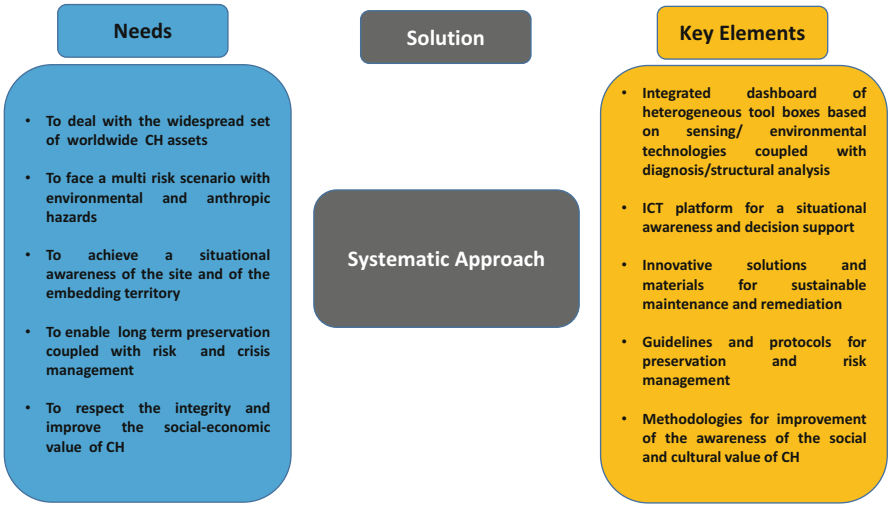

Fig. 1.1 The systematic approach for cultural heritage management, protection, and fruition

– Methodologies and strategies aiming at improving the awareness of the social and cultural value of cultural heritage from the different communities

Specifically, the integrated observation and monitoring of the cultural heritage assets is planned at two scale levels: (1) a macrolevel for a wide vision of the site and of the territory and (2) a local level through monitoring and diagnosis of buildings and artifacts present on the sites. The integration is made possible by combining data collected by the different observational platforms (satellite, aerial, traditional as well as innovative in situ sensing technologies, including multifunctional self-sensing materials).

Innovative flexible and scalable ICT platform solutions has to be designed and developed in order integrate, correlate, and manage the data collected over a long period of time from external sources/causes and intrinsically related to cultural heritage object behavior and to its physicochemical status in terms of these needs:

- Integration with historical information of the site (including past critical events)
- Integration of different monitoring data to obtain an online updated situation of the site and surroundings situation
- Vulnerability and risk evaluation by means of advanced modeling
- Integration of information about the structural and physicochemical status of materials and site
- Visualization of information through maps and three-dimensional (3D) models
- Situational assessment, information for awareness building, and decision support system (including warning and alert messages)

Such structured information will be crucial for the development of effective solutions for the mitigation and remediation of the hazards effects.

1.4 Why Sensing the Past?

In the cultural and social context just described, the idea was born of writing a book on sensing technologies for cultural heritage involving scientists and experts in different disciplines and technological applications.

This book has been thought to answer to a number of issues, which in the last decade have animated the debate of scientists, end-users, and institutions operating in the field of cultural heritage management, conservation, archaeology, and heritage science.

In particular, one wonders to what extent today the technologies are operational to address the needs of archaeological research and conservation of monuments and works of art? Are the potentialities of science fully exploited for applications in the field of cultural heritage? These are the crucial questions reflecting the fact that technology and science are tools seen and considered as being of service to cultural heritage issues.

Less frequent are questions of this type: Can cultural heritage and archaeology become a smart specialization area for the development of new scientific methods and technologies? Or, again, to complete the first question: How far do you have to go in the application of science and technology for a real and recognized benefit for cultural heritage?

Returning to the second question: Is the time ripe to create an economy based on the development of technologies designed ad hoc for cultural heritage? What are the limits in terms of operational effectiveness in using technology for cultural heritage that was primarily designed for other purposes and fields of application (from environment to security)?

Around these questions, the idea arises to do a survey of sensing technologies applied to different operational purposes: from the site discovery to the study of the ancient landscape and paleo-environment, from the characterization of construction materials to the analysis of the degradation of monuments, from risk assessment to the fruition of cultural heritage.

The book starts with remote sensing, which is one of the scientific areas that significantly increased the capability to address the issues of the knowledge (historical and archaeological), protection, conservation, and management of cultural heritage and landscape. This choice was mainly the result of both the dramatic advancement of earth observation technologies, in terms of performance of sensors (passive and active) and software data processing, and the greater awareness of end-users (archaeologists, conservators, etc.) of the usefulness of satellite remote sensing. In fact, remote sensing provides "a large variety of information capable to support multipurpose projects: from the archaeological research activity to risk monitoring, from the landscape analysis and protection to the promotion and valorization of cultural identity," as pointed out by Masini and Lasaponara (2016, this volume) and Lasaponara and Masini (2016, in this volume). In the first one the authors present a selected set of approaches to site detection with a number of

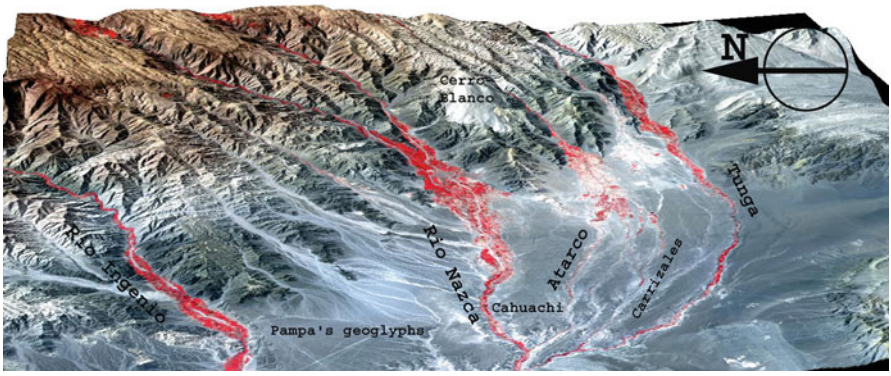

Fig. 1.2 Nasca drainage basin (Peru): false color of 3D satellite image

applications in Italy, Peru (see Fig. 1.2), and Turkey such as (i) the reconnaissance, processing, and interpretation of archaeological proxy indicators; (ii) the geographic information system (GIS)-based development of predictive models; and (iii) the data integration at different scales and details of requested information. In this way, it is possible to evaluate large areas of archaeological interest for driving the choices of urban planning in territories with a rich cultural heritage and to predict with high detail the presence of possible buried archaeological remains. In the second chapter (by Lasaponara and Masini 2016), an overview of possible applications of earth observation technology for risk assessment and monitoring is presented and discussed.

Earth observation technologies not only offer new opportunities to "sense" the past and its witnesses, known and unknown, but also enable novel approaches to the knowledge of cultural heritage and historical and archaeological research. This is the case of LiDAR (light detection and ranging) in archaeology, which since the first applications has truly acted as "a catalytic enabler of rapid transformational change in archaeological research and interpretation" as indicated by Chase et al. (2012) (see also Chase et al. 2016, this volume). Many studies and investigations of ancient landscapes and settlement have significantly benefited from LiDAR, especially in areas covered by tropical canopy as in Belize. The discoveries in Caracol cast new light on Mayan archaeology. The case of Belize demonstrated that LiDAR, although more expensive with respect to other remote sensing techniques, is cost efficient "when contextualized in terms of the sizeable landscapes that are revealed and the time involved" (see Chase and Chase 2016, this volume).

Synthetic aperture radar (SAR) represents the last frontier of Earth observation for cultural heritage. Thanks to the availability of several multifrequency, multi-polarization, and very high resolution (VHR) radar systems and great advances in data processing (Franceschetti and Lanari 1999), SAR increases the possibility to study the earth in its various facets, and consequently has great potential for use

for the study of the human past (Lasaponara and Masini 2013) and the analysis of deformation phenomena affecting the historical structures in their interaction with the subsoil. In this context, Tapete and Cigna (2016) open a window on landscape archaeology, the environmental processes as well as the anthropogenic impact on past and present landscapes, as observed, analyzed, and interpreted by means of SAR imagery. A number of emblematic and impressive case studies, from the Nasca landscape study in the context of the ITACA Mission in Peru (Masini et al. 2016a), to archaeological looting detection in Syria, demonstrate the potentialities of SAR by using the two key SAR parameters such as amplitude and phase.

A SAR application, presented in this volume by Chen et al. (2016), was utilized in the territory of Luoyang, the ancient capital city during five dynasties: from the Xia Dynasty (1900 BCE) to the Sui-Tang Dynasty (700–900 AD). The characteristics of the expected archaeological buried remains, in rammed earth, and the subsoil composed of clay, are not ideal for applications based on remote sensing and geophysics. The investigations were carried out on two test areas and pointed out the capability of SAR to provide indications for planning future extensive archaeological field surveys. The results were promising for the first investigation, whereas in the second one, because of the surface characteristics, the results were not significant. However, the results of UAV surveys and geoelectrical prospecting indicate the presence of some buried roads and channels, typical of the Sui Tang urban planning and architecture.

In this volume, Bonano et al. (2016) discuss how the monitoring of deformation by means of the differential SAR interferometry (DInSAR) techniques could be useful for the development of operative preservation strategies, showing the results obtained for the emblematic case study of Pompeii. A large archive of SAR data collected by the ERS-1/2 and ENVISAT SAR sensors of the European Space Agency (ESA), as well as by the Italian COSMO-SkyMed constellation, has been processed to monitor the ground deformations in the archaeological site of Pompeii from 1993 to 2015. The obtained results do not suggest particular and heavy problems of displacement with the exception of localized areas characterized by significant deformations. These results point out the need to enlarge the spectrum of sensing technologies, to increase the detail of information to characterize conservative problems, considering also the weathering pathologies and the constructive characteristics of buildings and artifacts.

This approach has marked the work of Masini et al. (2016b, in this volume), focused on the integration of geophysical techniques and other noninvasive sensing technologies, including ground-penetrating radar (GPR), seismic tomography, and infrared tomography, to support the conservation and to indicate efficient and compatible techniques and strategies of restoration in the Regio VIII of Pompeii (see Fig. 1.3). To this aim, the information requested is the identification and mapping of cracks, voids, dishomogeneities of masonry structures, among other data. It is also necessary to contextualize these data in a broader framework of knowledge (by the constructive characteristics of the walls to the knowledge of the risk factors, some of which can be inferred by SAR), which allow us to go

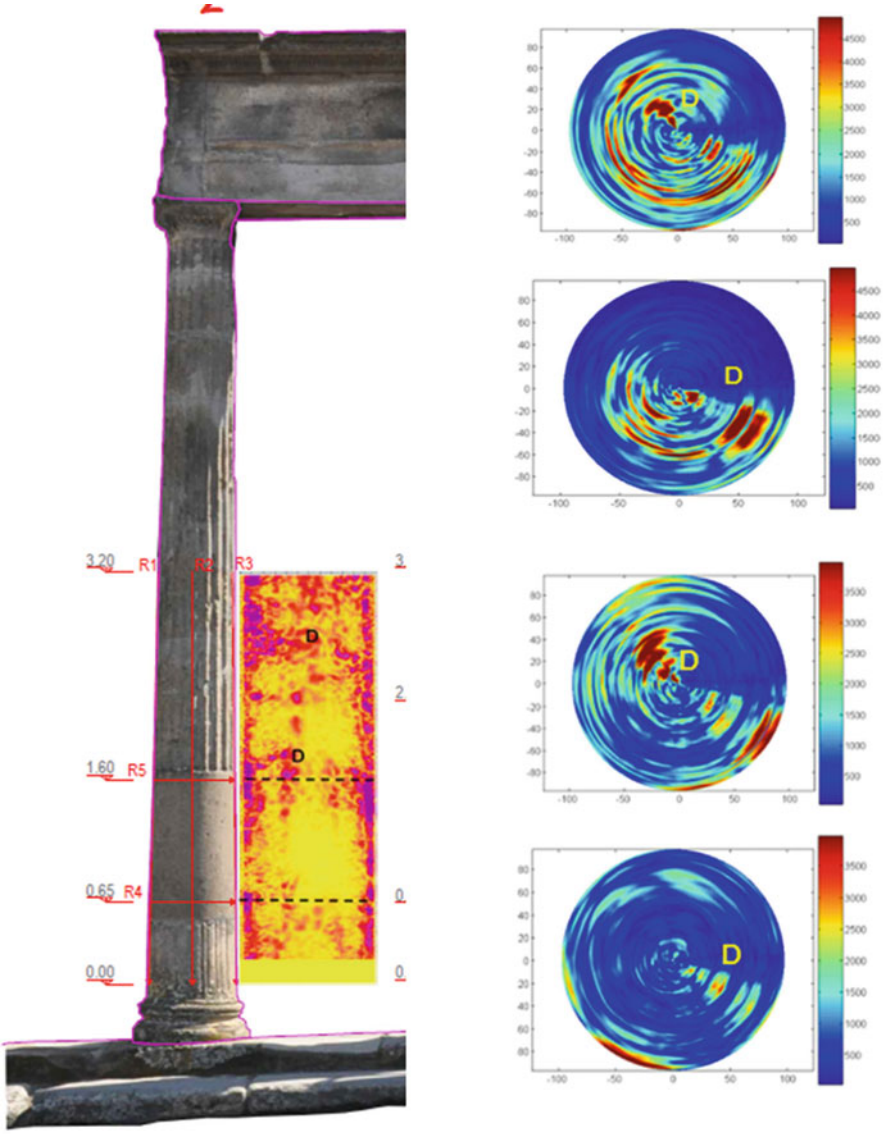

Fig. 1.3 Pompeii: GPR-based investigation of columns (Courtesy of G. Leucci)

beyond the simple "radiography" of the object and provide a real diagnosis of the conservation problems.

An integration approach, but for archaeological purposes, has been presented by Agapiou (2016, in this volume). The aim is the detection of archaeological crop marks by means of ground spectroradiometric measurements for calibrating and

simulating multispectral/hyperspectral satellite images and for better understanding the interaction in terms of EM radiation between buried remains, the surrounding soil, and the vegetation cover. This approach proved to be useful for test beds and historical sites in Cyprus.

When the crop marks are not the most effective proxy indicators of the presence of archaeological features, attention should be addressed to other surface or subsurface "anomalies" such as a magnetic one. After a global vision and analysis of the landscape by space and aerial remote sensing, geomagnetic prospecting is in many cases the following step aimed at providing information at an operational scale on the presence of possible archaeological features. Fedi et al. show the potentialities of the magnetic surveying as one of the most effective techniques supporting the archaeological prospecting (see Chap. 10 in this book). The effectiveness of this technique has benefited advances in signal enhancement and boundary analysis of potential field anomalies and new 3D imaging techniques, which provide an estimate of the magnetization distribution within the subsoil by means of high-resolution images of the source distribution. However, the limits of geomagnetometry in characterizing the "cultural" anomalies in the subsoil, especially in the perspective of archaeological excavations, make necessary the use of other geophysical prospecting methods such as GPR.

Despite its wide and well-assessed operational capability, the GPR technique needs knowledge of the underlying physical concepts, which make possible a full comprehension of the signal–target interaction to interpret in a correct way GPR products, from the single radargrams to time slice, in the case of possible buried archaeological remains. The quality of the results in terms of rate of success in identifying and characterizing "cultural" target depends also on positioning of the results. This aspect is often neglected or not taken into account by geophysicists, especially those who have not particular experience in archaeological missions. With such regard, Persico and Sato (2016) introduced some of the latest advancements achieved, with particular reference to systems equipped with arrays of antennas and precise positioning systems. Furthermore, the relevance of GPR for archaeological prospection is shown by Sato in another chapter of this book. In particular, GPR enhanced by advanced navigation systems permitted investigation of the inner of several "Kofun," which are burial mound structures (tumuli built mostly in the fourth to sixth centuries AD) and are considered the most important archaeological targets in Japan. The results demonstrate that the method provides very precise three-dimensional imaging also for surveys on non-flat ground surfaces.

GPR precision is still more important when the target are steel rebars of 2-cm diameter in a concrete structure such as the Musumeci Bridge in Potenza, which represents one of the most important bridges in Italy from the architectural point of view. GPR along with other noninvasive sensing technologies including infrared thermography has been used for detecting decay superficial patterns and surveying steel rebars. The aim was to provide a diagnosis of decay problems, to assess the structural vulnerability of the bridge, and to provide the mechanical parameters for the finite element computation (Soldovieri and Dumoulin 2017).

Important complementary results for the diagnostics of buildings, in masonry or in concrete, can be provided by seismic and sonic prospecting methods, as shown by Leucci (2016), who discussed their potentialities and limits for a number of cultural heritage applications along with the description of rational basis and some laboratory tests. Leucci (2016) also underlined how the environmental conditions affect the results of sonic and ultrasonic tests. In particular, moisture content however does not preclude the possibility to investigate the historical building materials (stone, brick, mortar), or influence the results, overestimating pulse velocity, because high saturation level may conceal flaws within the masonry.

The analysis of propagation of elastic waves could be used not only to detect cracks inside masonry but also to map and characterize surficial alterations of natural stone by ultrasonic transmission measurements. With such regard Meier et al. (2016) developed a methodological approach, reproducible and highly accurate, to evaluate and quantify surficial alterations of natural stone considering that the velocity of ultrasonic waves depends on a number of properties such as stone matrix and texture, the contacts between mineral grains, and pore filling. Some stone materials including marble, sandstone, and tuff have been studied with laboratory and in situ measurements to evaluate the changes of seismic velocities caused by weathering and conservation treatments. As for GPR, the interpretation needs effective approaches to data processing and to the analysis of the results, such as the analysis of amplitudes of the waveforms and comparison of average P- and Rayleigh wave velocities.

The operational effectiveness of ultrasonic measurements to address specific issues related to stone conservation improves if they are combined with petrographic and petrophysical analyses, as proposed by Alvarez de Buergo and Fort Gonzales (2016). The authors show and discuss six case studies in Spain related to a typological variety of artifacts, buildings, and stone materials such as a Roman carved granite megalith, a Gothic sandstone cross, granite and limestone ashlars of the façade of the Royal Palace at Madrid, monzogranite and porphyritic granite elements of church historical stylistic phases (from Mozarab to Baroque), sandstone stela, and finally different types of limestone used in the fourteenth century in Real Alcázar at Sevilla. The results demonstrate the capability of ultrasonic investigations in determining the degree of decay and the fissures and cracks located in different materials to provide indications useful for the planning and development of preventive and restoration measures. When the requested information is the characterization of the compounds (organic and inorganic) and, consequently, the detection of black crusts and changes in roughness on stone surfaces, the analysis of biological growth, and of chemical and physical transformation of painted surfaces, diagnostics requires different tools capable of increasing the detail of investigation.

A number of methods of analysis are available for applications not only in the laboratory but also in situ. Some of them are mature for extensive applications such the spectroscopic techniques, other are still at the beginning for their operational use on works of art, such the Terahertz, both of which are shown and discussed in this volume.

Among the spectroscopic techniques, the hyperspectral method acquiring imagery in the visible-near infrared and short-wave infrared are capable of discriminating lithological features and mineralogical characteristics. Camaiti et al. (2016) developed procedures for use of hyperspectral imaging for mapping and monitoring the gypsum of black crust that is found on historical architectural surfaces. These techniques can be also applied to characterize pigments, varnishes, and binding mediums for paintings, and in general for monitoring of protective coatings on stone or for evaluating the progress of cleaning treatments on painted surfaces. Although hyperspectral imaging does not offer the same level of detail of FT-IR spectroscopy, it has the advantage to investigate a large surface at relatively low cost and time.

The recent technological advancements regarding the development of portable devices working at terahertz (THz) frequencies, together with the ability of these radiations to perform noninvasive investigations, is motivating a widespread use of this technology also for cultural heritage as showed and discussed by Catapano et al. (2016a). The authors put in evidence the promising potentialities of spectroscopic and imaging devices working in the THz range to discriminate different material layers and detect inner features of artworks, in particular paintings and ceramics. Catapano et al. (2016b) applied this technology to three case studies, two concerning paintings (an oil-canvas and a tempera-wood panel) and one that referred to a ceramic object. The comparison of the results with those obtained by using X-ray radiography and infrared thermography evidence the capability of terahertz in providing different types of information useful for the analysis of the state of conservation and historical study, such as the presence of (i) optically invisible lines from an underpainting of oil on canvas; (ii) gesso layers under the pictorial layer, typical of medieval painting techniques; and, (iii) finally, varnish layers in majolica tiles.

For these materials and other which typically could be found in works of art, a number of sensing technologies capable in detecting and quantifying chemical and mineralogical components are available and employed. Romano et al. (2016) in this volume discussed the integration of particle-induced X-ray emission (PIXE), full field X-ray fluorescence (FF-XRF), and X-ray diffraction (XRD) for the analysis of ancient pictorial pigments of ceramics. In particular, by means of a protocol for the quantitative analysis of pigments, they obtained the global elemental composition and the chemical associations among elements, allowing new insights into the nature of pigments, production technology, and conservation state for samples related to Nasca polychrome ceramics and Neolithic fragments coming from Sicily.

The spectrum of sensing technologies mature for an operational use includes surely infrared thermography as demonstrated by Dumoulin (2016) who, starting from the radiation theory to introduce infrared thermography and radiative heat transfer, presented and discussed some processing analysis approaches to be applied to concrete elements for defect detection in laboratory and in real field conditions. In particular, the author shows two approaches, one based on the signal and image processing domain, the second on thermal domain, with different capabilities for

quantitative characterization of defect: the greater the second with respect to the first, especially if infrared thermography measurements are efficient and accurate.

A multiscale and multisensor approach proved to be the most effective investigation strategy to provide useful data for technical choices on how to intervene for conservation. To this aim, it is also important to analyze and characterize features and decay patterns of buildings and artifacts in relationship to the monitoring of environmental parameters.

With such respect, Martínez Garrido and Fort González (2016a, in this volume) reviewed the range of possibilities of ICT and in particular wireless sensor networks for monitoring cultural heritage, ranging from indoor or museum microclimatic conditions to the conditions prevailing inside walls or specific materials. They also discussed the main characteristics of this technology (RF bands, transceiver models, network topologies, etc.) in the context of demanding long-term monitoring of parameters of interest such as moisture movement, salt content inside construction materials, and capillary absorption-induced rises in damp levels inside walls. As a whole, new perspectives for a large operational use can be derived by low-cost and open design software/hardware, such as Arduino and Memsic platforms, or Libelium and Smartmote platforms, characterized by greater ease of integration and development. The latter proved to be effective in terms of quality of the communications also in difficult environmental contexts such as a volcanic tunnel in the island of Lanzarote (Martínez Garrido and Fort González, 2016b).

With the reduction of user interfaces, the functional capabilities of sensing technologies increase, not only for monitoring but also for security, as shown by Buzzi and Senette (2016). The authors introduce basic features of RFID systems and discusses their potential in the field of cultural heritage protection and promotion. In particular, they described the last research improvements aimed at integrating sensor ability in RFID (semi)-passive tags.

If ICT has produced great advances in the observation capability of phenomena linked to cultural heritage degradation, with great benefit for conservation studies, in the field of documentation and valorization they have represented a real revolution, thanks to the impressive progress of digitization technologies in the past two decades from the 2D and 3D digital sampling instruments to the platforms to support cross-analysis of multimedia assets.

Gobbetti et al. (2016) reviewed the available approaches for solving image-to-geometry registration and color mapping and blending. The authors discussed the image registration methods, such as manual, feature based, color based, statistical, and multiview methods. The latter exploits the intrinsic grouping nature of the input images and the relationships among them, recasting the 2D–3D matching problem into a 3D–3D alignment by means of structure from motion (SfM) approaches. For good final results it is also necessary to determine the correct color information that has to be projected, solving the "blending problem."

Scopigno and Dellepiane (2016) reviewed the platforms in the single or cross-analysis of multimedia representations that could support the CH/DH professional and the available approaches for integrating and managing the available data, presenting both the GIS-based solutions and the more recent web-based systems.

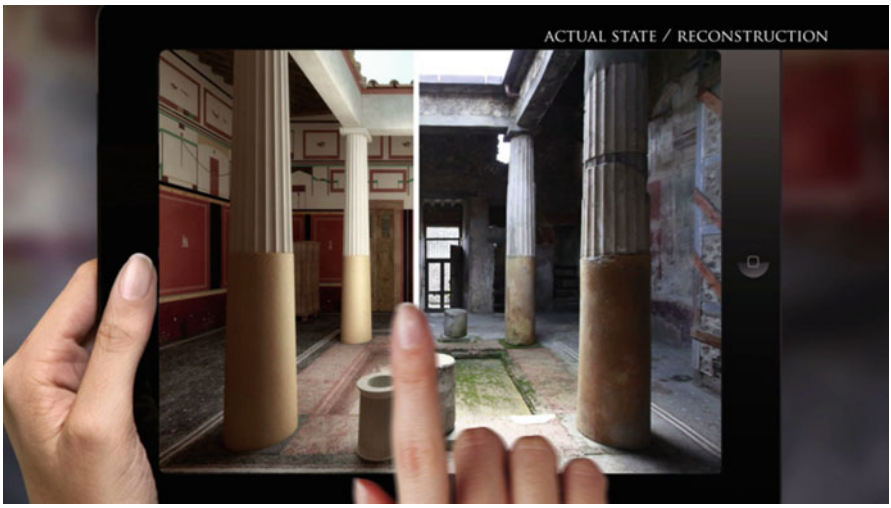

Fig. 1.4 Pompeii: visualization by tablet of virtual reconstruction of a domus (Courtesy of F. Gabellone)

The development of ICT benefited in tools that allow the user to rely on his position and field of view, by using smart devices and the new emerging wearable devices, such as smart glasses and smart watches (Amato et al. 2016, this volume). Technologies for visual localization and augmented reality in smart cities have been treated by Amato et al. (2016), wherein the authors present a good overview of the techniques enabling a precise positioning of the user and the subsequent experience in augmented reality.

ICT developed new tools not only for visualizing artifacts and landscapes but also for improving their interpretation, as demonstrated by the impressive applications of Gabellone (2016), whose approach to the reconstruction of archaeological contexts (see Fig. 1.4) is based on a dialectical relationship between historical and aesthetic values and the principles of building construction.

References

Agapiou A (2016) A window for the hidden past: revealing architecture remains based on ground spectroscopy data analysis. In: Masini N, Soldovieri F (eds) Sensing the past. Geoscience and sensing technologies for cultural heritage. Springer, Cham, pp 135–152, chapter 7

Alvarez de Buergo M, Fort Gonzalez R (2016) Ultrasonic analysis of the Spanish cultural heritage: six case studies. In: Masini N, Soldovieri F (eds) Sensing the past. Geoscience and sensing technologies for cultural heritage. Springer, Cham, pp 469–484, chapter 23

Amato G, Cardillo A, Falchi F (2016) Technologies for visual localization and augmented reality in smart cities. In: Masini N, Soldovieri F (eds) Sensing the past. Geoscience and sensing technologies for cultural heritage. Springer, Cham, pp 419–434, chapter 20

Bonano M, Manzo M, Casu F, Manunta M, Lanari R (2016) DinSAR for the monitoring of cultural heritage sites. In: Masini N, Soldovieri F (2016) Sensing the past. Geoscience and sensing technologies for cultural heritage. Springer, Cham, pp 117–134, chapter 6

Buzzi M, Senette C (2016) RFID sensors and artifact tracking. In: Masini N, Soldovieri F (eds) Sensing the past. Geoscience and sensing technologies for cultural heritage. Springer, Cham, pp 435–451, chapter 21

Camaiti M, Benvenuti M, Costagliola P, Di Benedetto F, Moretti S (2016) Hyperspectral sensors for the characterization of cultural heritage surfaces. In: Masini N, Soldovieri F (eds) Sensing the past. Geoscience and sensing technologies for cultural heritage. Springer, Cham, pp 289–312, chapter 13

Catapano I, Picollo M, Fukunaga K (2016a) TeraHertz waves and cultural heritage: state-of-the-art and perspectives. In: Masini N, Soldovieri F (eds) Sensing the past. Geoscience and sensing technologies for cultural heritage. Springer, Cham, pp 313–324, chapter 14

Catapano I, Picollo M, Fukunaga K (2016b) Case study regarding the application of THz imaging to cultural heritages. In: Masini N, Soldovieri F (eds) Sensing the past. Geoscience and sensing technologies for cultural heritage. Springer, Cham, pp 523–534, chapter 26

CCE-EP (2015) Report towards an integrated approach to cultural heritage for Europe, (2014/2149(INI)). Committee on Culture and Education of European Parliament

CEU (2014) Conclusions on cultural heritage as a strategic resource for a sustainable Europe. Education, Youth, Culture and Sport Council Meeting (Council of the European Union), Brussels

Chase AF, Chase DZ, Fisher CT, Leisz SJ, Weishampel JF (2012) Geospatial revolution and remote sensing LiDAR in Mesoamerican archaeology. PNAS 109(32):12916–12921

Chase ASZ, Chase DZ, Chase AF (2016) LiDAR for archaeological research and the study of historical landscapes. In Masini N, Soldovieri F (eds) Sensing the past. Geoscience and sensing technologies for cultural heritage. Springer, Cham, pp 89–100, chapter 4

Chase AF, Chase DZ (2016) Detection of Maya ruins by LiDAR: applications, case study, and issues. In: Masini N, Soldovieri F (eds) Sensing the past. Geoscience and sensing technologies for cultural heritage. Springer, Cham, pp 455–468, chapter 22

Chen F, Masini N, Rizzo R, Romano G, Pecci A, Lasaponara R (2016) Uncovering Luoyang by remote sensing. In: Masini N, Soldovieri F (eds) Sensing the past. Geoscience and sensing technologies for cultural heritage. Springer, Cham, pp 535–556, chapter 28

Cultural Heritage Assets (2012) Addressing climate change impacts on infrastructures, Preparing for Change. USAID Fact Sheet

Dumoulin J (2016) Infrared thermography: from sensing principle to nondestructive testing considerations. In: Masini N, Soldovieri F (eds) Sensing the past. Geoscience and sensing technologies for cultural heritage. Springer, Cham, pp 233–256, chapter 11

Fedi M, Cella F, Florio G, La Manna M, Paoletti V (2016) Geomagnetometry for archaeology. In: Masini N, Soldovieri F (eds) Sensing the past. Geoscience and sensing technologies for cultural heritage. Springer, Cham, pp 203–230, chapter 10

Franceschetti G, Lanari R (1999) Synthetic aperture radar processing. CRC Press, Boca Raton

Gabellone F (2016) The reconstruction of archaeological contexts: a dialectical relationship between historical-aesthetic values and principles of building construction. In: Masini N, Soldovieri F (eds) Sensing the past. Geoscience and sensing technologies for cultural heritage. Springer, Cham, pp 395–418, chapter 19

Gobbetti E et al. (2016) Techniques for seamless color registration and mapping on dense 3D models. In: Masini N, Soldovieri F (eds) Sensing the past. Geoscience and sensing technologies for cultural heritage. Springer, Cham, pp 355–376, chapter 17

IPCC (2014) Climate change 2014: synthesis report. Contribution of Working Groups I, II and III to the Fifth Assessment Report of the Intergovernmental Panel on Climate Change [Core Writing Team, Pachauri RK, Meyer LA (eds)]. IPCC, Geneva, Switzerland, 151 pp

Key Figures (2014) Activity 2013, construction in Europe. http://www.fiec.eu/en/library-619/keyfigures.aspx

Lasaponara R, Masini N (2013) Satellite synthetic aperture radar in archaeology and cultural landscape: an overview. Archaeol Prospect 20:71–78. doi:10.1002/arp.1452

Lasaponara R, Masini N (2016) Preserving the past from space: an overview of risk estimation and monitoring tools. In Masini N, Soldovieri F (eds) Sensing the past. Geoscience and sensing technologies for cultural heritage. Springer, Cham, pp 61–88, chapter 3

Leucci G (2016) Seismic and sonic applications on artifacts and historical building. In: Masini N, Soldovieri F (eds) Sensing the past. Geoscience and sensing technologies for cultural heritage. Springer, Cham, pp 153–174, chapter 8

Martínez-Garrido MI, Fort Gonzalez R (2016a) Wireless monitoring to detect decay factors in natural heritage scenarios in Spain: a case study at Lanzarote. In: Masini N, Soldovieri F (eds) Sensing the past. Geoscience and sensing technologies for cultural heritage. Springer, Cham, pp 485–498, chapter 24

Martínez-Garrido MI, Fort Gonzalez R (2016b) Wireless communications platforms for built and natural heritage monitoring. In: Masini N, Soldovieri F (eds) Sensing the past. Geoscience and sensing technologies for cultural heritage. Springer, Cham, pp 339–354, chapter 16

Masini N, Lasaponara R (2016) Sensing the past from space: approaches to site detection. In: Masini N, Soldovieri F (eds) Sensing the past. Geoscience and sensing technologies for cultural heritage. Springer, Cham, pp 23–60, chapter 2

Masini N, Rizzo E, Capozzoli L, Leucci G, Pecci A, Romano G, Sileo M, Lasaponara R (2016a) Remote sensing and geophysics for the study of the human past in the Nasca drainage. In: Lasaponara R, Masini N, Orefici G (eds) The ancient Nasca world: new insights from science and archaeology. Springer International Publishing, pp 469–527. doi:10.1007/978-3-319-47052-8_20

Masini N, Sileo M, Leucci G, Soldovieri F, D'Antonio A, De Giorgi L, Pecci A, Scavone M (2016b) Integrated in situ investigations for the restoration: the case of Regio VIII in Pompeii. In: Masini N, Soldovieri F (eds) Sensing the past. Geoscience and sensing technologies for cultural heritage. Springer, Cham, pp 557–586, chapter 29

Meier T, Aura M, Fehr M, Köhn D, Cristiano L, Sobott R, Mosca I, Ettl H, Eckel F, Steinkraus T, Erkul E, Schulte-Kortnack D, Sigloch K, Bilgili F, Di Gioia E, Parisi Presicce C (2016) Investigating surficial alterations of natural stone by ultrasonic surface measurements. In: Masini N, Soldovieri F (eds) Sensing the past. Geoscience and sensing technologies for cultural heritage. Springer, Cham, pp 257–288, chapter 12

Persico R, Sato M (2016) Ground penetrating radar: technologies and data processing issues for applications in the field of cultural heritage. In: Masini N, Soldovieri F (eds) Sensing the past. Geoscience and sensing technologies for cultural heritage. Springer, Cham, pp 175–202, chapter 9

Romano F P , Pappalardo L, Biondi G, Caliri C, Masini N, Rizzo F, Santos HC (2016) FF-XRF, XRD and PIXE, for the non-destructive investigation of archaeological pigments. In: Masini N, Soldovieri F (eds) Sensing the past. Geoscience and sensing technologies for cultural heritage. Springer, Cham, pp 326–336, chapter 15

Sato M (2016) A case study in Japan. In: Masini N, Soldovieri F (eds) Sensing the past. Geoscience and sensing technologies for cultural heritage. Springer, Cham, pp 523–534, chapter 27

Scopigno R, Dellepiane M (2016) Integration and analysis of sampled data: visualization techniques and platforms. In: Masini N, Soldovieri F (eds) Sensing the past. Geoscience and sensing technologies for cultural heritage. Springer, Cham, pp 377–394, chapter 18

Soldovieri F, Dumoulin J (2017) Integrated monitoring at a modern architectural masterpiece: the case of Viaduct Basento in Potenza. In: Masini N, Soldovieri F (eds) Sensing the past. Geoscience and sensing technologies for cultural heritage. Springer, Cham, pp 499–514, chapter 25

Tapete D, Cigna F (2016) SAR for landscape archaeology. In: Masini N, Soldovieri F (eds) Sensing the past. Geoscience and sensing technologies for cultural heritage. Springer, Cham, pp 101–116, chapter 5

WHC (2006) Predicting and managing the effects of climate change on world heritage. A joint report from the World Heritage Centre, its Advisory Bodies, and a broad group of experts to the 30th session of the World Heritage Committee (Vilnius, 2006)

Part I
Remote Sensing and Geophysics Technologies: Data Analysis for Applications in the Field of Archaeology and Cultural Heritage

Chapter 2
Sensing the Past from Space: Approaches to Site Detection

Nicola Masini and Rosa Lasaponara

Abstract This chapter is concerned with site detection by using earth observation technologies with particular reference to optical satellite data. Three different approaches are discussed: (1) the reconnaissance, analysis, and interpretation of proxy indicators; (2) remote sensing data integration; and (3) geographic information system (GIS)-based prediction modeling. Most of the chapter is dedicated to proxy indicators and in particular to how recognize them and which kind of data processing can be fruitfully employed for their enhancement. The proxy indicators are the result of physical and chemical interaction between archaeological remains and their surroundings that can produce changes in vegetation, moisture content, and microrelief. The reconnaissance of the proxy indicators is performed by means of the observation and processing of tones, shadows, shapes, textures, and patterns. For each of them some data processing methods (from the computation of spectral indices to semiautomatic and automatic features/object extraction) are shown and discussed with case studies. Two other approaches to site detection are prediction models based on GIS analyses and the integration of different remote sensing data. The prediction models aim at predicting the presence of sites of archaeological sites on the basis of observed patterns and on assumptions about human behavior, to be analyzed with environmental and geographic context, by using remotely sensed imagery and terrain models. Finally, different opportunities to integrate passive and active remotely sensed data to improve the characterization of microtopographic features related to shallow remains and the identification of paleo-environmental features are shown and discussed.

N. Masini (✉)
CNR-IBAM Institute for Archaeological and Monumental Heritage,
C. da Santa Loja, 85050, Tito Scalo, Potenza, Italy
e-mail: n.masini@ibam.cnr.it

R. Lasaponara (✉)
CNR-IMAA, Institute of Methodologies for Environmental Analysis,
C. da S. Loya, 85050 Tito Scalo, Potenza, Italy
e-mail: rosa.lasaponara@imaa.cnr.it

N. Masini, F. Soldovieri (eds.), *Sensing the Past*, Geotechnologies
and the Environment 16, DOI 10.1007/978-3-319-50518-3_2

Keywords Optical satellite remote sensing • Archaeology • Proxy indicator • Prediction models • Image enhancement

2.1 Introduction

The space technologies today more than ever provide an essential base of information for a wide range of operational applications and research fields, as, for example, regional and urban planning, design and construction of infrastructures, environmental monitoring, cultural heritage, and landscapes.

In particular, in the field of cultural heritage, the investigation of the human past needs remote sensing data to find both traces of the past and signs of the present. Past, present, and future are the temporal prospectives to consider when we observe from afar a portion of territory, a village, a river, a region. The traces, the color, the patterns visible from a remotely sensed scene are the interaction result of natural phenomena and human activities. Such a result is the landscape.

From an ecological perspective the landscape is a mosaic of interacting ecosystems (McGarigal 2013) and, considering human actions, it is also a social dynamic product, the result of the perception of the population, in which we recognize cultural values. According to the European Landscape Convention (2000), "Landscape means an area, as perceived by people, whose character is the result of the action and interaction of natural and/or human factors."

We can undoubtedly say that "we are" the landscape "we see" and contribute to change: landscape meant as a reflection of cultural identity and diversity, as well as a living natural and cultural heritage which needs to be investigated in its diachronic evolution and monitored for its protection, risk management, mitigation strategies, and further recovery.

In this context, earth observation (EO) technologies have a fundamental role in providing a large variety of information for different aims and applications: from archaeological research to risk monitoring, from landscape analysis and protection to the promotion and valorization of cultural identity.

In particular, EOs are particularly useful for multipurpose applications, thus resulting also in a ever more effective approach for these aims:

(i) Improving the quality and quantity of archaeological information content
(ii) Reducing the perception of complexity among the archaeological community that still today limits their use for operational purposes

Points (i) and (ii) have a crucial importance. The multipurpose applications allow us to reduce the costs and, at the same time, obtain more information whose integration makes a more comprehensive knowledge of the cultural heritage possible. As an example, SAR provide information on the characteristics of the landscape and data useful for risk analysis (i.e., radar interferometry for the monitoring of ground motions). Another example we cite is a well-known project conducted by Sever (1998) in Guatemala for which satellite data were used for both

the identification of archaeological features and the documentation of the sequence of deforestation of the forests in the territory of Peten. This project contributed to the increase of interest in using space technologies for cultural heritage in the United States (US) in the 1990s.

From the 1990s until today, the use of EO technologies in cultural heritage has been strongly increasing for a number of reasons, among which are the improvement of the performance of sensors able to reveal ever more detailed information for the study of the human past and ancient landscapes, the identification of unknown sites, and the detection of buried remains. The increased interest of the archaeological community to exploit space technologies has been the result of the availability of user-friendly and low-cost software and routines for data processing and of increased interest in the study of the dynamics of human frequentation in relationship to environmental changes that traditionally are investigated by remote sensing.

As a whole, with respect to the past archaeologists are more aware of the benefits of EO technologies in terms of reduction of cost and required time of archaeological excavations, and opportunities to support strategies addressed to conservation and preservation of cultural assets, as a result of the following:

(i) Improvement in spectral and spatial resolution of imagery that allows providing detailed information useful for preventive archaeology
(ii) Multiscale and multisensor views of satellite imagery that make possible correlating biophysical characteristics to possible changes from human activity of cultural interest
(iii) Ever more detailed digital elevation models (DEMs) that allow improving data analysis and the interpretation of microtopography of cultural interest
(iv) Availability of long satellite time series useful to detect the changes of landscape and to monitor hazard and risk in archaeological sites

The launch in 1999 of the satellite IKONOS, the first platform capable of acquiring images at 1-m spatial resolution, opened new perspectives for archaeological prospecting by using remote sensing. Later, submetric resolution allowed the availability for the first time of data complementary to those traditionally captured by aircraft for searching the classical proxy indicators, such as crop marks, damp marks, and soil marks, results of the physical interaction between archaeological deposits, the soil, and vegetation cover (Crawford 1929; Dassie 1978; Masini and Lasaponara 2007).

The crop marks appear as differences of height or color of vegetation from stress caused by the lack of water or deficiencies in other nutrients resulting from the presence of archaeological deposits. Damp marks, visible on bare ground, are caused by the variations of drainage capability of the soil in the presence of buried ditches and walls. Soil marks are differences in soil color, which are particularly visible after plowing of embankments that can bring to light dry material referable to buried walls or wet material related to pits and moats. In the same site, the proxy indicators change with the changing of environmental conditions, climate, and land cover, as in the case shown in Fig. 2.1 depicting a Neolithic

Fig. 2.1 Area of archaeological interest near Lucera (Southern Italy) observed in two different seasons: in autumn (**a**) and in spring (**b**). The circular features likely referable to Neolithic settlement are visible as damp marks in autumn and as crop marks in spring (Courtesy of Google Earth)

settlement in Apulia (Southern Italy) visible in spring and autumn by means of crop and damp marks, respectively. Moreover, the higher capability with respect to panchromatic photography from the multispectral content of satellite imagery adds new opportunities to enhance and quantify the information content associated

with the proxy indicators, exploiting their different spectral signature by means of approaches based on data fusion, classification, and geospatial analyses. As an example, the classification of land cover, soil, and water content also makes possible analyzing known and possible archaeological features in an environmental setting, providing archaeological predictive information.

Where the physical interaction between anthropic transformations of cultural interest (buried walls, ditches, pits, etc.) does not manifest through vegetation and moisture content changes, one cannot rely on only optical remote sensing for detecting archaeological features. In such cases, the passive data should be integrated with other kinds of earth observation technologies including the active ones, such as LiDAR and SAR, especially where the microtopography is a valuable archaeological proxy indicator. Further opportunities to improve the knowledge could be provided by integrating remote sensing with geophysics.

Another approach is based on the building of predictive models aimed at evaluating the archaeological sensitivity of large areas, useful for urban planning and the design of civil infrastructures.

This chapter is concerned with the aforementioned approaches to site discovery. In particular, the reconnaissance and analysis of proxy indicators by optical satellite remote sensing are shown and discussed in Sect. 2.3. Sections 2.4 and 2.5 approaches based on data integration and predictive modeling. The aforementioned sections are preceded by a brief history of the use of space remote sensing applied to archaeology (Sect. 2.2). The chapter ends with some final conclusions and future perspectives.

2.2 Brief History of Space Remote Sensing Applied to Archaeology

Early applications of space technologies in archaeology date back to the 1980s. Substantially, they were pioneering attempts to evaluate the potentiality of the Landsat multispectral scanner (MSS) and Thematic Mapper (TM), acquiring multispectral data at 60-m and 30-m m resolution, for investigating the human past in relationship to environmental changes. The 1980s were also characterized by intense successful experimentation of SAR systems for civil applications, among which were some pioneering investigations for the identification of features of geo-archaeological interest, such as the buried rivers and channels discovered by McCauley et al. (1982) in the eastern Sahara desert, using SAR data acquired by SIR-A, launched in 1981. A similar application was made in the Taklamakan desert in northwest China, where an ancient buried river system was detected using SIR-A data (Holcomb 1992).

In the 1990s the launch of Landsat ETM+ and active satellite sensors (ERS-1 SAR) encouraged a number of applications ranging from landscape archaeology to paleo-environmental study. At the beginning such applications were mostly aimed at evaluating the capability of satellite imagery for the identification of archaeological

features, as done by Parry (1992). Parry assessed the detectability of earthworks, part of a water control and storage system in northeastern Thailand, by using Landsat-TM imagery. Then, the satellite data were beginning to be used in the context of multidisciplinary research.

Clark et al. (1998), by using a multitemporal set of TM, SPOT, and ERS-1 SAR images, demonstrated how remote sensing could be applied to study the relationship between environmental variations and long-term social changes in southern Madagascar. To this aim it was fundamental: the double key of reading of the forest, analyzed both as part of the environment and as a place of sacred significance.

Sever (1998) identified a number of archaeological features, such as roadways and temples, as well as providing important information on ancient agriculture and water management in the forest of Peten in Guatemala by using a Landsat Thematic Mapper (TM) with airborne imagery. Sever was the first to use spectral indices as an enhancement tool of imagery. In particular, the results of normalized difference vegetation index (NDVI), principal component analysis, and a modified version of the Kauth–Thomas transformation (Kauth and Thomas 1976) allowed revealing Mayan causeways not visible at ground level.

In the 1990s, satellite remote sensing was also employed to monitor environmental changes in important archaeological contexts such as the Nile Delta, whose shoreline variations were analyzed by using Landsat MSS (Blodget and Taylor 1991) and Landsat TM imagery (White and El Asmar 1999).

After the end of the Cold War, American intelligence satellite photographs were declassified and made commercially available for civilian purposes, from global change research to the detection of archaeological buried remains (Fowler 2013). They are panchromatic images (among which are those acquired in stereo) downloadable from the USGS Earth Explorer (http://earthexplorer.usgs.gov/). These images were taken on film from American spy satellite missions launched from 1960 to 1980. The films were dropped back to earth by using a parachute opening so that they could be captured in midair by airplanes. The first set of imagery was declassified in 1995: these are photographs collected by the satellite platforms Lanyard, Corona, and Argon at the spatial resolution of 6, 6 to 40, and 460 ft, respectively. The second set of imagery was declassified in 2002, including photographs collected by KH-7 (2–4 ft) and KH-9 (20–30 ft).

The availability of images taken before the dramatic changes of landscape (caused by the diffuse urbanization process) that occurred from the 1970s onward with a geometric resolution ranging from 2 to 40 has been promptly exploited by archaeologists. They exploited this precious source of information to detect archaeological residues that have subsequently been destroyed by mechanized agriculture and by urban sprawl, in particular in the Middle East, which is covered by very high resolution declassified imagery.

For a limited period also Russian spy satellite imagery was made available, such as KVR-1000 and Soyuz Kate-200 images. The first images were exploited by Fowler (1996) for the detection of crop marks in Stonehenge, and by Comfort (1997) for archaeological investigations in the Greek and Roman city of Zeugma on

the Euphrates in Turkey; the second set of images were used by Marcolongo and Morandi Bonacossi (1997) to study ancient areas in Yemen.

The Russian declassified data were available for only 4 years, after which the use of American declassified imagery increased over time. In particular, Corona images "offered archaeologists a retrospective look" at the ancient landscapes of the Middle East (Challis 2007). For sake of brevity, we cite only the investigations of Kennedy (1998) in the Euphrates valley (Turkey), the discovery of ancient roads of the Early Bronze Age in the Upper Khabur basin in Northeastern Syria by Ur (2003). In the Middle East, Corona is the only data source for recording archaeological features that are no longer visible.

In China, the opportunities to discover new sites using declassified data are very promising because of the dramatic changes affecting the landscape from the 1990s onwards (Lu et al. 2016), in particular in those regions where economic development and urban expansion have been very rapid. This is the case of the Lake Dian basin in southwest China, where Corona images revealed prehistoric mounds of the Bronze Age (ca. 900–100 BC) that have since been razed by modernization projects (Yao et al. 2015).

Over time Corona images were also used, integrating them with other remote sensing data with different spectral characteristics or spatial resolution. Altaweel (2005) identified hollow ways, canals, and sites in North Iraq integrating Corona photographs with ASTER multispectral satellite imagery. Beck et al. (2007) and Scardozzi (2012), integrated very high resolution (VHR) satellite imagery with Corona: the first for studying tell settlements and field systems in Western Syria and the second for mapping Hierapolis in Turkey. In particular, Scardozzi (2012) used and interpreted a rich declassified satellite data set from 1961 to 1980 with a geometric resolution between 2.7 and 9 m, along with images taken by QuickBird-2 and Ikonos-2 between 2002 and 2009, which have been the cartographic basis of the Atlas of Hierapolis, the Hellenistic-Roman city of Phrygia, excavated by an Italian archaeological mission of the University of Lecce.

More recently, Palmer (2013) used photographs taken of Armenia of the Corona KH-4B mission for the identification of more than 200 "sites" in Armenia, which were then examined on the ground and recorded by oblique aerial photographs taken at low altitude from a paramotor.

As said before, a new era for remote sensing in archaeology started in 1999 with the launch of IKONOS, the first satellite platform capable of acquiring images at 1-m resolution. Later, the spatial resolution has strongly increased (see Fig. 2.5) up until today with WorldView-3, which acquires panchromatic and multispectral imagery at 0.31–0.34 m and 1.24–1.38 m, respectively (see Table 2.1).

Very high resolution satellite imagery allows obtaining information from the landscape up to site scale and to single artifacts and structure. The multispectral content has opened new perspectives for the use of remote sensing, from site discovery and documentation, with different approaches including semiautomatic and automatic procedures of feature extraction.

Nevertheless, at the beginning, because of the lack of data processing procedures developed for archaeological purposes, the potential of VHR satellite imagery was still not adequately exploited in the field of cultural heritage.

Table 2.1 List of optical very high resolution (VHR) satellite data

Satellite data	Launch	Country	Pan	Ms
IKONOS 2	1999	USA	1 m	4 m
QuickBird	2001	USA	0.6 m	2.4 m
TES	2001	India	1 m	
OrbView 3	2003	USA	1 m	4 m
Cartosat 1	2005	India	1 m	2.5 m
Kompsat 2	2006	S. Korea	1 m	4 m
Resurs DK2	2006	Russia	1 m	2–3 m
EROS B	2006	Israel	0.7 m	
WorldView-2	2007	USA	0.5 m	2 m
Cartosat 2	2007	India	0.8 m	
RapidEye	2008	Germany	5 m	5 m
GeoEye-1	2008	USA	0.41/0.5 m	1.65/2 m
Pleiades 1a-1B	2011–2012	France	0.5 m	2 m
Spot 7	2014	France	1.5 m	6 m
WorldView-3	2014	USA	0,31–0,34 m	1.24–1.38

Since 2006 the first multidisciplinary scientific community has been developing and growing, thanks to the first conferences and workshops on remote sensing applied to archaeology, among which we cite the conference "From Space to Place" (Rome 2006), the EARSeL Workshop "Advances in Remote Sensing for Archaeology and Cultural Heritage Management..." held in Rome in 2006 and 2008, respectively (Campana and Forte 2006; Lasaponara and Masini 2008).

The scientific debate was immediately characterized for its liveliness and richness of contents and methodological approaches.

Summarizing, we distinguish two positions:

1. One is focused on the development of data enhancement data approaches aimed at emphasizing crop, soil, and damp marks (see, for example, Lasaponara and Masini 2007a; Traviglia and Cottica 2011; Beck 2007; Garrison et al. 2008).
2. The second is more interested in extracting features of archaeological interest in a semiautomatic and automatic way (De Laet et al. 2007; Trier et al. 2009).

The search for new ways of using and processing satellite data is also boosted by the specificity of the case studies. For example, Menze and Ur (2011) adopted a multitemporal classification strategy, integrating information from different multispectral sensors, for mapping in a systematic way anthrosols accumulated over time in ancient landscapes in Mesopotamia. For the detection of buried earthen structures in the desert of Nasca in Peru, Masini et al. (2012) developed an archaeogeophysical approach in which satellite data processing and interpretation have a central role (see also Masini et al. 2009).

The effectiveness of automatic approaches has been evaluated for case studies and, therefore, their performance is "site dependent." We cite the case of the

Aztec pathways in the Valley of Mexico that have been identified and extracted by texture segmentation, linear pattern detection, and spatial filtering (Argote-Epino and Chavez 2005), and pixel-based and object-based classification techniques which extracted, with variable success, archaeological remains in Hisar, in southwest Turkey (De Laet et al. 2007).

As a whole, the scientific literature demonstrated that if VHR imagery is integrated with other data sources, and information derived from geosciences and field surveys, the information content is better exploited. These are the cases of the integrated approach, based on GIS and remote sensing for geomorphology and DEM analysis, used by Alexakis et al. (2011), for locating settlements, modeling, and reconstructing landscapes and habitations of the Neolithic Age in Thessaly, and the archaeo-geophysical data integration adopted by Ciminale et al. (2009) for the detection and reconstruction of a ditched Neolithic settlement in Apulia (Southern Italy).

2.3 Proxy Indicators for Site Detection: From the Reconnaissance to Processing Strategy and Interpretation

2.3.1 Proxy Indicators: Generalities

The proxy indicators of cultural interest are those marks through which subsurface archaeological features may become visible from above because of the physical and microtopographical changes caused by buried archaeological structures and deposits. According to the consolidated scientific literature the most common proxy indicators are the crop/damp/soil/shadow marks (Crawford 1929; Dassie 1978; Wilson 1982).

In particular, the crop marks are the result of the differential growth of plants: a buried wall affects their growth at the top of it, as its presence channels water from its area, thus stressing the plants (Fig. 2.2, upper). Conversely, a buried trench or ditch, filled with more organic matter than the natural land, provides much more favorable conditions for water that will flow naturally nourishing the plants growing on it (Fig. 2.2, middle). The damp marks are the result of the variations of soil drainage capability induced by the presence of buried stone structures, and filling of ditches, moats, and pits of cultural interest. The soil marks appear as soil color caused by plowing, which can bring to light stony material of shallow walls, and wet and organic clods of soil related to pits and moats. The shadow marks are caused by microrelief, the residues of eroded shallow remains and earthworks viewable from above when the sun is low in the sky (Fig. 2.2, bottom).

Before processing satellite images, geometric and radiometric corrections must be done. The first are necessary to reduce distortions from errors in the satellite positioning on its orbit and the effects of the Earth's rotation and camera angles and,

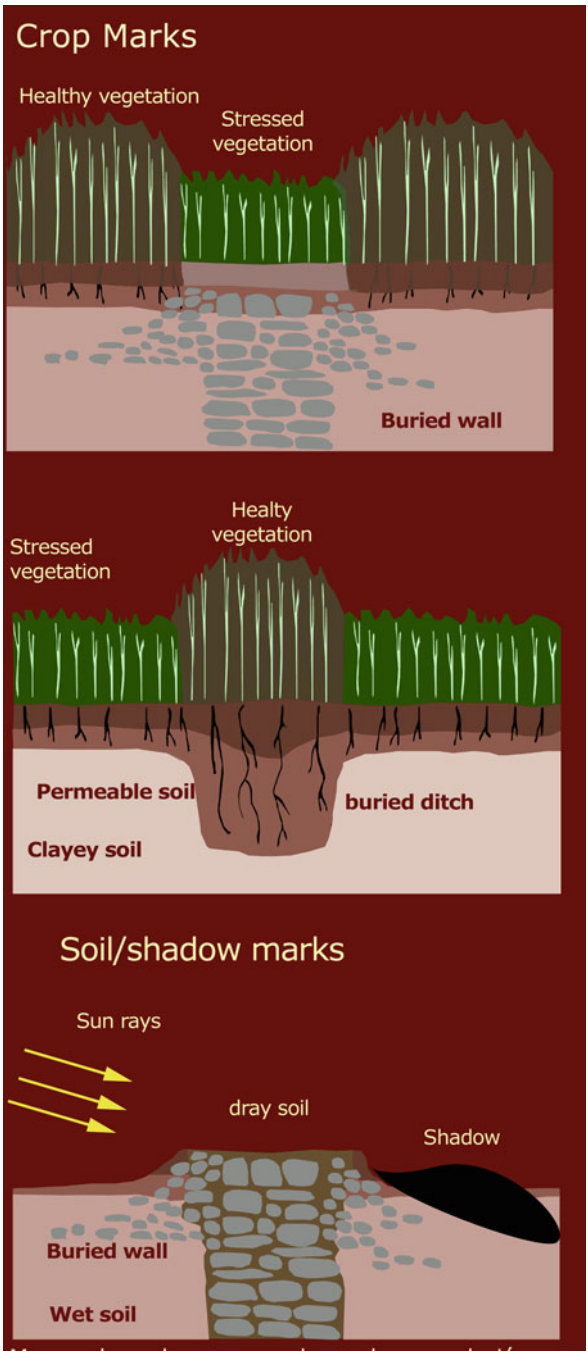

Fig. 2.2 Sketched diagrams of negative crop marks above a wall (*upper*), positive crop marks above a ditch (*middle*), and a mix of shadow and soil marks (*bottom*)

consequently, to convert data to coordinates of a given reference system. Moreover radiometric errors from sensor defects, atmospheric effects, variations in scan angle, and system noise need to be compensated to obtain the true spectral radiance at the sensor. To this aim, calibration to reflectance and radiance must be performed, enabling converting relative radiance into absolute radiance (in units of [(μW)/(cm^2 *nm*sr)]), using the calibration factors of the VHR metadata.

2.3.2 *Reconnaissance of Archaeological Features by Tone, Shadow, Shape, Texture, Pattern, and Association and Image Processing Strategies*

The reconnaissance of the proxy indicators and the subsequent archaeological interpretation are based on the observation, analysis, and enhancement of the *tone* (or the color), the *shadow* caused by microtopography, the *shape* and the *texture*, given by tonal variations, and the *pattern*, the result of the spatial arrangement of lines and figures. The weight of each of these depends on the scale of observation, surface characteristics (bare, vegetated, desert), the types of archaeological marks (crop/soil/damp), and the expected archaeological features (buried structures, ditches, moat).

In many cases the tone is the most significant key interpretation for the identification of traces of cultural interest, especially when linked to changes in vegetation growth and moisture content. A number of processing approaches based on the computation of spectral indices allows us to improve the information content. Also, the shapes could help in the identification of the "cultural nature" of marks as well as, in some cases, in the archaeological interpretation itself. For example, consider the "typical" circular double-trenched ditches of Neolithic settlements (see Fig. 2.1), the plants of the Roman villas typically based on the presence of a "patio" (Fig. 2.3), and the "motte and bailey"-based medieval castles.

The patterns are important in the identification and interpretation of archaeological features, especially in the presence of a rich archaeological and historical record. When varying the different weights of the four key interpretations of landscape (tones, shapes, textures, patterns), the image processing strategy varies accordingly.

Being aware of this distinction is important because it facilitates the choices of the most appropriate approaches to be taken and the most suitable algorithms to be used: from the radiometric to geometric enhancement using techniques in the image domain, from the multispectral transformation to supervised classification and clustering. The choice of the technique to be used depends also on the aims of the investigation and on what the archaeologist expects from the remote sensing images.

Fig. 2.3 Durres in Albania: IGM aerial photos of 1936 depict traces of a Roman villa (courtesy of G. Scardozzi)

2.3.2.1 Tone

The *tone* is given by the reflectance/emittance characteristics (or values) with respect to wavelengths for a given material. Each material has its spectral signature, which is a function of the incident electromagnetic (EM) wavelength and material interaction with that section of the EM spectrum. The vegetation exhibits higher reflectance values in the near-infrared (NIR) with respect to other bands of the visible spectrum. Also, the differences of height or color of vegetation are more discriminable from NIR, whereas damp and soil marks are generally more visible from the red band (Lasaponara and Masini 2007a; Masini and Lasaponara 2007).

A further improvement of the information content could be obtained by computing spectral indices, which in many cases can emphasize crop, soil, and damp marks. In particular, the spectral combinations of two or more bands including green, red, and NIR bands allow a more reliable evaluation of photosynthetic activity and the vegetation cover variations. These evaluations usually operate by contrasting chlorophyll pigment absorption in the red band with the NIR reflectance of leaf mesophyll, thus allowing the emphasis of archaeological crop marks. The most widely used index in archaeology (Lasaponara and Masini 2006; Oltean and Abell 2012) is the normalized difference vegetation index (NDVI) obtained by the following formula:

$$\mathrm{NDVI} = \frac{(\mathrm{NIR} - \mathrm{RED})}{(\mathrm{NIR} + \mathrm{RED})}$$

Garrison et al. (2008) assessed the potential of VHR satellite imagery in detecting and predicting a subcanopy Maya settlement in Peten (Guatemala) of the Pre-classic and Classic periods. The investigation focused on the search of vegetation proxies by experiencing different pansharpening methods. Pansharpening is a data fusion method consisting of extracting high-resolution geometric information from the panchromatic image and injecting it into the multispectral (MS) bands through proper models. For archaeological applications, pansharpening allows the improved enhancement of cultural marks, facilitating their detection. The performance depends on the characteristics of the expected archaeological features and the algorithm used. With such respect a number of pansharpening algorithms is available, which can be categorized into two groups: (1) one is based on a spectral transformation of the MS data and the substitution of the first transformed component with the pan image [the most widely used are principal components analysis (PCA), intensity-hue-saturation (IHS), and the Gram-Schmidt (GS) orthogonalization procedure (Laben and Brower 2000)]; and (2) the second employs multiresolution analysis such as wavelets and Laplacian pyramids.

The comparative analysis performed on case studies characterized by high noise such the ceremonial center of Cahuachi, in the desert of Nasca in Southern Peru, has shown evidence that the methods based on the GS algorithms provide fused images with high geometric quality but with some spectral impairments, whereas other algorithms are more accurate spectrally but unsatisfactory in terms of spatial enhancement (Aiazzi et al. 2008).

Some approaches are aimed at maximizing archaeological signatures by the selection of an optimal spectral domain (Cavalli et al. 2009); others are focused on the search for the optimal temporal and spectral region for detection and monitoring of crop marks (Agapiou et al. 2013a).

Another line of research is based on the re-projection of the initial VNIR bands of satellite imagery into a new coordinate system such as tasseled cap transformations (TCT) (Lasaponara and Masini 2007b; Keeney and Hickey 2015). The TCT is a linear affine transformation given by the following formula

$$TC = W_{TC}DN + B$$

where W_{TC} is the transformation coefficient, DN is the digital number, and B is bias. W_{TC} depends on the considered sensor, because different sensors have different spectral responses. TCT converts a given input channel data set in new bands typically denoting the brightness or variation in soil reflectance, the amount of green vegetation (greenness), and wetness (a sort of moisture index). The original TCT was derived (Kauth and Thomas 1976) for the four bands of the Landsat MSS sensor. Later, the TCT was extended to the Landsat TM (Crist and Cicone 1984), IKONOS (Horne 2003), and QuickBird sensors (Yarbrough et al. 2005). Agapiou et al. (2013b) proposed a new coordinate system based on orthogonal equations. The results are three components named crop marks, vegetation, and soil computed by a large ground spectral signature analyzed separately for each different satellite image in Cyprus.

2.3.2.2 Shadows

The shadow can reveal the presence of earthworks or microrelief of cultural interest that could derive from the presence of embankments and ditches, holes, slots, or other elements of possible anthropogenic nature. For the identification of archaeological shadow marks, the grazing light is fundamental. In fact, the most suitable period is winter. In addition to the incidence of light, ice, frost, and snow can improve the visibility of the microrelief. It should also be said that the microrelief either constitutes exposed archaeological structures or represents the top part of the partially buried archaeological walls. A typical situation is given by settlements located on hills (for example, medieval villages abandoned in the late Middle Ages in Central and Southern Italy; see Fig. 2.4, upper left) where erosion prevented a complete cover of archaeological remains.

This scenario created a microtopography from which it is possible to reconstruct the shapes in plan of the original structures, visible by shadow, and dispersed on surface building materials and pottery, useful for field survey, but sometimes reflecting or making noisy the scene to be observed. Also, in arid and desert environs

Fig. 2.4 Examples of archaeological microrelief for three different environs and surface characteristics: on a hill with herbaceous cover (medieval settlement in Monte Serico in Italy: *upper left*), on bare soil in an arid environment (pre-Inca settlement of later intermediate period in Rio Taruga in Peru: *upper right*), and on bare soil in a desert environment (Roman town of Sabratha in Libya: *bottom*)

microrelief related to shallow remains could be observed (Fig. 2.4, upper right and bottom). Visibility depends on the sun angle, orientation, and the color and height of the microrelief.

The shadow reveals traces of the past but can also prevent the detection of archaeological features. The shadow caused by the clouds can cover the scene, prevent observation of the landscape, or make difficult the reconnaissance of landscape features. To reduce the covering effect of this shadow, the spectral indices, including ratios of bands and NDVI, are effective. It is a recent application conducted by the authors in some sites of archaeological interest characterized by crop and damp marks (Agapiou et al. 2016).

Figure 2.5 shows a scene including circular marks referable to ditches of a possible Neolithic settlement in Apulia (Italy). Such marks are very difficult to see from the panchromatic, green, red, and NIR bands. The ratio NIR/RED and NDVI reduce the "shadow effect" that covers the scene, making the reconnaissance of the circular features easier.

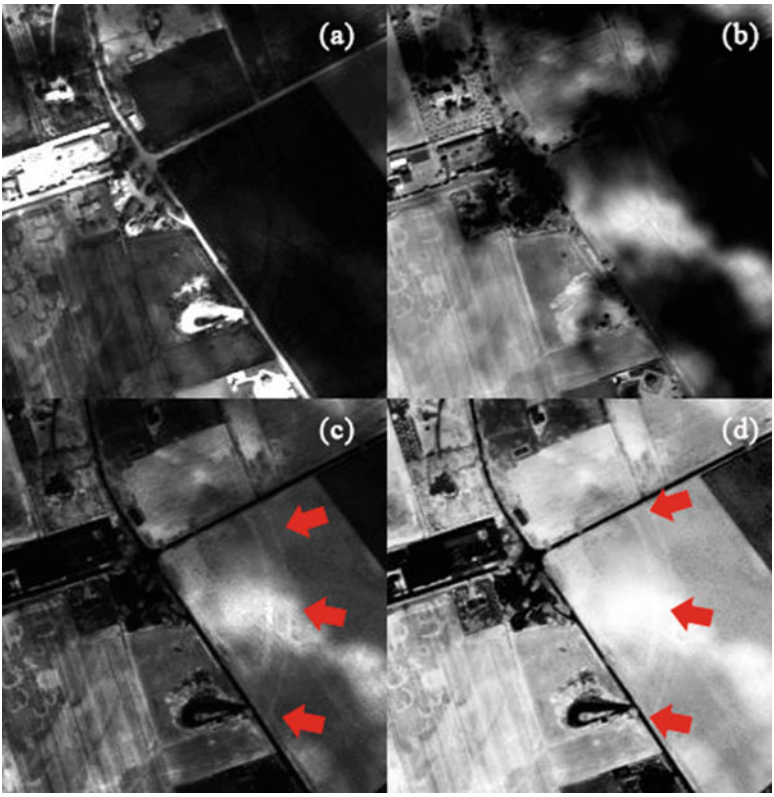

Fig. 2.5 Cloud shadow removal by using spectral indices. The scene refers to a Neolithic settlement in Apulia. The shadow of some clouds partially covers the image ((**a**) and (**b**), related to panchromatic and NIR band, respectively). The ratio NIR/RED (**c**) and NDVI (**d**) can remove the shadow, making visible two concentric circular features related to possible buried ditches

2.3.2.3 Shape

The *shape* denotes the general form of an individual artifact, building, infrastructure, or sites, revealing in some cases their functions and the period. We cite, for example, the Neolithic curvilinear ditches, linear Roman centuriations, the Nasca biomorphic geoglyphs, the quadrangular Roman villa, the semicircular exedra of Roman therma or the apse of a medieval church, the curvilinear motte of Norman castles, and the "cul de sac" pattern of Arab towns.

With respect to the tones, the reconnaissance of shapes is an advanced stage of remote sensing in archaeology. Their extraction allows us to make a significant step forward in the interpretation of traces of cultural interest. It could be performed by visual analysis, with the help of edge enhancement methods and semiautomatic and automatic feature extraction approaches.

The enhancement of edges could be obtained by using different filtering methods such as Roberts, Sobel, Prewitt, Laplacian, or Gaussian or Hessian matrix, which rely on the intensity change around the boundaries (Pellegrino et al. 2004). Therefore, weaker edges related to subtle proxy indicators such as crop marks and damp marks (Lasaponara and Masini 2012) or those marks from texture variations and those unevenly illuminated may not be detected (D'Orazio et al. 2015).

Other methods that are less affected by noise are the Hough (1962) transform and analysis of variance (ANOVA)-based approaches.

The first has been used by Lei Luo et al. (2014) for detecting some circular shafts used as proxy indicators of the presence of qanats (aqueducts) in northern Xinjiang, China. The approach is based on four steps: (i) circle average filtering to suppress noise; (ii) mathematical morphological processing performed on the binary images; (iii) Canny edge operator used to enhance the edges (Canny 1986); and (iv) Hough transform for extracting the circular shafts. The Canny edge detector frequently used for the detection of archaeological features is in its turn composed of the following four steps: (1) removal of noise by applying a Gaussian low filter; (2) determination of edge gradient and direction; (3) edge thinning applying nonmaximum suppression, thus removing pixels that are not considered to be part of an edge; (4) double threshold to determine potential edges; and (5) hysteresis to track edges.

The ANOVA-based approach has been employed by D'Orazio et al. (2015) for the extraction of archaeological crop marks in a Neolithic settlement in Apulia (Southern Italy). In particular, the authors exploited the analysis of variance to decide if a point belongs to a mark of archaeological interest by comparing their neighbor with the expected line shape. The effectiveness of this method as well as others proposed by other authors depends on the characteristics of the site, especially when the target is crop marks and the area to be investigated is plowed. The plowing direction creates a texture of lines that could be extracted along with the crop marks. To reduce the false-positive detections the automatic procedure should be integrated by a semantic processing of the extracted objects. Such an approach has been adopted by Marani et al. (2015), who improved the linear trace extraction within farmland modifying the ANOVA-based method by means of semantic treatment.

Automatic approaches have been developed also for extracting circular marks. One of these has been developed and applied by Trier et al. (2009) for the extraction of circular soil and crop marks related to burial mounds in Norway. The method is based on decision tree-based classification applied to VHR satellite images, elaborated by using local contrast enhancement, template matching, and feature extraction.

There are other shapes whose borders are not so well defined because of the presence of scattered building material from erosion (or in some cases, landslides). The erosion has generally a double effect on the chances to detect archaeological marks: (1) prevents the deposit of a significant soil layer on the archaeological remains such that crop and damp marks could not occur; or (2) spreads constructive material on the surface, making the detection of archaeological features difficult.

However, the building material, although chaotic on the surface, along with microrelief of shallow remains, allows us to still see something of the original construction. In these cases the most effective approach seems to be the use of clusterization procedures.

Such an approach has been adopted by the authors of this chapter (Lasaponara et al.) for extracting features linked to the presence of ancient farms and an aqueduct in the territory of Hierapolis, an archaeological site included in the World Heritage list, from two VHR satellite images acquired in March 2005 and April 2007 (see Fig. 2.6).

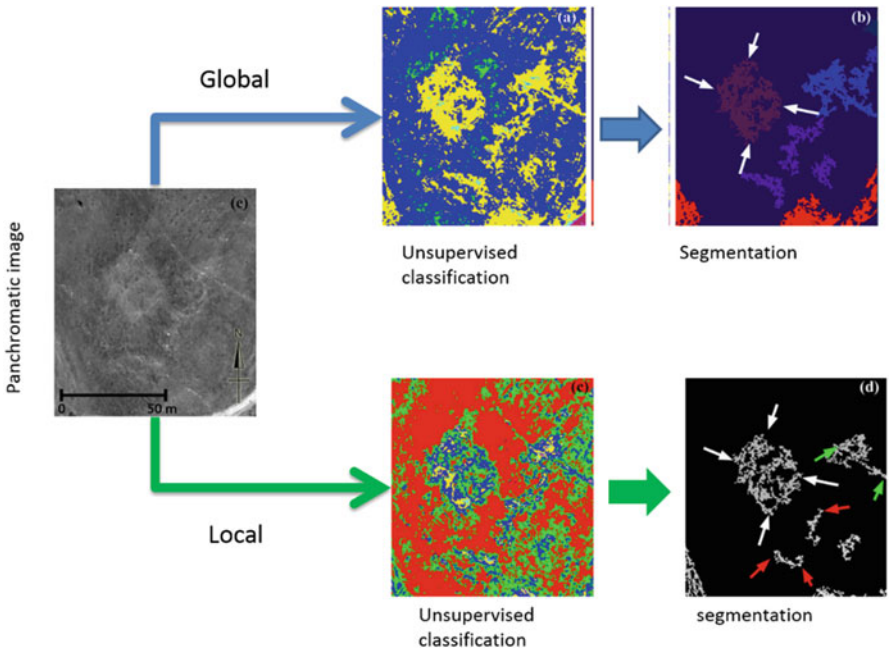

Fig. 2.6 Ancient farm in the territory of Hierapolis (Turkey). From *left* to *right*: QuickBird panchromatic image acquired on 10 April 2007, unsupervised classification, and segmentation of the result of unsupervised classification by a global (*up*) and a local (*bottom*) analysis

The farms have roughly quadrangular shapes characterized by microrelief linked to the presence of shallow walls and incoherent stone material. An object extraction approach based on the use of unsupervised classification and subsequent segmentation allowed the extraction of features referable to rural farms and an aqueduct dating back to a historical period spanning from the Hellenistic to Roman ages. The features extracted have been then validated by geophysical prospecting (Lasaponata et al. 2016a). Object-oriented classification algorithms are usually based on two main steps: (i) first the segmentation, (ii) then the classification. In Hierapolis, we first performed the supervised classification step and then the segmentation. The choice is given by the specificity of the archaeological issue. In particular, the subtle features/targets to be identified are partially or totally unknown. Therefore, to accommodate this issue, the first step is based on the unsupervised classification step, which provides a first "rough" categorization, followed by the segmentation to extract the geometric shape of the clusterized pixels. This approach has two advantages: (1) it does not require knowing and assigning a priori preestablished statistical distribution of classes as in the case of supervised classifications; and (2) it allows us the identification and extraction of subtle signals/patterns, which exhibit geometric shapes, even if veiled, as in the case under investigation, by the presence of scattered building material (stone blocks, tiles, bricks).

2.3.2.4 Textures, Patterns, Associations, and Remote Sensing Approaches

A fundamental aspect of the detection of information of cultural interest is the observation, analysis, and interpretation of textures, patterns, and associations.

The texture denotes the arrangement and frequency of tonal variation and strongly depends on the scale of observation. For example, rough textures are related to irregular surfaces such as microrelief linked to the presence of shallow walls, forest canopy, or rocky outcrops whereas smooth textures are linked to more uniform surfaces such as fields, asphalt, desert sand, or ancient land divisions.

Pattern denotes the spatial arrangement of objects. Distinctive patterns are generally a repetition of similar tones and textures: for example, linear Roman centuriations, Neolithic patterns with double curvilinear ditches, the orthogonal layout the Roman city planning composed, and some urban layouts of ancient cities in Mesoamerica and Mesopotamia that reveal spatial division into districts or neighbourhoods (Smith 2010).

Association takes into account the relationship between objects or features in proximity to the target of interest, for example, the paleo-riverbeds close to ancient settlements which allow us to study the relationship between environmental changes with human frequentation. The associations are also important for building predictive models (see paragraph 4).

Figure 2.7 shows two different textural patterns of ancient landscapes. One is related to roman centuriations in ancient Dalmatia (current Croatia; see Fig. 2.7,

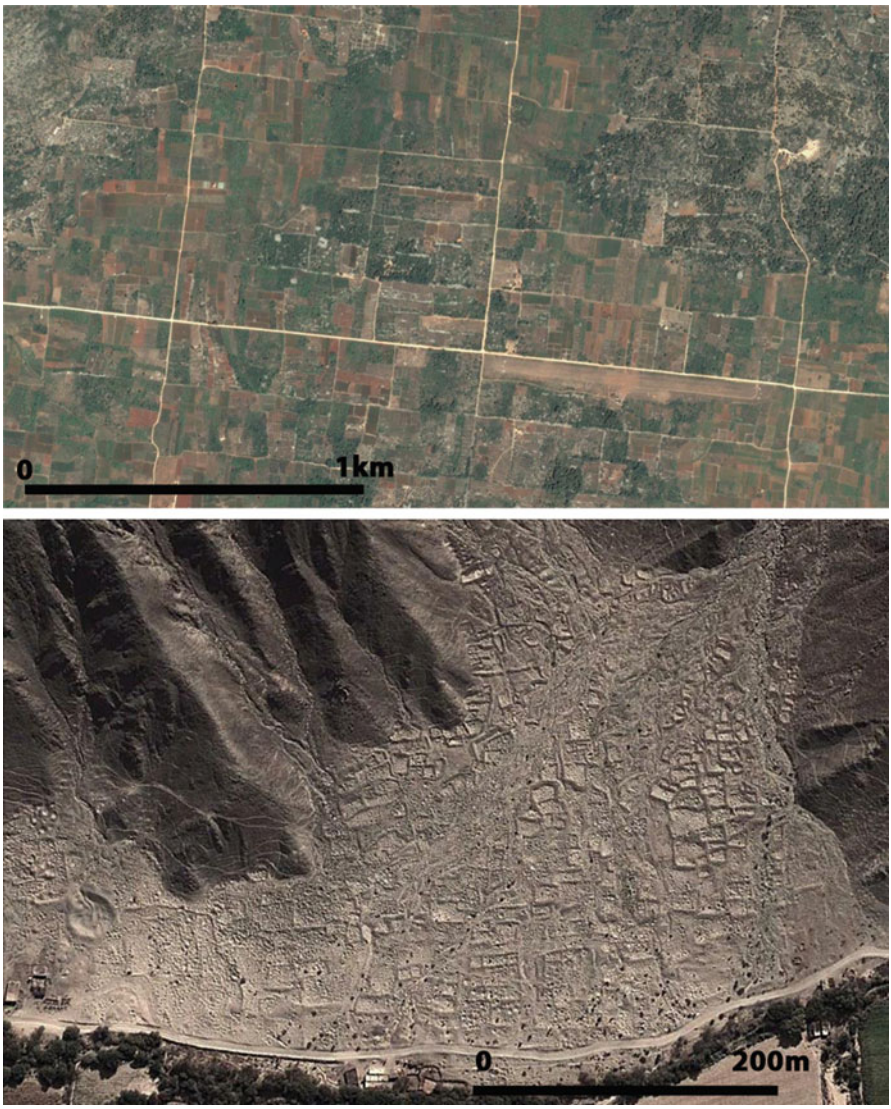

Fig. 2.7 Two different landscape patterns reveal traces of cultural interest. The first (*upper*) is a geometric grid of roads in Croatia that are traces of persistence of more ancient features: the centuriations that are Roman land divisions. The second (*bottom*) is an intricate network of microrelief that borders quadrangular spaces with rounded corners. These spaces are mainly domestic units of a settlement dated to Later Intermediate Period (1000–1450 AD) close to Rio Taruga, tributary of Nasca River in Southern Peru

upper). Romans delimitated the land to be farmed by means of the techniques of centuriations (*centuratio* in Latin), which were orthogonal and with equidistant borders (*limites* in Latin). They had also the function of roads, ditches, or channels. Their reconnaissance is usually facilitated by the identification of crop marks and signs of persistence of the landscape such as roads, divisions, and channels. The signs of persistence characterize the modern landscape but that assumes the value for the possibility that offers to reconstruct an ancient context or because they reflect past functions (as in the case of the roman centuriations in Croatia in Fig. 2.7, upper) or for the survival of all or part of their function.

Figure 2.7 (bottom) shows a different textural pattern characterized by less geometric shapes than those observed in Croatia. It is related to a pre-Inca settlement in Peru, located in Rio Taruga, in Southern Peru, dating back to the Late Intermediate Period (1000–1450 AD). The settlement is identified by a composed microrelief pattern that borders spaces with different shapes, such as quadrangular with rounded corners, oval, and curvilinear. Being that in the current case under investigation the archaeological remains are partially exposed as microrelief (which are proxy indicators of possible shallow and/or buried remains), a satellite-based analysis has been conducted to spatially characterize the urban shape that is not evident on the ground (see Fig. 2.8, upper) because of the presence of sparse material and the erosion process.

To this aim, the extraction of archaeological features is carried out by using an object-oriented approach that exploits both the texture and the spectral values related to the tone of stone surfaces and the shadow caused by the microrelief.

Similarly to the case of Hierapolis, the object-oriented approach of the classification (in this case supervised) preceded the segmentation. The aim was to extract only one class, that of the "archaeological microrelief," considering as training areas the polylines on the top of the microrelief of about ten units (see Fig. 2.8, middle).

Step I: Support Vector Machines

For the categorization of the pixels related to cultural features, we adopted the SVM (support vector machine) approaches that have also shown great potential for data classification also in VHR satellite data processing (Mountrakis et al. 2011). They are nonparametric classifiers that show a great ability to optimize classification issues, minimizing the empirical classification errors while maximizing the class separations. The main objective is to generalize the problem, avoiding overfitting. SVMs produce a model, based on the training data set, to predict the target values of the test data given only the test data attributes. As in other supervised classifications the first step is the training, which involves the random separation of datasets into training and testing subsets. The selected training area includes polylinear masks choiced along on some microrelief inside a subset whose area is about 5% of the total area.

As a whole, a support vector machine is a maximal margin hyperplane in the featured space built by using a kernel function in spectral space. The selection of SVM kernel classifier (along with kernel parameters) is considered as one of the

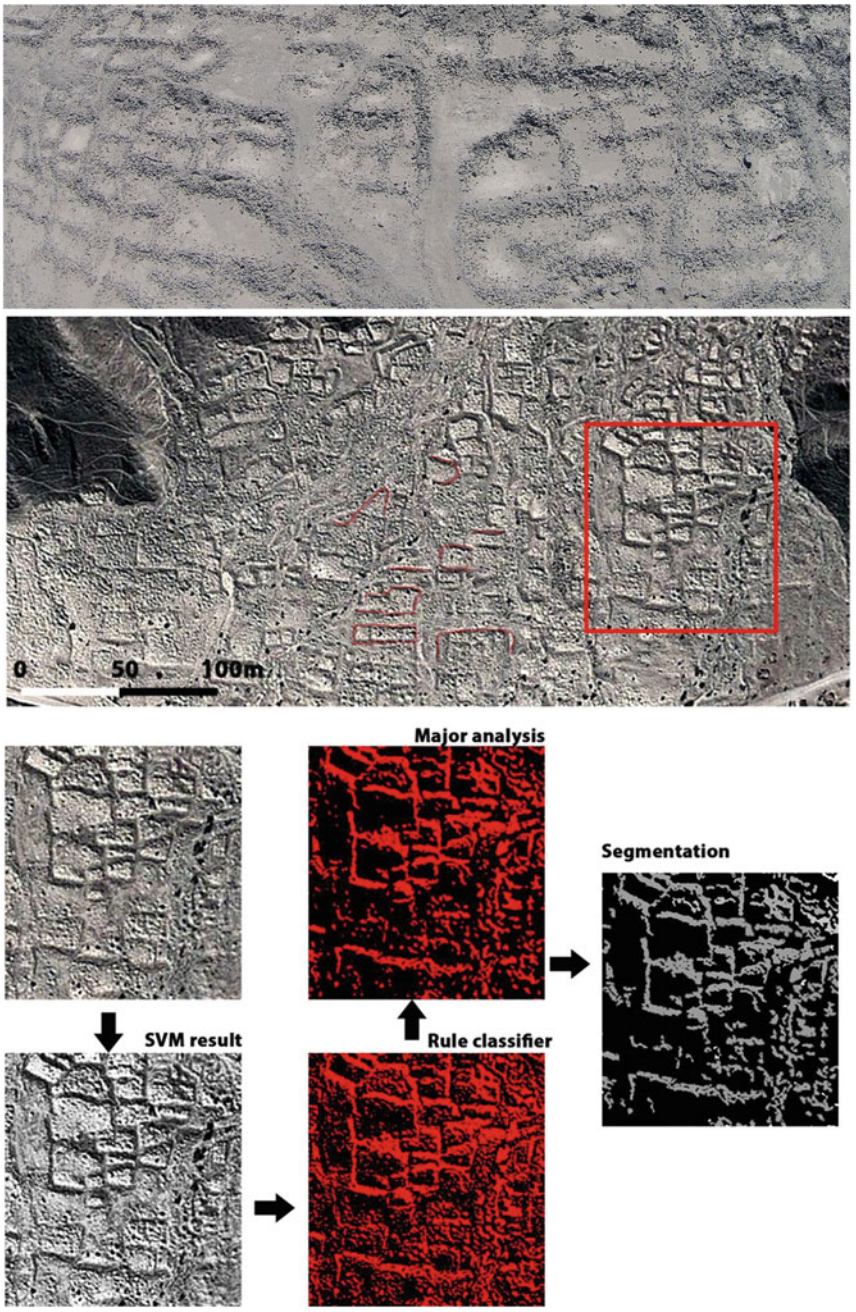

Fig. 2.8 Rio Taruga (Peru), settlement of the Late Intermediate Period: satellite-based object extraction of microrelief. *Upper*: detail of microrelief. *Middle:* Pleiades satellite image acquired in 2013. The training area is indicated by *red lines* along the microrelief. *Red box* denotes a detail in which the results of the processing are shown in the bottom image. *Bottom*: data processing workflow

most important steps in the implementation of SVM classifier. The lower the number of parameters to be defined, the greater the robustness of the SVM implementation.

Herein, we adopted a polynomial kernel.

Step II–III: Rule Classifier and Majority Analysis

Between SVM and segmentation, rule classifier and majority analyses have been performed: (1) the first to generate new classification images from different thresholds, and (2) the second to change spurious pixels within a large single class to that class. In particular, assumed a kernel size, the center pixel in the kernel is replaced with the class value of the majority of the pixels in the kernel.

In our case the two routines served just to reduce the number of pixels included in the unique class related to archaeological microrelief. These two steps have been fundamental to remove all the holes of looters contained inside each quadrangular room.

Step IV: Segmentation

Finally, segmentation has been performed. It generally can be manipulated by the following three parameters: (i) color, (ii) form, and (iii) scale.

In this chapter we focus on linear and rectangular shapes because the main interest of our investigations is the detection of geometric shape features. This choice is not restrictive because the same procedure may be carried out several times according to the different expected geometric patterns and shapes. The segmentation was made to reduce the parameters to be selected to extract geometric features that are obtained setting only (i) the minimum number of pixels to be considered in a region for building a segment and (ii) the number of neighbouring pixels, which determines the separability/connectivity of the segments. For the investigated areas we assumed the following values of (i) and (ii) were equal to 30 and 8, respectively.

2.4 Passive and Active Data Integration

Notwithstanding the tremendous increase of radiometric, spectral, and spatial resolution, optical remote sensing presents some limits in detecting all the possible archaeological features. In remains covered by dense vegetation, in particular forest, optical space technologies are able to detect only structures of large dimensions, as in the case of a large Maya settlement in the jungles of northeast Guatemala detected by Garrison et al. (2008) using IKONOS imagery. Also for bare ground surfaces, in the presence of earthworks and other topographic features of cultural interest the detection capability of optical imagery depends on time of image acquisition, viewing angle of the collected imagery, surface characteristics, and sun angle. The aforestated restrictions of optical imagery could be overcome by LiDAR and SAR.

LiDAR provides direct range measurements mapped into three-dimensional (3D) point clouds between a laser scanner and Earth's topography. The high detail of the digital terrain models allows us a precise characterization of geomorphological

features and the identification of relief linked to human activity. The interpretation of LiDAR products aimed at identifying potential traces of cultural interest is based on the visual criteria and the degree to which the features appeared anthropogenic versus nonanthropogenic: shape, pattern, texture, and shadow, as in the case of passive data (from the panchromatic to multispectral and hyperspectral imagery). To this aim, it is crucial (1) to process the point clouds and classify terrain and off-terrain objects by applying adequate filtering methods to obtain very accurate Digital terrain Model (DTM); (2) to "manipulate" the DTMs with appropriate techniques of visualization aimed at emphasizing changes of morphology, discontinuities of the landscape, platforms, and any kind of earthworks attributable to human work.

For task 1, a number of algorithms and tools are available for filtering LiDAR, categorized in five groups: morphological filtering, progressive densification, surface-based filtering, segment-based filtering, and spline interpolation filtering (for more detail, refer to Masini et al. 2011). Task 2 could be obtained by a relief shading procedure, slope gradient, and convexity, which are, respectively, the first and second derivatives of the DEM image processing filters to detect high-frequency variation, a local relief model to separate local small-scale features from large-scale landscape forms, and Sky view factors based on the measure for the portion of the sky visible from a certain point (for an overview of visualization techniques of LiDAR-derived relief models, see Stular et al. 2013; Fig. 2.9 shows the results of LiDAR-based investigation of an abandoned medieval village near Matera, Italy). The integration of passive and active remotely sensed data allowed the reconstruction of the "forma urbis" of the settlement, thanks also to the support of visualization techniques, among which is slope and profile convexity; see Lasaponara and Masini (2009).

LiDAR sensors are also and mainly a powerful tool for investigating archaeological heritage in wooded areas. These sensors can penetrate vegetation canopies and model accurately underlying terrain elevation. The recent discoveries of Evans in Angkor and those of Chase in Belize demonstrate the effectiveness of this technology for archaeological research. For sake of brevity, we refer to Chase et al. (2016) in this same volume for additional information and issues concerning LiDAR applied to archaeology.

Radar sensors are able to sense areas at any time of day or night, to "penetrate" clouds, making it possible to map and study also those regions, tropical and subtropical, where cloud cover is one of the major limitations of optical imaging. Moreover, radar SAR at low-frequency bands (L and P) can penetrate the vegetation and even soil down to several meters in hyperarid environments (for additional detail on SAR for archaeology, see Chap. 4 by Tapete and Cigna, this volume). As a whole the availability of numerous multifrequency, multipolarization SAR data and VHR opened new perspectives for remote sensing in archaeology (Chen et al. 2015; Lasaponara and Masini 2013; Chen et al. 2016). To obtain significant results for archaeological prospecting it is important to know the "object" or the surface to be investigated to analyze and process SAR data, taking into account the key parameters of the radar energy–target interaction. In particular, they are the (1) surface roughness, (2) moisture content and electrical properties, and (3) radar

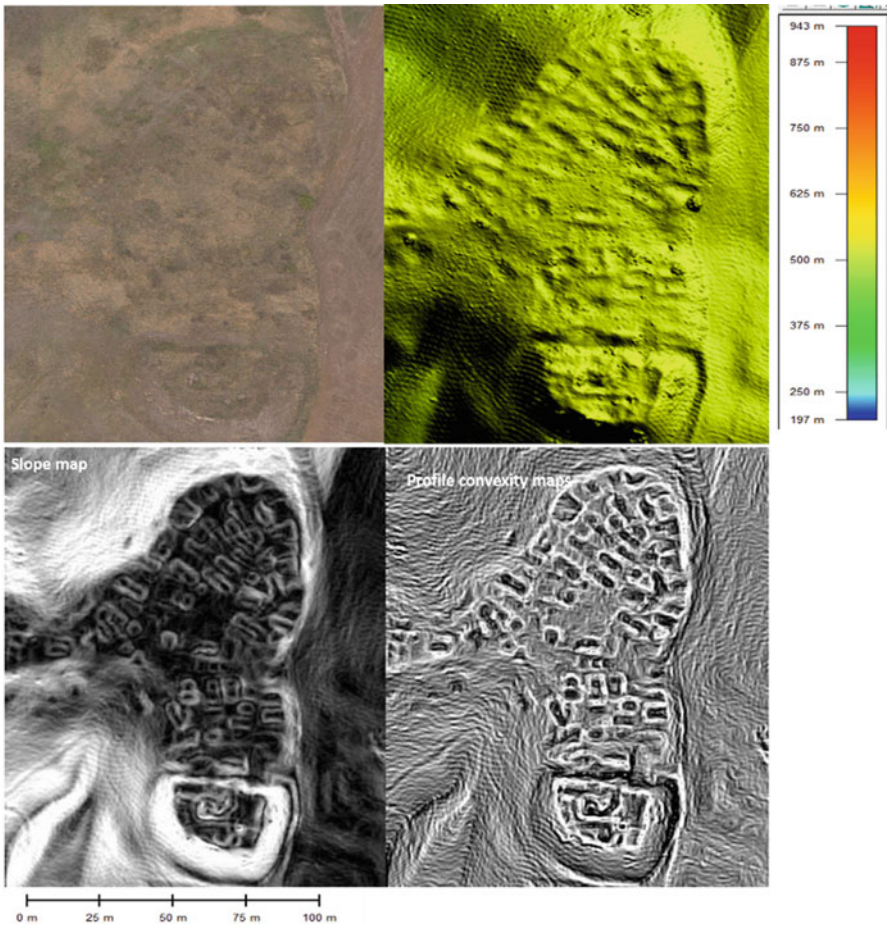

Fig. 2.9 LiDAR-based investigation of the medieval village of Yrsum near Matera (Southern Italy), founded in the eleventh century and abandoned in the fifteenth century. The microrelief visible from the DEM derived from LiDAR (*upper right*) is more significant in respect to the crop marks of the optical image (*upper left*). The slope and profile convexity maps allow us to extract way the urban shape of the village

viewing and surface geometry relationship. The most recent application of SAR in archaeology is evidenced in the need to integrate this technology with optical (airborne and space-borne). Examples of SAR and optical data integrations are related to the Phoenician and Roman town of Sabratha in Libya (Chen et al. 2014), the Greek town of Metaponto and its surroundings in Southern Italy (Lasaponara and Masini 2015), and the ancient town of Pelusium in Northern Egypt (Stewart et al. 2013; Lasaponara and Masini 2015).

Sabratha, located 64 km west of Tripoli and characterized by an arid climate in a desert environment, was founded in the seventh century BC by the Phoenicians

of Tyre. It became a trading post at the mouth of a major caravan route. Because of its strategic location, it had a rapid development. Then it fell under the control of Carthage before and of the Kingdom of Numidia afterwards. Sabratha was later taken by the Romans in 46 BC, under which it enjoyed a new prosperity. The city was rebuilt under Roman period when it achieved its greatest prosperity during the second and third centuries AD. The Roman town was just the object of some analyses conducted by using active and passive remotely sensed data. In particular, X-band Cosmo SkyMed added new data on a buried urban sector of the town, nearby the amphitheater, with respect to optical VHR satellite imagery. In particular, X-band data proved to be very capable in imaging the microrelief referable to shallow structures of urban blocks of the town (Fig. 2.10).

Metaponto, located between the Basento and Bradano Rivers, near the Ionian Sea, in the south of Italy, was founded by Greeks coming from the Achaea region. Between Greek colonization (700 BC to 200 BC) and the Roman Age (200 BC to 400 AD), the territory was characterized by an intensive use of soil as revealed by the several rural sites and extensive system of parallel land divisions and drainage channels (Adamesteanu 1973; Carter 1990) and by the spatial and temporal relationship between hydrography and human settlements.

The city of Pelusium (the modern Tell Farama) is located upon the easternmost bank of the Nile River, named the Ostium Pelusiac, closed at the mouth of a branch of the Nile, named Pelusiac, founded by Pharaoh Psamtik I (664–610 BC), of the twenty-sixth dynasty of Egypt. It was a very important defensive center exposed to numerous attacks by invaders from the east side. It was the place where the battle between Egyptians and Persians occurred. The whole area is characterized

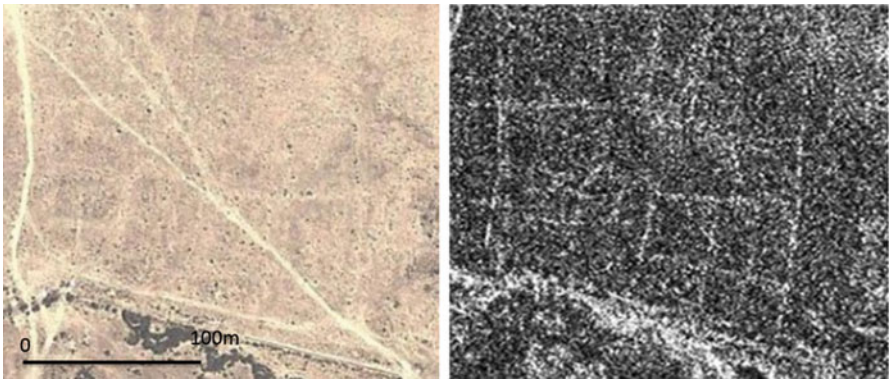

Fig. 2.10 Sabratha (Libya). (**a**) VHR satellite image from Google Earth acquired 20 August 2011. (**b**) COSMO-SkyMed Spotlight image acquired on 12 December 2012, at 1 m geometric resolution, in ascending orbit, with an angle of incidence of 27.32° and HH polarization. The active and passive are complementary in terms of discriminability of archaeological microrelief. The high reflectance of the microrelief from the optical data makes visibility difficult in some cases, although the backscattering response of radar band allows identifying a greater number of linear features of the urban shape

by several changes from the hydrogeological and geomorphological point of view since the first century BC. At the time of its construction, Pelusium was about 2.5 miles from the sea, located between the seaboard and the Nile Deltaic marshes. At approximately 25 AD, the Pelusiac branch was chocked by sand and silt deposits from beach accretion processes. During the third century AD the coastline advanced far beyond its ancient limits, so that the city was at least 4 miles from the coast (Coutellier and Stanley 1987; Goodfriend and Stanley 1999; Jakubiak 2012).

In Metapontum and in Pelusium the key parameter has been the moisture content that influences, as is well known, soil electrical properties of soil and consequently the reflection, transmission, and absorption characteristics of microwave energy. Generally, radar image "brightness" tends to increase with the increasing of moisture content. In Metaponto the high value of backscattering (highlighted with high pixel brightness) of radar data corresponds to high reflectance value of NIR named of the optical satellite imagery (QuickBird, Pleiades).

As a whole the integration of passive satellite data with X-band data allowed us to map ancient paleo-riverbeds, some of them coeval to archaeological sites, thus providing new information useful to analyze the spatiotemporal relationship between settlements and environmental/landscape change from 800 BC to 200 BC (Lasaponara and Masini 2015; Chen et al. 2014) (Fig. 2.11).

In Pelusium, with the X-band Cosmo SkyMed, the sensitiveness of X-band radar signal to surface dielectrical properties permitted discriminating moisture areas also visible by ASTER and Pleiades imagery, thought to be a sector of the defunct Pelusiac branch (Fig. 2.5e–f). In this case Pleiades and Spotlight Cosmo SkyMed data proved to be complementary for the extraction of information of cultural interest and to identify some paleo-environmental features such as coastal ridges when Pelusium was much closer to the sea compared to today (Quintanar et al. 2013).

New promising applications of data integration include the use of SAR with other remote sensing methods including geophysics as in the case of the investigations performed by Linck et al. (2013) aimed at comparing Terra SAR data with results of georadar survey to assess the penetration capability of the TERRA-SAR X band at a test site near the Roman fortress Qreiye in Syria, or the integrated archaeological prospectings in Pachacamac by using SAR data, Pleiades imagery, UAV, and geomagnetic techniques (Lasaponara et al. 2016b).

Concerning the integration between space and ground remote sensing we rely on a vast scientific literature, which deserves a separate chapter. For sake of brevity we limit to saying that now satellite imagery, thanks to the possibility of integration with geophysics, is ever more a fundamental source of information, not only for research but also for preventive archaeology.

Satellite remote sensing is generally the first step of a knowledge process that follows a multiscale approach and a multisensor integration. From the satellite to aerial images, from the UAV survey to geophysics (and inside it from geomagnetic to georadar), the investigated areas decrease and the obtainable detail increases together with its complexity.

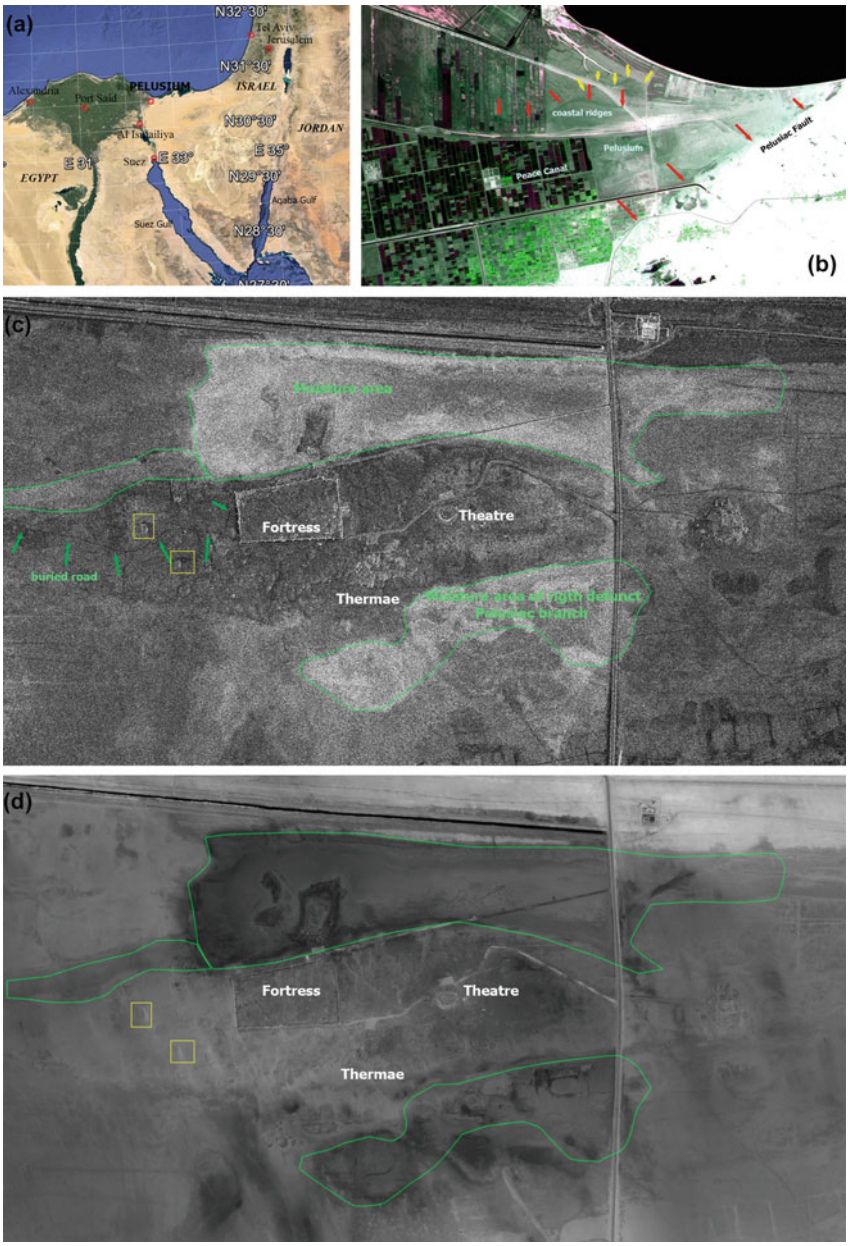

Fig. 2.11 Pelusium (Egypt). (**a**) Geographic setting. (**b**) RGB composition of ASTER image acquired on 24 October 2013 that puts into evidence some paleo-environmental and environmental features in the surrounding of Pelusium, such as the ancient coastline. (**c**) Spotlight Cosmo SkyMed scene (acquired on 15 November 2013). (**d**) Pleiades image acquired on 26 July 2013. The information derived from satellite and optical data is complementary, thus allowing improving their knowledge from the physical and morphological aspects. This is the case of the moisture areas referable to a part of the defunct Pelusiac branch and topographic relief of cultural interest, visible from both datasets (**c**, **d**) (Image drawn by Lasaponara and Masini 2015)

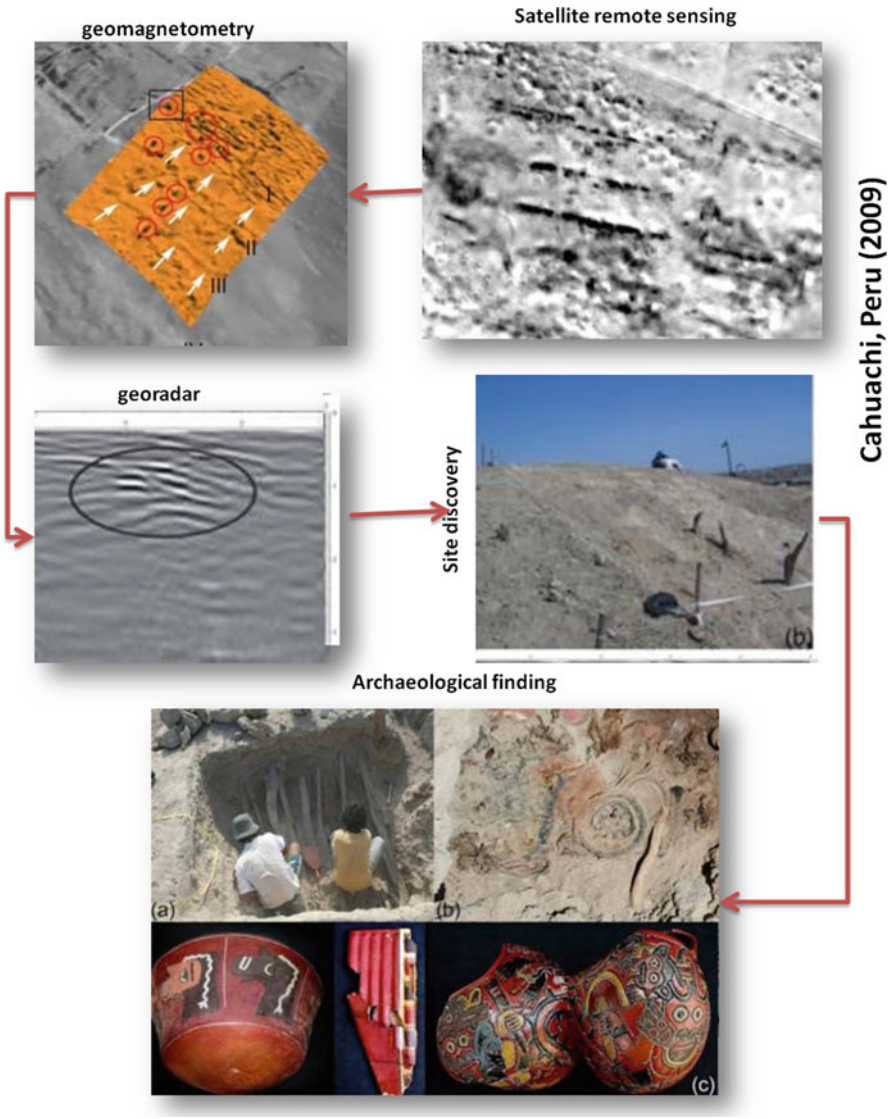

Fig. 2.12 From space to place: multiscale and multisensor approach adopted in Cahuachi (Nasca, Southern Peru)

It is a work based on the comparison of data acquired with different sensors and resolution on which to base the choices following insights until defining the grid to dig: this is what happens, for example, in the context of an archaeological mission. (See Fig. 2.12, related to the multiscale and multisensor approach adopted in the Nasca ceremonial center of Cahuachi; see Rizzo et al. 2010). Sometimes the work

does not follows directions coming from large to small areas but on the opposing paths in which the detail improves the knowledge of a landscape, in agreement with a discipline, such as archaeology, in which a few grams of carbon may change the dating of a tomb, the chronology of a site, the history of a civilization.

2.5 Predictive Modeling

Predictive modeling was initially applied in Peru and later developed in the US since the late 1970s and early 1980s (Kohler 1988). Today it is widely used in the US (Wescott and Brandon 2000), Canada (Dalla Bona 2000), and many countries in Europe (Deeben et al. 2002; Münch 2003; Danese et al. 2014).

The use of spatial statistics and predictive modeling has been under lively discussion for more than 20 years (Kvamme 1988, 1990; Parker 1985; Woodman and Woodward 2002) and today, also thanks to the availability of much open-sourced GIS software, is generally considered as an important operational tool for preventive archaeological investigations.

Traditional applications of predictive modeling in archaeological studies have been generally focused on estimation in areas that have not been previously investigated of statistical occurrence of sites, on the basis of observed patterns, or, on assumptions about human behavior.

Starting from well-known archaeological sites, it is possible to use them as test sites to understand and model the factors that influenced the selection of their locations. Observed patterns (location of sites) or assumptions about human behavior and relationships between natural and social environment parameters are statistically investigated to obtain " settlement rules" to be used inside the model. The selection of parameters depends on many factors; of course, different cultures, locations, and historical periods require different approaches. Moreover, in the literature a great variability of parameters is used (Danese et al. 2014); some are site dependent (directly linked to archaeological area characteristics), others are site independent, namely, linked to environmental or biophysical characteristics such as slope, relief, aspect, soil type, elevation, vegetation, distance to water, and proximity to food source. Actually, generally just a few are always present, such as land use, elevation, and water bodies. Other parameters, both environmental and social, are less employed.

Therefore, in a given region, known archaeological sites along with proxy variables and environmental context parameters are used to assess their relationships and statistical correlation to exploit this information as reference knowledge similarly as training sets are used in remote sensing-supervised image classification.

The environmental profile obtained from the statistical analysis of the mutual relationship of sites and environment is used to identify areas matching with this profile to predict and map potential occurrence of archaeological sites.

GIS-based tools make it relatively easy to produce statistical models offering significant insight; nevertheless, the identification and selection of variables that

refer to past land use and availability of resources (water, arable land, etc.) remains today one of the most important and critical issues, being that some attributes may be strongly involved in significant differences between current and past conditions.

Satellite data can provide useful data related to past environments and human activities and therefore can be used as a useful source to "feed" predictive models, enlarging the number and reliability of proxy and parameters that refer to past environs and human attitudes, etc., thus potentially improving the performance obtainable from the statistical tools.

Approaches based on the joint use of remote sensing and prediction modeling allowed the prediction of archaeological sites as in Danese et al. (2014) or Clark et al. (1998) exploiting the spectral properties of known archaeological sites observed using passive and active satellite imaging.

Remote sensing, GIS, and predictive models allow a new and more effective way to conduct archaeological research, storing, handling, and sharing geospatial data from heterogeneous sources. There are two main uses of predictive archaeology. The first is practical: its goal is to map sensitive areas and to protect our archaeological heritage. The second is scientific and is linked to the will to reconstruct the past, to better understand settlement patterns on the basis of parametric models.

The models can be classified in inductive and deductive approaches. The inductive model approach is the most common, based on the extraction of rules from datasets made up of information related to well-known sites or obtained from field surveys or remote sensing. In deductive modeling the location rules are derived from a theoretical knowledge and approach that support an easier understanding and interpretation of the results. For this reason, the deductive modeling approach is considered superior compared to the inductive one.

Concerning the methods adopted for analysis, the most common reported in the literature use statistics, in particular Markov's chain, Dempster–Shafer's belief theory, logistic or linear regression, or multifractal analysis. However, more simple methods such as map algebra functions are also used.

The most commonly used approaches are (i) logistic regression analysis and (ii) weighted ranking analysis.

Logistic regression analysis is applied to a large variety of modeling contexts. It is based on binary data (presence/absence) and estimates a relationship between predictor variables and an outcome variable.

The weighted ranking analysis considers that each environmental variable contributes in different amounts to predicting the presence or absence of archaeological sites. Therefore, the considered variables are weighted differently based on their impact on the feature being modeled.

Recently, an innovative approach has been proposed by Danese et al. (2014), who also include the assessment of the presence of spatial autocorrelation in the distribution of archaeological sites.

The testing of predictive models has been discussed for more than 20 years (Kvamme 1988, 1990; Parker 1985; Woodman and Woodward 2002) and still today

can stimulate a lively debate. However, the validation is generally carried out by a comparison of the model results with independent data sets, as, for example:

- Locations of known archaeological sites
- Surveys in areas classified as having high or moderate potential

Today, predictive models are generally regarded as useful tools for archaeological research. They can constitute an important decision support system providing useful information for defining survey priority and facilitating new site discovery, saving time and money, especially in large areas.

Moreover, predictive models can also contribute to preserving archaeological areas and features that are witnesses of the human past, providing information useful for reducing archaeological risk linked both to atrophic and to natural risk factors

The example in Fig. 2.13 related to the Neolithic sites in the Tavoliere (Apulia, Italy) in Danese et al. (2014) explains and resumes better the steps followed for the construction of a predictive model: there are three main steps, followed by a validation moment that is useful also for reviewing the entire process.

2.6 Conclusion and Future Perspectives

From the 1980s to date, the use of remote sensing for the study of ancient civilizations and for cultural resources management strongly increased as a few technologies were experienced in the same field of application.

This upgrade was the result of the long wave of the development of space technologies for civil applications and also to the increased awareness of end-users and stakeholders, from the archaeologists to conservators from private companies for archaeological excavations and restorations to policy makers, of the economic benefit and the improvement of knowledge.

These technologies are not only tools to improve address issues and solve problems for the study of the human past and protection and monitoring of ancient landscapes. These tools can also benefit for their development by countless and challenging applications in the field of archaeology and conservation.

In the past, the technologies and scientific methodologies were borrowed from other fields of application and disciplines from environmental to life sciences. If on the one hand this ensured a general availability of the technological products in the field of cultural heritage, on the other hand it has delayed ad hoc products for the specific needs of the archaeological research and heritage management aims. This was also the case of EO technologies whose potential was not fully exploited because of the difficulty of interpreting the results.

Something is changing. Cultural heritage is now not only an object of investigations but also a laboratory: (1) to experiment with new challenging tools and scientific approaches for site discovery and the documentation of landscapes and civilizations in danger; and (2) to develop low-cost and user-friendly technologies to enlarge the community of users.

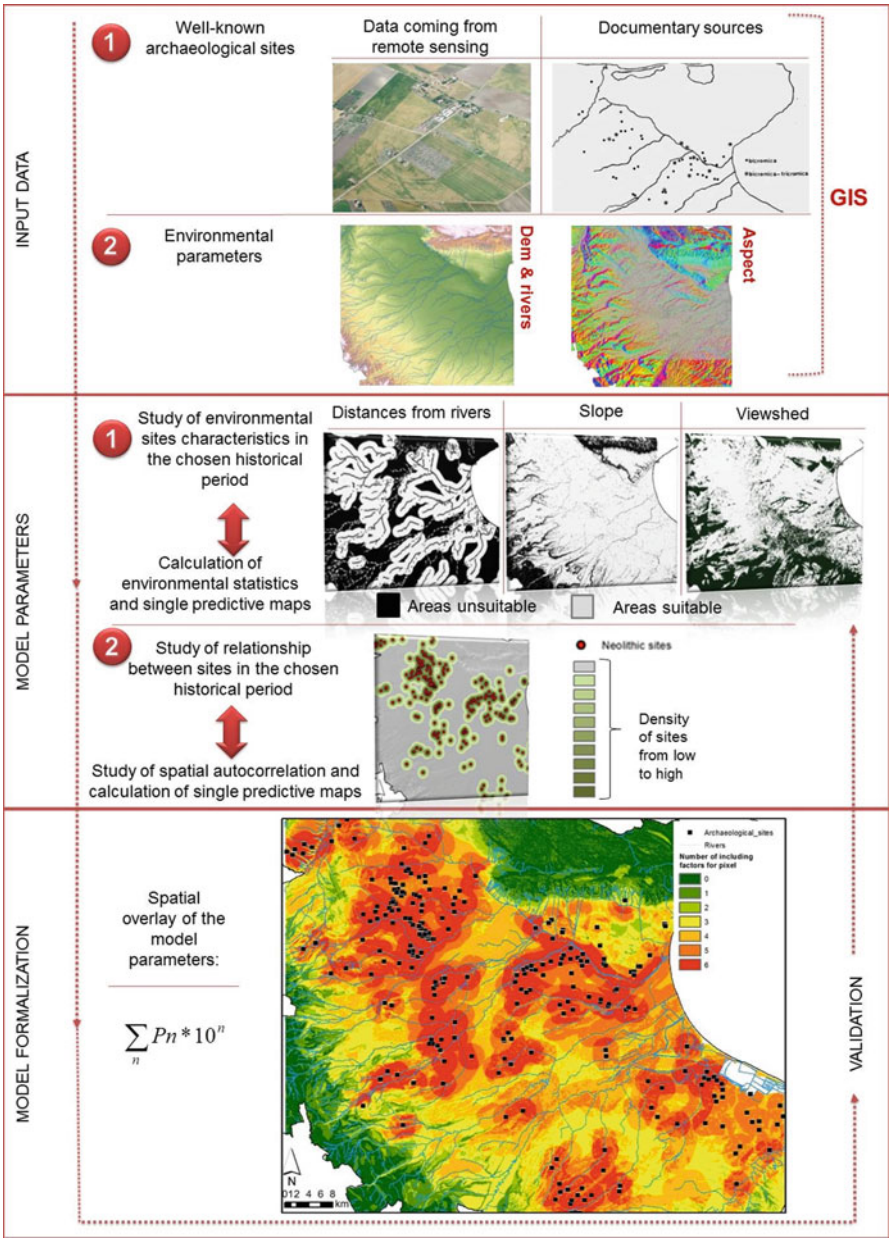

Fig. 2.13 Example of a predictive model: summarizing scheme for the Neolithic sites of Apulia (Italy)

We are living the era of digital humanities within which Earth observation data are fundamental in changing the notion of heritage as well as that of knowledge and landscape. This development favored data integration in the context of holistic approaches to improve the interpretation.

New exciting possibilities for the study and monitoring of cultural heritage are offered by Google Earth, Google Maps, NASA WorldWind, and other "geobrowsing" technologies (Myers 2010). Citizen scientists, defined as "volunteers who collect and/or process data as part of a scientific enquiry" (Silvertown 2009; Smith 2014), are favoring global participation in the problems of the environment and protection issues of World Cultural Heritage at risk, especially in those countries at war.

Acknowledgements The present publication is under the "ATHENA" project H2020-TWINN2015 of European Commission. This project has received funding from the European Union's Horizon 2020 research and innovation program under grant agreement No. 691936. This chapter is an annex of the deliverable 2.1 "RS systems use for application in archaeology research assessment report."

Author Contributions: Nicola Masini and Rosa Lasaponara conceived the study. Nicola Masini wrote the paper. Rosa Lasaponara reviewed the manuscript.

References

Adamesteanu D (1973) Le suddivisioni di terra nel metapontino. In: Finley MI (ed) Problems de la terre en Grece Ancienne. Paris, pp 49–61

Agapiou A, Hadjimitsis DG, Sarris A, Georgopoulos A, Alexakis DD (2013b) Optimum temporal and spectral window for monitoring crop marks over archaeological remains in the mediterranean region. J Archaeol Sci 40:1479–1492

Agapiou A, Alexakis DD, Sarris A, Hadjimitsis DA (2013a) Orthogonal equations of multispectral satellite imagery for the identification of un-excavated archaeological sites. Remote Sens 5:6560–6586. doi:10.3390/rs5126560

Agapiou A, Lysandrou V, Lasaponara R, Masini N, Hadjimitsis DG (2016) Study of the variations of archaeological marks at neolithic site of Lucera, Italy using high-resolution multispectral datasets. Remote Sens 8(9):723. doi:10.3390/rs8090723

Aiazzi B, Baronti S, Alparone L, Lasaponara R, Masini N (2008) Data fusion techniques for supporting and improving satellite-based archaeological research. In: Lasaponara R, Masini N (eds) Advances in remote sensing for archaeology and cultural heritage management. Aracne, Roma, pp 31–36

Alexakis D, Sarris A, Astaras T, Albanakis K (2011) Integrated GIS, remote sensing and geomorphologic approaches for the reconstruction of the landscape habitation of Thessaly during the Neolithic period. J Archaeol Sci 38:89–100

Altaweel M (2005) The use of ASTER satellite imagery in archaeological contexts. Archaeol Prospect 12:151–166

Argote-Espino D, Chavez RE (2005) Detection of possible archaeological pathways in Central Mexico through digital processing of remote sensing images. Archaeol Prospect 12:105–114

Beck AR (2007) Archaeological site detection: the importance of contrast. In: Proceedings of the 2007 annual conference of the Remote Sensing and Photogrammetry Society. The Remote Sensing and Photogrammetry Society, Newcastle, 11–14 September 2007

Beck A, Philip G, Abdulkarim M, Donoghue D (2007) Evaluation of Corona and Ikonos high resolution satellite imagery for archaeological prospection in western Syria. Antiquity 81:161–175

Blodget PT, Taylor JH (1991) Roark shoreline changes along the Rosetta–Nile promontory. Monitoring with satellite observations. Mar Geol 99:67–77

Campana S, Forte M (ed) (2006) Proceedings of 2nd international conference on Remote Sensing in Archaeology, BAR International Series, 4–7 December, 2006, Rome

Canny J (1986) A computational approach to edge detection. IEEE Trans Pattern Anal Mach Intell 8(6):679–698

Carter JC (1990) Between the Bradano and Basento: archaeology of an ancient landscape. In: Kelso W, Most R (eds) Earth patterns. Essays in landscape archaeology. University of Virginia Press, Charlottesville, pp 227–243

Cavalli RM, Pascucci S, Pignatti S (2009) Optimal spectral domain selection for maximizing archaeological signatures: Italy case studies. Sensors 9:1754–1767. doi:10.3390/s90301754

Challis K (2007) Archaeology's Cold War windfall – the CORONA programme and lost landscapes of the near East. JBIS 60:21–27

Chase ASZ, Chase DZ, Chase AF (2016) LiDAR for archaeological research and the study of historical landscapes. In: Masini N, Soldovieri F (eds) Sensing the past. Geoscience and sensing technologies for cultural heritage. Springer, Cham, pp 89–100, chapter 4.

Chen F, Lasaponara R, Masini N (2015) An overview of satellite synthetic aperture radar remote sensing in archaeology: from site detection to monitoring. J Cult Herit. http://dx.doi.org/10.1016/j.culher.2015.05.003

Chen F, Masini N, Yang R, Milillo P, Feng D, Lasaponara R (2014) A space view of radar archaeological marks: first applications of COSMO-SkyMed X-Band data. Remote Sens 2015(7):24–50. doi:10.3390/rs70100024

Chen F, Masini N, Liu J, You J, Lasaponara R (2016) Multi-frequency satellite radar imaging of cultural heritage: the case studies of the Yumen Frontier Pass and Niya ruins in the western regions of the silk road corridor. Int J Digit Earth 9(12):1224–1241. doi:10.1080/17538947.2016.1181213

Ciminale M, Gallo D, Lasaponara R, Masini N (2009) A multiscale approach for reconstructing archaeological landscapes: applications in Northern Apulia (Italy). Archaeol Prospect 16:143–153

Clark CD, Garrod SM, Parker Pearson M (1998) Landscape archaeology and remote sensing in southern Madagascar. Int J Remote Sens 19(8):1461–1477

Crawford OGS (1929) Air photography for archaeologists, Ordnance survey professional papers, new series, 12. HMSO, Southampton

Comfort A (1997) Satellite remote sensing and archaeological survey on the Euphrates. Archaeol Comput Newsl 48:1–8

Coutellier V, Stanley DJ (1987) Late Quaternary stratigraphy and paleogeography of the eastern Nile Delta. Egypt Mar Geol 77:257–275

Crist EP, Cicone RC (1984) A physically-based transformation of thematic mapper data: the TM tasseled cap. IEEE T Geosci Remote GE 22(33):256–263

Danese M, Masini N, Biscione M, Lasaponara R (2014) Predictive modeling for preventive archaeology: overview and case study. Cent Eur J Geosci 6(1):42–55. doi:10.2478/s13533-012-0160-5

Dalla Bona L (2000) Protecting cultural resources through forest management planning in Ontario using archaeological predictive modeling. In: Wescott KL, Brandon RJ (eds) Practical applications of GIS for archaeologists: a predictive modelling kit. Taylor & Francis, London, pp 73–99

Dassie J (1978) Manuel d'archeologie aerienne, Paris

Deeben J, Hallewas DP, Maarlevelt TJ (2002) Predictive modelling in archaeological heritage management of the Netherlands: the indicative map of archaeological values (2nd generation). Berichten ROB, vol 45. ROB, Amersfoort, pp 9–56

De Laet V, Paulissen E, Waelkens M (2007) Methods for the extraction of archaeological features from very high-resolution Ikonos-2 remote sensing imagery, Hisar (southwest Turkey). J Archaeol Sci 34(5):830–841. doi:10.1016/j.jas.2006.09.013

D'Orazio T, Da Pelo P, Marani P, Guaragnella C (2015) Automated extraction of archaeological traces by a modified variance analysis. Remote Sens (7):3565–3587. doi:10.3390/rs70403565

European Landscape Convention (2000)

Fowler MJF (1996) High resolution satellite imagery in archaeological application: a Russian satellite photograph of the Stonehenge region. Antiquity 70:667–671

Fowler MJF (2013) Declassified intelligence satellite photographs. In: Hanson WS, Oltean IA (eds) Archaeology from historical aerial and satellite archives. Springer, New York, pp 47–66. doi:10.1007/978-1-4614-4505-0

Garrison TG, Houston SD, Golden C, Inomata T, Nelson Z, Munson J (2008) Evaluating the use of IKONOS satellite imagery in lowland Maya settlement archaeology. J Archaeol Sci 35:2770–2777

Goodfriend GA, Stanley DJ (1999) Rapid strand-plain accretion in the northeastern Nile Delta in the 9th Century A.D. and the demise of the port of Pelusium. Geology 27(2):147–150

Holcomb DW (1992) Shuttle imaging SAR and archaeological survey in China's Taklamakan Desert. J Field Archaeol 19(1):129–138

Horne JH (2003) A tasselled cap transformation for IKONOS images. In: ASPRS 2003 annual conference proceedings, Anchorage, Alaska

Hough PVC (1962) Method and means for recognizing complex patterns. U.S. Patent 3,069,654, 18 December 1962

Jakubiak K (2012) Water distribution in Pelusium – a short note on a larger problem. In: Żuchowska M (ed) The archaeology of water supply. BAR international series, vol 2414, pp 49–59. http://earthexplorer.usgs.gov/, http://earthexplorer.usgs.gov/

Kauth RJ, Thomas GS (1976) The Tasseled Cap – a graphical description of the spectral-temporal development of agricultural crops as seen by Landsat. In: Proceedings of the symposium on machine processing of remotely sensed data. Purdue University, West Lafayette, Indiana, pp 4B41–4B51

Keeney J, Hickey R (2015) Using satellite image analysis for locating prehistoric archaeological sites in Alaska's Central Brooks Range. J Archaeol Sci Rep 3:80–89

Kennedy D (1998) The twin towns of Zeugma on the Euphrates: rescue work and historical studies. J Roman Archaeol Suppl Ser 27:1–247

Kohler TA (1988) Predictive locational modelling: history and current practice. In: Judge JW, Sebastian L (eds) Quantifying the present and predicting the past: theory, method and application of archaeological predictive modelling. U.S. Department of the Interior, Bureau of Land Management, Denver, pp 19–60

Kvamme KL (1988) Development and testing of quantitative models. In: Judge WL, Sebastian L (eds) Quantifying the present and predicting the past: theory, method and application of archaeological predictive modeling. US Bureau of Land Management, Denver, pp 324–428

Kvamme KL (1990) The Fundamental principles and Practice of Predictive Archaeological modeling. In: Voorrips A (ed) Mathematics and information science in archaeology: a flexible framework, Studies in modern archaeology, vol 3. Holos verlag, Bonn, pp 275–295

Laben CA, Brower BV (2000) Process for enhancing the spatial resolution of multispectral imagery using PanSharpening. U.S. Patent 6,011,875. Jan 4, 2000

Lasaponara R, Masini N (2006) Identification of archaeological buried remains based on Normalized Difference Vegetation Index (NDVI) from Quickbird satellite data. IEEE Geosci Remote Sens Lett 3(3):325–328. doi:10.1109/LGRS.2006.871747, ISSN: 1545-598X

Lasaponara R, Masini N (2007a) Detection of archaeological crop marks by using satellite QuickBird multispectral imagery. J Archaeol Sci 34:214–221

Lasaponara R, Masini N (2007b) Improving satellite quickbird-based identification of landscape archaeological features through Tasseled Cap Transformation and PCA., ISPRS International Archives of the Photogrammetry, Remote Sensing and Spatial Information Sciences, volume XXXVI-5/C53. Proceedings of 21st CIPA symposium, Atene, 1–6 giugno 2007, pp 812–816

Lasaponara R, Masini N (eds) (2008) Advances in remote sensing for archaeology and cultural heritage management. In: Proceedings of I international EARSeL workshop "Advances in Remote Sensing for Archaeology and Culturale Heritage Management", Rome 30 septembre-4 October, 2008, Aracne, Roma, 2008. ISBN: 978–88–548-2030-2

Lasaponara R, Masini N (2009) Full-waveform airborne laser scanning for the detection of medieval archaeological microtopographic relief. J Cult Herit 10S:78–82. doi:10.1016/j.culher.2009.10.004

Lasaponara R, Masini N (2012) Image enhancement, feature extraction and geospatial analysis in an archaeological perspective. In: Lasaponara R, Masini N (eds) 2012, satellite remote sensing: a new tool for archaeology. Springer Verlag, Berlin/Heidelberg, pp 17–64. ISBN 978-90-481-8800-0, doi:10.1007/978-90-481-8801-7_2

Lasaponara R, Masini N (2013) Satellite Synthetic Aperture Radar in archaeology and cultural landscape: an overview. Archaeol Prospect 20:71–78. doi:10.1002/arp.1452

Lasaponara R, Masini N (2015) Reconnaissance of archaeology marks through satellite Synthetic Aperture Radar. In: Chavarría A, Reynolds A (eds) Detecting and understanding historic landscapes. SAP Società Archeologica s.r.l, Mantiva, pp 93–108

Lasaponara R, Leucci G, Masini N, Persico R, Scardozzi G (2016a) Towards an operative use of remote sensing for exploring the past using satellite data: the case study of Hierapolis (Turkey). Remote Sens Environ 174:148–164. doi:10.1016/j.rse.2015.12.016

Lasaponara R, Masini N, Pecci A, Perciante A, Pozzi Escot D, Rizzo E, Scavone M, Sileo M (2016b) Qualitative evaluation of COSMO SkyMed in the detection of earthen archaeological remains: the case of Pachamacac (Peru. J Cult Herit. doi: http://dx.doi.org/10.1016/j.culher.2015.12.010

Linck R, Busche T, Buckreuss S, Fassbinder JWE, Seren S (2013) Possibilities of archaeological prospection by high-resolution X-band satellite radar-a case study from Syria. Archaeol Prospect 20:97–108

Lu P, Yang R, Guo Y, Chen F, Masini N, Lasaponara R (2016) On the use of historical archive of aerial photographs for the discovery and interpretation of ancient hidden linear cultural relics in the alluvial plain of eastern Henan, China. J Cult Herit. doi:10.1016/j.culher.2015.09.010

Luo L, Wang X, Guo H, Liu C, Liu J, Li L, Du X, Qian G (2014) Automated extraction of the archaeological tops of Qanat Shafts from VHR imagery in Google Earth. Remote Sens 6:11956–11976

Marani R, Reno' V, Stella E, D'Orazio T (2015) An improved ANOVA algorithm for crop mark extraction from large aerial images using semantics. In Azzopardi, Petkov N (eds) CAIP 2015, Part II, LNCS 9257, Springer International Publishing, Switzerland, pp 591–603

Marcolongo M, Morandi Bonacossi D (1997) Abandonment of the Qatabanian irrigation system in the Wadi Bayhan valley (Yemen): a geoarchaeological analysis. C R Acad Sci 325:79–86

Masini N, Lasaponara R (2007) Investigating the spectral capability of QuickBird data to detect archaeological remains buried under vegetated and not vegetated areas. J Cult Herit 8(1):53–60. doi:10.1016/j.culher.2006.06.006

Masini N, Lasaponara N, Orefici G (2009) Addressing the challenge of detecting archaeological adobe structures in Southern Peru using QuickBird imagery. J Cult Herit 10S:e3–e9. doi:10.1016/j.culher.2009.10.005

Masini N, Coluzzi R, Lasaponara R (2011) On the airborne Lidar contribution in archaeology: from site identification to landscape investigation. In: Chau-Chang Wang (ed) Laser scanning, theory and applications. Publisher Intech, pp 263–290. ISBN 978–953–307-205-0

Masini N, Lasaponara R, Rizzo E, Orefici G (2012) Integrated Remote Sensing Approach in Cahuachi (Peru): studies and results of the ITACA Mission (2007–2010). In: Lasaponara R, Masini N (eds) 2012, Satellite remote sensing: a new tool for Archaeology, Springer Verlag, Berlin/Heidelberg, pp 307–344. ISBN 978–90–481-8800-0, doi: 10.1007/978–90–481-8801-7_14

McCauley JF, Schaber GG, Breed CS, Grolier MJ, Haynes CV, Issawi B, Elachi C, Blom R (1982) Subsurface valleys and geoarchaeology of the Eastern Sahara revealed by Shuttle SAR. Science 218:1004–1020

McGarigal K (2013) Landscape pattern metrics. Ecological Statistics. doi:10.1002/9780470057339.val006.pub2

Menze BH, Ur JA (2011) Mapping patterns of long-term settlement in Northern Mesopotamia at a large scale. PNAS 109(14):E778–E787. doi:10.1073/pnas.1115472109

Mountrakis G, Im J, Ogole C (2011) Support vector machines in remote sensing: a review. ISPRS J Photogramm Remote Sens 66:247–259

Münch U (2003) Conceptual aspects of the Ärchäoprognose Brandenburg" project: archaeological site predictions for various test areas in Brandenburg. In Doerr M, Sarris A (eds) CAA 2002. The Digital Heritage of Archaeology. Proceedings of the 30th CAA conference held at Heraklion, Crete, Greece, 2–6 April 2002, pp 185–190

Myers A (2010) Camp Delta, Google Earth and the ethics of remote sensing in archaeology. World Archaeol 42(3):455–467. doi:10.1080/00438243.2010.498640. Archaeology and Contemporary Society, Taylor & Francis

Oltean I, Abell L (2012) High-resolution satellite imagery and the detection of buried archaeological features in ploughed landscapes. In: Masini N, Lasaponara R (eds) Satellite remote sensing. Springer, Dordrecht, pp 291–305

Palmer R (2013) Uses of declassified corona photographs for archaeological survey in Armenia. In: Hanson WS, Oltean IA (eds) Archaeology from historical aerial and satellite archives. Springer, New York, pp 279–290. doi:10.1007/978-1-4614-4505-0

Parker S (1985) Predictive modelling of site settlement systems using multivariate logistics. In: Carr C (ed) For concordance in archaeological analysis. Bridging data structure, quantitative technique, and theory. Westport Publishers, Kansas City, pp 173–207

Parry JT (1992) The investigative role of Landsat TM in the examination of pre-proto-historic water management sites in northeast Thailand. Geocarto Int 4:5–24

Pellegrino FA, Vanzella W, Torre V (2004) Edge detection revised. IEEE Trans Syst Man Cybern Part B Cybern 34:1500–1518

Rizzo E, Masini N, Lasaponara R, Orefici G (2010) ArchaeoGeophysical methods in the Templo del Escalonado (Cahuachi, Nasca, Perù). Near Surface Geophys 8(5):433–439. doi:10.3997/1873-0604.2010030

Quintanar J, Khan SD, Fathy MS, Zalat AF (2013) Remote sensing, planform, and facies analysis of the Plain of Tineh, Egypt for the remains of the defunct Pelusiac River. Sediment Geol 297:16–30

Scardozzi G (2012) Integrated methodologies for the archaeological map of an ancient city and its territory: the case of hierapolis in Phrygia. In: Lasaponara R, Masini N (eds) Satellite remote sensing: a new tool for archaeology, Remote sensing and digital image processing, vol 16. Springer Verlag Berlin/Heidelberg. ISBN:978-90-481-8800-0

Sever TL (1998) Validating prehistoric and current social phenomena upon the landscape of Peten, Guatemala. In: Liverman D, Moran EF, Rinfuss RR, Stern PC (eds) People and pixels: linking remote sensing and social science. National Academy Press, Washington, DC

Silvertown J (2009) A New Dawn for Citizen Science. Trends Ecol Evol 24:467–471

Smith ME (2010) The archaeological study of neighborhoods and districts in ancient cities. J Anthropol Archaeol 29:137–154

Smith ML (2014) Citizen science in archaeology. Am Antiq 79(4):749–762

Stewart C, Lasaponara R, Schiavon G (2013) ALOS PALSAR Analysis of the Archaeological Site of Pelusium. Archaeol Prospect 20:109–116

Stular B, Kokalj Z, Ostir K, Nuninger L (2013) Visualization of lidar-derived relief models for detection of archaeological features. J Archaeol Sci 39(2012):3354–3360

Tapete D, Cigna F (2016) SAR for landscape archaeology. In: Masini N, Soldovieri F (eds) Sensing the past. Geoscience and sensing technologies for cultural heritage. Springer, Cham. pp 101–116, chapter 5

Traviglia A, Cottica D (2011) Remote Sensing applications and archaeological research in the Northern Lagoon of Venice: the case of the lost settlement of Constanciacus. J Archaeol Sci 38(9):2040–2050

Trier ØD, Larsen SØ, Solberg R (2009) Automatic detection of circular structures in high-resolution satellite images of agricultural land. Archaeol Prospect 16:1–15
Ur J (2003) CORONA satellite photography and ancient road networks: a northern Mesopotamian case study. Antiquity 77:102–115
Wescott KL, Brandon RJ (eds) (2000) Practical applications of GIS for archaeologists. A predictive modeling kit. Taylor & Francis, London
White K, El Asmar HM (1999) Monitoring changing position of coastlines using Thematic Mapper imagery, an example from the Nile Delta. Geomorphology 29:93–105
Wilson DR (1982) Air photo interpretation for archaeologists. St. Martin's Press, London
Woodman PE, Woodward M (2002) The use and abuse of statistical methods in archaeological site location modelling. In: Wheatley D, Earl G, Poppy S (eds) Contemporary themes in archaeological computing. Oxbow Books, Oxford
Yao A, Jiang Z, Chen X, Liang Y (2015) Bronze age wetland/scapes: complex political formations in the humid subtropics of southwest China, 900–100 BC. J Anthropol Archaeol 40:213–229
Yarbrough LD, Easson G, Kuszmaul JS (2005) QuickBird 2 tasseled cap transform coefficients: a comparison of derivation methods Pecora, pp 23–27

Chapter 3
Preserving the Past from Space: An Overview of Risk Estimation and Monitoring Tools

Rosa Lasaponara and Nicola Masini

Abstract Earth observation (EO) technologies can enable advanced performance and new operational applications specifically addressed to security and risk (see, for example Copernicus program and Sentinel missions), also including the monitoring and preservation of heritage sites. EO techniques can provide operative tools for supporting heritage protection, conservation, and presentation identifying and monitoring factors that can adversely affect the property (see, for example, those listed in the UNESCO web site http://whc.unesco.org/en/factors/). In this context, UNESCO, in partnership with some space agencies of the world (NASA, ESA, DLR, ASI, CNES, Chinese), over the years has strongly promoted the use of space technologies to assess the state of conservation of cultural and natural heritage sites. Nevertheless, even if the potential of EO technologies for assessing and monitoring natural and man-made disasters is well known, still today the application of RS data in operational disaster management and monitoring is a difficult task. To move from scientific to operational applications there are gaps to be filled and needs to be addressed. To improve the risk estimation and management based on remote sensing data, it is particularly important to set up operational approaches and methods for diverse applications and risks, with protocols and quantitative evaluations of accuracy and reliability.

Keywords Optical satellite remote sensing • Archaeology • Proxy indicator • Prediction models • Image enhancement

R. Lasaponara (✉)
CNR-IMAA, Institute of Methodologies for Environmental Analysis,
C. da S. Loya, 85050 Tito Scalo, Potenza, Italy
e-mail: rosa.lasaponara@imaa.cnr.it

N. Masini
CNR-IBAM Institute for Archaeological and Monumental Heritage,
C. da Santa Loja, 85050, Tito Scalo, Potenza, Italy
e-mail: n.masini@ibam.cnr.it

N. Masini, F. Soldovieri (eds.), *Sensing the Past*, Geotechnologies
and the Environment 16, DOI 10.1007/978-3-319-50518-3_3

3.1 Introduction: Context Definition

The preservation of cultural heritage is a pressing issue, especially for the territories subjected to a long period of human action that has adversely influenced both environment and landscape, producing a significant deterioration of archaeological features and alteration of historical landscape. The preservation and enhancement of natural and cultural heritage, including landscape, is today one of the topics of great economic and social significance. It is a strategic priority not only to transmit cultural treasure and evidences of the human past to future generations (for more detail, see Masini and Lasaponara 2016, this volume) but also to exploit them as a strategic and valuable economic asset, if inspired to sustainable development strategies. Cultural heritage can be a resource for economic development based on the principles of sustainable use of resources, not only for the benefit of society but also as a useful source of human development. This is an extremely important key factor for the countries that are owners of an extraordinary cultural legacy which must be preserved from the significant potential alterations from anthropogenic activities having a significant effect upon atmosphere, water, soil, and in turn on heritage and landscape. In this context, systematic monitoring activities may provide effective information and tools for assessing threats and risks on historical buildings, landscape, and buried remains.

In this context, it is important to highlight that cultural heritage and historical landscapes, especially where heavily influenced by human activities, have to be systematically monitored and accordingly managed and preserved.

Today, as also highlighted by UNESCO (Fig. 3.1), cultural heritage is "increasingly threatened with destruction not only by the traditional causes of decay, but also by changing social and economic conditions which aggravate the situation with even more formidable phenomena of damage or destruction" (from the general conference of the United Nations Educational, Scientific and Cultural Organization meeting in Paris from 17 October to 21 November 1972, at its 17th session, available online (http://whc.unesco.org/en/conventiontext/)).

According to UNESCO the factors that most of all threaten cultural heritage sites are these:

1. Urban sprawl
2. Pollution
3. Biological resource use/modification
4. Physical resource extraction
5. Local conditions affecting physical fabric
6. Deliberate destruction and vandalism (Fig. 3.2)
7. Social/cultural uses of heritage
8. Climate change
9. Severe weather events (Fig. 3.3)
10. Sudden ecological or geological events
11. Management and institutional factors
12. Transportation and utilities infrastructure

Fig. 3.1 World heritage sites in danger (http://whc.unesco.org/en/danger/)

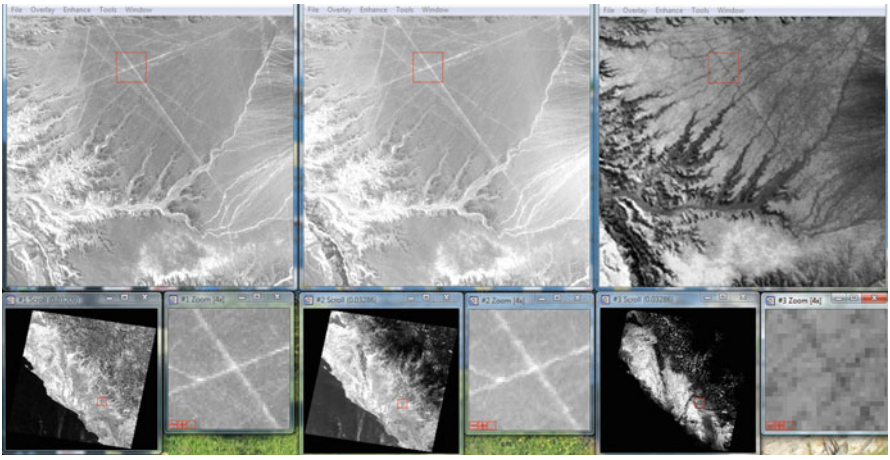

Fig. 3.2 Nasca lines threatened by vandalism and other human activities. The picture shows some detail from ASTER satellite data of the geoglyphs at different scales and spectral bands (VNIR, SWIR, TIR)

13. Invasive/alien or hyperabundant species
14. Terrorism or civil unrest

In past decades, many countries across the world have been involved and are today experiencing increasing frequency and impact of disasters, such as extreme

Fig. 3.3 Metaponto on the Ionian coast of Southern Italy: detail of the archaeological site affected by floods

hydrometeorological events, most probably related to climate change, floods, landslides, earthquakes, volcano eruptions, fires, uncontrolled urbanization, and air pollution.

To face the increasing frequency and adverse impact of disasters it is necessary to set up systematic monitoring activities and tools to identify issues and changes that can destroy or deteriorate heritage, increasing its vulnerability. This need may require the use of heterogeneous data essential to identify the major threats as well as to reconstruct the historical landscape and to compare it with the current one, so as to detect remains of the past, analyze the transformations, and detect ongoing changes and potential threats.

Although cultural heritage sites are documented and preserved, to date there have been limited monitoring actions and documentation of how cultural heritage sites are affected by the recent increasing impact of both natural and man-made disasters.

The potential of remote sensing technologies for assessing and monitoring natural and man-made disasters is well known, even if the application of remote sensing (RS) data in operational disaster management and monitoring is still a difficult task. There are gaps to be filled and a need to move from scientific to operational applications. In the past 20 years, the improved performance offered by space optical and radar sensors have opened the possibility of using RS data and tools for a large variety of applications ranging from landslide and subsidence to surface deformation, land cover degradation, flood, forest fire, volcanic eruptions, air pollution, and degradation phenomena.

At present it is particularly important to also improve risk estimation, mitigation, and management using information and data from remote sensing to set up operational approaches and methods for diverse applications and risks, as well as protocols and quantitative evaluations of their accuracy and reliability.

These needs and gaps have been also recently highlighted by ICOMOS (http://www.iccrom.org/ifrcdn/pdf/ICCROM_17_RiskPreparedness_en.pdf). Examples of the most critical and urgent needs to preserve cultural heritage are listed here:

- Environmental assessment and monitoring (pollution, climate change, seismic risk)
- Anthropic pressure evaluation and management
- Telesurvey and Geographic Information Systems (GIS) for protection and management of tangible cultural heritage
- Prenormative studies for the guaranteed protection and management of tangible cultural heritage
- Study of environmental changes over time (Fig. 3.4)

A preventive approach against extreme natural events (seismic events, flooding, storms, landslides, fire) and measures of "first aid" requires these assessments:

- Changes in hydrogeological conditions in the ground: technologies for stabilizing historic structures
- Best conservation practices against specific attacks (physical, chemical, biological) to prevent damage of specific materials
- Intelligent multisensor systems for early warning (modeling, local network for monitoring systems), including telediagnosis

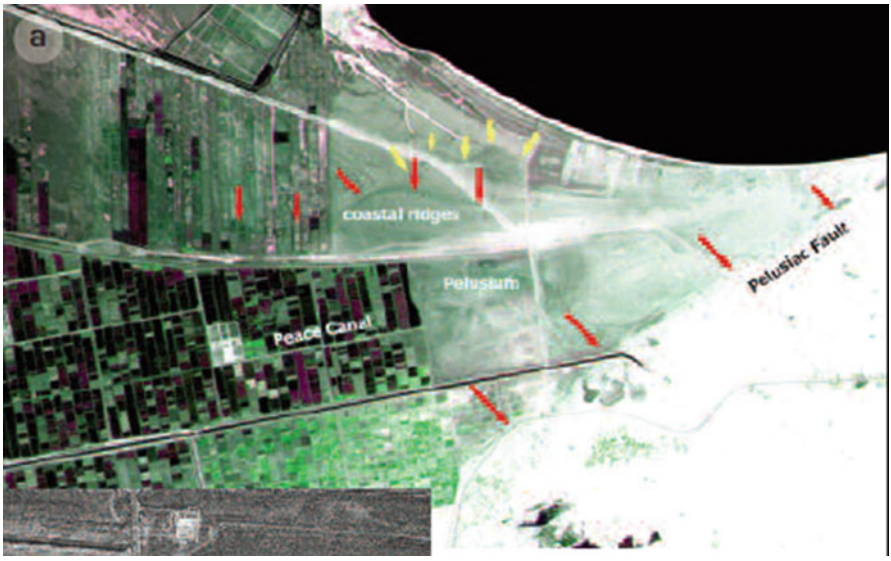

Fig. 3.4 Pelusium in Northern Egyptum. ASTER satellite imagery indicates traces of the coastal regression and the Pelusiac fault, which extends southwest from the Levant to the northwest part of Sinai and ends on the eastern extent of the Nile Delta (Lasaponara and Masini 2015)

- Techniques for inventory, cataloguing, and traceability of cultural heritage objects

With these requirements:

- Critical levels of synergic pollutants in a context of environmental conditions (indoor/outdoor)
- Impact of climate change on materials and structures and adaptation of technologies to mitigate negative effects
- New solutions for development, assessment, and reporting of analysis protocol for the time effects evaluation of treatments (e.g., cleaning, biocides) and materials
- Web mapping and web GIS innovative tools for the telemonitoring and remote control of archaeological sites and cultural landscapes
- Development of advanced systems for telesurvey and remote fruition of underwater cultural heritage
- Preservation of twentieth-century military heritage: objects, buildings, and landscapes
- Safeguard of areas of archaeological interest with particular reference to crop mark sites (Fig. 3.5)

The different areas of intervention for cultural heritage require the availability of rigorous information for study and documentation, protection and conservation, monitoring, risk assessment, and management.

Fig. 3.5 Crop marks: proxy indicators of the presence of archaeological buried sites that are threatened by wind turbines. The site is in Apulia (Southern Italy)

For these aims it is necessary to improve capacity in the use of remote sensing technologies and data to monitor the state of conservation of cultural heritage, moving from scientific exercises to operational applications and tools.

3.2 Environmental Assessment and Monitoring for Preservation of Cultural Heritage

Satellites provide reliable tools not only for the identification but also for the analysis, monitoring, and management of landscape resources, as well as for supporting the conservation (at least from a digital aspect) of the features that define the cultural identity of a specific territory.

Earth observation (EO) is being successfully used for providing ongoing monitoring of natural and cultural sites, for assessing natural and man-made risks including emerging threats to heritage sites. The current availability of long-term satellite time series provides an excellent tool to observe and monitor changes from a global view down to a local scale. National (DLR, CNES, ASI, JAXA) and international space agencies, such as NASA and ESA, provide valuable satellite data very useful for capturing regional environmental changes along with the impact induced by human activities at a site level. In particular, from NASA website satellite time series (as AVHRR, SPOT-VEGETATION, MODIS, Landsat TM, etc.) are available free. More recently, ESA delivers Sentinel products and open source software tools specifically set up for processing active and passive data. Moreover, the availability since 2000 of very high resolution (VHR) data with spatial resolution less than 1 m up to pixels at 30 cm (TERRA-SAR, WorldView-3, today) enables the creation of accurate and updated maps.

Satellite images provide "a means to improve the information flow and communication among site managers and conservation authorities: "an image is worth a thousand words" (UNESCO web-site site http://www.unesco.org/science/remotesensing/?id_page=74&lang=en).

Many national, regional, and global assessments of environmental degradation were undertaken during the past 30 years, including soil, subsoil, water, vegetation degradation, urban expansion, and atmospheric pollutants. However, available procedures for the assessment of environmental degradation are still unsatisfactory because these methods are often too costly for surveying large areas and rely on specific components of the degradation process without being able to integrate them in a unique process. The availability of satellite time series provides useful tools for capturing environmental degradation processes at different spatial and temporal scales. Satellite time series enable the monitoring of subtle long-term variations of important parameters, such as surface temperature, moisture content, vegetation indices, and aerosols.

Detecting temporal changes by observing surfaces at different times is one of the most important applications of satellite sensors because they can provide

multidate imagery at short intervals on a global scale. National and international agencies provide long time series of the aforementioned products obtained from MODIS, AVHRR, VEGETATION, and also Landsat TM data useful to assess environmental degradation and capture changes from global to local-scale change detection analyses.

Detecting regions of change in images of the same scene taken at different times has widespread interest because of the large number of applications in diverse disciplines. Important applications of change detection include remote sensing (see, for example, Bruzzone and Prieto 2002; Collins and Woodcock 1996; Huertas and Nevatia 2000), civil infrastructure (Landis et al. 1999; Nagy et al. 2001), and underwater sensing (Edgington et al. 2003; Singh 1989).

Earth observation data provide important and useful spatial and temporal information that can be used to make better decisions, design policies, and address problems that range in scale from local to global. Costs go down, quality increases, and data become increasingly available for important everyday applications.

Despite the diversity of applications, change detection researchers employ many common processing steps and core algorithms [see the overviews on change detection by Singh (1989) and Coppin and Bauer (1996)]. Starting from early application, nowadays much experience has already been accumulated in exploring change detection techniques for medium/high spatial resolutions, but very few methods can be found for the new generation of very high spatial resolution satellite sensors: passive such as IKONOS, QuickBird, or GeoEye, or active such as Cosmo SkyMed and TERRA SAR.

The availability of VHR data greatly increases the potentiality in monitoring changes from space, but at the same time, the relatively large amount of data may induce a decrease in our ability, because VHR data better resolve the details of changes but present a new challenge over other data processing approaches and methodologies. The large amount of data stored in VHR satellite sensors must be analyzed using advanced procedures; this makes it possible to overcome the mixed pixel problem inherent with more moderate resolution satellite systems.

3.2.1 Landscape Degradation: Nonnative Plant Invasion

Identification of nonnative plants by monitoring is quite complex and difficult to accomplish in situ; moreover, field surveys are time consuming and expensive. The use of satellite remote sensing techniques can effectively support the detection and categorization of areas characterized by invasion of alien plants as well as the identification of other vulnerable habitats.

Analysis based on multitemporal and multisensor remote sensing data can provide operational tools for the monitoring and mapping of invasive plants, which are generally quite aggressive, characterized by fast and continued spread, so that they reduce and strongly compromise local biodiversity.

Several investigations have pointed out that satellite imagery can suitably help us to control and prevent exotic plant populations as well as to effectively and systematically monitor vegetation dynamics and identify anomalies.

Maps based on the multitemporal investigation of satellite-based parameters, such as the commonly used normalized difference vegetation index (NDVI) enhances the signal of photosynthetically active reactions, providing information on changes in ecosystems as well as on the types and quantity of vegetation cover.

3.2.2 Landscape Degradation: Soil Erosion

Remote sensing is now recognized worldwide as an effective, accurate, and economical method to monitor changes in land cover from the global down to a local scale (Fig. 3.6). For large areas, the use of remote sensing data is an essential tool for change monitoring and mapping as well as for monitoring and evaluating the ongoing land degradation processes, which have been particularly evident in the past 30 years. The so-called erosion processes affect large areas and are frequently strongly related to land degradation processes. Satellite technologies provide systematic and periodical multitemporal observations that can be fruitfully adopted for multitask and multipurpose investigations and aims, ranging from natural and anthropogenic hazards such as land-use changes, landscape deterioration, and soil degradation in the surroundings of archaeological sites (Fig. 3.7) and geoparks (Fig. 3.8).

3.2.3 Landscape Degradation: Coastal Erosion

Coastal zones are under threat from both natural and anthropogenic activities linked to the unsustainable use and overexploitation of resources. At present, more than 70% of the world's beaches are affected by coastal erosion, today considered as a serious hazard for many countries including those in Europe. The use of multitemporal, multisensory satellite data from high- and moderate-resolution sensors can support the monitoring and assessment of shoreline variations as well as analysis of water temperature, salinity, and pollution, along with other potential threats to our coasts. Assessments of shoreline changes and coastal monitoring are needed not only to predict events (such as floods) that may adversely affect environment, human health, and archaeological sites and built heritage but even to set up mitigation strategies.

Figure 3.9 shows the use of different data for the monitoring of shoreline variations close to the Metaponto archaeological area. The use of multitemporal analysis (1950, 1961, 2004, 2013) enabled estimating the changes of the Ionian coast, which from the middle of the twentieth century was characterized by alternating phases of growth and regression. The latter has prevailed since the early 1960s and continues today with varying rates of erosion.

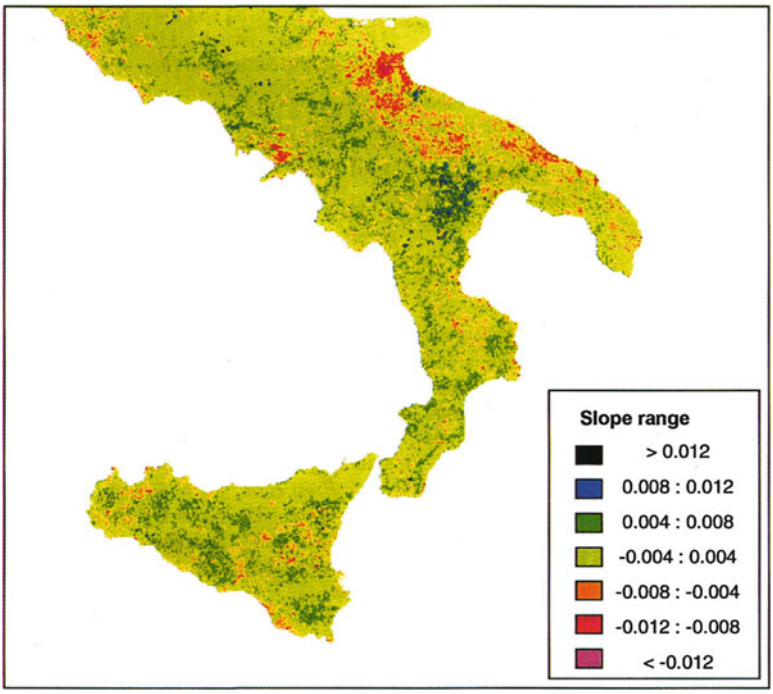

Fig. 3.6 Land degradation based on satellite data obtained for the south of Italy using a time series of AVHRR data

3.2.4 Landscape Degradation: Urban Sprawl

Urban sprawl indicates the expansion of urban areas generally referring to an uncontrolled and massive urbanization process, considered today as one of the most important transformations of our planet and considered now a global concern.

Even if the phenomenon is particularly dramatic in developing countries, unfortunately continuing low-density sprawl is also observed in industrialized countries. This sprawl not only adversely impacts environments with significant loss of prime agricultural lands and negative effects on carbon emissions and energy use, but also frequently impacts heritage sites and even UNESCO sites, as in the case of Giza in Egypt (Fig. 3.10), Pachacamac (see Fig. 3.11), and Chan Chan in Peru.

3.2.5 Landscape Degradation: Pollution

Assessment of air pollution has been performed by different means over the years, and recently the use of satellite data for detecting and monitoring atmospheric

Fig. 3.7 Satellite-based identification of fragile areas surrounding the archaeological park of Metaponto

pollution has received considerable attention, especially for application in industrial and urban areas (Hadjimitsis et al. 2002). Methods based on satellite data (such as Landsat TM, SPOT MODIS images) are focused on the estimation of aerosol optical thickness (AOT), which is a measure of aerosol loading in the atmosphere and therefore is considered as the main significant parameter of the presence or absence of atmospheric pollutants. A higher AOT value expresses the degree to which aerosols prevent the transmission of light; therefore, higher columnar of aerosol loading means lower visibility and higher aerosol concentration (Wang and Christopher 2003). AOT has been used as an indicative parameter for assessing air pollution close to cultural heritage sites.

Several state-of-the-art aerosol retrieval techniques provide aerosol properties on a global scale, as, for example, products from the moderate resolution imaging spectroradiometer (MODIS) on board the Earth Observing System (EOS) Terra and Aqua satellites (King et al. 1999). MODIS measures the total solar radiance scattered by the atmosphere as well as the sunlight reflected by the Earth's surface and attenuated by atmospheric transmission. Therefore, MODIS offers useful data for optical thickness (Tang et al. 2004).

Nevertheless, the spatial resolution of the current aerosol optical thickness (AOT) products from MODIS (available free of charge from the NASA website) is 10 km. This product is suitable for global research, but it faces difficulties in local area research, especially in urban areas. However, new aerosol retrieval algorithms for

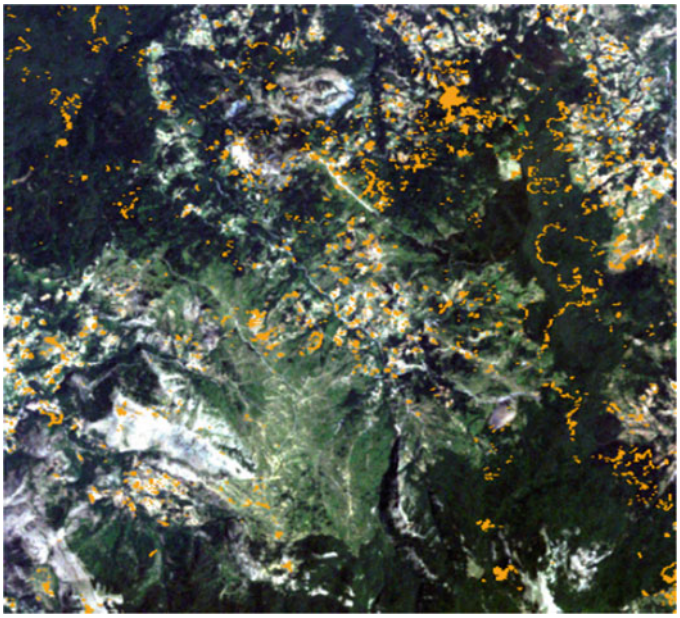

Fig. 3.8 Pollino National Park inside the Geopark UNESCO since 2016: negative anomalies (fragile areas)

the (MODIS) 500-m resolution data (see, for example, Dabin et al. 2010) have been developed to retrieve aerosol properties over land, which helps with addressing the aerosol climatic issues at a local or urban scale.

Over the years, several algorithms for determining aerosol optical thickness have been developed. For example, Kaufman et al. (1990) used the radiance difference recorded between a clear and a hazy day for land and water dark targets. Sifakis and Deschamps (1992) calculated the aerosol optical depth by using SPOT images and exploiting the difference between one reference image (acquired under clear atmospheric conditions) and a polluted image. Their method was based on the fact that, after correction of solar and observation angle variations, the remaining deviation of apparent radiances is mainly caused by pollutants.

Retalis (1998) and Retalis et al. (1999) estimated air pollution in the urban areas of Athens by using the Landsat TM band 1 and correlating the aerosol optical thickness with the acquired air pollutants.

Hadjimitsis and Clayton (2009) developed a method combining the darkest object subtraction (DOS) principle and the radiative transfer equations to evaluate the AOT value for Landsat TM bands 1 and 2. Hadjimitsis (2009) developed a method to determine the aerosol optical thickness through application of the contrast tool (maximum contrast value), radiative transfer calculations, and the "tracking" of the suitable darkest pixel in the scene for Landsat, SPOT, and high-resolution imagery such as IKONOS and Quickbird.

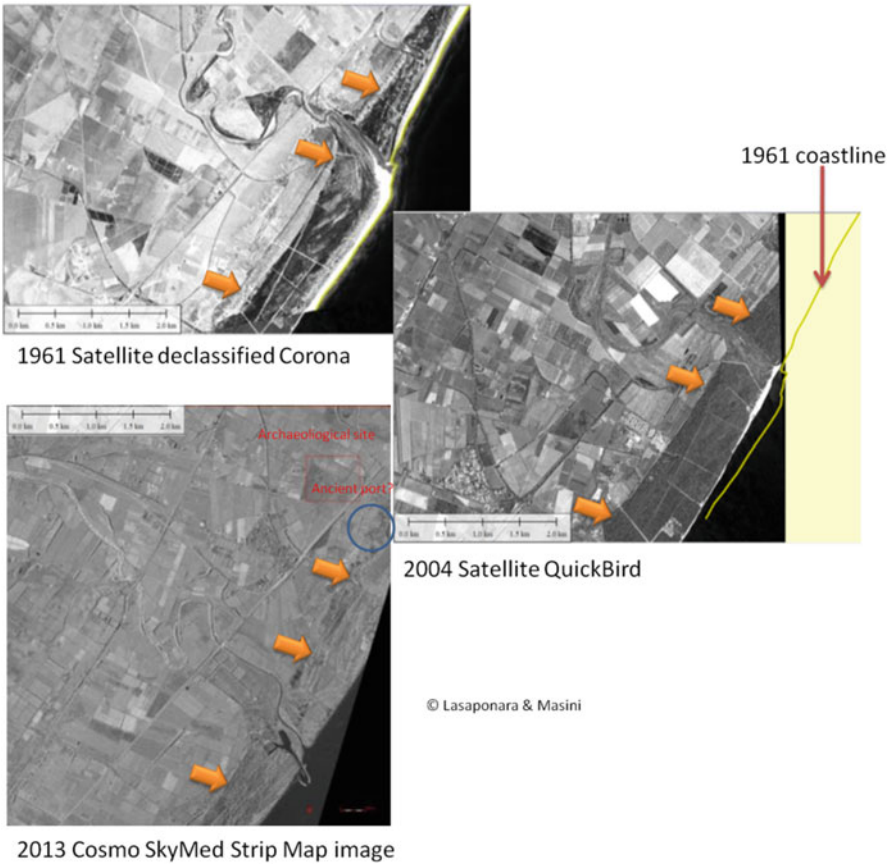

Fig. 3.9 Change detection of Ionian coastline near the ancient Metapontum (see *red box*(?), *bottom left*) by using different remote sensing data: Corona (1961), QuickBird (2004), and Cosmo SkyMed Strip Map (2013). The *orange arrows* denote the possible coastline in ancient times (Greek/Roman) when in Metapontum there was a port (indicated with *blue circle*, *bottom left*)

The future availability of data from the Sentinel-5 precursor (to be launched in 2017) will assure measurements of ozone, NO_2, SO_2, CH_4, CO, and aerosols. It will bridge the gap between Envisat/EOS Aura and Sentinel-5 (the latter expected to be launched in 2020). It will provide measurements of elements of atmospheric chemistry at high temporal and spatial resolution.

The availability of systematic measurements of the main atmospheric pollutants will promptly provide estimation of their impact on the natural and cultural heritage, on the basis of proxy ad hoc defined for the specific purposes. Moreover, this will address the current lack of information from in situ measurements and the strong limits of their statical spatialization that today affect these analyses.

In past decades, awareness related to the impact of pollution on cultural heritage has increased as well as attention to the interaction between microclimate (in particular, moisture) and pollutants on indoor and outdoor heritage. As is well

Fig. 3.10 Urban aggression near the Giza pyramids (WorldView2 true color image)

known, cultural heritage, with particular reference to architecture and built heritage, is constantly exposed to strong fluctuations (diurnal, seasonal, decadal) of meteorological parameters that can strongly accelerate the degradation mechanisms. To understand well this phenomenon, it is important to perform systematic monitoring of meteorological parameters and their fluctuations along with their interaction with atmospheric pollutants, at least in the most precious and vulnerable areas. Moisture and temperature fluctuations negatively impact not only vegetation but also have an important role in the degradation phenomena of buildings and artifacts. In particular, it should be considered that variations in temperatures induce material expansions, which in turn cause strain between surfaces and underlying structures. It must be considered that cyclic variations tend to damage the materials, and the faster the cycles the greater the damage.

Therefore, it is quite important to have information related to daily cycles of temperatures, because the shorter variations impact the material more significantly than longer as, for example, higher seasonal variations.

Moreover, moisture content has a strong influence on the material and artifacts decay process because the negative impacts are activated in different ways. In the presence of pollutants, humidity favors chemical reactions that alter stone material as in the case of the transformation of calcareous rocks in gypsum in the presence of SO_2 (the so-called black crust)[1] (see Fig. 3.12).

[1] It is the result of the sulfation process that is the transformation of calcium carbonate into calcium sulfate dihydrate.

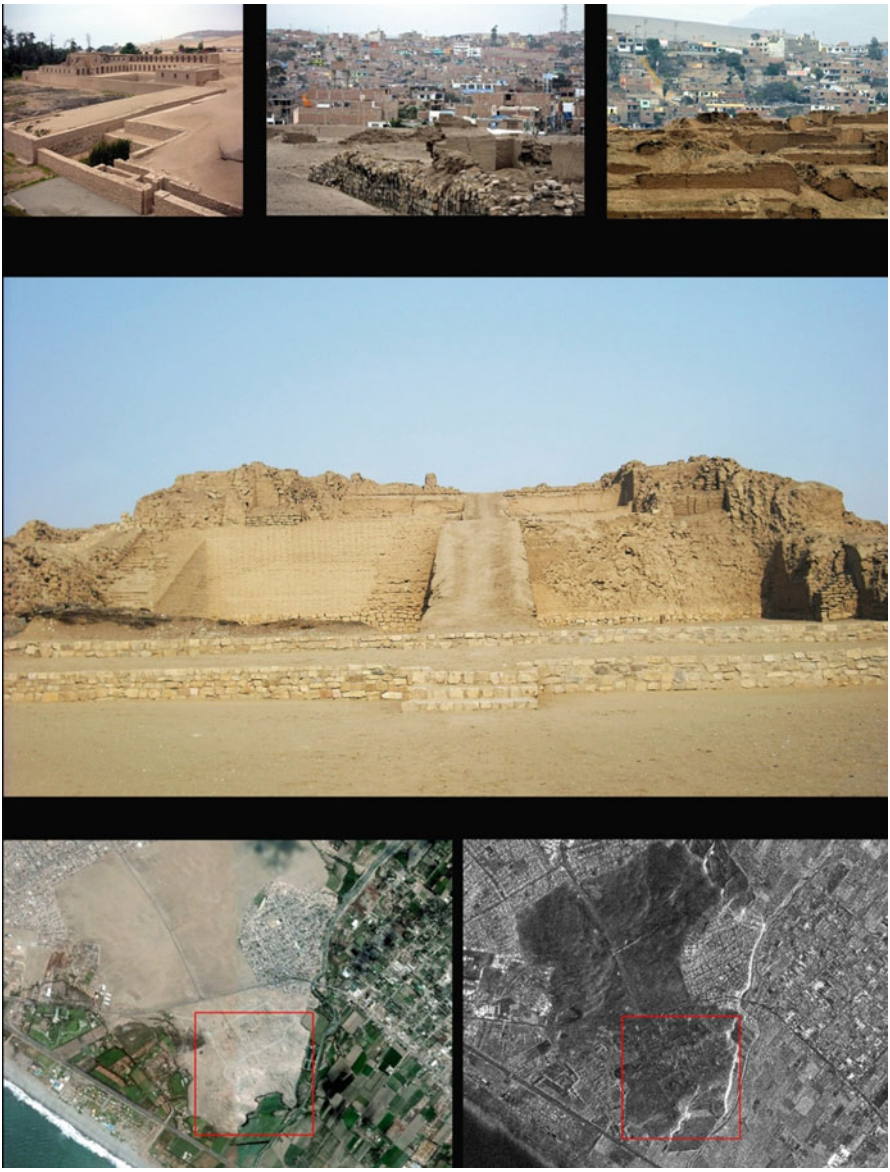

Fig. 3.11 Urban sprawl around the archaeological site of Pachacamac near Lima in Peru. *Top*, from *left* to *right*: details of Acclahuasi, other ruins, and the building of the modern Pachacamac very close to the archaeological site. *Middle*: detail of a pyramid with ramp. *Bottom*: optical and SAR satellite image of Pachacamac including the archaeological site (denoted by *red box*)

Fig. 3.12 Historical center of Dubrovnik: molded frame affected by the black crust

Fig. 3.13 Historical center of La Valletta: calcarenite blocks affected by alveolarization

Water acts in synergy with temperature: water temperature-induced changes in the quantity of water that can be absorbed. As a consequence, variation in temperature and increasing or decreasing of water absorbed by material cause expansion and contractions that can seriously damage material and artifacts.

In porous rocks, as, for example, calcarenite, alveolarization is particularly relevant. As practical examples we can consider the UNESCO site of Sassi and the Park of the Rupestrian Churches of Matera, the Baroque town of Lecce, the castle and historical palaces in La Valletta (also exposed to marine aerosol) where the evaporation process causes an increasing concentration of dissolved salts (see Fig. 3.13).

This information can be obtained using free-of-charge satellite data provided by MODIS (Figs. 3.14 and 3.15) and TM time series.

Moreover, it is important to consider that pollutants also affect the conservation of the material and strongly accelerate and increase the decay processes. The

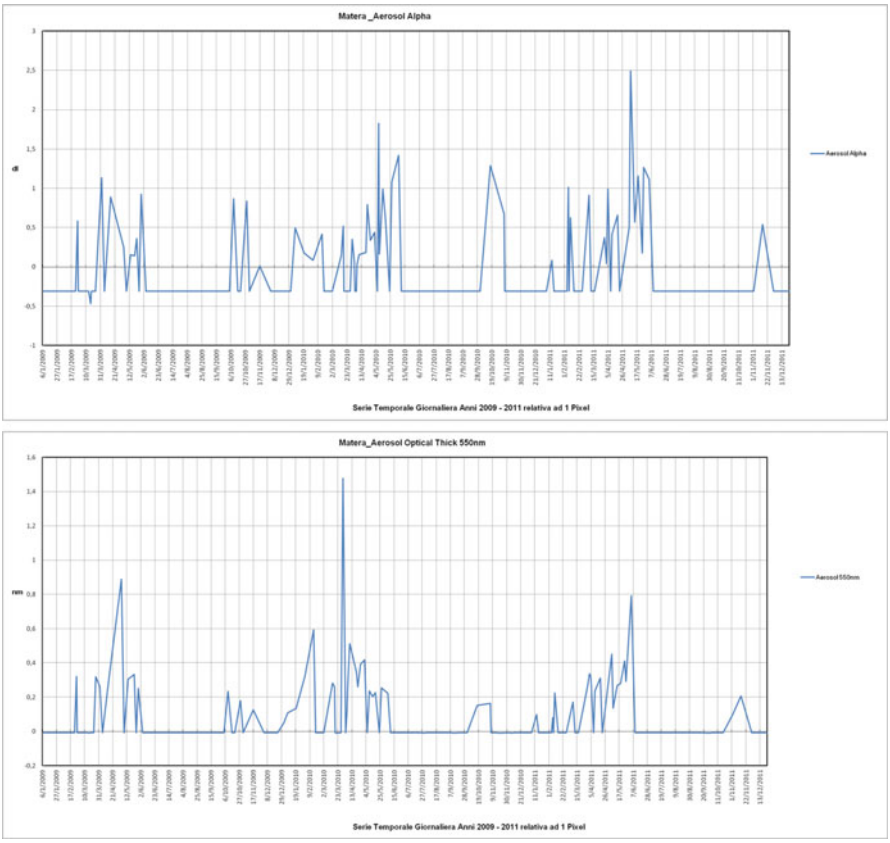

Fig. 3.14 MODIS-derived estimation of aerosol content obtained from 2009 to 2011 for the UNESCO site of Sassi Matera

state of the conservation of monuments and artifact depends on the quantity and quality of the pollutants as well as on their interaction with moisture and rain; for example, heavy showers wash away pollutants whereas a light drizzle activates the pollutants without removing them. Moreover, the frequency and the duration of humidification as well the typology of materials, their roughness, porosity, and intrinsic characteristics determine the specific decay characteristics as well as their dynamics and local effects. Therefore, to mitigate these critical conditions, knowledge of pollutants present in the atmosphere is important along with their effect on the specific materials of both indoor and outdoor heritage.

For these purposes, the satellite can provide systematic global monitoring tools at different temporal and spatial scales using different data sources, such as MODIS, Landsat TM, and Sentinel 2 time series.

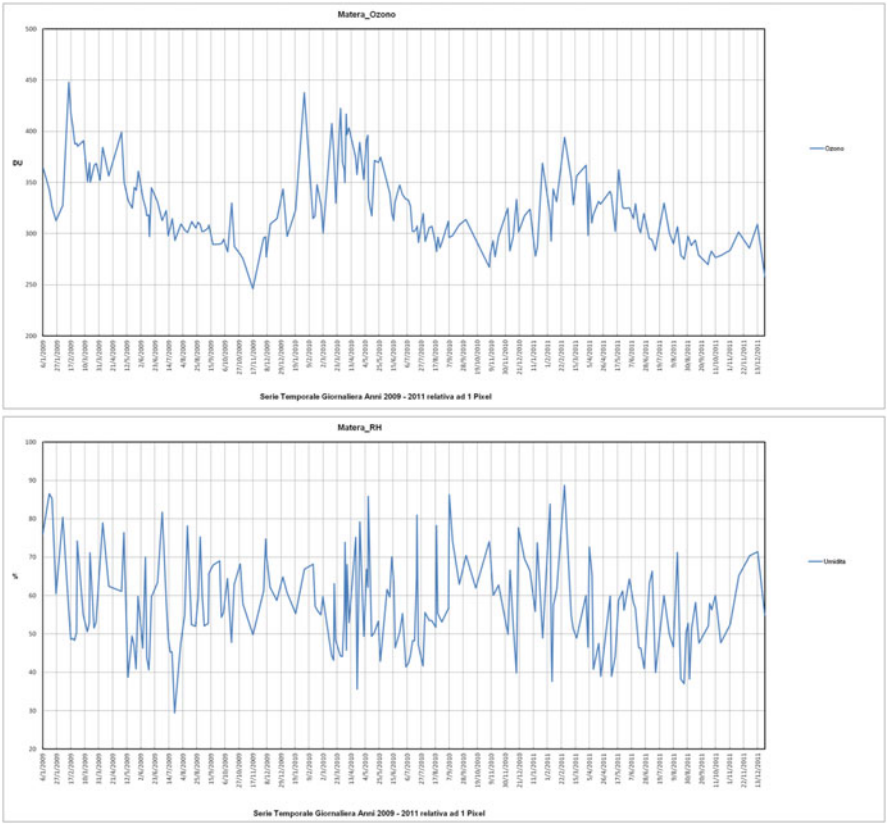

Fig. 3.15 MODIS-derived estimation of ozone and air moisture content obtained from MODIS data from 2009 to 2011 for the UNESCO site of Matera

3.3 Climate Change

Climate change during the next 100 years will likely have a range of direct and indirect effects on both natural and material environments, including the historic built environment. Important changes will include alterations in temperature, precipitation, extreme climatic events, soil conditions, groundwater, and sea level. Some processes of building decay will be accelerated or worsened by climate change whereas others will be mitigated. The impacts on individual processes can be described by linking meteorological parameters to the response of material surfaces of archaeological and historic structures, and this step is critical:

- To determine the meteorological parameters and changes most critical to the built cultural heritage
- To develop mitigation and adaptation strategies for historic buildings, sites, monuments, and materials that are likely to be most affected by climate change

As a whole, and even suggested by UNESCO, indicators can be used to complement direct monitoring or as an alternative where monitoring is not available. Table 3.1 lists the indicators recommended by UNESCO for assessing the impact of climate change on our heritage.

Scientific understanding of traditional materials and assemblies is the foundation of sustainable management of World Heritage sites in a changing climate, including chloride loading, high summer temperatures, and prolonged rainfall. The latter is often the main cause of weathering also in a desert environment as in the case of the Great Sphinx at Giza (Fig. 3.16), strongly weathered by heavy rain, probably caused by a climate change, occurred during the 4th Dynasty. Information based on cross-field monitoring must be sensitive to the scale and time of problems and guidance must be designed accordingly.

Not only should extreme events be documented but also short cycles of change that together can make significant changes to cultural heritage. Records of short cycle changes will gradually expand the notion of climate change impact on cultural heritage and enrich understanding of this phenomenon.

3.4 Space Assessment and Monitoring of Ground Displacements, Landslide, and Floods

In recent years, Spaceborne differential interferometric synthetic aperture radar (DInSAR) techniques have demonstrated their potential as land deformation measurement and ground displacements, and as such they are of great interest as possible operational tools for civil protection institutions needed to address landslide risk.

DInSAR techniques date back to 1989 when L-band SEASAT SAR data were first exploited to this aim as described in (Gabriel et al. 1989). For a general review of SAR interferometry, see Rosen et al. (2000). In the last few years, the capability of interferometric techniques has been considerably improved by using persistent scatterer interferometry (PSI) techniques based on large stacks of SAR images acquired over the same area, instead of the classical two images. PSI techniques were first published in the article by Ferretti et al. (2000). A general review of DInSAR can be found in Crosetto et al. (2005). An extensive list of successful examples is provided in Rosen et al. (2000). The significant advances of the DInSAR techniques have made them quantitative geodetic tools for deformation monitoring, rather than simple qualitative tools. A specific review of PSI applications in urban areas is provided in Crosetto et al. (2010).

Nevertheless, it is important to highlight that today the available DInSAR techniques are still not universal and robust because of two main intrinsic limitations: (i) coherence loss (or lack of persistent scatterers, PS) and (ii) the need to handle phase ambiguities (or wrapped phases). More information on the limitations of the DInSAR techniques is given by Crosetto et al. (2010).

Table 3.1 Impacts matrix, namely indicators defined and recommended by UNESCO for assessing main climate change impact on the heritage

Climate indicator	Climate change risk	Physical, social, and cultural impacts on cultural heritage
Atmospheric moisture change	Flooding (sea, river)	pH changes to buried archaeological evidence
	Intense rainfall	Loss of stratigraphic integrity because of cracking and heaving from changes in sediment moisture
	Changes in water table levels	Data loss preserved in waterlogged/anaerobic/anoxic conditions
	Changes in soil chemistry	Eutrophication accelerating microbial decomposition of organics
	Groundwater changes	Physical changes to porous building materials and finishes caused by rising damp
	Changes in humidity cycles	Damage caused by faulty or inadequate water disposal systems; historic rainwater goods not capable of handling heavy rain and often difficult to access, maintain, and adjust
	Increase in time of wetness	Crystallization and dissolution of salts caused by wetting and drying affecting standing structures, archaeology, wall paintings, frescos, and other decorated surfaces
	Sea salt chlorides	Erosion of inorganic and organic materials by flood waters
		Biological attack on organic materials by insects, molds, fungi, invasive species such as termites
		Subsoil instability, ground heave, and subsidence
		Relative humidity cycles/shock causing splitting, cracking, flaking and dusting of materials and surfaces
		Corrosion of metals
		Other combined effects, e.g., increase in moisture combined with fertilizers and pesticides
Temperature change	Diurnal, seasonal, extreme events (heat waves, snow loading)	Deterioration of facades by thermal stress
		Freeze–thaw/frost damage
		Damage inside brick, stone, ceramics that has become wet and frozen within material before drying
	Changes in freeze–thaw and ice storms, and increase in wet frost	Biochemical deterioration
		Changes in “fitness for purpose” of some structures. For example overheating of the interior of buildings can lead to inappropriate alterations to the historic fabric by the introduction of engineered solutions
		Inappropriate adaptation to allow structures to remain in use

(continued)

Table 3.1 (continued)

Climate indicator	Climate change risk	Physical, social, and cultural impacts on cultural heritage
Sea level rises	Coastal flooding	Coastal erosion/loss
		Intermittent introduction of large masses of "strange" water to the site, which may disturb the metastable equilibrium between artifacts and soil
		Permanent submersion of low-lying areas
	Seawater incursion	Population migration
		Disruption of communities
		Loss of rituals and breakdown of social interactions
Wind	Wind-driven rain	Penetrative moisture into porous cultural heritage materials
	Wind-transported salt	Static and dynamic loading of historic or archaeological structures
	Wind-driven sand	Structural damage and collapse
	Winds, gusts and changes in direction	Deterioration of surfaces by erosion
Desertification	Drought	Erosion
	Heat waves	Salt weathering
	Fall in water table	Impact on health of population
		Abandonment and collapse
		Loss of cultural memory
Climate and pollution acting together	pH precipitation	Stone recession by dissolution of carbonates
		Blackening of materials
	Changes in deposition of pollutants	Corrosion of metals
		Influence of biocolonialization
Climate and biological effects	Proliferation of invasive species	Collapse of structural timber and timber finishes
	Spread of existing and new species of insects (e.g. termites)	Reduction in availability of native species for repair and maintenance of buildings
	Increase in mold growth	Changes in the natural heritage values of cultural heritage sites
	Changes to lichen colonies on buildings	Changes in appearance of landscapes
	Decline of original plant materials	Transformation of communities
		Changes in the livelihood of traditional settlements
		Changes in family structures as sources of livelihoods become more dispersed and distant

Fig. 3.16 The Great Sphinx at Giza. Its conservation is threatened by strong weathering processes

The most important limitation of DInSAR is coherence loss, which means that the measure deformation is only over the available coherent pixels and PSs. Statistical analysis provides the estimation for the whole image data. The second limitation is related to the ambiguous nature of the DInSAR observations: it suffers severe limitations in the capability to measure fast deformation phenomena.

To overcome these drawbacks, several DInSAR data analysis procedures have been devised in the last 20 years ranging from a very simple approach, such as the standard DInSAR configuration (based on a single interferogram computed from a pair of complex SAR images) to PSI techniques, based on the use of redundant SAR data and quite refined estimation procedures.

Recently, Crosetto et al. (2011) proposed different complementary DInSAR methods, used together to obtain improved performance and flexibility. In particular, Crosetto et al. (2011) proposed the joint use of the (i) standard DInSAR analysis [see, for example, Biescas et al. (2007) and Crosetto et al. (2002)]; (ii) PSI analysis over small areas [see, for example, Biescas et al. (2007), Monserrat et al. (2011)]; (iii) full PSI analysis with linear deformation model [see, for example, Berardino et al. (2002) and Lanari et al. (2004)]; and (iv) full PSI analysis with free deformation model (see Crosetto et al. 2011). During the past decade, the listed methodologies were implemented, tested, and validated using different types of spaceborne SAR data acquired by the following sensors: ERS-1 (C-band), ERS-2 (C-band), ASAR-Envisat (C-band), TerraSAR-X (X-band), and Cosmo SkyMed (X-band), also for detecting deformation at a single-building scale from the perspective of conservators. This analysis has been done for the historical center of Rome by Cigna et al. (2014) by processing X-band COSMO-SkyMed StripMap HIMAGE time series of 2 years (2011–2013) and for the archaeological park of Pompeii

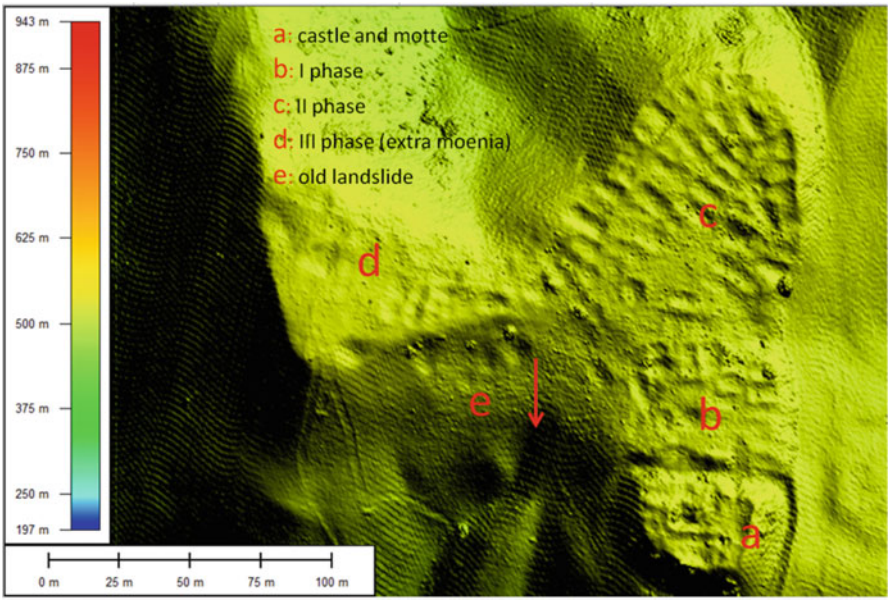

Fig. 3.17 Medieval village in Southern Italy: the DTM derived from LiDAR survey allowed not only reconstructing the historical urban phases (**a**, **b**, **c**, **d**) but also detecting an old landslide (**e**) that likely contributed to the abandonment of the settlement

by CNR-IREA (Bonano et al. 2016, in this volume) applying the SBAS-DInSAR technique to two C- and X-band satellite datasets, collected during the 1993–2015 time interval from the "first" (ERS and ENVISAT) and the "second" (CSK) SAR sensor generations

Landslide monitoring can be successfully approached by using drones, high-resolution optical satellite data, and LIDAR. Figure 3.17 shows the evidence of a landslide close to a medieval village in Basilicata as obtained by a survey based on LIDAR, which probably was one of the causes of the abandonment of this village that occurred in the fifteenth century (Lasaponara and Masini 2009).

3.5 Archaeological Looting and Vandalism

Looting of archaeological sites and ancient artifacts has a long history. Over the centuries looting has usually been a part of war; starting at least since 333 BC (http://www.smithsonianmag.com/making-a-difference/looting-iraq-16813540/) during the war of Alexander the Great against King Darius III.

In past centuries, clandestine excavation activities have been mainly linked to illicit trade of antiquities. To contend with this phenomenon, in many countries

repressive measures were adopted along with restrictive laws to impose the returning of objects derived from clandestine excavations or theft to their own countries

In 1956 the General Conference of the United Nations Educational, Scientific and Cultural Organization recommended all the Member States to take "all necessary measures to prevent clandestine excavations and damage to monuments and also to prevent the export of objects thus obtained" (UNESCO 1956)." In 1970, UNESCO promulgated the Convention on the Means of Prohibiting and Preventing the Illicit Import, Export and Transfer of Ownership of Cultural Property (UNESCO 1970), also including (in UNESCO 2001) underwater archaeology. Additional actions have been adopted recently to condemn and contrast the looting and illegal excavations that have exponentially increased in the Middle East since the beginning of the conflict in Syria. The United Nations Security Council, on 12 February 2015, adopted Resolution 2199 that convicts the destruction of cultural heritage and adopts legally binding measures to counter illicit trafficking of antiquities and cultural objects.

Despite these efforts, looting and artifact trafficking remain a pervasive broad-based phenomenon through the world, and important cultural property has disappeared from many countries, as revealed from the survey conducted by Proulx (2013). Therefore, illegal excavations represent one of the main risk factors affecting the archaeological heritage throughout the world.

Actions oriented to preventing looting can be supported by aerial (including UAV, see Fig. 3.18) and satellite systems. Aerial surveys and the use of UAV can be limited by the extent of the areas under surveillance, whereas the use of satellites can provide reliable information useful to (i) quantify the looting phenomenon even if it is at an "industrial scale" over large areas; and (ii) set up a systematic monitoring tool also for remote areas not accessible because of war or other limiting factors.

Taking advantage of large-spatial coverage, high-spectral and sensitivity satellite remote sensing can be usefully adopted for contrasting looting. Satellite technologies offer a suitable chance to quantify and analyze this phenomenon, especially in those countries, from South America to the Middle East, where the surveillance on site is not very effective and is time consuming or impractical as the result of military or political restrictions.

Recent applications, mainly focused in Peru (Lasaponara et al. 2012, 2014, Lasaponara and Masini 2010, Contreras 2010) and in areas of ongoing conflicts such as Iraq and Iran (Casana and Panahipour 2014; Stone 2008; Van Ess et al. 2006), have shown that VHR satellite imagery is of great help in the remote surveying of archaeological heritage and in monitoring of the damage from looting.

In particular, focusing on Peru, Contreras (2010) used remote sensing imagery from aerial and space platforms to assess looting damage via photointerpretation in the Virù valley. From the methodological perspective, Lasaponara and Masini (2010) provided a significant contribution by devising a pioneering semiautomatic looting classification, which was applied to Cahuachi just in Peru. To enhance the circular holes that typically characterized the spatial patterns of looting, they adopted statistical analysis based on local indices of spatial autocorrelation (LISA). The highly satisfactory results, further validated by ground survey (Lasaponara et al.

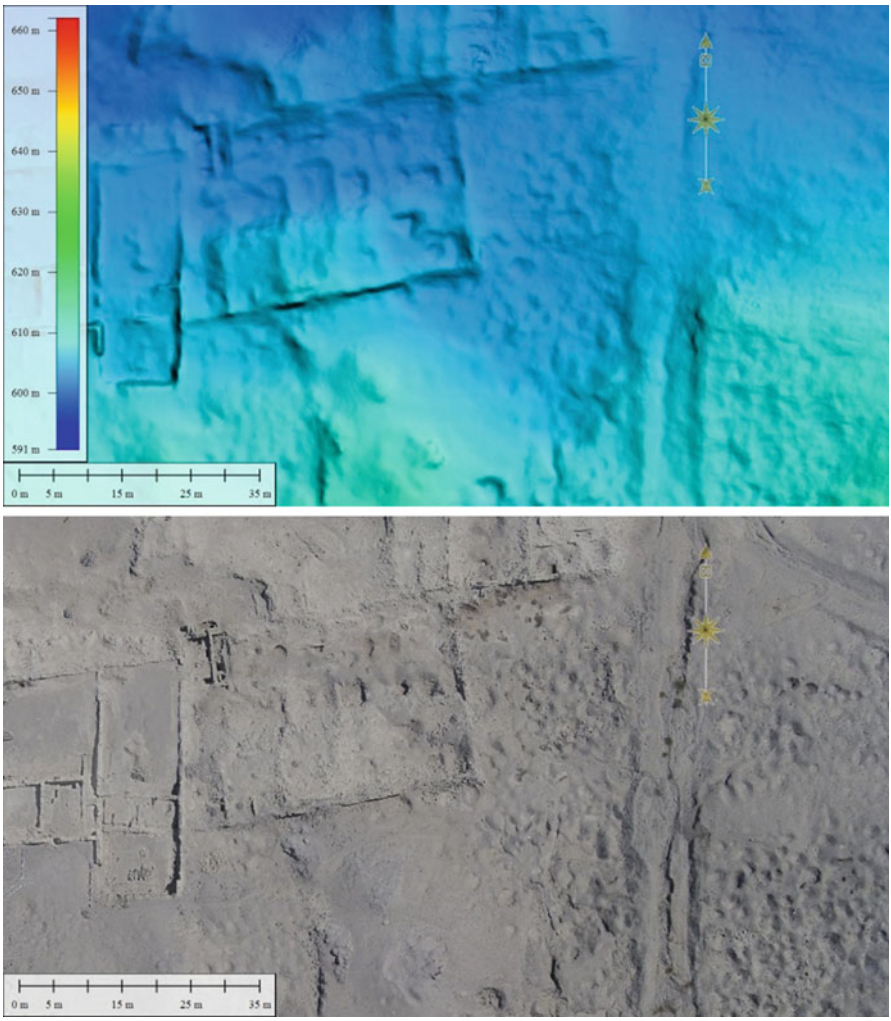

Fig. 3.18 Inca site of Paredones near Nasca (Southern Peru). The DEM and the orthophoto derived by aerial images taken from drone evidence the intense looting activity

2012), encouraged the authors to further improve the methodological approach. A fully automatic procedure (Lasaponara et al. 2014) was developed and tested in one of the most ancient archaeological sites in Southern America, Ventarron in Northern Peru.

Focusing on the Middle East and areas of ongoing conflicts, Van Ess et al. (2006) compared prewar and postwar IKONOS images to identify looted areas near Uruk-Warka, situated 300 km south of Baghdad. They located looting activities by using supervised classification methods. Stone (2008, 2015) estimated the extent of the damaged areas and the chronology of looting by using multidate QuickBird

images. Casana and Panahipour (2014) worked for several years, in the framework of a NASA-funded research project, to develop a comprehensive archaeological site database that includes 15,000 sites in Syria and surrounding regions.

3.6 Conclusions

Space technologies offer great availability of active and passive data that have a multitude of applications in the detection, documentation, monitoring, and management of natural and cultural sites. Satellite imagery can fruitfully cope with the need to providing documentation by visualization of natural and cultural heritage that improves support and data which can be promptly integrated with ancillary information and any other data sources. In particular, the high resolution of satellite images (currently up to 30 cm) enables deriving accurate maps of the current and ongoing status by analyzing changes and human-induced activities and assessing their impact at landscape down to building level. Moreover, by exploiting multidate satellite images or time series, remote sensing enables identifying emerging threats to the heritage sites, setting up mitigation strategies, and assessing if conservation measurements are being effective.

Acknowledgements The present publication is under the result of the project "Smart Cities and Communities and Social Innovation" Project (Avviso MIUR n.84/Ric 2012,PON 2007–2013 del 2 marzo 2012- Misura IV.1, IV.2, 2013–2015).

Author Contributions: Rosa Lasaponara and Nicola Masini conceived the study. Rosa Lasaponara wrote the paper. Nicola Masini reviewed the manuscript.

References

Berardino P, Fornaro G, Lanari R, Sansosti E (2002) A new algorithm for surface deformation monitoring based on small baseline differential SAR interferograms. IEEE Trans Geosci Remote Sens 40:2375–2383

Biescas E, Crosetto M, Agudo M, Monserrat O, Crippa B (2007) Two radar interferometric approaches to monitor slow and fast land deformations. J Surv Eng 133:66–71

Bonano M, Manzo M, Casu F, Manunta M, Lanari R (2016). DinSAR for the monitoring of cultural heritage sites. In Masini N, Soldovieri F (eds) Sensing the past. Geoscience and sensing technologies for cultural heritage. Springer, Cham, pp 117–134, chapter 6.

Bruzzone L, Prieto DF (2002) An adaptive semiparametric and context-based approach to unsupervised change detection in multitemporal remote-sensing images. IEEE Trans Image Process 11(4):452–466

Casana J, Panahipour M (2014) Satellite-based monitoring of looting and damage to archaeological sites in Syria. J East Mediterr Archaeol Herit Stud 2(2):128–150. doi:10.5325/jeasmedarcher-stu.2.2.0128

Cigna F, Lasaponara R, Masini N, Milillo P, Tapete D (2014) Persistent Scatterer Interferometry processing of COSMO-SkyMed StripMap HIMAGE time series to depict deformation of the historic centre of Rome, Italy. Remote Sens 6:12593–12618. doi:10.3390/rs61212593

Collins JB, Woodcock CE (1996) An assessment of several linear change detection techniques for mapping forest mortality using multitemporal Landsat TM data. Remote Sens Environ 56:66–77

Contreras DA (2010) Huaqueros and remote sensing imagery: assessing looting damage in the Viru Valley, Peru. Antiquity 84(324):544–555

Coppin P, Bauer M (1996) Digital change detection in forest ecosystems with remote sensing imagery. Remote Sens Rev 13:207–234

Crosetto M, Tscherning CC, Crippa B, Castillo M (2002) Subsidence monitoring using SAR interferometry: reduction of the atmospheric effects using stochastic filtering. Geophys Res Lett 29:26–29

Crosetto M, Crippa B, Biescas E, Monserrat O, Agudo M, Fernández P (2005) Land deformation monitoring using SAR interferometry: state-of-the-art. Photogrammetrie, Fernerkundung, Geoinformation 6:497–510

Crosetto M, Monserrat O, Herrera G (2010) Urban applications of persistent scatterer interferometry. In Soergel U (ed) Radar remote sensing on urban areas, Remote sensing and digital image processing series, vol 15. Springer Science+Business Media B.V, Berlin, pp 233–246

Crosetto M, Monserrat O, Cuevas M, Crippa B (2011) Spaceborne differential SAR interferometry: data analysis tools for deformation measurement. Remote Sens 3:305–318. doi:10.3390/rs3020305

Dabin Ji Lin Sun, Jiancheng Shi, Tao Jiang (2010) High resolution AOT retrieval based on MODIS surface reflectance product. Geoscience and Remote Sensing Symposium (IGARSS), 2010 IEEE International July 2010, pp 1703–1706

Edgington D, Dirk W, Salamy K, Koch C, Risi M, Sherlock R (2003) Automated event detection in underwater video. In Proceedings of the MTS/IEEE oceans 2003 conference

Ferretti A, Prati C, Rocca F (2000) Nonlinear subsidence rate estimation using permanent scatterers in differential SAR interferometry. IEEE Trans Geosci Remote Sens 38:2202–2212

Gabriel AK, Goldstein RM, Zebker HA (1989) Mapping small elevation changes over large areas: differential radar interferometry. J Geophys Res 94:9183–9191

Hadjimitsis DG, Retalis A, Clayton CRI (2002) The assessment of atmospheric pollution using satellite remote sensing technology in large cities in the vicinity of airports. Water Air Soil Pollut Focus 2:631–640. Monitoring Air Pollution in the Vicinity of Cultural Heritage Sites in Cyprus 547

Hadjimitsis DG, Clayton CRI (2009) Determination of aerosol optical thickness through the derivation of an atmospheric correction for short-wavelength Landsat TM and ASTER image data: an application to areas located in the vicinity of airports at UK and Cyprus. Appl Geomat J 1:31–40

Hadjimitsis DG (2009) Description of a new method for retrieving the aerosol optical thickness from satellite remotely sensed imagery using the maximum contrast value principle and the darkest pixel approach. Trans GIS J 12(5):633–644

http://whc.unesco.org/en/conventiontext

http://www.unesco.org/science/remotesensing/?id_page=74&lang=en

http://www.iccrom.org/ifrcdn/pdf/ICCROM_17_RiskPreparedness_en.pdf

http://www.smithsonianmag.com/making-a-difference/looting-iraq-16813540/

Huertas A, Nevatia T (2000) Detecting changes in aerial views of man-made structures. Image Vis Comput 18(8):583–596

Kaufman YJ, Fraserr RS, Ferrare RA (1990) Satellite measurements of large-scale air pollution: methods. J Geophys Res 95:9895–9909

King MD, Kaufman YJ, Tanré D, Nakajima T (1999) Remote sensing of tropospheric aerosols from space: past, present, and future. Bull Am Meteorol Soc:2229–2259

Lanari R, Mora O, Manunta M, Mallorquí JJ, Berardino P, Sansosti E (2004) A small-baseline approach for investigating deformations on full-resolution differential SAR interferograms. IEEE Trans Geosci Remote Sens 42:1377–1386

Landis E, Nagy E, Keane D, Nagy G (1999) A technique to measure 3D work-of-fracture of concrete in compression. J Eng Mech 126(6):599–605

Lasaponara R, Masini N (2009) Full-waveform airborne laser scanning for the detection of medieval archaeological microtopographic relief. J Cult Herit 10S:78–82. doi:10.1016/j.culher.2009.10.004

Lasaponara R, Masini N (2010) Facing the archaeological looting in Peru by local spatial autocorrelation statistics of Very high resolution satellite imagery. In: Taniar D et al. (eds) Proceedings of ICSSA, The 2010 INTERNATIONAL Conference on Computational Science and its Application (Fukuoka-Japan, 23–26 March, 2010), Springer, Berlin, pp 261–269.

Lasaponara R, Danese M, Masini N (2012) Satellite-based monitoring of archaeological looting in Peru. In: Lasaponara R, Masini N (eds) 2012, Satellite remote sensing: a new tool for Archaeology. Springer Verlag, Berlin/Heidelberg, pp 177–193. ISBN 978–90–481-8800-0, doi: 10.1007/978–90–481-8801-7_8

Lasaponara R, Leucci G, Masini N, Persico R (2014) Investigating archaeological looting using satellite images and georadar: the experience in Lambayeque in North Peru. J Archaeol Sci 42:216–230. http://dx.doi.org/10.1016/j.jas.2013.10.032

Lasaponara R, Masini N (2015) Reconnaissance of archaeology marks through satellite Synthetic Aperture Radar. In: Chavarría A, Reynolds A (eds) Detecting and understanding historic landscapes. SAP Società Archeologica s.r.l, Mantiva, pp 93–108

Masini N, Lasaponara R (2016) Sensing the past from space: approaches to site detection. In Masini N, Soldovieri F (eds) Sensing the past. Geoscience and sensing technologies for cultural heritage. Springer, Cham, pp 23–60, chapter 2

Monserrat O, Crosetto M, Cuevas M, Crippa B (2011) The thermal dilation component of persistent scatterer interferometry observations. IEEE Geosci Remote Sens Lett 8(5):864–868

Nagy G, Zhang T, Franklin W, Landis E, Nagy E, Keane D (2001) Volume and surface area distributions of cracks in concrete. Visual Form 2001 (Springer LNCS 2059):759–768

Proulx BB (2013) Archaeological site looting in "global" perspective: nature, scope, and frequency. Am J Archaeol 117(1):111–125

Retalis A (1998) Study of atmospheric pollution in large cities with the use of satellite observations: development of an atmospheric correction algorithm applied to polluted urban areas. Phd thesis, Department of Applied Physics, University of Athens

Retalis A, Cartalis C, Athanasiou E (1999) Assessment of the distribution of aerosols in the area of Athens with the use of Landsat TM. Int J Remote Sens 20:939–945

Rosen PA, Hensley S, Joughin IR et al (2000) Synthetic aperture radar interferometry. Proc IEEE 88:333–382

Sifakis N, Deschamps PY (1992) Mapping of air pollution using SPOT satellite data. Photogramm Eng Remote Sens 58:1433–1437

Singh A (1989) Digital change detection techniques using remotely-sensed data Internet. J Remote Sens 10(6):989–1003

Stone EC (2008) Patterns of looting in Iraq. Antiquity 82:125–138

Stone EC (2015) An update on the looting of archaeological sites in Iraq. Near East Archaeol 78(3):178–186

Tang J, Xue Y, Yu T, Guan Y (2004) Aerosol optical thickness determination by exploiting the synergy of Terra and Aqua MODIS. Remote Sens Environ 94:327–334

UNESCO (1956) Recommendation on international principles applicable to archaeological excavations

UNESCO (1970) Convention on the means of prohibiting and preventing the illicit import, export and transfer of ownership of cultural property

UNESCO (2001) Convention on the protection of the underwater cultural heritage

Van Ess M, Becker H, Fassbinder J, Kiefl R, Lingenfelder I, Schreier G, Zevenbergen A (2006) Detection of Looting Activities at Archaeological Sites in Iraq Using Ikonos Imagery," Angewandte Geoinformatik, Beiträge zum 18. Wiechmann-Verlag, Heidelberg, pp 668–678.

Wang J, Christopher SA (2003) Intercomparison between satellite derived aerosol optical thickness and PM2.5 mass: implications for air quality studies. Geophys Res Lett 30(21):2095

Chapter 4
LiDAR for Archaeological Research and the Study of Historical Landscapes

Adrian S. Z. Chase, Diane Z. Chase, and Arlen F. Chase

Abstract Remote sensing technologies have helped to revolutionize archaeology. LiDAR (light detection and ranging), a remote sensing technology in which lasers are used as topographic scanners that can penetrate foliage, has particularly influenced researchers in the field of settlement or landscape archaeology. LiDAR provides detailed landscape data for broad spatial areas and permits visualization of these landscapes in ways that were never before possible. These data and visualizations have been widely utilized to gain a better understanding of historical landscapes and their past uses by ancient peoples.

Keywords LiDAR • Visualization techniques • Landscapes • Archaeology

4.1 Introduction

Archaeological survey and settlement pattern research is becoming increasingly dependent on LiDAR (light detection and ranging) for enhancing the interpretation of historical landscapes. LiDAR is of value even in areas of the world where there is a long tradition of studying ancient landscapes in the context of environment and history. In Europe, LiDAR has been utilized to aid cultural heritage analysis in conjunction with written historic records. Within European countries, LiDAR has enabled researchers to gain detailed information on specific features such as castles, cairns, furrows, and coal pits that were obscured by covering vegetation. LiDAR has been perhaps even more significant for research in tropical and subtropical areas

A.S.Z. Chase
School of Human Evolution and Social Change, Arizona State University, P.O. Box 872402, Tempe, AZ, 85287-2402, USA

D.Z. Chase
Office of the Executive Vice President and Provost, University of Nevada, Las Vegas, 4505 S. Maryland Parkway, Box 451002, Las Vegas, NV, 89154-1002, USA

A.F. Chase (✉)
Department of Anthropology, University of Nevada, Las Vegas, 4505 S. Maryland Parkway, Box 451002, Las Vegas, NV, 89154-5003, USA
e-mail: arlen.chase@unlv.edu

N. Masini, F. Soldovieri (eds.), *Sensing the Past*, Geotechnologies and the Environment 16, DOI 10.1007/978-3-319-50518-3_4

such as Mesoamerica and Southeast Asia where there is often neither great time depth to the written history of landscapes nor a detailed understanding of the specific spatial parameters being investigated. In the tropics, LiDAR has dramatically changed perceptions of largely unknown landscapes, serving to document both the settlement and the spatial parameters of anthropogenic activity and tropical urbanism. Thus, the focus, applications, and effects of LiDAR to archaeological data have varied markedly in different parts of the world. In temperate zones, LiDAR is often used to focus on specific features or areas that are historically known or identified, whereas in the tropics LiDAR is used to understand a largely undocumented settlement distribution on an ancient landscape. Not only is LiDAR moving forward in archaeological interpretation, but its use by archaeologists is also changing the way in which LiDAR is collected and subsequently analyzed in an attempt to maximize interpretations within different environmental parameters.

4.2 What Is LiDAR?

LiDAR uses laser pulses to measure discrete distances and is able to produce three-dimensional (3D) points that measure both the canopy and earth surface (Glennie et al. 2013). Although new in the field of archaeology, LiDAR has actually been in use for more than half a century and directly derives from optics research with lasers. Even though initially unable to penetrate these bodies of vapor, LiDAR was utilized for meteorological remote sensing of clouds (Goyer and Watson 1963). The use of lasers in this technology eventually resulted in the word LiDAR, which originally stood for "light radar" (Ring 1963). Because RADAR was an acronym for "radio detection and ranging," the technology was ultimately called "light detection and ranging" or LiDAR. The public became aware of the impact of this technology as early as 1971, when a laser altimeter was used to map the surface of the moon by the Apollo 15 mission; a descendant system was also used to map the surface of Mars (Zuber et al. 1998). In the 1980s, NASA developed two airborne laser instruments that were precursors for modern LiDAR systems: (1) Atmospheric Oceanographic LiDAR (AOL) and (2) Airborne Topographic Mapper (ATM) (Anderson et al. 2010: 875). Most of the airborne systems used today derive from the ATM.

Modern researchers use various filtering algorithms to classify ground returns for future analysis. This method provides LiDAR with a distinct advantage over traditional aerial photography within forested survey regions (Fernandez-Diaz et al. 2014: 9971–9986). Early comparisons of different vegetation classification and removal algorithms (Sithole and Vosselman 2004) have facilitated archaeological LiDAR use by European researchers (Devereux et al. 2005; Risbøl et al. 2006; Sittler 2004). In parallel with new algorithms and advances in classification and removal algorithms, many researchers have highlighted—time and time again—the importance of considering the vegetation of the survey region when selecting which filtering algorithms to use (Crow et al. 2007; Prufer et al. 2015; Raber et al. 2002). After raw data collection, many additional processes and analyses facilitate

the creation of useful LiDAR data; however, to determine the best processes to use, researchers must balance the vegetation in their study region in conjunction with the features they wish to study (Fernandez-Diaz et al. 2014).

LiDAR has quickly become useful in a wide variety of disciplines. Modern agriculture uses LiDAR to determine how fertilizer should be applied to crop fields based on previous yield, land slope, and sun intensity (Hammerle and Hofle 2014). Atmospheric sciences first used LiDAR for profiling clouds and measuring winds (Rees and McDermid 1990), eventually for studying aerosols and the quantification of atmospheric components (Ansmann and Muller 2005). In biology, LiDAR permits measurement of canopy heights, biomass, and leaf area (Drake et al. 2002). Geologists leverage LiDAR in landform surveys and in studies of the physical and chemical processes that shape landscapes (Bellina et al. 2005); in mining, LiDAR terrestrial scanning has been used to calculate ore volumes (Lato et al. 2009: 194). In everyday life, law enforcement uses LiDAR in speed guns. LiDAR use is known for both unmanned drones and the detection of biological agents (Veerabuthiran and Razdan 2011). LiDAR has multiple uses in physics as well; it is used for robotics, cruise control, rangefinding, and the spaceflight detection of cloud droplets and industrial pollution (Glennie et al. 2013; Grob et al. 2013). Finally, in archaeology (the field focused upon in this chapter), LiDAR has provided a level of spatial understanding of the past that did not exist previously and which helps researchers to refine and redefine the settlement models that are applied to ancient societies (A. Chase et al. 2012).

Various kinds of LiDAR are being used by archaeologists, as well as a host of different visualization techniques for post-processing the collected data. Archaeologists have used three different forms of LiDAR: airborne LiDAR to investigate the surfaces of ground; terrestrial LiDAR to gain detailed scans of features; and bathymetric LiDAR to gain information from underwater. Terrestrial LiDAR usually involves the laser scanning of specific features such as monuments or buildings (Cheng et al. 2013) but has also been extended to the level of scanning complete sites (Romero and Bray 2014; Weber and Powis 2014). Terrestrial LiDAR has also been used to make reconstructions of archaeological stratigraphy, with successive scans being undertaken during excavation (Galeazzi et al. 2014). Although terrestrial LiDAR generally has limited use when analyzing large-scale historical landscapes because of scale, it does have application in terms of hydrological modeling of landscapes for potential flooding (Fewtrell et al. 2010). Bathymetric LiDAR works with features that are underwater and thus has application for shipwrecks (Shih et al. 2014) and submerged sites (Doneus et al. 2013). Airborne LiDAR has been successfully applied to historical landscapes throughout the world, ranging from Europe (Bernardini et al. 2013; Cifani et al. 2007; Masini and Lasaponara 2013; Risbøl et al. 2013) to North America (Harmon et al. 2006; Johnson and Ouimet 2013; Rochelo et al. 2015; Wienhold 2013) to Mesoamerica (Chase et al. 2011, 2012, 2014b) to Pacific islands (McCoy et al. 2011) to Southeast Asia (Evans et al. 2013).

4.3 Visualization of Landscapes with LiDAR

Much general background material has been written about the interpretation and analysis of LiDAR data (Challis et al. 2011; Glennie et al. 2013; Fernandez et al. 2014). The most basic product of airborne LiDAR is the creation of a DEM (digital elevation model), which "has a precise meaning as an xyz elevation raster" (A. Chase et al. 2011: 391). Analysis is made easier by applying various visualization techniques. Those that have been developed to view these data range from the traditional hill-shaded terrain model (Yoeli 1967) to slope analysis (McCoy et al. 2011) to local relief modeling (Hesse 2010) to sky-view factor (Kokalj et al. 2011) to geomorphons (Stepinski and Jasiewicz 2011).

The hill-shaded terrain model is one of the original visualizations applied to LiDAR (Devereux et al. 2008; also see Yoeli 1967 for detailed analytical hill-shading methods). This analysis is based on techniques that were used for traditional aerial photography, where flights where often scheduled to take advantage of the naturally raking light during different times of the year. The similarity between hill-shades and aerial photographs facilitated interpretation. There is also a long history of artists creating hill-shades from elevation maps (Yoeli 1967). The effect of a hill-shade is the same as raking a flashlight over a three-dimensional (3D) printout of the DEM, and this is essentially the computation process behind hill-shading (Fig. 4.1). Shadows highlight elevation differences that reveal natural hills and human-made features. This visualization type sees very common use because of the ease of manual interpretation; however, multiple hill-shades with variable azimuths and altitudes are required to see all the features on the landscape (White 2013).

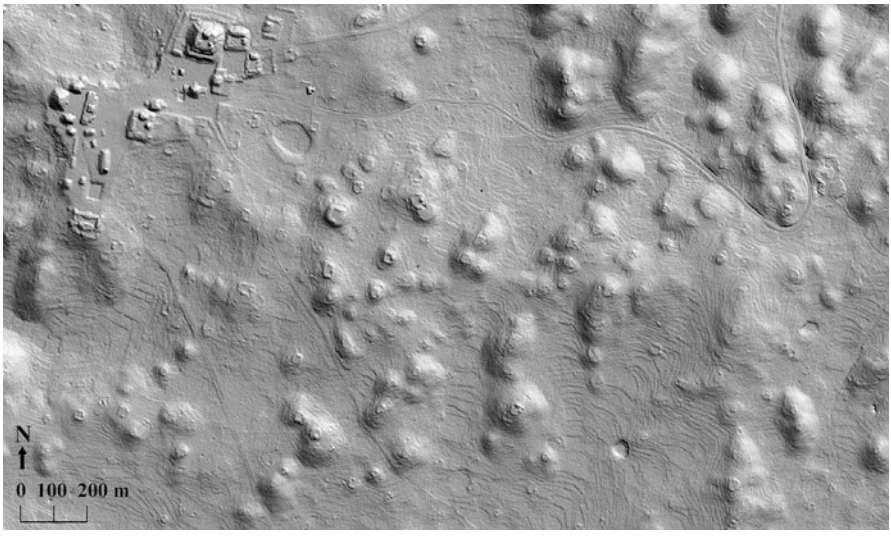

Fig. 4.1 A standard two-dimensional (2D) hillshade of the central part of Caracol, Belize

Future use of this analysis type has been superseded both by principal components analysis (PCA) hill-shades (Devereux et al. 2008) and more recently by sky-view factor (Kokalj et al. 2011).

Slope analysis (McCoy et al. 2011: 2148) uses the value of the angle representing the change in elevation between cells and reclassifies the slope into expected classes. In general, both slope and aspect, the compass direction of a cell's slope, find use in hydrological DEM applications. Additional measurements created from slope include the curvature along a cell's slope, the curvature perpendicular to a cell's slope, the first derivative of cell slopes along a specified direction, and the second derivative of cell slopes along a specified direction. These measures help identify anomalous slopes that may be archaeological features of interest, data errors, or changes in the underlying regional topography. After running these analyses, reclassification of the varying datasets of slopes into types can help further visualization and identification of features within these datasets. For example, the simplest classification utilizing only slope could be flat, low slope, and high slope; however, more complex systems utilizing various slope datasets mentioned earlier can be used in tandem to create more complex classifications based on research interests.

The local relief model (Hesse 2010) considers the microtopography of a DEM. Although the output is often considered noisy and messy, it also includes many of the humanly constructed features of archaeological interest. A small moving window of analysis is applied over every cell in the DEM to observe the difference between average elevation around a cell and the elevation of the cell itself. This technique effectively, but not actually, flattens hills and raises valleys so that only the minor landscape variations are visible.

Since being introduced by Kokalj and his colleagues (2011), sky-view factor has become the visualization of choice in airborne LiDAR. Sky-view factor asks one question: what proportion of the sky can I see from my location? Each point is analyzed looking at the full horizon. The angles from where the sky can be seen along the horizon are taken and recorded. This is a very good alternative to traditional hill-shaded terrain models.

Yet another visualization technique uses geomorphons (Stepinski and Jesiewicz 2011). This visualization does not produce a photograph-like image, as a hill-shade does. Rather, this analysis breaks down the landscape into distinct units that highlight flat space and elevated space. Each location has its unit type determined by the relative elevations of its neighbors along both cardinal and ordinal directions. Neighbors can be higher, lower, or equivalent (i.e., flat). These signatures, called geomorphons, are then classified into one of the 498 possible distinct types (Stepinski and Jesiewicz 2011: 110). This analysis essentially breaks the entire landscape into unique types; it is exceedingly good in differentiating and classifying landscapes by type, thus permitting the interpretation of archaeological landscapes in ways not possible through the previous methods (Fig. 4.2).

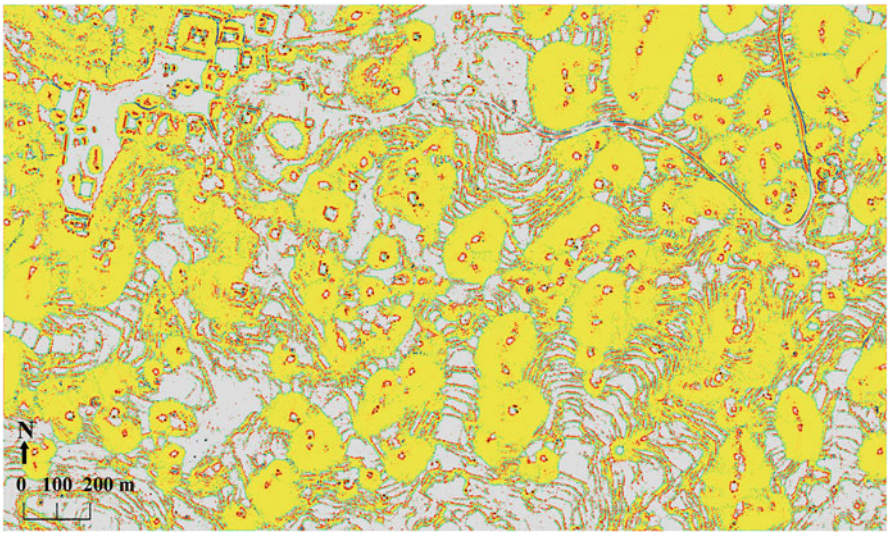

Fig. 4.2 A geomorphon of the central part of Caracol, Belize (same area as Fig. 4.1)

4.4 Applications of LiDAR to Landscape Analysis

There is a long history of landscape study using LiDAR, with the first applications occurring in Europe. Stonehenge was one of the earliest sites examined with airborne LiDAR. Examination of LiDAR originally collected for environmental monitoring (rather than archaeological purposes) led to the discovery of previously unidentified archaeological features, agricultural fields, and ditched banks. LiDAR provided surface traces of features with "no visible surface expression" and previously undiscovered data about Stonehenge that caused the researchers to comment that "the technique reveals new details and new levels of survival even in well-researched landscapes" (Bewley et al. 2005: 645).

Italian researchers are quite familiar with the use of LiDAR in terms of landscape analysis (see Masini and Lasaponara 2013 for a brief history of LiDAR research through 2012). As early as 2007, a 100 km^2 survey area in southern Italy showcased the effectiveness of LiDAR in recording archaeological remains in a "complex Mediterranean landscape" (Cifani et al. 2007: 3). LiDAR was also used to build on previous research that had detected a medieval village and led to a reconstruction of its urban boundaries using aerial photographs and Quickbird images. The LiDAR provided additional benefits and permitted researchers to examine "micro-topographic relief linked to archaeological and geomorphological factors" that was related to "the urban shape of a medieval village," allowing researchers to analyze small differences in height that were not visible in the other datasets (Lasaponara et al. 2010: 155). Using LiDAR that had previously been flown for environmental monitoring in 2006 at a low density of 4–5 points/km^2, Bernardini and his colleagues (2013: 2153) analyzed 212 km^2 of hillshaded LiDAR from the

Trieste Province in northeastern Italy for examples of prehistoric and historic sites in a karstic area. They identified previously unknown fortified structures, possible funerary barrows, agricultural terraces, and other buildings (Bernardini et al. 2013: 2152, 2159), noting the usefulness of the technique even for "relatively urbanized territories investigated for a long time," concluding that "LiDAR images yield information that surpasses that obtained after years of archaeological surveys." Masini and Lasaponara (2013: 673) also report on the effectiveness of LiDAR in terms of archaeology; the LiDAR that they used at an Etruscan site in Blera under a densely wooded area "made possible the identification of a large number of circular 'craters,' clearly referable to looted tombs or attempts to find and plunder tombs."

Researchers in Norway have also utilized LiDAR to better understand the history of their landscapes and have extensively tested how to best employ the technology. Risbøl and his colleagues (2013) utilized airborne laser scanning to observe the effect of point density on hill-shade identifications of linear features as opposed to irregular features; this study comprises a useful demonstration of the effects of size and shape in the detection of archaeological remains through the use of LiDAR. They concluded that "large cultural remains with clear geometrical shape (ovals and circles) and large elevation difference were more successfully detected and classified compared to smaller ones" and further noted that a point density greater than 10 points/m^2 "could potentially contribute to better identification of smaller features" (Risbøl et al. 2013: 4688).

Among the earliest LiDAR applications in the United Sates was its use in historic archaeology to gain information on the spatial layout and gardens of two eighteenth-century Maryland plantations. As a result of investigating these two plantations, the researchers concluded that LiDAR "can be used to identify areas of potential archaeological interest with ephemeral or no surface expression" (Harmon et al. 2006: 668). More recently, LiDAR has been used to examine past landscapes in North America. One of the more interesting applications has been the use of LiDAR data to examine the historic landscape of southern New England. Similar to some of the European applications, the New England study used an already extant database produced for environmental monitoring; even though the point density only averaged 2 points/m^2, the results from the LiDAR analyses were far better than any other database available. Within a heavily forested environment, Johnson and Ouimet (2014) were able to identify stone wall networks, building foundations, farmsteads, dams, mills, and old roads and pathways within the DEMs that they used. They also suggest that the large-scale LiDAR that they are using can be used to "interpret the data or results in terms of theoretical anthropological questions regarding landscape … and how humans have interacted with, shaped, viewed, and even divided the landscape" (Johnson and Ouimet 2014: 19). Their use of field systems and walls in New England mirrors the use of ancient agricultural terraces in the Maya area to answer similar landscape questions (D. Chase and A. Chase 2014).

Another recent study in the United States using LiDAR successfully documented ancient earthworks in the northern Everglades of Florida (Rochelo et al. 2015: 632–634), using post-processing techniques to improve on previous usage of the same LiDAR (Pluckhahn and Thompson 2012). Using lower-resolution 2-m data,

Rochelo and his colleagues (2015: 642) were able to process the raw data with alternative software systems to eliminate some of the vegetation problems that were not resolved with originally available DEMs. Their innovative solution only highlights the need for cross-disciplinary fusion in using LiDAR point files not only with other existing off-the-shelf programs but also with specially written algorithms for specific environmental and climatic circumstances.

Another study in North America used LiDAR data in conjunction with archaeological data and a GIS platform to study the hydrology and agricultural practices of the prehistoric Hohokam in the American Southwest (Wienhold 2013). Because of the three-dimensional points produced through LiDAR, it was possible to model the flow of water over the landscape and to demonstrate that prehistoric rock alignments were used to modify both the channel and surface flow of water. Constructed rock alignments "were placed within suitable areas for collecting rainfall and runoff and for maximizing crop production during a time period of substantial drought" (Wienhold 2013: 857). This water harvesting is an example of an ancient complex land-use strategy in a marginal environment.

Studies of Pacific island landscapes have specifically focused on ancient agricultural systems (McCoy et al. 2011; Ladefoged et al. 2011). Ladefoged and his colleagues (2011: 3605) used an area of 173 km^2 of LiDAR to examine "agricultural processes of expansion, segmentation, and intensification" on Hawaii that could then be combined with potential productivity modeling to understand the agricultural development of this area. The landscape that they sampled contained long horizontal walls that were believed to have served as windbreaks for crops planted behind them and also to "result in increased moisture levels ca. 2–3 m immediately upslope of the alignment centerline due to microorographic precipitation" (Ladefoged et al. 2011: 3616). The LiDAR data here also permitted the "identification of the spatial relationships between trails and agricultural alignments" as well as "evidence of segmentation and intensification" in the agricultural landscape, "something that was not apparent in the aerial photograph data" (Ladefoged et al. 2011: 3618). Simultaneously, the LiDAR data from Hawaii also helped identify diverse ancient agricultural strategies that included "terrace complexes used for irrigated agriculture" within small valleys, permitting the development of a new method of "slope contrast mapping" using the LiDAR data "and thus defining where irrigated agriculture could have expanded in the past" (McCoy et al. 2011: 2153). The use of LiDAR for understanding the ancient Hawaiian landscape illustrates how these data can be used for complex environmental reconstructions and modeling.

Finally, we would note that exceedingly successful application of LiDAR to landscapes has occurred in the tropics where it has documented the impressive cities of vanished civilizations, first in the Maya area in Central America at Caracol (A. Chase et al. 2010) and subsequently in Southeast Asia at Angkor (Evans et al. 2013). At Caracol, Belize, a 200 km^2 area was flown in 2009 that revealed a landscape covered with archaeological terraces, urban settlement, and roads (A. Chase et al. 2011). This LiDAR campaign firmly established the usefulness of this technology for understanding a large area of heavily forested landscape and

led to a more expansive campaign that covered an additional 1057 km^2 to better understand regional settlement patterns among the ancient Maya (A. Chase et al. 2014a, 2014b; this volume). Spurred on by the success of the Caracol LiDAR results, an area of 370 km^2 was surveyed with LiDAR in 2012 in northwest Cambodia associated with the medieval site of Angkor (Evans et al. 2013: 12, 596). Both the Caracol, Belize and the Angkor, Cambodia LiDAR data indicated the need for reevaluating the nature of urbanism and landscape use within tropical environments (A. Chase et al. 2011: 397; Evans et al. 2013: 12,599). As in the Maya case, a second LiDAR campaign is being carried out in Cambodia by Evans (this volume) to add 1200 km^2 to the previously surveyed area.

4.5 Final Remarks

Because of the ability of LiDAR to accurately detect relatively minor elevation differences and penetrate forest canopy over a vast spatial area, the technology has provided researchers the ability to better understand, model, and survey historical landscapes. In most cases, the application of LiDAR to a landscape has revealed previously unrecorded archaeological features that can then be investigated on the ground, and in some cases LiDAR has truly acted as "a catalytic enabler of rapid transformational change in archaeological research and interpretation" (A. Chase et al. 2012: 12,916), particularly for tropical regions where there is rapid vegetative growth that can obscure a landscape. LiDAR accurately portrays the palimpsest of features that covers the Earth's surface, but more detailed work is necessary to add a temporal dimension to the spatial one. Almost from the inception of the use of LiDAR by archaeologists, this limitation was noted. "The application of these methods will ultimately be most successful when the data are used in conjunction with information derived from the field, the laboratory, and from archival sources . . . and reinforces the need for integration of multiple techniques when attempting to understand archaeological landscapes" (Harmon et al. 2006: 668). More than a decade has now passed since LiDAR was first utilized to study archaeological landscapes, and we are now beginning to see the successful fusion and interplay between different scholarly fields (Fernandez et al. 2014; Chase et al. 2016) as new and innovative ways to better utilize LiDAR are developed and tested. In the future, LiDAR use will become even more ubiquitous as the technology is placed into common devices such as phones. The future will also witness the integration of LiDAR data that have been collected at multiple scales (terrestrial, mobile, different altitudes) with other kinds of remotely sensed data (e.g., thermal, hyperspectral, and/or multispectral data and synthetic aperture radar) that will again provide new research avenues and insights into past landscapes.

References

Anderson J, Massaro R, Lewis L, Moyers R, Wilkins J (2010) LiDAR-activated phosphors and infrared retro-reflectors: emerging target materials for calibration and control. Photogramm Eng Remote Sens August:875–879

Ansmann A, Muller D (2005) Lidar and atmospheric aerosol particles. In: Weitkamp C (ed) Lidar range-resolved optical remote sensing. Springer, New York, pp 105–141

Bellina JA, Kerans C, Jennette DC (2005) Digital outcrop models: applications of terrestrial scanning LiDAR technology in stratigraphic modeling. J Sediment Res 75:166–176

Bernardini F, Sgambati A, Montagnari Kokelj M, Zaccaria C, Micheli R, Fragiacomo A, Tiussi C, Dreossi D, Tuniz C, De Min A (2013) Airborne LiDAR application to karstic areas: The example of Trieste province (north-eastern Italy) from prehistoric sites to Roman forts. J Archaeol Sci 40:2152–2160

Bewley RH, Crutchley SP, Shell CA (2005) New light on an ancient landscape: LiDAR survey in the Stonehenge world heritage site. Antiquity 79:636–647

Challis K, Forlin P, Kincey M (2011) A generic toolkit for the visualization of archaeological features on airborne LiDAR elevation data. Archaeol Prospect 18:279–289

Chase DZ, Chase AF (2014) Path dependency in the rise and denouement of a classic Maya city: the case of Caracol, Belize. In: Chase AF, Scarborough V (eds) The resilience and vulnerability of ancient landscapes: transforming Maya archaeology through IHOPE. American Anthropological Association, Arlington, pp 142–154

Chase AF, Chase DZ, Weishampel JF (2010) Lasers in the jungle: airborne sensors reveal a vast Maya landscape. Archaeology 63(4):27–29

Chase AF, Chase DZ, Weishampel JF, Drake JB, Shrestha RL, Slatton KC, Awe JJ, Carter WE (2011) Airborne LiDAR, archaeology, and the ancient Maya landscape at Caracol, Belize. J Archaeol Sci 38:387–398

Chase AF, Chase DZ, Fisher CT, Leisz SJ, Weishampel JF (2012) Geospatial revolution and remote sensing LiDAR in Mesoamerican archaeology. PNAS 109(32):12916–12921

Chase AF, Chase DZ, Awe JJ, Weishampel JF, Iannone G, Moyes H, Yaeger J, Brown MK (2014a) The use of LiDAR in understanding the ancient Maya landscape: Caracol and western Belize. Adv Archaeol Pract 2:208–221

Chase AF, Chase DZ, Awe JJ, Weishampel JF, Iannone G, Moyes H, Yaeger J, Brown MK, Shrestha RL, Carter WE, Fernandez Diaz J (2014b) Ancient Maya regional settlement and inter-site analysis: the 2013 west-central Belize LiDAR survey. Remote Sens 6(9):8671–8695

Chase AF, Reese-Taylor K, Fernandez-Diaz JC, Chase DZ (2016) Progression and issues in the Mesoamerican geospatial revolution: an introduction. Adv Archaeol Pract 4:219–231

Cheng L, Tong L, Li M, Liu Y (2013) Semi-automatic registration of airborne and terrestrial laser scanning data using building corner matching with boundaries as a reliability check. Remote Sens 5:6260–6283

Cifani G, Opitz R, Stoddart S (2007) LiDAR survey in southern Etruria, Italy: a significant new technique for the study of cultural landscapes. Eur Archaeol 27:2–3

Crow P, Benham S, Devereux BJ, Amable GS (2007) Woodland vegetation and its implications for archaeological survey using LiDAR. Forestry 80:241–252

Devereux BJ, Amable GS, Crow P, Cliff AD (2005) The potential of airborne LiDAR for detection of archaeological features under woodland canopies. Antiquity 79:648–660

Devereux BJ, Amable GS, Crow P (2008) Visualisation of LiDAR terrain models for archaeological feature detection. Antiquity 82:470–479

Doneus M, Doneus N, Briese C, Pregesbauer M, Mandlburger G, Verhoeven G (2013) Airborne laser bathymetry: detecting and recording submerged archaeological sites from the air. J Archaeol Sci 40:2136–2151

Drake JB, Dubayah RO, Clark DB, Knox RG, Blair JB, Hofton MA, Chazdon RL, Weishampel JF, Prince S (2002) Estimation of tropical forest structural characteristics using large-fooprint LiDAR. Remote Sens Environ 79:305–309

Evans DH, Fletcher RJ, Pottier C, Chevance J-B, Sourtif D, Tan BS, Im S, Ea D, Tin T, Kim S, Cromarty C, De Greef S, Hanus K, Baty P, Kuszinger R, Shimoda I, Boornazian G (2013) Uncovering archaeological landscapes at Angkor using LiDAR. PNAS 110:12595–12600

Fernandez-Diaz JC, Carter WE, Shrestha RL, Glennie CL (2014) Now you see it... now you don't: understanding airborne mapping LiDAR collection and data product generation for archaeological research in Mesoamerica. Remote Sens 6:9951–10001

Fewtrell TJ, Duncan A, Sampson CC, Neal JC, Bates PD (2010) Benchmarking urban flood models of varying complexity and scale using high resolution terrestrial LiDAR data. Phys Chem Earth 36:281–291

Galeazzi F, Moyes H, Aldenderfer M (2014) Comparing laser scanning and dense stereo matching techniques for 3D intrasite data recording. Adv Archaeol Pract 2:353–365

Glennie CL, Carter WE, Shrestha RL, Dietrich WE (2013) Geodetic imaging with airborne LiDAR: the Earth's surface revealed. Rep Prog Phys 76:086801

Goyer GG, Watson R (1963) The laser and its application to meteorology. Bull Am Meteorol Soc 44:564–575

Grob SM, Esselborn M, Abicht F, Wirth M, Fix A, Minikin A (2013) Airborne high spectral resolution LiDAR observation of pollution aerosol during EUCAARI-LONGREX. Atmos Chem Phys 13:2435–2444

Hammerle M, Hofle B (2014) Effects of reduced terrestrial LiDAR point density on high resolution grain crop surface models in precision agriculture. Sensors 14:24212–24230

Harmon JM, Leone MP, Prince SD, Snyder M (2006) LiDAR for archaeological landscape analysis: a case study of two eighteenth-century Maryland plantation sites. Am Antiq 71:649–670

Hesse R (2010) LiDAR-derived local relief models: a new tool for archaeological prospection. Archaeol Prospect 17:67–72

Johnson KM, Ouimet WB (2014) Rediscovering the lost archaeological landscape of southern New England using airborne light detection and ranging (LiDAR). J Archaeol Sci 43:9–20

Kokalj Z, Zaksek K, Ostir K (2011) Application of sky-view factor for the visualization of historic landscape features in LiDAR-derived relief models. Antiquity 85:263–273

Ladefoged TN, McCoy MD, Asner GP, Kirch PV, Puleston CO, Chadwick OA, Vitousek PM (2011) Agricultural potential and actualized development in Hawai'i: an airborne LiDAR survey of the leeward Kohala field system (Hawai'i Island). J Archaeol Sci 38:3605–3619

Lasaponara R, Coluzzi R, Gizzi FT, Masini N (2010) On the LiDAR contribution for the archaeological and geomorphological study of a deserted medieval village in southern Italy. J Geophys Eng 7:155–163

Lato M, Diederichs MS, Hutchinson DJ, Harrap R (2009) Optimization of LiDAR scanning and processing for automated structural evaluation of discontinuities in rockmasses. Int J Rock Mech Min Sci 46:194–199

Masini N, Lasaponara R (2013) Airborne LiDAR in archaeology: overview and a case study. In: Murgante B, Misra S, Carlini M, Torre C, Nguyen H-Q, Taniar D, Apduhan B, Gervasi O (eds) Computational science and its applications. ICCSA 2013: lecture notes in computer science 7972. Springer, Berlin, pp 663–676

McCoy MD, Asner GP, Graves MW (2011) Airborne LiDAR survey of irrigated agricultural landscapes: an application of the slope contrast method. J Archaeol Sci 38:2141–2154

Pluckhahn TJ, Thompson VD (2012) Integrating LiDAR data and conventional mapping of the Fort Center Site in south-central Florida: a comparative approach. J Field Archaeol 37(4):289–301

Prufer KM, Thompson AE, Kennett DJ (2015) Evaluating airborne LiDAR for detecting settlements and modified landscapes in disturbed tropical environments at Uxbenká, Belize. J Archaeol Sci 57:1–13

Raber GT, Jensen JR, Schill SR, Schuckman K (2002) Creation of digital terrain models using an adaptive LiDAR vegetation point removal process. Photogramm Eng Remote Sens 68:1307–1314

Rees D, McDermid IS (1990) Doppler lidar atmospheric wind sensor: reevaluation of a 355-nm incoherent doppler LiDAR. Appl Opt 29:4133–4144

Ring J (1963) The laser in astronomy. New Scientist 344:672–673
Risbøl O, Gjertsen AK, Skare K (2006) Airborne laser scanning of cultural remains in forests: some preliminary results from a Norwegian project. In: From Space to Place. Proceedings of the 2nd international conference on remote sensing in archaeology: BAR International Series.
Risbøl O, Bollandsås OM, Nesbakken A, Ørka OH, Næsset E, Gobakken T (2013) Interpreting cultural remains in airborne laser scanning generated digital terrain models: effects of size and shape on detection success rates. J Archaeol Sci 40(12):4688–4700
Rochelo MJ, Davenport C, Selch D (2015) Revealing pre-historic native American Belle Glade earthworks in the northern Everglades utilizing airborne LiDAR. J Archaeol Sci Rep 2:624–643
Romero BE, Bray TL (2014) Analytical applications of fine-scale terrestrial LiDAR at the imperial Inca site of Caranqui, northern highland Ecuador. World Archaeol 46:25–42
Shih PT-Y, Chen Y-H, Chen J-C (2014) Historic shipwreck study in Dongsha Atoll with bathymetric LiDAR. Archaeol Prospect 21:139–146
Sithole G, Vosselman G (2004) Experimental comparison of filter algorithms for bare-Earth extraction from airborne laser scanning point clouds. ISPRS J Photogramm Remote Sens 59:85–101
Sittler B (2004) Revealing historical landscapes by using airborne laser scanning. A 3-D Modell of Ridge and Furrow in Forests near Rastatt (Germany). In: Proceedings of Natscan, Laser-Scanners for Forest and Landscape Assessment: Instruments, Processing Methods and Applications, International Archives of Photogrammetry and Remote Sensing
Stepinski TFF, Jasiewicz J (2011) Geomorphons – a new approach to classification of landforms. http://geomorphometry.org/2011
Veerabuthiran S, Razdan AD (2011) LiDAR for detection of chemical and biological warfare agents. Def Sci J 61(3):241–250
Weber J, Powis TG (2014) Assessing terrestrial laser scanning in complex environments. Adv Archaeol Pract 2:123–137
White DA (2013) LiDAR, point clouds, and their archaeological applications. In: Comer DC, Harrower MJ (eds) Mapping archaeological landscapes from space. Springer, New York, pp 175–186
Wienhold ML (2013) Prehistoric land use and hydrology: a multi-scalar spatial analysis in central Arizona. J Archaeol Sci 40:850–859
Yoeli P (1967) The mechanization of analytical hill shading. Cartogr J 4(2):82–88
Zuber MT, Smith DE, Solomon SC, Abshire JB, Afzal RS, Aharonson O, Fishbaugh K, Ford FG, Frey HV, Garvin JB, Head JW, Ivanov AB, Johnson CL, Muhleman DO, Neumann GA, Pettengill GH, Phillips RJ, Sun X, Zwally HJ, Banerdt B, Duxbury TC (1998) Observations of the north polar region of Mars from the Mars orbiter laser altimeter. Science 282:2053–2060

Chapter 5
SAR for Landscape Archaeology

Deodato Tapete and Francesca Cigna

Abstract This chapter provides an overview of the opportunities that image analysts, archaeologists, and conservation scientists currently have by using space-borne synthetic aperture radar (SAR) imagery for purposes of *landscape archaeology*. The latter in this context is meant as the discipline to study and interpret the anthropogenic impact on past and present landscapes, alongside the environmental and land surface processes that can alter the condition of heritage assets. The benefits of the recent developments in SAR satellite sensors toward higher resolution (up to less than 1 m) and shorter revisiting times (up to a few days) are discussed in relationship to established techniques using the two key SAR parameters—amplitude and phase—to detect subtle archaeological features in modern landscapes, monitor sites, and assess damage in areas of conflict.

Keywords Synthetic aperture radar • Landscape archaeology • Radar backscatter • Change detection • Polarimetry • DEM • Nasca • Syria

5.1 Synthetic Aperture Radar (SAR)

5.1.1 Definitions and Main Properties

The acronym SAR stands for synthetic aperture radar and indicates a coherent active satellite system operating in the radar wavelength domain (most exploited bands: *L* 1–2 GHz, 15–30 cm; *C* 4–8 GHz, 3.75–7.5 cm; *X* 8–12.5 GHz, 2.5–3.75 cm) which collects, independently of weather conditions, the received signal ("radar backscatter") over successive pulses from elements of a synthetic aperture to create an image (ESA 2007). Magnitude ("amplitude") and phase of the wavelength are recorded for each pixel of the complex SAR image. As the line-of-sight direction changes along the space-borne radar trajectory, a synthetic aperture is produced by signal processing with effect of lengthening (i.e., synthesizing) the antenna.

D. Tapete (✉) • F. Cigna
Natural Environment Research Council, British Geological Survey, Keyworth, Nottingham, UK
e-mail: deodato@bgs.ac.uk; fcigna@bgs.ac.uk

N. Masini, F. Soldovieri (eds.), *Sensing the Past*, Geotechnologies and the Environment 16, DOI 10.1007/978-3-319-50518-3_5

The achievable azimuth resolution (i.e., along the satellite flight track) of a SAR image is approximately equal to one half the length of the actual (real) antenna and does not depend on the platform altitude (distance). The ground surface is imaged along the ground range direction (i.e., across-track, perpendicular to the satellite orbit) with side-looking radar beaming along slant-range direction with a certain "incidence angle" that varies across the image swath (ESA 2007). The signal intensity relies on the amount of radar return from the surface, the roughness of which compared to the wavelength size determines the type and amount of backscattering and, in contrast, the penetration capability. The latter is theoretically higher with longer wavelengths (L- > X-band) and in drier and fine-grained soils.

5.1.2 State-of-the-Art

The earliest use of SAR for landscape archaeology dates back to the 1980s with investigations in both tropical and subtropical territories (Adams et al. 1981) and arid environments (Elachi et al. 1984). Since then, several studies have revealed hidden features and paleo-landscapes exploiting the peculiar penetration capability of the radar signal (El-Baz 1998; Comer et al. 2005; Wiseman and El-Baz 2007; Moore et al. 2007). This capability has been proved valuable in particular in sandy plain environments such as the Great Sahara where homogeneous fine-grained sand, with very limited moisture content less than 1%, allowed penetration to the bedrock. An earlier example was published by Elachi and Granger (1982) using space-borne imaging radar (SIR-A) imagery. Recent reviews on SAR for archaeological prospection and the achievements with current satellites (Lasaponara and Masini 2013; Chen et al. 2015a, b) prove this is already an established field in remote sensing and archaeological sciences.

5.2 Current Opportunities from Space

The scientific advances of satellite radar research for landscape archaeology was possible because of the increasing availability, from the early 1990s, of SAR imagery in the catalogues of the space agencies, covering with more regular frequency not only the Western countries but also remote areas of South America, Asia, and Africa. Furthermore, since the early 2000s, the beam modes with which SAR images are acquired have been continuously improved, so that nowadays image analysts, archaeologists, and conservation scientists can access data with a wide swath to spotlight coverage, kilometer to submeter spatial resolution, historical and present dates of acquisition, longer to shorter wavelength (L/C/X bands), and monthly to daily revisiting time if collecting time series.

At present radar remote sensing is witnessing the revolutionary turn of the satellites from the first (ERS-1/2, ENVISAT, ALOS, RADARSAT-1/2) to the

second generation (TerraSAR-X, COSMO-SkyMed, Sentinel-1 and ALOS-2). In this context there is a range of opportunities for feature detection, and condition and damage assessment (Tapete et al. 2015c; Tapete and Cigna 2015).

5.2.1 Space-Borne Data

5.2.1.1 Legacy SAR Archives

The ERS-1/2 and ENVISAT catalogues of the European Space Agency (ESA) are the most complete and abundant archives of C-band time series with almost uninterrupted temporal coverage from 1991 to April 2012. Their Image Mode spatial resolution of 25–30 m and swaths of 100 km make these images suitable for wide-area and regional assessments (e.g., detection of paleo-channels, trade route reconstruction), alongside investigation of sites as wholes and contextualized in their surrounding environments (Fig. 5.1a). Similarly, the archives built by the Japanese Space Agency (JAXA) with the L-band ALOS PALSAR sensor provide an historical view of cultural landscapes from 2006 to May 2011, with resolution up to 7 m in fine beam mode, both single and dual polarized (HH, VV, HH+HV, VV+VH).

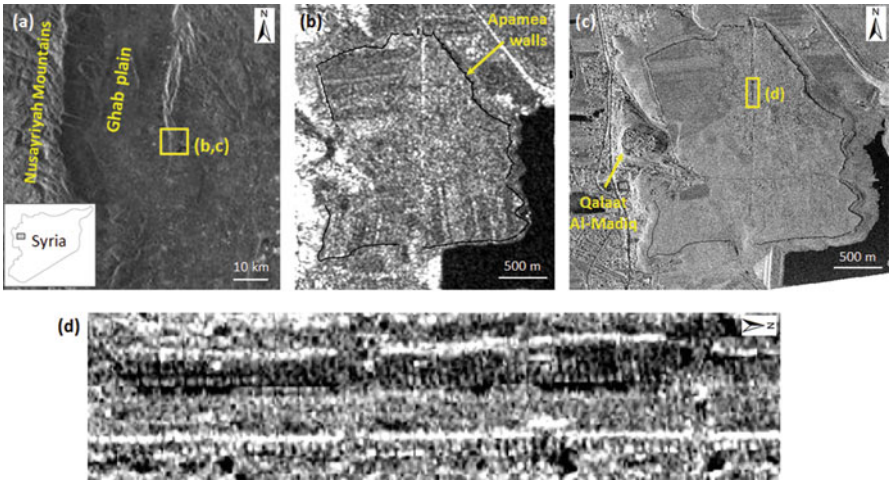

Fig. 5.1 SAR opportunities for site investigation. (**a**) 25-m resolution ENVISAT IS2 VV, 9 June 2006. (**b**) 17-m geocoded TerraSAR-X ScanSAR, 17 May 2011 (© DLR 2014). (**c**) 0.24-m resolution geocoded Staring Spotlight ascending mode image, 27 December 2014 (© DLR 2014) of Apamea, western Syria. (**d**) Detail of the monumental colonnade from the Staring Spotlight mode, enhancing the unprecedented very high spatial resolution currently achievable with space-borne SAR

5.2.1.2 New Satellites and SAR Imaging Modes

The TerraSAR-X constellation of the German Aerospace Center (DLR) is a clear example of how SAR can nowadays support studies of landscape archaeology.

Acquiring X-band imagery since mid-2007 with the twin satellite TanDEM-X launched 3 years later, TerraSAR-X (TSX) is building an image archive with repeat cycle of 11 days (i.e., a third of ESA's first-generation sensors) and a range of spatial resolutions, from 16 m and scene size of 100 km (width) × 150 km in ScanSAR mode, to azimuth resolution of 0.24 m over a scene extent varying between 2.5 and 2.8 km in azimuth and 4.6 to 7.5 km in range in Staring Spotlight mode (Mittermayer et al. 2014).

The Hellenistic town of Apamea, Syria, well demonstrates the paradigm of multitemporal and multiscale analysis using different satellites. ScanSAR time series 2011-2014 (Fig. 5.1b) complemented the historical analysis with ERS-1/2 and ENVISAT by providing regional-scale coverage to assess the recent impact on landscape caused by the construction of the dam nearby the Justinian walls (see Sect. 5.2.2.4) and the agricultural activities in the Ghab plain (Fig. 5.1a). Coeval submeter resolution Staring Spotlight imagery (Fig. 5.1c), instead, allows up-scaling the observations at the level of individual structures, such as the monumental colonnade of Apamea (Fig. 5.1d). Given the current exposure of the site to war damage and vandalism, the strong backscatter return from the marble columns provides a reliable SAR marker to assess whether the ancient ruins are still standing or have collapsed (see Sect. 5.3.2).

Archaeologists can also benefit from the full range of beam modes and incidence angles offered by the same satellite mission to improve the detection and delineation of subtle archaeological features, while relating them to the landscape over a wide swath. Figure 5.2 demonstrates the stunning improvement in SAR imaging from ScanSAR to high-resolution spotlight modes to discriminate the UNESCO World Heritage List Nasca Lines, Southern Peru. The distinctive radar signature of the "negative geoglyphs" (exposed unpatinated and lighter-colored ground) can be analyzed by drawing a backscatter profile from the feature to the nearby soil (dark gravels) and checking its consistency or variations by year or by season (Tapete et al. 2013b).

The suitability of SAR remote sensing to the specific purposes of landscape archaeology relies on the flexibility offered by the radar sensors to tune up the acquisition parameters. In this regard the successor to ALOS PALSAR, namely ALOS-2, launched in May 2014, can acquire images with single to full polarization, range-azimuth resolution up to 3 × 1 m, and incidence angles between 8° and 70° in the various beam modes. Operating in L-band, the sensor PALSAR-2 is expected to penetrate more of the topsoil, depending on the incidence angle (see Sect. 5.2.2.3) at equal environmental conditions (e.g., feature roughness and soil moisture).

Conversely, the coeval ESA C-band Sentinel-1A satellite launched in April 2014, with its twin Sentinel-1B launched 2 years later, is building a consistent and regular SAR catalogue with the predefined interferometric wide swath (IW) mode acquiring data at 5 m × 20 m spatial resolution over 250-km swaths, allowing conflict-free

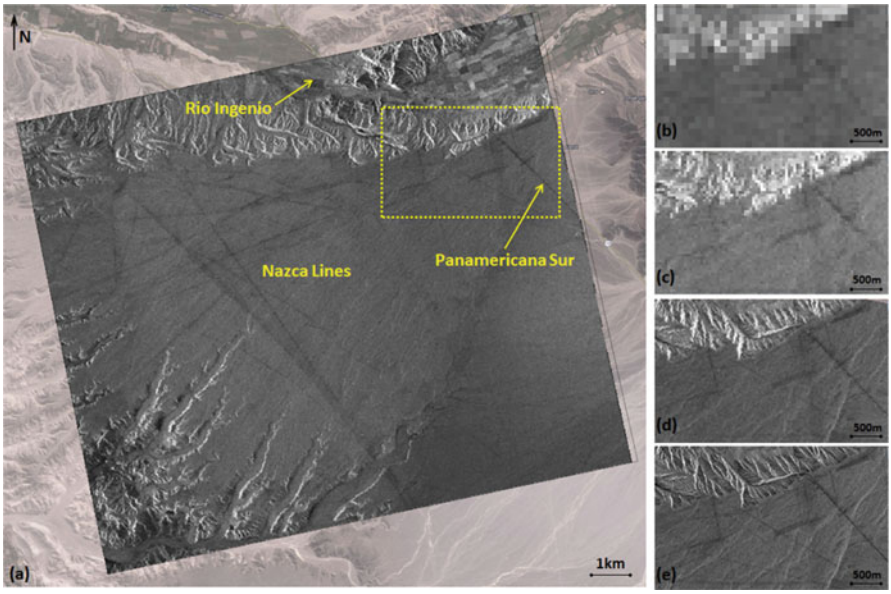

Fig. 5.2 SAR opportunities for feature detection. (**a**) TerraSAR-X (TSX) SpotLight 13 August 2008 ascending mode with VV polarization, 32.5°–33.6° incidence angles over the Nasca Lines (© DLR 2014), overlapped onto optical imagery (© 2013 Google Imagery © Cnes/Spot Image, DigitalGlobe, Map data © Google). Comparison of ScanSAR TSX, HH, ascending, range res. 17.0–19.2 m (**b**) with StripMap TanDEM-X (TDX), HH, ascending, range res. 3.3–3.5 m (**c**), SpotLight TSX, HH, descending, range res. 1.7–3.5 m (**d**), and High Resolution SpotLight TDX, HH, descending, range res. 1.1–3.5 m (© DLR 2014) (**e**) (Modified from Tapete et al. 2015b)

high-resolution coverage of dual polarization and interferometric data potentially over all global landmasses (ESA 2013, 2015). Therefore, the areas where the Sentinels can support archaeology and heritage conservation mostly relate to routine monitoring and condition assessment over wide areas but, as this mission is still new, more experimental research is needed to assess at what extent Sentinel-1 images would suit this purpose. Emergency observation requests altering the predefined observation scenario are foreseen, possibly exploiting the 5 × 5 m resolution StripMap (SM) mode over the narrow swath width of 80 km with adjustable beam incidence angle and the elevation beamwidth (ESA 2013). Section 5.3.3 illustrates a simulation of the operational capability of Sentinel-1A SM in such a circumstance (Tapete et al. 2015c).

A further element that undoubtedly will encourage the use of Sentinel data for landscape archaeology is their accessibility. The data are free for download and use from the Sentinels Scientific Data Hub (https://scihub.esa.int/), in various formats: SAR Level-0 (compressed and unfocused SAR raw data), Level-1 (focused data), and Level-2 (geo-located geophysical products). In particular, Level-1 ground range detected (GRD) products are focused SAR data that have been detected, multilooked, and projected to ground range using an Earth ellipsoid model, and

provided in GeoTIFF format. These rasters have approximately square resolution pixels and square pixel spacing with reduced speckle, although at the cost of reduced geometric resolution and loss of phase information. Although this means that interferometric analysis is not possible with GRD products (for an introduction to interferometric SAR, see Chap. 6 by Bonano et al. in this volume), image analysts can use them straightforwardly with GIS software for purposes of amplitude change detection (see Sect. 5.2.2.1) or geospatial analysis and data integration.

The other satellite mission operating in X-band is the Italian Space Agency (ASI) constellation COSMO-SkyMed, consisting of four satellites able to collect up to 1800 images of the Earth's surface per day under three different operative modes: routine, crisis, and very urgent (Covello et al. 2010). It is outside the scope of this chapter to review the abundant literature proving the well-known benefits of this constellation for emergency response. For what concerns the applications on landscape archaeology, Chen et al. (2015b) is one of the few papers that have investigated the use of COSMO-SkyMed images for archaeological prospection and identification of archaeological marks (see Sect. 5.3.1); this suggests that further research can be done to benefit from the huge archive that COSMO-SkyMed has already built to cover the globe.

5.2.2 Processing Methods

SAR processing methods can be distinguished by the radar parameter used: amplitude and radar backscatter; coherence; polarization; phase.

5.2.2.1 Amplitude Change Detection

This method allows the investigation of spatial and temporal changes of the backscattering coefficient σ^0 which indicates the radar signal backscattered to the sensor, normalized, to a first approximation, to the horizontal ground surface and referred to as per unit area on the ground.

Cigna et al. (2013) illustrated the typical workflow to extract, convert to decibels (dB), and compare values of σ^0 for purposes of landscape archaeology. An example of amplitude change detection consists in the computation of ratios between SAR pairs. Two SAR images, k and j, acquired by using the same acquisition mode and geometry at the times t_k and t_j, respectively, are spatially filtered to reduce the effects of radar speckle and increase the signal content of the image pixels. Their backscatter ratio ($R_{\sigma 0}$) is computed, pixel by pixel, as follows:

$$R_{\sigma_i^0} = \frac{\sigma_i^0 (t_k)}{\sigma_i^0 (t_j)}$$

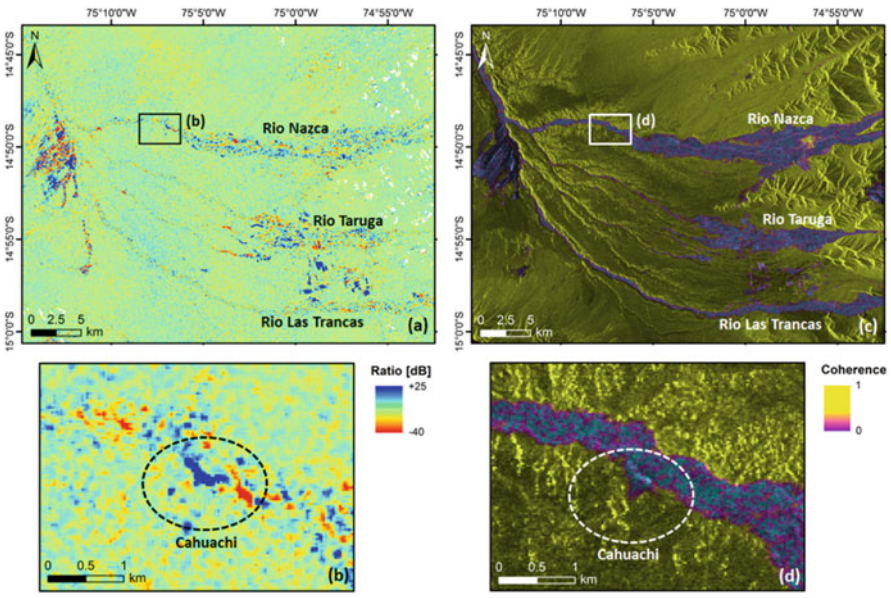

Fig. 5.3 Change detection maps based on the ratio of the backscattering coefficient between ENVISAT ascending mode images acquired on 2 February 2005 and 7 October 2007 (**a**–**b**) and the corresponding coherence maps (perpendicular baseline of 4 m) over the Nasca Civilization region in Peru and the archaeological site of Cahuachi (**c**–**d**). The *dotted circles* highlight areas where changes in the ratio (*blue-red patterns*) are associated with loss of coherence (*pink-purple patterns*), likely the result of soil moisture and vegetation changes along the river plain as seen in **a** for the Rio Nasca, Taruga, and Las Trancas plains, and archaeological excavations in the area of the ceremonial center of Cahuachi

where R is a dimensionless parameter that takes on values between 0 and 1 when the considered pixel i has higher backscattering coefficient at the time j with respect to time k, while values exceeding 1 occur when the pixel i has lower backscattering coefficient at the time j with respect to time k.

The result is a map showing the spatial patterns of σ^0 increase and decrease (Fig. 5.3a, b) that offers potential for correlation with changes in soil moisture content, vegetation coverage, or morphology, the latter being, for example, caused by legal or illegal excavations, collapses, or demolitions (see Sect. 5.3.3).

5.2.2.2 Multitemporal Coherence

Coherence (γ) is a measure of interferometric phase correlation and can be computed as the cross-correlation coefficient of two SAR images that is estimated over a small window of a few pixels in range and azimuth, once all the deterministic

phase components (mainly caused by terrain elevation) are compensated for (ESA 2007). Computation of the absolute value of γ using a moving window over the whole SAR image results in a coherence map of the observed scene, where values can range from 0 to 1, that is, from no to perfect correlation. Strong coherence means high homogeneity with no change of land surface properties such as soil moisture, vegetation cover, roughness, elevation, or geometry, whereas low γ values are found over altered surfaces.

Figure 5.3d shows how coherence maps can complement an amplitude-based change detection analysis.

Between 2005 and 2007 $R_{\sigma 0}$ patterns were observed in association with loss of coherence in the floodplain of Rio Nasca, Peru, in proximity to Cahuachi, the world largest adobe ceremonial center (Tapete et al. 2013b). Historically the whole area was affected by flood events to the extent that the settlements were heavily damaged or destroyed (Cigna et al. 2013). Although the river brings fresh mud yearly, thereby creating a fertile strip for agriculture, it still represents a threat for the local archaeological heritage, also caused by extreme meteorological events occurring in the mountain range to the east of the plain. Alteration of the radar backscatter between dry, wet, and flooded unvegetated surfaces can be also used to infer the impact in the recent past and assess flood hazard and susceptibility.

5.2.2.3 Polarimetric SAR (PolSAR)

Polarimetry is the measurement and interpretation of the polarization of electromagnetic waves and, for landscape archaeology, is used to detect proxies indicating the existence of buried features. SAR scattering mechanisms of the targets on the ground may differ as a consequence of the type and health of overlying vegetation (Stewart et al. 2014).

The typical PolSAR workflow consists of: multilooking to reduce speckle and obtain a squared pixel (or multitemporal averaging in the case of a stack of SAR images); analysis of target decompositions; and extraction and analysis of the polarimetric signatures to enhance the visibility of suspected buried structures. As demonstrated by Dore et al. (2013) in the sites of Samarra, Iraq, and Djebel Barkal, Sudan, Pauli RGB image of multilooked polarimetric SAR data is the first qualitative map to identify areas of different polarimetric response, while polarimetric descriptors of entropy (H) and alpha angle (α) are obtained by extracting the coherency matrix T3, to quantitatively analyze the randomness of the scattering mechanism and assess the predominant scattering mechanism between single-bounce, double-bounce, or volume scattering. The contribution of these three mechanisms can be then modeled using the Freeman decomposition (Dore et al. 2013), especially when ground-truth measurements are not available.

Patruno et al. (2013) provide an interesting discussion about how different bands, incidence angles, and spatial resolution can be negotiated in a polarimetric analysis to detect subtle to buried features. In the case of Samarra, although L-band ALOS PALSAR imagery is expected to penetrate more of the topsoil, better results are obtained with the higher resolution C-band RADARSAT-2 full-polarization image

acquired with a 26.63° incidence angle to detect the *qanāt* outside the octagonal city. This configuration also proves more suitable than the RADARSAT-2 image at 43.43° incidence angle.

Fully polarimetric ALOS PALSAR and RADARSAT-2 images have been also recently used by Gaber et al. (2013, 2015) to detect and characterize a well-defined geometric target hidden under sand deposits in the Western Desert of Egypt and to classify the surface sediments along El-Gallaba Plain.

These examples further confirm that PolSAR can be very helpful in dry and arid environments, where no interference is caused by soil moisture. Nevertheless, research is needed to assess at what extent PolSAR can support landscape archaeology also in temperate zones and exploit the highest resolution SAR beam modes and the flexibility of incidence angle offered by the current space missions.

5.2.2.4 Digital Elevation Model (DEM) Generation

To generate DEMs from radar data, SAR image pairs are acquired by two sensors flying along parallel tracks in across-track formation (not dissimilar to stereocomposition of optical sensors), so as the same point on the ground is imaged simultaneously from two slightly different directions. The typical workflow to generate DEMs with interferometric SAR processing (InSAR) is fully discussed in ESA (2007).

InSAR DEMs of Earth's surface have been generated since the 1990s, during the Space Shuttle SIR-C/X-SAR missions in 1994, and the "tandem" mission of the ESA ERS-1 and ERS-2 satellites from 16 August 1995 until mid-May 1996, with ERS-1 and ERS-2 phasing of 1 day (ESA 2007). In February 2000 the first single-pass radar interferometer in space flew on board the NASA Shuttle Radar Topography Mission (SRTM; Farr et al. 2007), which generated the first homogeneous, validated, and freely available 90-m resolution global DEM of the Earth. Figure 5.4a shows the SRTM Digital Surface Model (DSM) over the archaeological site of Apamea, Syria, from which the main topographic features and the northern dam are clearly visible.

Papers published by Wiseman and El-Baz (2007) report various examples where SRTM was used to extract slope and elevation information and in combination with land cover maps and natural resource mapping to identify anthropogenic settlements, trade routes, and migration pathways, alongside prediction of future flood and landslide hazards.

The release, since 2014, of the global 1 arc-second (∼30-m) resolution SRTM elevation data will certainly move landscape research forward.

In this context, the DLR TanDEM-X mission is revolutionary. In addition to the generation of a worldwide, consistent, and high-precision global digital elevation model (DEM) at 12-m resolution, StripMap (SM) and High Resolution Spotlight (HS) data at 3-m and 2-m resolution are acquired using the operational alternating bistatic and monostatic acquisition modes. A comprehensive quantitative appraisal of the absolute and relative vertical accuracy of these elevation products in an archaeological context was recently published by Erasmi et al. (2014). The authors

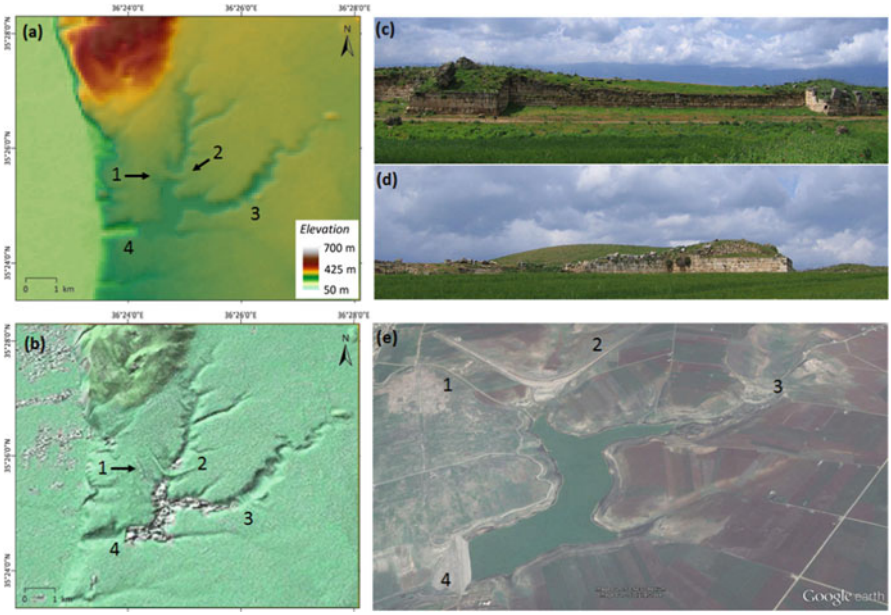

Fig. 5.4 90-m resolution SRTM DSM (**a**) and shaded relief (**b**) of 3-m resolution TanDEM-X StripMap Bistatic HH DEM 27 February 2012 with indication of the archaeological and landscape features of interest for the site of Apamea, Syria (cf. Fig. 5.1): (*1*) eastern Justinian walls; (*2–4*) dams of the Apamea lakes. (**c**, **d**) Details of the eastern walls before looting (© R. Piperno, romeartlover.tripod.com). (**e**) Google Earth image of the Apamea lake and dams (© 2015 CNES/Astrium; © 2015 DigitalGlobe)

showed that SM data were suitable to reconstruct a paleo-channel in the alluvial plain of Cilicia, Turkey, and enhanced the microtopography of the fortification towers, gates, theater, and stadium of the ancient city of Magarsos using HS data.

Similar results are obtained in Apamea (Fig. 5.4). SM bistatic DEM HH polarization not only improves the delineation of the three dams of the Apamea lake and the topographic features of the natural relief where the ancient town was built, but also allows the recognition of the eastern walls (Fig. 5.4b, d). This is a clear example of the usefulness of these data to analyze the regional context in which a site can be studied up to the local scale, and anthropogenic impacts on the landscape can be assessed.

5.3 Cultural Heritage and Landscape Applications

5.3.1 Detection of Archaeological Features

Given the heritage of historical data and the diverse options for new acquisition with the current space missions (see Sect. 5.2.1), it would be simplistic and reductive to

state that only the highest resolution SAR imagery should be used for detection of archaeological features. Images are to be selected accounting for the size, morphology, location, and degree of exposure of the features on the ground to investigate.

Tapete et al. (2013b) demonstrated that even medium-resolution SAR images such as 30-m resolution ENVISAT ASAR were suitable to delineate major geoglyphs of the Nasca Lines or detect buried and abandoned *puquios*, although the obvious limitation relates to the precision with which the feature is delimited from the nearby soil and its land use. Furthermore, despite their lower resolution, historical data are sometimes the only imagery available from the space agencies archives, and can be used to look at past landscapes that have been modified by human actions such as extensive plowing, dam construction, urban sealing, war damage, and vandalism.

At present, except for the L-band ALOS-2 mission, the highest resolution SAR imagery is acquired in X-band (e.g., TerraSAR-X Staring Spotlight and Spotlight COSMO-SkyMed; see Fig. 5.1d), which is expected to have lower penetration capability than L-band, at equal environmental conditions. As mentioned earlier (see Sect. 5.2.2.3), the combination of incidence angle, soil properties, and surface roughness has a key role. An example is presented by Chen et al. (2015a) as part of a review of archaeological marks in SAR imagery. A 1-m resolution COSMO-SkyMed Spotlight HH polarization image acquired with 27.32° incidence angle revealed shallow remains of walls and foundation close to the amphitheater of Sabratha in Libya.

Figure 5.5 shows the clear archaeological mark detected over the deserted village of Dar es-Salaam, north of the city of Homs in western Syria, using a 3-m resolution TerraSAR-X StripMap image. The size, shape, and location of the amplitude pattern match with the corresponding mark observed in Google Earth, thereby proving that SAR imagery can be an effective alternative to optical data when the latter are not available or are cloud covered. The radar backscatter also enhances the site as a distinctive feature compared with the nearly regular orthogonal agricultural fields in the surroundings, also testifying the extensive program of cadastration or centuriation of the basalt landscape. Dar es-Salaam is nowadays mostly a mass of rubble, with no standing structures: these apparently were demolished over the centuries to source good worked stone for use in local farms. Therefore, spatial investigation of the site extent is crucial to understand the relationship between Dar es-Salaam and the field systems, alongside its physical outreach, that is, the area of influence and control on the surrounding hinterland.

5.3.2 Condition Assessment and Environmental Monitoring

There is a wealth of recent literature concerning the use of multitemporal InSAR for condition assessment of monuments and sites threatened by natural and human-induced hazards (Cigna et al. 2012, 2014; Tapete and Cigna 2012a, b;

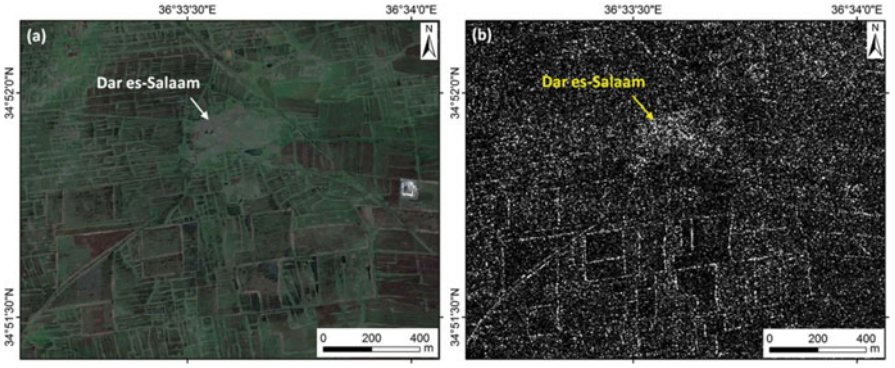

Fig. 5.5 Detection of the archaeological features of the deserted village of Dar es-Salaam, northwest of Homs, Syria: Google Earth image (© DigitalGlobe 2015) (**a**) and TerraSAR-X 3-m resolution StripMap VV image (© DLR 2014-2015) (**b**) from which the site and surrounding agricultural fields are clearly visible

Pratesi et al. 2015; Tapete et al. 2012, 2013a, 2015a; Zhou et al. 2015; see chapter by Bonano et al. in this book). Multitemporal InSAR provides sparse grids of pointwise deformation estimates that inform us about the stability of the objects on the ground.

On the other side, amplitude change detection techniques (see Sect. 5.2.2.1) highlight alteration of the landscape and heritage assets in the form of backscatter change patterns (Fig. 5.3c). At a regional scale this can be exploited to investigate the impact of land surface dynamics occurring in a river catchment or as a consequence of extensive cultivation (Cigna et al. 2013). Geospatial analysis of backscatter changes can suggest a correlation between the distribution and extension of seasonal floodable areas and human settlements (Conesa et al. 2014). At a local scale, depending on the spatial resolution of SAR imagery used, it is possible to identify changes caused by intentional alteration of archaeological features, such as illegal excavations (Tapete et al. 2013b). In this regard, the new TerraSAR-X Staring Spotlight mode is opening a new frontier, as it brings, for the first time, SAR data to image looting features at resolutions comparable with VHR QuickBird, GeoEye, and WorldView optical imagery (Tapete et al. 2016; Tapete and Cigna 2015).

As mentioned in Sect. 5.2.2.2, interferometric coherence provides another option to investigate the environmental impact on cultural landscape and features (Ruescas et al. 2009; Baade and Schmullius 2010) and is increasingly used in post-disaster damage assessment.

Last but not least, it is worth mentioning that the availability of SAR image stacks can be beneficial to analyze, on a seasonal or yearly basis, geomorphological features relating to past, even vanished or hidden, landscapes, such as Quaternary paleo-environments and paleo-shorelines (Bachofer et al. 2014).

5.3.3 *Damage Assessment in Areas of Conflict*

An area in which SAR can complement optical remote sensing is in the assessment of war damage to support the monitoring and protection of cultural heritage in situation of crisis, such as those ongoing in the Middle East and northern Africa. The advantage of operating under any weather conditions and the possibility of acquiring data on a regular basis make SAR a gap-filler and an alternative option to optical or aerial imagery whenever the latter are not feasible.

Figure 5.6 shows the results of change detection analysis in the city of Homs based on the comparison of 3-m resolution TerraSAR-X and TanDEM-X VV polarization StripMap acquisitions of August 2009 and December 2014, that is, before and after major impacts of the recent Syrian civil war. Damage and war-related

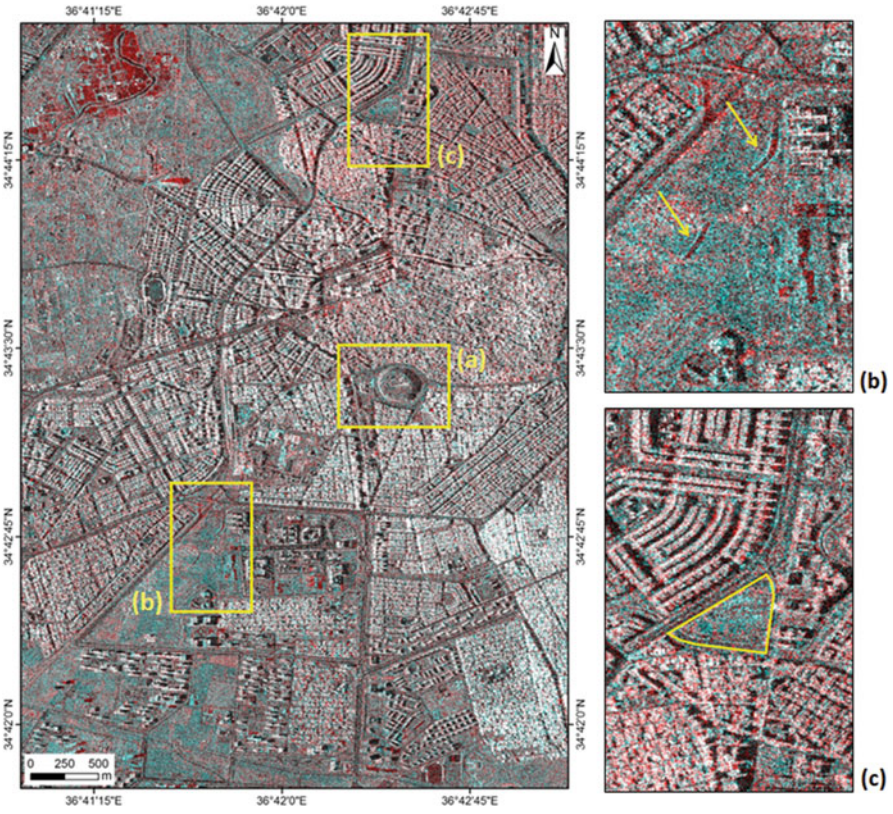

Fig. 5.6 RC color composite of 17 August 2009 and 5 December 2014 VV SM TSX over Homs, Syria (© DLR 2014–2015), with examples of damage and changes in the urban setting: Homs Tell with evidence of alteration at the bottom of the tell (**a**); trenches and embankments in the area of Homs University (**b**); and area of prewar building demolition, northern quarter of Homs (**c**) (Modified from Tapete et al. 2015c)

alteration include military blockages (Fig. 5.6a) and excavations and trenches (Fig. 5.6b) (Tapete et al. 2015c). Background information and environmental considerations also help to correctly interpret the other change patterns, apparently not caused by the conflict, such as prewar demolitions (Fig. 5.6c) and the flooded area in the top-left corner of Fig. 5.6.

As mentioned in Sect. 5.2.1.2, this is a type of analysis that might be undertaken in emergency contexts using Sentinel-1 StripMap mode over wide areas of investigation, coupled with local-scale assessment based on exploitation of L- and X-band imagery at high to very high resolution.

Acknowledgments TerraSAR-X and TanDEM-X imagery of Syrian sites were provided by the German Aerospace Center (DLR) via the TSX-New-Modes-2013 LAN2377 and TDX XTI-HYDR0399 grants. ENVISAT ASAR data over Apamea (Syria) and the Nasca region (Peru) were provided by ESA via the Cat-1 projects id. 28439 and 11073, respectively. Data processing was carried out using GAMMA SAR and Interferometry Software licensed to BGS, NERC. The authors publish with the permission of the Executive Director of BGS, NERC.

References

Adams R, Brown W, Culbert T (1981) Radar mapping, archeology, and ancient Maya land use. Science 213:1457–1463

Baade J, Schmullius C (2010) High-resolution mapping of fluvial landform change in arid environments using TerraSAR-X images. In: Geoscience and Remote Sensing Symposium (IGARSS), 2010 IEEE International, pp 2159–2162

Bachofer F, Quénéhervé G, Märker M (2014) The delineation of paleo-shorelines in the lake Manyara Basin using TerraSAR-X data. Remote Sens 6:2195–2212

Chen F, Masini N, Yang R et al (2015a) A space view of radar archaeological marks: first applications of COSMO-SkyMed X-band data. Remote Sens 7:24–50

Chen F, Lasaponara R, Masini N (2015b) An overview of satellite synthetic aperture radar remote sensing in archaeology: from site detection to monitoring. J Cult Herit. doi:10.1016/j.culher.2015.05.003

Cigna F, Ventisette C, Gigli G et al (2012) Ground instability in the old town of Agrigento (Italy) depicted by on-site investigations and Persistent Scatterers data. Nat Hazards Earth Syst Sci 12:3589–3603

Cigna F, Tapete D, Lasaponara R et al (2013) Amplitude change detection with Envisat ASAR to image the cultural landscape of the Nasca region, Peru. Archaeol Prospect 20:117–131

Cigna F, Lasaponara R, Masini N et al (2014) Persistent scatterer interferometry processing of COSMO-SkyMed StripMap HIMAGE time series to depict deformation of the historic Centre of Rome, Italy. Remote Sens 6:12593–12618

Comer D, Blom R, Golden C, Quilter J, Chapman B (2005) Inventory of archaeological sites using radar and multispectral data. Lecture presented at National Geographic Society, Washington, DC

Conesa F, Devanthéry N, Balbo AL et al (2014) Use of satellite SAR for understanding long-term human occupation dynamics in the monsoonal semi-arid plains of North Gujarat, India. Remote Sens 6(11):11420–11443

Covello F, Battazza F, Coletta A et al (2010) COSMO-SkyMed an existing opportunity for observing the earth. J Geodyn 49(3–4):171–180

Dore N, Patruno J, Pottier E et al (2013) New research in polarimetric SAR technique for archaeological purposes using ALOS PALSAR data. Archaeol Prospect 20:79–87

Elachi C, Granger J (1982) Space-borne imaging radars probe “in depth”. IEEE Spectrum 19:24–29

Elachi C, Roth L, Schaber G (1984) Spaceborne radar subsurface imaging in hyperarid regions. IEEE T Geosci Remote 4:383–387

El-Baz F (1998) Prehistoric artifacts near paleo-channels revealed by radar images in the western desert of Egypt. In: Remote sensing in archaeology from spacecraft, aircraft, on land, and in the deep sea. Boston University, Boston

Erasmi S, Rosenbauer R, Buchbach R et al (2014) Evaluating the quality and accuracy of TanDEM-X digital elevation models at archaeological sites in the Cilician Plain, Turkey. Remote Sens 6:9475–9493

ESA (2007) TM-19 InSAR principles: guidelines for SAR interferometry processing and interpretation. Part B InSAR processing: a practical approach. TM-19_ptB http://www.esa.int/esapub/tm/tm19/TM-19_ptB.pdf

ESA (2013) ESA Sentinel-1 user handbook. ESA Standard Document, GMES-S1OP-EOPG-TN-13-0001. 1 September 2013, 80 pp. https://sentinel.esa.int/

ESA Sentinel Online (2015) SENTINEL-1 SAR Technical Guide. Glossary. https://sentinel.esa.int/web/sentinel/sentinel-1-sar-wiki/-/wiki/Sentinel%20One/Glossary

Farr TG, Rosen PA, Caro E et al. (2007) The shuttle radar topography mission. Rev Geophys 45:RG2004/2007. doi:10.1029/2005RG000183

Gaber A, Koch M, Griesh MH et al (2013) Near-surface imaging of a buried foundation in the Western Desert, Egypt, using space-borne and ground penetrating radar. J Archaeol Sci 40:1946–1955

Gaber A, Soliman F, Koch M et al (2015) Using full-polarimetric SAR data to characterize the surface sediments in desert areas: a case study in El-Gallaba Plain, Egypt. Remote Sens Environ 16:11–28

Lasaponara R, Masini N (2013) Satellite synthetic aperture radar in archaeology and cultural landscape: an overview. Archaeol Prospect 20:71–78

Mittermayer J, Wollstadt S, Prats-Iraola P et al (2014) The TerraSAR-X staring spotlight mode concept. IEEE T Geosci Remote 52:3695–3706

Moore E, Freeman T, Hensley S (2007) Spaceborne and airborne radar at Angkor: introducing new technology to the ancient site. In: Wiseman JR, El-Baz F (eds) Remote sensing in archaeology, technology to the ancient site. Remote sensing in archaeology, Springer, New York, pp 185–218

Patruno J, Dore N, Crespi M et al (2013) Polarimetric multifrequency and multi-incidence SAR sensors analysis for archaeological purposes. Archaeol Prospect 20:89–96

Pratesi F, Tapete D, Terenzi G et al (2015) Rating health and stability of engineering structures via classification indexes of InSAR Persistent Scatterers. Int J Appl Earth Obs 40:81–90

Ruescas AB, Delgado JM, Costantini F et al (2009) Change detection by interferometric coherence in Nasca Lines, Peru (1997–2004). In: Fringe workshop proceedings 2009, European Space Agency SP-677, ESA-ESRIN, Frascati, 30 November–4 December 2009

Stewart C, Lasaponara R, Schiavon G (2014) Multi-frequency, polarimetric SAR analysis for archaeological prospection. Int J Appl Earth Obs 28:211–219

Tapete D, Cigna F (2012a) Rapid mapping and deformation analysis over cultural heritage and rural sites based on Persistent Scatterer Interferometry. Int J Geophys. doi:10.1155/2012/618609

Tapete D, Cigna F (2012b) Site-specific analysis of deformation patterns on archaeological heritage by satellite radar interferometry. In: 20th international materials research congress, symposium 8 cultural heritage and archaeological issues in materials science, MRS proceedings 1374, Cambridge University Press, pp 283–295

Tapete D, Cigna F (2015) A novel VHR SAR solution to monitor archaeological looting from space. Paper presented at ESA Workshop Advances in remote sensing for cultural heritage, ESA-ESRIN, Frascati, 12–13 November 2015

Tapete D, Fanti R, Cecchi R et al (2012) Satellite radar interferometry for monitoring and early-stage warning of structural instability in archaeological sites. J Geophys Eng 9:S10–S25

Tapete D, Casagli N, Luzi G et al (2013a) Integrating radar and laser-based remote sensing techniques for monitoring structural deformation of archaeological monuments. J Archaeol Sci 40:176–189

Tapete D, Cigna F, Masini N et al (2013b) Prospection and monitoring of the archaeological heritage of Nasca, Peru, with ENVISAT ASAR. Archaeol Prospect 20:133–147

Tapete D, Morelli S, Fanti R et al (2015a) Localising deformation along the elevation of linear structures: an experiment with space-borne InSAR and RTK GPS on the Roman Aqueducts in Rome, Italy. Appl Geogr 58:65–83

Tapete D, Cigna F, Lasaponara R et al. (2015b) Multi-scale detection of changing cultural landscapes in Nasca (Peru) through ENVISAT ASAR and TerraSAR-X. In: Lollino G et al (eds) Engineering geology for society and territory, vol 8. Springer, pp 339–343

Tapete D, Cigna F, Donoghue DNM et al. (2015c) Mapping changes and damages in areas of conflict: from archive C-band data to new HR X-band imagery, towards the Sentinels. In: Proceedings of FRINGE'15: advances in the science and applications of SAR interferometry and sentinel-1 InSAR workshop, Frascati, Italy, 23–27 March 2015, Ouwehand L., Ed., ESA Publication SP-731. doi:10.5270/Fringe2015.149

Tapete D, Cigna F, Donoghue DNM (2016) 'Looting marks' in space-borne SAR imagery: measuring rates of archaeological looting in Apamea (Syria) with TerraSAR-X staring spotlight. Remote Sens Environ 178:42–58

Wiseman J, El-Baz F (eds) (2007) Remote sensing in archaeology. Springer, New York

Zhou W, Chen F, Guo H (2015) Differential radar interferometry for structural and ground deformation monitoring: a new tool for the conservation and sustainability of cultural heritage sites. Sustainability 7:1712–1729

Chapter 6
DInSAR for the Monitoring of Cultural Heritage Sites

Differential SAR Interferometry for the Investigation of Deformations Affecting Cultural Heritage Sites: The Case Study of the Ancient Roman City of Pompeii (Italy)

Manuela Bonano, Mariarosaria Manzo, Francesco Casu, Michele Manunta, and Riccardo Lanari

Abstract Detection and monitoring of deformations affecting cultural heritage sites and their surroundings represent a key issue for developing strategies for their preservation, particularly in the case of extended archaeological areas. In this chapter, we first introduce the differential SAR interferometry (DInSAR) techniques that, thanks to their capability of performing noninvasive deformation analyses, provide valuable information about the spatial and the temporal evolution of the detected displacements. Subsequently, we present the DInSAR results achieved over the whole archaeological site of the ancient Roman city of Pompeii (Italy), and focus on some historical buildings where small displacements, involving portions or the whole complex structure, have been detected.

The performed analysis confirms the relevance of the DInSAR techniques for developing sustainable strategies aimed at the preservation of cultural and historical heritage sites.

M. Bonano (✉)
Institute for Electromagnetic Sensing of the Environment, National Research Council, Via Diocleziano 328, 80124, Naples, Italy

Institute of Methodologies for Environmental Analysis, National Research Council, C.da S. Loja, 85050, Tito Scalo, Potenza, Italy
e-mail: bonano.m@irea.cnr.it

M. Manzo • F. Casu • M. Manunta • R. Lanari
Institute for Electromagnetic Sensing of the Environment, National Research Council, Via Diocleziano 328, 80124, Naples, Italy

N. Masini, F. Soldovieri (eds.), *Sensing the Past*, Geotechnologies and the Environment 16, DOI 10.1007/978-3-319-50518-3_6

6.1 Introduction

Investigation of the deformation phenomena affecting the artistic, archaeological, and architectural heritage is of key relevance for its preservation. Indeed, heritage sites and their surroundings are prone to be affected by both natural and human-induced phenomena, which can cause structural and ground deformation, thus leading, in the worst case, to dislocation or even collapse of portions or entire historical monuments.

Traditionally, monitoring of the deformations occurring in cultural and historical heritage sites is carried out by exploiting portable or in situ installed sensors, such as GPS, automatic total stations, spirit leveling, and theodolites, which allow achieving single or continuous measurements. These systems have several advantages, such as highly accurate measurements, as well as a large flexibility in the monitoring system design; conversely, they can only acquire data in correspondence to the monitored structures, not permitting overall observation of the entire heritage site and its surrounding landscape. In the past two decades, the differential synthetic aperture radar interferometry (DInSAR) technique has emerged as an effective, noninvasive, microwave methodology to detect and map surface displacements with centimeter to millimeter accuracy (Gabriel et al. 1989). Indeed, DInSAR overcomes the main limitations of the traditional in situ methods because of its extensive spatial coverage without requiring the installation of instruments over the investigated area and structures. Accordingly, the exploitation of this methodology is rapidly growing within the framework of structural and ground deformation monitoring of cultural and historical heritage sites and for supporting the preventive diagnosis of deformation threats (Bock et al. 2012; Tapete et al. 2012; Zeni et al. 2011).

In this chapter, we investigate the capability of the DInSAR technique to identify and monitor deformation phenomena affecting historical buildings, by focusing on the archaeological site of the ancient Roman city of Pompeii (Italy), which because of its invaluable inheritance represents a very relevant case study. In particular, we analyze the displacements involving the whole archaeological site during the 1993–2015 time interval, through the generation of deformation time series computed from large archives of SAR data collected by the ERS-1/2 and ENVISAT SAR sensors of the European Space Agency (ESA), as well as by the Italian COSMO-SkyMed constellation.

The chapter is organized as follows. First, we describe the conventional DInSAR technique and its advances developed during the past decades; then, we present and discuss the results achieved in correspondence to the whole archaeological site of the ancient Roman city of Pompeii, focusing on some relevant and well-known historical buildings. Finally, we provide some concluding remarks.

6.2 The Conventional DInSAR Technique

A synthetic aperture radar (SAR) sensor is a coherent active radar system, typically mounted onboard aircraft or satellites, whose capability to effectively map the scattering properties of the Earth's surface is nowadays well established. It operates

in a side-looking illumination configuration, emits microwave pulses, and measures the amplitude and the phase of the signals backscattered from the Earth's surface. It is able to accurately measure the distance between the system moving platform and the observed ground surface. The proper processing of the received backscattered radar signal (echo), which accounts for both the physical characteristics of the imaged scene and the acquisition geometry, allows reconstructing high spatial resolution complex radar images relevant to Earth's surface, independently from the sensor altitude. Being an active sensor, SAR provides its own illumination system; therefore, it does not need any external radiation source to work, thus permitting continuous (day and night) operation. Moreover, by working at the microwave frequencies of the electromagnetic spectrum (significantly lower than those of the visible spectrum region), it can be effectively used in presence of fog, clouds, precipitation, and ashes, thus allowing all-weather imaging.

Thanks to its flexibility, SAR technology has been largely applied during the past decades and several new techniques have also been developed for an advanced use of SAR data in both scientific and commercial scenarios, making it a fundamental instrument for Earth Observation. One of the major applications of this technology is represented by the SAR interferometry (InSAR), which exploits the phase difference (i.e., interferogram) between pairs of SAR images, collected over the same area at different epochs (temporal baseline) and with different orbital positions (spatial baseline), to retrieve Earth's surface geophysical parameters, such as scene topography or surface deformation. In particular, the differential SAR interferometry (DInSAR) technique (Burgmann et al. 2000; Gabriel et al. 1989; Massonnet and Feigl 1998) allows extracting information on the radar line-of-sight (LOS) projection of the surface displacements, which occurred between two temporally separated observations (referred to as *master* and *slave* acquisitions) acquired with the same illumination geometry over an investigated area (Franceschetti and Lanari 1999).

As a consequence of its capability to produce spatially dense maps of the surface displacements caused by a large variety of natural and anthropogenic hazards, such as earthquakes, volcanic eruptions, and subsidence phenomena (Massonnet et al. 1993, 1995; Peltzer and Rosen 1995; Rignot 1998; Tesauro et al. 2000), with accuracies of the order of fractions of the used wavelength (Gabriel et al. 1989), DInSAR technique has progressively emerged as an effective, noninvasive tool in civil protection scenarios, with limited monitoring costs with respect to the traditional in situ surveys. Nevertheless, standard DInSAR analyses are intrinsically limited, because a single interferogram contains the information relevant to the overall deformation that occurred between the two acquisitions, whose separation in time can range from a few days to some months. Moreover, the presence of atmospheric disturbances that may characterize the SAR data pairs, as well as of the residual topographic phase components because of inaccuracies of the exploited external digital elevation models (DEMs), is particularly difficult to filter out from the single DInSAR interferograms, if no rather sophisticated atmospheric models or precise DEM relative to the investigated area are available. To overcome these limitations, in the past 25 years several advanced DInSAR approaches have been developed, also fostered by the large availability of SAR data collected by the so-called first-generation satellite systems, continuously acquiring data of the Earth's

surface since 1992 (e.g., ERS-1/2, ENVISAT, RADARSAT-1) with a nearly monthly revisit time, and ground resolution ranging from a few to tens of meters. Such advanced DInSAR approaches are based on the exploitation of large sequences of SAR images collected over an investigated area, with the aim to follow the temporal evolution of the detected displacements via the generation of deformation time series.

6.3 The Advanced DInSAR Techniques

Originally applied to investigate single deformation episodes, the DInSAR technique has subsequently been extended to manage large stacks of SAR acquisitions to provide useful information on both the spatial and the temporal patterns of the detected LOS-projected displacements through the generation of deformation time series (Berardino et al. 2002; Crosetto et al. 2005; Ferretti et al. 2000, 2011; Hooper et al. 2004; Hooper 2008; Kampes 2006; Lanari et al. 2004a; Mora et al. 2003; Werner et al. 2003). In particular, the so-called advanced DInSAR techniques are based on a proper combination of a set of multitemporal differential interferograms relevant to an area of interest, to compute the deformation time series of the observed area through the inversion of a system of linear equations. In the past decades, several advanced multitemporal DInSAR algorithms, characterized by different interferogram selection criteria, have been developed; they are usually grouped into two main categories, commonly referred to as persistent scatterers (PS) (Ferretti et al. 2000; Hooper et al. 2004; Kampes 2006; Werner et al. 2003) and small baseline (SB) (Berardino et al. 2002; Crosetto et al. 2005; Lanari et al. 2004a; Mora et al. 2003) techniques, even though a solution that incorporates both PS and SB approaches has also been proposed (Ferretti et al. 2011). The PS-based approaches rely on the selection of all the interferometric data pairs with respect to one common master image, without imposing any baseline constraint on the used interferograms; accordingly, only single dominant scatterers are analyzed, which are less affected by noise (temporal and spatial decorrelation) effects (Zebker and Villasenor 1992). Conversely, the SB algorithms are able to investigate also distributed scatterers (DS), by properly selecting multitemporal interferometric data pairs characterized by small spatial and temporal baselines. Such an accurate selection, which involves the introduction of constraints on the maximum allowed spatial and temporal baseline values of the DInSAR interferograms, permits mitigating the decorrelation phenomena that affect the interferometric pairs, and thus drastically increases the spatial density of the retrieved DInSAR measurements, especially in semi-urbanized and rural areas.

Among these methods, the DInSAR approach referred to as Small Baseline Subset (SBAS) (Berardino et al. 2002; Lanari et al. 2004a) has successfully been applied to detect surface deformations caused by several natural and human-induced hazards, such as volcanic events, earthquakes, landslides, oil and gas extraction, subsidence phenomena, and tunnelling excavations (Bonano et al. 2013; Calò et al. 2014; D'Auria et al. 2015; Lanari et al. 2004b, 2007a, b, 2010; Manzo et al.

2006; Sansosti et al. 2010; Stramondo et al. 2007; Tizzani et al. 2009, 2013; Trasatti et al. 2008; Zeni et al. 2011). It relies on the proper selection of a large number of SAR data pairs, which are used to generate small baseline DInSAR interferograms to limit decorrelation effects. The combination of the selected interferometric data pairs allows generating mean deformation velocity maps and corresponding time series for each coherent measure point, with an accuracy of about 1–2 mm/year for what concerns the mean deformation velocity information and 5–10 mm for the single deformation measurement (Bonano et al. 2013; Casu et al. 2006; Lanari et al. 2007b). The deformation time series are easily computed by searching for a least squares solution with a minimum norm energy constraint (the SVD technique is applied in presence of different data subsets separated by large baselines) (Berardino et al. 2002).

The SBAS approach allows producing ground deformation time series at two distinct spatial scales: at the regional (low resolution) scale, it exploits average (multi-look) interferograms to detect and analyze deformation phenomena relevant to very large areas, with a ground spatial resolution ranging from about 30 to 100 m (Sansosti et al. 2014); at the local (full resolution) scale, the SBAS approach exploits single-look interferograms, generated at the full sensor spatial resolution (down to a few meters), to study local deformation that may affect buildings and man-made features (Arangio et al. 2013; Bonano et al. 2013; Cascini et al. 2007). Moreover, the multiscale SBAS algorithm allows handling multisensor SAR data acquired by different radar systems but with the same illumination geometry, as for the case of the C-band ERS-1/2 and ENVISAT sensors (Bonano et al. 2012; Pepe et al. 2005). Accordingly, the SBAS approach allows generating LOS displacement maps and associated time series spanning very long periods (decades), thus guaranteeing the continuity in the monitoring of the Earth's surface deformation phenomena, as well as providing unprecedented information for studying long-term ground movements at different spatial scales.

In the most recent past years, advanced DInSAR technologies have been rapidly changing to take into account the large availability of SAR data acquired by the so-called second-generation satellite constellations, such as the X-band Italian COSMO-SkyMed (CSK) and German TerraSAR-X (TSX) systems. These new-generation SAR systems are mainly characterized by a higher spatial resolution (of about 3 m for the stripmap mode, but potentially down to 1 m or less for the spotlight mode case) and a reduced revisit time (11 days for the TSX system, but as short as a few days for the CSK constellation) compared to the ERS and ENVISAT ones, thus leading to the creation of large SAR data archives. Moreover, a massive data volume will be further supplied by the C-band Sentinel-1A (S1A) SAR satellite, recently launched (3 April 2014) within the framework of the Copernicus (formerly GMES) Programme of the European Union. Indeed, S1A, designed to work over land by exploiting the innovative acquisition mode referred to as terrain observation with progressive scans (TOPS) mode (Torres et al. 2012), which allows collecting S1A interferometric wide swath (IWS) scenes, acquires SAR images with a spatial resolution comparable to that of the ERS and ENVISAT satellites, but with a very wide swath (about 280 km) and a "free and open access" data policy.

Moreover, its current revisit time (12 days) will be soon halved (to 6 days) when the Sentinel-1B (S1B) twin satellite, just launched (25 April 2016), will be fully operative. Accordingly, innovative and appropriate solutions, aimed at handling these massive SAR data archives, more and more increasing in terms of both temporal and spatial coverage, are needed to effectively and routinely exploit the advanced DInSAR methodologies (Rucci et al. 2012).

In the following, we discuss the relevance of the multiscale and multisensor SBAS-DInSAR technique to detect and monitor deformation phenomena affecting cultural and historical heritage. To this aim, we focus on the archaeological site of Pompeii and show, through a comparative analysis between ERS/ENVISAT and CSK SBAS-DInSAR results, how the improved spatial resolution and reduced revisit time characterizing the CSK constellation impacts on the capabilities of detecting and mapping deformation phenomena relevant to single historical buildings and complex structures.

6.4 The DInSAR Results on the Archaeological Site of Pompeii

The excavations over the archaeological site of Pompeii have brought to light the remains of the ancient Roman city, buried under a thick layer of ashes and lapilli when the devastating eruption of Mt. Vesuvius occurred in 79 AD, destroying the city of Pompeii and the neighboring city of Herculaneum. The ancient Pompeii site was rediscovered during the seventeenth century, when the excavations started under King Charles III of Bourbon, and continued systematically throughout the twentieth century, providing an outstanding and valuable heritage of architecture, sculptures, paintings, and mosaics.

To carry out our overall deformation analysis, we have applied the multiscale, multisensor SBAS approach (Bonano et al. 2012; Lanari et al. 2004a; Pepe et al. 2005) to two large SAR data archives, acquired from both the C- and X-band sensors over the Napoli Bay area (Italy), which includes also the selected case study. In particular, the C-band dataset consists of 75 ERS-1/2 and 63 ENVISAT-IS2 SAR images (Fig. 6.1a), collected over ascending orbits between January 1993 and September 2010, whereas the X-band set comprises a sequence of 388 CSK data frames (see Fig. 6.1b), acquired over ascending orbits during the 6-year time interval between July 2009 and July 2015. Starting from the available SAR acquisitions, two sets of SB interferometric data pairs have been identified, by imposing constraints on the maximum spatial baseline values: 400 m for the C-band dataset, and 800 m for the CSK set. Then, 404 ERS/ENVISAT and 1189 CSK DInSAR interferograms were generated, using precise satellite orbital information and the 3-arcsec Shuttle Radar Topography Mission (SRTM) DEM of the study area to remove the topographic phase component (Gabriel et al. 1989).

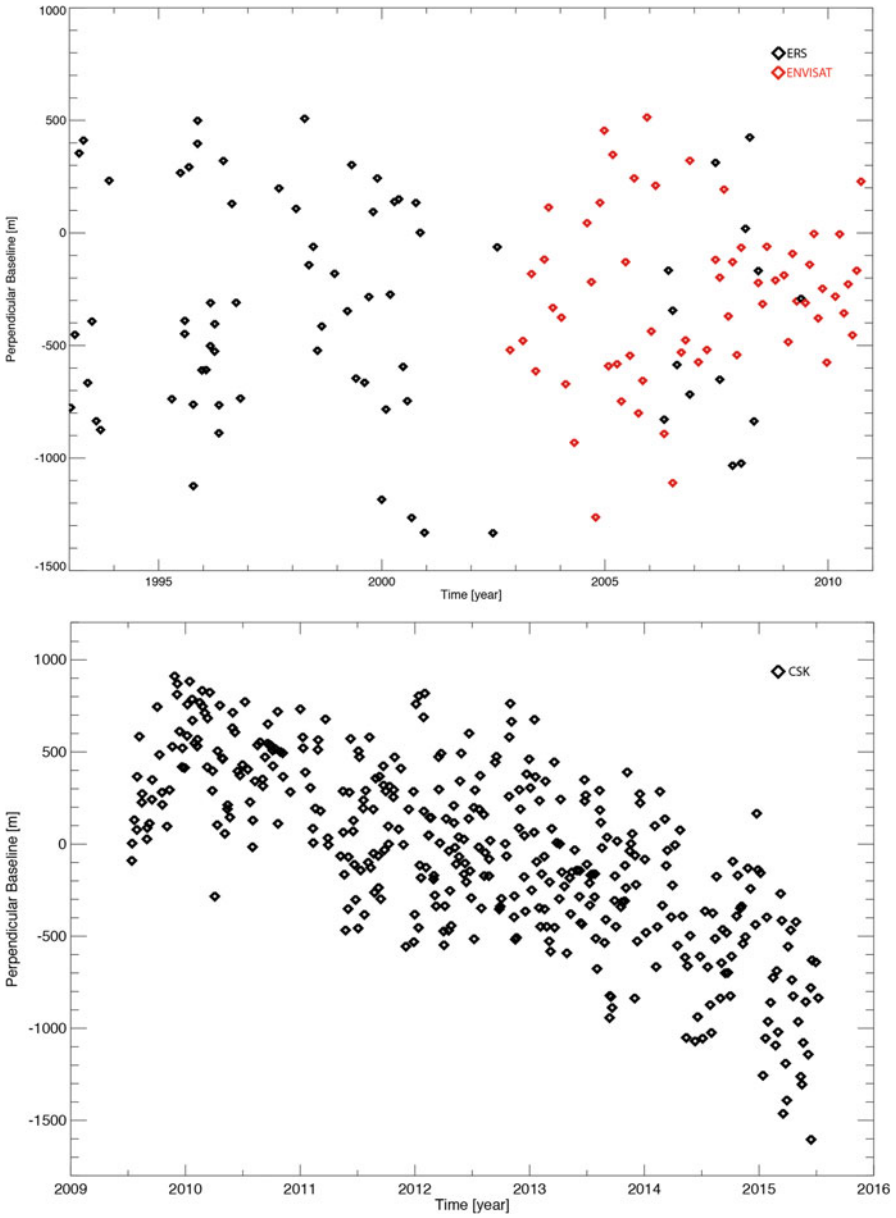

Fig. 6.1 Synthetic aperture radar (SAR) acquisition distribution in the temporal/perpendicular baseline plane for the exploited C- and X-band datasets. (**a**) ERS-1/2 and ENVISAT acquisitions (*black* and *red diamonds*, respectively). (**b**) COSMO-SkyMed images (*black diamonds*)

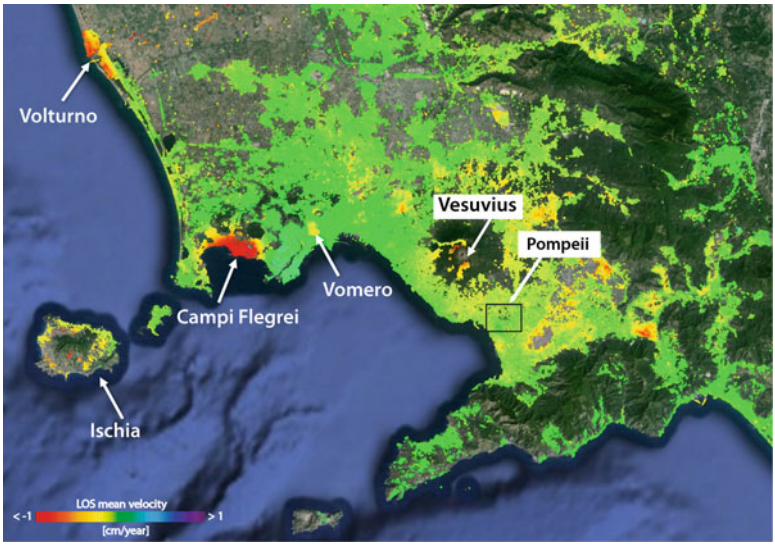

Fig. 6.2 Low-resolution (ground spatial resolution of about 100 × 100 m) SBAS-DInSAR deformation velocity map superimposed on an optical image of the Napoli Bay area (Southern Italy). The results are relevant to the 1993–2010 ERS/ENVISAT dataset. The Volturno River, the Ischia Island, the Campi Flegrei Caldera, the Vomero quarter within the city of Napoli, Mt. Vesuvius, and the city of Pompeii are *highlighted*. The *black box* indicates the area relevant to the archaeological site of the ancient Roman city of Pompeii

To provide an overall view of the deformation phenomena affecting the whole Napoli Bay area, we present in Fig. 6.2 the SBAS DInSAR results achieved by performing a low-resolution analysis via the 1993–2010 ERS/ENVISAT dataset. In particular, Fig. 6.2 reports the geocoded ERS/ENVISAT mean deformation velocity map, superimposed on an optical image of the investigated area, relevant to the coherent pixels only. The presented results show the well-known deformation patterns affecting the area during the observed time period. In particular, we can clearly identify, from left to right, the subsidence phenomena along the delta region of the Volturno River, the displacements characterizing the Ischia volcanic Island, the large deformation pattern (of more than 1 cm/year) related to the Campi Flegrei Caldera, the subsidence phenomena (some mm/year) relevant to the highly urbanized Vomero quarter within the Napoli city centre, as well as the displacements in correspondence to the summit of Mt. Vesuvius. Such a representation is visually effective and allows us to retrieve average information on the detected displacements. However, the presented low-resolution results, because of the multi-look operation (with an average factor of 20 and 4 pixels along the azimuth and range directions, respectively, which leads to a ground pixel size of about 100 m × 100 m) carried out within the interferogram generation, are particularly suitable to investigate regional trends or deformation phenomena over large areas, but are not appropriate to monitor displacements related to single structures, as in the case of

historical buildings and archaeological sites. Accordingly, in the following we move to the full-resolution analysis and present a comparative SBAS-DInSAR study of the ground deformation time series and velocity maps relevant to the archaeological site of Pompeii, achieved by exploiting both the C- and X-band SAR datasets.

Before going into the details of the retrieved SBAS-DInSAR results, we highlight how the higher spatial resolution of the CSK acquisitions (down to a few meters) with respect to the ERS/ENVISAT data (some tens of meters) allows having a complete and detailed image of the whole archaeological site, making the X-band radar images more and more geometrically comparable to the optical ones. In Fig. 6.3 we report a sketch of the full-resolution SAR amplitude images (in radar geometry) relevant to the Pompeii site obtained by exploiting the C-band (Fig. 6.3a) and X-band (Fig. 6.3b) data; it is evident the impressive level of details achievable via the CSK systems (the historical buildings and the structures are clearly recognizable) with respect to the ERS/ENVISAT data. Accordingly, the improved spatial resolution of the X-band sensors allows us to detect an increased number of coherent points within the SBAS deformation maps. Such an improvement in the coherent pixel density is shown in Fig. 6.4, where the sketches of the full-resolution deformation velocity maps relevant to the ERS/ENVISAT (Fig. 6.4a) and the CSK (Fig. 6.4b) datasets over the ancient Pompeii ruins are reported. Both the maps reveal that most of the human-made buildings and monuments within the investigated area are detected; however, the spatial distribution of the retrieved CSK pixels is extremely much denser than the corresponding C-band one, allowing us to identify nearly all the historical monuments and complex structures located within the archaeological site. This is the case of the large complex structures known as the Major Amphitheatre on the right (identified by the label *c* in Fig. 6.4) and the Big Theatre, close to the Isis temple, on the bottom (label *d* in Fig. 6.4), where no ERS/ENVISAT pixels have been detected; concerning other well-known historical buildings, as for the Temple of Apollo (label *e*) and the Roman Forum (label *f*), characterized by the long column lines, the CSK results are able to depict the whole structure, whereas only a few ERS/ENVISAT pixels fall within the relevant perimeters. In this framework, it is worth noting that the pixel density enhancement can be also beneficial for investigating possible displacements associated with portions of the analyzed structures, thus easily detecting intra-building differential movements affecting single elements of a complex historical monument.

Moving to a qualitative analysis of the retrieved SBAS-DInSAR measurements, the displacement velocity maps in Fig. 6.4a, b do not show any significant deformation pattern, thus revealing a general stable behavior of the entire archaeological site. Nevertheless, thanks to the improved pixel density achieved for the CSK data processing, a few localized buildings affected by significant subsidence phenomena have been detected, as clearly shown in Fig. 6.4b. In particular, we first focus on a prestigious historical building known as the “House of the Vettii” (see the white circles in Fig. 6.4 for its location), and show the corresponding CSK deformation velocity map in the zoomed view of Fig. 6.5. The Domus, for which the excavation works started in 1894, is one of the most beautiful, richest, and well-preserved houses of the ancient Pompeian town. The house is characterized by a large number

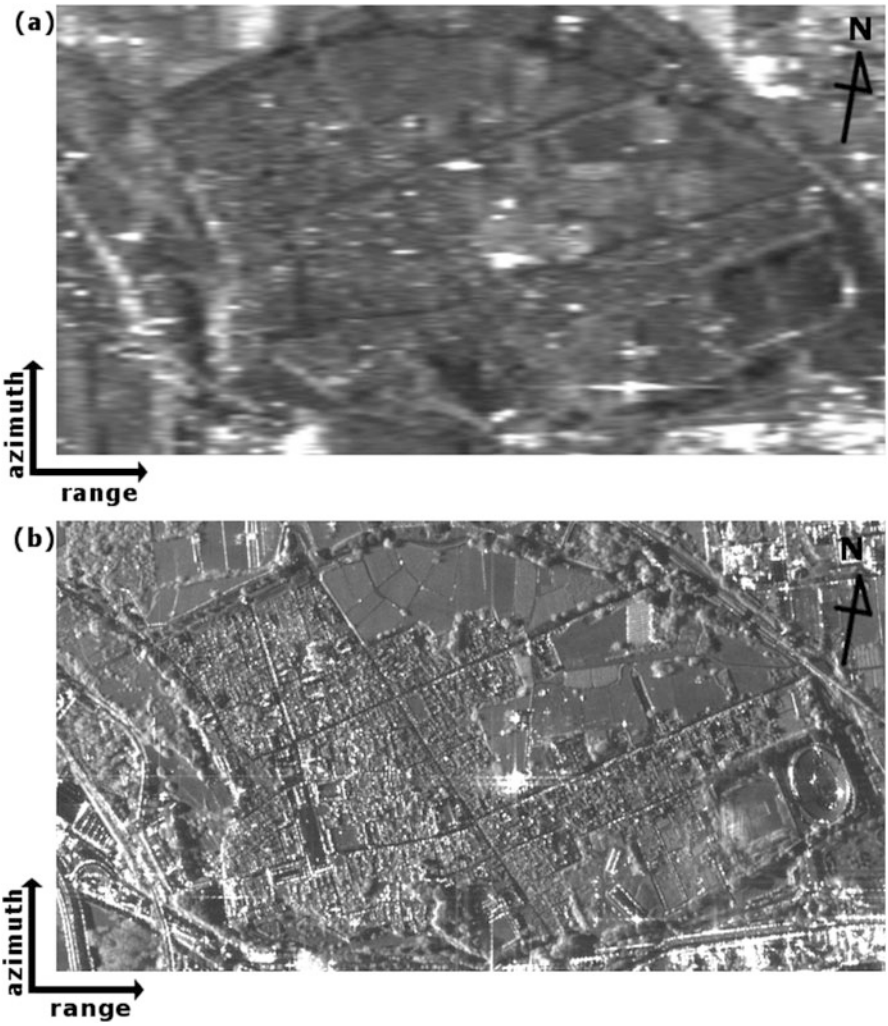

Fig. 6.3 SAR amplitude images of the Pompeii archaeological site in the radar coordinate geometry (the *pictured area* is approximately the one reported in the *black box* of Fig. 6.2). (**a**) ERS-1/2 and ENVISAT data. (**b**) CSK data. The *black arrows* indicate the corresponding SAR sensor azimuth and range directions. The north direction is also shown as a reference

of paintings and decorations in an excellent state of preservation, which testify the high economic and social level of the owners, the Vettii, and their devotion to Priapus, the god of prosperity, who is pictured in the main entrance.

The CSK results retrieved in correspondence to the investigated structure show a maximum subsidence trend of about 7 mm/year, as also evidenced by the displacement time series reported in the plot of Fig. 6.5. It is worth noting

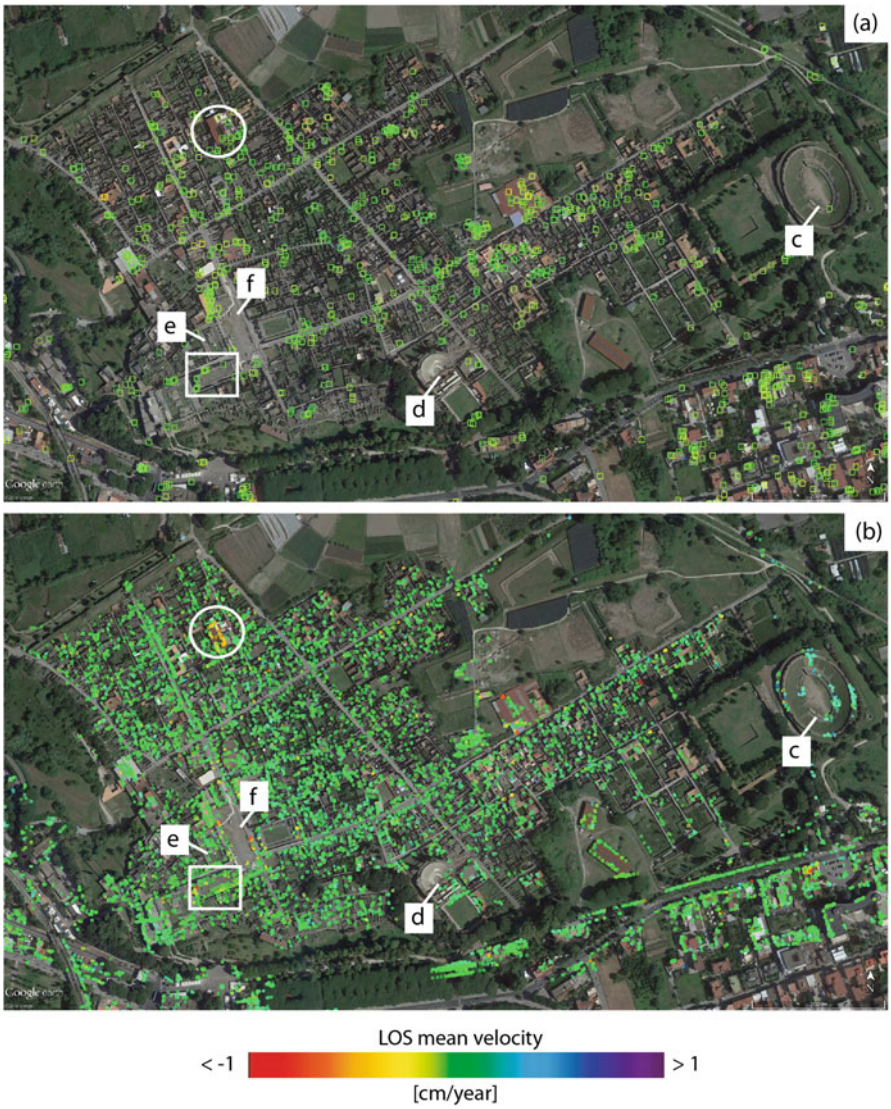

Fig. 6.4 Comparison between the ERS/ENVISAT and the CSK SBAS-DInSAR results relevant to the selected area shown in Fig. 6.3. (**a**) Zoomed view of the full-resolution SBAS-DInSAR results achieved through the 1993–2010 ERS-1/2 and ENVISAT SAR data archive. (**b**) Zoomed view of the full-resolution SBAS-DInSAR results achieved through the 2009–2015 CSK SAR data archive. Some well-known historical and archaeological monuments, such as the Major Amphitheatre (*label c*), the Big Theatre (*label d*), the Temple of Apollo (*label e*) and the Roman Forum (*label f*) are also *highlighted*. The *white circles* indicate the position of the historical building (the "House of Vettii") investigated in Fig. 6.5, whereas the *white rectangles* show the location of the "Basilica," analyzed in Fig. 6.6

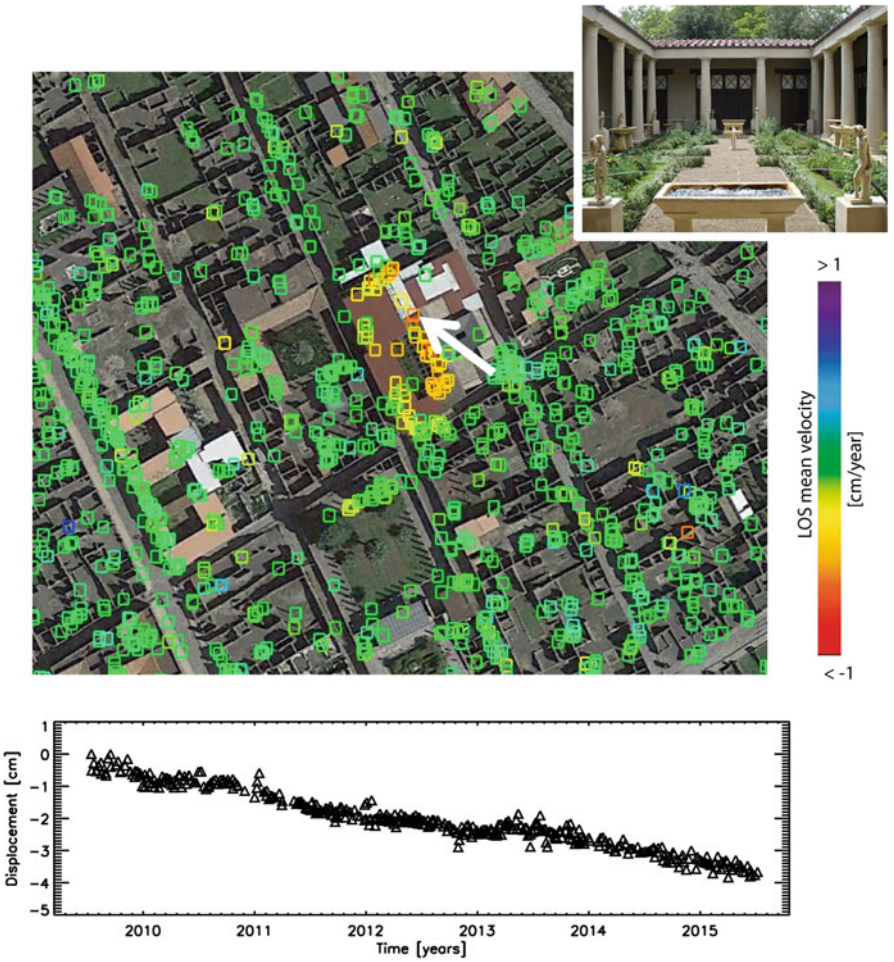

Fig. 6.5 Zoomed view of the CSK SBAS-DInSAR results relevant to the historical building known as "House of Vettii," pictured in the *inset* on the top (see the *white circles* in Fig. 6.4 for its location). On the *bottom* is shown the CSK deformation time series for the pixel highlighted by the *white arrow*

that the high temporal sampling rate guaranteed by the CSK constellation has a large impact on the capability to follow and monitor small-rate, fast-varying, and nonlinear deformation signals over time, compared to the monthly ERS/ENVISAT revisit frequency. Such a reduced revisit time is particularly effective in presence of deformation analyses related to short time intervals, where a possible limited number of collected SAR acquisitions may compromise the typical performances of the SBAS-DInSAR approach (Bonano et al. 2013; Casu et al. 2006), leading to a drastic decrease of the accuracy of the achieved results. Therefore, the almost 4-day revisit pass offered by the CSK constellation makes available the

collection of a large SAR data archive, allowing us to handle a sufficient number of SAR acquisitions also in restricted time periods (in this case, almost 400 CSK acquisitions in about 6 years).

We then concentrate on another historical building known as the "Basilica," identified in Fig. 6.4 by the white rectangles. The Basilica of Pompeii is dated at the end of the second century BC and is the oldest known basilica of the Roman Empire. It is located at the southwest corner of the Roman Forum (see label *f* in Fig. 6.4) with the short side adjacent to it, and is characterized by a long colonnade of both Ionic and Corinthian orders all along its perimeter. Such an important building represented the core of both the civil and commercial activities in Pompeii because the court and the market were placed there.

In this case, the SBAS-DInSAR velocity map pictured in Fig. 6.6 does not show any particular deformation pattern within the investigated structure, revealing a quite stable behavior of the whole building; nevertheless, a few localized pixels in correspondence to the northwestern corner exhibit a maximum subsidence rate of about 5 mm/year, as also portrayed in the displacement time series reported in the plot of Fig. 6.6. This example confirms the capability of the full-resolution SBAS-DInSAR approach to detect and also monitor also small displacements affecting single elements of a whole historical building.

The experiments performed over the archaeological site of Pompeii clearly demonstrate how the full-resolution SBAS approach is able to monitor and follow the temporal evolution of very localized deformation phenomena related not only to extended man-made features, but also to portions of a single historical monument or building, thanks to the large number of coherent targets detected over the investigated structures.

6.5 Conclusions and Further Developments

This chapter is devoted to highlighting the key role of the advanced DInSAR techniques for the preservation of our cultural, artistic, and archaeological heritage, thanks to their capability to detect and monitor deformation phenomena affecting historical monuments. To this aim, we focused on the well-known archaeological site of Pompeii, and applied the multiscale and multisensor SBAS-DInSAR technique to two C- and X-band satellite datasets, collected during the 1993–2015 time interval from the "first" (ERS and ENVISAT) and the "second" (CSK) SAR sensor generations, respectively. The comparative analysis between the C- and X-band SBAS-DInSAR results clearly shows the significant impact of the improved spatial resolution and reduced revisit time of the CSK data on the investigation of the space–time characteristics of the revealed displacement phenomena at the scale of single buildings and structures. More specifically, the higher spatial resolution (down to a few meters) characterizing the X-band CSK SAR images allows analyzing the detected deformations with a great level of spatial detail, thanks to the increased number of coherent points within the SBAS-DInSAR deformation

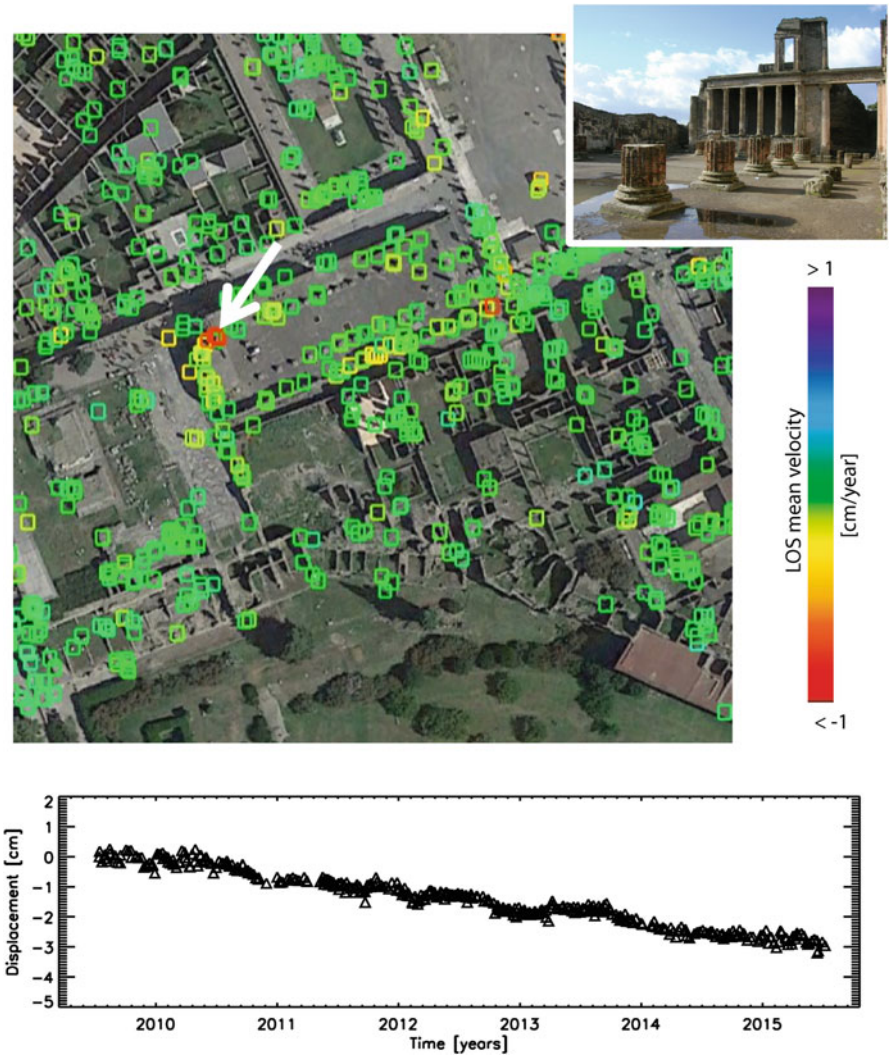

Fig. 6.6 Zoomed view of the CSK SBAS-DInSAR results relevant to the historical building known as the "Basilica," located close to the Apollo Temple, pictured in the *inset* on the top (see the *white rectangles* in Fig. 6.4 for its location). On the *bottom* is shown the CSK deformation time series for the pixel highlighted by the *white arrow*

maps. This capability is particularly relevant because it permits the investigation of most of the historical monuments and structures located within the archaeological site. Moreover, in presence of possible displacements associated with portions of a building, it allows identifying even small and very localized deformation patterns. These findings may also allow revealing intra-building differential movements, thus resulting particularly appropriate for geotechnical and structural engineering

analyses. Moreover, the reduced revisit time of the CSK SAR constellation is very relevant when considering small rates and fast-varying and nonlinear deformation phenomena, thus opening new possibilities of the operational use of the advanced DInSAR techniques in early warning monitoring scenarios.

In this framework, a further advance is represented by the availability of the new C-band SAR data archives provided by the twin satellites of the Sentinel-1 constellation. However, the high data volume provided by these new-generation SAR sensors (i.e., CSK and Sentinel-1) is moving the DInSAR scenario toward a 'big data' challenge, which is expected to have a strong impact on the data storage and the computational requirements needed to generate the advanced DInSAR products. In this context, the innovation brought by the new information and communication technologies (ICT) can be very relevant but, to profitably exploit the performances of the new generation of SAR sensors, it is also crucial to develop much more advanced DInSAR methodologies (and codes) able to effectively compact the information associated with these huge amounts of SAR data. Accordingly, both large-storage and high-performance computing capabilities are needed, as well as development of efficient algorithms, to tackle this huge data flow. In this scenario, cloud computing technologies, which are well established within the ICT community (Badger et al. 2012), may represent an efficient solution within the advanced DInSAR application framework. It is worth noting that a parallel implementation of the SBAS approach (Casu et al. 2014), referred to as P-SBAS, suitable to run efficiently in large computing infrastructures, such as those based on GRID and Cloud solutions (Zinno et al. 2015), has recently been developed. It allows overcoming the problem of the computational efficiency of advanced DInSAR approaches, becoming strategic in the light of the extremely large data flow provided by the aforementioned new-generation SAR sensors in the next years. This solution can be particularly relevant for the development of a preservation strategy for the archaeological sites and historical buildings spread all over the world.

Acknowledgments This work has partially been funded by the Italian Department of Civil Protection (DPC); the manuscript contents reflect authors' positions that could be different from the DPC official statements. The work has also been supported by the I-AMICA project (PONa3 00363). We thank the European and Italian Space Agency for providing the ERS/ENVISAT and COSMO-SkyMed data, respectively. We also thank the NASA SRTM mission for the DEM of the Napoli Bay area.

References

Arangio S, Calo' F, Di Mauro M, Bonano M, Marsella M, Manunta M (2013) An application of the SBAS-DInSAR technique for the assessment of structural damage in the city of Rome, Struct Infrastruct Eng Maint, Manag Life-Cycle Des Perform:1–15

Badger L, Grance T, Patt Corner R, Voas J (2012) Cloud computing synopsis and recommendations, NIST special publication 800–146. National Institute of Standards and Technology, US. Department of Commerce, Gaithersburg, MD

Berardino P, Fornaro G, Lanari R, Sansosti E (2002) A new Algorithm for surface deformation monitoring based on small baseline differential SAR Interferograms. IEEE Trans Geosci Remote Sens 40:2375–2383

Bock Y, Wdowinski S, Ferretti A, Novali F, Fumagalli A (2012) Recent subsidence of the Venice Lagoon from continuous GPS and interferometric synthetic aperture radar. Geochem Geophys Geosyst 13:Q03023

Bonano M, Manunta M, Marsella M, Lanari R (2012) Long-term ERS/ENVISAT deformation time-series generation at full spatial resolution via the extended SBAS technique. Int J Remote Sens 33:4756–4783

Bonano M, Manunta M, Pepe A, Paglia L, Lanari R (2013) From previous C-Band to New X-Band SAR systems: assessment of the DInSAR mapping improvement for deformation time-series retrieval in urban areas. IEEE Trans Geosci Remote Sens 51(4):1973–1984

Burgmann R, Rosen PA, Fielding EJ (2000) Synthetic aperture radar interferometry to measure Earth's surface topography and its deformation. Annu Rev Earth Planet Sci 28:169–209

Calò F, Ardizzone F, Castaldo R, Lollino P, Tizzani P, Guzzetti F, Lanari R, Angeli M, Pontoni F, Manunta M (2014) Enhanced landslide investigations through advanced DInSAR techniques: the Ivancich case study, Assisi, Italy. Remote Sens Environ 142:69–82

Cascini L, Ferlisi S, Peduto D, Fornaro G, Manunta M (2007) Analysis of a subsidence phenomenon via DInSAR data and geotechnical criteria. Ital Geotech J 41(4):50–67

Casu F, Manzo M, Lanari R (2006) A quantitative assessment of the SBAS algorithm performance for surface deformation retrieval from DInSAR data. Remote Sens Environ 102(3–4): 195–210

Casu F, Elefante S, Imperatore P, Zinno I, Manunta M, De Luca C, Lanari R (2014) SBAS-DInSAR parallel processing for deformation time-series computation. IEEE J Sel Top Appl Earth Obs Remote Sens 7(8):3285–3296

Crosetto M, Crippa B, Biescas E (2005) Early detection and in-depth analysis of deformation phenomena by radar interferometry. Eng Geol 79(1/2):81–91

D'Auria L, Pepe S, Castaldo R, Giudicepietro F, Macedonio G, Ricciolino P, Tizzani P, Casu F, Lanari R, Manzo M, Martini M, Sansosti E, Zinno I (2015) Magma injection beneath the urban area of Naples: a new mechanism for the 2012-2013 volcanic unrest at Campi Flegrei caldera. Scientific Reports 5:13100. doi:10.1038/srep13100

Ferretti A, Prati C, Rocca F (2000) Non-linear Subsidence Rate Estimation Using Permanent Scatterers in Differential SAR Interferometry. IEEE Trans Geosci Remote Sens 38:2202–2212

Ferretti A, Fumagalli A, Novali F, Prati C, Rocca F, Rucci A (2011) A new algorithm for processing interferometric data- stacks: SqueeSAR. IEEE Trans Geosci Remote Sens 49:3460–3470

Franceschetti G, Lanari R (1999) Synthetic aperture radar processing. CRC Press, Boca Raton

Gabriel AK, Goldstein RM, Zebker HA (1989) Mapping small elevation changes over large areas: differential interferometry. J Geophys Res 94(B7):9183–9191

Hooper A, Zebker H, Segall P, Kampes B (2004) A new method for measuring deformation on volcanoes and other natural terrains using InSAR persistent scatterers. Geophys Res Lett 31(23):L23611

Hooper A (2008) A multi-temporal InSAR method incorporating both persistent scatterer and small baseline approaches. Geophys Res Lett 35:L16302., http://dx.doi.org/10.1029/2008GL034654

Kampes BM (2006) Radar interferometry: persistent scatterer technique. Springer, Dordrecht

Lanari R, Mora O, Manunta M, Mallorquí JJ, Berardino P, Sansosti E (2004a) A small baseline approach for investigating deformations on full resolution differential SAR interferograms. IEEE Trans Geosci Remote Sens 42:1377–1386

Lanari R, Lundgren P, Manzo M, Casu F (2004b) Satellite radar inter- ferometry time series analysis of surface deformation for Los Angeles, California. Geophys Res Lett 31(23):L23 613–1–L23 613–5

Lanari R, Casu F, Manzo M, Zeni G, Berardino P, Manunta M, Pepe A (2007a) An overview of the small BAseline subset algorithm: a DInSAR technique for surface deformation analysis. Pure Appl Geophys (PAGEOPH) 164(4):637–661

Lanari R, Casu F, Manzo M, Lundgren P (2007b) Application of the SBAS-DInSAR technique to fault creep: a case study of the Hayward fault, California. Remote Sens Environ 109(1):20–28

Lanari R, Berardino P, Bonano M, Casu F, Manconi A, Manunta M, Manzo M, Pepe A, Pepe S, Sansosti E, Solaro G, Tizzani P, Zeni G (2010) Surface displacements associated with the L'Aquila 2009 Mw 63 earthquake Central Italy: new evidence from DInSAR time series analysis. Geophys Res Letter 37:L20309, doi:101029/2010GL044780

Manzo M, Ricciardi GP, Casu F, Ventura G, Zeni G, Borgström S, Berardino P, Del Gaudio C, Lanari R (2006) Surface deformation analysis in the Ischia island (Italy) based on spaceborne radar interferometry. J Volcanol Geotherm Res 151:399–416. doi:10.1016/j.jvolgeores.2005.09.010

Massonnet D, Rossi M, Carmona C, Adragna F, Peltzer G, Feigl K, Rabaute T (1993) The displacement field of the Landers earthquake mapped by radar interferometry. Nature 364(6433):138–142

Massonnet D, Briole P, Arnaud A (1995) Deflation of Mount Etna monitored by spaceborne radar interferometry. Nature 375:567–570

Massonnet D, Feigl KL (1998) Radar interferometry and its application to changes in the earth's surface. Rev Geophys 36:441–500

Mora O, Mallorquí JJ, Broquetas A (2003) Linear and nonlinear terrain deformation maps from a reduced set of interferometric SAR images. IEEE Trans Geosci. Remote Sens 41:2243–2253

Peltzer G, Rosen PA (1995) Surface displacement of the 17 May 1993 Eureka Valley earthquake observed by SAR interferometry. Science 268:1333–1336

Pepe A, Sansosti E, Berardino P, Lanari R (2005) On the generation of ERS/ENVISAT DInSAR time-series via the SBAS technique. IEEE Geosci Remote Sens Lett 2(3):265–269

Rignot E (1998) Fast recession of a west Antarctic glacier. Science 281:549–551

Rucci A, Ferretti A, Monti Guarnieri A, Rocca F (2012) Sentinel 1 SAR interferometry applications: The outlook for sub millimeter measurements. Remote Sens Environ 120:156–163

Sansosti E, Casu F, Manzo M, Lanari R (2010) Space-borne radar interferometry techniques for the generation of deformation time series: an advanced tool for Earth's surface displacement analysis. Geophys Res Lett 37:L20305

Sansosti E, Berardino P, Bonano M, Calo' F, Castaldo R, Casu F, Manunta M, Manzo M, Pepe A, Pepe S, Solaro G, Tizzani P, Zeni G, Lanari R (2014) How second generation SAR systems are impacting the analysis of ground deformation. Int J Appl Earth Obs Geoinf 28:1–11. doi:10.1016/j.jag.2013.10.007.

Stramondo S, Saroli M, Tolomei C, Moro M, Doumaz F, Pesci A, Loddo F, Baldi P, Boschi E (2007) Surface movements in Bologna (Po Plain—Italy) detected by multitemporal DInSAR. Remote Sens Environ 110:304–316

Tapete D, Fanti R, Cecchi R, Petrangeli P, Casagli N (2012) Satellite radar interferometry for monitoring and early-stage warning of structural instability in archaeological sites. J Geophys Eng 9:S10–S25

Tesauro M, Berardino P, Lanari R, Sansosti E, Fornaro G, Franceschetti G (2000) Urban subsidence inside the city of Napoli (Italy) observed by satellite radar interferometry. Geophys Res Lett 27(13):1961–1964

Tizzani P, Battaglia M, Zeni G, Attori S, Berardino P, Lanari R (2009) Uplift and magma intrusion at Long Valley caldera from InSAR and gravity measurements. Geology 37(1):63–66. doi:10.1130/G25318A.1

Tizzani P, Castaldo R, Solaro G, Pepe S, Bonano M, Casu F, Manunta M, Manzo M, Pepe A, Samsonov S, Lanari R, Sansosti E (2013) New insights into the 2012 Emilia (Italy) seismic sequence through advanced numerical modeling of ground deformation InSAR measurements. Geophys Res Lett 40(10):1971–1977. doi:10.1002/grl.50290

Trasatti E, Casu F, Giunchi C, Pepe S, Solaro G, Tagliaventi S, Berardino P, Manzo M, Pepe A, Ricciardi GP, Sansosti E, Tizzani P, Zeni G, Lanari R (2008) The 2004–2006 uplift episode at Campi Flegrei caldera (Italy): constraints from SBAS-DInSAR ENVISAT data and Bayesian source inference. Geophys. Res. Lett. 35:L073078. doi:10.1029/2007GL033091

Torres R, Snoeij P, Geudtner D, Bibby D, Davidson M, Attema E, Potin P, Rommen B, Floury N, Brown M, Navas Traver I, Deghaye P, Duesmann B, Rosich B, Miranda N, Bruno C, L'Abbate M, Croci R, Pietropaolo A, Huchler M, Rostan F (2012) GMES Sentinel-1 mission. Remote Sens Environ 120:9–24

Werner C, Wegmüller U, Strozzi T, Wiesmann A (2003) Interferometric point target analysis for deformation mapping. In: Proceedings of the geoscience and remote sensing symposium, Toulouse, France, 21–25 July 2003, 7, 4362–4364

Zebker HA, Villasenor J (1992) Decorrelation in interferometric radar echoes. IEEE Trans Geosci Remote Sens 30:950–959

Zeni G, Bonano M, Casu F, Manunta M, Manzo M, Marsella M, Pepe A, Lanari R (2011) Long term deformation analysis of historical buildings through the advanced SBAS-DInSAR technique: the case study of the city of Roma Italy. J Geophys Eng 8:S1 doi:101088/1742-2132/8/3/S01

Zinno I, Elefante S, Mossucca L, De Luca C, Manunta M, Terzo O, Lanari R, Casu F (2015) A first assessment of the P-SBAS DInSAR algorithm performances within a cloud computing environment. IEEE J Sel Top Appl Earth Obs Remote Sens 8:10

Chapter 7
A Window for the Hidden Past: Revealing Architectural Remains Based on Field Spectroscopy Data Analysis

Athos Agapiou

Abstract Field spectroscopy is the quantitative measurement of the radiance, irradiance, reflectance, or transmission in the field. It is principally used to understand the interaction of different materials based on electromagnetic radiation. Although field spectroscopy has been systematically exploited for the calibration of remote sensing sensors, nowadays spectroscopy is being used for a variety of remote sensing applications. This chapter aims to provide an overview of the potential use of field spectroscopy for supporting archaeological research. The overview is based on examples and applications from different archaeological environments in the eastern Mediterranean basin, specifically targeted for the detection of underground architectural remains. As is demonstrated in this chapter, field spectroscopy uses hyperspectral signatures to validate or calibrate the space-borne or airborne images, while at the same time spectroscopy may assist in better understanding of the interaction of the electromagnetic radiation with the different targets and therefore in developing new algorithms to support future archaeological applications.

Keywords Ground spectroscopy • Remote sensing archaeology • Crop marks • Buried archaeological remains

7.1 Introduction to Remote Sensing Archaeology

The wider cultural heritage (CH) sector is facing a number of challenges including the decrease of public budgets, urbanization, and technological changes. Within this context, CH experts seek to improve the methodologies applied in the field to better understand and preserve the past. Remote sensing offers new perspectives

A. Agapiou (✉)
Department of Civil Engineering and Geomatics, Faculty of Engineering and Technology, Cyprus University of Technology, 2-6, Saripolou str, 3603, Limassol, Cyprus
e-mail: athos.agapiou@cut.ac.cy

N. Masini, F. Soldovieri (eds.), *Sensing the Past*, Geotechnologies and the Environment 16, DOI 10.1007/978-3-319-50518-3_7

Fig. 7.1 Examples of crop (*left*) and soil (*right*) marks as a result of buried archaeological sites. *Left*: the archaeological site of Ilis in southern Greece; *right*: UNESCO cultural heritage site of Nea Paphos is western Cyprus

in archaeological research (Garrison et al. 2008; Giacomo et al. 2011; Deroin et al. 2011; Agapiou et al. 2013a, 2014a; Lasaponara et al. 2014). It is a nondestructive technique that can be used as part of an investigation of an archaeological or historical site before the commencement of any excavation or other modern human intervention. In particular, the exposure of buried archaeological features using satellite, aerial data, or unmanned autonomous vehicles (UAVs) is based on the identification of crop or soil marks (Fig. 7.1).

Recently, several applications have demonstrated that satellite images are efficiently useful for the detection of crop marks, which are formed in areas where vegetation overlies near-surface architectural remains (Parcak 2009; Alexakis et al. 2009, 2011; Lasaponara and Masini 2006; Altaweel 2005; Agapiou et al. 2012a). These remains retain soil moisture with a different percentage of moisture compared to the rest of the crops in an area. Depending of the type of feature, crop vigour may be enhanced or reduced by buried archaeological features (Winton and Horne 2010). When vegetation grows above buried ditches or a moat, then the crop growth is likely to be enhanced because the topsoil holds more moisture than in the surrounding context (especially during periods when water stress develops). This phenomenon can be recorded from any airborne or space-borne platform and is referred to as a positive crop mark (Lasaponara and Masini 2007; Jonson 2006; Sharpe 2004; Stanjek and Fabinder 1995).

However, in cases where there is not enough moisture in the retentive soil and there is a lack of available water for evapotranspiration (e.g., vegetation growth above building remains or compacted ground), the developed marks are

characterized as negative crop marks (Lasaponara and Masini 2007; Jonson 2006; Sharpe 2004). Comparing the two different kinds of marks, the positives are normally taller with darker green and healthy foliage than the negative crop marks, which tend to be paler green with lighter-colored appearance when monitored from the air (Sharpe 2004; Jonson 2006).

Figure 7.2 indicates an example of positive crop marks from barley crops compared to a cultivated barley crop. Both seed types were planted the same day very close to each other. Differences both in size and color are easily recognized in Fig. 7.2.

Fig. 7.2 *Top*: Positive barley crop mark (*right*) compared with normal barley (*left*). *Bottom*: Photograph from the formation of positive crop mark (Photograph by A. Agapiou)

7.2 Research Today Related with Crop Marks

Although there has been significant progress in increasing the resolution of space/aerial sensors and image processing, the detection of crop marks is challenging using satellite and airborne images, as these marks may not be visible in the images if observed in different periods of the year or in different spatial/spectral resolution (see example in Fig. 7.3).

Recent studies argue that there are many complex factors involved in the capturing of these marks (Kaimaris and Patias 2012). Indeed, the detection of crop marks in satellite data can be problematic for a number of reasons, such as atmospheric impact of the satellite data; noise of the data from the soil background; and limitations by the spatial resolution of the sensors (mixed pixels). In addition, several parameters affect the formation of crop marks, such as climatic conditions, soil characteristics, or water availability. Consequently, there is a need to understand better the formation procedure of such marks as well to improve or develop new algorithms to improve the detection of crop marks in satellite images.

Moreover, it is essential to link remote sensing analysis with pure archaeological questions. In this way, image anomalies (i.e., crop marks) can provide further information to archaeologists investigating a site. A digital atlas of geolocated crop

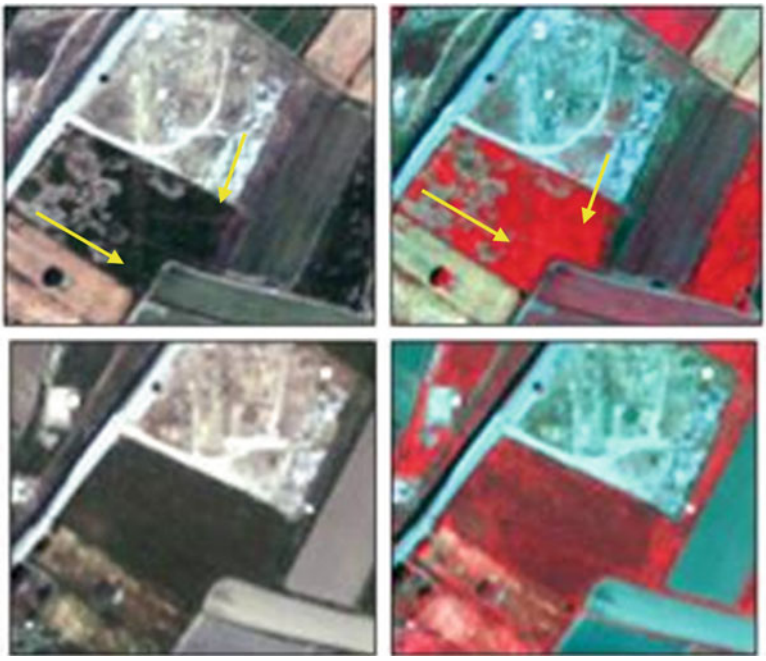

Fig. 7.3 Detection of crop marks, indicated with arrows, at Ilis, Greece (*top*) and disappearance from a second satellite image (*bottom*) resulting from the different phenological stage of the crops (Agapiou et al. 2013a)

marks linked with archaeological investigations can be used as a systematic tool for both local authorities and researchers to protect and study the archaeo-landscape.

7.3 Contribution of Field Spectroscopy

Field spectroscopy is the quantitative measurement of the radiance, irradiance, reflectance, or transmission in the field and is principally used to understand the interaction of targets with electromagnetic radiation (Milton 1987; Milton et al. 2009). Therefore, field spectroscopy provides accurate, reliable ground-truth data over a target in the ground. Although field spectroscopy has been used in several environmental applications, its application for archaeological research is still limited. In the following sections the contribution of field spectroscopy is presented in different examples from field campaigns in the eastern Mediterranean region. Based on these examples, it is demonstrated that field spectroscopy can assist towards this direction, improving remote sensing algorithms as well as providing better insight regarding the formation of crop marks.

7.3.1 Spectral Libraries of Crop Marks

To develop a complete phenological spectral library of crop marks for the area of Cyprus, two test fields were built in different areas. The first area, presented here, is located near Alampra village, in central Cyprus. In this agricultural site, a "simulated" archaeological environment was created. Specifically, local stones normally used for construction were buried in different depths (25 cm or 50 cm below ground surface) and rock-cut tombs were also simulated in the same environment (Fig. 7.4). Ground spectroradiometric measurements were collected systematically for a complete phenological cycle of the crops. The phenological cycle of barley crops, in Cyprus, begins from late September to early November and lasts until mid-April to early May.

Each diagram of Fig. 7.5 corresponds to a different observation day. Measurements were taken on top of the simulated archaeological environment (Fig. 7.5, red line) as well in the surrounding cultivated area (Fig. 7.5, blue line). The mean reflectance value from each campaign was calculated in the range of 400 nm to 950 nm, covering both the visible and VNIR spectra. Standard deviations are also plotted in Fig. 7.5 (indicated with dashed lines). Special attention was given to the red and near-infrared part of the spectrum. As shown in Fig. 7.5, the detection of buried archaeological remains using electromagnetic radiation (i.e., spectroradiometer) is a very difficult task, especially before the full growth of the crops. Actually, as was demonstrated (see Agapiou et al. 2013b), the optimal window for detecting crop marks is limited to only 15 days throughout the year. During this period (boot stage of the crops), the crop mark is enhanced.

Fig. 7.4 Photographs taken during the construction of the test field in Alampra village, in central Cyprus (Photograph by A. Agapiou)

7.3.2 Simulation of Ground Data to Satellite Sensors

Hyperspectral signatures can provide more details regarding the multispectral signatures of the satellite sensors. As presented in Fig. 7.6, the narrowband spectral signatures can assist further the detection of possible stress vegetation (especially in the red edge area) although information is lost in the resampled spectral signature of multispectral sensors such as the Landsat 7 ETM+. Resampling was achieved using the appropriate relative spectral response (RSR) filter of the Landsat 7 ETM+ sensor. The reflectance recorded from the spectroradiometer was calculated based on the wavelength of each band and the RSR filter, as shown in Eq. 7.1:

$$R_{\text{bandi}} = \Sigma\,(R_i * \text{RSR}_i) \,/\, \Sigma \text{RSR}_i \tag{7.1}$$

where the R_{bandi} is the reflectance at a range of wavelength (e.g., band 1), R_i is the reflectance at a specific wavelength (e.g., $R_{0.450}$ μm), and the RSR_i is the relative response value at the specific wavelength. In cases where no information regarding the spectral sensitivity of the sensor exists, then the mean value for each bandwidth may be taken as an approximation.

The selection of the best multispectral sensor to support archaeological investigations, based not only on its spatial resolution but also its spectral characteristics, is therefore of great importance. As demonstrated from previous studies (see Agapiou et al. 2014a), some existing sensors such as IKONOS can better enhance the detection of crop marks because of their spectral characteristics.

In a similar way, ongoing designed satellite sensors can be also evaluated even before their application using real satellite data. For instance, the new Sentinel-2 sensor launched recently in 2015 was evaluated and compared with other existing

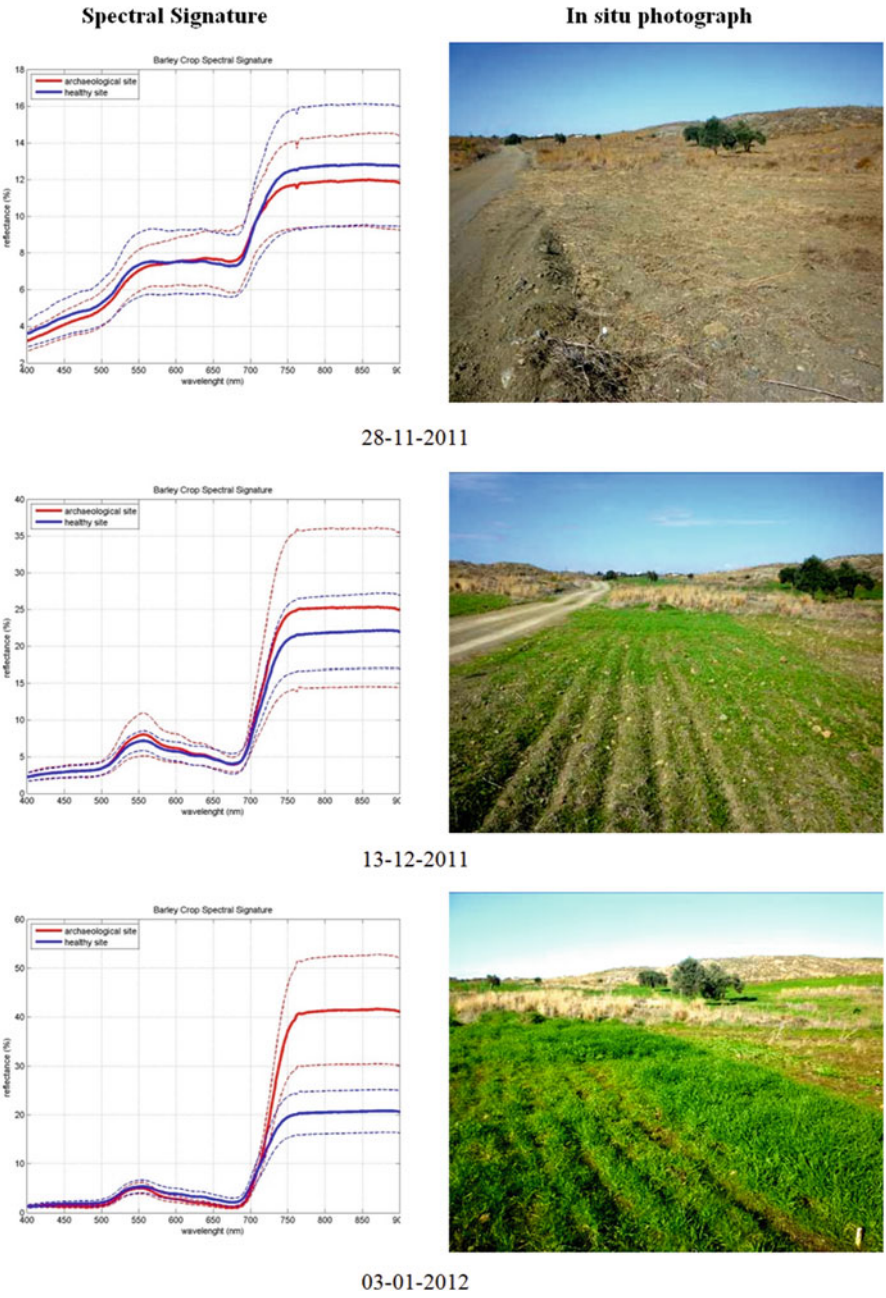

Fig. 7.5 Spectral signatures of crop marks (*red line*) and healthy barley crops (*blue line*) during a complete phenological cycle. Next to the spectral signature is a photograph from the in situ test field (Alampra, Cyprus)

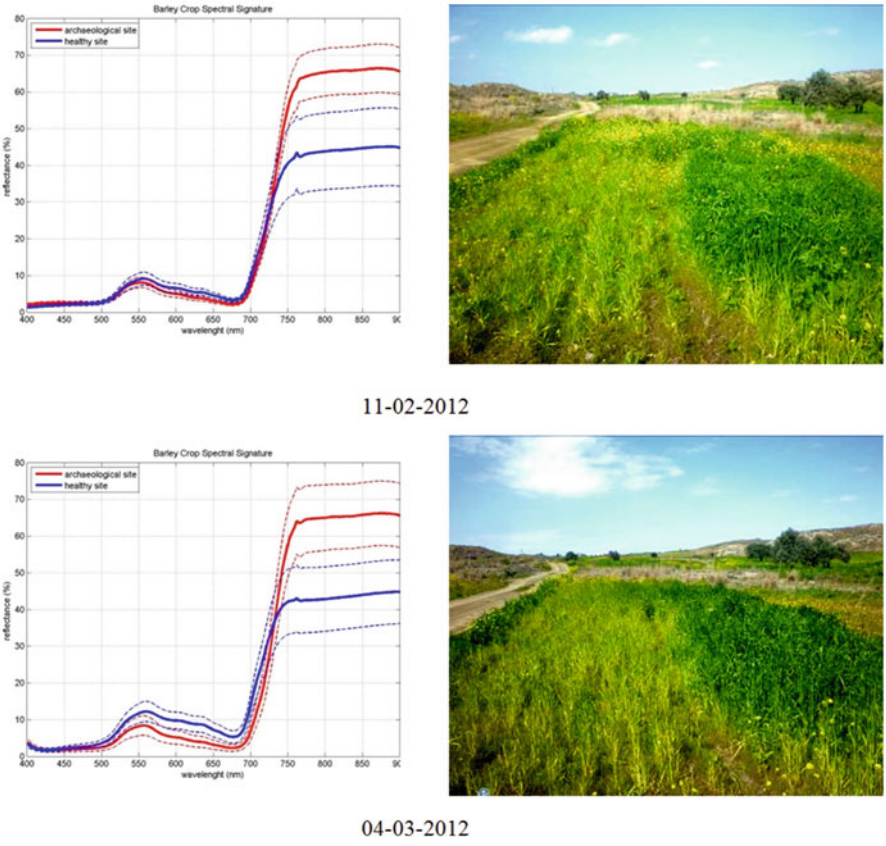

Fig. 7.5 (continued)

sensors (Fig. 7.7) (Agapiou et al. 2014b). As it was found that the spectral characteristics of the new sensor are closer to the optimum spectral region (700 nm and 800 nm) to detect crop marks, therefore it seems suitable to enhance crop marks.

A simulated Sentinel-2 image was processed using a pansharpened EO Hyperion and IKONOS image over Neolithic settlements of Thessaly, central Greece. The EO-Hyperion narrow bands were resampled into the specific bandwidths of bands 5 and 7 of the Sentinel-2 sensor using the relevant RSR filters. Specifically, the Hyperion bands 33–36 and 39–45 were resampled to Sentinel-2 bands 5 and 7, respectively. The high-resolution IKONOS image of the same area was used for improving the spatial resolution of the EO-Hyperion image. A relative geometric correction between the EO-Hyperion and the IKONOS image was achieved [total root mean square error (TRMSE) <2 m] using a second-order polynomial order correction algorithm. Then, the IKONOS image was merged into the EO-Hyperion dataset using the PCA approach. This procedure was used to merge the high-resolution image (IKONOS, 1-m pixel size) with the lower-resolution image

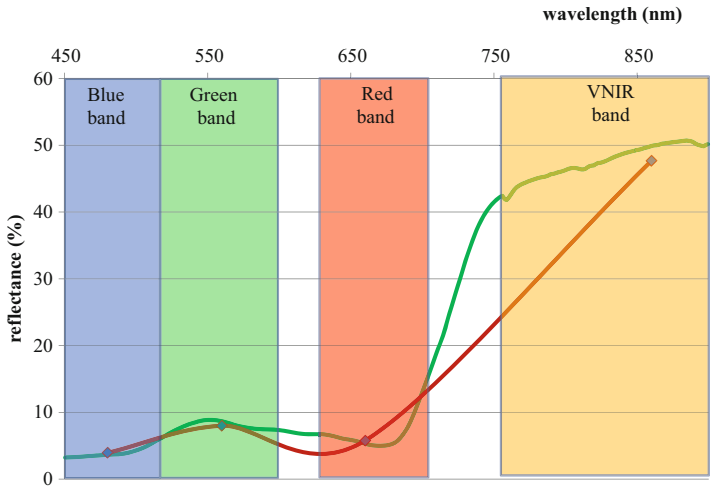

Fig. 7.6 Spectral signature from the GER1500 spectroradiometer (*green line*) and the resampled signature using the RSR filter of Landsat 7 ETM+ in the same spectral region

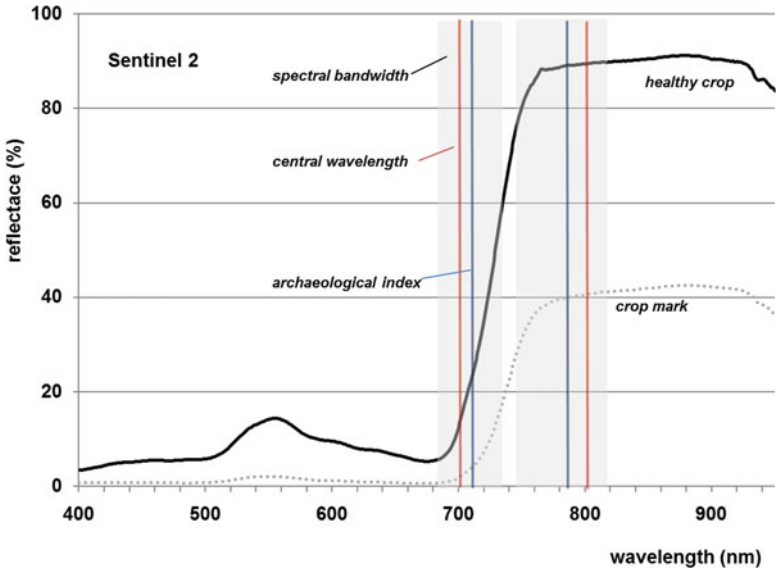

Fig. 7.7 Spectral characteristics of Sentinel-2 compared to the optimum spectral region (700 nm and 800 nm) to detect crop marks

(EO-Hyperion, 30 m). Finally, the end product was resampled to 20 m as the Sentinel-2 spatial resolution (Agapiou et al. 2014b).

As shown in Fig. 7.8, some already known *magoules* (i.e., tells in the form of low hills; indicated with yellow color in Fig. 7.8a, b) were detected using simple

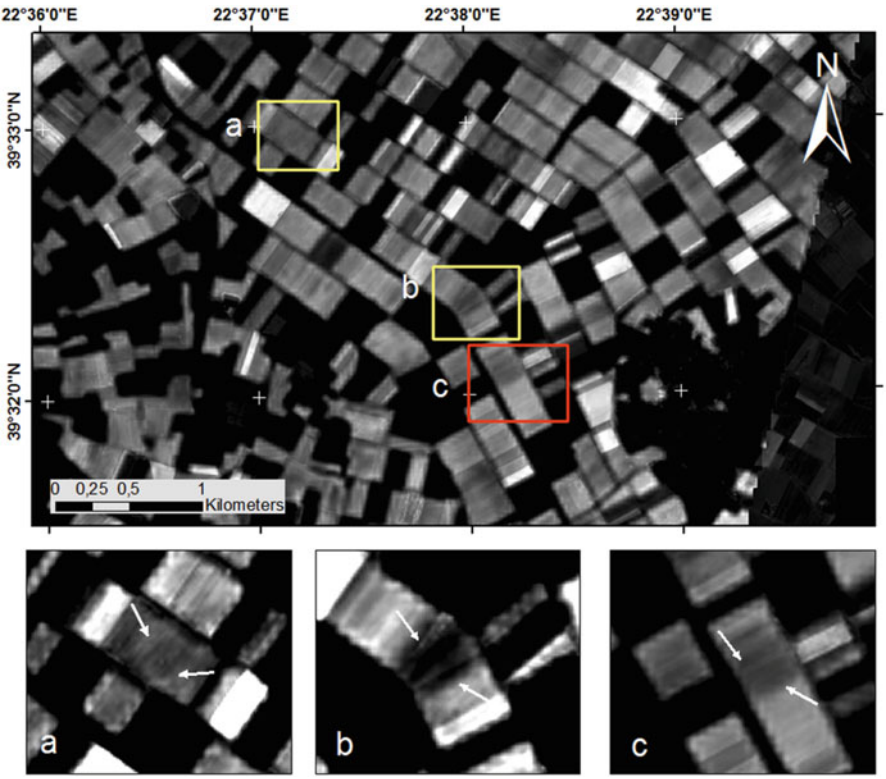

Fig. 7.8 Simulated Sentinel-2 image over the Thessalian plain, based on the EO-Hyperion dataset. Known archaeological vegetation marks are indicated with *yellow color*; another unknown vegetation mark is indicated in a *red square* (Agapiou et al. 2014b)

photointerpretation of the image. These archaeological vegetation marks can be detected mainly by the difference of the vegetation mark against the surrounding area, but also based on their circular shape. However, the most promising of this analysis was the detection of still unknown archaeological crop marks. Indeed, as demonstrated in Fig. 7.8, at least one other potential site has been found in this area. The site (red color in Fig. 7.8c) is in very close proximity to existing known sites and, therefore, the hypothesis of the existence of new sites is strengthened (Agapiou et al. 2014b).

7.3.3 Spectral Unmixing Using Spectral Libraries

Spectral libraries can be further used to support future remote sensing applications for archaeology. These libraries are useful for training new researchers and at the same time can be used for linear unmixing techniques in low-resolution

satellite data. Mixed pixels can be problematic for several applications, not only for archaeological research. Classification techniques, which are widely used for the taxonomy of a multispectral/hyperspectral image to thematic classes, are characteristic examples of this phenomenon: mixed pixels, because of their spectral signature, are classified in the wrong class. To overcome this limitation of the satellite raster datasets, scale-down techniques are used. Scale-down techniques (top-down approach) aim to decompose information at a certain geographic scale into its constituents at smaller scales.

In detail, spectral unmixing is the procedure according which the measured spectrum of a mixed pixel is decomposed into a collection of constituent spectra, or endmembers, and a set of corresponding fractions, or abundances, that indicate the proportion of each endmember present in the pixel. An example of this approach is given in Figs. 7.9 and 7.10 where in situ spectroradiometric measurements over possible archaeological remains were taken over Palaepaphos (southwest Cyprus), simultaneously with the Landsat 5 TM overpass. Geophysical prospection was carried out before indicating potential archaeological remains mainly in the southern part of the area.

The spectral signatures from the in situ observation were used for the spectral unmixing technique. The constrained linear spectral unmixing (LSU) model was applied in this study (Agapiou et al. 2012b). The foregoing spectral signatures were used in the LSU algorithm to record any stress vegetation similar to the

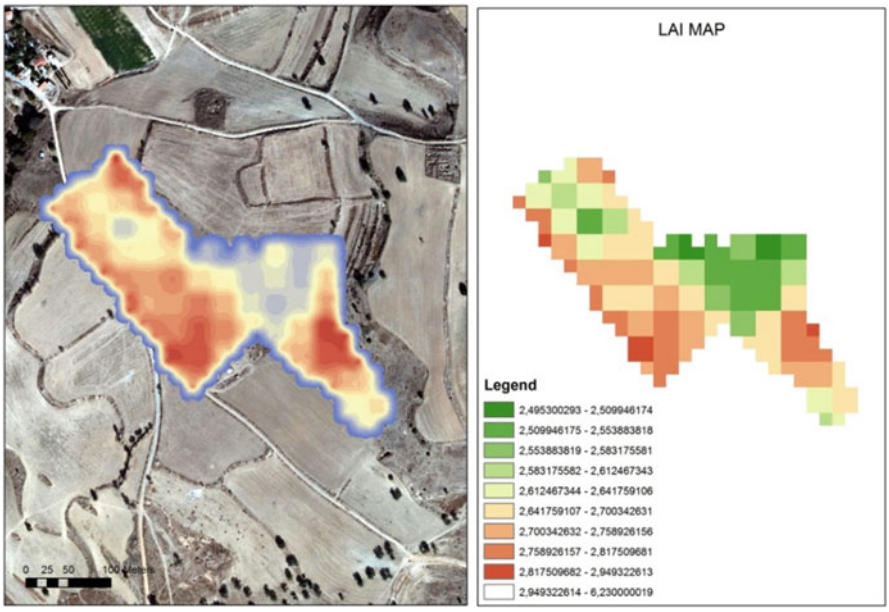

Fig. 7.9 LSU application of the case study area (*left*). *Red color* indicates stressed vegetation. An LAI map was also calculated for the same area (*right*)

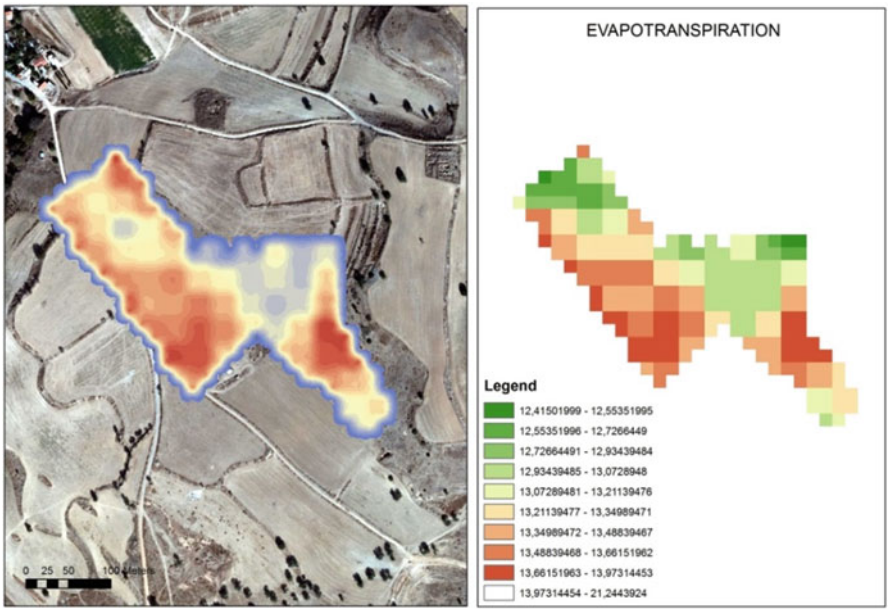

Fig. 7.10 LSU application of the case study area (*left*). *Red color* indicates stressed vegetation. An ETc map was also calculated for the same area (*right*)

spectroradiometric results over the geophysical anomalies. The LSU algorithm was applied at a multispectral Landsat 5 TM image. Initially, geometric correction was carried out to the satellite image using standard techniques with ground control points and a second-order polynomial fit. Then, the conversion of Digital Numbers (DN) values to radiance values was performed, and finally reflectance values were calculated. It should be also noticed that atmospheric correction was applied as well, using the darkest pixel algorithm.

Figures 7.9 and 7.10 (left) indicate the results after the application of the LSU algorithm in the case study area. Red colors indicate areas with stressed vegetation and blue colors correspond to nonstressed vegetation. A great similarity has been observed between the stressed vegetation and the geophysical results (Agapiou et al. 2012b). Figures 7.9 and 7.10 (right) also indicate the leaf area index (LAI) and evapotranspiration (ETc) of the crops for the same area. In the same figures, the stress condition of the crop is also highlighted, especially over the geophysical anomalies.

7.3.4 Development of New Image Equations

New linear orthogonal equations for the enhancement of crop marks, for several existing medium- and high-resolution satellite sensors, have been also proposed

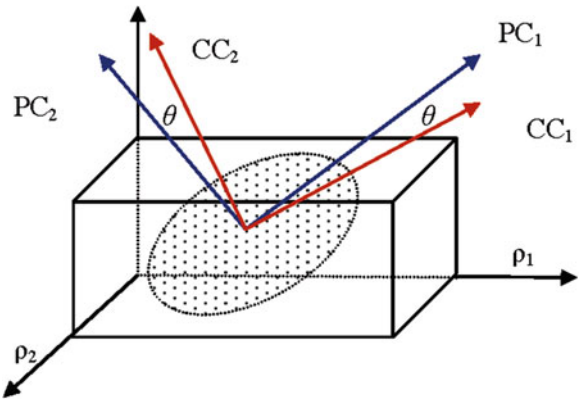

Fig. 7.11 Illustration of the third step. The original data axes (ρ_1, ρ_2, ρ_3) are transformed into new axes based on the PCA rotations (PC1, PC2, PC3) and then a rotation θ is applied to be associated with soil, vegetation, and crop marks characteristics (CC1, CC2, CC3)

recently using spectral libraries (Agapiou et al. 2013a). For the calculation of the *n*-space coefficients for several high-resolution satellite sensors, the sequential methodology was followed for each sensor individually, as indicated in Fig. 7.11:

- *Step 1*: First, all narrowband spectral signatures were recalculated based on the appropriate RSR filters of each sensor; this was necessary to simulate the ground data to at-satellite broadband reflectance.
- *Step 2*: Then, principal component analysis (PCA) was applied to create the initial eigenspace. These eigenvalues are used to define the initial feature space before selective rotations occur.
- *Step 3*: The next step concerns the definition by the user of the spectral data used in the transformation. Three types of datasets were determined by the user, namely, soil, vegetation, and crop marks. Major concerns can be expanded similar to those of the T-K transformation because the basis vectors depend on the data set selected to construct the transform. To overcome such limitations a large dataset has been evaluated, taking into consideration the dynamic nature of the formation of crop marks. In addition, the basis vectors were selected based on the results from previous studies performed by the authors. Indeed, the data selected were taken during the best phenophase (time window) where crop marks are enhanced (boot stage of the crops).
- *Step 4*: After the basis vectors were defined, rotation of the PCA *n*-space was performed into a new three-dimensional (3D) orthogonal space (soil, vegetation, crop marks). In the end, the coefficients for all satellite sensors were calculated based on the 3D rotation angles. These coefficients were expected to enhance the crop marks, vegetation, and soil for each specific sensor selected.

For each sensor, three new linear equations were derived. The coefficients for each sensor can be found in Agapiou et al. (2013a). In each case, different existing algorithms, vegetation indices, and false composites were compared with the proposed linear transformations of this study. Figure 7.12 presents the results from the application of linear equations (**d–f**), as well the RGB pseudo-composite

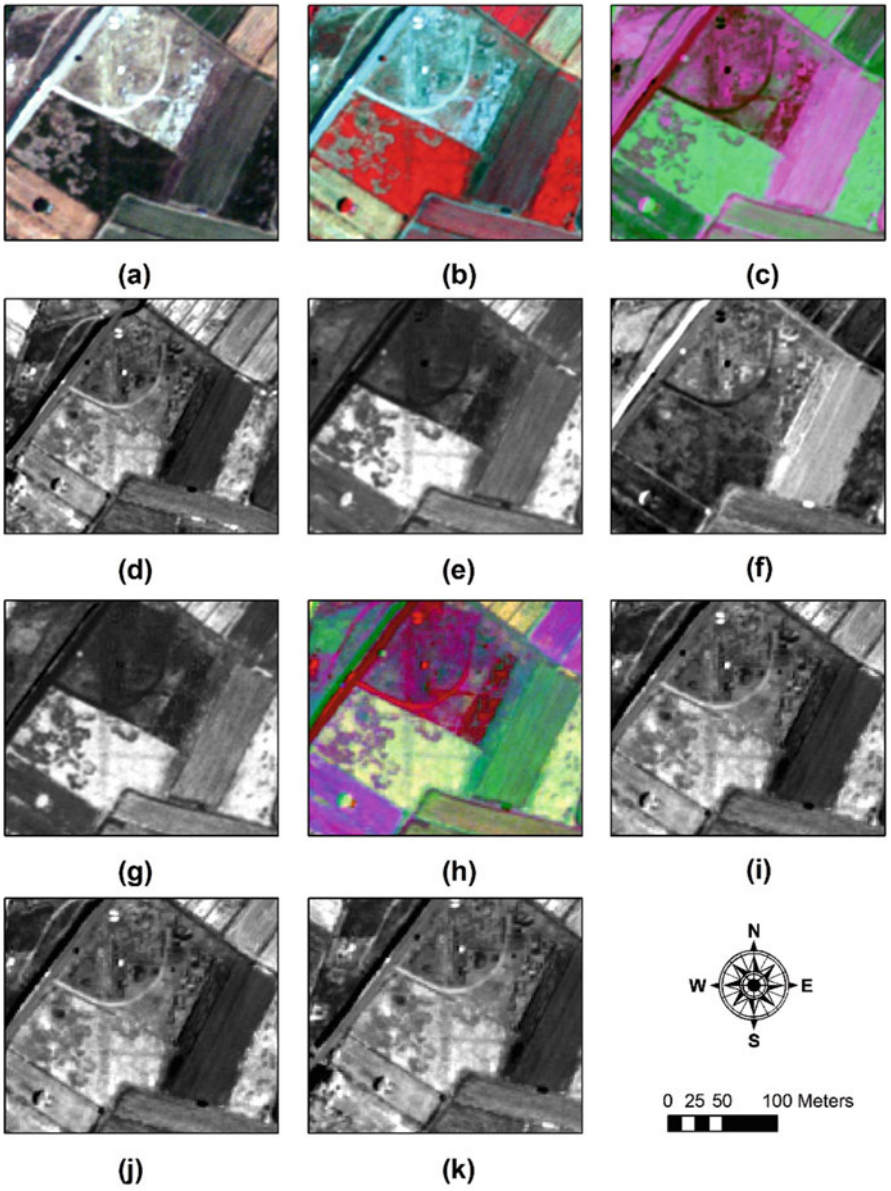

Fig. 7.12 Results from GeoEye-1 dataset from the western part of Ilis archaeological site (37°53′18.05″N, 21°22′24.48″E). (**a**) RGB composite. (**b**) NIR-R-G composite. (**c**) Proposed linear transformation RGB pseudo-color. (**d**) First component. (**e**) Second component. (**f**) Third component. (**g**) NDVI. (**h**) PCA composite. (**i**) First PCA component. (**j**) Second PCA component. (**k**) Third PCA component (Agapiou et al. 2013a)

of the proposed transformation components (**c**). In addition, RGB and NIR-R-G composites are presented (**a** and **b**, respectively) and the result from the NDVI index (**g**). Finally, the results from the PCA analysis are also displayed (**h**–**k**).

Two interesting linear features are also detected in Fig. 7.12 from the same archaeological site, using again the GeoEye-1 satellite imagery. A linear feature with direction from north to south seems to continue from an already excavated area at the northern part. At the center of this feature, another linear finding, perpendicular to the previous one, has been also detected. Although both linear features are detectable to several algorithms applied to the GeoEye-1 image, the second component of the proposed transformation (Fig. 7.12e) tends to further enhance these buried archaeological features.

7.4 Discussion

This chapter aims to demonstrate the great potentials of ground spectroscopy for archaeological research. A critical point for the future, success, and improvements of remote sensing in archaeology is the integration of archaeological questions within the technological improvement of the different sensors. Until now, the different remote sensing sensors have been evaluated only a posteriori for their capability in archaeological research. It is of great importance, therefore, to experiment and provide, a priori, to remote sensing engineers with specific needs (e.g., spectral windows) so as to build these sensors capable of assisting archaeologists.

In this perspective, ground spectroscopy can be used as a "ground-truth" tool for satellite remote sensing archaeological research and applications. As presented in this chapter, ground spectroscopy is a methodological tool capable of providing details in terms of both spatial and spectral range that are normally lost if using satellite sensors. Simulated environments or known buried archaeological remains can be used to build a complete spectral library for crop marks to be used for supporting future remote sensing applications. Researchers may benefit from ground spectroscopy so as to schedule an efficient airborne campaign or even to improve the methodologies—algorithms applied for the specific area. Finally, ground spectroscopy can be used to develop more sophisticated sensors specifically designed for archaeological research and archaeological questions.

Acknowledgments The results presented here are in part from the Ph.D. thesis of the author as well from other research projects. Thanks are given to the Remote Sensing Laboratory of the Department of Civil Engineering & Geomatics at the Cyprus University of Technology for the support (http://www.cut.ac.cy/) as well to Prof. Diofantos Hadjimitsis for his continued support. Thanks also are given to my colleague Dr. Dimitrios Alexakis. Acknowledgments also are given to Dr. Apostolos Sarris and Dr. Nikos Papadopoulos from the Laboratory of Geophysical-Satellite Remote Sensing & Archaeo-environment, Institute for Mediterranean Studies, Foundation for Research & Technology, Hellas (F.O.R.T.H.). Sincere thanks to my colleague Dr. Vasiliki Lysandrou for her fruitful comments and suggestions.

References

Agapiou A, Hadjimitsis DG, Alexakis D, Papadavid G (2012a) Examining the phenological cycle of barley (*Hordeum vulgare*) using satellite and in situ spectroradiometer measurements for the detection of buried archaeological remains. GISci Remote Sens 49(6):854–872

Agapiou A, Hadjimitsis DG, Sarris A, Georgopoulos A, Alexakis DD (2012b) Linear spectral unmixing for the detection of Neolithic settlements in the Thessalian Plain, central Greece. In: Perakis K, Moysiadis A (eds) Proceedings of the 32nd EARSeL symposium 2012, Advances in geosciences, pp 125–140

Agapiou A, Alexakis DD, Sarris A, Hadjimitsis DG (2013a) Orthogonal re-projection of spectral bands using medium and high resolution satellite images for the detection of archaeological crop marks. Remote Sens 5(12):6560–6586. doi:10.3390/rs5126560

Agapiou A, Hadjimitsis DG, Sarris A, Georgopoulos A, Alexakis DD (2013b) Optimum temporal and spectral window for monitoring crop marks over archaeological remains in the Mediterranean region. J Archaeol Sci 40(3):1479–1492. doi:10.1016/j.jas.2012.10.036

Agapiou A, Alexakis D, Hadjimitsis DG (2014a) Evaluation of spectral sensitivity of ALOS, ASTER, IKONOS, LANDSAT and SPOT satellite sensors intended for the detection of archaeological crop marks. Digital Earth 7(5). doi:10.1080/17538947.2012.674159

Agapiou A, Alexakis DD, Sarris A, Hadjimitsis DG (2014b) Evaluating the potentials of Sentinel-2 for archaeological perspective. Remote Sens 2014(6):2176–2194

Alexakis A, Sarris A, Astaras T, Albanakis K (2009) Detection of neolithic settlements in Thessaly (Greece) through multispectral and hyperspectral satellite imagery. Sensors 9:1167–1187

Alexakis A, Sarris A, Astaras T, Albanakis K (2011) Integrated GIS, remote sensing and geomorphologic approaches for the reconstruction of the landscape habitation of Thessaly during the neolithic period. J Archaeol Sci 38:89–100

Altaweel M (2005) The use of ASTER satellite imagery in archaeological contexts. Archaeol Prospect 12:151–166

Deroin J-P, Téreygeol F, Heckes J (2011) Evaluation of very high to medium resolution multispectral satellite imagery for geoarchaeology in arid regions – Case study from Jabali, Yemen. J Archaeol Sci 38(1):101–114

Garrison GT, Houston DS, Golden C, Inomata T, Nelson Z, Munson J (2008) Evaluating the use of IKONOS satellite imagery in lowland Maya settlement archaeology. J Archaeol Sci 35(10):2770–2777

Giacomo DG, Ditaranto I, Scardozzi G (2011) Cartography of the archaeological surveys taken from an Ikonos stereo-pair: a case study of the territory of Hierapolis in Phrygia (Turkey). J Archaeol Sci 38(9):2051–2060

Jonson KJ (2006) Remote sensing in archaeology. An explicitly North America perspective. The University of Alabama Press

Kaimaris D, Patias P (2012) Best period for high spatial resolution satellite images for the detection of marks of buried structures. Egypt J Remote Sens Space Sci. doi:10.1016/j.ejrs.2011.12.001

Lasaponara R, Masini N (2006) Identification of archaeological buried remains based on Normalized Difference Vegetation Index (NDVI) from Quickbird satellite data. IEEE Geosci Remote Sens Lett 3(3):325–328

Lasaponara R, Masini N (2007) Detection of archaeological crop marks by using satellite QuickBird multispectral imagery. J Archaeol Sci 34:214–221

Lasaponara R, Leucci G, Masini N, Persico R (2014) Investigating archaeological looting using satellite images and GEORADAR: the experience in Lambayeque in North Peru. J Archaeol Sci 42:216–230

Milton EJ, Schaepman ME, Anderson K, Kneubühler M, Fox N (2009) Progress in field spectroscopy. Remote Sens Environ 113:92e109

Milton EJ (1987) Principles of field spectroscopy. Remote Sens Environ 8(12):1807e1827

Parcak SH (2009) Satellite remote sensing for archaeology. Routledge Taylor and Francis Group Press, London/New York

Sharpe L (2004) Geophysical, geochemical and arable crop responses to archaeological sites in the Upper Clyde Valley, Scotland, PhD thesis, Department of Archaeology, Faculty of Physical Sciences, University of Glasgow

Stanjek H, Fabinder JWE (1995) Soil aspects affecting archaeological details in aerial photographs. Archaeol Prospect 2(1):91–101

Winton, H., Horne, P., (2010). National archives for national survey programmes: NMP and the English heritage aerial photograph collection. In: Landscapes through the lens. Aerial photographs and historic enviroment. Aerial Archaeology Research Group No. 2, pp 7–18

Chapter 8
Seismic and Sonic Applications on Artifacts and Historical Buildings

Giovanni Leucci

Abstract Historic buildings, no matter whether they are famous monuments or so-called "minor," or even vernacular, architecture, represent an important part of our cultural heritage. This patrimony, which is the living memory of the country history and development, must be preserved as much as possible as an historic document of our past. Unfortunately, wars and dramatic events (earthquakes, floods, slides, fires, etc.), but also abandonment and lack of maintenance, are constant menaces to the cultural heritage in every country of the world.

Difficulties exist when is necessary to evaluate the degree of the degradation process inside the heritage buildings. The degradation processes affect many structural levels (cracks, fissures, detachments, displacements . . .) as much as the aesthetic values (dirt, crusts, efflorescence . . .) of the historical buildings. The knowledge of this reality is important for the valuation of its stability conditions and also for a restoration planning environment. The main pathologies that can result in the breakdown of historical buildings are humidity damage caused by capillarity ascent, breeze, or high humidity environments, successive freeze–thaw cycles that result in crystallization, broken mortar joints, and loss of the most exposed material, and finally erosion damage caused by lack of vegetation. Centering on structural pathologies (cracks, fissures), the detection and characterization of the aforementioned problems are important to estimate the status and to plan the possible repair.

This chapter describes the possible applications of a nondestructive testing (NDT) method related to the study of the propagation of sonic and ultrasonic waves to analyze the conservation state of heritage buildings. Some tests for masonry investigations and the conditions for applicability are here reported, providing necessary information and decision criteria for the planned application of the methods to historic masonry buildings. The chapter comprises a short summary of the basic technical principles of the method and describes the required equipment, measurement setup, application, and relevant limits and site conditions, data analysis and interpretation, and the required safety cautions.

G. Leucci (✉)
Istituto per i Beni Archeologici e Monumentali (IBAM) – Consiglio Nazionale delle Ricerche (CNR), Lecce, Italy
e-mail: giovanni.leucci@cnr.it

N. Masini, F. Soldovieri (eds.), *Sensing the Past*, Geotechnologies and the Environment 16, DOI 10.1007/978-3-319-50518-3_8

8.1 Introduction

Non destructive geophysical methodologies have been implemented, tested, and validated as diagnostic or monitoring tools in artworks or historical monuments. These methods provide an image of internal structure of the investigated structure and medium at different scales. Detailed knowledge of the internal structure of historical monuments is an important key for their effective preservation and restoration. For example, a building could be structured of different types of stones, or bricks, with wooden or iron elements inserted into walls and cavities as ties, etc. Assuming great importance for the wall thickness, recognition of detachments and cracks is needed to verify the stability of buildings. For cultural built heritage, there are additional constraints related to the impossibility of touching or taking samples to be studied in the laboratory or even in situ (Yasar and Erdogan 2004; Vasconcelos et al. 2008).

Evaluation of the degree of decay can be performed using various geophysical methods (Lualdi and Zanzi 2004; Abad et al. 2007; Abu-Zeid and Santarato 2006). These methods had different levels of accuracy. In general, evaluation can be carried out by qualitative and quantitative methods (Abu-Zeid et al. 2010; Bavusi et al. 2012; Binda et al. 2003b).

Depending on the frequencies of the waves, it is possible to distinguish between seismic, sonic, and ultrasonic waves. The first are low-frequency waves between 1 Hz and 100 Hz. Sonic or acoustic waves are between 20 Hz and 20 KHz, and ultrasonic waves present frequencies higher than 20 KHz, a typical frequency ranging between 100 KHz and 20 MHz. Resolution and penetration depth depends on the frequency, the penetration depth being higher and the resolution of waves lower with lower frequencies, as the selection of the frequency range depends on the type of studied structures, based on these two limiting parameters (Epperson and Abrams 1989).

Seismic (sonic and ultrasonic) techniques are able to give important information about the quality and conservation state of the element under investigation.

These investigations exploit propagation of elastic waves; the seismic wave velocity propagation depends on the mechanical characteristics of the rock (Kearey et al. 2002; Reynolds 2011). By generating seismic waves and measuring the travel time required for the waves from the sources to the receivers, it is possible to determine the two-dimensional (2D) or three-dimensional (3D) velocity distribution and accordingly the nature of the subsurface layers. Therefore, these methods can provide information to detect the thickness and position of the weathering layer, and the physical properties of the different materials, including mechanical characteristics and the state of cracking, fractures, and other discontinuous elements (Leucci and De Giorgi 2006; Cosentino et al. 2009; Leucci et al. 2011; Calia et al. 2013; Leucci and De Giorgi 2015; Vasanelli et al. 2015). The ultrasound technique is also exploited in the cultural heritage field and allows evaluating the degradation status of the element. In fact, it is possible to localize areas of decay and structural weakness hidden within the analyzed structures by assessing the extent

of decay visible on the surface and measuring the depth and extent of fractures (Valle et al. 1998; Binda et al. 2003a; Leucci et al. 2011, 2012). In addition, such a nondestructive technique can be carried out in situ and in laboratory samples as well (Vasanelli et al. 2015). Sonic or ultrasonic transducers are used to transmit a pulse through a material in question (Fais et al. 2002; El-Gohary 2013; Martinho and Dionísio 2014). Two probes are used, one emitting and the other receiving ultrasonic pulses. The measured travel time of the pulse through the material depends on the distance between the elastic wave source and receiver. If the reciprocal location of the probes is known, the elastic wave velocities can be calculated (Reynolds 2011).

The elastic wave velocities measured in a material mainly depend on its water content (degree of saturation), density (composition), and state of preservation (Calia et al. 2010; Calia et al. 2012; Vasanelli et al. 2012). Usually the surveys are carried out with a 2D array; sometimes many 2D tomographic profiles are arranged to construct a 3D model. The full 3D sonic or ultrasonic tomographic approaches are especially devoted to the internal study of artifacts (Leucci et al. 2011; Cosentino et al. 2011; Calia et al. 2013).

8.2 Background Theory

In seismic surveys, waves are emitted by a controlled source and propagate through the subsurface. Several waves will be backscattered at the surface by refraction or reflection at boundaries within the surveyed materials. Receivers distributed along the surface detect the motion caused by these returning waves and measure the arrival times of the waves at different distances from the source. The travel times are then converted into velocity values, and the spatial distribution of the velocities can be systematically mapped. Sources suitable for seismic surveying usually emit pulses, which are associated to a wide range of frequencies (Reynolds 2011). With the exception only of the areas near to the source, the strains associated with the passage of a seismic pulse are very low and may be assumed to be elastic. Based on this assumption, the propagation velocities are determined by the elastic moduli and densities of the materials.

The elastic waves can be classified in two groups, that is, body waves and surface waves.

Body waves can propagate through the inside of an elastic solid and can be of two types. Compressional waves (the longitudinal, primary or P-waves) propagate by compression and expansion of uniaxial strains in the direction of wave travel (Fig. 8.1a). Shear waves (the transverse, secondary or S-waves) propagate by a pure shear strain in a direction perpendicular to the direction of wave travel (Fig. 8.1b). Body waves are nondispersive, that is, all frequency components in a wave train or pulse propagate through any material at the same velocity, which is determined only by the elastic moduli and density of the material.

Surface waves can propagate along the boundary of the solid. Rayleigh waves are seismic surface waves causing the ground to shake in an elliptical motion, with

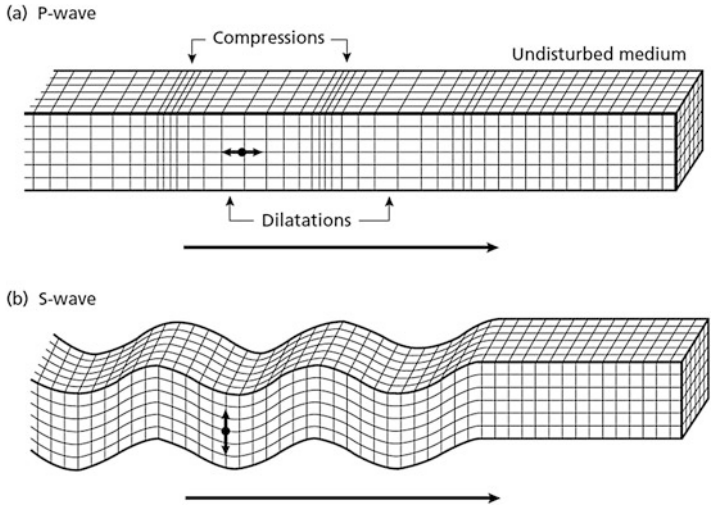

Fig. 8.1 Elastic deformation and ground particle motion associated with the passage of body waves: P-wave (**a**) and S-wave (**b**)

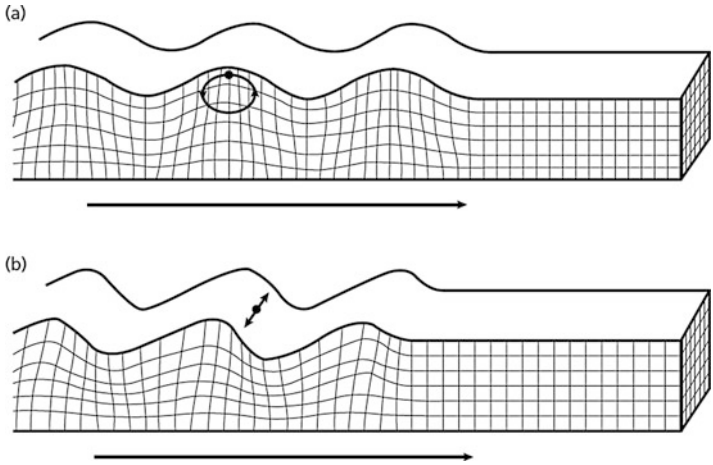

Fig. 8.2 Elastic deformation and ground particle motion associated with the passage of surface waves: Rayleigh wave (**a**) and love wave (**b**)

no transverse, or perpendicular, motion (Fig. 8.2a). Love waves are surface waves having a horizontal motion that is transverse (or perpendicular) to the direction the wave is traveling (Fig. 8.2b).

A seismic pulse propagates at a velocity determined by the physical properties of the surrounding materials. If the pulse travels through a homogeneous material, all

the waves will travel at the same velocity, and accordingly the wavefront, defined as the locus of all points which the pulse has reached at a particular time, will be a sphere.

For sonic and ultrasonic standard surveys, only the body waves P and S are considered. The travel time and the sonic pulse velocity provide basic information about the quality and conservation state of the medium element under investigation.

The sonic pulse velocity test is very similar to the ultrasonic pulse velocity test for what concerns basic theories, purpose of the tests, and application of the method. The difference between the two methods is relative to the frequency of the emitted wave, as already described.

The commonly used sonic methods are the sonic transmission method, sonic/seismic tomography, sonic/seismic reflection method, and ultrasonic reflection method.

The sonic transmission method involves the propagation of a sonic wave through the thickness of the wall (or the structure) under investigation. Emission of the wave is performed on one side of the structure by the impact of the force hammer or pulsed generator; an accelerometer, positioned directly opposite the force hammer, receives the transmitted signal on the other side of the wall (Fig. 8.3a). The resulting wave velocity is an average of the local velocity along the path, and it is not possible to evaluate the position and the extent of any possible inhomogeneity. The velocity variations may be plotted in a contour map format, with grid points as X and Y coordinates and the pulse velocity as the Z coordinate. This format allows a simple evaluation of the status of the masonry or concrete walls of the structure or an evaluation of the internal condition of a structure. It has generally been recognized that the direct transmission arrangement is a simple technique to apply in the analysis of structures because it provides a defined pathlength through the structure. Furthermore, because the arrival time of the first wave is of primary concern, no

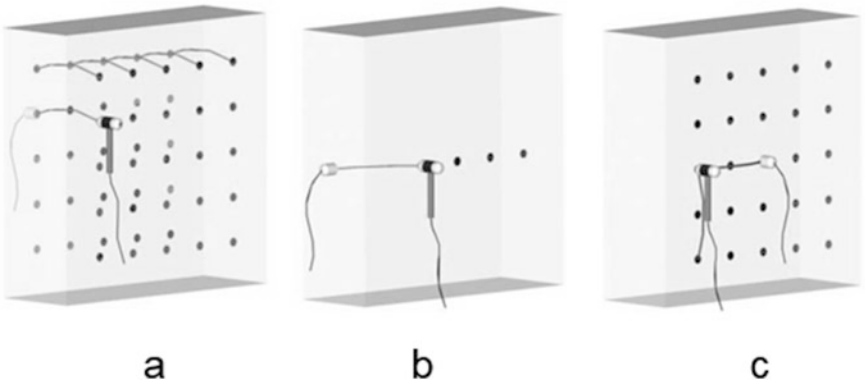

Fig. 8.3 Transmission modes for sonic wave tests: direct (**a**), semidirect (**b**), indirect (**c**)

attempt to distinguish complex wave frequencies and reflections is required for the analysis. This method has been successfully used to evaluate material uniformity, detect the presence of voids, estimate the depth of a surface crack, and calculate an average compressive strength for the structure or the material. The detection of flaws is possible because sonic waves cannot transmit across an air gap, which could be the result of a crack, void, or delamination at the interface between brick or stone and mortar. A propagating wave must find a path around the void, resulting in attenuation and an increase in the transit time of the signal. Figure 8.3b, c illustrates the semidirect and indirect transmission modes mainly used for tomographic surveys, respectively.

Sonic tomography represents an improvement in the sonic transmission test method because tests are performed not only in the direct mode but also along paths that are not perpendicular to the wall surfaces. The wall of the structure or the masonry section is thus crossed by a dense network of ray paths, each of which defines a specific travel time between the sonic source and receiver. These values of travel time are processed to achieve a three-dimensional reconstruction of the velocity distribution across the structure or selected cross section; in this way, local variations of the velocity can be identified and correlated to zones of weakness or flaws in the internal fabric of the structure (Fig. 8.4).

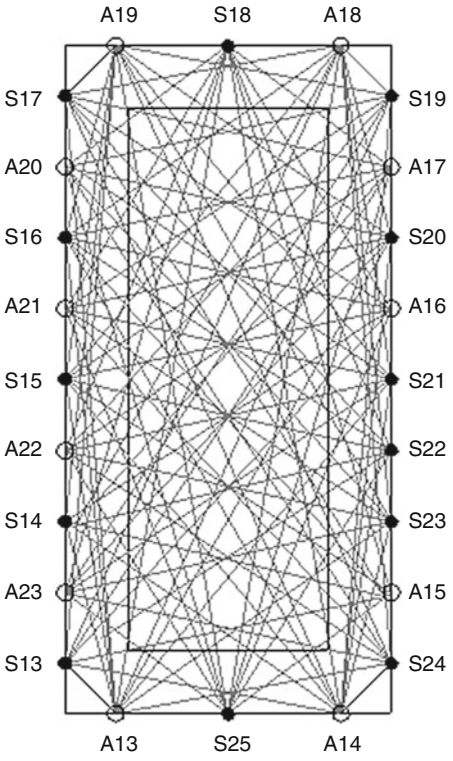

Fig. 8.4 Typical ray path in a tomography acquisition (*S* sources, *A* receivers)

It is usual to assume a homogeneous structural response in the application of the tomographic method because the response is measured by transducers far from the location of the impact, where nonhomogeneous behavior may arise. Therefore, any variation from the expected travel time is attributed to inhomogeneity in the structure or damage occurred. To increase the accuracy of the measurements, it is necessary to maximize the amount of experimental data included in any calculation u by ensuring that all areas of the proposed tomographic section have adequate ray path coverage. A number of inversion algorithms are available commercially for tomographic reconstruction (Cheeke 2002).

In the sonic reflection method the emitters and receivers are on the same side of the masonry; thus, the stress wave recorded is the direct stress wave reflected from any internal flaw or the rear face of the structure investigated. The value of velocity calculated from the rear wall or face of a structure is a measure of the local velocities along the path. The problems for which reflection methods may be used in the investigation of retaining walls/wing walls/spandrel walls are (1) internal dimensions and shape; (2) type and properties of fill; (3) voiding within the fill material; and (4) cracks and voids within the internal fabric of the structure.

Seismic reflection techniques is not a currently recommended method because the resolution achievable with the low-frequency energy is poor, and it is often difficult to distinguish reflections from surface waves and refracted arrivals. Ultrasonic waves, which are generated by a piezoelectric transducer at frequencies above 20 kHz, propagate with a wavelength around 50–100 mm (as function of the wave velocity propagation). This form of testing is used successfully for the detection of flaws in metal castings and is the first nondestructive technique to be developed for the testing of concrete. However, it is much less practical in concrete and masonry, which have much higher attenuation characteristics, and hence lower-frequency signals are required to obtain a reasonable penetration.

At present the method is not commonly used for these purposes because of a number of technical difficulties. In the case of ultrasonic signals the main factors to overcome are the need for good coupling of the transducer to the surface, which is often rough, and the scattering of the wave by material heterogeneity. The need for effective coupling requires the use of a coupling agent, such as grease or petroleum jelly, to temporarily adhere the transmitter and receiver to the surface. This requirement makes the process of moving the points of measurement quite slow, and it is often difficult to achieve adequate coupling on some uneven surfaces. Scattering of the signal limits propagation through the material and also leads to a complicated series of return signals, which makes it difficult to identify defects among the noise. In addition, surface waves, which travel more slowly than the compression waves, may arrive at the receiver within the same time interval and confuse interpretation. Further developments of the ultrasonic technique, for example, improvements in signal generation, detection, and data processing, are underway and may lead to a practical tool if the problems mentioned here are overcome.

Seismic resolution is a measure of how large an object needs to be that it can be seen in seismic. The vertical resolution is derived from the length of the sound wave,

and layers can be discerned when their thickness is less than 1/4 the wavelength. Still, it is possible to detect layers down to 1/32 wavelength. When referring to vertical resolution, it is normally the 1/4 wavelength. The wavelength is calculated by Reynolds (2011):

$$\lambda = V/F$$

The vertical seismic resolution is calculated by $\lambda/4$ where λ is the wavelength, F is the seismic frequency, and V is the seismic velocity.

The seismic waves sent out from the source move in three dimensions and spread out over a larger area the further away they move from the source. The horizontal resolution is derived from the Fresnel zone, the part of a reflector covered by the seismic signal at a certain depth. On a buried horizon, all features with a lateral extent exceeding the Fresnel zone are visible. The radius of this zone is often taken as the horizontal resolution for unmigrated seismic data. As with the wavelength, the Fresnel zone size also increases rapidly with depth (Reynolds 2011).

$$\text{Fresnel zone} = V\,(D/F)^{0.5}$$

where F is the seismic frequency, V is the seismic velocity, and D is the depth in time.

8.3 Targets of Sonic and Ultrasonic Measurements

Sonic (S) and ultrasonic (US) can be used on built heritage with direct tomography (DT), semidirect tomography (ST), indirect tomography (IT) transmission method, or with tomographic (T) mode, depending on the objective of the investigation. Problems that can be analyzed are listed in Table 8.1, with indications of the most appropriate acquisition mode.

Table 8.1 Targets of sonic and ultrasonic measurements

Target	Acquisition type
Detection of inhomogeneities (e.g., variation of material texture, repair interventions, presence of different materials...)	DT, T
Detection of multiple leaves and measurement of the thickness of each leaf	T
Detection of detached external leaves	DT, T
Detection of voids or chimney flues	DT, T
Evaluation of effectiveness of repair interventions (e.g., grout injections, repointing)	DT, T, ST
Detection of damaged portions of structure or of crack patterns	DT, IT, T

8.4 When to Apply

The successful application of S and US methods depend on the appropriate application of the method, but there also exist unfavorable conditions in which the application to some of these problems might fail. Sonic pulses do not undergo significant signal attenuation. The execution of the tests is thus generally successful. On the other side, these methods are characterized by low resolution, which cannot be sufficient for the detection of small voids or small inclusions or when considering the detection of multiple leaves, of detached external leaves, of cracks, etc.

Higher frequencies and smaller wavelengths are needed to improve the resolution, and this entails the use of the US waves. The resolution of S and US tomography depends also on the dimension of the grid used to transmit/acquire the sonic waves. However, very dense grids, if not accompanied by the use of higher-frequency stress waves, may not lead to improved resolution. As the presence of moisture produces an apparent S and US pulse velocity increase, the application of the method to a very moist masonry should be carefully evaluated. If metal elements (ties or anchorages) are placed inside the investigated structure, is possible to observe an apparent S and US pulse velocity increase, which is caused by the faster propagation of the wave on the metal element; thus the tests should be carried out at a certain distance from the position where the ties are placed. Particular care is needed when the hammer/accelerometer must be used on a precious surface decorated with frescos or plasters; in these cases, a good practice consists in protecting the surface (when hitting/receiving) from the contact with a simple piece of clean paper.

8.5 Equipment, Investigation Design, and Data Acquisition

The equipment required to carry out sonic and ultrasonic pulse velocity tests consists of several components. The stress wave is generated by means of an impulse force hammer or from a pulse generator, instrumented with a piezoelectric sensor to record the impulse force. The frequency and energy content of the impulse force are dictated by the characteristics of the source. The hammer tip hardness determines the amplitude and duration of the impulse force, where harder tips generate higher-amplitude, shorter-duration signals. The mass of the hammer determines the initial energy content of the input stress wave. The hammer can be substituted by a calibrated impactor. The small vibrations of the material are measured by means of accelerometers, which can be fixed to the surface by means of steel angles or plates glued with epoxy or screwed to the wall, or simply leaned against the wall and hand-supported for a fully nondestructive test procedure. The signals of both the impact hammer and the accelerometer pass through a power amplifier and an analogue-to-digital converter and are subsequently displayed or recorded by means of an external

Fig. 8.5 Experimental setup for sonic and ultrasonic measurements

device such as an oscilloscope or digital waveform recorder. Figure 8.5 shows a typical instrumentation for both S and US pulse velocity measurements.

The sensitivity of the acceleration transducers may vary between 100 and 1000 mV/g, being sufficient for the scope of the signal acquisition. The sampling rate is an important issue concerning the accuracy of the acquired data. In fact, the use of digital computer technology means that the analogue signal must be sampled at regular intervals in time to be processed. Figure 8.6 shows a signal sampled at two different intervals. The top slide shows that a good representation of the 20-Hz signal can be made by samples taken every 25 ms (marked by the dark stars). In the bottom slide, samples are taken every 75 ms. An insufficient number of samples are taken, and the higher-frequency information is "lost" or aliased. The original 20-Hz blue curve appears as a 6.7-Hz red dotted curve. The highest frequency F that can be sampled by interval d is 1/2 day: this is called the Nyquist frequency. Higher frequencies than this are said to be temporally aliased because they will

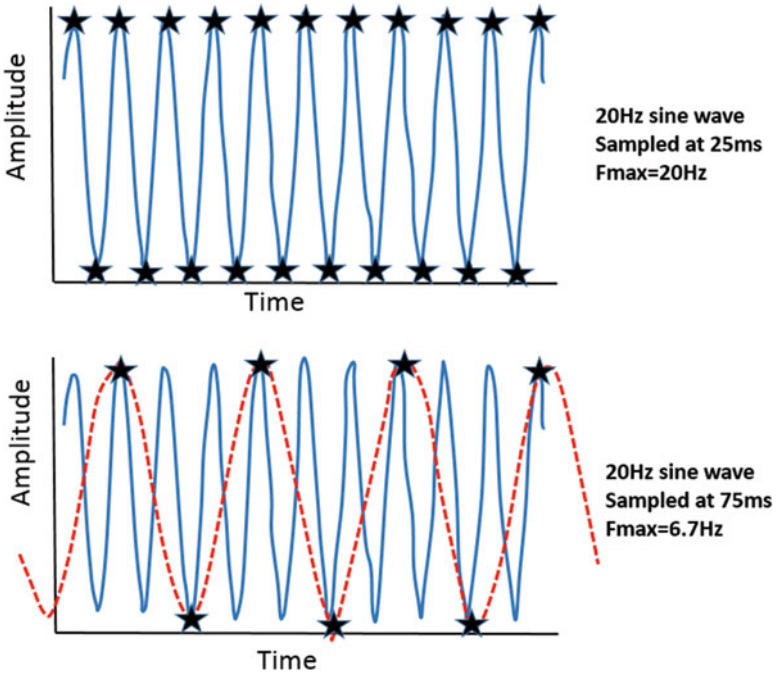

Fig. 8.6 Example of sample rate

appear as if they are lower frequencies. Typical sampling intervals are 10, 20, 40, and 80 microseconds (μs), with aliasing occurring above 5000, 2500, 1250, and 625 Hz, respectively. Before the data are sampled, the higher frequencies that would be aliased should be cut off by an analogue filter in the recording system.

The design of the investigations should take into account the aims of the survey and the onsite conditions. The plan of the investigation campaign should be done by the S and US test experts in cooperation with the designer, who should be expert about built heritage structures and of the particular building under investigation and should define the aims of the tests and the relevant areas to be tested. The interaction with historic experts and the study of available documentation and drawings of the building is essential to define the target of the investigations and to evaluate the probability of success. An onsite preliminary inspection of the multidisciplinary expert team is very useful to select the optimal measurement positions. It is then necessary to take into account several factors, such as, for example, geometry and morphology of the structures to be tested and access to the experiment location. The typology of the S or US test to be performed (DT, ST, IT, or T) has to be chosen according to the aim of the investigation, in agreement with the possible targets testing problems, the cost-effectiveness of the specific investigation, the required in-depth of the investigation and the accessibility of the site. To have significant

data, a minimum distance from transmitter to receiver, related to the texture and unit dimension, must be considered. Lower distances are indicative of limited structure portions and lead to local results.

As already stated, the accuracy of the data recorded depends on the sampling rate of the acquiring device and on the average velocity of the seismic wave within the tested structure [i.e., when acquiring at 100,000 samples per seconds (10 μs or at a frequency sampling of 100 KHz), and considering an average velocity of 1500 m/s, the accuracy in terms of distance is ±1.5 cm, corresponding to an error of 10%, if the distance between source and receiver is 15 cm]. Tomographic experiments are quite time consuming. The design of transmitter and receiver positions is an essential issue for tomographic tests. The tomographic approach is more effective on pillars and columns because a reliable tomographic reconstruction requires a good coverage of the scanned section. The goal in designing the acquisition scheme is to ensure that any region of the tomographic section is crossed by a number of transmitter–receiver (TX–RX) ray paths arriving from any possible direction. As a result, for a pillar, TX and RX positions should be designed to collect transmission data from every accessible side toward any other side (not only toward the opposite sides). The distance between subsequent TX and RX positions along each side of the tomographic section should be calibrated according to the expected resolution. The experiment area should be properly prepared to ensure an accurate execution of the S or US measurements. Important issues to be considered are the accessibility of the site (easy access, need of ladders or scaffoldings to reach the testing position, possibility to have a safe working position . . .), the presence of a power line, and the indoor or outdoor conditions. The preparation depends on the type of experiment (DT, ST, IT, or T), being in any case quite similar for the different testing typologies.

The test preparation starts with the survey of the area to be tested. If the test crosses the structure section, it is necessary to mark a reference point on the different sides of the structure. Because in many cases to reach the two sides of a structure it is necessary to make a long detour, the reference point must be chosen with the help of meters or distance meters and levels. Subsequently, the complete acquisition grid has to be marked on the surface or surfaces of the area to be measured. When the structure surface cannot be directly marked or when the surface is delicate (frescos, bas-reliefs,..), pre-marked paper should be placed over the experiment area. It is advisable that the rows and/or columns chosen for the data acquisition have a regular prefixed spacing. If, for any reason, a point of the line/grid has to be shifted, the changed position must be immediately reported on the drawings of the structural elements. Once the marking work has been done, the exact position of the measurements must be reported with respect to selected reference points.

The most common testing arrangement consists in drawing a rectangular/square grid on the masonry wall to be tested and the corresponding grid on the other side of the wall. The numeration must be unequivocal and corresponding from one side to the other. The minimum number of rows and columns depends on the aims of the investigation (Fig. 8.7).

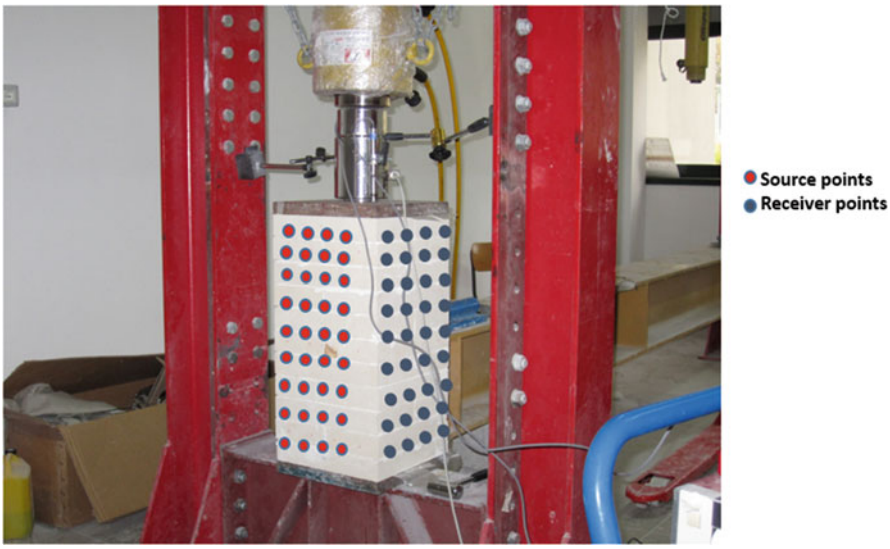

Fig. 8.7 Example of acquisition geometry

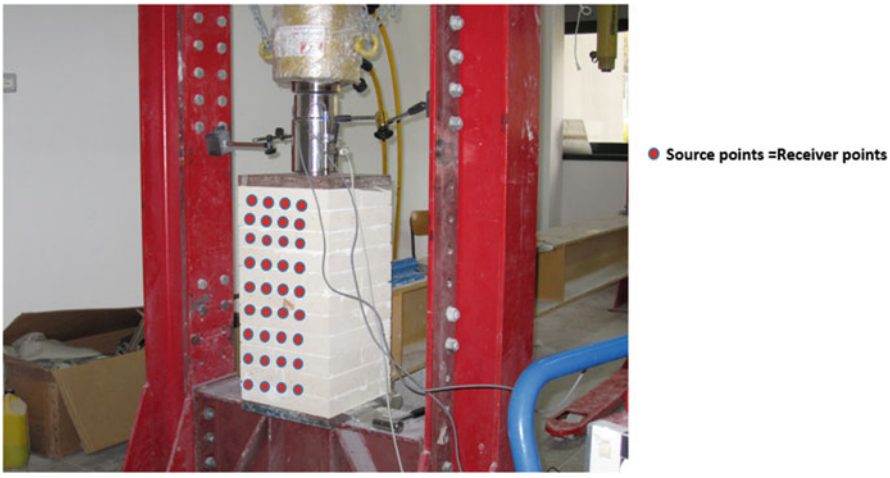

Fig. 8.8 Example of acquisition geometry for IT

A similar arrangement has to be considered for the indirect sonic test, on one side of the structure. It is necessary to set the acquisition grid to have several horizontal and vertical paths, considering meaningful distances, where performing the test (Fig. 8.8).

In the case of the tomography, performed on two or more sides of a structure (wall/pillar), the most common testing arrangement considers a cross section (horizontal or vertical) of the structure to be tested. The source transmits the signal that is received on all the positions chosen on the other side/sides (Fig. 8.7).

A good strategy to ensure a proper recording is to take pictures of the experiment areas after the marking work; pictures of the marked profiles with a measuring tape that shows the distance from the reference points of the area are also a good practice. Pictures taken from a distance long enough to include the whole area of an experiment will be very useful to prepare the final report by superimposing the sonic results on the exact position of the investigation. In principle, the final criterion in producing the field documentation is that this documentation must be sufficient to repeat the experiments exactly in the same positions and in the same way at a later time. Any evidence of metal elements observed on the surface of the experiments (tie-rods, nails, hooks, etc.), as for other evident different material inclusion within the masonry wall portion tested, should be reported (e.g., with pictures or drawings) to facilitate the final interpretation of the results.

8.6 Data Acquisition and Processing

All the instruments needed in the data acquisition chain must be checked before starting the test. A cross check of the source and receiving devices, with their connection cables, can be easily achieved by verification of the signal input in the power amplifier and the corresponding visualization of the signal in the display. A proper setup of the acquisition parameters is extremely important to ensure a successful investigation. The acquisition system may have different parameters to be checked. The factors that are usually be set are the sampling rate and the signal gain. If possible, it is recommended to calibrate the acquisition system on some masonry samples, or brick/stone units, whose geometry and morphology are directly observable. It is a good practice to report on the field documents the final parameters that have been selected for the experiment (Fig. 8.9).

Data acquisitions should be performed according to the investigation design. An unambiguous naming convention must be chosen for the data files and this convention must be indicated in the drawings. Any variation with respect to the design or to the naming convention must be properly reported on the field documents. Similarly, any variation of the setup parameters must be monitored. Because it is necessary to have a clean signal record, it is recommended to choose a firm position where to hit with the instrumented hammer or to position the acceleration transducer. When the chosen point of the grid is located on an unsteady masonry unit or deteriorated mortar joint, it would be better to shift the point a few centimeters to select a more suitable position. To obtain more accurate results, it is advisable to have more than one record file per each ray path. Three record files per acquisition point would be convenient.

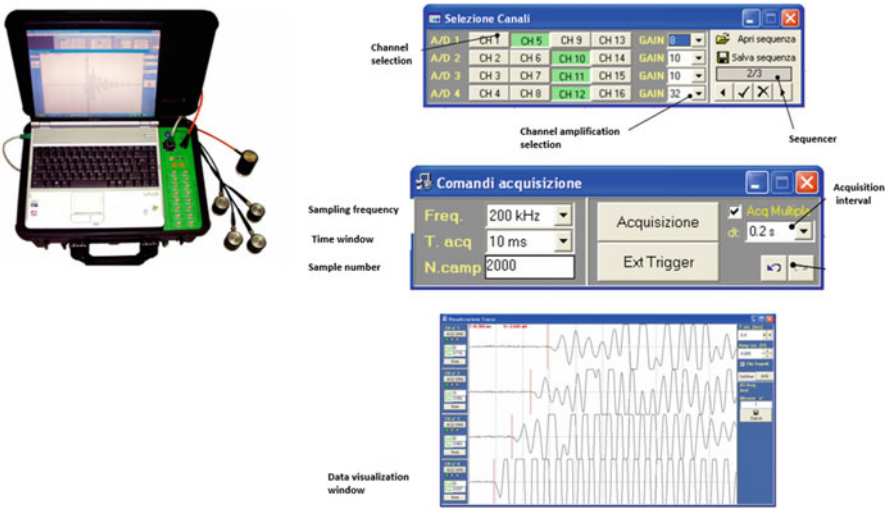

Fig. 8.9 Example of instrument setup

Data processing must be performed by a sonic test processing expert using dedicated software products. It consists in evaluating the pulse transit time by measuring the elapsed time of the recorded waveforms, that is to say, by picking in an amplitude versus time diagram the starting point of the hammer pulse and the first arrival recorded by the accelerometer. In the case that time picking is performed with automated procedures, by using a threshold value to find the wave onset, the reliability of the procedure and appropriateness of the threshold value should be checked. After evaluating the transit time, the pulse velocity is calculated as follows: $v = l/t$ where v is the pulse velocity (m/s); l is the distance between transducer (m); and t is the transit time (s). This simple procedure should be followed for S and US pulse velocity tests with direct, semidirect, and indirect transmission method.

Data processing for tomography requires specific software codes. The tomographic inversion is a challenging problem, and the performances and the flexibility of tomographic programs can vary significantly. The standard procedure in a tomographic reconstruction consists of picking the travel times first of the direct wave traveling from TX to RX positions through the masonry section. The transit times are then inverted by the tomographic software to obtain a velocity map. The problem is typically nonlinear and the final solution is the result of several iterations where ray paths are iteratively updated by using a ray-tracing module. Critical issues within this procedure are the design of the inversion grid and the control of the stability and reliability of the inversion. The grid size should be defined with special care considering the expected resolution of the experiment and the spacing between acquisition points. Pillars with complex geometries may create data where the direct wave partially or totally travels in air. These data should be removed before the

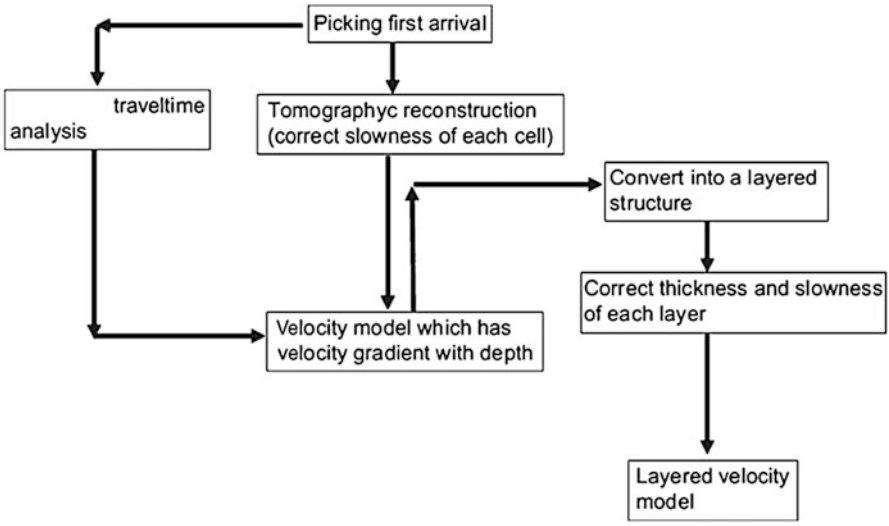

Fig. 8.10 The seismic tomography data inversion scheme

inversion stage to prevent artifacts in the final velocity map. The processing flow used in the method is shown in Fig. 8.10.

The first step in the tomography survey consists of measuring the travel times of seismic wave first arrivals related to source–receiver distances located along the profile. These travel times would be picked manually on a PC. To determine the velocity distribution, the travel times of each source and each receiver must be combined to achieve a an initial velocity model, by assuming a homogeneous medium. The model is represented by N × M cells. Rays are traced through this model to give calculated travel times. A misfit function, consisting of the squared difference between the observed and computed travel times, is calculated. The model is adjusted until the misfit is minimized. The iterations are stopped when the root mean square (RMS) travel time residual (difference between the calculated travel times for the initial model and the observed ones) is less than the average travel time pick error. The results of data processing may be visualized in the form of 3D or 2D gray- or color-scale contour maps, or others (Figs. 8.11 and 8.12).

Tomographic results can be presented as velocity maps, color images in which the color is associated with a given velocity (Figs. 8.11 and 8.12). This visualization allows directly evaluating the internal composition of a surveyed material structure, being in general areas with higher or lower velocity representative of changing in terms of material, of presence of flaws/voids or diffuse crack patterns. Whatever the representation is, it is essential to include a drawing of the structural element (wall, pillar, etc.) with an accurate indication of the position of the experiment. An effective method to facilitate the location of the results is to superimpose the images on the drawings or on the pictures of the structure (Fig. 8.13).

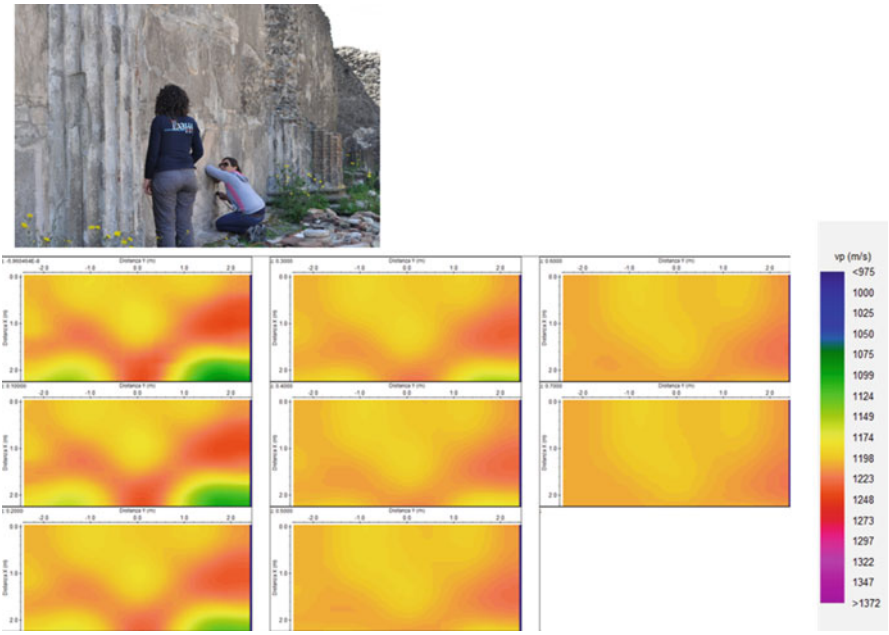

Fig. 8.11 Velocity distribution shown as 2D depth slices

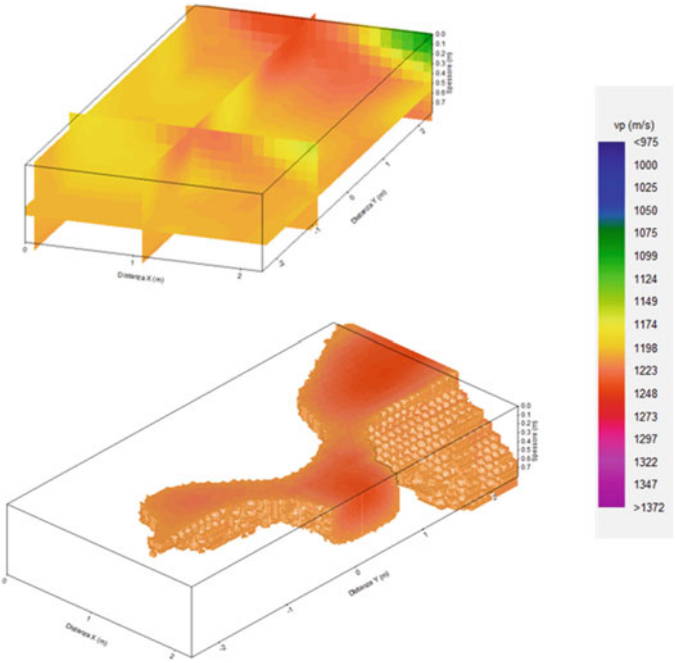

Fig. 8.12 The velocity distribution shown as 3D volumes

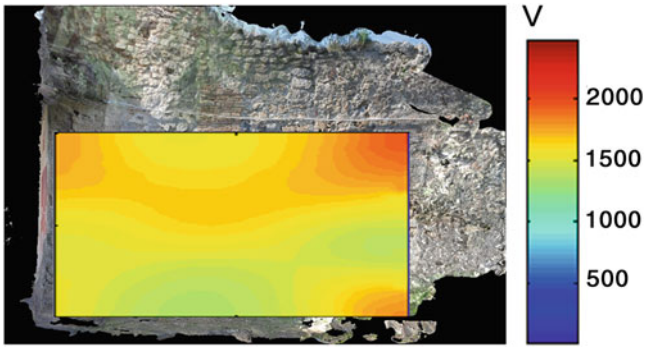

Fig. 8.13 Velocity distribution superimposed with surveyed wall

For an easier visualization and for the correct interpretation of the tests results, it is also necessary to use the same color scale throughout all the testing report, even if the values of S pulse velocity are very different (e.g., the quality of different structural elements varies a lot, or the same test is carried out before and after injection, etc.). A calibration of the color scale after all the tests are finished and the data processed may be needed.

8.7 Interpretation of Results

Interpretation of the results is a fundamental and critical step. In many cases, S and US tests alone cannot resolve all the ambiguities and some additional information or calibrations (from complementary investigations, from local invasive and other noninvasive measurement, from a priori knowledge of the building, from expertise on construction techniques, etc.) is required. Macroscopic inclusions (e.g., beams, voids, chimney flues, presence of different materials) can be detected by means of direct test or tomography. In general, it is not possible to associate the velocity anomalies to the nature of the targets. The defaulters of the targets can be only inferred from assumptions or other information or directly checked with a local invasive test, whose positioning can be chosen on the basis of the S or US test results. If the resolution of sonic tomography is sufficient, it is possible to detect outer leaves and internal filling, appearing as areas with different sonic velocities (Fig. 8.14). The detection of damaged portions of masonry or of crack patterns is in general possible by examining the retrieved low velocity values. The dimension of cracks being far lower than the sonic wavelength, it is not possible to localize them but only to record a decrement in terms of velocity. The tests also permit evaluating the effectiveness of repair interventions (e.g., grout injections, repointing, etc. . . .) on the basis of the outcomes of the investigation campaign before and after the strengthening intervention. In this case, a ratio between the local/average sonic

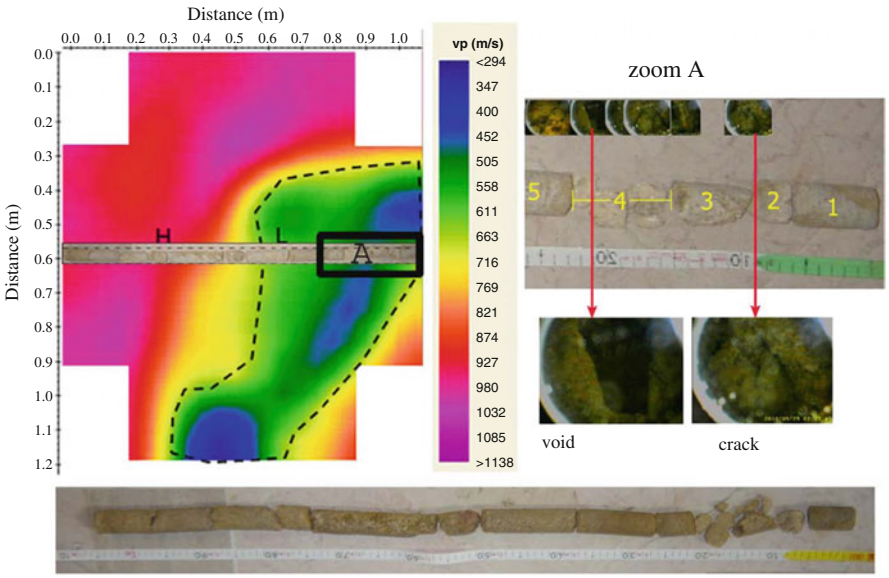

Fig. 8.14 Sonic tomogram with the overlaid core. *Upper right*: zoom A of the core with an endoscopic image that puts into evidence a void and a crack that are the cause of the low velocity values of the sonic wave (Leucci et al. 2011)

velocity value before and after the intervention can be considered a quantitative parameter. Variations in moisture levels can be indicated by an apparent sonic pulse velocity increase. For a quantitative calibration, local measurements of moisture level with other methods are needed.

Figure 8.14 shows results obtained in the sonic tomography survey performed by Leucci et al. in 2011 on a pillar in the Cathedral of Tricarico (South Italy). The core and endoscopic images were captured inside the hole. The core and the endoscopy analysis evidenced the presence of a void and a crossing crack between the right pilaster and the central nucleus where very low elastic waves velocity values have been measured.

8.8 Conclusions

A brief discussion about noninvasive sonic and ultrasonic methods for the built cultural heritage was addressed. It is important to underline that the environmental conditions can affect the results of sonic and ultrasonic tests. Sonic and ultrasonic tests inside a building are generally always applicable. Moist conditions of the built heritage do not preclude the possibility of running the experiments, but high

moisture content affects the test results, determining an apparent pulse velocity increase (a high saturation level may conceal flaws within the masonry).

For outdoor investigations, intense rain might preclude the possibility of running the experiments because of its effects on both the state of the masonry and the instrumentation. The sonic and ultrasonic techniques applied to the study of cultural heritage must be refined to obtain investigation tools that can be applied and interpreted as best as possible. Future developments should include the creation of appropriate instruments and software for certain types of studies. Transducers of reduced dimensions for performing sonic or ultrasonic tomography must be developed for both laboratory studies (very small size laboratory samples) and in situ surveys (small-dimension artifacts or very irregular surfaces). Laboratory investigations are necessary to predict the behavior of materials in specific situations and to assess the accuracy of the method. The study of cultural artifacts of small size requires increasingly higher resolution of the techniques.

References

Abad R, García G, Abad R, Blanco R, Conesa M, Marco B, Lladró C (2007) Non-destructive assessment of a buried rainwater cistern at the Carthusian Monastery Vall de Crist (Spain, 14th century) derived by microgravimetric 2D modeling. J Cultur Heritage 8:197–201

Abu-Zeid N, Santarato G (2006) Non-invasive imaging of ancient foundations status in venice (italy) using the electrical resistivity tomography technique. heritage, weathering and conservation – fort Alvarez de Buergo eds Gomez-Heras and Vasquez-Calvo. Taylor and Francis Group. London. ISBN 0-415-41272-2

Abu Zeid N, Balducci M, Bartocci F, Regni R, Santarato G (2010) Indirect estimation of injected mortar volume in historical walls using the electrical resistivity tomography. J Cultur Heritage 11:220–227

Bavusi M, Loperte A, Soldovieri F (2012) A low cost ERT prototype in the Cultural Heritage monitoring. Geophys Res Abstr 14:EGU2012–EG10064

Binda L, Saisia A, Tiraboschi C, Valle S, Colla C, Forde M (2003a) Application of sonic and radar tests on the piers and walls of the Cathedral of Noto Constr. Build Mater 17:613–627

Binda L, Saisi A, Zanzi L (2003b) Sonic tomography and flat jack tests as complementary investigation procedures for the stone pillars of the temple of S.Nicolo' L'Arena (Italy). NDT&E Int 36:215–227

Calia A., Leucci G., Masini N., Persico R., Quarta G. (2010) Integration of in situ NDT tests with petro-physical analyses for the characterization of materials and constructive techniques of ancient masonries Geophys Res Abstr 12:EGU2010–12963, 2010, EGU General Assembly 2010

Calia A, Sileo M, Leucci G (2012) The assessment of ultrasonic tests as a tool for qualification and diagnostic study of traditional highly porous and soft stone materials used in the built heritage of the past. EGU General Assembly 14:EGU2012–9860

Calia A, Lettieri M, Leucci G, Matera L, Persico R, Sileo M (2013) The mosaic of the crypt of St. Nicholas in Bari (Italy): integrated GPR and laboratory diagnostic study. J Archaeol Sci 40:4162–4169. doi:10.1016/j.jas.2013.06.005

Cheeke JDN (2002) Foundamental and applications of ultrasonic waves. CRC Press LLC, Boca Raton, p 462

Cosentino PL, Capizzi P, Martorana R, Messina P, Schiavone S (2011) From geophysics to microgeophysics for engineering and cultural heritage. Int J Geophys 2011:Article ID 428412 8

Cosentino PL, Capizzi P, Fiandaca G, Martorana R, Messina P (2009) Advances in micro geophysics for engineering and cultural heritage. J Earth Sci 20:626–639

El-Gohary MA (2013) Evaluation of treated and un-treated Nubia Sandstone using ultrasonic as a non-destructive technique. J. Archaeol. Sci. 40:2190–2195

Epperson GS, Abrams DP (1989) Non destructive evaluation of masonry buildings. Advanced Construction Technology Center, Doc. N. 89-26-03, Urbana Illinois, October 1989, 208 pp

Fais S, Ligas P, Palomba M and Tocco R (2002) Evaluation of preservation state of monumental buildings by ND acoustic techniques and mineralogical Studies. In: Proceedings of the 5th international symposium on protection and conservation of the cultural heritage of the Mediterranean cities, pp 307–314

Kearey P., Brooks M., Hill I (2002) An introduction to geophysical exploration. Blackwell Science Ltd, Oxford

Leucci G, De Giorgi L (2006) Experimental studies on the effects of fracture on the p and s wave velocity propagation in sedimentary rock ("calcarenite del salento"). Eng Geol 84:130–142. doi:10.1016/j.enggeo.2005.12.004

Leucci G, Masini N, Persico R, Soldovieri F (2011) GPR and sonic tomography for structural restoration: the case of the Cathedral of Tricarico. J Geophys Eng 8:76–92. doi:10.1088/1742-2132/8/3/S08

Leucci G, De Giorgi L (2015) 2D AND 3D seismic measurements to evaluate the collapse risk of cave in soft carbonate rock. Central Eur J Geosci. doi:10.1515/geo-2015-0006

Lualdi M, Zanzi L (2004) 2D and 3D experiments to explore the potential benefit of GPR investigations in planning the mining activity of a limestone quarry. In: Proceedings of the 10th international conferences on Ground Penetrating Radar GPR 2004 June 21–24 Delft 613–616

Martinho E., Dionísio A (2014) Main geophysical techniques used for non-destructive evaluation in cultural built heritage: a review. J Geophys Eng 11(2014):053001 (15 pp)

Reynolds JM (2011) An introduction to applied and environmental geophysics. Wiley, Chichester

Valle S, Zanzi L, Binda L, Saisi A Lenzi G (1998) Tomography for NDT applied to masonry structures: sonic and/or EM methods Arch Bridges ed A Sinopoli (Rotterdam: Balkema) pp 243–252

Vasanelli E, A Calia, MA Aiello, M Sileo, G Leucci (2012) Mechanical DT and NDT: characterisation of building stones and research of correlation for in situ analysis of ancient masonries. EGU General Assembly 14:EGU2012–10333

Vasanelli E, M Sileo, G Leucci, A Calia, MA Aiello, F Micelli (2015) Mechanical characterization of building stones through DT and NDT tests: research of correlations for the in situ analysis of ancient masonry. Key Eng Mater 628:85–89. Online available since 2014/Aug/28 at www.scientific.net Trans Tech Publications, Switzerland doi:10.4028/www.scientific.net/KEM.628.85

Vasconcelos G, Lourenço PB, Alves CAS, Pamplona J (2008) Ultrasonic evaluation of the physical and mechanical properties of granites. Ultrasonics 48:453–466

Yasar E, Erdogan Y (2004) Correlating sound velocity with the density, compressive strength and Young's modulus of carbonate rocks. Int J Rock Mech Mining Sci 41:871–875

Chapter 9
Ground-Penetrating Radar: Technologies and Data Processing Issues for Applications in the Field of Cultural Heritage

Raffaele Persico and Motoyuki Sato

Abstract In this contribution, the possibilities offered by the some of the most advanced ground-penetrating radar (GPR) instruments are shown, with particular reference to the Yakumo GPR system. To make more clear the exposition and the advantages offered by this new technology, some theoretical aspects about GPR prospecting are also briefly recalled. In particular, sampling and resolution aspects are mentioned, as well as aspects relative to the measure of the propagation velocity of the waves in the soil.

9.1 Introduction

In this chapter, we introduce some of the most advanced technologies and methodologies in GPR prospecting. In particular, we refer to the techniques for a precise positioning of the results and to the large measurement campaign that can be performed thanks to the modern systems equipped with arrays of antennas, which can allow a narrow interline spacing of the data, a multiview processing, and a fast measure of the propagation velocity of the waves in the soil because there is an instantaneous common midpoint (CMP) measure that can be extracted for any position of the array from the same GPR data. Indeed, a full understanding of the underlying physical concepts would require a deep, and consequently not immediate, discussion about the physics and mathematics of the problem, which would amount to a discussion based on Maxwell's equations. We avoid such an effort here, referring the interested reader to other texts (Daniels 2004; Persico 2014; and references therein). Notwithstanding, a minimal awareness of the meaning of

R. Persico (✉)
Institute for Archaeological and Monumental Heritage IBAM-CNR, Via Monteroni 199/A, 73100, Lecce, Italy
e-mail: r.persico@ibam.cnr.it

M. Sato
Center for Northeast Asian Studies, Tohoku University, 41 Kawauchi, Sendai, 980-8576, Japan

N. Masini, F. Soldovieri (eds.), *Sensing the Past*, Geotechnologies and the Environment 16, DOI 10.1007/978-3-319-50518-3_9

the most exploited terms is well advised for a fuller comprehension of the second part of this chapter. In particular, sections 2–6 are devoted to the introduction of the quantities taken for granted in the following sessions.

9.2 Sinusoidal Waves: Frequency and Wavelength

It is well known that a GPR radiates and receives electromagnetic waves, but it is less known, or in some cases it has been forgotten, what an electromagnetic wave indeed is. As said, a complete exposition on this is beyond our purposes, but we want to introduce gradually the concepts. So, we introduce first of all a sinusoidal wave propagating along a straight line, that without loss of generality will be identified with the x-axis of a Cartesian system. That said, a sinusoidal wave SW is a quantity that can be expressed according to the expression

$$SW(x,t) = A\cos(kx - \omega t + \varphi) \tag{9.1}$$

In Eq. 9.1, x[m] is the spatial position of the observation point, t[s] is the time, k[rad/m] is a constant called the wavenumber, and ω[rad/s] is another constant called the pulsation, or angular frequency. The wavenumber k has the dimensions of the inverse of a length, whereas the angular frequency has the dimension of the inverse of a time. A is the amplitude of the wave (an ideal observation instrument able to perceive the instantaneous value of the wave would record a maximum modulus of the field equal to A), and ϕ is the initial phase, that is, a quantity that can be extracted from the value of the field at the time zero and at the abscissa zero.

Equation 9.1 can be obviously rewritten as

$$SW(x,t) = A\cos\left(k\left(x - \frac{\omega}{k}t\right) + \varphi\right) = A\cos(k(x - ct) + \varphi) \tag{9.2}$$

and the quantity $c = \frac{\omega}{k}$ [m/s] has the physical dimensions of a velocity. Indeed, it is easily recognized that Eq. 9.2 represents the graph of a sinusoid that shifts along the positive verse of the x-axis with velocity c. Therefore, c is called the propagation velocity of the waves. Moreover, Eq. 9.2 represents the graph of a sinusoid along the spatial x-axis for any fixed time instant t, and at the same time represents the graph of a sinusoid along the time axis t for any fixed abscissa x. Because the shift of the function is "rigid," which characterizes the concept of "wave," the sinusoidal wave is characterized by a unique spatial period, for any time instant, and is characterized by a unique temporal period at any spatial abscissa. The temporal period is customarily just called "the period" and is usually indicated with T[s]. Instead, the spatial period is called wavelength and is usually indicated with λ[m]. The reader has probably heard the concept of period and even more that of wavelength. What is important to outline at this moment is that, rigorously, period and wavelength are definitions that apply in rigorous terms only to periodic (in particular sinusoidal, but not only) waves (afterward, there

are extensions of these concepts, which are described in the next section). In fact, the period is the interval after which a function repeats equal to itself, that is, the interval after which that function assumes the same values, and so by definition the period and the wavelength make rigorous sense only for periodic waves. Beyond the period, it is often of interest considering the inverse of the period, which is called frequency. In particular, for a periodic wave we have a temporal frequency $f = \frac{1}{T}\,[1/s] = [\text{Hz}]$ and a spatial frequency $f_s = \frac{1}{\lambda}\,[1/\text{m}]$. Conventionally, when using the word "frequency" we mean the temporal frequency. So, the frequency indicates the number of times at which the periodic wave assumes its maximum (or minimum) value in the interval of 1 s at any fixed observation point, whereas the spatial frequency indicates the number of points at which the periodic wave assumes its maximum (or minimum) value in the interval of 1 m at any fixed time instant. Finally, as the wave is characterized by a rigid shifting of the function (which physically means a rigid shift of the electric and magnetic fields radiated by the antenna), there must be a relationship between the period and the wavelength. After some easy mathematics, it can be shown that this relationship is expressed by

$$c = \frac{\lambda}{T} = \lambda f \ [\text{m/s}] \tag{9.3}$$

Now, the propagation velocity c is a characteristic of the propagation medium: in air it is about 3×10^8 m/s, in freshwater it is about 3.3×10^7 m/s, and the values for several kinds of propagation media are tabled by, for example, Daniels (2004) and Jol (2009). So, passing from one medium to another, the waves change their propagation velocity (further than other properties, as the direction along which they propagate). So, it is licit to ask whether, passing through the interface between two different media, a periodic wave changes its wavelength, its frequency, or both. The answer to this question resides in Maxwell's equations, and the conclusion is that the frequency does not change, whereas the wavelength changes in agreement with Eq. 9.3; that is, a condition to be respected in both media. In particular, in the literature on GPR prospecting, we can find terms such as "wavelength in air" (or "external wavelength") and "wavelength in the soil" (or "internal wavelength"), but not "external frequency" or "internal frequency."

Before closing this section, it is worth specifying something more about the propagation velocity. In particular, the reader might meet in the literature a parameter of the soil called dielectric permittivity and (even if more rarely) also another parameter of the soil called magnetic permeability. These are two quantities related to the electric and magnetic forces that act on any free charge, and the propagation velocity in the medium at hand is related to them. We avoid formal definitions of the dielectric permittivity and of the magnetic permeability, referring the interested reader to general results of electromagnetism, and in particular to the expressions of Coulomb's law and of the force of Lorentz (Franceschetti 1997). Physically, the dielectric permittivity is related to the electric attraction (or repulsion) force that acts on a still point-like charge in presence of an electric field in the position occupied by the given charge. Also, the electric force is inversely proportional to the dielectric

permittivity, in the sense that the larger is the dielectric permittivity, the weaker is the force that a still charge "feels" at the parity of the electrical field in that point. With regard to magnetic permeability, given a point-like charge in a given point and moving at a fixed velocity, this charge 'feels' a further force with respect to that perceived by a still charge in the same point. This further force is directly proportional to the magnetic permeability of the medium in that point, in the sense that the larger is the magnetic permeability, the stronger is the force perceived by the moving charge at the parity of the magnetic field in that point.

With regard to the free space, the values of the dielectric permittivity and the magnetic permeability have been evaluated once and for all. In particular, they are equal to $\varepsilon_o = 8.854 \times 10^{-12}$ Farad/m and $\mu_o = 1.25710^{-6}$ Henry/m. It can be shown that the product of one Farad times one Henry is equal to the square of 1 s, and in particular the propagation velocity in free space is equal to

$$c_o = \frac{1}{\sqrt{\varepsilon_o \mu_o}} \cong 2.997 \times 10^8 \quad [\text{m/s}] \tag{9.4}$$

This value is often approximated with 3×10^8 m/s, which was the value previously provided.

Now, in a propagation medium different from the free space, it is praxis to describe the dielectric permittivity and the magnetic permeability as the product of the values in free space times a dimensionless constant. Namely, for a generic medium, we can write[1]:

$$\begin{cases} \varepsilon = \varepsilon_o \varepsilon_r \\ \mu = \mu_o \mu_r \end{cases} \tag{9.5}$$

where ε [Farad/m] and μ [Henry/m] are the absolute dielectric permittivity and magnetic permeability of the propagation medium at hand, respectively, whereas ε_r and μ_r are two dimensionless quantities called the relative dielectric permittivity and the relative magnetic permeability of the medium at hand. The relative dielectric permittivity and the relative magnetic permeability of the free space are by definition unitary, and indeed no other medium different from the free space (i.e., the vacuum) is known whose relative dielectric permittivity and magnetic permeability are both equal to 1. However, in general the values of ε_r and μ_r in air are quite close to 1. Consequently, in GPR applications, the air and the free space are substantially identified with each other at all times. The reader is warned about the fact that this "confusion" is licit with regard to (and only with regard to) the considered application. In particular, we have specified "in GPR applications." In other applications, as in the meteorological previsions, it is not licit at all to confound the air with the free space.

[1] Indeed, not all the media can be described in a so simple fashion, but we can accept this model for many soils of interest.

That said, the propagation medium of the electromagnetic waves in the medium at hand is given by

$$c = \frac{1}{\sqrt{\varepsilon\mu}} = \frac{1}{\sqrt{\varepsilon_o\varepsilon_r\mu_o\mu_r}} = \frac{1}{\sqrt{\varepsilon_o\mu_o}\sqrt{\varepsilon_r\mu_r}} = \frac{c_o}{\sqrt{\varepsilon_r\mu_r}} \tag{9.6}$$

Indeed, most media do not present appreciable magnetic properties in the frequency range of the GPR prospecting, so that in most cases we can approximate $\mu_r \approx 1$. In these cases, we have, of course:

$$c \approx \frac{c_o}{\sqrt{\varepsilon_r}} \tag{9.7}$$

In the following we also take for granted this assumption and will take for granted the validity of Eq. 9.7. However, the reader should be aware of a few aspects. First of all, the assumption that the medium has no magnetic property is valid in most cases but exceptions exist. In particular, when some minerals such as magnetite, but also hematite or maghemite, are present, the soil might show magnetic properties, as well as in some cases when strongly polluting substances are present (Nabighian 1987). Also, the martial soil is suspected to have (at least in some areas) magnetic properties (Stillman and Olhoeft 2004). Moreover, the dielectric permittivity and the magnetic permeability (either absolute or relative) might be expressed by matrixes instead of scalar quantities. In these cases, the medium is said to be anisotropic, and the propagation velocity of the waves in general depends on their direction of propagation. Still, the dielectric permittivity and the magnetic permeability of a medium in general change from point to point, and can change also versus time (e.g., after rain, they are probably different than their values in the previous "dry" soil). We can usually neglect the variation versus time during the time of the measure, but in general not the changes that occur over seasonal periods, and in general we cannot ignore the changes of the electromagnetic parameters of the medium versus the position. In other words, we can often assume the medium to be homogeneous versus the time but not versus the spatial point. Notwithstanding, in many GPR applications people measure and make use of some medium value of the propagation velocity. The reason is twofold; namely, it is because this allows us to achieve satisfying results and because a punctual characterization of the propagation velocity is not an easy task. If a more refined analysis is required, we can try to achieve and exploit a more refined characterization of the medium. In particular, a so-called analysis of velocity (Sheriff 1980) can provide in some cases the propagation velocity (and consequently the dielectric permittivity in a nonmagnetic medium) versus the buried point. Last but not least, the reader might be familiar with other noninvasive techniques, and in particular with magnetometry. Consequently, one might wonder why we are stating that most soils do not show magnetic properties if there are instruments that identify the buried targets exactly on the basis of their magnetic properties. The point is that all the characteristics of the soil depend in general also on the frequency of the solicitation that probes

it. Indeed, a magnetometer works in general with at a few kHz at most, whereas a GPR works around a central frequency of 20 MHz at least (and often quite higher). Therefore, the magnetic properties possibly present at lower frequencies in most cases vanish in the GPR range of frequencies.

That said, Eq. 9.7 puts in relationship the propagation velocity in the medium at hand with that in free space. It is immediate, replacing Eq. 9.7 into Eq. 9.3, that we have also a relationship between the wavelength in free space λ_o and that in the medium of interest λ. This relationship is

$$\lambda \approx \frac{\lambda_o}{\sqrt{\varepsilon_r}} \tag{9.8}$$

It is worth reminding a nontechnical reader that, according to the theory of relativity published by Albert Einstein in 1916, there is in the world nothing faster than the electromagnetic waves in free space. Consequently, the reader should be aware that, if for any reason he/she measures a propagation velocity larger than c_o some error must have occurred, at least to the current state of art. As a consequence, the relative permittivity of any medium different from the free space should be never smaller than one, and still the wavelength in the medium of interest in general is smaller than the wavelength in free space at the same frequency.

9.3 General Waves: Central Frequency, Band, and Central Wavelength

In general, an electromagnetic wave is not a sinusoidal wave, but it is a quantity variable along the propagation direction and versus the time according to a law of the following kind:

$$W(x,t) = g(x - ct) \tag{9.9}$$

where g is the function that characterizes, at the same time, the shape of the wave along x at any time instant and the behavior of the quantity versus the time in any fixed position x. The reader can easily recognize that Eq. 9.9 represents the graph of a function rigidly shifting with velocity c along the x-axis. So, the general wave shares with a sinusoidal wave the characteristic of translating at constant velocity. However, its shape can be quite general, and in general it is not only not sinusoidal, but it is not periodic either. In the case of GPR prospecting, the wave is in most cases pulse shaped, and of course it physically represents the electric field radiated by the transmitting antenna in the medium at hand.

That said, what sense does it make to speak of frequency or wavelength for a general electromagnetic wave?

To fully answer this question, some nonelementary mathematics would be needed, based on the Fourier analysis. Here, we propose a simplified reasoning, as follows. Indeed, it is possible to show that any generic wave is "composed" by sinusoidal waves, in the sense that it can be expressed as a suitable sum of sinusoidal waves. In conditions of ideal propagation, the sinusoidal components (at different frequencies) propagate with the same velocity, so that the wave given by their superposition translates rigidly (i.e., by definition, propagates) with the same velocity. So, in a sense, the sinusoidal waves are the "bricks" with which we can express any kind of wave. However, these bricks are not all of the same relevance and, in most cases, there is an interval of frequencies where the sinusoidal components have an amplitude quite larger than the amplitude of the sinusoidal components at a frequency outside this interval. The interval of frequencies where the sinusoidal components of the wave at hand are relevant is called "the frequency band" of the signal, and the central point of this interval is called "the central frequency." The reader is thus invited to devote attention to the difference: the frequency band is an interval of frequencies and the central frequency is a single point of this interval. There is sometimes a term that identifies the frequency band (also just called "the band") with a single number. For example, we might state that a given antenna has a band of 400 MHz. Indeed, this identifies only the width of the frequency band, but the information is not complete. Indeed, that antenna might have a frequency band ranging from 100 to 500 MHz, or perhaps a frequency band ranging from 250 to 650 MHz. Therefore, indeed one should either specify the extreme points of the band or the band width and the central frequency.

Another common term is to label the central frequency as just the frequency, but the (non)technical) reader could confuse these. When saying, for example, that a system is equipped with antennas at 600 MHz, we mean that that GPR system is equipped with antennas with a frequency band such as the central frequency is equal to 600 MHz. Rigorously, the behavior of the antennas also depends on the conditions of the soil at hand, or more in general on the conditions of the propagation medium at hand. Therefore, the central frequency of a given pair of antennas changes from case history to case history, and what we know a priori is a nominal value of the central frequency, referred to a prefixed situation. In general, these changes are secondary and the nominal central frequency can be accepted as a good approximation of the actual (i.e., current) central frequency. At any rate, if for a particularly refined application a more correct value of the central frequency is needed or at least is "well advised," this can be retrieved from the data. That said, the central wavelength is defined as the wavelength corresponding to the central frequency. Of course, the central wavelength has to be referred to a propagation medium, and so in general we distinguish an internal central wavelength (in the soil) from an external central wavelength (in air). Without further specifications, the wavelength relative to a GPR signal is customarily meant as the central wavelength (i.e., the wavelength relative to the central frequency) in the soil.

9.4 Resolution and Data Rate

The frequency band of the signal is an important parameter, because it is related to the quantity of information available from the data. In particular, if the band is larger, the data contain more information and this reverses on a better available resolution.

The resolution is defined as the minimum distance at which we can distinguish two small buried targets from each other in the final image. In general, the resolution is different also in dependence of the reciprocal positions of the considered small targets, and in particular it is customary to distinguish a horizontal resolution from a vertical one. The horizontal resolution is meant as the minimum distance at which we can distinguish two small targets put side by side at the same depth along the direction of the B-scan, whereas the vertical resolution is defined as the minimum distance at which we can distinguish two small targets piled on each other under the same point of the surface. The reader should be aware that a "small target" is meant as a target whose extent is small with respect to the internal central wavelength, and should also be aware that the resolution is implicitly defined on processed data. Sometimes there are attempts to measure the resolution on the basis of the raw (not processed) data. This is incorrect, because one of the steps of the processing is in most cases the migration of the data, which tends to focus the apparent sources of reflection toward their actual size (within certain limits, of course). So, the resolution available from processed data is in general better than that available from raw data.

A necessary "drawback" of having a large band is the need of a narrower data rate, both in time and in space. In other words, the spatial step along any observation line, the needed interline space, and also the needed time step for the data gathered in each observation point, depend both on the band and on the central frequency. In particular, coherently with the fact that a larger band is an index of data containing "more information," we need to make narrower the data rate just to really gather the information contained in the data.

As said, the resolution capabilities (and consequently the needed data rate) of the system are related, among other things, to the frequency band. However, customarily in GPR systems ultra-wideband antennas (UWB) are exploited, which means that the central frequency and the band are quantities of the same order of size. So, in the formulas provided in the following for resolution and data rate, the band can be roughly replaced by the central frequency, that in its turn can be expressed in terms of the central internal wavelength and propagation velocity of the electromagnetic waves in the medium at hand (see Eqs. 9.3 and 9.7).

So, there are also well-known formulas that derive the resolution in terms of wavelength. This drives to simple and "smart" formulas, because both the resolution and the wavelength have the physical dimension of a length. In Table 9.1, values for the available resolution and the needed data rate are reported, where B is the frequency band, λ_c is the central internal wavelength, and $c = \frac{c_0}{\sqrt{\varepsilon_r}}$ is the propagation velocity of the electromagnetic wave in the medium at hand (presumed to be nonmagnetic).

Table 9.1 Sampling and resolution in ground-penetrating radar (GPR) prospecting

Available horizontal resolution	$\frac{\lambda_c}{2}$
Available vertical resolution	$\frac{c}{B}$
Needed spatial sampling rate along the B-scan	$\frac{\lambda_c}{4}$
Needed interline spacing (transect)	$\frac{\lambda_c}{4}$
Needed time spacing	$\frac{1}{2B}$

For a fuller understanding of Table 9.1, let us remember that, as already said, in most GPR systems the frequency band is of the same order as the central frequency. Coherently, from Table 9.1 we can appreciate the fact that the resolution improves when the wavelength is smaller, that is, at high frequency. Actually, it might be shown that, at parity of wideness of the band, antennas with a higher central frequency provide more information than antennas with a lower central frequency. At any rate, being the extent of the band and the central frequency of the same order, indeed antennas at higher frequencies have in general also a larger band with respect to antennas at lower frequency and so even more they are able to provide more details about the buried scenario.

Incidentally, the provided time step and spatial steps have been calculated according to general well-known "rules" for the sampling, established by Harry Theodor Nyquist (1889–1976). Therefore, they are also often labeled as "Nyquist (sampling) rates."

The reader should be aware of a few considerations about Table 9.1, in particular:

1. The table expresses a complex physical problem in a synthesized and necessarily simplified way. The underlying calculations contain assumptions and approximations (Persico 2014). Consequently, the results are to be meant as an order of size and not as exact values. In particular, in the literature one might find also different values, but of the same order (Daniels 2004; Persico 2014; Jol 2009).
2. The values provided in Table 9.1 have to be meant for shallow targets. Indeed, for deeper targets there is a progressive degradation of the resolution, expressed in more detail elsewhere (Persico 2014; Sheriff 1980). As a theoretical consequence, if one were interested exclusively in deep targets, one might relax the spatial rate and also the time rate. However, in general this does not correspond to the real situations.
3. It is worth outlining that in general we do not know the propagation velocity in the soil, but retrieve it from the data (as will be shown). Therefore, it is advised to gather data with a little redundancy, thus making the data rate even slightly narrow than the nominal (alleged) values of the parameters suggested in Table 9.1.
4. The fact that antennas at higher frequency allow achieving more information with respect to those at lower frequency does not mean that the low-frequency antennas are useless because, as is well known, low-frequency antennas are likely to

achieve a better penetration, that is, they can provide an image for deeper targets. There is no contradiction in these two statements, because the information should not be meant as a merely quantitative entity, but the information of interest in the problem at hand is something specific and consequently, let us say, qualitative. In particular, exactly as in daily life, in GPR prospecting we are usually interested in some specific kind of information, and not in any kind of "news," even if we should be (and usually are) attentive also to the main novelties "unlooked for" that we might meet.

Some considerations apart seem to us well advised with regard to the experimental difficulties, if any, met while adopting the suggested data rates. Indeed, from a practical point of view, a spatial rate of one quarter of the wavelength is in many cases a quantity of the order of a few centimeters (from 2 to 20 depending on the exploited antennas and on the soil at hand), and it is not troublesome to have such a sampling along the B-scan, that is, along each measurement line. Similarly, to have a time rate along each trace of the order suggested in Table 9.1 is in general nothing critical. It is instead practically troublesome to have an interline step of the order of just a few centimeters, at least with a classical GPR system equipped with a unique couple of antennas. In particular, this might lead to meaningful amounts of time needed for the measurement campaign, and consequently to meaningful, if not prohibitive, costs of the work. Fortunately, in many cases the targets looked for are quite larger than one quarter of wavelength, and so a larger interline step (customarily of the order of 50 cm) can be usefully exploited, in many cases, even if this means, rigorously, to undersample the data.

Nowadays, GPR systems equipped with an array of antennas allow a meaningful reduction of the interline step, being the distance between adjacent lines automatically of the order of 25 cm or less. In general, this is not yet as narrow as one quarter of the wavelength but approaches this limit.

9.5 Pulsed and Stepped Frequency Systems

In the past sections we have stated that a GPR signal can be decomposed as the sum of suitable sinusoidal components. This condition implicitly states the equivalence between a GPR signal, essentially meant as an electromagnetic pulse transmitted (and propagating) in the soil, and the set of its sinusoidal (also said harmonic) components, which is more rigorously called its spectrum. Further than mathematical, this equivalence can be also translated into technological aspects. In fact, it is possible, instead of radiating and receiving an electromagnetic pulse, to radiate and receive sequentially its harmonic components. A system working in this modality is called a stepped frequency system, whereas a GPR working in the classical modality is called a pulsed system. The idea underlying a stepped frequency system is that of transmitting and receiving one after the other the bricks that compose a pulsed GPR signal, whereas a pulsed GPR transmits and receives them together. Clearly, a stepped frequency requires that eventually it is possible,

from the received "bricks," to compose again the signal that we would have received if we had exploited a pulsed system. Done by means of Fourier transforms, this is a standard and straightforward operation. The question about what solution is "better" between the pulsed and the stepped frequency technologies has not been definitively answered yet, and perhaps a response in an absolute sense does not exist, it depending also on the situation at hand, and in particular on the required range of frequencies for the application at hand (Sato and Takahashi 2009; Pieraccini et al. 2006). Stepped frequency systems have been stated to be theoretically better performing (Noon 1996), but this should be discussed with experimental updated compared results. On the other hand, historically, stepped frequency systems were more heavy, but also this aspect should be rediscussed in the framework of the latest technological state of art. Another recent development has been the reconfigurability of the GPR systems (Persico and Prisco 2008), which contains several aspects more easily implementable with the stepped frequency technology, but at least partially exportable also to pulsed systems. So, the debate is still open.

Comprehensively, most of the commercial systems are pulsed, even if there are also commercial stepped frequency systems. As a matter of fact, a pulsed GPR is in most cases less expensive than a stepped frequency instrument. However, this might be a consequence of the current diffusion rather than of a different technological difficulty for the construction of the instrument. When exploiting a stepped frequency system, a new kind of sampling problem appears. In fact, the time sampling in this case does not make sense, because we are radiating frequencies, that is, harmonic components. Indeed, we are sampling the spectrum of the signal rather than the signal itself, and therefore in this case we have the problem of establishing a frequency step rather than a time step. The needed frequency step can be established on the basis of some mathematical considerations that we will avoid here, providing directly the result. Incidentally, however, similarly to the time step and the spatial steps given in Table 9.1, the provided frequency step for stepped frequency systems is also based on the sampling rules identified by Nyquist, and therefore it is a Nyquist rate too.

That said, if we label as $T_{\max}$ the maximum time after which we can receive a perceivable signal, then the needed frequency step is

$$\Delta f = \frac{1}{T_{\max}} \tag{9.10}$$

Now, the maximum depth reached by the signal within the time interval $T_{\max}$ is given by $D_{\max} = \frac{cT_{\max}}{2} = \frac{c_o T_{\max}}{2\sqrt{\varepsilon_r}}$, where c is the propagation of the electromagnetic waves in the medium at hand. The factor 2 derives from the round trip, namely, the fact that in the time $T_{\max}$ the signal reaches the depth $D_{\max}$ and "goes back," so traveling a comprehensive distance $2D_{\max}$. Substituting Eq. 9.10 into Eqs. 9.7–9.8, we retrieve

$$\Delta f = \frac{c}{2D_{\max}} = \frac{c_o}{2\sqrt{\varepsilon_r} D_{\max}} \tag{9.11}$$

There is sometimes a misunderstanding about Eq. 9.11, because $D_{\max}$ (also called nonambiguous depth) is in many cases implicitly identified with the maximum depth of interest, that is, the maximum depth at which we presume there are targets of interest. Indeed, $D_{\max}$ is the maximum depth from which the instrument is able to perceive some signal, independently from the fact we seek targets in that entire depth range or in a smaller sub-range. This limitation has strong practical consequences because if we look for targets expected to be buried in the first 50 cm (e.g., unexploded mines), for example, and the propagation velocity of the waves in the soil has been measured to be equal to 15 cm/ns (or, equivalently, the relative permittivity of the soil has been measured to be equal to 4), we might erroneously think that we need a frequency step equal to $\Delta f = \frac{30 \text{ cm/ns}}{2\times 50 \text{ cm}\times\sqrt{4}} = 150$ MHz. Indeed, the signal is likely to propagate beyond 50 cm, and perceivable signals might arrive also (in optimistic cases) from the depth of 5 m, which narrows the required frequency step to $\Delta f = \frac{30 \text{ cm/ns}}{2\times 500 \text{ cm}\times\sqrt{4}} = 15$ MHz. It is also to be said, however, that stepped frequency systems usually do not allow a free choice of the frequency step, but leaves at most some options, and the possible choices rarely overcome the upper limit $\Delta f = 5$ MHz. So, the risk of undersampling the stepped frequency signal in frequency domain is, as a matter of fact, quite remote.

With regard to the needed spatial steps, instead, the parameters given in Table 9.1 hold both for a pulsed and a stepped frequency system, as well as the values provided for the available resolution.

9.6 Common Midpoint

Propagation of the electromagnetic waves in the soil occurs at a velocity different (and in particular lower, as said) than in free space. One important point is the fact that such a propagation velocity is not known a priori in general. Depending on the kind of soil, there are tables of probable values that can help (in most cases the tables are referred to the dielectric permittivity rather than directly to the propagation velocity; Daniels 2004; Jol 2009). However, these table values are just indicative. Indeed, the water content and the chemical and physical properties are strongly dependent on the material at hand (e.g., the dissolved salts, if any, or the porosity, or also possibly the temperature) and make it well advised to measure this propagation velocity in the field. In particular, this parameter is essential both to have a correct time depth conversion of the data and to focus the data in a proper way by migration algorithms (Persico 2014; Stolt 1978; Schneider 1978), as described in the next sections. There are several techniques for the measure of the propagation velocity. We focus here on the common midpoint (CMP) technique (Daniels 2004; Persico 2014; Jol 2009), which is, to our knowledge, the most precise noninvasive available technique. To describe the classical CMP technique, let us suppose that we have a target at some depth d and let us place the transmitting and receiving antennas of the GPR in two symmetrical positions with respect to this target. Then, let us vary

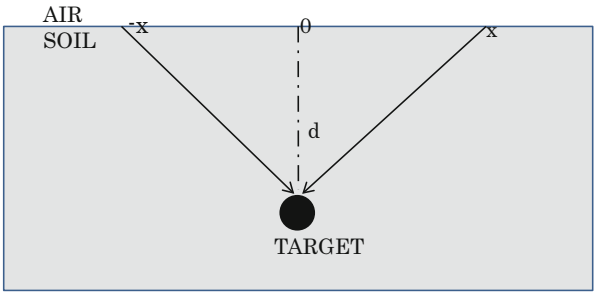

Fig. 9.1 Basic scheme for a common midpoint (CMP) measure

the positions of the two antennas, but keeping the condition that the target is placed under the central point between them. Let us choose a reference system where the target is at the abscissa zero. In this way, the transmitting antenna will be placed at several abscissas x, and the receiving antennas will be placed correspondingly in the point $-x$. According to the scheme in Fig. 9.1, the time after which the signal radiated by the transmitting antenna reaches the buried reflector and then the receiving antenna is given by the following:

$$t = \frac{2}{c}\sqrt{x^2 + d^2} \tag{9.12}$$

Indeed, Eq. 9.12 is not sufficient to retrieve the propagation velocity because the depth of the target is not known a priori in general. However, if the two antennas are placed just over the target at the zero abscissa, we record the minimum return time, necessarily equal to

$$t_o = \frac{2d}{c} \tag{9.13}$$

Solving d versus t_o we have that Eq. 9.12 can be rewritten as

$$t = \frac{2}{c}\sqrt{x^2 + \left(\frac{ct_o}{2}\right)^2} \Rightarrow \frac{t^2}{t_o^2} - \frac{x^2}{0.25c^2t_o^2} = 1 \tag{9.14}$$

Equation 9.14 is the equation of a hyperbola in the plane (x, t). However, the graph that we "see" is only one half of one branch of the hyperbola. In fact, only positive times makes sense, and only positive values of x. In particular, to consider a negative x amounts to exchanging the positions of the transmitting and receiving antennas, which provides the same signal. Equation 9.14 is parametric in c, so that we can look for the propagation velocity matching the diffraction hyperbola visible in the data with the model of Eq. 9.13 at variance of a trial propagation velocity.

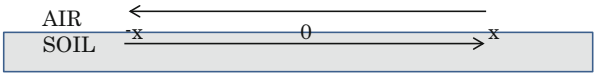

Fig. 9.2 Common midpoint (CMP) based on the direct coupling of the antennas

An advantage of the CMP is that the size of the buried target is not important (in contrast to other techniques, as the diffraction hyperbolas in common offset, for example) (Mertens et al. 2015). In particular, the target can be also just the interface between two consecutive layers of soil, and the reasoning is the same. Another thing worth outlining is that, on condition that the soil is homogeneous (at least from the surface up to the buried target), it is unimportant that the positions of the transmitting and of the receiving antenna move along a straight line passing over the target: the only important thing is that the projection of the target on the surface is kept in the middle between the two antennas.

Last but not least, we have to outline that the common midpoint technique can work even in absence of a centered buried target. In fact, the mere direct signal from the transmitting to the receiving antenna is equivalent to two equivalent small targets centered between the two antennas (see Fig. 9.2), one of which placed immediately over the surface and another one immediately under the surface.

It is immediately recognized that the coupling underground is equivalent to a target at zero time depth. Now, for $t_o \to 0$, accounting for the fact that we consider only positive values of x, Eq. 9.12 degenerates into

$$t = \frac{2}{c}x \tag{9.15}$$

Equation 9.15 is the equation of a straight line with slope $\frac{2}{c} = \frac{2\sqrt{\varepsilon_r}}{c_o}$, which provides immediately the propagation velocity in the soil. The coupling in air, instead, is equivalent to a "soil composed of air" so that it provides a signal of the kind

$$t = \frac{2}{c_o}x \tag{9.16}$$

In Fig. 9.3, a simulation of CMP data is shown, performed with the code GPRmax2D. In the simulation, a soil with relative permittivity equal to 3 and a conductivity equal to 0.001 S/m has been chosen. Source and receiver simulate antennas at 500 MHz and move with a step of 2.5 cm from the starting point. At the starting point, source and observation point are 5 cm distant from each other. The two straight lines are evident, and the same happens with real data, as is widely known.

Where c_o is, as said, the propagation velocity in free space. In particular, the "upper" features that characterize any CMP signal are two oblique lines, one of which with slant $\frac{2}{c_o}$ and another one with slant $\frac{2\sqrt{\varepsilon_r}}{c_o}$. The reader is warned fact that, in

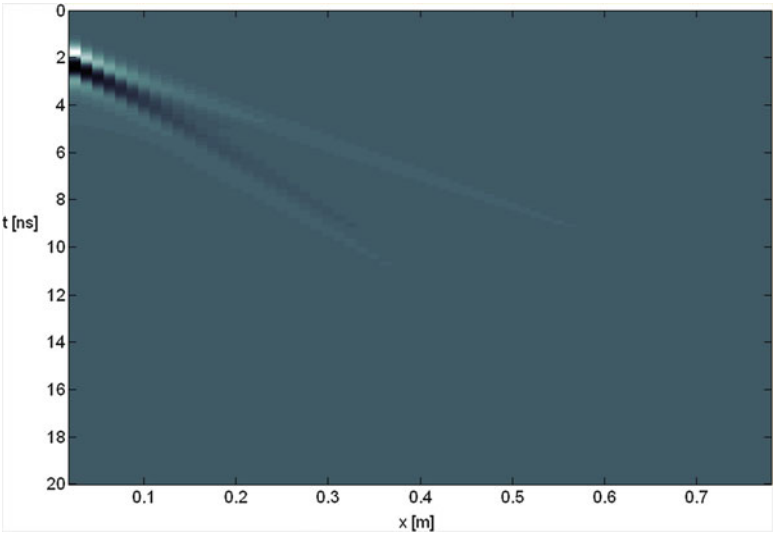

Fig. 9.3 Simulation of CMP data

the common representations of the CMP signal, the line relative to the propagation of the signal in the soil (with slant $\frac{2\sqrt{\varepsilon_r}}{c_o}$) appears to be lower than that relative to the propagation in air (with slant $\frac{2}{c_o}$) because the time axis is conventionally directed downward, so that the proportional depth levels are represented as positive quantities.

A drawback of the "classical" CMP technique is that it requires two separable antennas (which are not available in a classical GPR system), and it is a slow procedure because it requires the punctual displacement of the two antennas in all the positions scheduled for the measure. However, a system equipped with an array of antennas can overcome this drawback, because if there is a center of symmetry common to several pairs of transmitting-receiving antennas, then that point can be exploited as a common midpoint, and the data needed for this CMP measure are just a subset of the GPR gathered within the performed survey. So, in this case the CMP measure can be performed in real time and without needing further equipment other than the GPR itself.

9.7 Method of GPR Data Acquisition

9.7.1 Antenna Scanning

Conventionally, GPR data acquisition is usually conducted as follows. A one-dimensional (1D) survey (data acquisition) is carried out by moving a GPR system

along a straight line. The data acquisition density is determined by the spacing of data acquisition points along the survey line, and the data can be observed as a B-scan image. A 2D survey is carried out by acquiring the data on a two-dimensional grid, which gives a three-dimensional GPR image. To acquire the data in 2D form, normally we set multiple parallel survey lines and acquire several sets of 1D data to create 2D data sets. If we need high-density data sets, the interval of the survey line spacing must be small. The data can be observed as a B-scan, but it can be used to create C-scan images as well.

9.7.2 Advanced GPR Navigation

9.7.2.1 GNSS

Sometimes the ground surface topography is quite rough and placing measuring tapes can prove to be difficult. Most current commercial GPR systems are able to record position data from a global navigation satellite system (GNSS) such as a GPS signal, enabling the user to acquire GPR data along with geographic position. This survey is easy, but we need additional methods to guide the GPR antenna along the desired survey locations. It should also be noted that the positioning accuracy of GPS is normally limited to a few meters. If we use RTK-GPS, the positioning accuracy can be drastically improved, down to a few centimeters. In addition, GNSS navigation is possible only when the survey area is open and wide, so that GNSS signals from spacecraft can be received reliably.

9.7.2.2 Total Station

When surveys are carried out in woods or inside or near buildings, GNS navigation cannot be used. Another approach in such a case is to use a total station.

A total station or TST (total station theodolite) is an electronic/optical instrument used in land surveying. A TST system measures the distance and angle of the location of a reflector from the location of the TST equipment. Robotic total stations can track the position of the reflector automatically. If we set the reflector on the top of a GPR antenna, the TST automatically measures the position of the antenna. TST combined with GPR is quite flexible in operation and can be used even for indoor surveys.

9.7.2.3 Data Acquisition Density

In practice, there is not much problem in acquiring very high density data sets along a survey line, because most commercial GPR systems can acquire data at a few

hundred cycles, and even if the GPR moves at 1 m/s, the data density can reach one measurement per centimeter; the latter interval is much shorter than a one-tenth wavelength at 500 MHz. Even if the data acquisition rate is increased, the survey time along the same length of a survey line does not change. In contrast, if we decrease the spacing between the survey lines, we can decrease the data acquisition density across the survey lines, but this will increase the data acquisition time for a given area under the survey because it simply increases the number of survey lines. Data acquisition time is a very important factor in field surveys, and unfortunately, minimizing acquisition time conflicts with a correct sampling of the data (indeed, especially the horizontal achievable resolution can be degraded by undersampling).

9.8 GPR Image Reconstruction

Raw GPR signals can be displayed as a B-scan or a C-scan; however, the raw GPR signals do not reproduce the actual shape of subsurface objects. "Migration" is the signal processing step that retrieves the shape of the subsurface objects from the raw GPR signals. The migration algorithm is mathematically very similar to that employed in synthetic aperture radar (SAR) processing, which is widely used in space-borne and airborne microwave remote sensing. Note that the situation is more difficult for GPR processing than for typical SAR observations, because one must image the near field, and through a very inhomogeneous medium.

Most SAR image reconstruction schemes use a Fourier transformation-based imaging approach. The radiation pattern of an array antenna is well understood, and a wider array size and denser array spacing give a narrower beam width, leading to a better azimuth resolution (the azimuth resolution can be roughly compared to the horizontal resolution, but rigorously it is not the same) (Franceschetti and Lanari 1999) in real aperture radar imaging. In SAR, this is equivalently given by a simple image reconstruction algorithm:

$$u(x,y) = \int d\left(x', t = \frac{2R(x'-x,y)}{c}\right) dx' \tag{9.17}$$

where

$$R = \sqrt{(x-x')^2 + y^2} \tag{9.18}$$

is the distance from the antenna position to the imaging point $u(x,y)$and $d(x',t)$is the acquired datum at the time t in the position $x = x'$. Moreover, $c$is the wave velocity in the medium (indeed, in SAR imaging the propagation of the signal occurs essentially in air and possibly also in the upper layers of the atmosphere or beyond,

so that the medium might be considered as free space, but Eq. 9.17 contains already the extension to the case of the GPR prospecting, where the propagation medium is essentially the soil). Equation 9.17 shows that the image is reconstructed by a phase compensation caused by the propagation delay R/c equated to the measured data.

If the scanning length is unlimited, such as with space-borne SAR, the Fourier-based image reconstruction algorithm gives the azimuth resolution $D/2$, where D is the size of the real aperture (i.e., the size of the antenna exploited for the SAR imaging) used in the SAR system, and this resolution is independent of the distance from the sensor to the objects. This condition will be satisfied if the data sampling spacing respects the Nyquist rate.

9.9 Advanced GPR Survey

9.9.1 Advanced GPR Navigation

Although migration and SAR processing are very useful for high-resolution image reconstruction in GPR, there are limitations to these technique, because differences exist between space-borne SAR and GPR. The strong attenuation of electromagnetic waves in the soil normally limits the distance observable with a synthetic aperture. Therefore, we also have investigated another approach, namely "3DGPR," which is a virtual realization of high-accuracy position control of the GPR system developed by Grasmueck (Grasmueck and Viggiano 2007). Instead of moving the GPR system along a straight survey line very accurately, we move the system roughly along survey lines, but the spacing of the survey lines is much smaller than in a normal survey. In addition, the positioning of the GPR system is measured by the GPS system very accurately. After being acquired on the "rough" 2D survey grid, the data were rearranged on the "accurate" 2D grid by 3D interpolation, as shown in Fig. 9.4. By this signal processing scheme, we can obtain very accurate 2D gridded GPR data sets. Regularly sampled data are easy to process by using the FFT algorithm.

To achieve high position accuracy for GPR measurements, we use a commercial laser positioning system (Nicon iGPS). We set at least two transmitters, each of which transmits position data by modulated laser signals. A receiver set on the GPR system receives and decodes the laser signals. More than two signals are used to calculate the receiver's position, which can be estimated to millimeter accuracy. The GPR system used in the 3DGPR does not require any special capabilities; a commercial GPR system (RAMAC GPR) was used in this study. The position information acquired by iGPS and the GPR data acquired by the RAMAC GPR must be synchronized, which is accomplished through small modifications of the hardware.

Tohoku University and University of Miami are collaboratively working on the application of 3DGPR (Mahmoud et al. 2009). This 3DGPR measurement has

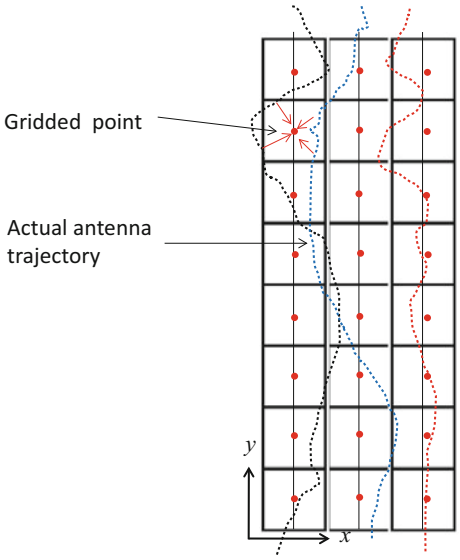

Fig. 9.4 The actual GPR antenna trajectory and the position of gridded data interpolated from the acquired GPR data sets

Fig. 9.5 3DGPR survey by 250-MHz GPR antenna (Saitobaru burial mounds, Miyazaki, Japan)

been applied to disaster mitigation, archaeological survey, and facility detection. Figure 9.5 shows a measurement from one of the archaeological surveys, conducted at Saitobaru, Miyazaki, Japan. There is a subsurface grave at this site. Figure 9.6 shows the 3D image that was obtained after migration. We could image the shape of the grave very clearly, and could find some buried objects, which would be made of

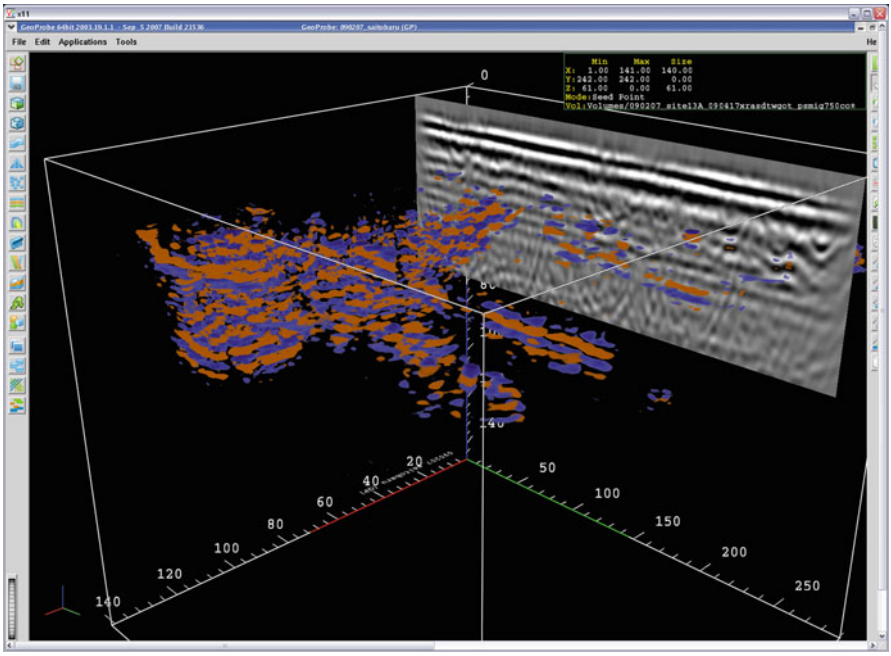

Fig. 9.6 3DGPR imaging at Saitobaru Archaeological Site, Miyazaki, Japan

metal. Although the site was detected by conventional GPR survey, such a detailed image could not have been obtained by conventional GPR survey.

9.10 Array GPR System

9.10.1 GPR for Massive and Fast Inspection

As an alternative approach for acquiring massive and highly dense data sets, GPR systems equipped with many array antenna elements are becoming more popular. One of the most important applications of this type of GPR system is road inspection. To maintain road pavement, a GPR system can be mounted on a vehicle and used for real-time road inspection. To acquire the data at normal highway speeds, the data acquisition rate must be quite high, but in many cases, the required range is relatively shallow. For this purpose, a very densly aligned transmitter and receiver antenna array can image many parallel B-scan images along the road and can be used for high-resolution imaging. In this case, the spacing of adjacent survey lines is fixed by the antenna spacing, and therefore a clear C-scan image can be produced.

9.10.2 The New "Yakumo" System: System Confuguration

Conventional GPR uses an antenna system that is composed of one transmitter and one receiver. The data acquisition by one pair of antennas is not slow, but the spacing of antenna survey lines is irregular when two-dimensional surveys are carried out. Therefore, advanced SAR processing or signal processing techniques such as 3DGPR must be employed. However, if we use a combination of antennas, namely, array antennas, we can solve this problem. Based on this idea, Tohoku University is now developing an array GPR system dubbed "Yakumo," which means "eight rising clouds" in Japanese.

This system, being developed with Mitsui Engineering & Shipbuilding Co. Ltd., is a stepped frequency continuous wave (SFCW) system, and by using a switching network, it will be possible to achieve fast data acquisition (Sato et al. 2013; Chen et al. 2013). We have designed a system having eight transmitting antennas and eight receiving antennas, and by switching we can acquire all 64 pairs of signals for each transmitter–receiver combination. The antenna element is a shielded bow-tie antenna, which can operate in a relatively low frequency range, namely, below 1 GHz.

Figure 9.7 shows the Yakumo array GPR system, and Fig. 9.8 shows the scheme of the array. The Yakumo is small and light enough to be scanned manually or can be pulled by a small vehicle. This small size and portability are important, because survey areas in Japan are generally not very large and have irregular terrain. The

Fig. 9.7 The array GPR system "Yakumo," developed by Tohoku University, is equipped with eight transmitting and eight receiving antennas (Nobiru Site, Japan)

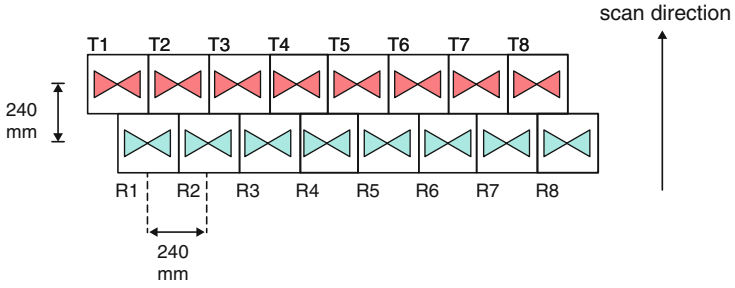

Fig. 9.8 Antenna configuration. Eight transmitting and receiving antennas are aligned. We use bow-tie antennas

antennas, transmitter, and receiver are connected through switching circuits and coaxial cables. Therefore, delays caused by the feeding circuit must be calibrated. Calibration was carried out in the laboratory, and then the system was tested in the field.

We can check the raw data but can use them for sophisticated migration for image reconstruction. Selection of frequency is one of the most important issues in a GPR survey. We think that frequencies around 500 MHz are most useful at many of the Japanese archaeological sites of interest. However, a wider operational frequency range is in general better for a system. We have decided to use 50 MHz to 1.5 GHz, which should provide a good balance of high resolution and deep penetration.

9.10.3 SAR Signal Processing

In the array GPR system, the antenna spacing in the cross-track direction is very accurately maintained, because antennas are fixed to each other, and we acquire GPR data every 1 cm along the track direction, using distance measured by a surveyor's wheel. The maximum data acquisition velocity is 7 km/h when we acquire 64 channels every 1 cm along the track. The data sampling interval in both the cross-track and the along-track direction is accurate in this system. This data sampling gives us unique advantages in signal processing.

Synthetic aperture radar processing has been widely used in space-borne and airborne microwave remote sensing. When we use SAR processing in GPR data sets, we should notice that the situation is more difficult compared to conventional SAR, because we have to image the near field, and through a very inhomogeneous medium. Most SAR image reconstruction schemes use a Fourier transformation-based imaging approach. The radiation pattern of an array antenna is well understood, and we designed our system so that the wider array size and denser array spacing gives a narrower beam width, thus enabling better azimuth resolution in real aperture radar imaging.

Most SAR data processing is based on the assumption of a mono-static antenna arrangement, where the positions of the transmitting and receiving antenna are the same. Yakumo has used a multi-static antenna configuration, in which the positions of the transmitting and receiving antenna are separated. Using this multi-static antenna configuration, we can adopt unique signal processes as follows.

We use the data for SAR/migration processing. For multi-static SAR processing, we employ

$$u(x,y) = \sum_i \int d_i \left(x', t = \frac{2R(x'-x,y)}{c} \right) dx' \tag{9.19}$$

where $d_i(x', t)$ denotes the time-domain signal of the ith pair of transmitter and receiver antennas. Multi-static radar can acquire radar data from wider incident angles, and it can improve the quality of the reconstructed images.

9.10.4 Velocity Analysis Using CMP Signal Processing

One unique feature of the Yakumo signal processing is its capability of application to CMP processing (Dix 1955), which can also provide a vertical velocity profile estimation in GPR. The velocity estimation is quite important in migration/SAR processing and accurate depth estimation of targets.

When we use Yakumo, CMP data acquisition can be done only by selecting transmitter and receiver pairs that satisfy the CMP conditions. If we select an antenna pair so that the path connecting the two antennas crosses the same CMP point as shown in Fig. 9.9, we can use the data sets for CMP processing, and we can move the CMP points by selecting the antenna pairs as shown in Fig. 9.9a, b. Although the CMP configuration is not exactly symmetrical, the practical effect is not significant.

We carried out a fundamental laboratory test for validation of CMP using Yakumo. Yakumo was set on a sandpit where the sand layer was 0.83 m thick and the bottom of the sand layer was a concrete floor. Figure 9.10a shows one example of a CMP data set acquired by CMP antenna pairs, and Fig. 9.10b shows the velocity spectrum estimated from the data shown in Fig. 9.10a. We estimated the velocity of the wave to be 0.15 m/ns and the layer depth to be 0.829 m, which is almost the same as the actual sand layer thickness.

An important advantage of using Yakumo for CMP data processing is that we can acquire the data at the same time as the normal GPR data acquisition, and we do not have to repeat the measurement for CMP data acquisition. Using this technique, we can estimate the vertical profile of the dielectric constant, which can be used for SAR processing.

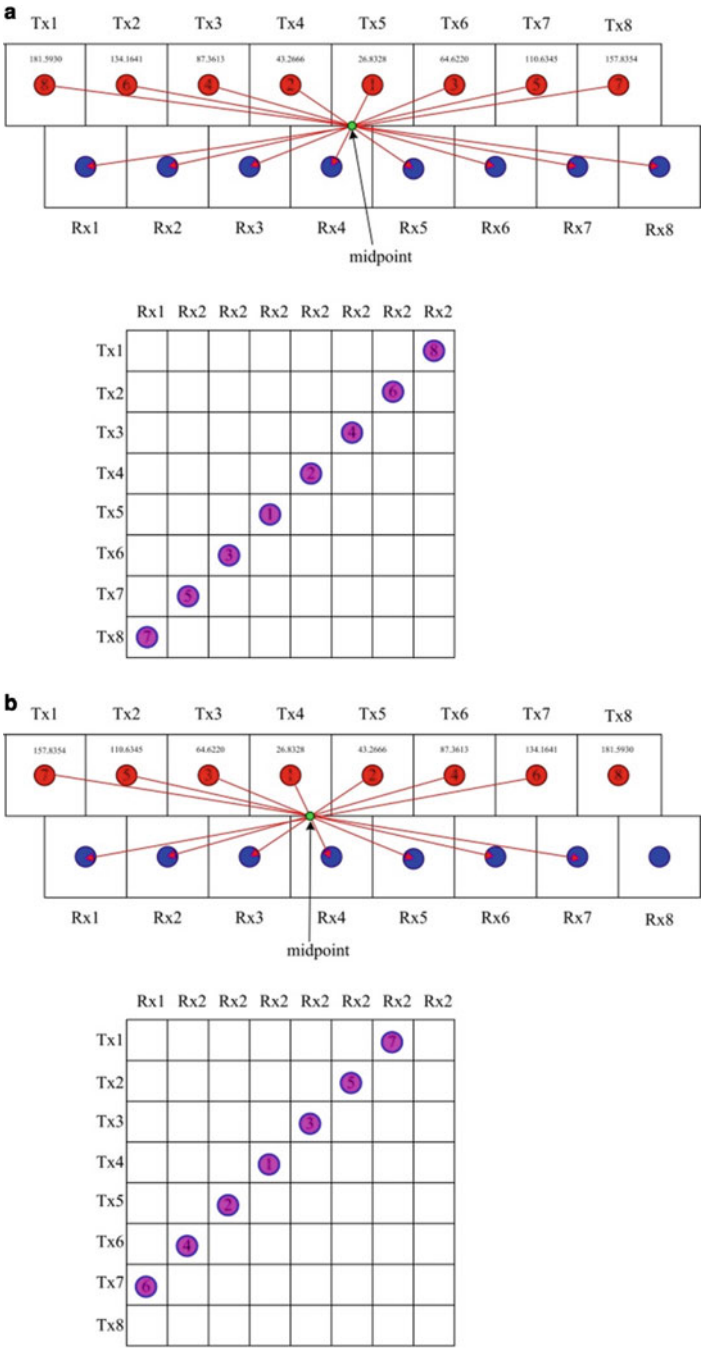

Fig. 9.9 Antenna pairs that satisfy the CMP condition: configuration #1 (**a**); configuration #2 (**b**)

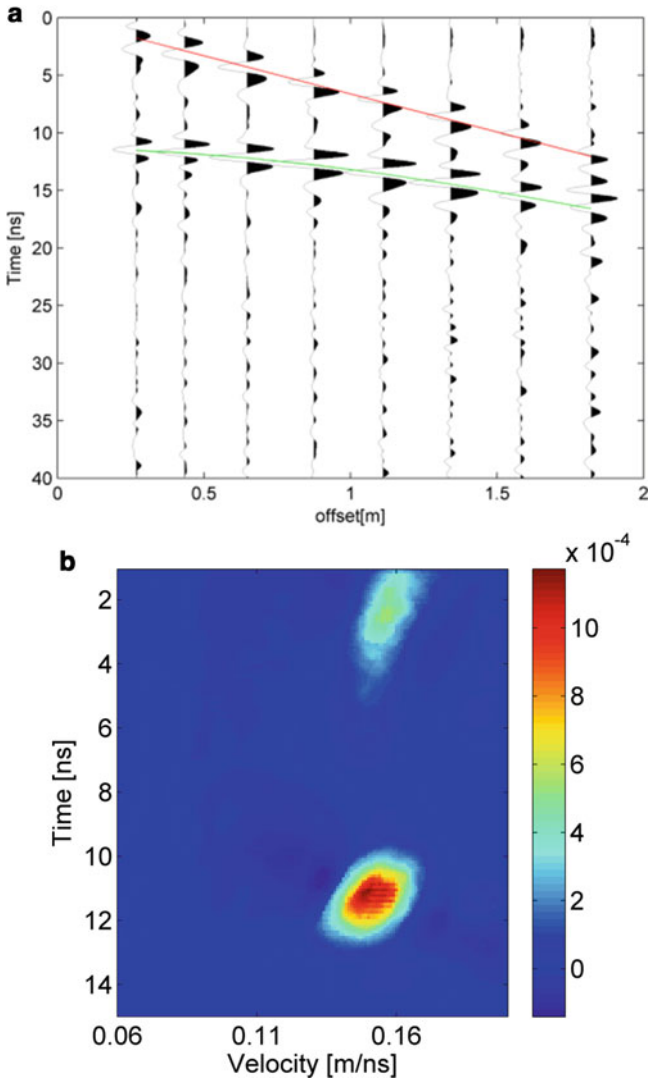

Fig. 9.10 CMP signal processing using Yakumo data. (**a**) Raw data acquired by Yakumo. (**b**) Velocity spectrum

9.11 Summary

In this chapter we have introduced some of the latest advances achieved in the framework of GPR prospecting, where particular systems equipped with arrays of antennas (instead of a single pair of transmitting-receiving antennas) have been introduced, and precise positioning systems have allowed to improve meaningfully the geo-referencing of the data.

It seems to us well advised to warn the reader that the positioning is an essential issue, also because it is rarely possible (or scheduled) to perform an immediate excavation in the points where the GPR prospecting revealed the most promising anomalies. Indeed, this excavation could be done at another time, after months or even years, and a bad positioning of the anomalies might lead to expensive excavation without any useful result. And this is just in the case of a "rigid" error, wherein the entire GPR image is shifted or rotated without deformations in the horizontal plane of the planking level. Even worse, of course, is the case where the relative positions of the B-scans with respect to each other are not well geometrically related: this leads to distortion of the image, possibly erasing some of the true buried anomalies and creating ghost targets that do not exist in the real ground truth.

Another aspect stressed has been the data rate, and in particular the possibility, introduced some years ago, to "almost" approach the Nyquist sampling rate with respect to the interline spacing between two adjacent B-scans. This possibility is offered by systems equipped with an array of antennas, and we have shown in particular the array system "Yakumo," developed by Tohoku University, that allows an interline spacing of 24 cm. As said, this is not the Nyquist rate that, depending on the kind of soil, is a quantity expected to be between 3 and 10 cm (because the band of the Yakumo array ranges from 50 to 1500 MHz). However, the distance 24 cm is about one half of the most refined (and reasonably possible on large areas) praxis, which outdoors is of the order of 50 cm as stated. At any rate, if for some particularly refined application a narrower interline is required, it is possibly to make, for example, two subsequent "slitherings" laterally, shifting the array of one half of the lateral distance between its antennas (this means 12 cm in the case of the Yakumo array), thus decreasing times a factor two the interline space, and doing it in a quite efficient way with respect to a classical GPR system equipped with a single pair of antennas.

Beyond these hardware aspects, it is to be said that, recently, a radar image reconstruction method using an optimization algorithm, "compressive sensing (CS)," has been investigated. We think CS can solve some of the problems mentioned here, at least partially, in a "software" way, that is, by means of a more refined post-processing. It is known that the approach including CS is "super resolution," which means that the data acquired at a rate larger than the Nyquist criterion can be used for image reconstruction. It may reduce the time for data acquisition, and we can obtain more accurate subsurface images.

Last but not least, we have considered the aspect of the measure of the characteristics of the soil (in particular the propagation velocity of the electromagnetic waves in the soil) from the GPR data. In particular, we have shown the possibility (not to be meant as theoretical, but rather already implemented and available) to perform CMP measurements, extracting the data required for it from the same GPR data. This method allows us to perform CMP measures in real time, which was not possible before the introduction of GPR systems equipped with an array of antennas. In particular, a system equipped with a single pair of antennas allows a real-time evaluation of the propagation velocity only based on the shape of the diffraction

hyperbolas gathered in common offset configuration. This is a method to be used with some care, because it is meaningfully related to the hypothesis of a small target, that is, the hypothesis that the considered diffraction hyperbolas are generated by a target with a size small with respect to the central internal wavelength. This hypothesis cannot be known a priori, and so in the end one has to postulate (on a heuristic basis) that the diffraction hyperbolas chosen for the evaluation of the propagation velocity have been generated by small targets. To provide an example with realistically possible values, let us consider, for example, a GPR signal at 500 MHz radiated in a soil with relative permittivity equal to 9. In this case, the internal wavelength is equal to 20 cm (see Eqs. 9.3 and 9.7), and so a target with a cross section of 20 cm cannot be considered "small." Previous simulation work has shown us that it is reasonable to consider as small a target extended up to one fourth of the internal wavelength, that is, 5 cm in the brought example. The CMP method overcomes this limit.

References

Chen J, Liu H, Takahashi K, Sato M (2013) Development of array GPR for archaeological survey and disaster mitigation. In: Proceedings of the near surface geophysics Asia Pacific conference, Beijing, July 2013

Daniels DJ (2004) Ground penetrating radar, 2nd. IEE Press, London

Dix CH (1955) Seismic velocities from surface measurements. Geophysics 20:68–86

Franceschetti G (1997) Electromagnetics: theory, techniques, and engineering paradigms. Plenum Press, New York/London

Franceschetti G, Lanari R (1999) Synthetic aperture radar processing, CRC Press, Boca Raton

Grasmueck M, Viggiano D (2007) Integration of ground-penetrating radar and laser position sensors for real-time 3D data fusion. IEEE Trans Geosci Remote Sens 45(1):130–137

Jol H (2009) Ground penetrating radar: theory and applications, Elsevier, Burlington

Mahmoud G, Grasumeck M, Sato M (2009) Non-destructive 3D ground penetrating radar for imaging tree root architecture. Tech Rep IEICE SANE 109(219):67–72

Mertens L, Persico R, Matera L, Lambot S (2015) Smart automated detection of reflection hyperbolas in complex GPR images, accepted for publication on IEEE Transaction on geosciences and Remote Sensing

Nabighian M (1987) Electromagnetic methods in applied geophysics-theory, vol 1. Society of Exploration Geophysics, Tulsa

Noon DA (1996) Stepped-frequency radar design and signal processing enhances ground penetrating radar performance, Ph.D. thesis, Department of Electrical & Computer Engineering, University of Queensland, Australia

Persico R (2014) Introduction to ground penetrating radar: inverse scattering and data processing. Wiley, Hoboken. ISBN 9781118305003

Persico R, Prisco G (2008) A reconfigurative approach for SF-GPR prospecting. IEEE Trans Antenn Prop 56(8):2673–2680

Pieraccini M, Noferini L, Mecatti D, Atzeni C, Persico R, Soldovieri F (2006) Advanced Processing Techniques for Step-frequency Continuous-Wave Penetrating Radar: the Case Study of "Palazzo Vecchio" Walls (Firenze, Italy). Res Nondestruct Eval 17:71–83

Sato M,Takahashi K (2009) Development of dual sensors and deployment in mine affected countries. In: Anti-personnel landmine detection for humanitarian demining, Spinkerlink ed

Sato M, Doi K, Takahashi K (2013) Advanced GPR for archaeological survey. In: Proceedings of the IGARSS2013, Melbourne, July 2013
Schneider WA (1978) Integral formulation for migration in two and three dimensions. Geophysics 43(1):49–76
Sheriff RE (1980) Nomogram for Fresnel-zone calculation. Geophysics 45(5):968–972
Stillman DE, Olhoeft GR (2004) GPR and magnetic minerals at mars temperatures. In: Proceedings of the tenth international conference on ground penetrating radar, pp 735–738
Stolt RH (1978) Migration by Fourier transform. Geophysics 43(1):23–48

Chapter 10
Geomagnetometry for Archaeology

M. Fedi, F. Cella, G. Florio, M. La Manna, and V. Paoletti

Abstract In past decades, magnetic surveying had become popular as one of the most effective techniques supporting archaeological prospecting. This is possible because the existence of susceptibility contrasts between the cover soil and several buried finds often causes detectable anomalies. More recently, great advances were made in signal enhancement and boundary analysis of potential field anomalies, thanks to methods allowing a suitable differentiation of the field without making the process unstable. New three-dimensional (3D) imaging techniques provided an estimate of the magnetization distribution within the subsoil by means of high-resolution images of the source distribution. Most of these methods are fast and reliable in the presence of shallow and compact sources, just as in the case of the sources usually occurring in archaeological prospecting. Nevertheless, great effort was spent by the scientific community to overcome serious problems causing low signal-to-noise ratio in the measurements. This chapter provides a step-by-step description of technical solutions adopted to improve the quality of data and to perform a better interpretation of the magnetic anomalies usually associated to the presence of archaeological finds. To this end, a summary of case histories is illustrated giving a general framework of the latest progress in archaeo-magnetism.

10.1 Introduction

Besides geological applications, geophysical methods are shown to be able to measure not only the physical properties of soil and rocks, but also the anthropically induced effects. The magnetic method is probably the most widely used and

M. Fedi (✉) • G. Florio • V. Paoletti
Dipartimento di Scienze della Terra, dell'Ambiente e delle Risorse, Università di Napoli Federico II, Largo san Marcellino 10, 80138, Naples, Italy
e-mail: fedi@unina.it

F. Cella
Dipartimento di Biologia, Ecologia e Scienze della Terra, Università della Calabria, 87036, Rende, CS, Italy

M. La Manna
INNOVA SCARL, Via Campi Flegrei 34, 80078, Pozzuoli, NA, Italy

N. Masini, F. Soldovieri (eds.), *Sensing the Past*, Geotechnologies and the Environment 16, DOI 10.1007/978-3-319-50518-3_10

effective geophysical technique to investigate archaeological sites. Its application to buried anthropic structures is also recognized as the first application of a geophysical method to be well documented in the scientific literature (Clark 1990). We refer to the field measurements made by Martin Aitken, in 1958, who used for the first time a proton magnetometer to detect archaeological remains at Water Newton (Aitken 1958). Since then, the number of archaeological applications of the magnetic method is quite high (Gibson 1986; Sternberg 1987; Jeng et al. 2003; Larson et al. 2003; Gaffney 2008). Aitken demonstrated that the well-burnt Romano-British kilns could be detected because the magnetic response of materials burned, at temperatures high enough to alter their magnetic properties, is not negligible. In fact, a contrast in magnetic remanence can occur when baked clay artifacts have acquired a thermoremanent magnetization after being heated to several hundred degrees Celsius (Sternberg 1987). During heating at high temperatures, small regions of magnetic materials (the magnetic domains) reorient themselves and, upon cooling, tend to align themselves more or less in the direction of the present Earth's magnetic field and thus parallel to each other; this creates a net magnetization that may give the artefact a strong thermoremanent magnetization (Smekalova et al. 1996). Furthermore, in most cases strong anomalies are associated with burned features as a result of the conversion of iron oxides to a more magnetic state (Weymouth 1986).

Magnetometric methods have been successfully employed for mapping not only well-burnt kilns and hearths, but also anomalies from very common archaeological targets, such as ditches and pits. The contrast in magnetic susceptibility between topsoil, subsoil, and rocks, with the topsoil normally more magnetic than subsoil, allows in fact locating ditches, pits, and other silted-up features, which were excavated in ancient times and then silted or backfilled with topsoil. The response to foundations and floors is influenced by the magnetic contrast between the construction materials and the surrounding soils. Many kinds of masonry, for example, limestone walls in topsoil, produce a negative susceptibility contrast (Smekalova et al. 1996). Even earthen features such as storage pits with humic content can produce observable anomalies because of the conversion of iron oxides to a more magnetic state taking place in an organic environment. Finally, concentrations of ferrous metal usually cause intense and detectable anomalies (Weymouth 1986).

Magnetic surveying is not limited to land surveys; it may be also applied to the marine environment. Meaningful examples of integrated geophysical surveys of wrecked ships are given, for example, in Arnold (1996), Quinn et al. (1997), and Quinn et al. (2002). The authors aimed to characterize the site and delineate the extent and geometry of the wrecks of the ships La Belle, Mary Rose, and La Surveillante, respectively. Although this application of magnetometry to marine archaeology is quite common, magnetic studies of submerged ancient harbors or towns are few. A meaningful example of this kind of application is given in Boyce et al. (2004), who performed a marine magnetic survey at Caesarea Maritima, Israel, to locate and map the buried structures of a Roman harbor from the time of King Herod. One more application is that of the submerged Roman ruins of the Bay of Baia, one of the most extensive submerged archaeological

sites known in Italy. The comparison of the magnetic anomaly field and its total gradient (often referred to as the amplitude of analytical signal) with the known submerged archaeological structures of the area gave some interesting insights into the lithological characteristics of the archaeological structures of the Baiae site and showed the effectiveness of the magnetic method for mapping remnants of building structures beneath the seabed (Paoletti et al. 2005). This case is more thoroughly described in the third section of this chapter.

As a matter of fact, underground archaeological remains can be successfully detected by magnetometric surveys on the basis of several factors:

(a) The magnetic susceptibility contrast between the buried archaeological features and the surrounding environment
(b) The remanent magnetization effects induced by old human activity
(c) Using an appropriate density of measurements and an adequate size of the area, with respect the expected size of the archaeological features
(d) Their depth with respect to the survey measurement level
(e) A high signal-to-noise ratio where the signal is that from the targeted anomaly
(f) A good choice of the most appropriate instrumentation
(g) Appropriate data processing, especially in case of weak effects of buried structures or of anthropic soil alterations

The range of magnetic anomalies generated by buried archaeological features is wide (Piro et al. 2007): remains (graves, dwelling walls, floorings) typically exhibit local magnetic anomalies in the range 1–20 nT; for 'fired' structures (hearths, kilns, crockery, pottery) anomalies can range between 10 and 1000 nT; magnetic anomalies of ferrous objects (weapons, tools, slag) range between 20 and 2000 nT.

With regard to the effective detectability of the magnetic effects, we note that the smaller items are generally harder to detect, except for the metal ones and large agglomeration of shards at a shallow depth from ceramic objects. The same may be said for waste products, such as fuel ash and associated burnt soil, used to fire a kiln; this is caused by the formation of enhanced magnetic particles of superparamagnetic grain size from magnetic alteration of fine-grained, weakly magnetic clay minerals in the soil. For similar reasons, we may also find tracks of human activity from land clearance through repetitive use of domestic fires or concentrated organic matter from the preferential colonization by bacteria (Fassbinder and Stanjek 1993) through a process called fermentation. By simple magnetic models, we may argue that a slight change in the natural magneto-stratigraphy among the organic rich surface layers and subsoil, as a result of construction of banks and ditch cut features, is able to produce detectable magnetic anomalies (Linford 2006).

Finally other, probably minor, effects may be noticed (Asandulesei 2011): the first is the creation of intracellular magnetite of a crystalline structure by magneto-tactical bacteria, used for navigation by reference to the Earth's magnetic field and remaining in the soil after the bacteria die; the other is pedogenesis, because the magnetic susceptibility is likely to increase during the genesis of the soil, without any human contribution, by means of ultrafine granular magnetite natural production

in sterile soil. Examples of pedogenesis effects are a ditch filled with plant material, much richer in iron oxides than the soil in which it was dug, or a pit filled with household refuse or construction debris.

On the other hand, it is worthwhile to note (item a) that the remains from buildings or similar structures can be instead more easily detected, either because of the net susceptibility contrast between the building materials and the soil (or the seawater) and even because their regular shapes makes easier them to be detected. This detection is the object of the case histories presented in the third section of the chapter.

Regarding the signal-to-noise ratio (item e) we note that it may be low when the sought target is at a large depth, or because of the scattering of metallic fragments on the soil, to agricultural works, to the occurrence of modern buildings from the immediate vicinity, to the perturbations caused by the activity of various wild animals in the soil, and especially because of the presence of metallic and electric fences and power lines. Moreover, archaeological deposits may have a dense stratigraphy, caused by intense and continuous inhabitation in different ages, thus complicating the process of identifying and accurately interpreting the measurements (Maher and Taylor 1988).

We turn now to the item related to the choice of the most appropriate instrumentation (item f). As noted by Gaffney (2008) the situation is much changed since the first experiment by Atkins. Now the choice is among these:

- Measuring vector, vertical, or total field
- Using a single or a multisensor to measure the magnetic or its tensor gradient field
- Using a handheld or a nonmagnetic cart, this last human- or vehicle powered

Nonetheless, one may also choose among many types of sensors: from the classical precession proton, Overhauser effect, and fluxgate magnetometers, to the highly sensitive optically pumped alkali vapor-magnetometer systems or to the SQUID (superconducting quantum interference device)-based systems. The different magnetometers are ranked in order of sensitivity, the main question being not which sensor is the ‘best’ but which is most appropriate.

We refer to Gaffney (2008) for a deeper discussion about this important topic and we here limit our discussion on the choice about multisensors (gradiometers) or single sensors (magnetometers). The most conventional gradient instrument measures the gradient component of the magnetic total field, which is the component of the anomalous field in the direction of the main geomagnetic field (Blakely 1995). However, in archaeo-geophysics also vector instruments are sometimes used, generally measuring the vertical component of the field. When the instruments are arranged in a gradiometric configuration, a pair of magnetic sensors is deployed at a fixed distance from each other and the field is measured at both sensors at the same time. This method allows the numerical computation of magnetic gradients as the difference between the two measurements divided by the distance between the sensors. In the most common configuration the two sensors are placed at different altitudes along a vertical rod, and the vertical gradient of the field is thus estimated.

In other cases, often when multisensor configurations are used, horizontal gradients can be measured as well. The magnetic field gradients will be correctly estimated when the distance between the sensors is 'small' with respect to the source depth. Typical distances between the sensors vary in the range 0.25–1 m. In some cases, however, to maximize the gradiometer 'sensitivity', greater distances between the sensors can be deliberately chosen.

In general, the gradiometer surveys are preferred to the simpler measurement of the only magnetic field for the following reasons:

I. The estimated gradients are insensitive to the temporal variations of the magnetic fields, because the two measurements are acquired at the same time. So, the fixed magnetic reference station is avoided.
II. The gradient field has increased sensitivity to shallow sources, as archaeological structures are, because the magnetic gradients decay is faster than the magnetic field decay. For instance, the magnetic decay of the field from a dipole is $1/r^3$, whereas that of its gradient is $1/r^4$, where r is the distance of the source from the sensor.
III. For the same reason, magnetic gradients are insensitive (or less sensitive than the magnetic field) to magnetic regional fields and also to magnetic fields generated by man-made structures in the proximity of the survey area (fences and other metallic structures).
IV. Again, thanks to the fast magnetic gradients spatial decay (see point II), the ability to separate signals coming from nearby sources ('resolution') is increased with respect to the magnetic field.

These advantages are partially counterweighed by the increase of high-wavenumber noise: it may be generated by small and shallow sources of natural as well as artificial origin, whose magnetic field is not adequately sampled.

Despite this drawback, magnetic gradients are now routinely used to investigate archaeological areas and there are many numerical techniques that can be used in the data processing phase to remove the noise.

We have now approached the discussion of the final item (g), that is, to the construction of an appropriate processing of the data collected in the field. Because of its relevance, the next section is devoted entirely to this issue.

10.2 Data Processing of Magnetic Data: A Quest for Signal Enhancement in Archeo-geophysics

In this section we analyze a number of numerical procedures that could be applied to measured magnetic data and, more specifically, to gradiometer data. We show that the procedures can be combined in a workflow transforming the raw magnetic gradient data into magnetic gradient anomalies, which can be finely interpreted from either a qualitative or quantitative point of view.

The need of establishing a data processing workflow is that both the magnetic field and its vertical gradient are not directly suitable for analysis and interpretation. As a matter of fact, the magnetic maps based on raw data are affected by errors from different causes. One more reason is that archaeo-magnetic signals are usually weak, so that they may need to be enhanced.

The errors must be necessarily removed (or minimized) by means of a pre-processing phase, consisting in a sequence of application of numerical techniques devoted to correct or filtering the raw data. Here we illustrate the complete pre-processing of a real magnetic gradient dataset in acquired in Northern Syria.

A first phase implies the removal of "spikes" ("despiking"). Spikes are extreme values of normal or reverse signs appearing in the gradient maps as single, localized points well distinguished by the surrounding values. Usually, they are the result of instrumental errors from temporary failure of one of the two sensors, or also to the presence of very shallow, small, ferrous objects. The presence of spikes expands the range of values and, consequently, compresses all the data in a narrow color range, with obvious degrading of the image (Fig. 10.1). Spikes can be removed (Fig. 10.2) by means of different methods such as median filters (Tabbagh 1999) and generalized extreme studentized deviation (GESD) (Rosner 1983; Iglewicz and Hoaglin 1993; Ciminale and Loddo 2001), although even a 'manual' removal of these outliers may be effective.

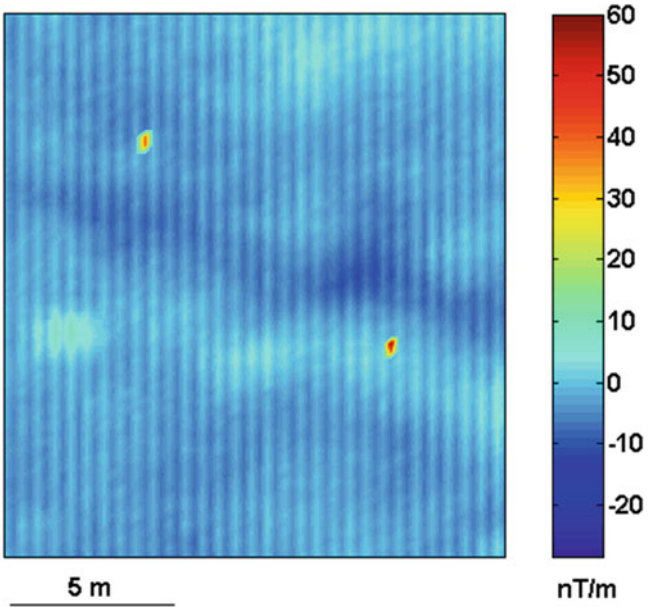

Fig. 10.1 Vertical gradient of the total magnetic field: raw data from a survey in Northern Syria

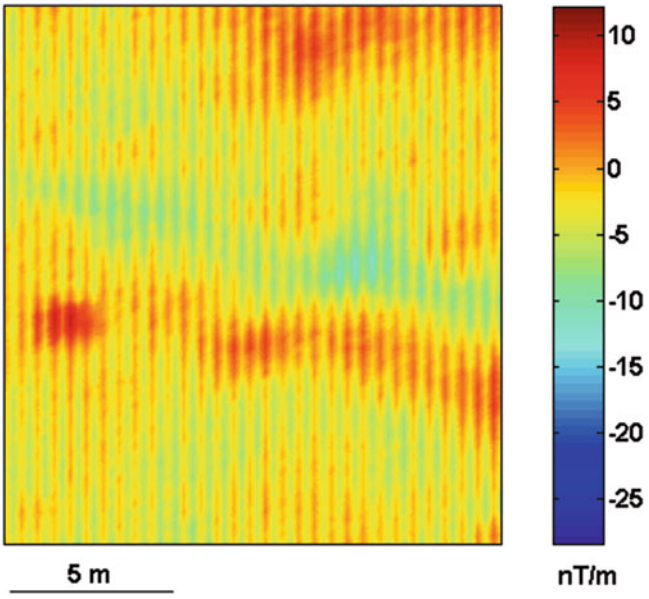

Fig. 10.2 Vertical gradient of the total field in Fig. 10.1, after removal of spikes

The field in Fig. 10.2 is still affected by a typical noise arising when magnetic measurements are acquired in the bi-directional mode. In this case, the different symmetry, along adjacent lines, of the instrument–operator system when traveling in opposite directions, generates maps showing a typical 'striping' ("heading error"; Scollar et al. 1990).

The effect caused by such an error can be removed (Fig. 10.3) by equalizing at the same mean value the data acquired along each line of the measured field (Ciminale and Loddo 2001). Obviously, this effect can also be eliminated by a one-way mode acquisition, in which the instrument–operator system is not rotated, but this good result is obtained at the price of a great slowdown of the survey operations.

Another error, typical of data acquired by the bi-directional mode, is generated by a systematic error in the positioning of the measurements. This error is caused by an offset between the operator, where the position is generally recorded, and the sensors, and results in a distortion of the anomalies ("zigzag effect" or "displacement error"). The map in Fig. 10.3 is affected by this problem.

This error may be corrected by an efficient statistical method based on the cross-correlation, suggested by Eder-Hinterleitner et al. (1996) and Ciminale and Loddo (2001). It was successfully applied producing the results shown in Fig. 10.4.

Even after the use of the aforedescribed techniques, it may happen that the some linear artifacts ('corrugations') still affect the vertical gradient map (Fig. 10.4). In this case, the solution is commonly found by application of directional filters, able

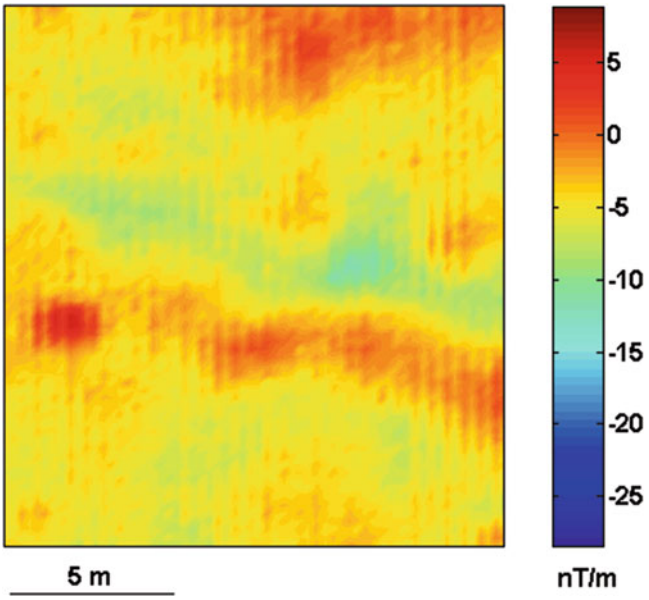

Fig. 10.3 Vertical gradient of the total field in Fig. 10.2, after removal of heading error

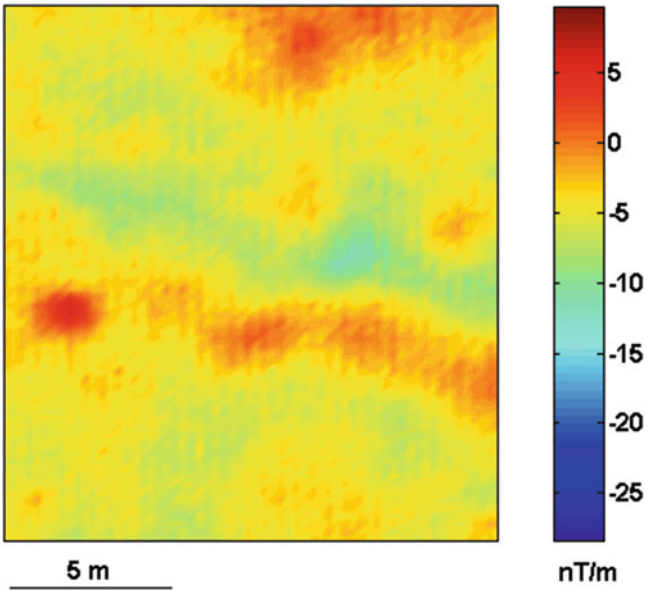

Fig. 10.4 Vertical gradient of the total field in Fig. 10.3, after removal of the zigzag effect

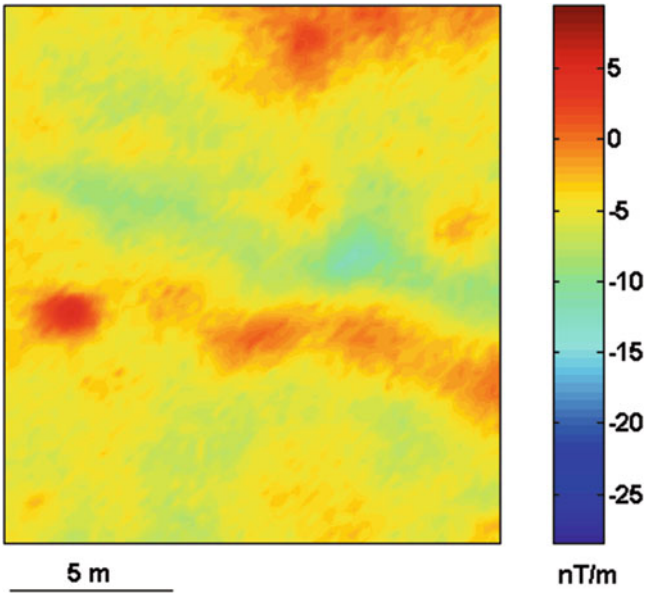

Fig. 10.5 Vertical gradient of the total field in Fig. 10.4, after directional filtering in the wavelet domain, through the application of the discrete wavelet transform (DWT)

to cancel or attenuate the signal along a specified direction. Such filters may be designed in the Fourier domain (such as the "directional cosine" filter) or, more efficiently, using the discrete wavelet transform (DWT; Fedi and Quarta 1998; Fedi and Florio 2003). In Fig. 10.5, to remove the striping still affecting the map in Fig. 10.4, the data were directionally filtered, using the DWT approach, to remove the anomalies elongated along the north–south direction.

After the previous filtering steps, the vertical gradient may be still disturbed by the presence of high wavenumber noise (Fig. 10.5). In this case, a light low-pass filtering may be necessary, and it can be performed again both in the Fourier and in the wavelet domains. It is important to highlight that a later quantitative interpretation of magnetic data may be strongly influenced by an improper filtering (Florio et al. 2014), so that this operation should be as light as possible. In any case, a careful check of the removed part of the signal should be done to ascertain that no significant portion of the signal has be removed. Thus the data were finally isotropically low-pass filtered using the DWT approach (Fig. 10.6). Now the anomalies are clearly defined, but an obstacle for a qualitative interpretation is their dipolar shape, preventing the unambiguous positioning of the magnetic sources.

Thus, when most of the mentioned noisy effects are removed from the field map, the reduction to the pole of the total field, or its vertical gradient, is commonly carried out as a final step.

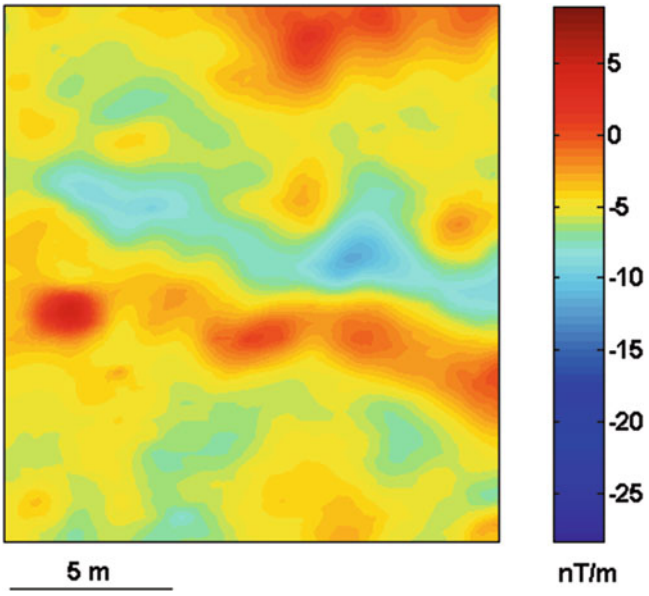

Fig. 10.6 Vertical gradient of the total field in Fig. 10.5 after isotropical removal of fine details, through the application of the discrete wavelet transform (DWT)

Owing to the dipolar nature of magnetism and the possibility that the magnetization of the source may be in any direction, magnetic responses are much more complex than gravity responses. The reduction to the pole is a transformation allowing the conversion of a total-field anomaly, generally dipolar, into that it would have been measured at the magnetic pole (Baranov 1975; Blakely 1995), which is instead monopolar, similar to the gravity anomalies. If the unknown direction of total magnetization vector is correctly assumed, the reduced-to-the-pole anomaly is shifted just above the causative source. Furthermore, the resolution of closely spaced sources is improved and thus the qualitative interpretation of the vertical gradient map results is much simplified after performing reduction to the pole (Figs. 10.6 and 10.7).

Other transformations of the field in a 'monopolar' shape are the total gradient (Roest et al. 1992) and the magnetic field modulus (Stavrev and Gerovska 2000). They have the advantage of not depending on the unknown magnetization direction, but have the drawback of the nonlinear combination of the transformed anomalies, potentially causing some ambiguous results.

At this point, the transformed field in Fig. 10.7 is ready to be analyzed for a preliminary interpretation phase. To this end, a large number of methods of signal enhancement and boundary analysis are significant in archaeo-geophysics. With 'boundary analysis' we indicate a group of algorithms designed to clearly locate the lateral changes of magnetization. Among these methods, Cordell and

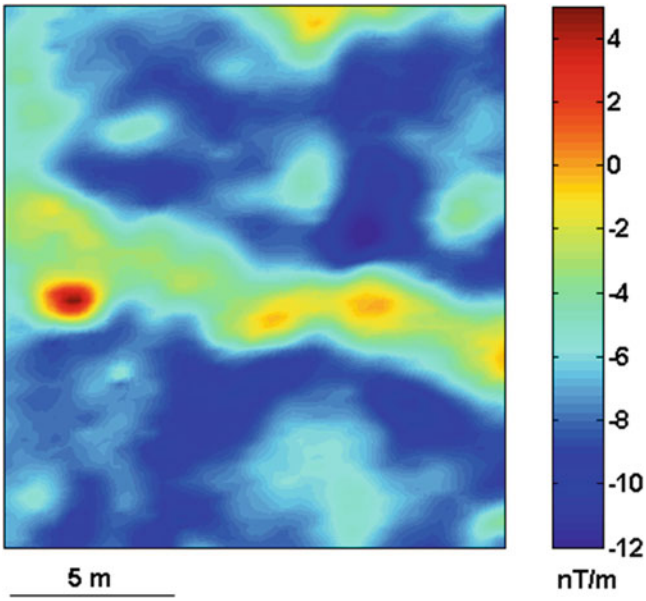

Fig. 10.7 Vertical gradient of the total field in Fig. 10.6, after reduction to the pole assuming that the sources have no remnant magnetization. The field now presents mainly maxima: the dipolar effects in Fig. 10.6 disappear almost completely in the reduced to the pole map. The declination of the geomagnetic field at this survey location is about 0° and the inclination is about 54°

Grauch (1985) and Blakely and Simpson (1986) showed how the maxima of the total horizontal derivative may help to identify the position of the source edges. Other authors (Nabighian 1984; Roest et al. 1992) demonstrated similar properties for the amplitude of the analytical signal. A generalization of the analytic signal method to higher-order derivatives (Hsu et al. 1998) was also proposed to this end. Other methods use the concept of normalized derivatives, such as total horizontal derivative of the tilt angle (Verduzco et al. 2004), hyperbolic tilt angle (Cooper and Cowan 2006), and theta map (Wijns et al. 2005). All these functions behave as an automatic gain control filter because they tend to equalize the amplitude of transformed total field magnetic anomalies. However, over areas where sources at different depths cause both large- and small-scale effects, results from these methods may be confusing because they produce a single map where source lineaments from sources at different depths are merged, potentially causing the occurrence of fictitious trends (Jeng et al. 2003; Stampolidis and Tsokas 2012; Cella et al. 2009).

In these cases, more refined techniques have to be employed to allow a selection of the lineaments because of sources at different depths. The multi-scale derivative analysis was explicitly proposed to this end (Fedi 2002). The analysis is based on the enhanced horizontal derivative (EHD; Fedi and Florio 2001), allowing

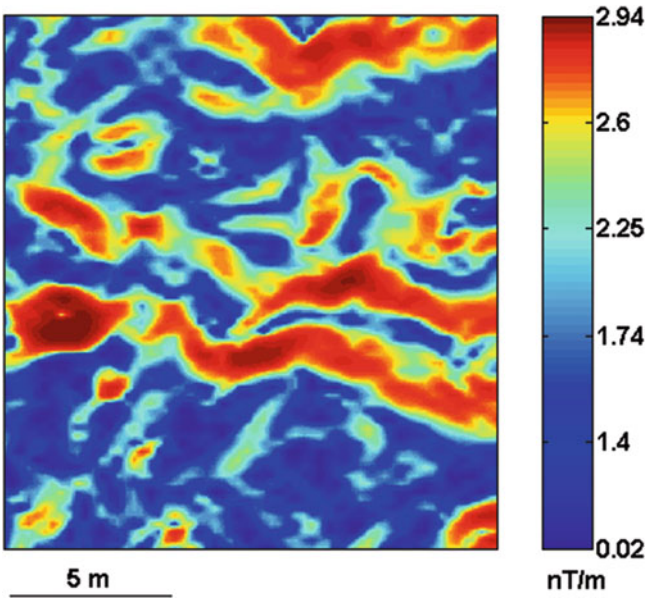

Fig. 10.8 Multiscale derivative analysis (MDA; Fedi 2002) computed starting from the total field in Fig. 10.7 up to its fourth vertical derivative. To better visualize the boundaries of the magnetic sources, a histogram equalization algorithm was used for plotting the map

different images of the causative body's edges at a variable resolution, so separating the effects generated at various scales by sources of different depth and extent (Figs. 10.8 and 10.9). With this method each maximum should correspond to a horizontal magnetization contrast at some depth. In these figures we used also a graphical utility, the histogram equalization (HE), suited to better enhance the weak field anomalies of archaeological interest of the magnetic/gradient field.

The pictured workflow describes how it is possible to identify and enhance the field contributions from archaeological features.

In particular, Figs. 10.8 and 10.9 show how to determine best the horizontal position of sources of potential archaeological interest. However, it may be also important not only to estimate the horizontal position of the archaeological structure but also to obtain a reasonable estimate of its depth. So, further data elaboration may be still needed to produce a 3D model of the underground susceptibility distribution, which could yield a complete description (horizontal and depth position) of the sought sources of archaeological interest.

To this end, the next section is dedicated to case histories, which will show not only the application of the techniques here described, but also the use of powerful interpretative methods, such as the depth from extreme points (DEXP; Fedi 2007).

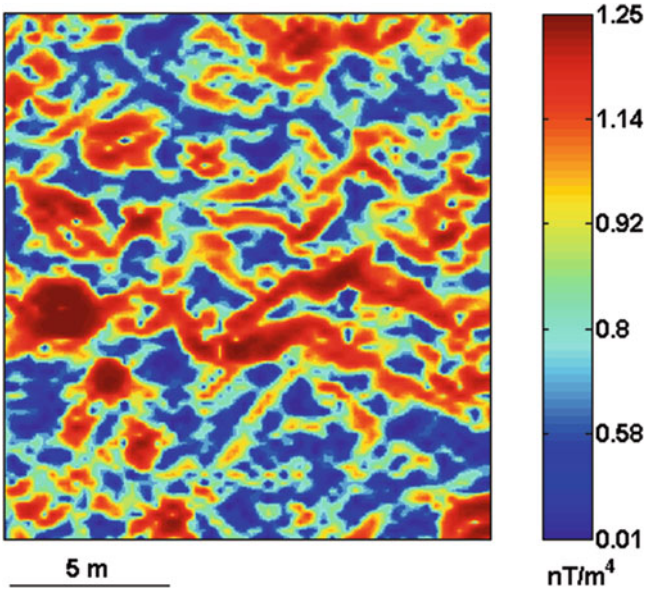

Fig. 10.9 Multiscale derivative analysis (MDA; Fedi 2002) of the field in Fig. 10.7 computed at high resolution. MDA is built starting from the third vertical derivative of the total field up to its fifth vertical derivative. To better visualize the boundaries of the magnetic sources, a histogram equalization algorithm was used for plotting the map

10.3 Case Histories: Investigations of Archaeological Sites through Magnetometric Methods

In this section, we aim at showing the effectiveness of magnetometric surveys in archaeo-geophysical investigations through several selected examples. These examples illustrate the use of advanced processing and interpretation methodologies of magnetometric data, yielding effective noise removal, signal enhancement, and source edge detection, under the guideline described in the previous section.

Moreover, 3D imaging (Fedi and Pilkington 2012) of the magnetization distribution can be used to obtain information on positions of the sources also in depth, so allowing virtual visualization of the archaeological structures. As imaging method, we show the usefulness of the depth from extreme points (DEXP; Fedi 2007; Baniamerian et al. 2016), which is an alternative method to data inversion and yields a fast 3D image of the source distribution. DEXP is a multiscale method allowing information on the source depth and structural index N, the latter being a parameter indicative of the source shape. It is a physically based transformation (mainly consisting of upward continuation and differentiation), so being able to decrease interference effects and infer the depth of the source distribution without any pre-filtering.

Fig. 10.10 Pian della Tirena (Cosenza, Southern Italy; *red box*)

The studies were carried out through magnetometric and high-resolution radiometric surveys in both marine and land contexts.

10.3.1 Pian Della Tirena (Cosenza, Southern Italy)

The first example shows the study of the site of Pian della Tirena (Cosenza, Southern Italy; Fig. 10.10) and is taken from Cella et al. (2015). The site gained archaeological interest because of the hypothesis of two adjacent but distinct settlements: the first one is of Hellenic/Hellenistic age (the ancient Temesa), and the second one (called Tempsa) is of Roman age.

Even though the site was recently excavated, extensive investigation was not possible because of the size of the area (more than 100,000 m^2). The area was investigated in 2006 and 2013 through detailed magnetic surveys to provide precise information about the possible existence of a well-developed Magna Graecia urban network. The survey aimed to confirm the existence of a true urban settlement instead of isolated dwellings and to locate centers of manufacturing activities (local pottery and metal handicrafts).

The area has gained archaeological interest since the 1980s following the hypothesis that it may be the site of Temesa, a town mentioned by Homer in the *Iliad* as an important market for trading metals. Some pottery from the sixth century BC, and thus preceding the Brethio period, has been found in different parts of the plain. Archaeological excavations conducted in 1982, 1987, and 1988 by the University of Naples 'Federico II' found the remains of different occupation phases dated from the sixth to the third century BC. Excavation findings suggest that the plateau was divided into areas with different functions (Cicala et al. 2013).

The geophysical investigations in Pian della Tirena were carried out in 2006 and in 2013 over a subhorizontal area of about 60,000 m^2 located in the central portion of the plain. The employed instrumentation was a gradiometer using two GEM GSM19 Overhauser magnetometers. The magnetic profiles were carried out along an east–west direction in 2006 and a northeast–southwest direction in 2013. The magnetic measurements were acquired along equidistant profiles with sampling rates of two to three measures per second, corresponding to an in-line sampling step of 0.3 m. The distance between the profiles was 0.5 m. Geo-referencing was made through high-precision global positioning system (GPS) measurements (Leica GPS System 500).

The gradiometer magnetic data measured along each profile in the 2006 and 2013 surveys were gridded to an interval of 0.25 m. The data needed some processing procedures to reduce noise (for details, see Sect. 10.2). The raw data were characterized by differences between the average values measured in adjacent cells. Thus, the different cells of the mesh were equalized based on the average value of each cell. Data showed some linear noise from the data acquisition procedures and geometry, removed by a filter built in the wavelet domain (Sect. 10.2), which allowed a localized and sharp filtering of directional noise (DWT; Fedi and Florio 2003; Paoletti et al. 2007). The two filtered data sets were then merged through several steps, including the removal of the mismatch between the two data sets through a polynomial surface of zero-order and interpolating the data with an interval of 0.25 m. The gradiometric data obtained after this processing are shown in Fig. 10.11a; in Fig. 10.11b we show the gradiometric data after pole-reduction, which performed using an inclination 55° and declination 2° for both the inducing field and the magnetization vector directions.

The data are characterized by several main linear trends with amplitude up to 20 nT m^{-1} (anomalies L1–L7 shown in plot b, having a length of 55–65 m) and by a set of small anomalies in the eastern and southwestern sectors of the map. Those anomalies may highlight the presence of archaeological features. The map also shows the presence of high-amplitude anomalies in the central sector of the study area, displaying the maximum-to-minimum axis in a direction very different from that of the present inducing field. This direction could be related to highly magnetized sources with a strong component of remnant magnetization, such as metallic objects or backed clay bricks or tiles. Finally, we notice a subcircular anomaly in the eastern sector of the plain, which is indicated as F1.

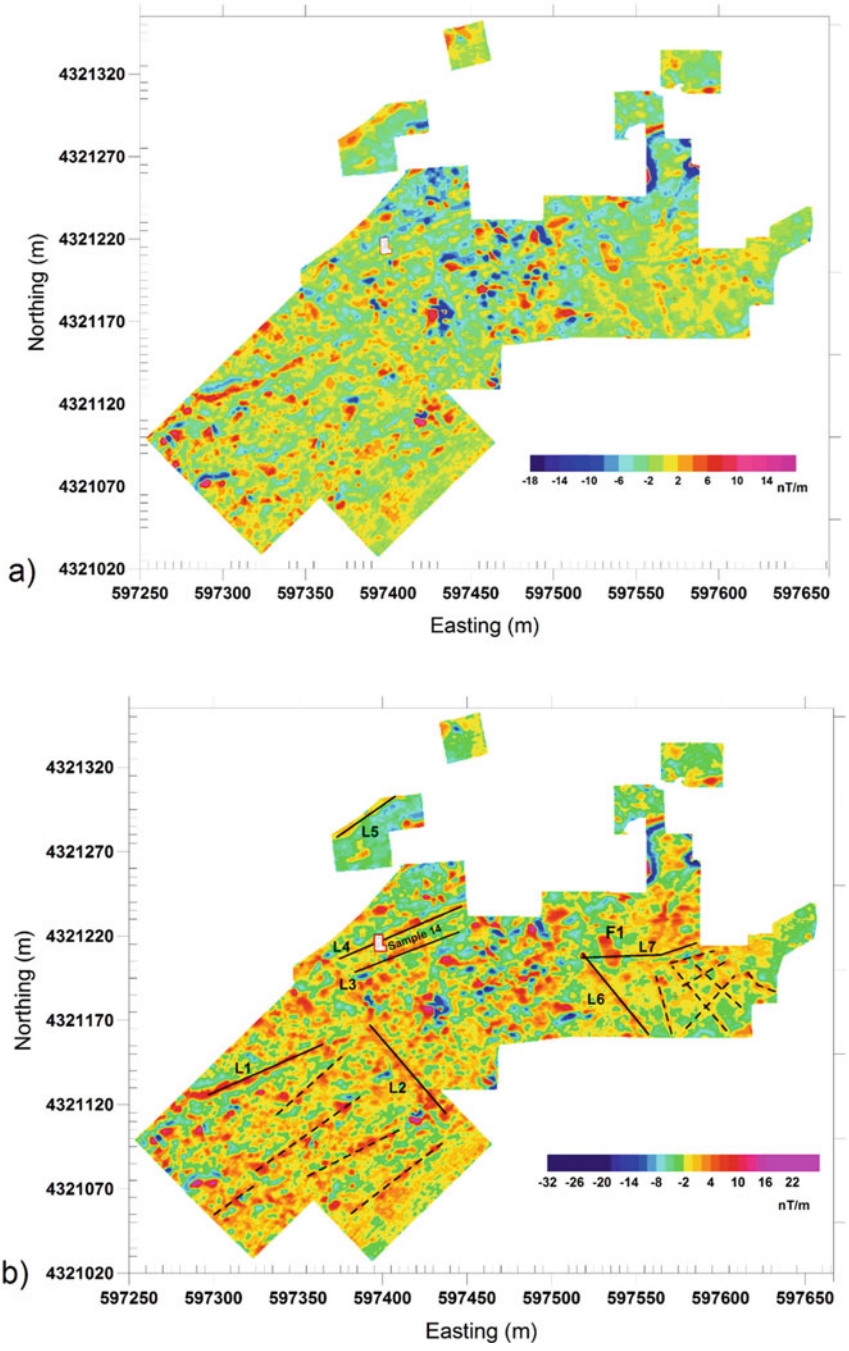

Fig. 10.11 Vertical gradient of the magnetic field, measured during the 2006–2013 surveys (**a**), and vertical gradient of the pole-reduced field, after pre-processing and filtering (**b**) (as described in Sect 10.2). *Solid lines L1–L7* mark the main linear trends of the field. *Dashed lines* highlight a network of less marked linear anomalies. Sample 14 is the excavation, which was driven in 2013 by the information provided by geophysics. (Modified after Cella et al. 2015)

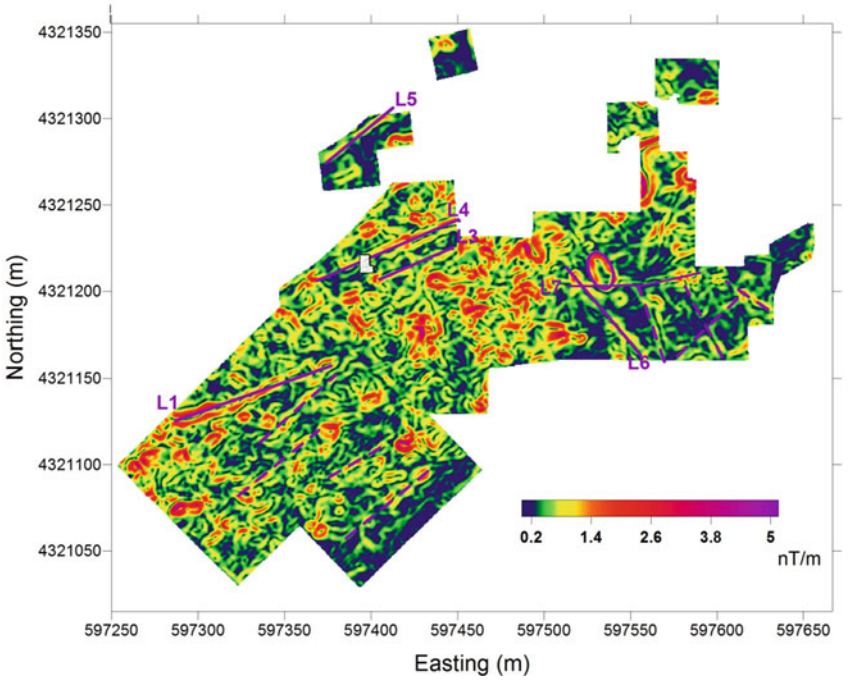

Fig. 10.12 Edge analysis by the EHD method (Fedi and Florio 2001). *Solid purple lines* mark the main linear trends. *Dashed purple lines* highlight minor linear trends. The *purple ellipse* points out the edges of the F1 anomaly. (Modified after Cella et al. 2015)

The position of the boundaries of the anomaly sources was highlighted through the computation of an enhanced horizontal derivative (EHD; Fedi and Florio 2001, see Sect. 10.2). The EHD was applied to pole-reduced data, after upward continuation of 2 m above the ground, implying the dataset is referred to 4 m above the ground.

The EHD map obtained by taking the first and second vertical derivatives of the data (Fig. 10.12) show many linear trends and boundaries in the eastern and southwestern sectors of the studied area.

We also notice a clear subcircular anomaly located east of anomaly L6 that corresponds with the F1 anomaly shown in Fig. 10.11b.

An estimation of the depth of some buried structures of the plain was performed through the DEXP (Fedi 2007; Fedi and Pilkington 2012). In Fig. 10.13, we show the depth analysis on linear anomaly L4 (Fig. 10.13a).

The results of the DEXP analysis show the presence of a trend of sources located about 0.5 m below the ground, possibly representing the base layer of Brett period roads (Fig. 10.13b). The estimated source depth is in agreement with what was found in Sample 14 (see Fig. 10.13c) from 0.3 m to 1.3 m The excavation found several layers of stones and brickwork, belonging to different construction phases,

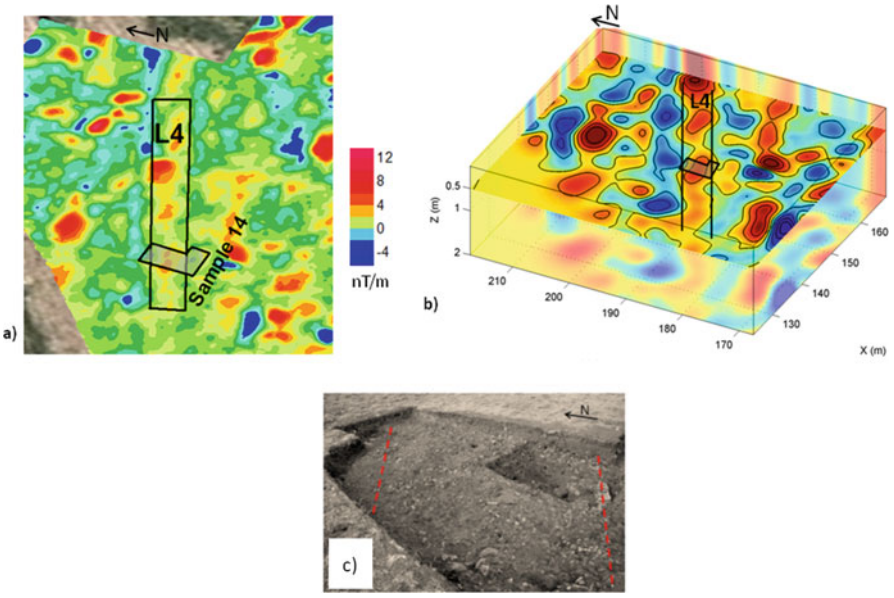

Fig. 10.13 Depth analysis along the linear anomaly L4. (**a**) Subarea of the pole-reduced vertical gradient map picked up for the DEXP analysis. *Light gray area* shows the excavation of Sample 14. (**b**) Results of the DEXP analysis: the depth of the anomaly source found by the analysis is 0.5 m. (**c**) Photograph of Sample 14, in which was found a layer of stones and brickwork. The average depth of the found remnants is in agreement with the depth inferred by the DEXP analysis. (Modified after Cella et al. 2015)

very likely representing the base layer of a Brett road. The results of the depth analysis performed along anomaly L1 and in correspondence with the subcircular anomaly F1 showed an average depth of 0.3 m below the ground for these structures.

10.3.2 Baiae (Naples, Southern Italy)

The second example concerns a magnetic survey over the submerged Roman ruins of Baiae (Southern Italy; Fig. 10.14), is taken from Paoletti et al. (2005).

The site of Baiae, one of the most extensive submerged archaeological sites known in Italy, is characterized by residential houses, thermal baths, fisheries, and harbor buildings. A magnetic marine survey was carried out in 2003 with the aim of establishing the typical magnetic signatures of building structures submerged in a volcanic marine environment. The comparison of the measured magnetic anomaly field with the known submerged archaeological structures of the area gave some interesting insights into the lithological characteristics of the archaeological structures of the Baiae site. Baiae is in the Phlegrean Fields area, of which the

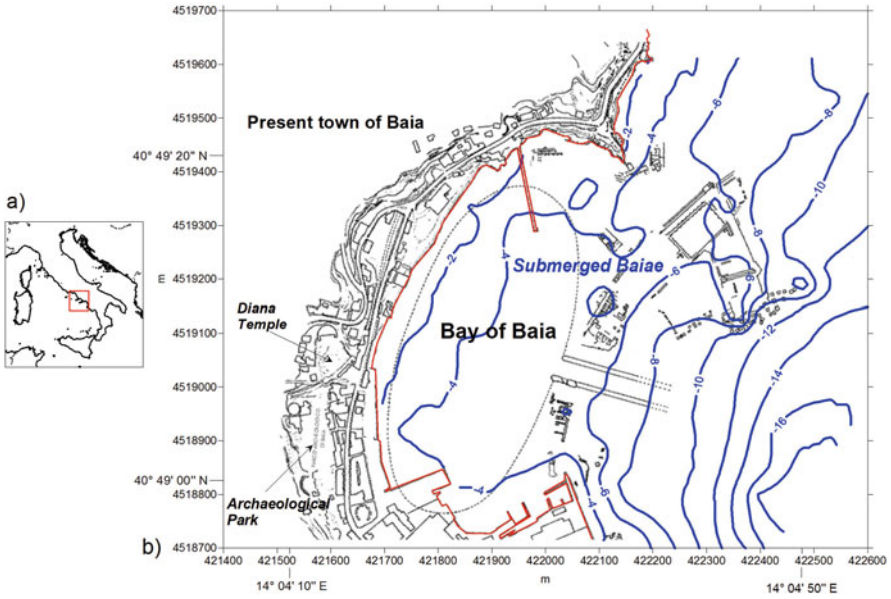

Fig. 10.14 Investigations at submerged Baiae (Naples, Southern Italy). (**a**) Location of the study area. (**b**) The Bay of Baia and its submerged archaeological site (from Scognamiglio 1993; Maniscalco and Severino 2002); coastline in *red*. (Modified after Paoletti et al. 2005)

submerged archaeological sites include Puteoli, Baiae, Bauli, Misenum, and Nisida. Because of the bradyseism most of these sites are currently submerged and still in part undiscovered. The main expansion of Baiae took place during the Roman age, starting from the second century before Christ. Baiae was mainly a residential center, consisting of villas, thermal baths, and inns. This town was active until at least the end of the fourth century after Christ (Pappalardo and Russo 2001); afterward, bradyseism induced inundation of entire areas of the town, causing a decline.

The sea level basically increased constantly until the seventh century after Christ. Between the seventh and eighth centuries after Christ most of the town was submerged by the sea (Tocco Sciarelli 1983). Currently, the coastline relative to Roman times is about 10 m below sea level and is marked by a drop in the seabed at about 400 m from the present coastline (Pappalardo and Russo 2001).

The submerged archaeological structures, whose distribution was mapped on the basis of dive surveys (Figs. 10.14 and 10.15), emerge from the seabed for a few meters (Scognamiglio 1993).

The magnetic data analyzed in this work were acquired in June 2003; the instrument was dragged behind the boat by a cable 20 m long at a depth of 2 m. Magnetic data were corrected for the offset, by repositioning the magnetic data in correspondence to the position of the GPS on board. The diurnal time-varying correction was performed using the magnetic data acquired by a base station located

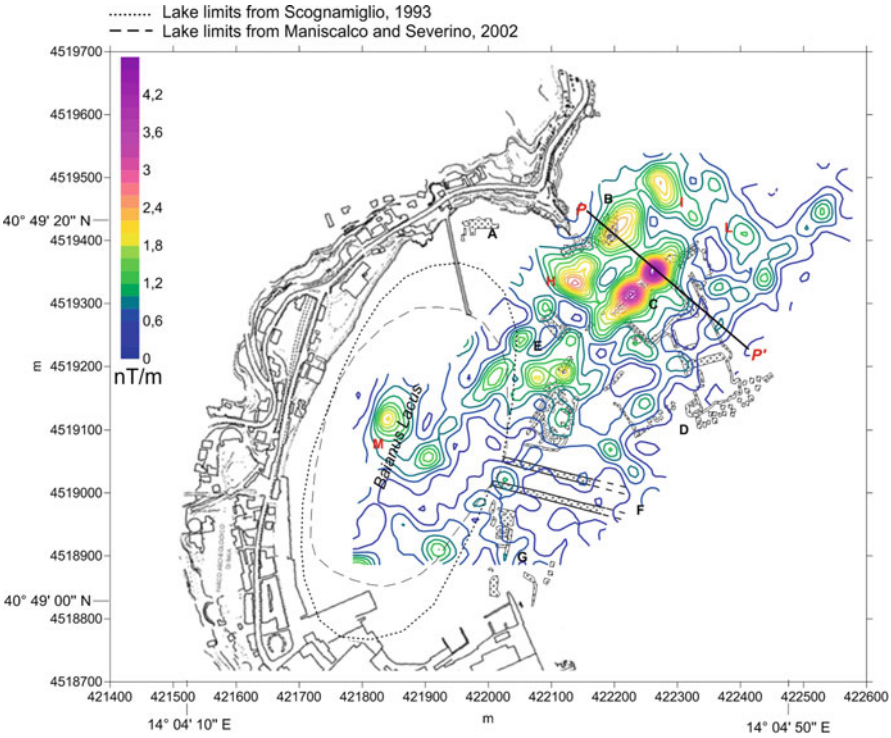

Fig. 10.15 Total gradient of the magnetic data at the archaeological site of Baiae overlying the known submerged archaeological features of the bay (from Scognamiglio 1993; Maniscalco and Severino 2002): Claudius' Ninfeo (**a**); Thermae (**b**); Palatium Adrianeo and Pisoni's villa (**c**); fishery and pilae (**d**); ruins of thermal baths and villa (**e**); channel connecting the Baianus Lacus to the sea (**f**); ruins in front of Baiae dockyards (**g**); fisheries (**h**) (Modified after Paoletti et al. 2005)

at Capri Island, integrated with the data from the Geomagnetic Observatory of L'Aquila (Italy). The data were then low-pass filtered to reduce the high-frequency components.

The field obtained after the processing and filtering is characterized by several dipolar anomalies with maximum amplitude of about 100 nT, which in some cases show a good correlation with the known position of the submerged structures. A clear relationship between the spatial location of magnetic anomalies and their sources can be yielded by the total gradient of magnetic data (Nabighian et al. 2005; see Sect. 10.2) (Fig. 10.15).

After comparing the total gradient to the known submerged archaeological features in the bay, we may see a very good correspondence between anomalies and structures for some areas (anomalies labelled by "b" and "c" in Fig. 10.15). In other cases (anomaly labelled by "e" in Fig. 10.15), the known archaeological ruins are characterized by a weaker magnetic signature, probably because of erosion. Finally, the structures labelled by "f" and "g" in Fig. 10.15 do not show magnetic signatures,

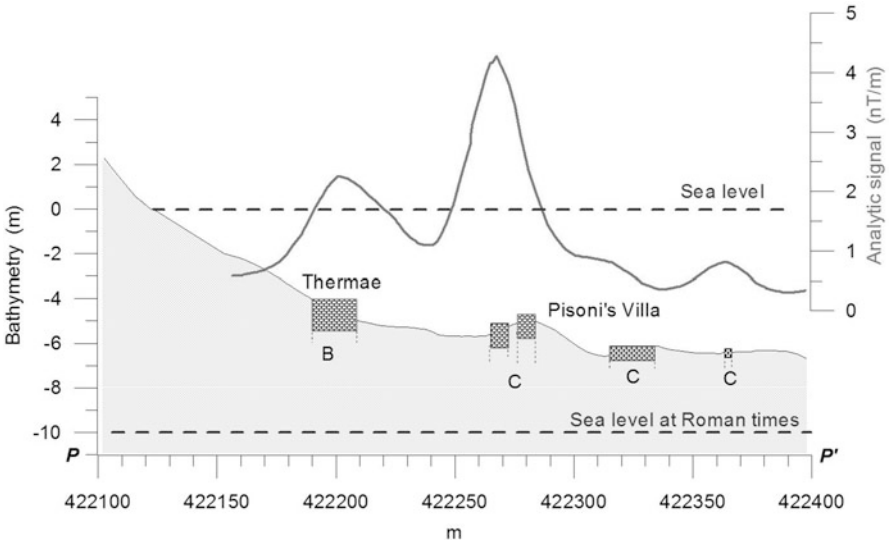

Fig. 10.16 Comparison between the total gradient data and the bathymetry of the bay along profile ***P–P′*** (see Fig. 10.15). Sea level in Roman times as quoted in Pappalardo and Russo (2001) (Modified after Paoletti et al. 2005)

perhaps because of the low susceptibilities of the construction materials, made of volcanics and limestone. On the other hand, there are anomalies not apparently corresponding to any known structure, for example, the anomalies marked with i, l, and m, which suggests the presence of undiscovered ruins buried beneath the seabed.

The study focused on the two main magnetic anomalies corresponding to the Pisoni family villa and to the Thermae (c and b in Fig. 10.15). These two anomalies have an amplitude of 105 and 55 nT and seem connected to a negative contrast of susceptibilities, possibly caused by yellow tuff walls. In Fig. 10.16 we show the total gradient and the bathymetry data along a profile (***P–P′***) over the mentioned structures. The profile shows three highs, clearly corresponding to the remnants of the Thermae and the Pisoni family villa.

10.3.3 Torre Galli (Vibo Valentia, Southern Italy)

The third example is Torre Galli (Vibo Valentia, Southern Italy; Fig. 10.17), one of the most significant sites of the early Iron Age in Italy; it is taken from Cella and Fedi (2015). The archaeological relevance of the site greatly increased after digs carried out in the 1920s (Orsi 2004) and again the 1980s, after excavations realized by Pacciarelli (1999). A high-resolution gradiometric survey was carried out in the summer of 2012, with the aim of providing information about the kind and position of buried archaeological structures. Advanced techniques of boundary

Fig. 10.17 Location of Torre Galli, Southern Italy (*small black rectangle*)

analysis (EHD; Fedi and Florio 2001) provided detailed maps of the edges of magnetized structures within the subsoil, whereas 3D imaging methods (DEXP; Fedi 2007) yielded information about the depth and shape of the buried remnants.

The studied area is located near Vibo Valentia, Southern Italy, on the Tyrrhenian side of the Calabria-Peloritani Arc (Fig. 10.17). The first campaign of archaeological excavations, during the 1920s (Orsi 2004), found a necropolis with 280 burial pits, dated to the Iron Age. The wide extent of the necropolis let us infer a thriving indigenous community, living in a small town since the ninth and for the entire eighth century BC. Analysis of the remains found in the graves suggests that the Torre Galli social framework was more complex than that hypothesized for the Late Bronze Age.

An excavation carried out by M. Pacciarelli (1999) recognized the remains of stone walls aligned with regular geometry and traces of a fireplace. This finding suggested that some defenses should have been located just within the area between the village and the necropolis.

A magnetometric investigation was carried out in the area in 2012 over a subhorizontal area of about 14,400 m^2. The surveyed area was divided into three sectors of variable size and shape (Fig. 10.18). Each of them was divided into smaller cells, variously sized, that were surveyed separately. The magnetometric method was used in gradiometric configuration, using a GEM GSM19 Overhauser magnetometer and a GEM potassium GSMP40 magnetometer. The two sensors were separated by 0.25 m (GSMP40) and 0.56 m (GSM19), with the gradiometer midpoint located, respectively, about 1.30 m and 2 m above the ground.

The profiles of gradiometric data were gridded to an interval of 0.25 m to provide maps of the vertical gradient of the magnetic field. Data were then processed by

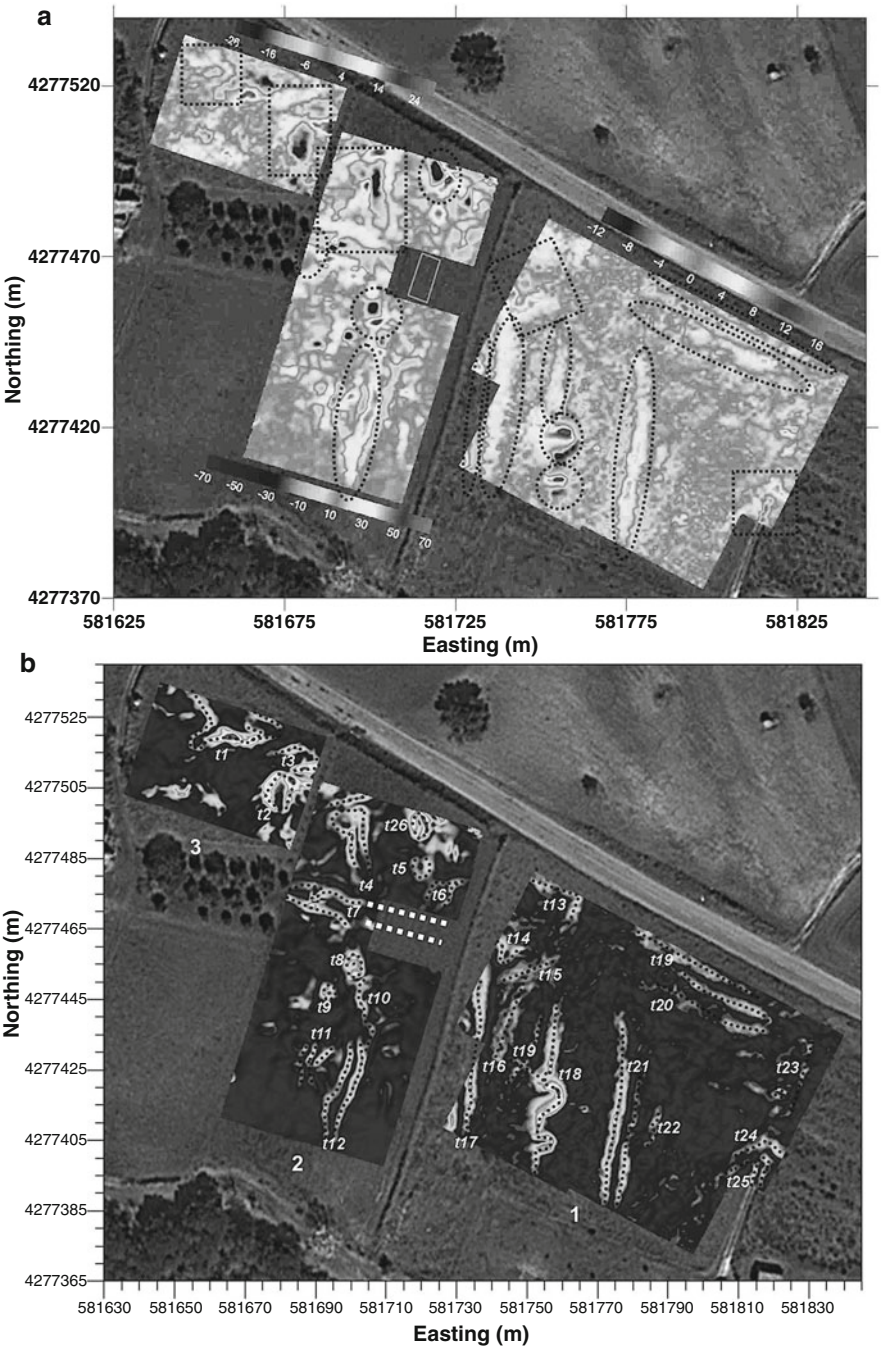

Fig. 10.18 (**a**) Vertical gradient of the magnetic anomaly field after processing and reduction to the pole (along guidelines on Sect. 10.2). *Dashed lines* outline the main patterns of anomalies. *Gray rectangle* is area of archaeological excavation before the geophysical survey. Data are in nT/m. (**b**) Large-scale EHD. Edges of the buried sources are identified by local maxima: *white dashed segments* indicate structures unearthed during a previous excavation. (Modified after Cella and Fedi 2015)

means of automatic gain control algorithms (AGC; Milligan and Rajagopalan 1995) and corrected to suppress spurious effects and noise linked to the survey geometry ("heading error," "zigzag," "staggering" effect, etc.) (see Sect. 10.2 for details). This noise was minimized by a cross-correlation procedure (Ciminale and Loddo 2001) and by equalizing the average value of the measured field among the alternate lines. Finally, we used the discrete wavelet transform (DWT; e.g., Fedi and Florio 2003) to remove any residual directional noise still affecting the data. Figure 10.18a shows the maps thus obtained of the vertical gradient of the reduced to the pole magnetic field, in the three sectors.

We noticed several anomalies with a linear shape trending NNE and WNW for some tens of meters, which suggested a correlation with elongated archaeological structures such as roads, walls, or moats. Other anomalies have such a geometric regularity to be possibly associated to the dwellings remains. Further intense anomalies have a dipolar shape with the high/low direction very different from that of the present inducing geomagnetic field (inclination 55°, declination 2°). A strong component of remnant magnetization could be therefore inferred for the causative sources of these anomalies, related to kilns, pottery, metal handicrafts, and slag.

Figure 10.18b shows the boundaries obtained through the EHD algorithm, using the first- and second-order vertical derivatives of the pole-reduced data (see Sect. 10.2). We note trends that are located along parallel alignments. We may focus our attention to lineaments *t*7 and *t*12. The eastward extension of *t*7 seems to coincide with two walls, unearthed during a previous excavation and interpreted by the archaeologists as structures bordering a small road. Lineament *t*12 marks one of the most significant linear anomalies of the magnetic vertical gradient (Fig. 10.18b). This anomaly seems to be separating the burial area, eastward, from the urban settlement, westward. DEXP imaging (Fig. 10.19) individuates a shallow thin source body (about 1 m deep), with significant longitudinal extent (more than 15 m) in the N–S direction.

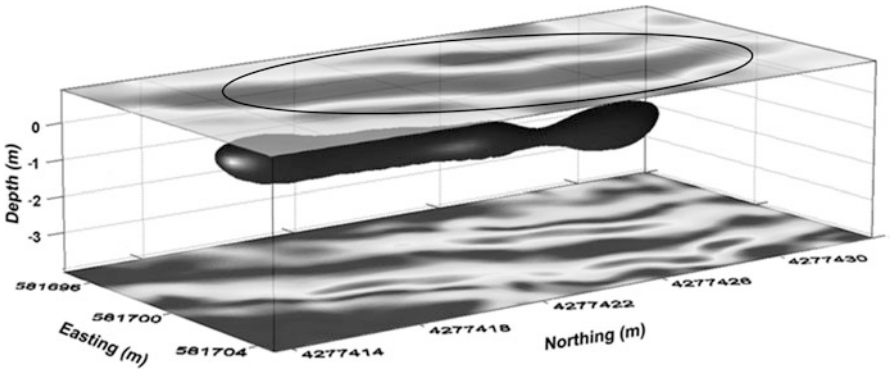

Fig. 10.19 DEXP analysis of the magnetic vertical gradient along lineament *t12* (see Fig. 10.18) shows a structure elongated for more than 15 m in the N–S direction and buried at about 1 m depth. *Upper map*: vertical magnetic gradient data; *lower map*: large-scale EHD. (Modified after Cella and Fedi 2015)

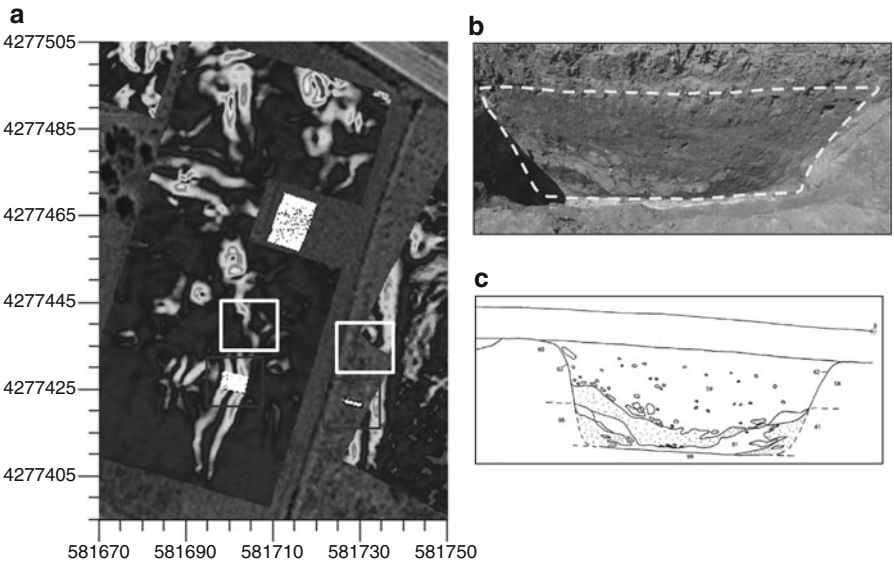

Fig. 10.20 (**a**) Detail of the EHD map of Fig. 10.18b. *Boxes* indicate the position of the two digs. Photograph (**b**) and drawing (**c**) show the cross section of the western excavation. (Modified after Cella and Fedi 2015)

A new excavation was planned following this geophysical information, and a trench was dug perpendicular to the main direction of the double EHD trend *t12* (Fig. 10.20a). The dig revealed the upper side of a moat elongated in the N–S direction and with lateral edges exactly matching with the double linear trend found by EHD (Fig. 10.18b) and a depth in agreement to the DEXP imaged structure (Fig. 10.19).

In fact, the discovered moat is about 2.5 m wide, showing steep walls and a flat bottom at a depth of 1.5 m, in correspondence with the bedrock (Fig. 10.20c).

10.4 Conclusions

Magnetic surveying is one of the most effective techniques supporting archaeological investigations, deriving from the often significant susceptibility contrast between the cover soil and most archaeological buried structures. The widespread applicability of the magnetometric surveys is related to its quick and flexible acquisition mode and low cost–benefit ratio. Nevertheless, the obtained magnetic maps may be hard to interpret, given the complex interference pattern among various buried structures and the low signal-to-noise ratio that frequently characterizes the field measurements. Noise is connected not only to present human activities but also to the acquisition procedures and to the geological environment itself.

In this chapter we described the use of advanced methodologies to improve the quality of magnetometric data and to yield an effective interpretation of the magnetic anomalies related to buried/submerged archaeological remnants. The reported examples illustrate how the use of such processing and interpretation methods allows efficient noise removal, signal enhancement, and source edge detection.

We illustrated that techniques such as the discrete wavelet transform (DWT; Fedi and Quarta 1998; Fedi and Florio 2003) allow a precise filtering of localized and directional noise. Furthermore, we showed how the enhanced horizontal derivative technique (EHD; Fedi and Florio 2001), a multiscale edge analysis method originally developed for earth science purposes, can be quite effective for positioning man-made features, by detecting the lateral edges of the buried structures of archaeological interest. Another multiscale advanced method illustrated here is the depth from extreme points technique (DEXP; Fedi 2007). It represents an alternative method to data inversion, yielding a fast 3D image of the source distribution and allowing the source to be characterized in terms of size, shape, and depth. This information may be crucial for archaeological digging and interpretation.

The reported case histories concerning magnetometric investigation of both buried and submerged archaeological sites (e.g., Baiae, Tirena, Torre Galli) confirmed that the combined use of the advanced techniques of data processing and interpretation described here is a reliable and useful resource also for archaeological investigations.

References

Aitken MJ (1958) Magnetic prospecting. I. The Water Newton survey. Archaeometry 1:24–26

Arnold JB III (1996) Magnetometer survey of La Salle's ship the Belle. The International Journal of Nautical Archaeology 25:243–249

Asandulesei A (2011) Geophysical Prospecting Techniques Used in archaeology magnetometry. In: *Studia antiqua et archaeologica*, XVII, Editura Universității Alexandru Ioan Cuza, Iaşi, 5–17

Baniamerian J, Fedi M, Oskooi B (2016) Compact depth from extreme points: a tool for fastpotential field imaging. Geophys Prospect 64:1386–1398. doi:0.1111/1365-2478.12365

Baranov W (1975) Potential fields and their transformation in applied geophysics, pp 1–72. Geoexploration monograph series, vol 6, 121 pp, Gebruder Borntraeger, Stuttgart, Germany

Blakely JR, Simpson RW (1986) Approximating edges of source bodies from magnetic or gravity anomalies. Geophysics 51(7)

Blakely RJ (1995) Potential theory in gravity and magnetic applications. Cambridge University Press, Cambridge

Boyce JI, Reinhardt EG, Raban A, Pozza MR (2004) Marine magnetic survey of a submerged Roman Harbour, Caesarea Maritima, Israel. Int J Nautic Archaeol 33:122–136

Cella F, Fedi M, Florio G (2009) Toward a full multiscale approach to interpret potential fields. Geophysical Prospecting 57:543–557

Cella F, Paoletti V, Florio G, Fedi M (2015) Characterizing elements of urban planning in Magna Graecia using geophysical techniques: the case of Tirena (Southern Italy). Archaeol Prospect 22:207–219

Cella F, Fedi M (2015) High-resolution geophysical 3D imaging for archaeology by magnetic and EM data: the case of the iron age settlement of Torre Galli, Southern Italy. Surv Geophys 36:831–850. doi:10.1007/s10712-015-9341-3
Cicala L, Grifa C, Franciosi L, Langella A, Germinario C, Morra V, (2013) Pottery production from Pian della Tirena, NoceraTerinese (Cz). Archaeometry: comparing experiences, Naus Editoria
Ciminale M, Loddo M (2001) Aspects of magnetic data processing. Archaeol Prospect 8:239–246
Clark A (1990) Seeing beneath the soil. Batsford, London
Cooper GRJ, Cowan DR (2006) Enhancing potential field data using filters based on the local phase. Comput Geosci 32:1585–1591
Cordell L., Grauch V.J.S., 1985. Mapping basement magnetization zones from aeromagnetic data in the San Juan basin, New Mexico. In: Hinze WJ (ed) The utility of regional gravity and magnetic anomaly maps. Society of Exploration Geophysicists, Tulsa, pp 181–197
Eder-Hinterleitner A, Neubauer W, Melichar P (1996) Restoring magnetic Anomalies. Archaeol Prospect 3:185–197
Fassbinder JWE, Stanjek H (1993) Occurrence of bacterial magnetite in soils from archaeological sites. Archaeologia Polona 31:117–128
Fedi M, Florio G (2001) Detection of potential fields source boundaries by enhanced horizontal derivative method. Geophys Prospect 49:40–58
Fedi M (2002) Multiscale derivative analysis: a new tool to enhance detection of gravity source boundaries at various scales. Geophys Res Lett 29(2):1029, 16–1/16–4
Fedi M, Florio G (2003) Decorrugation and removal of directional trends of magnetic fields by the wavelet transform: application to archeological areas. Geophys Prospect 51(4):261–272
Fedi M (2007) DEXP: a fast method to determine the depth and the structural index of potential field sources. Geophysics 72(1):I1–I11.
Fedi M, Pilkington M (2012) Understanding imaging methods for potential field data. Geophysics 77(1):G13–G24
Fedi M, Quarta T (1998) Wavelet analysis for the regional-residual and local separation of potential field anomalies. Geophys Prospect 46(5):507–525
Florio G, Fedi M, Pasteka R (2014) On the estimation of the structural index from low-pass filtered magnetic data. Geophysics 79(6):J67–J80
Gaffney C (2008) Detecting trends in the prediction of the buried past: a review of geophysical techniques in archaeology. Archaeometry 50:313–336
Gibson T (1986) Magnetic prospection on prehistoric sites in western Canada. Geophysics 51:553–560
Jeng Y, Lee YL, Chen CY, Lin MJ (2003) Integrated signal enhancements in magnetic investigation in archaeology. J Appl Geophys 53:31–48
Hsu S, Coppens D, Shyu C (1998) Depth to magnetic source using the generalized analytic signal. Geophysics 63:1947–1957
Iglewicz B, Hoaglin DC (1993) How to detect and handle outliers. ASQ Press, Milwaukee
Larson DO, Lipo CP, Ambos EL (2003) Application of advanced geophysical methods and engineering principles in an emerging scientific archaeology. First Break 21:51–62
Linford NT (2006) The application of geophysical methods to archaeological prospection. Rep Prog Phys 69:2205–2257
Maher BA, Taylor RM (1988) Formation of ultrafine-grained magnetite in soils. Nature 336(6197):368–370
Maniscalco F, Severino N (2002) Recenti ipotesi sulla conformazione del Lacus Baianus, Ostraka. Rivista di Antichità 11(1):167–176
Milligan P, Rajagopalan S (1995) Image enhancement of aeromagnetic data using automatic gain control. Explorat Geophys 25(4):173–178
Nabighian MN (1984) Toward a three-dimensional automatic interpretation of potential field data via generalized Hilbert transforms: fundamental relations. Geophysics 49:780–786
Nabighian MN, Grauch VJS, Hansen RO, LaFehr TR, Li Y, Peirce JW, Phillips JD, Ruder ME, (2005) The historical development of the magnetic method in exploration. Geophysics 70:33ND–61ND

Orsi P (2004) Le necropoli preelleniche calabresi. Torre Galli, Canale, Ianchina, Patariti. FPE-Franco Pancallo Ed., ISBN 8864561323, 9788864561325 (in Italian)
Pacciarelli M (1999) Torre Galli. La necropoli della prima età del ferro (scavi di Paolo Orsi 1922–23). Rubbettino Ed., Iraceb., ISBN 8872847257 (in Italian)
Paoletti V, Secomandi M, Piromallo M, Giordano F, Fedi M, Rapolla A (2005) Magnetic survey at the submerged archaeological site of Baia, Naples, Southern Italy. Archaeol Prospect 12(1): 51–59
Paoletti V, Fedi M, Florio G, Rapolla A (2007) Localized cultural de-noising of high-resolution aeromagnetic data. Geophys Prospect 55:412–432
Pappalardo U, Russo F (2001) Il bradisismo dei Campi Flegrei (Campania): dati geomorfologici-ed evidenze archeologiche. In Forma Maris, eds. Gianfrotta P.A., Maniscalco F. Forum Internazionale di Archeologia Subacquea, Pozzuoli(Naples), September 22–24, 1998. Massa Editore, Napoli, 107–129 (in Italian).
Piro S, Sambuelli L, Godio A, Taormina R (2007) Beyond image analysis in processing archaeomagnetic geophysical data: case studies of chamber tombs with dromos. Near Surface Geophys 5(6):405–414
Quinn R, Bull JM, Dix JK, Adams JR (1997) The Mary Rose site – geophysical evidence for palaeo-scour marks. Int J Naut Archaeol 26:3–16
Quinn R, Breen C, Forsythe W, Barton K, Rooney S, O'Hara D (2002) Integrated geophysical surveys of the French Frigate La Surveillante (1797), Bantry Bay, Co. Cork, Ireland. J Archaeol Sci 29:413–422
Roest WR, Verhoef J, Pilkington M, (1992) Magnetic interpretation using the 3-D analytic signal. Geophysics 57:116–125
Rosner B (1983) Percentage points for a generalised ESD many-outlier procedure. Technometrics 25:165–172
Scognamiglio E (1993) Il rilievo di Baia sommersa. Note tecniche e osservazioni. Archeologia Subacquea. Studi, ricerche e documenti I:65–70 (in Italian)
Smekalova T, Abrahamsen N, Voss O (1996) Magnetic investigation of a Roman/Early Germanic Iron Age iron-smelting center at Snorup, Denmark. In: Proceedings of the sixth Nordic conference on the application of scientific methods in archaeology 1993. ArkæologiskeRapporter No. 1, Esbjerg Museum, pp 227–245
Stampolidis A, Tsokas GN (2012) Use of edge delineating methods in interpreting magnetic archaeological prospection data. Archaeol Prospect. 19(2):123–140
Sternberg RS (1987) Archaeomagnetism and magnetic anomalies in the American Southwest. Geophysics 52:368–371
Scollar I, Tabbagh A, Hesse A, Herzog I (1990) Archaeological prospecting and remote sensing. Cambridge University Press, Cambridge
Stavrev P, Gerovska D (2000) Magnetic field transforms with low sensitivity to the direction of source magnetization and high. Geophys Prospect 48:317–340
Tabbagh J (1999) Filtrage numérique des donnes géophysiques. In: Pasquinucci M, Trément F (eds) Non-destructive techniques applied to landscape archaeology. Oxbow Books, Oxford
Tocco Sciarelli G (1983) Baia, inquadramento storico e topografico. In: Baia—il Ninfeo Imperiale sommerso di Punta Epitaffio. Edizione Banca Sannitica, Naples, pp 17–24 (in Italian)
Verduzco B, Fairhead JD, Green CM, Mackenzie C (2004) New insights into magnetic derivatives. The Leading Edge 22:116–119
Weymouth JW (1986) Archaeological site surveying program at the University of Nebraska. Geophysics 51:538–552
Wynn JC (1986) Archaeological prospection: an introduction to the special issue. Geophysics 51:533–537
Wijns C, Perez C, Kowalczyk P (2005) Theta map: edge detection in magnetic data. Geophysics 70:39–43

Part II
In Situ Noninvasive Technologies for Investigating Monuments and Artifacts

Chapter 11
Infrared Thermography: From Sensing Principle to Nondestructive Testing Considerations

Jean Dumoulin

Abstract This chapter addresses a short review on radiation theory to introduce infrared thermography. Infrared thermography is presented in both passive and active mode. Then, several processing analysis approaches are described, which belong to the signal and image processing domain or to the heat transfer domain. Illustration of results obtained through such analysis approaches are described by two experiments carried out in nonlaboratory conditions. Finally, a conclusion and perspectives are proposed.

11.1 Introduction

This section is devoted to introducing the nature of radiative heat transfer (more information can be found in Siegel and Howell 2002), which is at the basis of infrared thermography applied to nondestructive evaluation.

One of the three mechanisms by which bodies at different temperatures can exchange energy is thermal radiation. Thermal radiation is characterized by the electromagnetic wave emission by a material (internal energy variation). Depending on material temperature, an object emits radiations from the ultraviolet to the far infrared. Each body acts at the same time as an emitter (continuous emission of thermal radiation) and a receiver (continuous reception of radiation even though from far bodies). Nonetheless, thermal radiation is linked to the molecular structure of emitter bodies, the receiver, and the propagation medium.

The mechanism of heat transfer by thermal radiation can be divided into three phases:

1. Energy transformation (internal energy variation of the body) in electromagnetic radiation (emission) by the body, which can be solid, liquid, or gas.

J. Dumoulin (✉)
IFSTTAR, COSYS-SII, Route de Bouaye, CS4, Bouguenais, F-44344, France

Inria, I4S Team, Campus de Beaulieu, Rennes, F-35042, France
e-mail: jean.dumoulin@ifsttar.fr; jean.dumoulin@inria.fr

N. Masini, F. Soldovieri (eds.), *Sensing the Past*, Geotechnologies and the Environment 16, DOI 10.1007/978-3-319-50518-3_11

2. Radiation through the vacuum, a transparent (as dry air over a short distance) or semitransparent atmosphere (as a gas such as CO_2, H_2O, or Cl_2).
3. Radiation interaction with one or several opaque or semitransparent receivers, where it converts part by absorption (internal energy variation), and the other part is then reflected or transmitted with or without scattering but retaining its electromagnetic wave nature.

Remarks

- For solid and liquid, thermal radiation begins near the surfaces [thickness from a few micrometers (μm) to a few millimeters (mm)].
- For gas, the full volume has to be considered.

The thermal radiation spectrum domain can be defined from 0.1 μm to 500 or 1000 μm (the higher the temperature, the shorter is the wavelength maximum peak of emission):

- 0.1–0.4 μm: ultraviolet
- 0.4–0.76 μm: visible spectrum
- 0.76–200 μm up to 500 or 1000 μm: infrared spectrum

The millimetric wave spectrum follows the infrared spectrum, but different lower limits can be found in the literature.

The first infrared cameras were developed in the twentieth century (Gaussorgues 1989), beginning with a mono-detector equipped with an opto-mechanical system to form an infrared image of the investigated object. Subsequently, infrared focal plane arrays including an adapted readout circuit have permitted suppressing the opto-mechanical components. At the end of the twentieth century, the development and realization of low-cost uncooled infrared thermography systems have favored its dissemination in laboratories and in various fields of application.

The use of the infrared camera can be divided into three categories. The first category is concerned with vision application such as law enforcement, security, or safety (for instance, human rescue). The second one concerns preventive maintenance or thermal monitoring such as electrical cabinet control, qualitative inspection of building insulation, and inline thermal survey of industrial plant production. The third and last category addresses nondestructive testing, which requires monitoring the thermal evolution of an object in a transient thermal regime. Such a thermal state can be reached by using artificial or, in some cases, natural, heat excitation sources. This last category requires developing processing tools for the analysis, where the first and natural approach belongs to the signal and image processing domain. To go further in the characterization of a surveyed body, the use of thermal models coupled or not coupled with an inverse approach is required.

In this chapter, we first recall a few fundamental considerations on radiation theory to introduce infrared thermography. After that, several processing analysis approaches are presented with illustrations. Conclusion and perspectives end this chapter, with a short list of references.

11.2 General Considerations on the Nature of Radiative Heat Transfer

In this section we first introduce the concept of the blackbody, an ideal body to introduce several specific aspects of heat radiation. Then, we focus on the definition and interpretation of thermo-optical properties and recommendations versus what can be encountered in experimental conditions.

11.2.1 Blackbody Concept

The blackbody is an ideal reference body that emits heat radiation uniformly in all directions and also totally absorbs all incident radiations. For a blackbody at local thermal equilibrium, the spectral emittance M_λ^0 is linked to the spectral radiance L_λ^0 (by multiplying it by π after integration over the space), which is defined by Planck's law (Eq. 11.1):

$$M_\lambda^0 = \pi L_\lambda^0 = \frac{2\pi h c_0^2 \lambda^{-5}}{\left(\exp \frac{hc_0}{K_B \lambda T} - 1\right)} \tag{11.1}$$

with

- h is Plank's constant: 6.626×10^{-34} J
- c_0 is velocity of light in vacuum: 2.998×10^8 ms^{-1}
- K_B is Boltzmann's constant: 1.3806×10^{-23} J/K
- λ is the wavelength of the emitted radiation (in m)
- T is the temperature of the blackbody (in K)

Typical wavelength distribution of emitted radiative heat flux at different temperatures for a blackbody is shown in Fig. 11.1.

It can be noted on these curves that the hotter is the temperature, the lower is the wavelength of maximum emission. The wavelength of maximum emission can be extracted from Planck's law. It leads to Wien's displacement law:

$$\lambda_{\max} T = 2898\ \mu\text{mK} \tag{11.2}$$

This law is useful when one wants to select in a first approach the bandwidth of an infrared camera for its application. For instance, by assuming that studied objects behave as blackbodies, the Sun with a surface temperature of about 6000 K has an emission centered in the visible spectrum (0.4–0.8 μm) whereas the Earth surface at about 300 K has an emission centered in the long wavelength band (8–12 μm).

In the case of real objects whose absorbance is limited, only part of the energy is radiated directly from the surface and part is reflected from the environment.

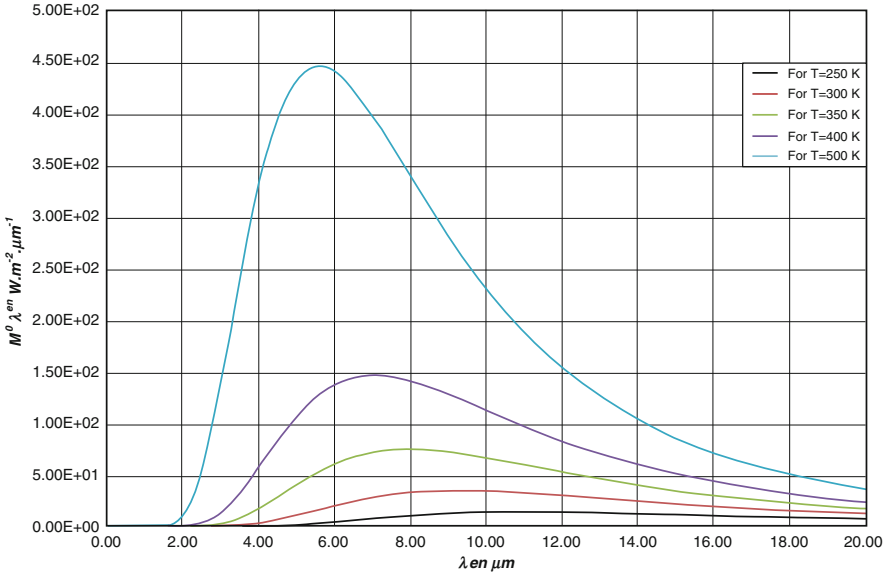

Fig. 11.1 Blackbody spectral emittance curves at different temperatures according to Planck's law

11.2.2 Thermo-optical Properties of Materials

The behavior of materials in front of an incident thermal radiation can be characterized by three quantities depending on the temperature, the direction, and the wavelength of the electromagnetic wave, that is, the absorption (α), reflectance (ρ), and transmission (τ) coefficients.

For a material submitted to a heat flux radiation, Φ_i (see Fig. 11.2), it can be observed that

- A part Φ_a is absorbed
- A part Φ_r is reflected
- A part Φ_t is transmitted

To describe such physical phenomenon, three parameters are introduced:

- Reflection coefficient: $\rho = \frac{\Phi_r}{\Phi_i} = \frac{\text{reflected radiation heat flux}}{\text{incident radiation heat flux}}$
- Absorption coefficient: $\alpha = \frac{\Phi_a}{\Phi_i} = \frac{\text{absorbed radiation heat flux}}{\text{incident radiation heat flux}}$
- Transmission coefficient: $\tau = \frac{\Phi_t}{\Phi_i} = \frac{\text{transmitted radiation heat flux}}{\text{incident radiation heat flux}}$

These parameters globally describe the behavior of a surface in front of an incident illumination. If the transmission coefficient is equal to zero, the notion of an opaque material can be introduced. Furthermore, if the reflection and absorption coefficients are independent of wavelength, the notion of gray body can be introduced. In the same way, if these two properties are direction independent, the notion

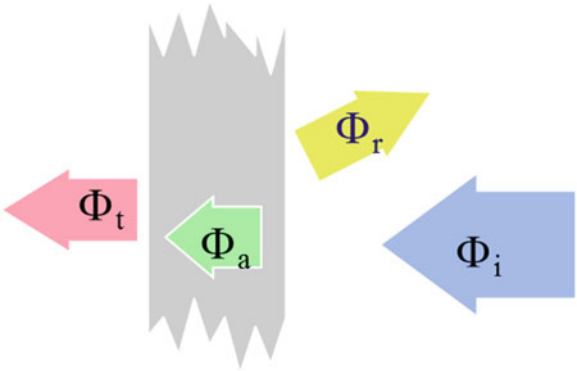

Fig. 11.2 Material behavior in presence of an incident radiation Φ_i

of diffuse bodies, which follow Lambert's law, can be introduced. Unfortunately, such coefficients very often depend on wavelength, direction, temperature, and surface roughness.

The behavior of materials versus their thermal radiation emission can also be characterized by a quantity function of temperature, direction, and wavelength: the emissivity (ε). The illumination notion can be then introduced: it is the heat flux radiation for a given direction and reported to the surface unit. This illumination depends on the body temperature and its emissivity.

At the local thermal equilibrium, Kirchhoff's second law (Eq. 11.3) shows that the absorption coefficient is equal to the emissivity coefficient for a given temperature, direction, and wavelength:

$$\varepsilon(\lambda, \theta, T) = \alpha(\lambda, \theta, T) \tag{11.3}$$

where λ is the wavelength, θ is the direction in the space, and T is temperature.

In the case of opaque gray and diffuse bodies, the emissivity at a given temperature is equal to its absorptivity independently of the direction and the wavelength. However, such common hypotheses on radiative heat exchanges are difficult to satisfy entirely in the real world. These hypotheses can be partly satisfied on reduced spectral bandwidths and for limited angles of observations, and are commonly adopted in basic infrared thermography measurements.

11.3 Infrared Thermography

In the infrared spectrum, three spectral bandwidths are typically available on the market for infrared cameras, with different techniques used for the detector:

- SWIR [short wavelength infrared (band I)]: spectral bandwidth (wavelengths) from 1 to 2.5 μm

- MWIR [mid-wavelength infrared (band II)]: spectral bandwidth (wavelengths) from 2.5 to 5.5 μm
- LWIR [long wavelength infrared (band III)]: spectral bandwidth (wavelengths) from 7–8 μm to 13–14 μm

Infrared thermal cameras are equipped with sensor and optical components that are efficient in a limited spectral bandwidth. Thermal images or a sequence of thermal images of the target's surface for detecting the radiation emitted and reflected from targets are built, followed by a digitization of the analogue signal. Under several assumptions, and by using a proper calibration, it is possible to convert radiometric values collected by the camera into apparent surface temperature values.

The retrieving of the apparent surface temperature (i.e., apparent net radiation) of the investigated object depends on the following conditions:

- Local thermal equilibrium
- The thermal properties of the materials (function of the wavelength, the temperature, and the direction of the incident electromagnetic (EM) wave
- The deployed infrared spectral bandwidth
- The radiative transmission

11.3.1 Passive Infrared Thermography

The nature of thermal radiation means that a description of radiative heat exchange is complex, and their qualification by an infrared thermography device can be affected by errors caused by the influence of the measurement scene environment. A schematic representation of the main parameters to be considered when making apparent surface temperature measurements by infrared cameras is shown in Fig. 11.3.

Most infrared cameras on the market integrate some in-line radiative correction in stabilized atmosphere (laboratory conditions), as presented in the following formula:

$$DL'_0 = \tau_{\text{atm}}\varepsilon_0 DL_0 + \tau_{\text{atm}}\left(1-\varepsilon_0\right)DL_{\text{env}} + \left(1-\tau_{\text{atm}}\right)DL_{\text{atm}} \tag{11.4}$$

where

- DL'_0 is the global received radiative heat flux converted in digital level at detector outlet level
- τ_{atm} is the atmospheric transmission computed for atmospheric conditions of measurements in the IR camera bandwidth
- ε_0 is object emissivity
- $(1-\varepsilon_0)$ is object reflectivity
- DL_0 matches the radiative contribution from the object

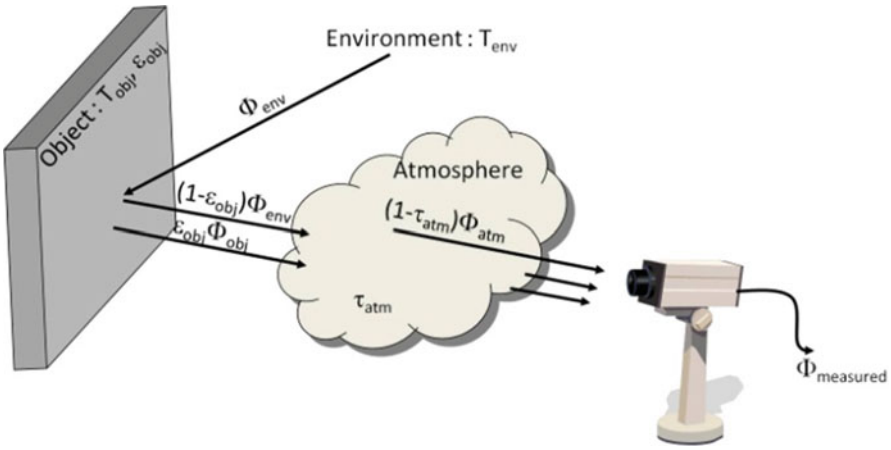

Fig. 11.3 Schematic representation of radiative heat flux composition received by the infrared camera

- DL_{env} and DL_{atm} match the respective contribution of the environment and the atmosphere, generally assumed to behave as a blackbody at an equivalent known temperature

All the respective contributions in Eq. 11.4 are affected by atmospheric transmission. All DL terms are connected with temperature through an equivalent radiance L in the spectral bandwidth of the infrared camera, obtained by using adequate calibration laws.

So, according to what was shown in Fig. 11.3, an IR camera in front of an object not only detects the emitted radiance but also a part of the radiance from reflection of the ambient fluxes by the object surface whose reflectivity is nonzero. Therefore, it is necessary to take into account this phenomenon for objects with partly reflective surfaces, such as painted walls or ceramic tiles, when analyzing the measurement results.

It should be stressed that this formula is applied to the whole matrix of the sensor and not independently to each pixel in standard commercial systems. For complex scenes, such as those encountered in cultural heritage and more generally on a real test site, it is useful to carry out post-processing temperature conversion by using at least an emissivity map of the surveyed object.

Furthermore, depending on measurement configuration, the atmosphere between the scene and the sensor needs to be taken into account. For instance, Fig. 11.4 shows the mean transmission behavior of the natural atmosphere in two bandwidths as a function of the distance and for a relative humidity of 50%.

So, when the effect of propagation in the atmosphere between the scene and the sensor can be neglected in the adopted infrared camera spectral bandwidth (according to measurement distance and atmospheric conditions), the transmission

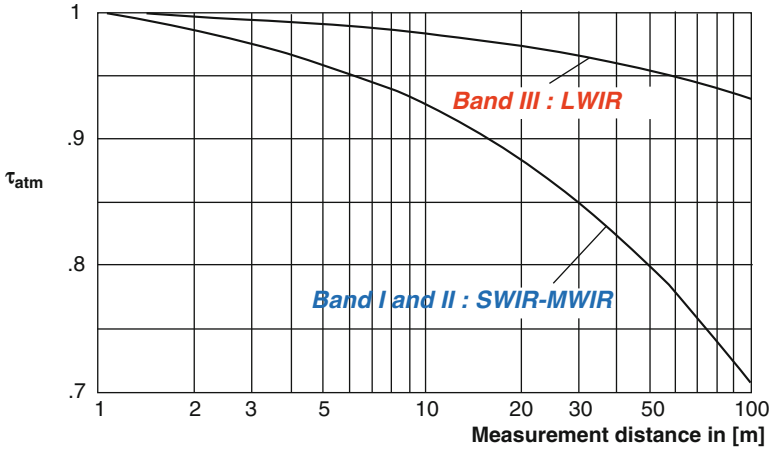

Fig. 11.4 Mean transmission coefficient behavior with measurement distance for two infrared spectral bandwidths and a relative humidity of 50% (see Gaussorgues 1989)

coefficient of the atmosphere τ_{atm} can be approximated by unity, and Eq. 11.4 can be simplified as follows:

$$DL'_0 = \varepsilon_0 DL_0 + (1 - \varepsilon_0)\, DL_{\text{env}} \tag{11.5}$$

In practice, when using thermal cameras, it is frequently assumed that the observed body behaves as a gray body in the spectral bandwidth of measurement and is supposed to have a diffusive behavior for the angle of observation used during measurements. For a given temperature range, care must be taken with angle of observation; in practice it is recommended to avoid normal to surface angle and grazing angle.

Therefore, to obtain an infrared measurement on the investigated object, knowledge of environmental conditions is required. For outdoor applications, the integration of a weather station is helpful to provide information to refine radiometric correction. In addition, it is necessary to take into account the geometry of the investigated target and the optical properties of the infrared sensor used to drive adequate radiometric corrections.

It is pertinent to use infrared (IR) techniques in dry atmospheric conditions; in fact, in bad weather conditions, such as rain showers or fog (Dumoulin et al. 2009; Dumoulin and Boucher 2014), all the elements of the scene are affected by a thermal quenching. If the thermal inertia is sufficient and if no water film was formed on the objects, infrared thermal images still may be used for measurements after radiometric corrections. In the presence of a scene with the target covered by a water layer and located in a semitransparent medium, a flat signal arises, and accordingly measurement is not directly possible. The thermo-optical properties of a material (i.e., depending on the investigated structure) have also to be known to retrieve the apparent temperature from the illumination distribution received at the

sensor level (focal plane array), or alternatively a reference area has to be used simultaneously during measurements.

11.3.2 Active Infrared Thermography

Nondestructive evaluation by active infrared thermography is based on the detection and the registration of the time evolution of net radiation flux emitted by the surface of of the object surveyed. It is necessary to set the object in a transient thermal regime by heating or cooling it during a long or short period. In the presence of a defective area in the apparently homogeneous material being studied, the apparent surface temperature will present a local perturbation versus the overall thermal evolution of the object surface. Time evolution of the thermal difference intensity and the shape of this anomaly depend on the volume of the defect and its location inside the material.

Various techniques can be used for the thermal excitation: optical means, inductive (if the material is compliant), ultrasound. Furthermore, it is also possible to modulate in space and time the thermal excitation to favor the detection of a particular defect.

Finally, in this configuration, at the end of the measurements a thermal image sequence is generated and analyzed. One will easily understand that depending on the characteristic thermal time of the object being studied, a large amount of infrared images (frames) can be generated (from a few hundred to a few thousand). So, efficient post-processing approaches are needed. The next section presents some post-processing approaches that can be used on thermal image sequences.

11.4 Thermal Image Sequence Qualitative Analysis: Detection of Anomalies

Three standard approaches for detection of areas affected by defects are presented here: the first is based on thermal contrast computation, and the other two are pulse phase thermography (PPT), based on the use of the fast Fourier transform, and principal component thermography (PCT), based on the use of the singular value decomposition tool.

11.4.1 Thermal Contrast Analysis

Thermal contrast is a basic procedure that, despite its simplicity, is at the origin of many PT (pulse thermography) algorithms. Numerous thermal contrast definitions exist but they all share the need for specifying a sound area, *Sa*, that is, a defect-free

region within the region of interest. For instance, the absolute thermal contrast Ct_{abs} and the running contrast Ct_{run} are defined as follows (Maldague 2001):

$$Ct_{\text{abs}} = \Delta T(t) = T_d(t) - T_{Sa}(t) \quad \text{and} \quad Ct_{\text{run}} = \frac{T_d(t) - T_{Sa}(t)}{T_{S_a}(t)} \tag{11.6}$$

where

$T_d(t)$ is the temperature of a pixel or the average value of a group of pixels on a defect area at time t

$T_{Sa}(t)$ is the temperature at time t over a sound area (Sa) on a pixel or for the average value of a group of pixels

It is also possible to use the standard contrast (Maldague 2001) as

$$Ct_{\text{std}} = \frac{T_d(t) - T_d(0)}{T_{Sa}(t) - T_{S_a}(0)} \tag{11.7}$$

Particular care has to be taken for the behavior of an inhomogeneous material during the heating phase. Locally, an object may not have the same diffusive thermal time constant. This phenomenon vanishes with the establishment of the three-dimensional (3D) heat diffusion according to the spatial resolution used for infrared measurements. Thus, the standard contrast formula has to be modified by substituting T_{sa} by the average of the sound area values. For instance, the sound area can be determined by labeling an empirical orthogonal functions (EOF) map obtained by singular value decomposition (SVD; as presented in Sect. 11.4.3) or by using the average of the overall thermal image, assuming that defect size is negligible versus the sound area (Dumoulin et al. 2010).

11.4.2 Pulse Phase Thermography (PPT) Analysis

The PPT analysis approach is a way to reduce the number of thermal images to be analyzed in a sequence and also to look at local delay induced by thermal property changes inside materials (for instance, in defect areas). The Fourier transform is applied to the time evolution of each pixel of the thermal image:

$$F_n = \Delta t \sum_{k=0}^{N-1} T\,(k\Delta t) \exp^{(-j2\pi nk/N)} = \text{Re}_n + \text{Im}_n \tag{11.8}$$

where

- n designates the frequency increment ($n = 0, 1, \ldots N$)
- Δt is the sampling interval
- Re and Im are the real and the imaginary parts, respectively, of the Fourier transform

In practice, the fast Fourier transform algorithm (Cooley and Tukey 1965) is used to reduce time computing.

Then, magnitude (A_n) and phase (Φ_n) maps are calculated:

$$A_n = \sqrt{\mathrm{Re}_n^2 + \mathrm{Im}_n^2} \quad \text{and} \quad \Phi_n = \tan^{-1}\left(\frac{\mathrm{Im}_n}{\mathrm{Re}_n}\right) \tag{11.9}$$

and can be analyzed to locate areas with different thermal behaviors.

Illustration of results obtained by using this image processing approach are proposed in Sect. 11.6.

11.4.3 Principal Component Thermography (PCT) Analysis

The PCT analysis is based on the singular value decomposition (SVD) approach (Rajic 2002; Valluzzi et al. 2009). It permits extracting the spatial and temporal information from a thermal image sequence in a compact or simplified manner. Instead of relying on a basic function (such as in PPT), which is based on the Fourier transform (relying in sinusoidal basis functions), SVD is an eigenvector-based transform that builds an orthonormal space.

The SVD of an $M \times N$ matrix $\mathbf{A}$ ($M > N$) can be calculated as follows:

$$\mathbf{A} = \mathbf{U}\Sigma\mathbf{V}^{\mathbf{T}} \tag{11.10}$$

where

- $\boldsymbol{U}$ is an $M \times N$ orthogonal matrix
- Σ is a diagonal $N \times N$ matrix (with the singular values of A on the diagonal)
- $\boldsymbol{V}^{\boldsymbol{T}}$ is the transpose of an $N \times N$ orthogonal matrix (characteristic time)

Hence, to apply the SVD to thermographic data, the 3D thermal images sequence matrix representing time and spatial variations has to be reorganized as a two-dimensional (2D) $M \times N$ matrix $\mathbf{A}$ as depicted in Fig. 11.5. This reordering can be done by rearranging the infrared images for every time as columns in $\mathbf{A}$, in such a way that time variations will occur column wise and spatial variations will occur row wise.

After rearranging the thermal image for every time as columns in $\mathbf{A}$ and applying the SVD, the columns of $\mathbf{U}$ represent a set of orthogonal statistical modes known as empirical orthogonal functions (EOF) that describe spatial variations of data. On the other hand, the principal components (PCs), which represent time variations, are arranged row wise in matrix $\mathbf{V}^T$. The first EOF will represent the most characteristic variability of the data; the second EOF will contain the second most important variability, and so on. Usually, original data can be adequately represented with only a few EOFs.

Results obtained by using this image processing approach are presented in Sect. 11.6.

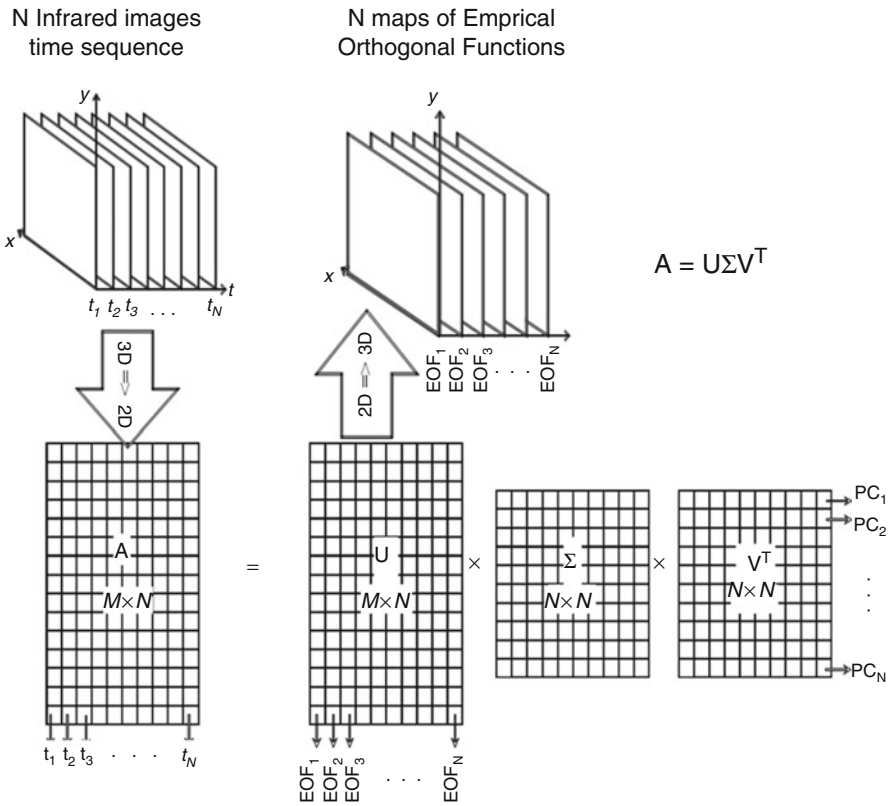

Fig. 11.5 Schematic representation of the application of the singular value decomposition (SVD) to infrared image sequence

11.5 Thermal Modeling Analysis (Quantitative Analysis)

Two approaches among various possibilities are presented here. The first one requires first locating the defect area whereas the second one does not require this information. Nevertheless, the second approach requires knowledge of the thermal properties of the object surveyed and the environmental parameters to obtain reliable apparent surface temperature field evolution during experiments.

11.5.1 Blind Frequency

Using phase maps and assuming defect location is known, absolute phase contrast can be calculated as:

$$\Delta\Phi = \Phi_{\text{def}} - \Phi_{\text{sound}} \tag{11.11}$$

where:

Φ_{def} is the phase evolution over a defect area
Φ_{sound} is the phase evolution over a sound area

If the defect area is small enough with respect to the overall inspected zone, it might be possible to use the average on the overall area as a sound one. Nevertheless, the contrast result might be affected.

It is then possible to use the blind frequency f_b approach, which is defined as the frequency limit for which a defect can be detected. Initially introduced in lock-in thermography, later it was extended to pulse thermography (Ibarra-Castanedo 2005). The condition of its extension to long-pulse thermography has been studied (Dumoulin et al. 2011) by working only on the thermal relaxation part of the trials.

Using blind frequency identified on absolute phase contrast evolution, defect depth can be retrieved by using the equation:

$$z_{def} = C_1 \sqrt{\frac{a}{\pi f_b}} \tag{11.12}$$

where

a is the studied thermal diffusivity
f_b is the identified blind frequency
C_1 is a correlation constant depending on materials studied

Using phase maps when the defect location is known allows us to generalize this approach. In that case, absolute phase contrast can be calculated as

$$\Delta\Phi = \Phi_{pix} - \Phi_{mean} \tag{11.13}$$

where

Φ_{pix} is the phase evolution over a pixel
Φ_{mean} is the mean phase evolution over an area of interest

In practice, the minimum size of the area for computing Φ_{mean} has to be characterized depending on the studied materials and their thermal behavior.

11.5.2 Defect Depth Estimation by a Semi-infinite Direct Thermal Model for Square Pulse Thermal Excitation

In this approach, we do not assume the location of the defect is known, and we compute maps of the overheating evolution using the temperature map acquired before the square heating at t_0 for each pixel (see Eq. 11.14, below). This is a

classical approach in wall heat transfer determination by infrared (IR) thermography (Dumoulin et al. 1995), also known as cold image subtraction (Maldague 2001):

$$\Delta T_{x,y}(t) = T_{x,y}(t) - T_{x,y}\,(t_0) \tag{11.14}$$

As a first approximation, heat transfer in massive materials can be assumed to behave as in a semi-infinite body. Nevertheless, care must be taken when choosing the time interval for the calculation and the experiments (according to material characteristic thermal diffusion time), to be compliant with the validity domain of such a model. Furthermore, by neglecting natural heat transfer on the surface of the inspected material, the heat equation system to be solved takes the following form:

$$\begin{cases} \frac{\partial^2\theta}{\partial z^2} = \frac{1}{a}\frac{\partial\theta}{\partial t} \text{ with } \theta\,(z,t) = T\,(z,t) - T_0 \\ \text{Initial condition :} \\ t \le 0 : \theta\ (z,t) = 0 \\ \text{Boundary condition :} \\ \text{t} > 0 \text{ and z} = 0 : -k\frac{\partial\theta}{\partial z} = \varphi_0(t) \end{cases} \tag{11.15}$$

In the case of active infrared measurement configuration, the surface solicitation is a constant square heat pulse of duration τ. Accordingly, the boundary condition at $t > 0$ (Eq. 11.15) takes the following expression where φ_0 is the constant heat flux density applied during the pulse:

$$\varphi_0(t) = \text{q}_0 \text{ if } t \le \tau \quad \text{and} \quad \varphi_0(t) = 0 \text{ if } t > \tau \tag{11.16}$$

The solution of such a system can be obtained by using the Laplace transform. Other approaches can be found in the literature. For instance, Vavilov (1992) presents different solutions for various thermal configurations. The solution for the surface temperature is

$$\begin{cases} \text{if } t < \tau : \theta\,(0,t) = \frac{2q_0\sqrt{t}}{b\sqrt{\pi}} \\ \text{if } t \ge \tau : \theta\,(0,t) = \frac{2q_0}{b\sqrt{\pi}}\left(\sqrt{t} - \sqrt{t-\tau}\right) \end{cases} \tag{11.17}$$

Combining this solution for the case of a square pulse solicitation over the surface of the studied material with the normalized effusivity approach proposed by Balageas et al. (1987), the depth of the defect can be determined using this relationship:

$$z_{\text{def}} = \sqrt{a}\sqrt{t_{\min}}(b_{n,\min})^{0.95} \tag{11.18}$$

where

a is the thermal diffusivity
b is the thermal effusivity, calculated with Eq. 11.19

$t_{\min}$ is the time when the effusivity curve is minimum
z_{def} is the depth of the defect in the material
$b_{n,\min}$ is the normalized minimum effusivity $b_n = \frac{b}{b_{\text{studied material}}}$

Finally, the evolution of apparent thermal effusivity for a square heat flux density pulse is obtained using Eq. 11.17 and takes the expression as reported below:

$$\begin{cases} \text{if } t < \tau \;\; \text{b}(t) = \frac{2q_0\sqrt{t}}{\theta(0,t)\sqrt{\pi}} \\ \text{if } t \geq \tau \;\; \text{b}(t) = \frac{2q_0}{\theta(0,t)\sqrt{\pi}}\left(\sqrt{t} - \sqrt{t-\tau}\right) \end{cases} \tag{11.19}$$

Illustrations of results obtained by using this image processing approach are presented in Sect. 11.6.

11.6 Application Examples

11.6.1 Example of PPT Analysis Applied to Defect Detection

Here, we show an illustration of the pulsed phase thermography analysis approach applied to carbon fiber-reinforced polymer (CFRP) glued on cement concrete.

Two concrete samples (300 × 300 mm^2) have been manufactured (Figs. 11.6 and 11.7). The defects are simulated by replacing the adhesive material by a Teflon disc (0.5 mm thick) between the concrete surface and the carbon/epoxy laminate. The CFRP used was a wrap.

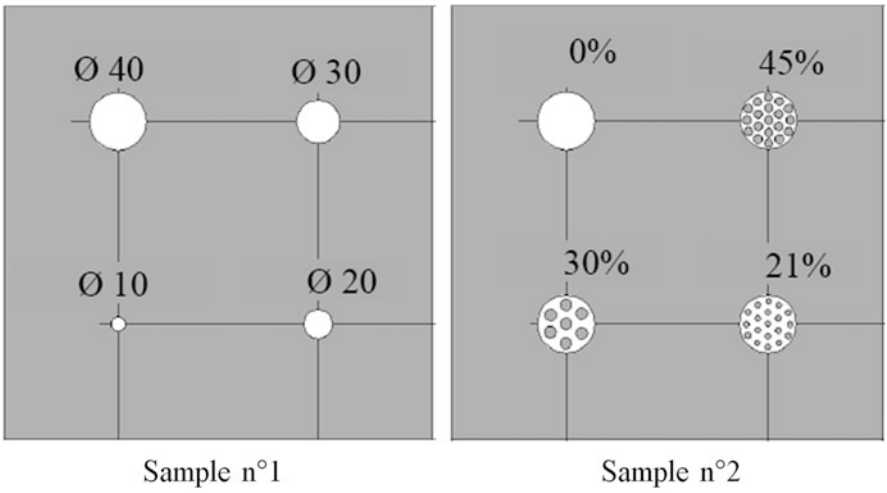

Fig. 11.6 Schematic view of laboratory samples

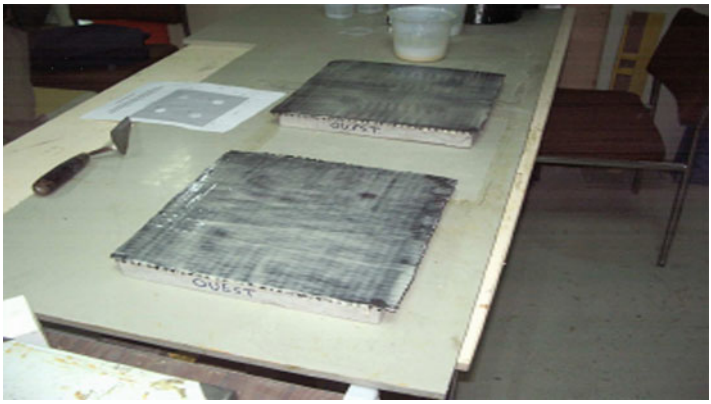

Fig. 11.7 View of laboratory samples realized

Fig. 11.8 View of the step heating test bench

Sample 1 contains four different discs (diameters 40, 30, 20, and 10 mm). Sample 2 contains four identical discs (Ø = 40 mm) drilled with different percentages of small holes to simulate the different qualities of the adhesive.

The experimental step heating bench for testing samples 1 and 2 (see Fig. 11.8) uses two halogen lamps of 500 W; a third lamp of 300 W can also be added onto the test bench.

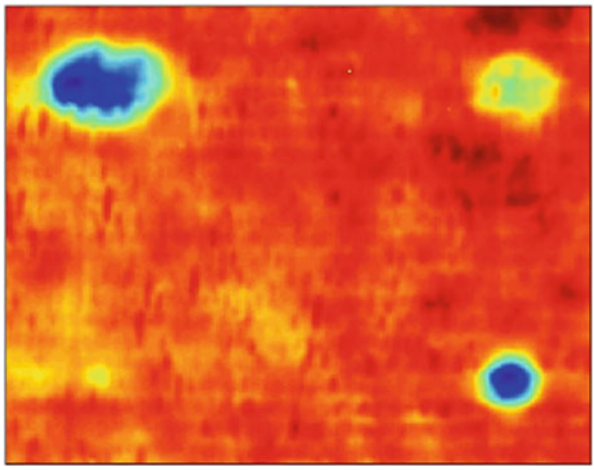

Fig. 11.9 Phase maps at $f = 1.10^{-2}$ Hz for a pulse heating duration of 60 s on sample 1

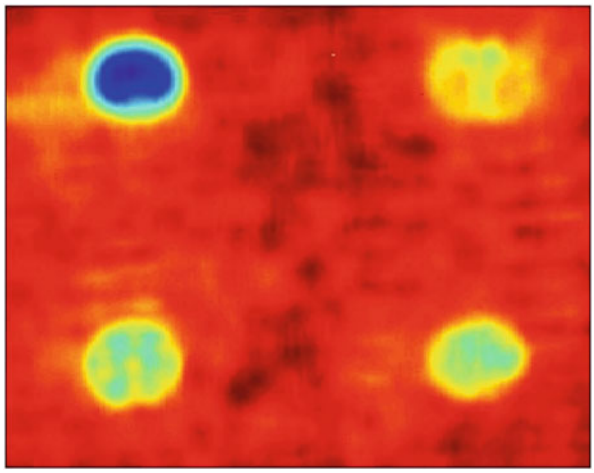

Fig. 11.10 Phase maps at $f = 1.10^{-2}$ Hz for a pulse heating duration of 60 s on sample 2

The step heating phase lengths were 5, 10, or 60 s. The heat flux density of the excitation during trials was assumed to be constant. Two infrared cameras were used during the trial: a FLIR A320 uncooled long wave band microbolometer focal plane array; and a CEDIP Jade 3 cooled InSb focal plane array in medium wave band. Each one has 320 × 240 sensitive elements.

Examples of results for measurements carried out with the band II cooled IR camera are shown here. The recovered detection and localization of the defects in samples 1 and 2, by using pulse phase thermography analysis, are provided in Figs. 11.9 and 11.10, respectively.

For sample 1, defects of 40 and 30 mm are easily detected, and even the 20-mm diameter defect. The smallest one (diameter 10 mm) is more difficult to detect. For sample 2, the four defects are easily detected and the range of the phase values for each defect is in agreement with the percentage of voids present in each one.

Magnitude maps produce similar results. Furthermore, analysis by using singular value decomposition achieves similar results, but this analysis requires fewer maps to be analyzed for the localization of debonding areas.

11.6.2 Example of Defect Detection and Characterization on a Civil Engineering Specimen in Real Field Conditions

Here, we show several results obtained by analyzing (with various approaches presented in Sects. 11.4 and 11.5) thermal image sequences acquired by active infrared thermography deployed on a real site in outdoor conditions. The specimen of the study is made of CFRP rigid plate glued onto cement concrete submitted to daily seawater effects in a dedicated pool located in an outdoor environment.

Figure 11.11 depicts a view of the inserted defect with no constant depth and shape during specimen construction; the black one is a deposit of pure bitumen and the yellow-white one is a slice of polyurethane (PU) insulating material. The shape and thickness of the defect are variable.

Figure 11.12 (left panel) shows a global view of the specimen on site with the glued CFRP plate on its surface with no protective layer. In Fig. 11.12, the north plate is on the bottom of the picture and the south plate on the top of the image.

Figure 11.12 (right panel) shows a detailed view of the delamination at the angle of the south plate, which occurred after 3 months of seawater solicitation.

A partial view of the outdoor sea pool with a different specimen is depicted in Fig. 11.13 (left panel) where also the experimental setup is present. Figure 11.13 shows the illuminated surface during optical heating.

The specimen was thermally solicited by two halogen spotlights of 500 W each. The distance between the specimen and the spot was 70 cm with an angle of 45°. The IR camera was viewing the specimen with a small angle from the normal to the specimen surface at a distance of 1.3 m. Thermal excitation was set to around 60 s.

Fig. 11.11 View of the defects insertion during building

Fig. 11.12 View of realized specimen on site (*Left panel*) – Detailed view at plate level

Fig. 11.13 View of outdoor test site with an active infrared (IR) test bench over the specimen (*left panel*). Detailed view of the specimen surface during thermal solicitation (*right panel*)

Figures 11.14, 11.15, and 11.16 show the processing results obtained before starting the daily periodic sea tide solicitation over the specimen. The results of the PPT analysis and the direct thermal model approaches are shown; this analysis was applied to the north plate.

The PPT analysis allows us to extract the location of the defect. The application of the thermal model allows us to characterize its apparent thermal effusivity and also its depth. Care must be taken when using the thermal model; the hypothesis of semi-infinite body requires working in a time-limited period respective to the heat diffusion time.

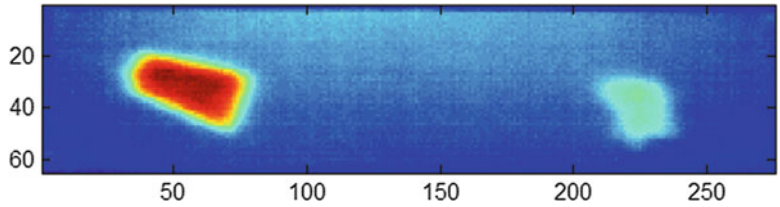

Fig. 11.14 North plate: pulsed phase thermography (PPT) analysis, amplitude map at initial state (t_0)

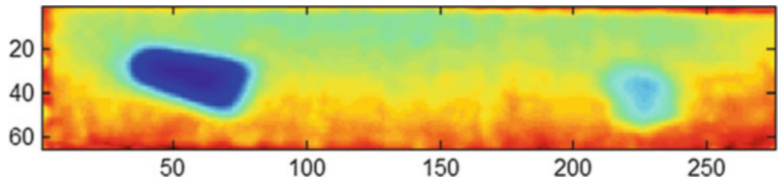

Fig. 11.15 North plate: direct semi-infinite model. Effusivity minima map at initial state (t_0)

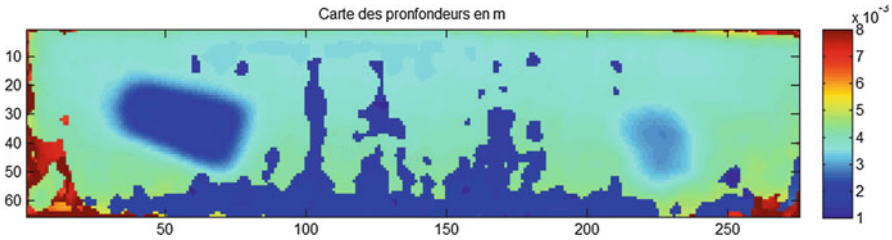

Fig. 11.16 North plate: direct semi-infinite model; depth map at initial state (t_0)

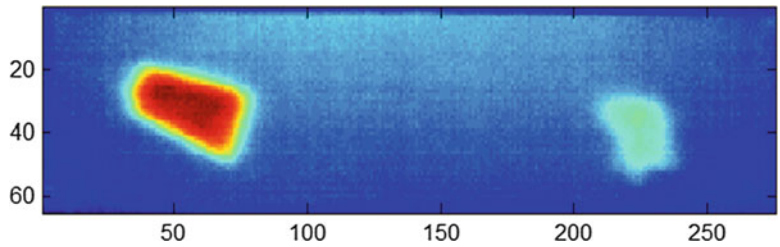

Fig. 11.17 North plate: PPT analysis, amplitude map at t_0 +3 months

Figures 11.17 and 11.18 show results obtained after 3 months of sea water solicitation without protective layer on the surface of the plates.

The PPT analysis allows to better reconstruct the shape of defect in that case. Only the PCT is able to help us to detect the initiation of a delamination, which can

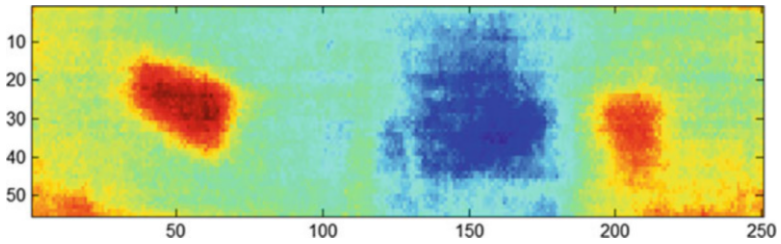

Fig. 11.18 North plate: PCT analysis, EOF 4 map at t_0 +3 months

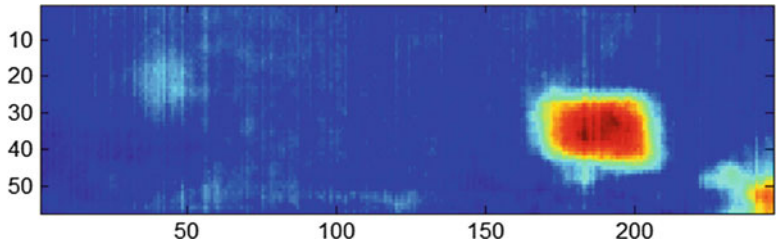

Fig. 11.19 South plate: PPT analysis, amplitude map at t_0 +3 months

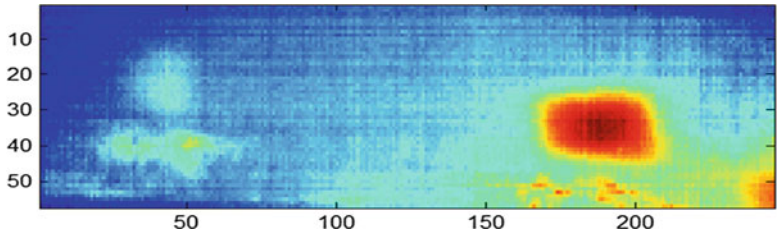

Fig. 11.20 South plate: PPT analysis, phase map at t_0 +3 months

be observed on right bottom corner on EOF map. When the delamination becomes more pronounced, as it is the case for the South plate after 3 months (see Figs. 11.19 and 11.20), PPT analysis is also able to detect the problem.

Both the phase and amplitude map allow us to observe the presence of the bitumen defect (on the left); however, its signature is thinner than the one observed previously for the north plate. The amplitude map shows also the initiation of the delamination on the corner, and the phase map helps us to follow it longitudinally.

11.7 Conclusion and Perspectives

After a short summary on radiative heat transfer theory, measurements by infrared thermography were introduced and the different features of passive and active IR thermography were highlighted. A generic use case of nondestructive evaluation that produces thermal image sequences was presented, and two analysis approaches were introduced.

The first approach belongs to the signal and image processing domain and is mainly concerned with the detection of the defect area, with limited capability for quantitative characterization of the defect, when they are used on a real object as encountered in cultural heritage. In these experimental test cases, it is difficult to construct calibration protocols.

The second approach belongs to the thermal modeling domain. If efficient and accurate infrared thermography measurements can be obtained, such an analysis approach can lead to more effective defect characterization, paving the way to nondestructive evaluation by the thermal method.

Finally, study cases from laboratory conditions were presented and discussed.

Nondestructive testing by active infrared thermography requires adapting the observation period and the nature of the thermal excitation to the depth of probing according to thermophysical properties of objects. Therefore, in a few configurations, such an approach should be avoided and other nondestructive techniques have to be used. As shown in the chapter, in this volume, presenting experiments at Basento Viaduct (Soldovieri and Dumoulin 2017), some IR analysis techniques introduced here have been used to monitor large-scale structures in outdoor conditions. For the Basento Viaduct study case, efforts have been also carried out to develop an adapted architecture for infrared thermography deployed in outdoor conditions, by accounting for not only the duration of experiments, but also enabling measurement corrections online or offline. This kind of application on large-scale structures in outdoor conditions is currently an open field of research and requires at least to combine informatics with applied thermal (i.e., mechanical) sciences and applied mathematics.

References

Balageas DL, Deom AA, Boscher DM (1987) Characterization and nondestructive testing of carbon-epoxy composites by a pulsed photothermal method. J Mater Eval 45(4):465–466

Cooley JW, Tukey JW (1965) An algorithm for the machine calculation of complex fourier series. Math Comput 19(90):297–301

Dumoulin J, Boucher V (2014) Infrared thermography system for transport infrastructures survey with inline local atmospheric parameter measurements and offline model for radiation attenuation evaluations. J Appl Remote Sens 8:084978-1–084978-19

Dumoulin J, Millan P, Plazanet M (1995) Steady and unsteady wall heat transfer mapping by active infrared thermography in perturbed aerodynamic situations. J Flow Visual Image Process 2:219–236

Dumoulin J, Boucher V, Greffier F (2009) Numerical and experimental evaluation of road infrastructure perception in fog and/or night conditions using infrared and photometric vision systems. In: SPIE proceedings of the 7543, infrared spaceborne remote sensing and instrumentation, XVII conference, San Diego

Dumoulin J, Ibos L, Ibarra-Castanedo C, Mazioud A, Marchetti M, Maldague X, Bendada A (2010) Active infrared thermography applied to defect detection and characterization on asphalt pavement samples: comparison between experiments and numerical simulations. J Modern Optics, Special Issue on Advanced Infrared Technology and Applications 57(18):1759–1769

Dumoulin J, Ibos L, Mazioud A, Marchetti M (2011) Detection of non emergent defects in asphalt pavement samples by long pulse and pulse phase infrared thermography. Eur J Environ Civil Eng, Special issue on Non Destructive Testing in Civil Engineering 15(4):557–574

Gaussorgues G (1989) La thermographie infrarouge: principes-technologies-applications, 3e édition, Technique et Documentation, Lavoisier

Ibarra-Castanedo C (2005) Quantitative subsurface defect evaluation by pulsed phase thermography: depth retrieval with the phase. PhD thesis Laval University, Quebec, Canada

Maldague XPV (2001) Theory and practice of infrared technology for non-destructive testing. John Wiley & Sons Inc

Rajic N (2002) Principal component thermography for flaw contrast enhancement and flaw depth characterisation in composite structures. Composite Struct 58:521–528

Siegel R, Howell J (2002) Thermal radiation heat transfer, 4th edn. Taylor and Francis, New York

Soldovieri F, Dumoulin J (2017) Integrated monitoring at a modern architectural masterpiece: the case of Viaduct Basento in Potenza. In: Masini N, Soldovieri F (eds) Sensing the past. Geoscience and sensing technologies for cultural heritage. Springer, Cham, pp 499–514, chapter 25

Valluzzi MR, Grinzato E, Pellegrino C, Modena C (2009) IR thermography for interface analysis of FRP laminates externally bonded to RC beams. Mater Struct 42:25–34

Vavilov V (1992) Transient thermal NDT: conception in formulae. In: Proceedings of QIRT 92, Paris, pp 229–234

Chapter 12
Investigating Surficial Alterations of Natural Stone by Ultrasonic Surface Measurements

Thomas Meier, Michael Auras, Moritz Fehr, Daniel Köhn, Luigia Cristiano, Robert Sobott, Ilaria Mosca, Hans Ettl, Felix Eckel, Tim Steinkraus, Ercan Erkul, Detlef Schulte-Kortnack, Karin Sigloch, Filiz Bilgili, Elena Di Gioia, and Claudio Parisi Presicce

Abstract The surface of buildings and monuments is essential for their visual appearance and their protection. Usually the surface is carefully designed and strongly related to the purpose of the object. Moreover, it is carrying information on the artistic and technical skills of the builders. It is however also prone to weathering and deterioration. A prerequisite for a careful restoration of the surface of historic buildings and monuments is a thorough analysis of surficial alterations. Quantitative measurements support visual inspections, but nondestructive characterization of material properties in the uppermost centimeters of an object represents a challenge. Here, the potential of ultrasonic surface measurements for the quantification of surficial alterations of natural stone is demonstrated by forward

The original version of this chapter was revised. An erratum to this chapter can be found at https://doi.org/10.1007/978-3-319-50518-3_30

T. Meier (✉) • M. Fehr • D. Köhn • L. Cristiano • F. Eckel • T. Steinkraus • E. Erkul
D. Schulte-Kortnack • F. Bilgili
Christian-Albrechts University Kiel, Kiel, Germany
e-mail: meier@geophysik.uni-kiel.de

M. Auras
Insitut für Steinkonservierung e.V, Mainz, Germany

R. Sobott
Labor für Denkmalpflege, Naumburg, Germany

I. Mosca
British Geological Survey, Edinburgh, UK

H. Ettl
Labor für Erforschung und Begutachtung umweltbedingter Gebäudeschäden, Munich, Germany

K. Sigloch
Department of Earth Sciences, Oxford University, Oxford, UK

E. Di Gioia • C. Parisi Presicce
Sovrintendenza Capitolina ai Beni Culturali, Rome, Italy

N. Masini, F. Soldovieri (eds.), *Sensing the Past*, Geotechnologies and the Environment 16, DOI 10.1007/978-3-319-50518-3_12

modeling, laboratory tests, and case studies. The fundamental Rayleigh mode is shown to dominate the waveform in the case of surface measurements. It is sensitive to changes in the shear wave velocity with depth and in anelastic damping of shear wave propagation. We report on ultrasonic surface measurements at facades made of marble (Neptungrotte, Park Sanssouci, Potsdam), sandstone (Porta Nigra, Trier), and tuff (Campidoglio, Rome). Average Rayleigh wave velocities are roughly proportional to measured P-wave velocities and are related to the overall state of the object in the uppermost centimeters. Rayleigh wave group velocities indicate changes in the material properties with depth, and waveform inversions allow for estimating depth profiles of velocity and damping of shear waves. The strong variability of weathering of natural stone is illustrated.

Keywords Cultural heritage • Weathering • Marble • Sandstone • Tuff • Non-destructive testing • Ultrasonic measurements

12.1 Introduction

Many buildings and monuments are made of natural stone, and their surfaces are exposed to aggressive agents, such as weather, air pollutants, and microorganisms. In addition, factors such as rising damp, soluble salts, or structural overload force the deterioration of stone. In many cases degradation processes work directly at the stone's surface or in small zones below the surface. In the initial stage, deterioration starts with minor changes without macroscopically visible damage. Therefore, nondestructive investigations of the uppermost centimeters of natural stones are crucial for characterizing surficial alterations, planning conservation measures, and evaluating their success.

Often ultrasonic transmission measurements are applied to detect alterations of natural stone. The velocity of ultrasonic waves depends on the properties of the stone matrix, stone texture, contacts between mineral grains, and pore filling. Caused by weathering, microcracks develop between the initially firmly interconnected mineral grains, the porosity increases, and the mechanical properties (e.g., strength and E-modulus) decrease. Deteriorations may be confined to the uppermost millimeters or may reach deeper levels. These processes may lead to a substantial decrease in seismic velocities down to a variable depth. Seismic velocities may also increase close to the surface because of thin surface films, which may seal and harden the surface. Furthermore, pore spaces may be filled with gypsum or other precipitated minerals, forming a surficial crust. Just beneath a hardened crust the stone fabric can be damaged, leading to low seismic velocities beneath a crust with high velocities. Therefore, changes in seismic velocities with depth are also to be detected by ultrasonic measurements.

Changes in ultrasonic P-wave velocity caused by weathering have been studied intensively for marble (Köhler 1991; Ruedrich et al. 2013) and have been observed for other types of stone as well (see review by Ahmad et al. 2009 and Siedel et al. 2011). Often transmission measurements are applied and average velocities for the entire path through the stone are determined. However, the detection and analysis of

surficial alterations with ultrasonic transmission measurements is difficult or often impossible. Average velocities are poorly estimated in the vicinity of the object's surface, especially for long paths, and transmission measurements are not applicable if the object is accessible from one side only.

Surficial alterations of natural stones often must be analyzed by ultrasonic surface measurements where both transmitter and receiver are located at the object's surface. An advantage of surface measurements is that beside P-wave velocities, the velocity of another seismic wave (i.e., the Rayleigh wave) can be determined by analyzing the entire waveform. Whereas the P-wave is a body wave that may propagate deeply into the medium, the Rayleigh wave represents a surface wave propagating along the free surface of an object. The Rayleigh wave is mainly sensitive to the shear modulus of the medium via its shear wave velocity. Furthermore, changes in the medium's properties with depth may be detected based on the frequency dependence of the Rayleigh wave propagation.

Here, we first give a brief introduction to the methodological fundamentals of ultrasonic surface measurements. Then, in Sect. 12.2 we report on laboratory experiments with frost-resisting tests and thunder-shower cycling applied to samples of natural stones. In Sect. 12.3 we present examples for the application of ultrasonic surface measurements to the investigation of the uppermost centimeters of facades of historic buildings made of marble (Neptungrotte at Park Sancoussi, Potsdam), sandstone (Porta Nigra, Trier), and tuff (basement of the Campidoglio, Rome). We discuss the reproducibility of ultrasonic surface measurements and their sensitivity to water saturation for measurements at the Porta Nigra. Results of ultrasonic surface measurements are also compared to destructive drilling experiments, and we show the effect of treatment with silicic acid ester on the seismic velocities.

12.2 Method

The recording of ultrasonic waveforms in the field requires a flexible, simple, and accurate acquisition geometry. In the case of ultrasonic surface measurements, a fixed vertical point source with a broadband, impulsive wavelet radiates an ultrasonic wavefield, which is recorded at discrete points along a 15- to 30-cm-long profile (Fig. 12.1) using a specifically designed coupling device. Measurements are performed in a frequency range between 10 and 300 kHz using a piezoelectric transducer and receiver by Geotron Elektronik Pirna. No couplant, such as oil, gel, or glue, is used to increase the coupling between source and test object. Although not contactless, this approach is nondestructive even on sensitive surfaces and porous media.

As a simple example, Fig. 12.2 shows measurements at the surface of a homogeneous Plexiglas block. The ultrasonic waveforms recorded at different source-receiver offsets are plotted as a function of time. The wavefield is dominated by the Rayleigh wave, propagating with a speed of $V_R = 1280$ m/s (left panel in Fig. 12.2). Also, the P-wave is observed. It is faster ($V_P = 2700$ m/s), but has a significantly weaker amplitude compared to the Rayleigh wave (right panel in Fig. 12.2).

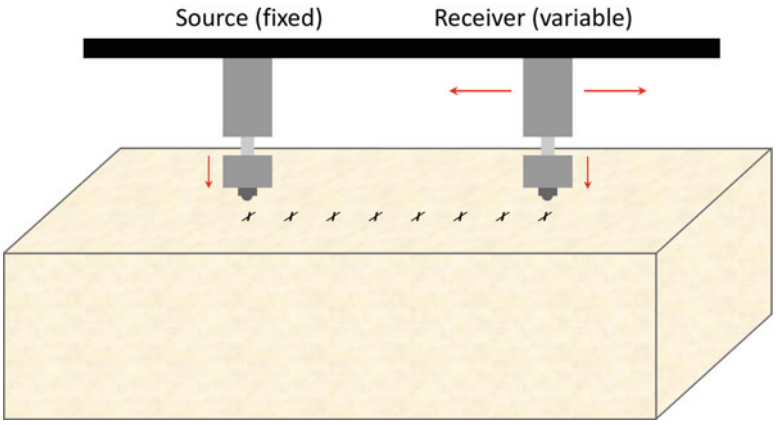

Fig. 12.1 Acquisition geometry of ultrasonic surface measurements. The position of the source is kept fixed, while the receiver position is varied such that the source–receiver distance is increasing stepwise along a profile on the surface

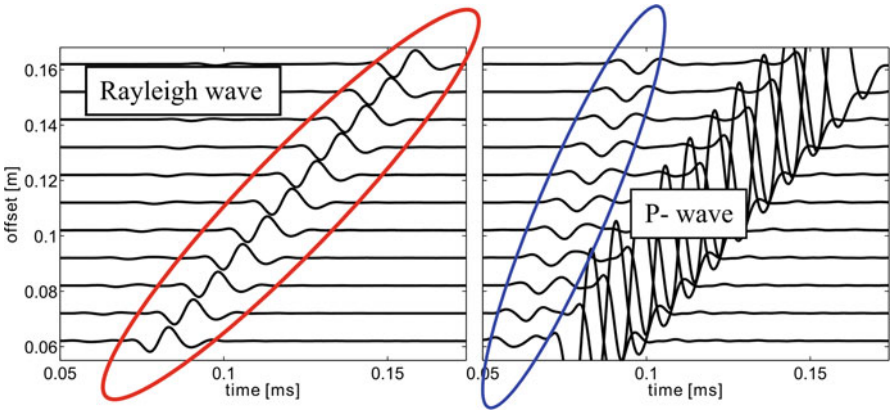

Fig. 12.2 Ultrasonic surface measurement for a homogeneous Plexiglas block with Rayleigh wave (*left panel*) and P-wave (*right panel*). In the right panel only the scaling of the waveforms is changed to enhance the P-wave, which is barely visible on the *left*

To illustrate the main properties of the expected ultrasonic waveforms and their sensitivity to alterations of the stones' properties with depth, a series of synthetic forward calculations is performed. Figure 12.3 shows the considered models, which consist of a surficial layer with gradual changes in seismic velocities with depth and a homogeneous half-space below. Ultrasonic waveforms are calculated for two different models: one with an increase in seismic velocities with depth and another with a decrease in the seismic velocities with depth. To analyze the sensitivity of the Rayleigh waveform on depth-dependent changes in material properties, the thickness of the surficial layer is varied stepwise from 0.1 to 30 mm. The synthetic waveforms are calculated using GEMINI-II (Dalkolmo 1993; Friederich

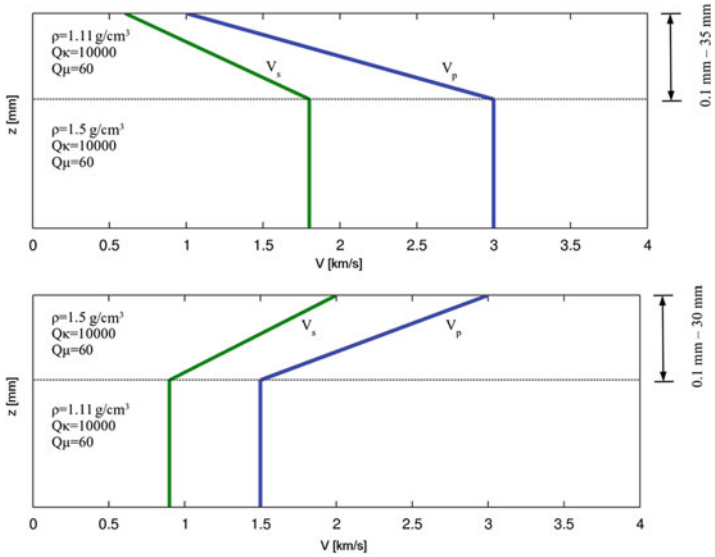

Fig. 12.3 Models for synthetic forward calculations of ultrasonic waveforms. Two models with different gradual changes in seismic velocities with depth are considered. The first model (*upper panel*) shows a linear increase of seismic velocities with depth, the second one (*lower panel*) a decrease with depth. S-wave velocities are shown in *green* and P-wave velocities in *blue*. Density and Q-values in the layer and half-space are assumed to be constant

and Dalkolmo 1995), which directly evaluates Green's functions for isotropic, viscoelastic one-dimensional (1D) media.

For each layer thickness the resulting synthetic waveform is plotted over recording time for a fixed source–receiver distance of 100 mm (Fig. 12.4). Each line of the images corresponds to a synthetic waveform for another layer thickness with color-coded amplitude (positive amplitudes are denoted in red, negative amplitudes in blue). The waveforms are plotted as a function of recording time (x-axis) and the thickness of the surficial layer (y-axis). As in the case of the recorded wavefield from the homogenous Plexiglas block, the wavefield is dominated by the Rayleigh wave whereas the P-wave is not visible. Changes in the waveform as a function of the layer thickness show the depth sensitivity of the Rayleigh waveform. In Fig. 12.4 it is clear that in the considered frequency range the Rayleigh waveform is highly sensitive to changes in the layer thickness between about 2 and 3 cm. Furthermore, the waveforms are very different for the two models, which means it is possible to detect an increase as well as a decrease in the seismic velocities with depth using ultrasonic surface measurements. More specifically, in case of model 1 (left panel in Fig. 12.3, upper panel in Fig. 12.4), for small thicknesses of the surficial layer the Rayleigh wave is fast, whereas with increasing thickness of the slow surficial layer the waveform is spreading progressively over time. The largest amplitudes at the end of the waveform represent an Airy phase of the fundamental Rayleigh mode. In front of it, the influence of higher modes becomes visible. In contrast, for model 2

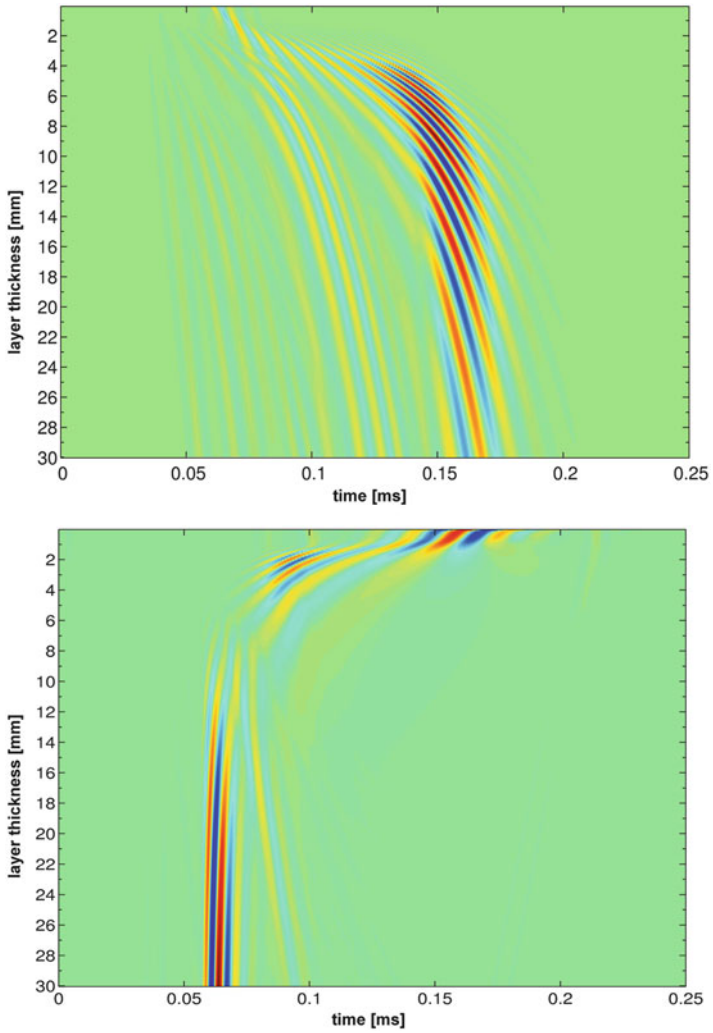

Fig. 12.4 Synthetic ultrasonic waveforms for the two models shown in Fig. 12.3. Amplitudes of the waveforms are color coded: positive amplitudes are shown in *red*, whereas negative amplitudes are shown in *blue*. The waveforms are depicted as a function of recording time (*x*-axis) and layer thickness (*y*-axis) for a fixed source–receiver distance of 10 cm. They are normalized to their absolute maximum amplitude. On the *above*, waveforms are shown for a gradual increase of the velocities with depth. On the *below*, waveforms are shown for a decrease of velocities with depth. See text for further explanations

(right panel in Fig. 12.3, lower panel in Fig. 12.4) the waveform is dominated by a rather simple waveform of the fundamental mode that is slower for smaller thicknesses of the fast layer than for larger thicknesses. Note the dispersion in the waveform with higher frequencies being faster than lower frequencies (thicknesses

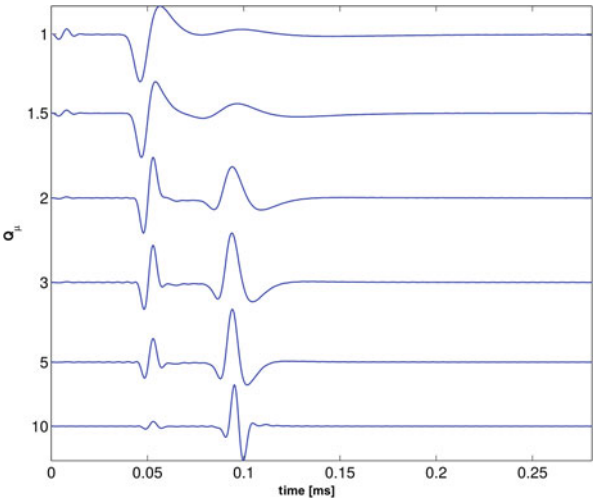

Fig. 12.5 Variability of synthetic ultrasonic waveforms in dependence of the attenuation of seismic waves. Different Q_μ values of a homogeneous half-space model are considered (y-axis). The source–receiver distance is fixed at 120 mm

between 2 and 10 mm in the lower panel in Fig. 12.4). This kind of dispersion is called anomalous dispersion.

The damping of seismic waves in surficial layers has a strong influence on the recorded waveforms. Figure 12.5 shows the influence of the quality factor Q_μ for values ranging from 10 to 1 on synthetic waveforms of a half-space model. The quality factor Q_μ is a measure for the damping of S-waves caused by anelastic deformation. For low-quality factors, indicating strong damping, high frequencies are strongly attenuated (Fig. 12.5). In Fig. 12.5, all seismograms are normalized by their respective maximum amplitude. For low Q_μ values between 1 and 2, the P-wave at 0.05 ms dominates the seismogram, whereas the Rayleigh wave is very weak and contains only low frequencies. Furthermore, the Rayleigh wave is strongly dispersive. For Q_μ larger than two, the Rayleigh wave amplitude increases, compared to the P-wave amplitude, higher frequencies are less attenuated, and the dispersion of the Rayleigh waveform decreases. Because the damping of seismic waves is influencing the recorded waveforms significantly, inversions of waveforms must be carried out for both the velocities and the damping of seismic waves.

In conclusion, the synthetic data examples in Figs. 12.4 and 12.5 show the significant impact of surficial structures and their physical properties on recorded ultrasonic waveforms. This evidence implies that crucial information about the surficial structures can be derived from ultrasonic surface measurements.

12.3 Laboratory Experiments

To understand changes in seismic velocities caused by weathering, ultrasonic surface measurements were performed before and after a first and second phase of artificial weathering of natural stone samples. Four samples were investigated:

Table 12.1 Properties of the samples according to Grimm (1990), INSK (n.d.), Simon (2001), and unpublished data

	Marble	Sandstone (Medard)	Sandstone (Schweinstal)	Tuff
Provenance	Carrara, Italy	Medard, Germany	Krickenbach, Germany	Weibern, Germany
Stratigraphy	Jurassic, Lias	Permian, Rotliegend	Triassic, Buntsandstein	Quarternary, Pleistocene
Macroscopic description	Homogeneous, fine-grained, white with irregular grayish veining	Yellowish, fine- to middle grained, lithic arenite, cement of clay minerals, iron hydroxides and silica	Brownish-red, middle grained lithic arenite, cement of silica and kaolinite	Yellowish tuff of phonolitic composition, consisting of a fine-grained matrix and coarse components (pumice, intraclasts, xenoclasts)
Bulk density (g/cm^3)	2.71	2.17	2.12	1.37
Porosity (vol %)	0.3	19	20	46
Compressive strength (N/mm^2)	133	30	59	15

marble, two sandstone samples, and tuff (Table 12.1). The size of the samples was 40 cm × 20 cm × 20 cm. The first weathering phase consisted of 50 cycles of thundershower simulations (DIN EN 13687–2) and 47 frost resistance cycles (freezing + thawing; DIN EN 12371). In the second phase, again 40 cycles of thundershower simulations and 47 frost resistance tests were carried out. In the last seven tests the freezing was performed under water saturation to simulate even stronger weathering.

In each cycle of the thundershower simulation, the surface of the samples had been heated to 65 °C for 7 h and 45 min by infrared lamps. Then, the surface was cooled for 15 min by sprinkling with water (water temperature: 12 °C). In each freezing and thawing cycle the samples were at first saturated by water at a temperature of 20 °C for 6 h. Subsequently, the water was drained and the samples were cooled completely to −20 °C.

Figure 12.6 shows an example of ultrasonic surface measurements recorded at the marble sample before weathering and after the second phase of weathering. Note the high quality of the waveforms and the strong change in the average Rayleigh wave velocity, which drops by about 50%, suggesting severe alterations in the properties of the rock matrix. Nevertheless, also after weathering clear and simple waveforms are recorded and the average Rayleigh wave velocity is straightforward to determine. Later arrivals in Fig. 12.6 are Rayleigh waves reflected at the edges of the sample. By changing the scaling, the P-wave arriving before the Rayleigh

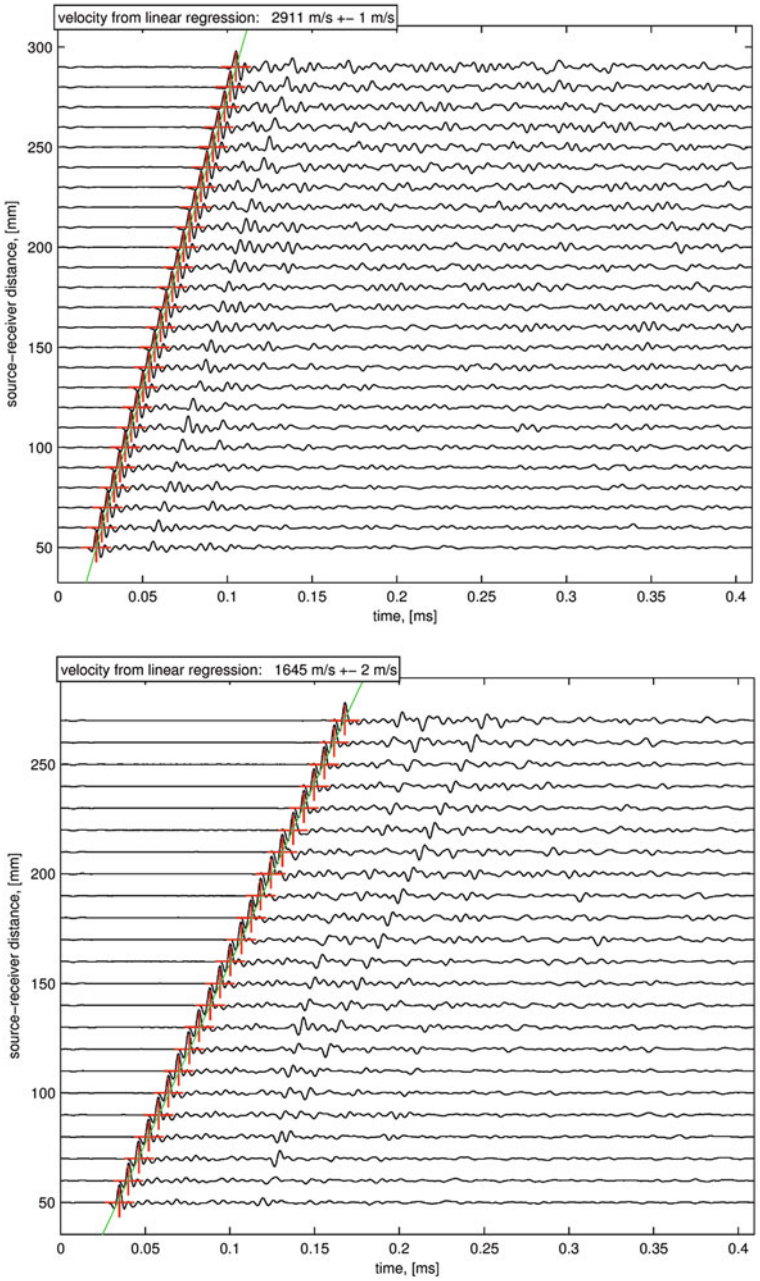

Fig. 12.6 Waveforms along a profile recorded at the marble surface before (*above*) and after (*below*) weathering. *Red crosses* mark the arrival of the Rayleigh wave. Average Rayleigh wave velocities are given in the boxes on the *above top*. Note the strong reduction in the average velocity caused by weathering. Comparison of average P-wave and Rayleigh wave velocities from surface measurements at stone samples

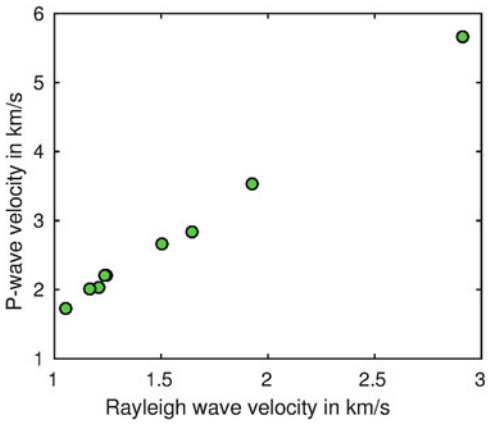

Fig. 12.7 Comparison of average P-wave and Rayleigh wave velocities from surface measurements at stone samples

becomes visible, and in many cases P-wave velocities may also be determined using surface measurements. Figure 12.7 shows a comparison between P-wave and Rayleigh wave velocities measured at the surface of the four samples before and after the first and second phases of weathering. Clearly, there is a strong correlation between average P- and Rayleigh wave velocities. The P-wave velocity is enlarged compared to the Rayleigh wave velocity by a factor of about 1.9, as expected for a homogeneous half-space with a Poisson ratio of 0.25; that means Rayleigh waves are well suited to characterize alterations of natural stone.

It is often sufficient to determine average Rayleigh wave velocities. However, the frequency dependence of the Rayleigh wave velocity, called dispersion, yields additional information. In Fig. 12.8, the Rayleigh wave group velocity is shown as a function of frequency. Group velocities are determined by time–frequency analysis of the Rayleigh waveform (Meier et al. 2004) for each source–receiver distance and then averaged along the profiles (Auras et al. 2015). As a rule of thumb, the Rayleigh wave at 200 kHz is sensitive to properties of the outermost millimeters of the medium. At 100 kHz it is mainly sensitive to depths of about 0.5 cm and at 50 kHz to depths of about 1 cm, meaning that higher frequencies are sensitive to shallower depths, whereas lower frequencies are sensitive to greater depths.

Major differences in the response to weathering become clear. After the first phase of weathering, Rayleigh wave velocities have already decreased strongly for marble. After the second phase, velocities reduce further but only slightly, indicating changes in the velocity are nonlinear. At the beginning of the exposure to weathering, velocities are strongly reduced, but later they decrease only mildly. In contrast, for sandstone and tuff, changes in the velocities after the first phase are essentially insignificant, suggesting that these stones are strongly resistant to weathering. After the second phase, however, changes in the velocities are significant. In addition, Fig. 12.8 reveals another remarkable difference between the rock samples. For marble and tuff, Rayleigh wave velocities do not change strongly with frequency. In contrast, in sandstone, after the second phase of

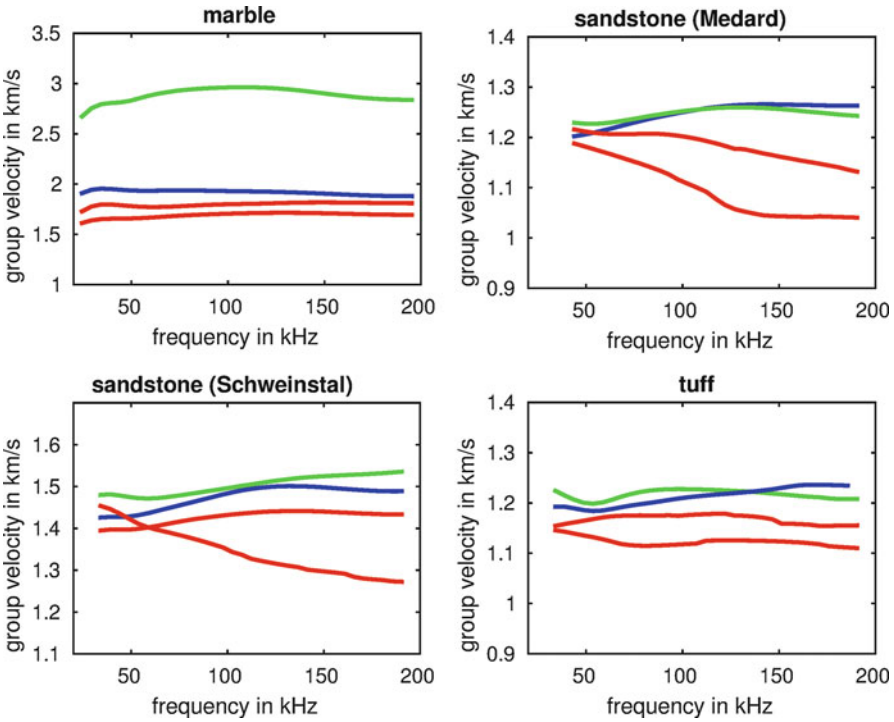

Fig. 12.8 Rayleigh wave group velocities as a function of frequency before weathering (*green*), after the first phase of weathering (*blue*), and after the second phase of weathering (*red*). After the second phase two results for two different profiles are shown to highlight lateral variability in Rayleigh wave velocities

weathering the Rayleigh wave becomes strongly dispersive: the Rayleigh wave group velocity decreases with increasing frequency. This observation indicates surficial deterioration of the sandstones. In contrast, changes are not confined to the outermost layers for marble and tuff. Changes at greater depths are similar to surficial layers as no dispersion is observed. After the second phase of weathering, two profiles were measured for all samples. Results differ significantly between these two measurements, especially for the sandstone samples (Fig. 12.8): thus, lateral variability is stronger for sandstones compared to marble and tuff.

In addition to ultrasonic nondestructive measurements, destructive test techniques were applied to fresh and artificially weathered samples. Results are compared to ultrasonic velocities in Fig. 12.9. For Carrara marble, porosity, ultrasonic velocities, and compressive strength show substantial change from weathering, whereas drilling resistance is affected only to a minor degree. Testing of the compressive strength provided misleading data for Schweinstal sandstone. Microscopic research on thin sections as well as pore radii distribution proved that the increase in compressive strength for Schweinstal sandstone is the result of

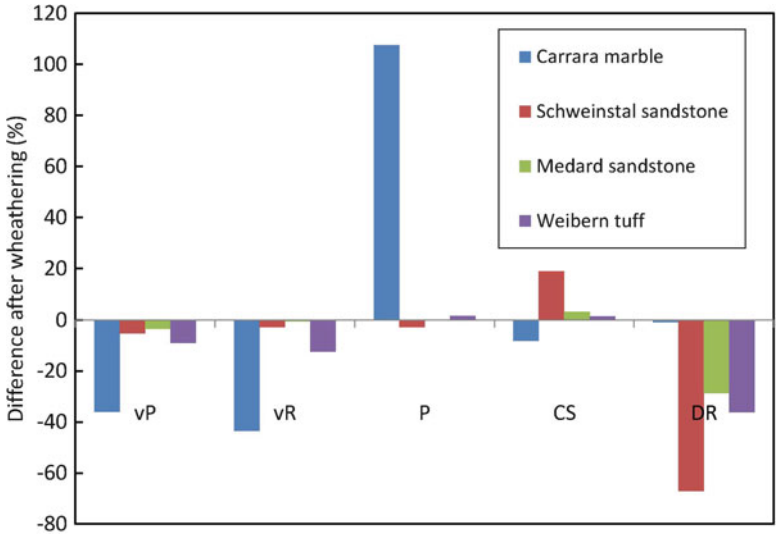

Fig. 12.9 Change in ultrasonic P-wave (*vP*) and average Rayleigh wave (*vR*) velocities by artificial weathering compared to alterations in total porosity (*P*), compressive strength (*CS*), and drilling resistance (*DR*) obtained by destructive testing

small petrographic differences between the fresh and the weathered sample. Apart from this experimental error, weathering of both sandstones shows little impact on porosity, but a remarkable change of drilling resistance. For tuff, porosity and compressive strength change very little by weathering, whereas ultrasonic velocities and drilling resistance are influenced to a higher degree.

These results demonstrate the different sensitivity of the test methods depending on the type of stone. Furthermore, drilling resistance tests and ultrasonic P-wave and Rayleigh wave velocities show a higher sensitivity to surficial alterations caused by weathering. Testing of core samples is important but may be not representative for surficial alterations and their spatial variability.

To analyze the revealed sensitivity of Carrara marble to temperature variations in greater detail, P-wave velocities at a core sample were measured after heating. Three core samples were cyclically heated to a variable maximum temperature and then cooled to 20 °C. In each cycle, the maximum temperature was stepwise increased from 40 ° to 100 °C. In Fig. 12.10, the average P-wave velocity is plotted in dependence on the maximum temperature. The P-wave velocity is already reduced significantly after heating to 40 °C. The higher the maximum temperature, the stronger is the decrease in the P-wave velocity. Subsequent repeated heating to 100 °C continuously lowers the P-wave velocity further.

The reason for this extraordinary response to an exposure to elevated temperature is the high degree of thermal expansion of calcite in the direction of the *c*-axis and the shrinkage perpendicular to the *c*-axis, resulting in the development of thermal stress in the grain fabric. This effect is further enhanced by the structure of Carrara

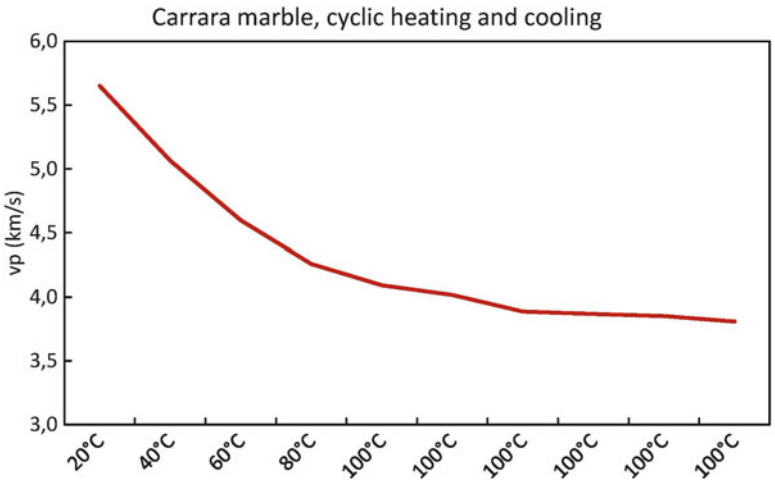

Fig. 12.10 Decline of average P-wave velocity measured at core samples of marble resulting from cyclic heating up to the indicated temperature. See text for further explanations

marble with equigranular calcite grains with low lattice preferred orientation (Weiss et al. 2001; Shushakowa et al. 2013). The thermal shrinkage of calcite crystals leads to the formation of microcracks along the crystal interfaces. These microcracks impede the wave propagation and cause the decrease of ultrasonic wave velocities.

In conclusion, these experiments show that the alterations caused by weathering are (1) significant; (2) depend strongly on the rock type, being very different for marble, sandstones, and tuff; and (3) may vary spatially on the surface of a sample, especially for sandstone and tuff. Nondestructive ultrasonic surface measurements yield valuable information on surficial alterations in the stone properties caused by weathering. Variations of the stone properties with depth may be detected by analyzing the frequency dependence of the Rayleigh wave propagation.

12.4 Application to Neptungrotte, Park Sanssouci, Potsdam (Marble)

In this section we describe the application of ultrasonic surface measurements to nondestructive testing of facades made of marble at the Neptungrotte in Park Sanssouci (Potsdam, Germany; Fig. 12.11). The grotto was built in in the eastern part of the Park of Sanssouci from 1751 to 1757 according to plans by Georg Wenzeslaus von Knobelsdorff. The name is derived from a larger than life size marble sculpture of Neptune with his trident crowning the attic with two naiads and tritons. The sculptures were made by Georg Franz Ebenhech and Johann Peter Benckert. The structure was built of bricks and decorated with ornaments (attic,

Fig. 12.11 Neptungrotte in Park Sanssouci, Potsdam (Photograph published with permission by Stiftung Preussische Schlösser und Gärten Berlin-Brandenburg)

cornice, porch and oculi frames, basins, columns) of Silesian (Kauffunger) and Italian (Carrara) marble. The marble parts exhibit typical forms of damage such as sanding, spalling, and fracturing. A characteristic weathering feature on marble surfaces is the formation of a dark gypsum layer (crust). After many cyclic changes of temperature and humidity, this crust is detached from the marble in response to differences in the hygric and thermal dilatation of the surface layer and substrate. The calcium needed for the formation of gypsum is derived from the rock-forming mineral of marble, calcite, and the dissolution of calcite on grain boundaries leads to a weakening of the calcite fabric under the gypsum layer. Once the dark gypsum layer is cracked or gone white sucrosic, strongly sanding marble emerges. This kind of weathering is typical for marbles of the Carrara type. The Kauffunger marble, which by definition is not a proper marble but a limestone, displays distinctly different weathering features. This limestone was subjected to tectonic stress and is marked by many stylolites and closed fractures acting as weak spots in the rock fabric. Therefore, the decay of this rock is caused by fracturing and shearing of small pieces.

To assess the degree of weathering, the two basic marble types were investigated in situ by transmission ultrasonic measurements in 1998 (Köhler 1998, Sobott 2002) and in 2014 (Sobott 2014). Basic information pertaining to the mechanical state of a rock can be gleaned from the P-wave travel-time diagram, the P-wave amplitude, and the frequency spectrum. The first was evaluated for all measurements while the amplitude was only interpreted if the source and receiver could be fixed to the surface under reproducible conditions. Most of the P-wave velocities of Carrara

marble were in the range of 1.5–4.5 km/s and those for Kauffunger marble in the range of 2.5–5.5 km/s, respectively. The data interpretation followed the principles expounded by Siegesmund et al. (1997), Ettl and Sobott (1999), and Fleischer (2002). The interpretation of on-site data was supported by laboratory data gained from drill cores. A significant change of P-wave velocities within 16 years could not be detected. The interpretation of data for the Kauffunger marble eludes the rather simple relationship between P-wave velocity and porosity as a weathering indicator.

In 2014, surface measurements were performed at 46 profiles at representative locations of the facade. In all cases the data quality is high, allowing the determination of profile-average Rayleigh wave velocities. Examples of recorded waveforms are shown in Figs. 12.12 and 12.13. Average P-wave velocities were determined for 28 profiles. As known from P-wave transmission measurements and in agreement with laboratory tests (Sect. 12.3), seismic velocities in marble may show a remarkable variability. Kauffunger marble shows average Rayleigh wave velocities between 2.68 and 2.99 km/s. Average velocities of Carrara marble may be much lower, varying between 0.67 and 2.25 km/s. Average Rayleigh wave velocities of Carrara marble treated with silicic ester increase to 2.35–2.8 km/s.

Figure 12.14 shows a linear correlation between the measured P-wave and Rayleigh wave velocities. However, only in roughly 60% of the profiles are P-wave velocities observable because of their low amplitude. Furthermore, errors in P-wave velocity are much larger compared to errors in Rayleigh wave velocity because of the lower signal-to-noise ratio. These observations show that Rayleigh wave velocities represent a reliable measure for surficial alterations. The alterations are very different for Kauffunger and Carrara marble. Although cracks are often observed in Kauffunger marble, deteriorations in Carrara marble may be significant, as indicated by a reduction of average Rayleigh wave velocities down to 30%. The effect of treatment can also be measured. In general, the velocities after treatment are larger than in untreated weathered marble.

Although average Rayleigh wave velocities are easy to determine and have proved to represent a useful measure for surficial alterations of marble, the frequency dependence of the Rayleigh wave (dispersion) may yield additional information on variations of alterations with depth. The dispersion is generally low in treated marble, in Kauffunger marble, and in Carrara marble with large average Rayleigh wave velocities. The lack of strong dispersion indicates homogeneity and low variations with depth.

However, on some profiles significant dispersion is present. Full waveform inversions are performed to quantify changes with depth. In Figs. 12.15 and 12.16, results of waveform inversions are shown for the data plotted in Figs. 12.12 and 12.13, respectively. Software tools for the inversion of ultrasonic waveforms for one-dimensional depth profiles have been developed (Forbriger et al. 2014; Meier et al. 2014, 2016). The inversion is performed for a gradual change in S-wave velocity with depth and an average, depth-independent quality factor Q_μ. The incorporation of the quality factor, describing the attenuation of S-waves, is required because of its strong influence on the waveforms (Sect. 12.2), even though the uncertainties in the quality factor may be large. A low-quality factor causes strong damping

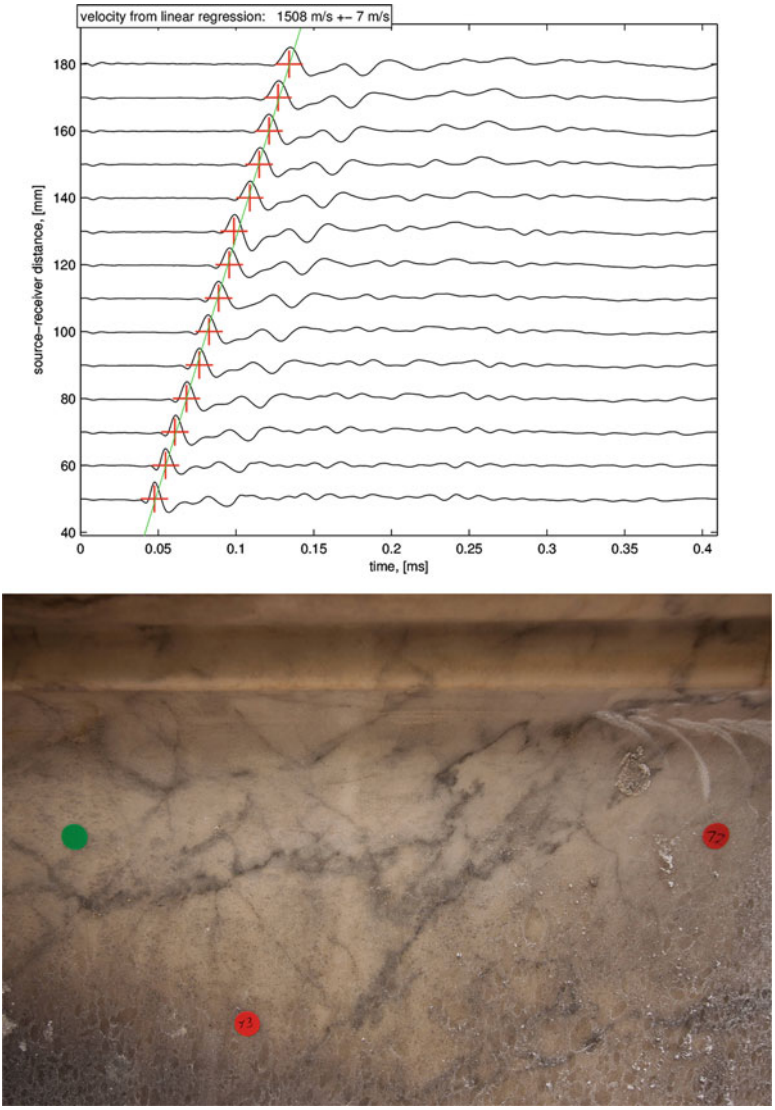

Fig. 12.12 Waveforms along a profile at the surface of the Carrara marble (*above*). *Red crosses* mark the arrival of the direct Rayleigh wave. The average Rayleigh wave velocity is given in the boxes on the *above top*. Location of the profile (*below*). The position of source is indicated by the *red point* to the *right*. (The *red point* below indicates the source position for another profile.) The end of the profile is marked by the *green dot* (Photograph published with permission by Stiftung Preussische Schlösser und Gärten Berlin-Brandenburg)

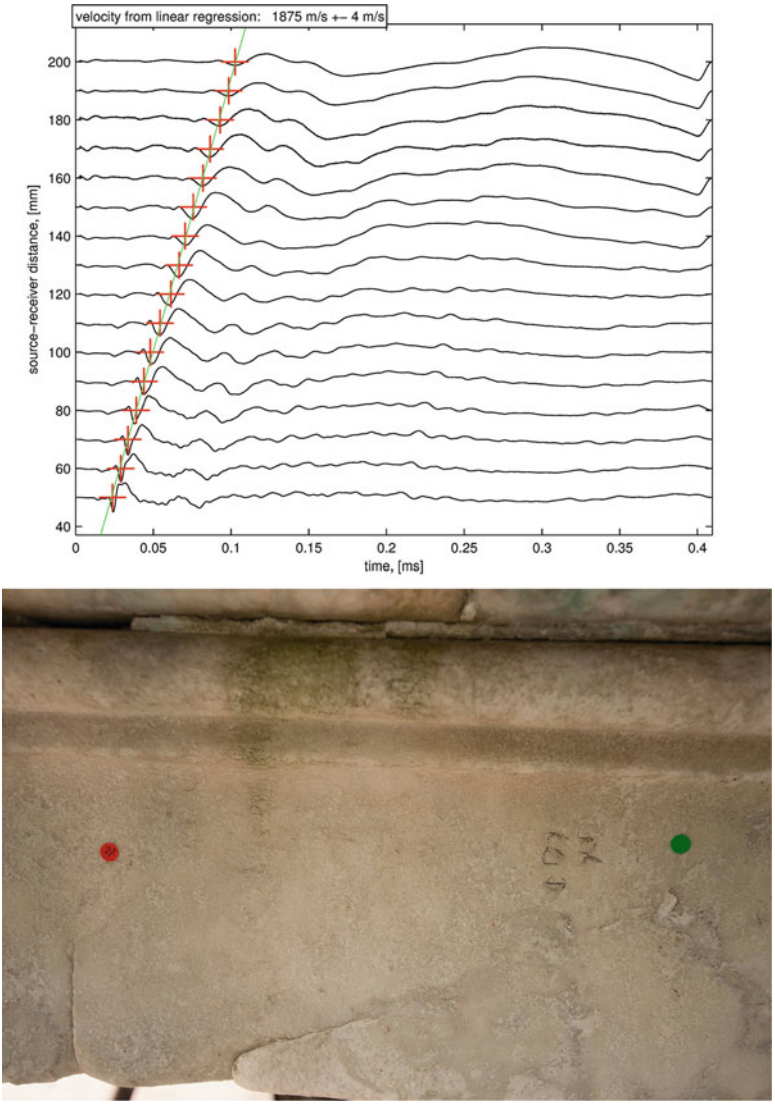

Fig. 12.13 Waveforms along a profile at the surface of the Carrara marble (*above*). *Red crosses* mark the arrival of the Rayleigh wave. The average Rayleigh wave velocity is given in the *boxes* on the *above top*. Location of the profile (*below*). The position of the source is indicated by the *red point*. The end of the profile is marked by the *green dot* (Photograph published with permission by Stiftung Preussische Schlösser und Gärten Berlin-Brandenburg)

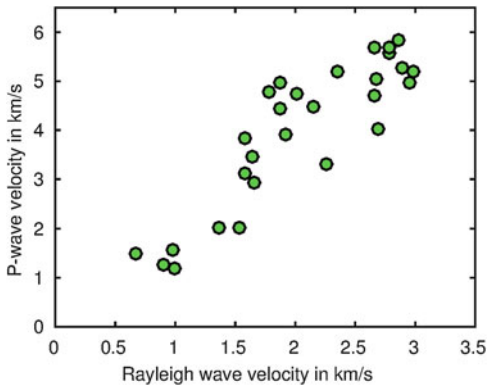

Fig. 12.14 Average P-wave and Rayleigh wave velocities measured at the facade of the Neptungrotte

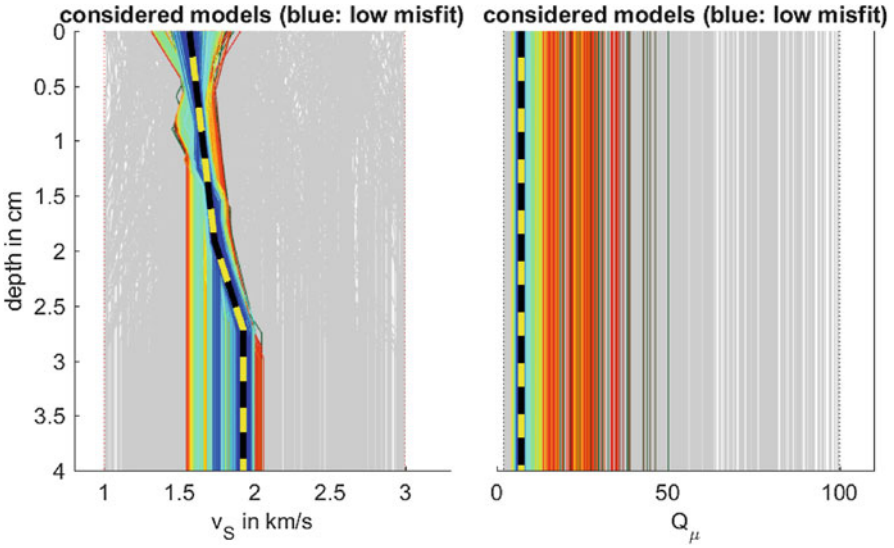

Fig. 12.15 Depth profile of S-wave velocity (*left*) and quality factor (*right*) observed at the Neptungrotte for the profile shown in Fig. 12.12. Acceptable models are plotted in *blue*. The *dashed line* indicates the optimal model. See text for further explanations

of high frequency and a measurable dispersion of the Rayleigh wave. This effect cannot be ignored in the waveform inversion. A grid search algorithm, namely, a particle swarm optimization algorithm, sampling the space of possible values of S-wave velocity and attenuation is applied to detect ambiguities and uncertainties in the model parameters (Steinkraus 2016). In Figs. 12.15 and 12.16, models yielding a low misfit between synthetic and measured waveforms, representing acceptable models, are plotted in blue; green, yellow, red, and gray colors indicate increasing misfit. The optimal model is denoted by a black-yellow *dashed line*.

Often changes with depth are rather small. However, in some cases an increase (Fig. 12.15) or a considerable decrease (Fig. 12.16) of the S-wave velocity with

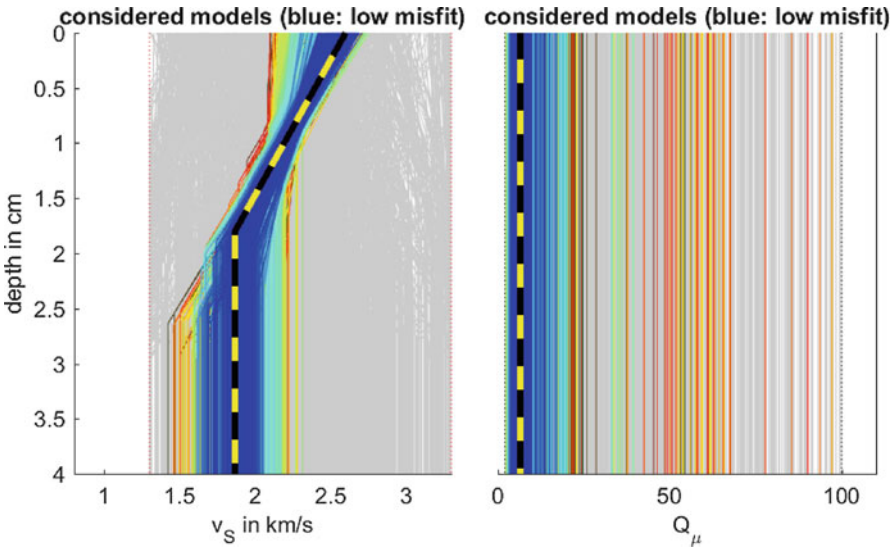

Fig. 12.16 Depth profile of S-wave velocity (*left*) and quality factor (*right*) observed at the Neptungrotte for the profile shown in Fig. 12.13. Acceptable models are plotted in *blue*. The *dashed line* indicates the optimal model. See text for further explanations

depth may be present. The Q_μ values are low (here about 5; Figs. 12.15 and 12.16), which means the damping is strong and is influencing the waveform significantly.

In many cases, the main properties of the waveforms are explained by a one-dimensional model consisting of an S-wave velocity varying with depth and a depth-independent quality factor. This observation confirms the sensitivity of the Rayleigh wave to depth-dependent stone properties. If surface alterations vary laterally along the profile, two-dimensional waveform inversions have to be applied. In this case, the resulting model is a function of depth as well as of the position at the profile (Köhn et al. 2016). Lateral heterogeneity may be detected and quantified. An average one-dimensional model is, however, needed as a starting model for the two-dimensional inversion.

12.5 Application to Porta Nigra, Trier (Sandstone)

Next, we describe the applicability of ultrasonic surface measurements to buildings of sandstone. Whereas the variability of seismic velocities in marble is mainly caused by alterations of the internal structure, fresh sandstones show a high variability in seismic velocities because of varying porosity and composition. As shown in Sect. 12.3, in sandstones seismic velocities may in addition change because of weathering. Because of the natural variability of sandstones, ultrasonic testing should be performed in terms of relative measurements: either weathered and

Fig. 12.17 Porta Nigra in Trier (Germany) (Photograph courtesy of M. Auras)

unweathered sandstones of the same type are compared or changes in the velocity with depth are investigated. The latter is possible if the frequency dependence of the Rayleigh wave propagation (i.e., dispersion) is analyzed. Here, we summarize results obtained by 71 ultrasonic surface measurements at various locations of the weathered facade of the Porta Nigra, a large Roman city gate in Trier (Germany) from the second century (Fig. 12.17).

In the Middle Ages this structure was converted to a church and at the beginning of the nineteenth century reconverted to its original form of a Roman gate (Gose 1969). The Porta Nigra consists of large blocks of a pale yellowish sandstone of local provenance. The name Porta Nigra is known since Medieval times and indicates a very old blackening of the sandstone surface (Sebald 2015). From many other monuments it is known that black crusts on the surface of sandstones can lead to severe damage. Consequentially, most monuments are cleaned in the course of conservation measures. Stone conservation at the Porta Nigra will be necessary in the coming years (Auras 2014). In this context it must be evaluated carefully whether stone cleaning is required to preserve the black color. And hence, detailed information on the causes and implications of the blackening is needed. Thin black surface films seal and harden the surface, gypsum may fill the pore space close to the surface, and the stone fabric just beneath black crusts may be damaged. Ultrasonic

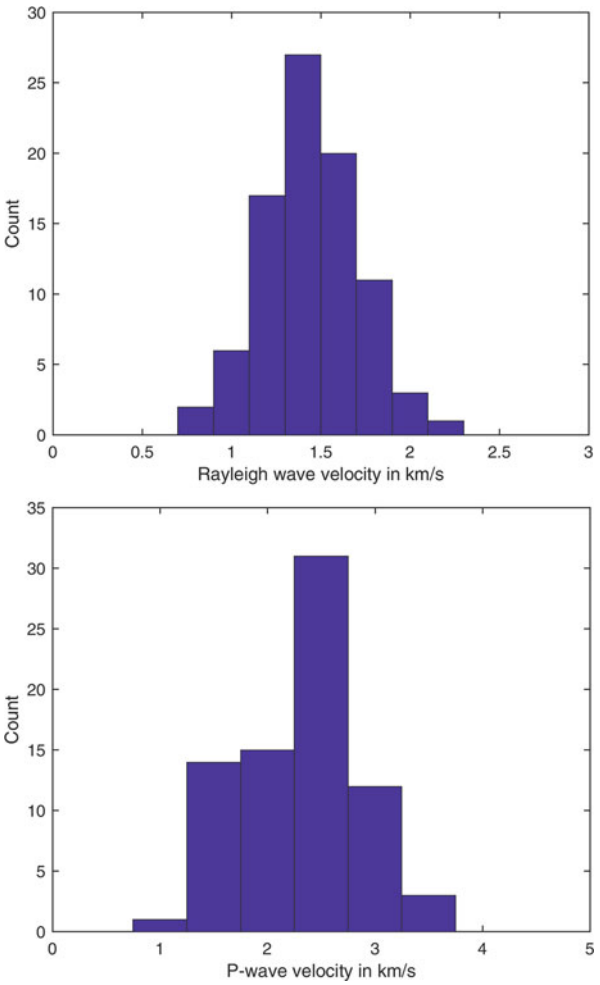

Fig. 12.18 Histograms of average Rayleigh wave velocities (*above*) and P-wave velocities measured at the Porta Nigra

surface measurements were performed on sandstone blocks of Roman and Medieval times that showed representative alterations to investigate surficial properties of the sandstones (Meier et al. 2014).

For all profiles, average Rayleigh wave group velocities were determined. They indicate a remarkable variability of surficial alterations. In Fig. 12.18 are shown histograms of measured Rayleigh and P-wave velocities. For sandstones with sanding parts at the surface, Rayleigh wave group velocities may be as low as 0.7 km/s whereas sandstones with dark crusts are characterized by increased group velocities up to 1.9 km/s. Intact sandstones show group velocities between about 1.3 and 1.5 km/s (Meier et al. 2014), meaning that average Rayleigh wave group velocities may be diminished by as much as 50% or may be enlarged by as much as 30% by weathering. A similar behavior is found for P-wave velocities. Those

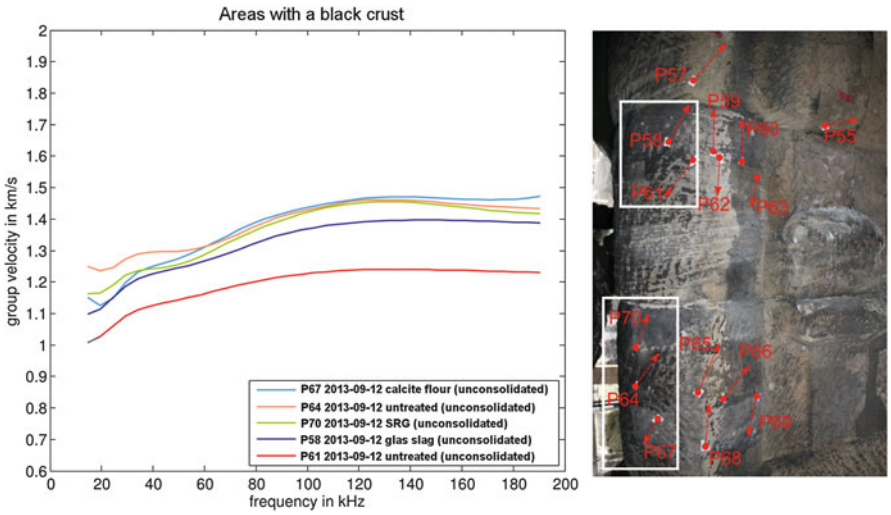

Fig. 12.19 Examples for path-average Rayleigh wave group velocities as a function of frequency (Porta Nigra). The profiles are located in areas with a *black crust* (*white boxes* in the photograph on the *right*). In the case of *black crusts*, Rayleigh wave group velocities show a distinct increase with frequency (*left*) (Photograph courtesy of D. Schulte-Kortnack)

strong variations are easily detectable as the reproducibility of the measurements is rather good. To test the reproducibility, the measurements were repeated at selected locations after 6 months. The resulting average Rayleigh wave group velocities deviate only by about 4%.

In the following we show examples for changes in the Rayleigh wave group velocity with frequency indicating changes of material properties with depth. For profiles at test sites, the Rayleigh wave group velocity was measured between about 20 and 200 kHz by applying an optimized time–frequency analysis to the individual recordings (Meier et al. 2004, 2014). Then, profile average group velocities were determined. Figure 12.19 shows examples of the frequency-dependent Rayleigh wave group velocity for profiles on a black crust. Note the increase of the group velocity with frequency, pointing to an increased density of the outermost layer by a moderate enrichment of gypsum and iron hydroxides in the pore space. The decrease in the group velocities to about 1.0–1.3 km/s at low frequencies indicates a loosened structure in the region below the outermost densified layer.

In Fig. 12.20, results are depicted for a crust composed of gypsum. Rayleigh wave group velocities show an even more pronounced increase with frequency as much as 20% from an almost complete filling of the pore space with gypsum crystals. In contrast, in areas of a sanding surface without a black crust, Rayleigh wave group velocities do not increase with frequency (Fig. 12.21). The velocities remain on a rather low level, indicating a beginning decomposition affecting the whole subsurface area.

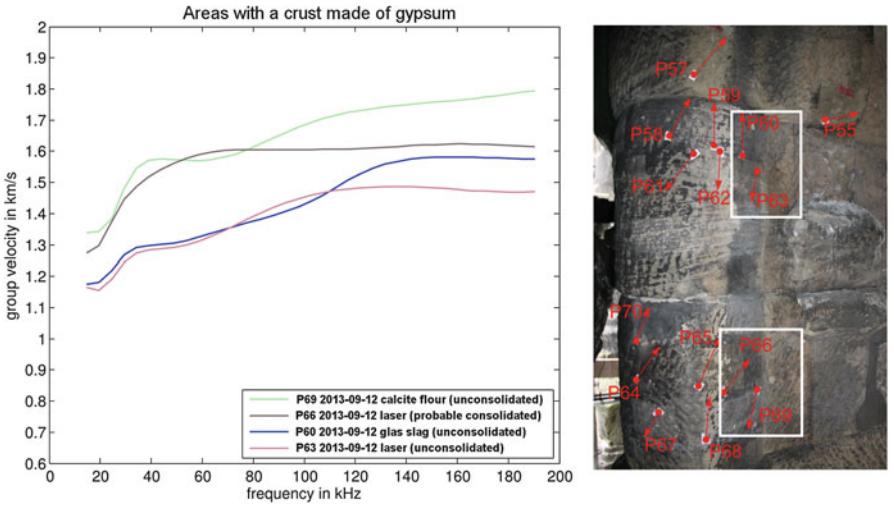

Fig. 12.20 Examples for path-average Rayleigh wave group velocities as a function of frequency (Porta Nigra). The profiles are located in areas with a gypsum crust (*white boxes* in the photograph on the *right*). Rayleigh wave group velocities (*left*) increase more strongly compared to profiles with *black crusts* (Fig. 12.19) (Photograph by D. Schulte-Kortnack)

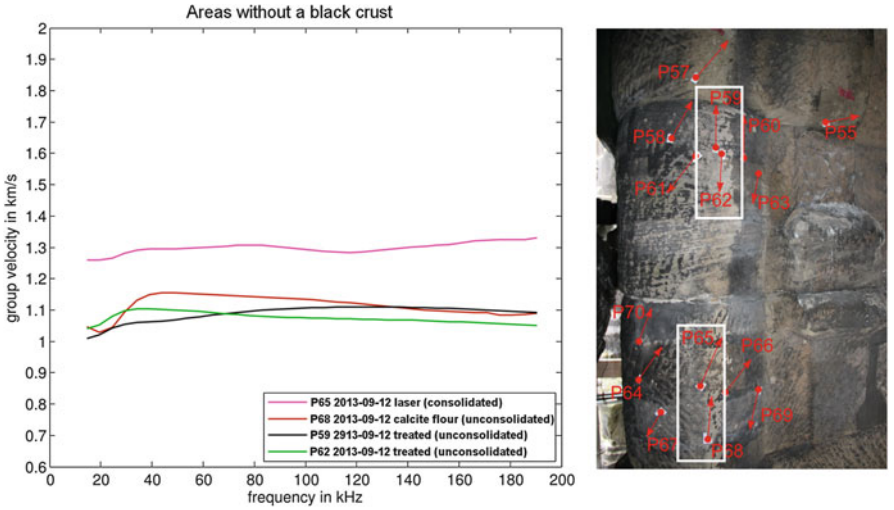

Fig. 12.21 Examples for path-average Rayleigh wave group velocities as a function of frequency (Porta Nigra). The profiles are located in areas without a *black crust* (*white boxes* in the photograph on the *right*). Rayleigh wave group velocities (*left*) do not show any significant increase with frequency (Photograph by D. Schult-Kortnack)

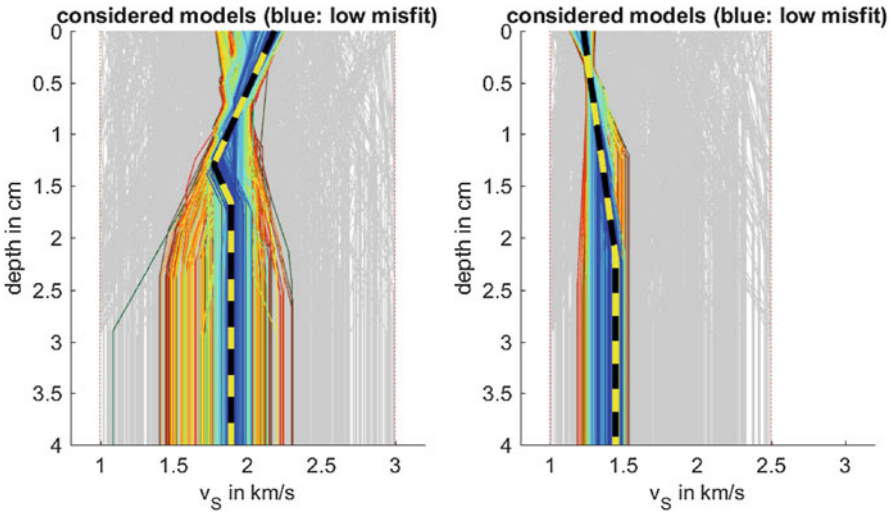

Fig. 12.22 Examples for depth profiles at the Porta Nigra resulting from waveform inversions. *Left*: profile 69 with gypsum crust. *Right*: profile 59 without a crust. All considered models are shown. Acceptable models are plotted in *blue*. The *dashed line* indicates the optimal model

The black crusts and films on the surface of the sandstones of the Porta Nigra are characterized by an increased content of iron oxides and varying portions of gypsum (Auras 2014), modifying the water transport into and out of the sandstone and sealing the surface more or less completely (Ettl 2014). The modification of the hygric, thermal, and mechanical properties of the stone surface can lead to loosening of the grain contacts and initial decomposition below the crusts. From Figs. 12.19, 12.20 and 12.21, it becomes clear that the presence and properties of a crust at the surface and the initial decomposition below the crusts may be detected on sandstones nondestructively by ultrasonic surface measurements. Based on waveform inversions similar to Sect. 12.4, the thickness of the crusts is estimated to vary between a few millimeters and nearly a centimeter (Meier et al. 2014). In Fig. 12.22, an example of a depth profile in a region with a gypsum crust is shown on the left. Note the deterioration indicated by low shear-wave velocities below the crust with increased velocities. For comparison, on the right a depth profile for a sandstone without a crust is shown. Here, the surficial shear-wave velocities are slightly decreased.

For two profiles, measurements were repeated after saturating the sandstones artificially with water. Those tests revealed that the Rayleigh wave propagation is strongly sensitive to water saturation: the damping is increased and the Rayleigh wave velocity may drop by about 20%. Changes in Rayleigh wave velocity from weathering may, however, be significantly larger than changes caused by water saturation. Nevertheless, to ensure the comparability of the measurements, the water saturation of the tested sandstones should be similar to diminish the influence of water saturation. Measurements on wet sandstones should be avoided.

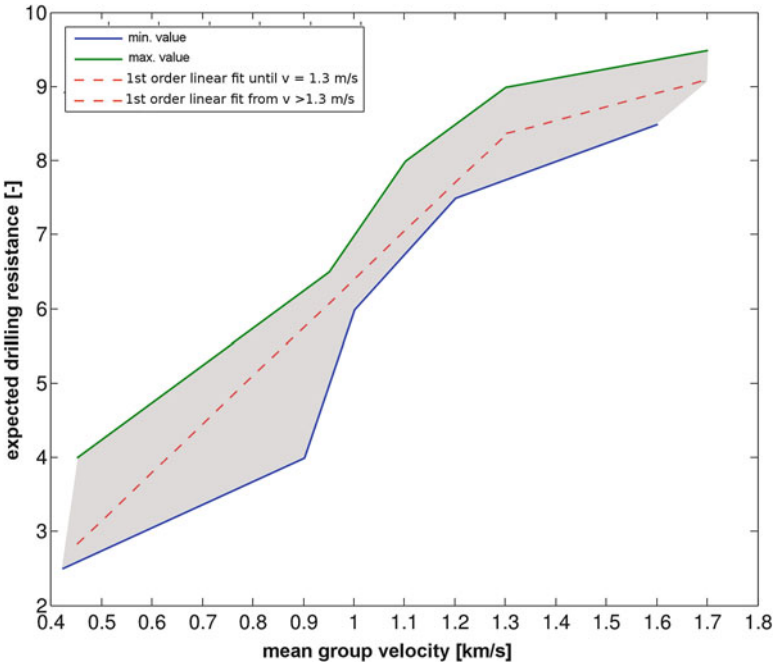

Fig. 12.23 Comparison of minimum (*blue*) and maximum (*green*) hardness obtained by drilling resistance tests with average Rayleigh wave group velocities determined by ultrasonic surface measurements at the Porta Nigra. Note the almost linear empirical relationship between the measurements

Also, the influence of treatment with silicic ester on the Rayleigh wave propagation was tested. Ultrasonic surface measurements in locations with sanding stones were repeated after treatment. The Rayleigh wave velocities increased remarkably, by 20–50%, which shows that the effect and success of the treatment may be quantitatively characterized by ultrasonic surface measurements.

In addition to nondestructive testing, drilling resistance tests were performed close to profiles in the test areas. In Fig. 12.23 average Rayleigh wave group velocities in the frequency range between 30 and 150 kHz are compared to the minimum and the maximum modified drilling hardness obtained by drilling resistance tests (Pfefferkorn 1998) for the depth range between 3 and 15 mm. Both measurements correlate linearly with each other up to a drilling hardness of about 8. Thus, the Rayleigh wave group velocity obtained by nondestructive testing is indeed a measure for the strength of the material. For a drilling hardness larger than about 8, the Rayleigh wave group velocity appears to be a more sensitive measure of changes in the material properties than the drilling resistance as small changes in the hardness are associated with larger changes in the Rayleigh wave group velocity.

12.6 Application to Campidoglio, Rome (Tuff)

In this section we summarize results obtained from ultrasonic surface measurements at the Campidoglio in Rome (Italy) where the most ancient structures are made of tuff. The Campidoglio, or Capitoline Hill, is one of the seven hills in Rome and was the citadel of the earliest Romans. It contains few ancient ground-level ruins because they are almost covered by Medieval and Renaissance palaces (e.g., Capitoline Museums) surrounding the square (La Regina et al. 2007; Aicher 2004; Wallace 2010). On the front slope of Campidoglio, the Roman Forum's main square is closed by the square structure of the Tabularium, the Roman public record office and public archive. Constructed around 78 BC, its name is derived from the tables of bronze containing the laws, that is, the tabulae. Only the foundations of the Tabularium are preserved. The upper floors, where the Roman state archive was hosted, have been replaced by the Medieval Senatorial Palace, characterized by four Medieval towers of different periods. In the Middle Ages, the Tabularium was partly used as storage space for goods and water. The facade of the Tabularium consists mainly of tuff, but there are a few elements of travertine and concrete. It is interesting to note the similarity in the shape of the stone blocks at the Porta Nigra and the Tabularium.

We performed ultrasonic surface measurements at the accessible southeastern part of the Tabularium at the lowermost floor of the Capitoline Museum (Fig. 12.24)

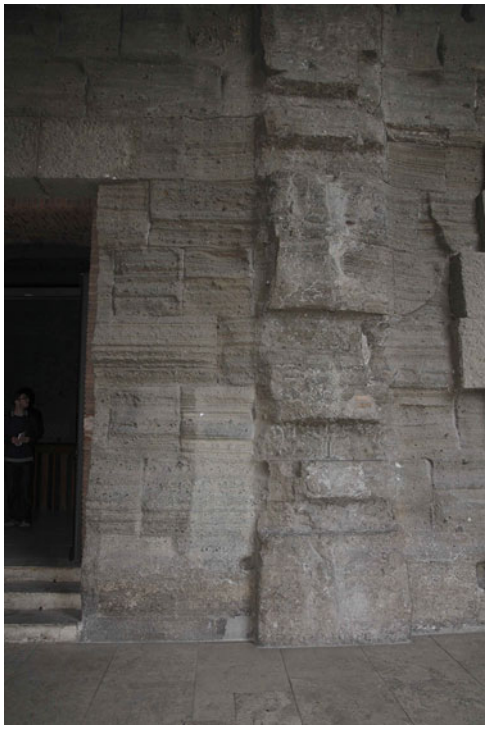

Fig. 12.24 Basement of the Campidoglio made of tuff (Photograph by D. Schulte-Kortnack)

to investigate the state of deterioration of the tuff walls. The reason for this deterioration is its continuous usage, together with weathering: the upper part of its walls at this site is exposed to winds, whereas the lower part of the walls is exposed to a constant humidity.

Surface measurements were performed along six profiles. An example of the recorded waveforms is shown in Fig. 12.25. At all profiles the Rayleigh waves as well as the P-waves are clearly visible. The amount of deterioration is largely variable, as indicated by average Rayleigh and P-wave velocities (Fig. 12.26). Note the strong correlation between the two velocities (Fig. 12.26). The fastest Rayleigh wave velocities are observed at surfaces without colored crusts. Relatively large velocities of about 1.8 km/s are also found at sites with strong topography caused by erosion by wind. Average Rayleigh wave velocities may, however, be variable and strongly reduced in areas with colored crusts. Along a profile at a surface with a brownish, partly sanding crust, a very low average Rayleigh wave velocity of about 1.2 km/s was found (Fig. 12.26). This value corresponds to a reduction of about 30%. The dispersion of the Rayleigh wave is lower compared to sandstone in agreement with the results of the laboratory experiments (Sect. 12.3). This observation hints at relatively deep weathering of the uppermost centimeters. Ultrasonic surface measurements are also applicable to tuff, indicating variable and in a few cases substantial surficial alterations at the Tabularium of the Campidoglio.

12.7 Conclusions

Based on theoretical forward calculations, laboratory measurements and applications to historic buildings, ultrasonic surface measurements are shown to represent a reproducible, highly accurate, nondestructive method to evaluate and quantify surficial alterations of natural stone. Recording of the entire waveform allows for analysis of both first-arriving P-waves and later-arriving Rayleigh waves. The prerequisite for the application of ultrasonic surface measurements is the existence of nearly flat surfaces along profiles about 15 cm to 30 cm in length. These measurements are ideally suited to investigate properties of facades or plane surfaces accessible from one side only. In contrast, classical transmission measurements are to be preferred in case of strongly curved surfaces as in cases of three-dimensional decoration and small objects that are accessible from all sides. Ultrasonic surface measurements in the frequency range between about 10 and 300 kHz allow for analyses of Rayleigh waves sensitive to the S-wave velocity and attenuation in the upper approximately 3 cm of the object under investigation. Rayleigh wave velocities are shown to correlate roughly with P-wave velocities. Rayleigh waves are, however, better to analyze in case of surface measurements because of their larger amplitudes and better signal-to-noise ratio.

Laboratory experiments show that weathering changes seismic velocities in natural stone significantly. A number of interesting results have been obtained. Seismic velocities in natural stone change generally nonlinearly because of continued

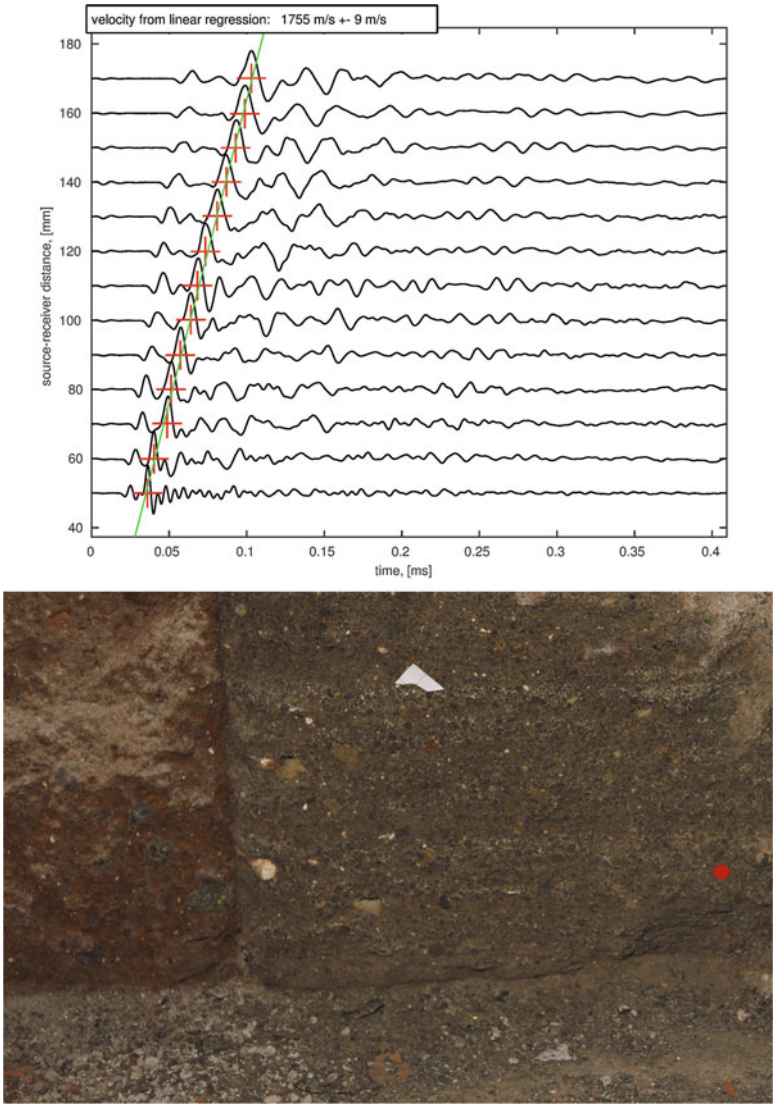

Fig. 12.25 Waveforms along a profile recorded at the surface of the tuff (*above*). *Red crosses* mark the arrival of the Rayleigh wave. The average Rayleigh wave velocity is given in the *boxes* on the *above top*. Also, the P-wave arrival before the Rayleigh wave is visible: its average velocity along the profile is 3340 m/s. Location of the profile (*below*). The position of the source is indicated by the *white paper*. The end of the profile is marked by the *red dot*

application of temperature variations and frost-resisting tests. Temperature variations lead to an immediate and very strong reduction of seismic velocities in Carrara marble. Further exposure to weathering decreases seismic velocities only moderately. Alterations of seismic velocities in Carrara marble penetrate deeply into

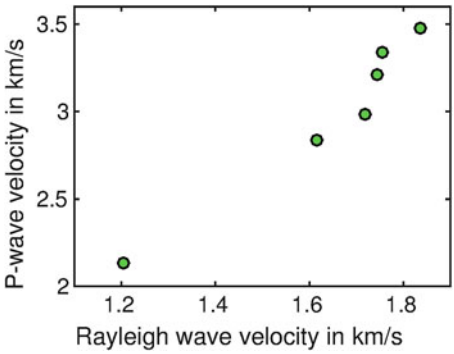

Fig. 12.26 Average P-wave and Rayleigh wave velocities measured at the Tabularium of the Campidoglio

the object. In contrast, alterations in sandstone may be spatially highly variable and are usually confined to outermost layers. A long exposure to weathering is needed before substantial changes in strength are observed in sandstones. Tuff samples may develop cracks, and also in tuff a rather deep penetration of the deterioration after long exposure to weathering is observed.

In addition to laboratory experiments we applied ultrasonic surface measurements to weathered facades of marble, sandstone, and tuff. The measurements proved to be a flexible tool allowing for evaluation of different types of weathering. In all cases high-quality recordings have been obtained. The determination of profile-average Rayleigh wave velocities represents a simple but effective analysis method that neglects, however, the frequency dependence of the Rayleigh wave propagation. The latter may be studied by time–frequency analysis, allowing for the determination of frequency-dependent group velocities and the detection of changes in S-wave velocities with depth. Quantitative depth profiles of S-wave velocity and attenuation may be determined by more sophisticated waveform inversions.

In general a strong variability of surficial alterations is observed. However, subtle alterations are detectable as well. In Carrara marble, strong reductions in seismic velocities by as much as 70% may occur. Seismic velocities at the Neptungrotte may increase or decrease with depth in dependence of the type of weathering. In sandstones, deteriorations as well as a densification in case of black crusts may develop. Seismic velocities in black crusts are enlarged by up to 20%. The thickness of the black crust has been estimated nondestructively at the Porta Nigra. It varies between a few millimeters and about a centimeter. The obtained Rayleigh wave velocities correlate strongly with results of drilling resistance testing and may be reduced by as much as 50%. Interestingly, saturation by water decreases Rayleigh wave velocities moderately and increases its damping strongly. The tuff at the Tabularium of the Campidoglio in Rome shows a considerable variability in surficial alterations and reductions of the velocities by as much as 30%. In addition, the measurements show that the success of treatment with silicic ester may be quantified in marble as well as in sandstone. A significant increase in seismic velocities after the treatment has been observed by ultrasonic surface measurements.

Ultrasonic surface measurements are well suited for nondestructive testing of the surfaces of cultural heritage objects. For about 25 years P-wave transmission measurements have been applied, but the investigation of flat surfaces remains a challenge. Ultrasonic surface measurements have the potential to become a standard test procedure for stone objects because they allow for evaluating surficial alterations including their variability with depth nondestructively and quantitatively.

Acknowledgments We thank Dr. Dorsemagen (Stiftung Preussische Gärten und Schlösser Berlin-Brandenburg) for the permission to carry out measurements at the Neptungrotte in Park Sanssouci, Potsdam. We thank the Landesbetrieb Liegenschafts- und Baubetreuung Trier for support of the measurements at the Porta Nigra. We thank the conservator L. Pelagalli and the Sovrintendenza Capitolina for the support of the measurements at the Campidoglio in Rome.

We are grateful to Deutschen Bundesstiftung Umwelt (project AZ 31010-45), German Science Foundation and German Ministry of Education and Research (project TOAST, 03G0752G) for providing funding for the presented studies.

We further thank L. Beckel, R. Behrendt, S. Christen, L. Goerik, H. Heinisch, K. Jepsen, C. Milde, P.-B. Riedel, M. Tesch, and M. Wenk for taking part in the measurements.

References

Ahmad A, Pamplona M, Simon S (2009) Ultrasonic testing for the investigation and characterization of stone: a non-destructive and transportable tool. Rev Conserv 10:43–53

Aicher PJ (2004) Rome alive: a source guide to the ancient city. Bolchazy-Carducci, Wauconda

Auras M (2014) Charakterisierung von schwarzen Krusten und anderen Oberflächenveränderungen der Sandsteine der Porta Nigra in Trier. IFS-Bericht Nr. 47, Institut für Steinkonservierung e. V., Mainz, pp 15–28

Auras M, Meier T, Fehr M, Erkul E, Bilgili F (2015) Anwendung von Rayleighwellen zur Untersuchung verwitterter Denkmaloberflächen aus Naturstein. In: Raupach M (ed) Tagungshandbuch zum 4. Kolloquium Erhaltung von Bauwerken. Technische Akademie Esslingen, Ostfildern, pp 355–360

Dalkolmo J (1993) Synthetische Seismogramme für eine sphärische symmetrische, nichtrotierende Erde durch direkte Berechnung der Greenschen Funktion. Diplomarbeit. Institut für Geophysik der Universität Stuttgart

Ettl H (2014) Reinigung der Porta Nigra aus naturwissenschaftlicher Sicht. IFS-Bericht Nr. 47, Institut für Steinkonservierung e. V., Mainz, pp 53–75

Ettl H, Sobott R (1999) Ultraschallmessungen an in-situ konservierten Marmorreliefs des Siegestors in München. Z Kunsttechnol. Konserv 13(1):92–102

Fleischer G (2002) Beurteilung von Ultraschallmessungen an Natursteinobjekten in der Denkmalpflege. Dissertation, Technische Universität Wien, Fakultät für Bauingenieurwesen, p 182

Forbriger T, Auras M, Bilgili F, Bohlen T, Butzer S, Christen S, Cristiano L, Friederich W, Giese R, Groos L, Igel H, Köllner F, Krompholz R, Lüth S, Mauerberger S, Meier T, Mosca I, Niehoff D, Richter H, Schäfer M, Schuck A, Schumacher F, Sigloch K, Vormbaum M, Wuttke F (2014) Toolbox for applied seismic tomography. In: Weber M, Münch U (eds) Tomography of the earth's crust: from geophysical sounding to real-time monitoring. Geotechnologien Science Report No. 21, pp 135–156

Friederich W, Dalkolmo J (1995) Complete synthetic seismograms for a spherically symmetric earth by a numerical computation of the Green's function in the frequency domain. Geophys J Int 122:537–550

Gose E (1969) Die Porta Nigra in Trier. Trierer Grabungen und Forschungen 4, Berlin, 2 vols
Grimm WD (1990) Bildatlas der Denkmalgesteine der Bundesrepublik Deutschland. Bayerisches Landesamt für Denkmalpflege, Lipp Verlag München, Arbeitsheft 50:255
INSK (n.d.) Internationale Natursteinkartei. Ebner Verlag, Ulm
Köhler W (1991) Untersuchungen zu Verwitterungsvorgängen an Carrara-Marmor in Potsdam-Sanssouci. Berichte zu Forschung und Praxis der Denkmalpflege in Deutschland, Steinschäden–Steinkonservierung 2, Hannover, pp 50–53
Köhler W (1998) Untersuchungsbericht für Stiftung Preußische Schlösser und Gärten Berlin-Brandenburg: Neptungrotte Potsdam Sanssouci, Carrara Marmor, Ultraschalluntersuchungen. 8 pp + supplements
Köhn D, Meier T, Fehr M, De Nil D, Auras M (2016) Application of 2D elastic Rayleigh waveform inversion to ultrasonic laboratory and field data. Near Surface Geophysics, 14, 461–476, doi:10.3997/1873-0604.2016027
La Regina A, Cadario M, Giustozzi N, Guerrieri MC, Sadleir R (2007) Archaeological guide to Rome. New Update, p 105
Meier T, Dietrich K, Stöckhert B, Harjes HP (2004) One-dimensional models of shear-wave velocity for the eastern Mediterranean obtained from the inversion of Rayleigh wave phase velocities and tectonic implications. Geophys J Int 156:45–58
Meier T, Auras M, Erkul E, Fehr M, Jepsen K, Milde C, Schulte-Kortnack D, Spangenberg E, Steinkraus T, Wilken D (2014) Physikalische Untersuchungen an der Porta Nigra–Ultraschall-Oberflächen-Messungen und thermische Untersuchungen. IFS-Bericht Nr. 47, Institut für Steinkonservierung e. V., Mainz, pp 50–62
Meier T, Auras M, Fehr M, Köhn D, Steinkraus T, Eckel F, Sobott R, Siegesmund S, Schulte-Kortnack D, Erkul E (2016) Untersuchung der Verwitterung von Naturstein mit Ultraschall-Oberflächen-Messungen. In: Patitz G Grassegger G Wölbert O (eds) Natursteinsanierung, Stuttgart, pp 57–72
Pfefferkorn S (1998) Auswertung von Untersuchungen mit dem Bohrhärte-Prüfgerät an Gesteinen mit makroskopisch inhomogenen Gefüge. In: Snethlage R (ed) Jahresberichte Steinzerfall: Steinkonservierung 1994–1996. Ebner Verlag, Ulm, pp 105–112
Ruedrich J, Knell C, Enseleit J, Rieffel Y, Siegesmund S (2013) Stability assessment of marble statuaries of the Schlossbrücke (Berlin, Germany) based on rock strength measurements and ultrasonic wave velocities. Environ Earth Sci 69(4):1451–1469
Sebald E (2015) , … ein Tor … aus außerordentlichen Steinen …“ – Bemerkungen zur Bau- und Restaurierungsgeschichte der Porta Nigra und der Kirche St. Simeon. In: Reinigung der Porta Nigra? Naturwissenschaftliche und restauratorische Aspekte zur Verschwärzung und Reinigung der Sandsteine. IFS-Bericht Nr. 47, Institut für Steinkonservierung e.V., Mainz, pp 1–14
Shushakowa V, Fuller ER Jr, Heidelbach F, Mainprice D, Siegesmund S (2013) Marble decay induced by thermal strains: simulations and experiments. Environ Earth Sci 69:1281–1297
Siedel H, Siegesmund S, Sterflinger K (2011) Characterisation of stone deterioration on buildings. In: Siegesmund S, Snethlage R (eds) Stone in architecture. Springer, Berlin, pp 347–410
Siegesmund S, Vollbrecht A, Ullemeyer K, Weiß T, Sobott R (1997) Die Anwendung der geologischen Gefügekunde für die Charakterisierung natürlicher Werksteine Fallbeispiel: Kauffunger (Schlesischer) Marmor. Internationale Zeitschrift für Bauinstandsetzen 3:269–292
Simon S (2001) Zur Verwitterung und Konservierung kristallinen Marmors. Dissertation, Ludwig Maximilians-Universität München, 256 pp.
Sobott R (2002) Ultraschallmessungen an Marmor-Werkstücken an der Neptungrotte im Park Sanssouci, Potsdam. Bericht No. 89/2002 für Stiftung Preußische Schlösser und Gärten, Berlin-Brandenburg, 9 + XXI pp
Sobott R (2014) Ultraschallmessungen an Marmor-Werkstücken an der Neptungrotte im Park Sanssouci, Potsdam. Bericht No. 28/2014 für Stiftung Preußische Schlösser und Gärten Berlin-Brandenburg, 16 + XX pp

Steinkraus T (2016) Untersuchung der Verwitterung von Natursteinen mittels Inversion von Ultraschallwellenformen. Master thesis, Institute for Geosciences University, Kiel
Wallace W (2010) Michelangelo: the artist, the man, and his times. Cambridge University Press, Cambridge, pp 229–231
Weiss T, Rasolofosaon PNJ, Siegesmund S (2001) Thermal cracking in Carrara marble. Z Dtsch Geol Ges 152((2–4):621–636

Chapter 13
Hyperspectral Sensors for the Characterization of Cultural Heritage Surfaces

Mara Camaiti, Marco Benvenuti, Pilario Costagliola, Francesco Di Benedetto, and Sandro Moretti

Abstract The characterization of artistic and historical surfaces in a wide, fast, low-expense, and noninvasive way is a necessity for the conservation of these cultural assets. Hyperspectral sensors having bands in the visible-near infrared and short-wave infrared (VNIR-SWIR) regions are commonly used for determining the characteristics and properties of many materials (such as soils, minerals, rocks, water, vegetation) because of their ability to provide information in a fast and nondestructive way. Among the existing VNIR-SWIR techniques, field spectroscopy and imaging spectroscopy (remote sensing) have a crucial part in the characterization of different kinds of surfaces. In this work, the potentialities of hyperspectral sensors (working in the range 0.35–2.5 μm) for cultural heritage applications are discussed. The attention is focused both on field spectroscopy as a method for accurate characterization of small, confined, and highly heterogeneous surfaces and on imaging spectrometry obtained through field sensors. A few case studies where both techniques were employed are also reported.

13.1 Introduction

Historical buildings, stone objects, and painted surfaces such as frescoes and paintings are the most common artifacts of cultural heritage to be preserved. Their degradation is mainly caused by exposure to environmental conditions and to the effects of climatic agents on the raw material of the artwork (Dolske 1995; Striegel et al. 2003; Gauri and Holdren 1981; Lluveras et al. 2010; Mugnaini et al. 2006).

Water polluted with acidic gases (SO_x, NO_x, CO_2) is responsible for dissolution or transformation of inorganic components (rocks, pigments, mortar, etc.) (Haneef et

M. Camaiti (✉)
CNR-Institute of Geosciences and Earth Resources, Via G. La Pira, 4, Florence, Italy
e-mail: mara.camaiti@igg.cnr.it

M. Benvenuti • P. Costagliola • F. Di Benedetto • S. Moretti
Department of Earth Sciences, University of Florence, Via G. La Pira, 4, Florence, Italy
e-mail: sandro.moretti@unifi.it

N. Masini, F. Soldovieri (eds.), *Sensing the Past*, Geotechnologies and the Environment 16, DOI 10.1007/978-3-319-50518-3_13

al. 1992). Physical or microbiological degradation is also governed by the presence of water. In the case of physical decay, although no new products are formed, changes in porosity of the rock are the main consequences.

It is ascertained that preservation of this important part of cultural heritage is affected by a sustainable conservation, including treatment with suitable products for reducing the effects and the consequences of the aging, as well as by timely maintenance (Siegesmund et al. 2002; Doehene and Price 2010; Tsakalof et al. 2007). For both original and restored surfaces, the monitoring of possible chemical/physical changes of the surfaces enables timely maintenance. Effective monitoring requires instruments able to characterize surfaces in a broad, fast, and inexpensive way. Moreover, because of the poor homogeneity of these surfaces, data on the same area must be collected periodically for progressive comparison. Therefore, nondestructive and noninvasive techniques are required for collecting information about the surface status changes.

Several spectroscopic techniques, including FT-IR (Fourier transform-infrared), Raman, XRF (X-ray fluorescence), XRD (X-ray powder diffraction), LiDAR (light detection and ranging), and FORS (fiber optics reflectance spectra) are frequently employed for the characterization and identification of many compounds such as minerals, organic matter, vegetation, and soils. Most of these instruments are now available in portable form, thus enabling their use in field spectroscopy as noninvasive and nondestructive techniques of analysis (Aloupi et al. 2000; Craig et al. 2007; Rosi et al. 2009; Ricci et al. 2006; Miliani et al. 2010; Raimondi et al. 1998; Vandenabeele et al. 2005; Bacci 1995; Bacci et al. 2003).

13.1.1 Basic Concept of Spectroscopy

Spectroscopic techniques are based on the study of light, at different wavelengths, which is emitted, reflected, or scattered from a solid, liquid, or gas. Different processes, depending on the wavelength at which the technique operates, cause the spectra generated in spectroscopic measurements. If wavelengths are in the range 0.1–100 μm (UV-far infrared region), the resulting molecular effects of the interaction of light with matter are the electronic and vibrational excitations (Clark 1999; Ramakrishnan and Bharti 2015). The UV-visible and infrared spectroscopy are possible because of these kinds of excitation.

The electronic excitations are observed in the UV-visible region (0.2–1.0 μm); they consist of the change of the states of the electrons from the ground state to the excited one, when transitions in the electronic energy levels of the bonds of the molecule are possible. Transitions involving electrons belonging to the same atom are observed in compounds where elements such as Ni, Cr, Co, and Fe are present. The identification of a specific mineral is possible because the orbital energy levels of the transition element are sensitive to the specific crystal structure hosting them ("crystal field effects"). On the other hand, transitions to an adjacent atom, or "charge transfer," are also possible and are responsible for the red color

of iron oxides. These last transitions cause stronger absorption bands compared to those associated with the crystal field transitions. Finally, promotion of an electron from the lower energy level called the "valence band" to a higher level called the "conduction band" is responsible for the yellow color of sulfur or the red color of cinnabar (HgS). The energy difference between the top of the "valence band" and the bottom of the "conduction band" is called the "band gap" and in semiconductors corresponds to the energy of visible and near-infrared regions.

The vibrational excitations or absorptions are detectable in the infrared spectrum when a change in the dipole moment of the molecule occurs. These excitations allow the identification of functional groups of a molecule. For a molecule with N atoms, there are 3 N-5 normal modes of vibration (or fundamentals) in the case of a linear molecule, and 3 N-6 fundamentals for nonlinear molecules. Additional vibrations, such as multiples of fundamental modes (overtone bands) or composition of different modes of vibrations, may also occur. Fundamental vibrations are detected in the mid-infrared (MIR) region (2.5–25 μm), whereas overtone and combination bands are found in the short-wave infrared (SWIR) region (1.0–2.5 μm). Although the peaks generated by overtones and combinations are much weaker than the fundamental ones, their absorptions can be measured providing diagnostic information on minerals and other materials (Clark et al. 1990). The advantage to use sensors in the visible-near infrared and short-wave infrared (NIR-SWIR) regions, instead of in the MIR, is the capability to excite the emitting target using the Sun as the illumination source and work in the same portion of the solar spectrum (0.38–3.0 μm) used directly for remote sensors (Campbell 2002).

13.1.2 Hyperspectral Techniques

Among the spectroscopic techniques, hyperspectral sensors having bands in the visible-near infrared and short-wave infrared (NIR-SWIR) regions are deployed to characterize many compounds (both inorganic and organic). Therefore, they are potential methods for detecting new mineral phases, biological growth, the presence of black crusts, and changes in roughness on rock surfaces, as well as the chemical and physical transformation of painted surfaces (Clark 1999). They can be used in remote sensing techniques for obtaining surface maps and exploited, for example, in lithological discrimination and mineral mapping.

Use of the hyperspectral techniques is relatively recent and their main advantage is the ability to acquire images in many continuous spectral bands with a narrow bandwidth (width of an individual spectral channel in the spectrometer), which permits acquisition of laboratory-like spectra also from remote sensors (Ramakrishnan and Bharti 2015). In contrast to multispectral sensors, which have coarse bandwidth and poor spectral contiguity, hyperspectral sensors are widely used for geological applications such as mineral exploration (Magendran et al. 2011; Kerr et al. 2011; Kruse 2012; Ramakrishnan et al. 2013; Zadeh et al. 2014) and localization of hydrocarbon deposits (Petrovic et al. 2012; Tangestani and Validabadi 2014).

Indeed, with hyperspectral sensors it is possible to combine spatially and spectrally contiguous images. However, for sake of clarity, it must be pointed out that the spectral database created in the laboratory using pure materials (i.e., minerals and rocks) has limited potential for geological and cultural heritage applications because of the complexity of the investigated surfaces, characterized by the contemporary presence of several compounds and the roughness of the substrates. New compact and sophisticated spectrometers and spectroradiometers allow researchers to address the natural heterogeneities, and to develop the so-called field spectroscopy, greatly improving the potential applications of the hyperspectral sensors. Moreover, field spectroscopy can be used to acquire accurate ground data to be used for the calibration of airborne or space-borne spectrometry (imaging spectrometry).

In this chapter, the potential for hyperspectral sensors (working in the range of 0.35–2.5 μm) in cultural heritage applications is discussed. Attention is focused both on field spectroscopy, as a method for accurate characterization of small, confined, and highly heterogeneous surfaces, and on imaging spectrometry obtained through field sensors. Finally, some case studies, where both techniques were employed, are reported.

13.2 Laboratory and Field Spectroscopy

Field spectroscopy is usually considered propaedeutic to remote sensing (imaging spectrometry) because it allows the acquisition of accurate measurements and involves the study of the effect of the environment on the spectral characteristics of objects (Milton 1987). It can be considered as a "connection" between laboratory measurements and spectral reflectance acquisitions in the field, becoming useful for the calibration of land, airborne, and satellite sensors. In the case of cultural heritage applications, field spectroscopy has an additional role of crucial importance when surfaces with small dimensions, or located in confined spaces where imaging spectrometry cannot be used, must be characterized.

However, although hyperspectral sensors can be used to identify many compounds, their application to cultural heritage is, at present, limited to archaeological research (Agapiou and Hadjimitsis 2011; Alexakis et al. 2012; Agapiou et al. 2012, 2013; Sarris et al. 2013) and to the characterization of stone (Vettori et al. 2008; Camaiti et al. 2011) or painted surfaces (Wang 2015).

In the case of archaeological research, one of the first applications of field spectroscopy was reported by Agapiou et al. (2012), where it was used to detect buried archaeological sites in Neolithic settlements in Tessaly. Spectral profiles of the investigated areas, collected from a GER 1500 field spectrometer covering a range from 400 to 1050 nm, were processed to retrieve the characteristics of vegetation and thus discriminate the archaeological sites in terms of vegetation indices (Agapiou et al. 2012; Alexakis et al. 2012).

In the case of the characterization of stone and painted surfaces, the subject of this chapter, the first application of laboratory and field spectroscopy was for the

detection of gypsum (calcium sulfate bihydrate) on monumental buildings (Vettori et al. 2008; Camaiti et al. 2011). Later, it was used to monitor and identify the organic materials applied on historical stone surfaces as protective agents (Alparone et al. 2011; Camaiti et al. 2013).

Only recently, this technique has been used for the identification of different components present in painted surfaces, such as pigments, binding mediums, and varnishes (Wang 2015). The spectral signatures of the different surfaces, in both laboratory and field, were collected with a portable spectroradiometer (ASD-FieldSpec FP Pro). The instrument is designed to acquire reflectance spectra in the region 350–2500 nm (0.35–2.5 μm) with spectral resolution of 3–10 nm, spectral sampling of 1.4–2 nm, and acquisition frequency of 10 spectra·s^{-1}.

Field spectroscopy typically involves the ambient solar illumination, but the ASD-FieldSpec FP Pro spectroradiometer can also collect spectra using the contact reflectance probe, which consists of a fixed geometry of illumination and shot with an internal light source and a constant field of view (FOV) of 1.2 cm^2 (Fig. 13.1). The internal light for its fixed illumination angle (12°) and shot provides for a uniform and constant illumination, thus allowing for spectra collection regardless of weather or time of day. Therefore, the spectral signatures were mainly collected using the contact reflectance probe.

13.2.1 Qualitative and Semiquantitative Detection of Gypsum

The detection of gypsum on historical buildings was used to estimate the degradation of carbonate surfaces. Indeed, gypsum is considered the precursor symptom of

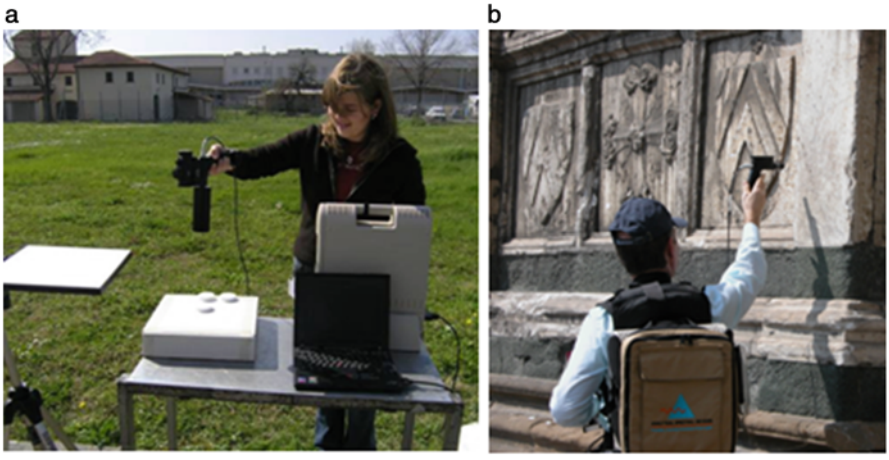

Fig. 13.1 ASD-FieldSpec FP Pro in environmental conditions (**a**) and with the contact reflectance probe configuration (**b**)

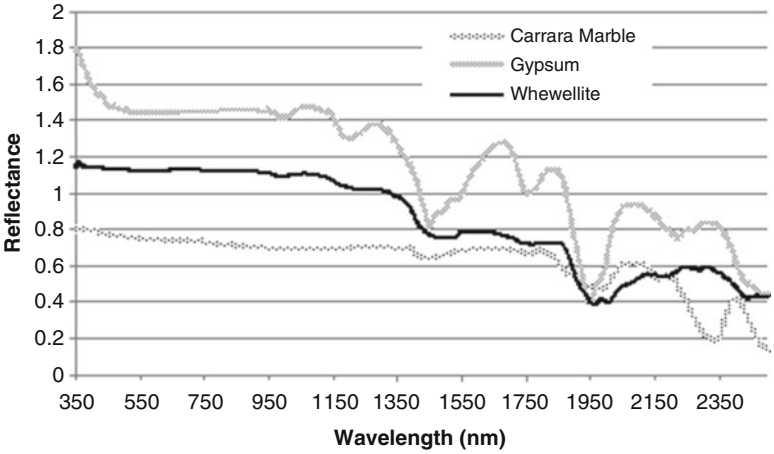

Fig. 13.2 Reflectance spectra of gypsum, calcite, and synthetic whewellite

the disintegration of carbonate rocks because of the reaction of calcium carbonate (i.e., marble) with acidic pollutants (such as sulfur oxides, SO_x). Although historical surfaces must be considered complex matrices, where several minerals (e.g., calcite, calcium oxalates, silicates) and other components (e.g., carbon particles in black crusts) are commonly found, the identification of gypsum is possible because of the different spectral signature of these compounds (Fig. 13.2). In particular, the peak at 1445 nm, associated with the weaker peaks at 1489 and 1536 nm, can be considered diagnostic for the identification of gypsum. On the other hand, the identification of calcium oxalates in the presence of calcium carbonate and gypsum appears more difficult because of the overlapping of the peaks of calcium oxalates with gypsum or calcite (Fig. 13.3). Carbon particles are an exception because they absorb and do not reflect light. However, the reflectance spectra obtained from matrices in which black carbon, also in small concentrations, is mixed with other minerals are characterized by a lower reflectance compared to the pure minerals, but the strongest peak of gypsum, at 1948 nm, is always present (Fig. 13.4).

The quantification of gypsum in a mixture appears more difficult because the amount of light reflected and absorbed by the detected surface depends not only on its concentration but also on several other factors, such as the grain size of gypsum crystals, the co-presence of other minerals having absorption peaks in the same regions of gypsum, or components that drastically reduce the reflectance of light (i.e., carbon particles). The grain size effects and the influence of dark grains on the reflectance of light was described by Clark (1999) and verified by Serraglini (2010). Particularly, Serraglini (2010) studied both the signal intensity of peaks of gypsum and calcite versus grain size, and the reflectance changes of mixtures of gypsum/calcite (1:1) where small percentages of carbon black were added. The influence of other minerals such as calcite and whewellite was studied by Camaiti et al. (2011).

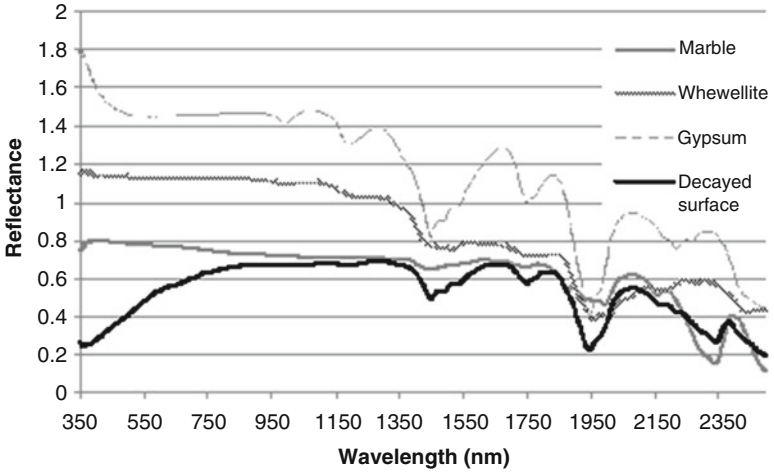

Fig. 13.3 Reflectance spectrum of a decayed carbonate surface where gypsum and calcium oxalates, detected by mid-FT-IR, are also present. The spectra of calcite, gypsum, and whewellite are reported for comparison

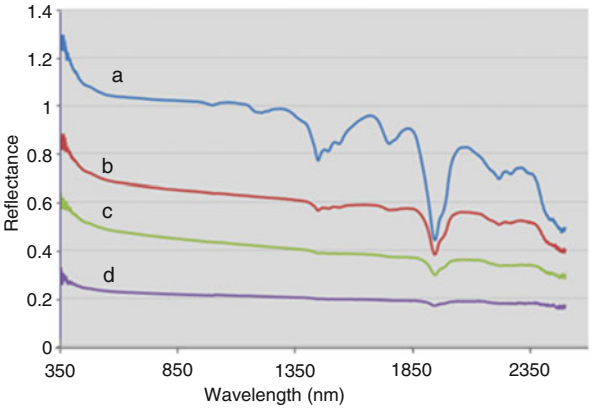

Fig. 13.4 Reflectance spectra of mixtures of gypsum and calcite (1:1) with different concentration of carbon black: 0% (*a*); 0.5% (*b*); 1.0% (*c*); 5.0% (*d*)

Because the absorbance of light, and therefore the signal intensity of the diagnostic peaks, is not related only to the concentration of the compounds, only a semiquantitative estimation of gypsum is possible. However, as the signal intensity of gypsum peaks does not change significantly for grain sizes in the range 15–50 μm (Serraglini 2010), a more accurate estimate of gypsum can be actually obtained in favorable situations. The situations can be assumed favorable when the grain size of gypsum falls in the above-reported range, and when it is possible to suppose that the grain size is homogeneous on the investigated surfaces because of homogeneous environmental conditions during the formation and growth of gypsum crystals. In fact, in these cases it is possible to use calibration curves generated in laboratory conditions from specific mixtures, where the minerals have similar

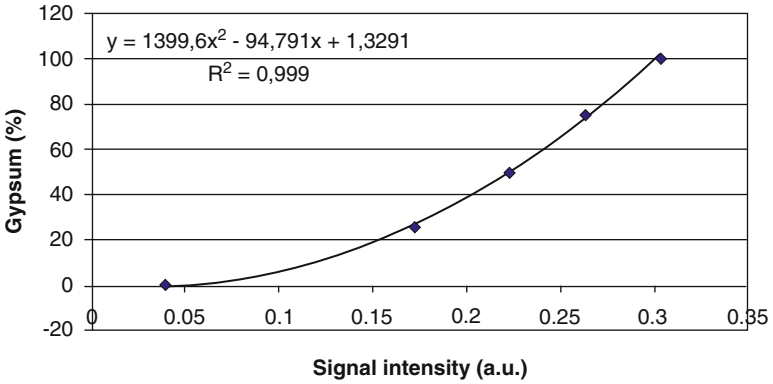

Fig. 13.5 Calibration curve for semiquantitative estimation of gypsum on carbonate surfaces. Mixtures of gypsum and calcite containing 0%, 25%, 50%, 75%, and 100% of gypsum were used

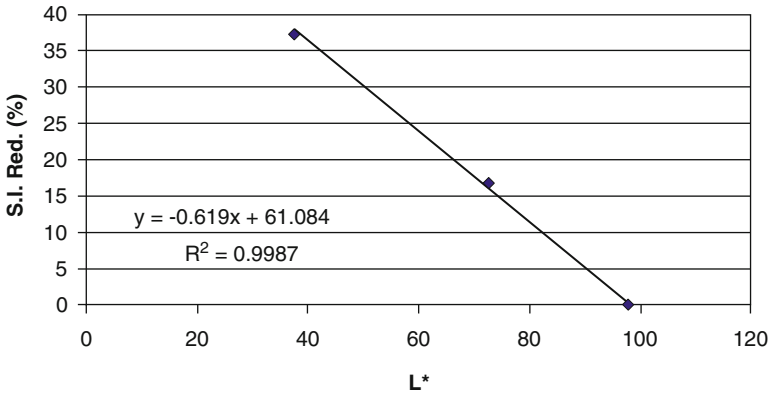

Fig. 13.6 Signal intensity reduction (%) of the peak of gypsum at 1445 nm versus brightness (L* parameter)

grain size to those found on the historical surfaces. An example of a calibration curve for estimating gypsum on two marble sepulchral arches (Avelli) of the left side of the façade of Santa Maria Novella church (Florence, Italy) is shown in Fig. 13.5 (Benvenuti et al. 2009). In this study, the calibration curve was obtained from synthetic powders of gypsum and calcite (grain size about 15–20 μm), and the signal intensity of the peak at 1445 nm was used as the reference peak. At the same time, the influence of dark particles, such as carbon particles in "black crusts," on the signal intensity of gypsum peaks may be properly corrected. In fact, the reduction of the signal intensity of the peak at 1445 nm, expressed as a percentage, can be related to the L* parameter, which is the brightness of the surface evaluated in accordance with the L*a*b* (CIE 1976) system. A direct proportionality between the reduction of signal intensity and the L* value was found for values of L* greater than 40 (Fig. 13.6). For values of L* less than 40 the surface is too dark, the light

is almost completely absorbed, and the diagnostic peak of gypsum is drastically reduced, thus hindering any quantitative analysis. The semiquantitative estimate of gypsum obtained with the foregoing calibration curve and corrected for the presence of black crust agreed well with an estimate obtained through traditional methods (SEM-EDS, scanning electron microscopy-energy dispersion system). The results are reported in 1.4.

A method based on the spectral decomposition of spectra of calcite–gypsum mixtures in individual spectral components assigned to calcite and gypsum was recently proposed for a semiquantitative estimation of gypsum (Di Benedetto et al. 2014; Suzuki 2014; Xinyue 2013; Montecchi 2013). The advantages of this method consist in the possibility, after a proper calibration process, to partially overcome some of the most critical drawbacks of the application of the SWIR spectroscopic field investigation to sulfated marble surfaces. Namely, the spectral overtone and combination bands exhibit a relevant width, mainly because of surface and crystallite inhomogeneities, but also the comparable dimension of the size of crystallites and of the SWIR wavelength. Moreover, the method is able to account for the different conditions of illumination or for the color of the stone surface, through a modeling of the background, performed simultaneously with the spectral decomposition.

13.2.2 Monitoring of Protective Treatments

Since the second half of the twentieth century, some synthetic polymers with hydrophobic properties have been widely employed as protective agents on buildings and other stone surfaces (Doehene and Price 2010; Tsakalof et al. 2007). The main advantage of the use of these compounds is their capacity to change the stone wettability and therefore to drastically reduce the degradation effects caused by water. All these protective agents, including those with the best chemical, thermal, and photo stability, show their highest protection performances immediately after their application with a progressive decay, which leads to substantially lower efficacy in a few years. This loss of efficacy has chemical and physical causes such as the slow and progressive degradation of some polymers by photooxidation processes, or the loss of adhesion to the substrate with consequent leaching effect. To ensure the protection of stone, the degradation of the protective agent or its depletion from the surface must be monitored to plan timely maintenance. Until now, water absorption tests by “pipette” method (Frediani et al. 1982), laboratory analyses of samples (Favaro et al. 2007), or, sometimes, in situ analyses using portable spectrometers (mainly mid-FT-IR) (Ricci et al. 2006) are the most common methods of investigation. All these methods allow the analysis only of restricted areas, so creating detailed maps of the permanence and efficacy of these treatments becomes particularly tedious and time consuming. When new restoration treatments for large surfaces of historical buildings are needed and decisions on the best choice of restoration protocols must be made, the lack of information can be also

detrimental. In these cases, hyperspectral techniques can be again successfully exploited to detect, and therefore monitor, the protective treatment. Indeed, thanks to the short time needed for the acquisition of spectra, it is possible to obtain compositional maps at relatively low cost.

Laboratory studies carried out on calcareous (marble and Lecce stone) and siliceous (Pietra Serena and Pietraforte) stones treated with some of the most widely used restoration products, such as Paraloid B72 (poly(ethyl acrylate-*co*-methyl acrylate)) and a fluoroelastomer (poly(hexafluoropropene-*co*-vinylidene fluoride)), proved the detection of the diagnostic peaks of the organic material in the SWIR region, on both calcareous and siliceous stones (Alparone et al. 2011; Vettori et al. 2012; Zecchi 2013). The reflectance spectra of Lecce stone treated with Paraloid B72 and Pietraforte treated with a fluoroelastomer, respectively, are reported as examples in Figs. 13.7 and 13.8.

The detection of the product depends on the amount of protective agent applied. However, it was found that when the amount was enough to provide a high hydrophobic effect, the treatment was clearly detected. In contrast, when the amount was too small or not well distributed on the surface, the hydrophobic effect was drastically reduced (more than 50%) and no product was detected.

The different spectral signatures of the protective agents allow us to identify the kind of product used in restoration treatments. However, in the case of treated sandstones, this identification requires an accurate analysis of the spectra because of

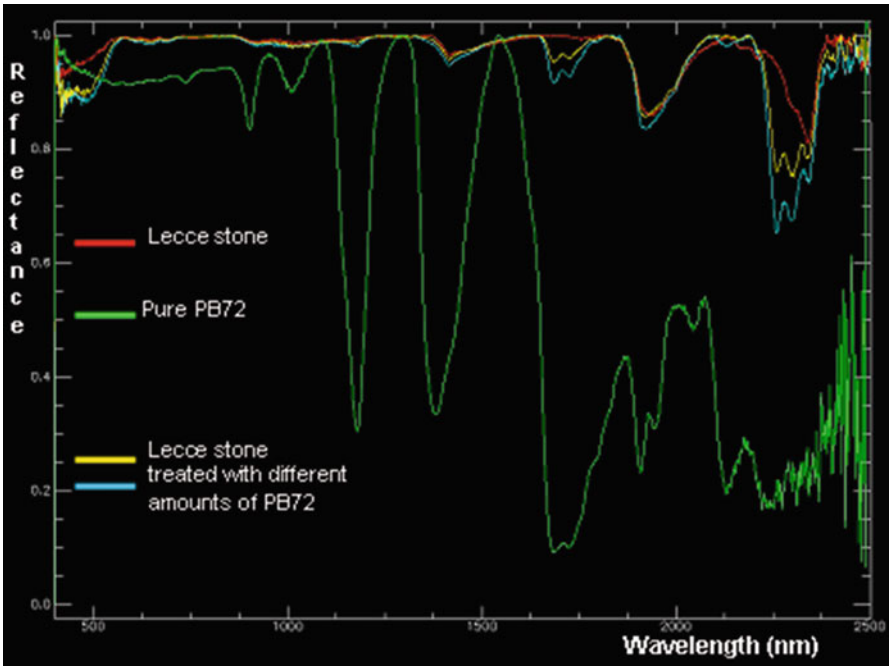

Fig. 13.7 Reflectance spectra of Lecce stone samples untreated and treated with Paraloid B72

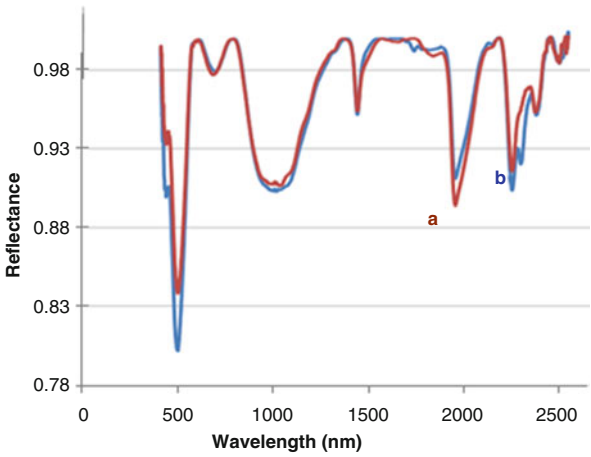

Fig. 13.8 Reflectance spectra of Pietraforte samples: (*a*) untreated and (*b*) treated with the fluoroelastomer

the interference from the peaks of the stone. Indeed, siliceous stones show medium to strong absorption peaks in the same SWIR region as the protective agents.

In spectroscopic analysis, calculation of the ratio of the intensity of diagnostic peaks is frequently used to detect a component in a mixture. The same method can be used to discriminate between these two polymers. In fact, when comparing the signal intensity of the peaks at 2212 nm (from the stone), at 2257 nm (from fluoroelastomer and Paraloid B72), and at 2335 nm (from Paraloid B72), it was found that the ratio of the signal intensity 2212/2257 with respect to the untreated stone changes for both PB72 and fluoroelastomer treatments, whereas the ratio 2212/2335 changes only for the stone treated with PB72 (Zecchi 2013).

13.2.3 Characterization of Painted Surfaces

The identification of the components of painted surfaces (including pigments, binding mediums, and varnishes) is commonly required for restoration or authentication of the object. Sophisticated laboratory analyses, such as SEM-EDS (scanning electron microscopy-energy dispersion system), FT-IR (Fourier transform-infrared), Raman spectroscopy, and GC-MS (gas chromatography–mass spectrometry), are often required to give qualitative and quantitative information of the stratigraphic composition of the painted object. Although these investigations give accurate results, the high cost of the analyses and in particular the invasiveness of the method (sampling of micro-fragments is required) limit their use to only a few samples from micro-areas that are not always representative of the entire object.

On the other hand, portable and noninvasive instruments, such as mid-FT-IR, micro-Raman, XRF (X-ray fluorescence), FORS (fiber optics reflectance spectra) are developed and successfully used for the identification of pigments, varnishes, and binding mediums (Rosi et al. 2009; Miliani et al. 2010; Bacci et al. 2003).

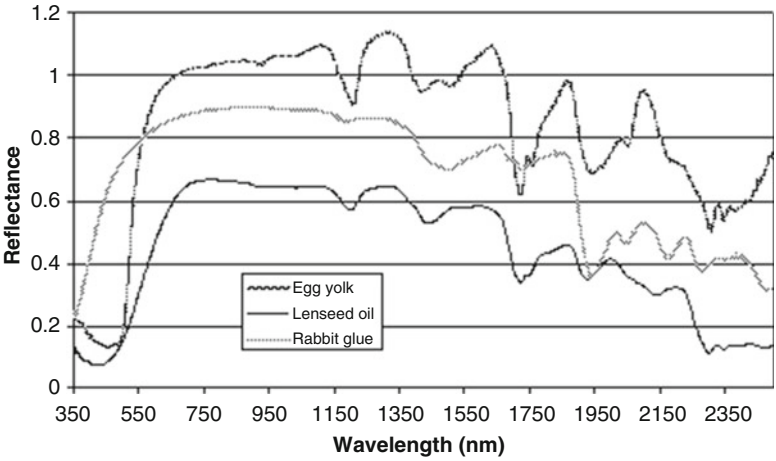

Fig. 13.9 Reflectance spectra of some binding mediums: egg yolk, linseed oil aged 4 years, and animal glue (rabbit glue)

In contrast, hyperspectral sensors in the range 350–2500 nm have been tested on painted surfaces only recently (Wang 2015). The results obtained from the analysis of several pigments, varnishes, and binding mediums show that this technique permits discriminating both organic and inorganic components, except for compounds with similar composition (e.g., natural resins such as dammar and mastic that give the same spectral feature). Other synthetic varnishes such as Paraloid B67 (poly isobutyl methacrylate) and a keton resin (a poly cyclohexanone resin) can be identified in the region of the overtone and combination bands. Similarly, good discrimination is obtained for the pigments (lead white or biacca, cinnabar, malachite, azurite, lapis lazuli, yellow ochre, Naples yellow) and the binding mediums (egg yolk, linseed oil, animal glue) investigated. In Fig. 13.9 the reflectance spectra of egg yolk, linseed oil, and animal glue are reported as examples. In Fig. 13.10, the reflectance spectra of two yellow pigments, yellow ochre and Naples yellow, are shown as examples of discrimination between pigments.

However, the reflectance spectra obtained from a painted surface appear more complex and their interpretation is more difficult than those from the pure materials. Moreover, paintings are made of a series of layers, where the pigments mixed with the binding medium are coated with natural or synthetic varnishes. If abundant varnish covers the pictorial layer, the identification of the pigments in the lower layers may fail.

The advantages of the hyperspectral techniques in the field of paintings lie mainly in the evaluation of cleaning treatments, where it is possible to detect the partial or total removal of varnish, or for a general screening of the superficial layer to determine the uniformity of the varnishes and the presence of retouched areas. After

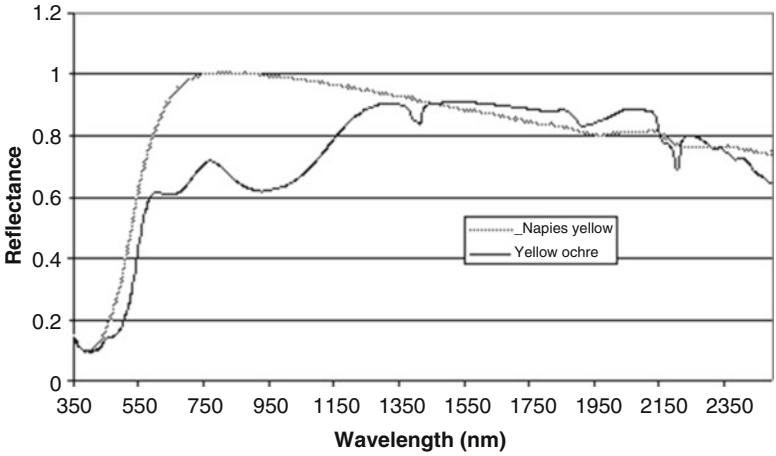

Fig. 13.10 Reflectance spectra of some yellow pigments: Naples yellow and yellow ochre

the removal of the thick or impenetrable superficial layer, the characterization of the pictorial layer with the identification of different pigments and binding mediums is made possible.

13.3 Imaging Spectroscopy

Imaging spectroscopy, or hyperspectral imaging, combines digital imaging and reflectance spectroscopy. A hyperspectral camera simultaneously collects spatial and spectral information and produces a three-dimensional hyperspectral cube from the data. The hyperspectral cube consists of two-dimensional (2D) spatial images, and each pixel in the 2D image provides a continuous spectrum, which forms the third dimension of the image.

The precision of hyperspectral sensors is typically measured in spectral resolution (width of each spectral band), but spatial resolution is the other factor to be taken into consideration. Indeed, if the pixels are too large, many objects or compounds are "captured" in the same pixel and their identification becomes more difficult. On the other hand, if the pixels are too small, the energy captured by each sensor gives a signal-to-noise ratio too low for measured features.

Hyperspectral sensors can work in the UV, visible, NIR, and SWIR regions. In fact, hyperspectral cameras can be configured from 280 up to 2500 nm.

The most important applications of imaging spectroscopy are in the geological field, where the ability of this technique to identify many minerals makes it ideal for mining and oil industries (Ramakrishnan and Bharti 2015). However, in the past 10–15 years hyperspectral imaging systems have been developed and used for

Fig. 13.11 SIM-GA (Selex Galileo Multisensor Hyperspectral System) in land configuration

the noninvasive study of artistic objects, mainly easel paintings and paper-based artifacts (Kubik 2007; Balas et al. 2003), or for the assessment of the degradation of historical building surfaces (Vettori et al. 2008). Only recently, they have been used for the investigation of mural paintings (Cucci et al. 2015).

In the case of easel paintings or movable objects, the hyperspectral imaging systems are composed of a high-resolution CCD detector having a wide wavelength response. These systems operate at short distances from the object; this operating mode has the advantages to eliminate the effects of the ambient light through calibration and to provide good spatial resolution. However, the main disadvantage of these systems is the limited size of covered surfaces (small FOV). The spectral range usually investigated is 400–1000 nm, which provides useful information for pigment identification, color, and UV fluorescence documentation (Kubik 2007).

In contrast, the hyperspectral imaging system used to assess stone decay and investigation of mural paintings is an airborne hyperspectral system, readapted for ground-based applications. It works in the 400–2500 nm range, exploiting the concept of pushbroom nadir imaging (Vettori et al. 2008; Melani et al. 2010). This system (Selex Galileo Multisensor Hyperspectral System, SIM-GA) consists of two cameras (electro-optical heads) physically separated but placed side by side on a common alignment plate inside the same protecting box (Fig. 13.11).

The first head operates in the VNIR region (400–1000 nm) with a spectral sampling of 1.2 nm (512 bands), and the second one in the SWIR region (1000–2500 nm) with a spectral sampling of 6.3 nm (256 bands). SIM-GA is able to collect hyperspectral images from distances in tens of meters, using a remote sensing approach. Then, an elaborate sequence of data processing steps is required, such as removal of atmospheric effects, transformation of remotely measured radiance (raw hyperspectral images) to reflectance, and data processing for noise and dimensionality reduction (Ramakrishnan and Bharti 2015; Melani et al. 2010). Finally, identification and mapping of surface materials can be accomplished by using reference reflectance spectra or spectral library. Because of the heterogeneity of architectural or painted surfaces, the reflectance spectra collected by a hyperspectral sensor are often a spectral mixture, which must be separated into spectra of single materials (endmembers) for the identification. This procedure, known as spectral unmixing, may be realized through different models; among them, the most popular is the linear mixing model (Ramakrishnan and Bharti 2015).

The main advantage of imaging spectroscopy, in respect to field spectroscopy, is the ability to map large areas (mainly in the case of hyperspectral sensors used in airborne/land configuration) faster and at relatively low cost. This ability makes possible not only the identification of materials on the entire surface, but also the monitoring of surface degradation. An example of application of the imaging spectroscopy for assessing the conservation state of a building surface is reported in Sect. 13.4.

13.4 Applications of Hyperspectral Sensors to Historical Building Surfaces

Two case studies are herein selected to illustrate the applications of hyperspectral sensors to the characterization of historical building surfaces.

The first case study regards the Basilica of Santa Maria Novella in Florence (Italy), where both field and imaging spectroscopy have been applied for the evaluation of marble decay through the estimation of gypsum content. The second study concerns with San Gaetano church in Florence (Italy), which was investigated through a portable spectroradiometer to detect the permanence of the protective treatment on the surface.

13.4.1 Basilica of Santa Maria Novella

The construction of the Church, one of the most important Gothic churches in Florence, began in 1246 and was ended with the adjacent convent by the middle of the fourteenth century. The façade, entirely made of white marbles, green serpentinites and red marly limestones, was created by Fra Jacopo Talenti (lower

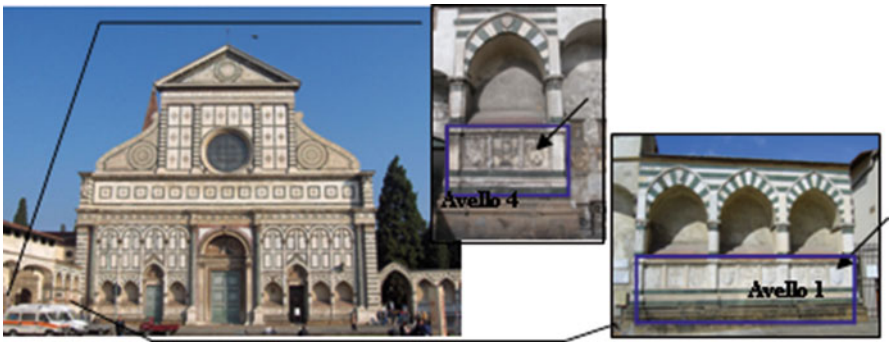

Fig. 13.12 Façade of the Basilica of Santa Maria Novella in Florence (Italy) with detail of the "Avelli" of the *left side* of the church. The *arrows* indicate the two escutcheons investigated by ACS-FieldSpec FP Pro. The areas *inside the rectangle* were studied with SIM-GA

part) and Leon Battista Alberti (upper part). The investigation was focused on the marble sepulchral arches ("Avelli") on the left side of the church façade (Fig. 13.12) (Vettori et al. 2008; Melani et al. 2010; Camaiti et al. 2011), which show clear evidence of deterioration, as well as areas with different chromatic characteristics (from white to black). Moreover, in this case the surface is substantially flat, making the (hyperspectral) reflectance spectra dependent only on the nature and structure of the surface or the intensity and position of light, but independent of the relative position of the observer.

The right escutcheons in the first and fourth "Avello" were selected for field investigation through the portable spectroradiometer (ASD-FieldSpec FP Pro), whereas all the "Avelli" of the left side were investigated by imaging spectroscopy using the hyperspectral system SIM-GA.

The field investigations were used to validate hyperspectral imaging, whereas traditional analyses, including SEM-EDS, FT-IR, and XRD, performed on small fragments sampled from representative areas of the Avelli, were used to validate the semiquantitative data obtained by ASD-FieldSpec FP Pro.

For the field investigations, systematic reflection measurements were carried out on the two escutcheons, where a grid with 5-cm mesh was used for mapping the distribution of gypsum. The estimate of gypsum abundance was determined by using the calibration curve reported in Fig. 13.5, and the results were mapped in ranges of concentration (Fig. 13.13).

The percentage of gypsum versus calcite in light-colored areas agreed well with the values obtained by SEM-EDS and FT-IR analyses. In contrast, in dark areas the concentration of gypsum was much less than the one estimated by SEM-EDS (29% instead of 72%) (Fig. 13.14a). As expected, the dark surfaces partially absorb the light, reducing the signal intensity of the peaks of gypsum (mainly, the diagnostic peak at 1445 nm), causing the percentage of gypsum found to be drastically reduced. To overcome this problem, it is useful to consider the reduction of the signal

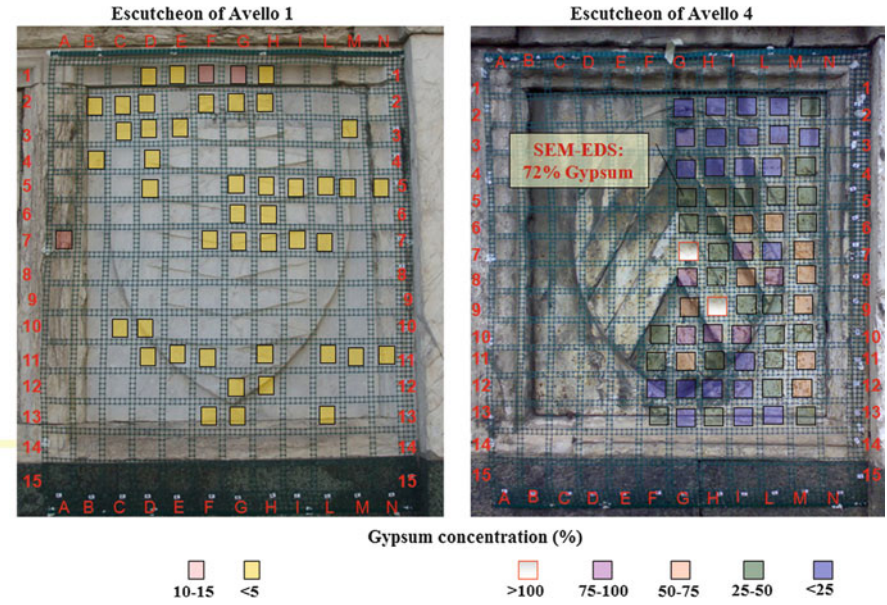

Fig. 13.13 Maps of the concentration of gypsum on the *right escutcheons* of Avello 1 and 4, determined by ASD-FieldSpec FP Pro measurements

intensity of gypsum as a function of lightness (the measured L* parameter). The equation used for the calculation of this reduction is reported in Fig. 13.6. After performing the necessary corrections of the signal intensity according to the L* parameter, the new values agreed well with those found by SEM-EDS (Fig. 13.14b).

Values of gypsum percentage higher than 100% were also found. These "nonobvious" (too high) values may be explained by the copresence of other components, mainly calcium oxalates, that is, whewellite. Although whewellite gives a different reflectance spectrum than gypsum, in the diagnostic region of gypsum there is a medium to weak peak of calcium oxalate at 1450 nm, which may interfere with the peak of gypsum at 1445 nm. In this situation, a more accurate processing of the spectra, which includes the contribution of calcium oxalates, is required.

Measurements with the hyperspectral system SIM-GA were performed in three sampling campaigns. The device was placed at a distance of about 10 m from the Avelli, with a instantaneous field of view (IFOV), or pixel dimensions, of about 1×1 cm in the VNIR region and about 1.5×1.5 cm in the SWIR region. Target areas, as well as the standards for gypsum, calcite, and whewellite, and mixtures of gypsum/calcite, were placed at the bottom of the Avelli and used for identification, mapping, and estimation of the gypsum concentration.

The radiance values were converted to reflectance using the empirical line method with ENVI (Environment for Visualizing Images) software.

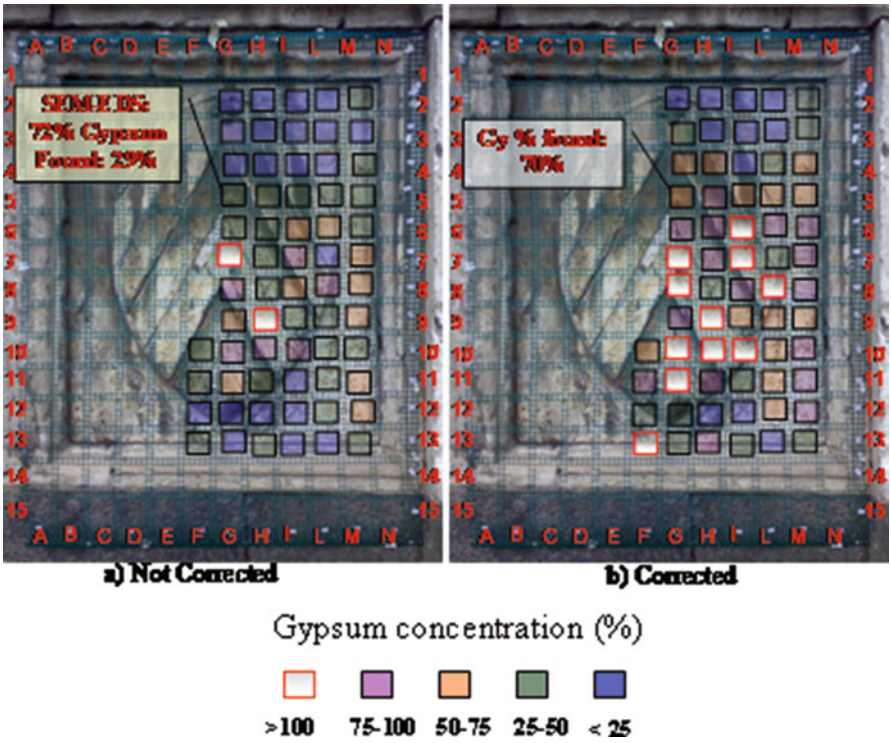

Fig. 13.14 Map of gypsum percentage on the *right escutcheon* of Avello 1 with a comparison with SEM-EDS analysis: (**a**) before correction; (**b**) after correction in accordance with the L* parameter

SAM (spectral angle mapper) classification was used for mapping gypsum/calcite/oxalates distribution when spectra of pure components were used as endmembers, and for the semiquantitative estimation of gypsum when reflectance spectra of standard mixtures of gypsum/calcite were used as endmembers.

The comparison of the results obtained by the portable spectroradiometer and the hyperspectral imaging system, reported in Fig. 13.15, were in good agreement.

13.4.2 San Gaetano Church

The church, one of the rare examples of Baroque churches in Florence, was built between 1604 and 1648. The façade is in Pietraforte, a calcareous sandstone, with sculptural decorations in marble. During the last restoration, completed in 1996, the entire surface in Pietraforte was treated with a fluoroelastomer (poly(hexafluoropropene-*co*-vinylidene fluoride)) as a protective agent. After about 20 years, the overall state of conservation of the façade is good, but verification

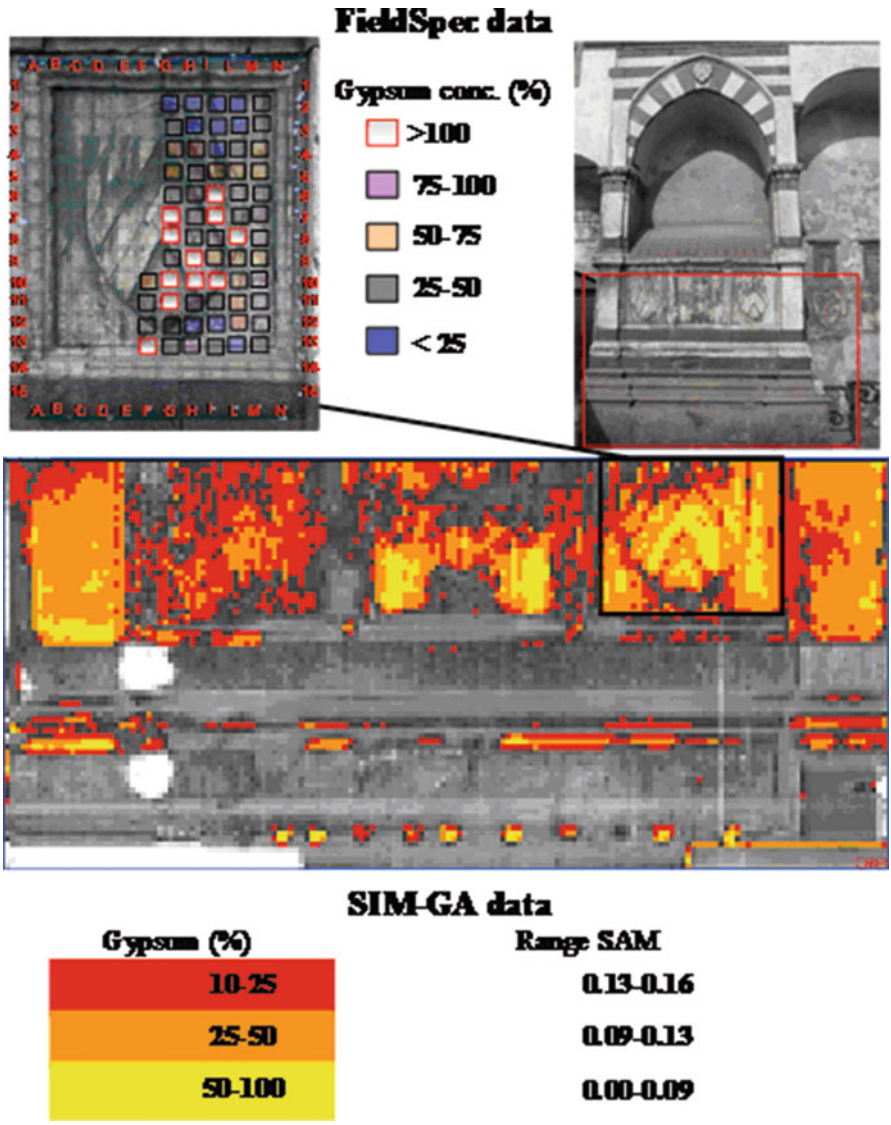

Fig. 13.15 Semiquantitative analysis of gypsum on the Basilica of Santa Maria Novella: comparison between ASD FieldSpec FP Pro and SIM-GA data

of the permanence of the protective treatment is essential for planning timely maintenance. Considering that the detection of a protective agent, specifically the fluoroelastomer, by the portable spectroradiometer is possible when it is present in quantities sufficient to give an effective hydrophobic capacity, several reflectance spectra were collected in different areas of the façade (Vettori et al. 2012).

Comparing the spectra of treated and small untreated areas, the diagnostic peak of the fluorinated elastomer was detected at 2256–2257 nm in many areas. These results were confirmed by the water absorption test performed through the "pipette" method" (Frediani et al. 1982), which gave high values of protective efficacy (or low amount of water absorbed).

13.5 Conclusions

Hyperspectral sensors, used both in the field and in imaging spectroscopy, were successfully applied to conserve artifacts of cultural heritage. Indeed, it was proved that the hyperspectral devices can be used for mapping and monitoring the gypsum abundance on historical building surfaces, even in presence of dark areas, because the reduction of the signal intensity of gypsum can be properly corrected with the lightness parameter (L*). Moreover, these techniques can be used to identify pigments and organic materials, such as agents for protecting stone and varnishes and binding mediums for paintings. Therefore, hyperspectral techniques can be exploited for monitoring the permanence of protective coatings on stone or the progress of cleaning treatments on painted surfaces. Although hyperspectral sensors do not offer the same level of specificity as FT-IR spectroscopy, they have the advantages of working under natural light and collecting spectra in a rapid and nondestructive way. It is also possible to produce large maps at relatively low cost.

Acknowledgments The authors wish to thank the teams that have worked on the collection of many field and laboratory data, namely, Silvia Vettori, Elena Pecchioni, Teresa Salvatici, Leandro Chiarantini, Francesca Serraglini, Diletta Zecchi, and Cong Wang. A part of this work was supported by Regione Toscana in the framework of the agreement for Research and Technological transfer to productive system between the Italian Government and Regione Toscana (SKY-EYE project).

References

Agapiou A, Hadjimitsis DG (2011) Vegetation indices and field spectral-radiometric measurements for validation of buried architectural remains: verification under area surveyed with geophysical campaigns. J Appl Remote Sens 5(1):053554–053551. doi:10.1117/1.3645590

Agapiou A, Hadjimitsis DG, Alexis D et al (2012) Osservatory validation of Neolithic tells ("Megoules") in the Thessalian plain, central Greece, using hyperspectral spectroradiometric data. J Archaeol Sci 35(5):1499–1512

Agapiou A, Hadjimitsis DG, Sarris A et al (2013) Optimum temporal and spectral window for monitoring crop marks over archaeological remains in the Mediterranean region. J Archaeol Sci 40:1479–1492

Alexakis D D, Agapiou A, Hadjimitsis D G et al (2012) Remote sensing applications in archaeological research. doi: 10.5772/37668

Aloupi E, Karydas AG, Paradellis T (2000) Pigment analysis of wall paintings and ceramics from Greece and Cyprus: the optimum use of X-ray spectrometry on specific archaeological issues. X-Ray Spectrom 29(1):18–24

Alparone L et al (2011) Hyperspectral instruments as potential tools for monitoring decay processes of historical building surfaces. In: Fioravanti M, Mecca S (eds) Proceedings of the safeguard of cultural heritage—a challenge from the past for the Europe of tomorrow, Florence, 2011

Bacci M (1995) Fibre optics applications to works of art. Sensor Actuat B 29:190–196

Bacci M, Casini A, Cucci C et al (2003) Non-invasive spectroscopic measurements on the Il ritratto della figliastra by Giovanni Fattori: identification of pigments and colourimetric analysis. J Cult Herit 4:329–336

Balas C, Papadakis V, Papadakis N et al (2003) A novel hyper-spectral imaging apparatus for the non-destructive analysis of objects of artistic and historic value. J Cult Herit 4:330s–337s

Benvenuti M et al (2009) A portable hyperspectral device for monitoring the chemical and mineralogical composition of historical buildings surfaces. Paper presented at the 4th International Congress on Science and Technology for the safeguard of cultural heritage in the Mediterranean Basin, Cairo, Egypt, 6–8 December 2009

Camaiti M, Benvenuti M, Chiarantini L et al (2011) Hyperspectral sensor for gypsum detection on monumental buildings. J Geophys Eng 8:S126–S131

Camaiti M et al (2013) Monitoring of chemical and physical characteristics of stone surfaces by a portable spectroradiometer. In: Geophysical Research Abstracts of EGU General Assembly 2013, Wien, 7–12 April 2013, vol 15, p 13552

Campbell JB (2002) Introduction to remote sensing, third edn. Taylor & Francis, London

Clark RN (1999) Spectroscopy of rocks and minerals, and principles of spectroscopy. In: Rencz A (ed) Manual of remote sensing. Wiley, New York, pp 1–63

Clark RN, King TVV, Klejwa M et al (1990) High spectral resolution reflectance spectroscopy of minerals. J Geophys Res 95(B8):12653–12680

Craig N, Speakman RJ, Popelka-Filcoff RS et al (2007) Comparison of XRF and PXRF for analysis of archaeological obsidian from Southern Perú. J Archaeol Sci 34(12):2012–2024

Cucci C et al (2015) Hyperspectral remote sensing techniques applied to the non invasive investigation of mural paintings: a feasibility study carried out on a wall painting by Beato Angelico in Florence. In: Pezzati L, Targowski P (eds) Proceedings SPIE 9527: Optics for Arts, Architecture, and Archaeology V, Munich, June 2015. doi:10.1117/12.2184743

Di Benedetto F et al (2014) Hyperspectral monitoring of marble in buildings: a case study of the Santa Maria del Fiore (Florence, Italy) facades. In: Abstracts of the 21st general meeting of the International Mineralogical Association (IMA 2014), Sandton, Johannesburg, 1–5 September 2014

Doehene E, Price CA (2010) Stone conservation: an overview of current research, second edition. Getty Publications, The Getty Conservation Institute, Los Angeles

Dolske DA (1995) Deposition of atmospheric pollutants to monuments, statues, and buildings. Sci Total Environ 167:15–31

Favaro M, Mendichi R, Ossola F et al (2007) Evaluation of polymers for conservation treatments of outdoor exposed stone monuments. Part II: Photo-oxidative and salt-induced weathering of acrylic silicone mixtures. Polym Degrad Stab 92:335–351

Frediani P, Manganelli del Fá C, Matteoli U et al (1982) Use of perfluoropolyethers as water repellents: study of their behaviour on Pietra Serena, a fiorentine building stone. Stud Conserv 27:31–37

Gauri K L, Holdren G C Jr (1981) Pollutant effects on stone monuments. Environ Sci Technol 15(4):386–390

Haneef SJ, Johnson JB, Dickinson C et al (1992) Effect of dry deposition of NO_x and SO_2 gaseous pollutants on the degradation of calcareous building stones. Atmos Environ A Gen 26(16):2963–2974

Kerr A, Rafuse H, Sparkes G et al (2011) Visible/infrared spectroscopy (VIRS) as a research tool in economic geology: background and pilot studies from Newfoundland and Labrador. Curr Res Rep 11(1):145–166

Kruse FA (2012) Mapping surface mineralogy using imaging spectrometry. Geomorphology 137:41–56

Kubik M (2007) Hyperspectral imaging: a new technique for the non-invasive study of artworkks. In: Creagh D, Bradley D (eds) Physical techniques in the study of art, archeology and cultural heritage, vol 2. Elsevier, Amsterdam, pp 200–259

Lluveras A, Boularand S, Andreotti A et al (2010) Degradation of azurite in mural paintings: distribution of copper carbonate, chlorides and oxalates by SRFTIR. Appl Phys A Mater 99(2):363–375

Magendran T, Sanjeevi S, Bhattacharya A K et al (2011) Hyperspectral radiometry to estimate the grades of iron ores of Noamundi, India: a preliminary study. In: 31st Asian Association on Remote Sensing 2010, Hanoi, 1–5 November 2010. Curran Associates, New York, pp 1–6

Melani A et al (2010) Hyperspectral data processing activities and applications with SIM-GA. In: Proceedings of the IEEE Gold Remote Sensing Conference, Livorno, 20–30 April 2010

Miliani C, Rosi F, Brunetti BG et al (2010) In situ noninvasive study of artworks: the MOLAB multitechnique approach. ACC Chem Res 43(6):758–738

Milton EJ (1987) Principles of field spectroscopy. Int J Remote Sens 8(12):1807–1827

Montecchi A (2013) Development of a methodology for monitoring surfaces of historic buildings using hyperspectral portable instrument (in Italian). Dissertation, University of Florence

Mugnaini S, Bagnoli A, Bensi P et al (2006) Thirteenth century wall paintings under the Siena Cathedral (Italy). Mineralogical and petrographic study of materials, painting techniques and state of conservation. J Cult Herit 7(3):171–185

Petrovic A, Khan SD, Thurmond AK (2012) Integrated hyperspectral remote sensing, geochemical and isotopic studies for understanding hydrocarbon-induced rock alterations. Mar Pet Geol 35(1):292–308

Raimondi V, Cecchi G, Pantani L et al (1998) Fluorescence LiDAR monitoring of historic buildings. Appl Opt 37:1089–1098

Ramakrishnan D, Bharti R (2015) Hyperspectral remote sensing and geological applications. Curr Sci 108(5):879–891

Ramakrishnan D, Nithya M, Singh KD et al (2013) A field technique for rapid lithological discrimination and ore mineral identification: results from Mamandar polymetal deposit, India. J Earth Syst Sci 122(1):1–14

Ricci C, Miliani C, Brunetti BG et al (2006) Non-invasive identification of surface materials on marble artifacts with fiber optic mid-FTIR reflectance spectroscopy. Talanta 69:1221–1226

Rosi F, Daveri A, Miliani C et al (2009) Non-invasive identification of organic materials in wall paintings by fiber optic reflectance infrared spectroscopy: a statistical multivariate approach. Anal Bioanal Chem 395:2097–2106. doi:10.1007/s00216-009-3108-y

Sarris A, Papadopoulos N, Agapiou A et al (2013) Integration of geophysical surveys, ground hyperspectral measurements, aerial and satellite imagery for archaeological prospection of prehistoric sites: the case study of Vésztő-Mágor Tell, Hungary. J Archaeol Sci 40:1454–1470

Serraglini F (2010) Verifica dell'efficacia di tecniche di restauro su marmo con sensori iperspettrali. Dissertation, University of Florence

Siegesmund S, Weiss T, Vollbrecht A (2002) Natural stone, weathering phenomena, conservation strategies and case studies. Geological Society Special Publications No. 205. The Geological Society, London

Striegel MF, Bede Guin E et al (2003) Air pollution, coatings, and cultural resources. Prog Org Coat 48:281–288

Suzuki A (2014) Study for the calibration of the hyperspectral FieldSpec Pro instrument for the characterization of carbonatic stone surfaces affected by saline efflorescences (in Italian). Dissertation, University of Florence

Tangestani MH, Validabadi K (2014) Mineralogy and geochemistry of alteration induced by hydrocarbon seepage in an evaporite formation; a case study from the Zagros Fold Belt, SW Iran. Appl Geochem 41:189–195

Tsakalof A, Manoudis P, Karapanagiotis I et al (2007) Assessment of synthetic polymeric coatings for the protection and preservation of stone monuments. J Cult Herit 8:69–72

Vandenabeele P, Lambert K, Matthys S et al (2005) In situ analysis of mediaeval wall paintings: a challenge for mobile Raman spectroscopy. Anal Bioanal Chem 383:702–712

Vettori S, Benvenuti M, Camaiti M et al (2008) Assessment of the deterioration status of historical buildings by hyperspectral imaging techniques. In: Tiano P, Pardini C (eds) SMS/08 Congress on in situ monitoring of monumental surfaces. Edifir, Firenze, p 55

Vettori S et al (2012) Portable hyperspectral device as a valuable tool for the detection of protective agents applied on historical buildings. In: Geophysical Research abstracts of EGU general assembly 2012, Wien, 22–27 April 2012, vol 14, p 9459

Wang C (2015) Hyperspectral sensor: a new approach for evaluating the efficacy of laser cleaning in the removal of varnishes and overpaintings. Dissertation, University of Bologna

Xinyue G (2013) Numerical elaboration of hyperspectral monitoring of the marble surface of Santa Maria del Fiore Cathedral (in Italian). Dissertation, University of Florence

Zadeh MH, Tangestani MH, Roldan FV et al (2014) Sub-pixel mineral mapping of a porphyry copper belt using EO-1 Hyperion data. Adv Space Res 53(3):440–451

Zecchi D (2013) Portable hyperspectral technique for detecting protective treatments on architectural stone materials (in Italian). Dissertation, University of Florence

Chapter 14
Terahertz Waves and Cultural Heritage: State-of-the-Art and Perspectives

Ilaria Catapano, Marcello Picollo, and Kaori Fukunaga

Abstract Noninvasive diagnostic technologies capable of gathering information on materials and the state of preservation of works of art are crucial to help conservators, archaeologists, and anthropologists plan and carry out their tasks properly. Among these technologies, those operating in the terahertz (THz) frequency range are among the newest and are deserving great attention as they allow both high-resolution imaging and material identification. A synthetic snapshot of the development today of THz spectroscopy and imaging is provided in this chapter together with practical examples assessing the advantages offered in the framework of cultural heritage surveys.

Keywords Noninvasive diagnostics • Spectroscopy • THz waves • Time-of-flight imaging

14.1 Introduction

Diagnostic technologies exploiting waves in the frequency range from 0.1 terahertz (THz) to 10 THz (corresponding to a free-space wavelength ranging from 30 μm to 3 mm) can be considered as the newest among the sensing and imaging techniques based on electromagnetic waves. As a matter of fact, although THz spectroscopy has a quite long history and THz waveforms have been widely used to perform spectroscopy in the far-infrared region (Karr and Kovach 1969; Nuss and Orenstein 1997; van Exter et al. 1989), the first THz images were provided only 20 years ago

I. Catapano (✉)
Institute for Electromagnetic Sensing of the Environment, National Research Council of Italy (IREA-CNR), Naples, Italy
e-mail: catapano.i@irea.cnr.it

M. Picollo
Nello Carrara Institute of Applied Physics, National Research Council of Italy (IFAC-CNR), Florence, Italy

K. Fukunaga
Applied Electromagnetic Research Center, National Institute of Information and Communications Technology, Tokyo, Japan

N. Masini, F. Soldovieri (eds.), *Sensing the Past*, Geotechnologies and the Environment 16, DOI 10.1007/978-3-319-50518-3_14

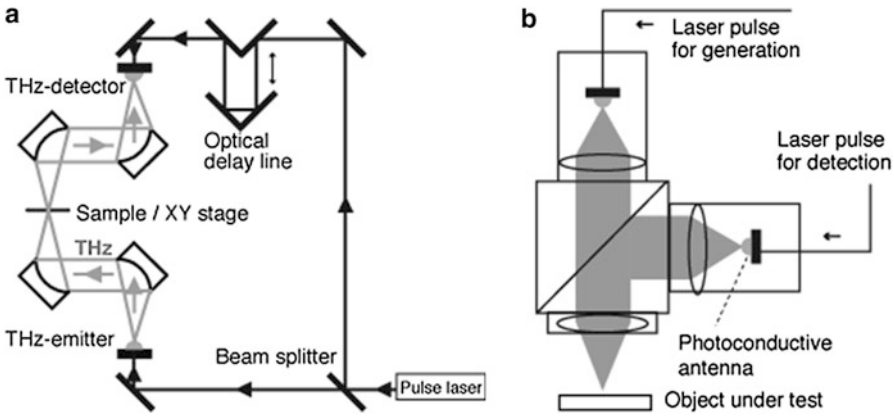

Fig. 14.1 Schematic representation of a THz system: (**a**) transmission mode; (**b**) reflection mode

by Hu and Nuss. These images were obtained by scanning test objects by means of sub-picosecond optical pulses, which were adopted to generate a broadband THz radiation, and by collecting the signal transmitted through the objects (Hu and Nuss 1995).

The delay of THz imaging development was the result of lack of stable and cost-effective sources and detectors. Such a lack has entailed the historical definition of "THz gap" and, for a long time, has limited the use of THz waves mainly for academic research purposes, wherein complex and bulky custom-made systems have been employed.

In past years, the technological progress, especially in the frame of laser technology, has significantly changed this scenario, and a new generation of flexible, compact, and portable THz systems is currently available. These systems are characterized by an optical fiber-coupled source and detector probes and do not require complex optical alignments. Hence, they can be easily reconfigured to scan objects under different measurement configurations as sketched in Fig. 14.1a, b, which show a schematic representation of a THz system working in transmission and reflection modalities, respectively.

Thanks to the massive technological progress, THz spectroscopy and imaging systems are currently experiencing a rapid expansion and deserving great attention in a wide range of applicative contexts (Tonouchi 2009; Jepsen et al. 2011; Axel Zeitler 2013; Saeedkia 2013; Perenzoni and Paul 2014; Song and Nagatsuma 2015).

As microwaves, THz signals are, indeed, nonionizing radiations capable of penetrating dielectric materials, which are opaque to both visible and infrared waves. Moreover, the energy of THz waves is sufficiently low to be considered as perfectly noninvasive in practice. On the other hand, several substances exhibit absorption spectra at THz frequencies with specific fingerprints, which depend on their molecular and intermolecular behavior. Therefore, THz waves allow a high-resolution characterization of the inner features of man-made objects, with the

possibility of recognizing the adopted materials while assuring negligible long-term risks to the molecular stability of the exposed objects. These potentialities motivate the current interest about the use of THz sensing as a complementary technique to classical analysis methodologies, such as those based on X-rays or mid-infrared radiations, in several applications among which are food process monitoring (Gowen et al. 2012; Qin et al. 2013), quality control (Yasui et al. 2005; Rutz et al. 2006), security (Kawase et al. 2003; Shen et al. 2005), biomedical investigations (Yu et al. 2012; Joseph et al. 2014), and artwork characterization (Fukunaga and Hosako 2010).

As far as artwork surveys are concerned, both THz spectroscopy and imaging can be profitably exploited to carry out scientific observations and analysis. These investigations are essential for both academic research and practical conservation to understand the materials and techniques used in original works as well as those used in previous interventions. In this frame, as an extension from the mid-infrared range, THz spectroscopy can be used to analyze artists' materials and identify pigments, dyes, and binders (Fukunaga and Picollo 2010). Conversely, THz imaging allows a noninvasive and high-resolution characterization of the inner structure of the investigated objects and provides information comparable with that achieved invasively by analyzing cross sections of micro-samples (Picollo et al. 2015).

These potentialities are assessed in the following sections, wherein the state-of-the-art of THz spectroscopy and imaging is briefly traced and several results are summarized.

14.2 THz Spectroscopy

THz spectroscopy allows the determination of material transmittance or reflectance. It is performed by computing the ratio, in the frequency domain, of the signal transmitted through or reflected by the material under test and a reference signal, that is, the signal measured without the object. Moreover, THz spectroscopy can be used to identify materials having similar features and chemical composition but different structure (e.g., titanium dioxide in its rutile and anatase forms). Gas, liquid, and solid materials exhibit, indeed, unique spectral fingerprints in the THz range depending on their molecular and intermolecular behavior, weak bonds, and phonon absorptions (Karr and Kovach 1969; Nuss and Orenstein 1997; van Exter et al. 1989; Axel Zeitler 2013; Saeedkia 2013; Perenzoni and Paul 2014; Song and Nagatsuma 2015).

In the frame of artwork investigations, THz spectroscopy has been successfully used to discriminate pigments having almost the same color and including the same mineral elements. As an example, we recall that, based on the spectra of more than 60 cobalt blue pigment and paint products, it was discovered that, in the THz region, aureolin and cobalt blue (two cobalt components) have distinct spectral signatures (Jackson et al. 2011).

However, in contrast to the mid-infrared range, a THz spectral database providing standards and comparative data is not available at this time. In addition, several open issues have yet to be faced to define measurement protocols, which must be applied to uniquely identify materials in terms of their THz spectral fingerprints.

A first step in this direction has been performed at the National Institute of Information and Telecommunication Technology (NICT), where a spectral library of art materials has been established (http://thzdb.org). Fukunaga and colleagues have measured more than 500 spectra to the NICT database by using Fourier transform infrared THz spectroscopy (FTIR-THz) and time-domain terahertz spectroscopy (TDS) and compared the results provided by the two methodologies to assess their consistency (Fukunaga 2008).

As an example, the spectra of cinnabar obtained by TDS and FTIR are compared in Fig. 14.2. This figure shows that the positions of the spectral peaks provided by the two methodologies, working in transmission mode, are in good agreement. This result corroborates that THz TDS is able to indicate the absorption peaks properly, although its applicable frequency range is usually limited to a bandwidth between 0.1 and 4.5 THz. Such constraints together with the observation that many artists' materials have characteristic spectral fingerprints at frequencies higher than

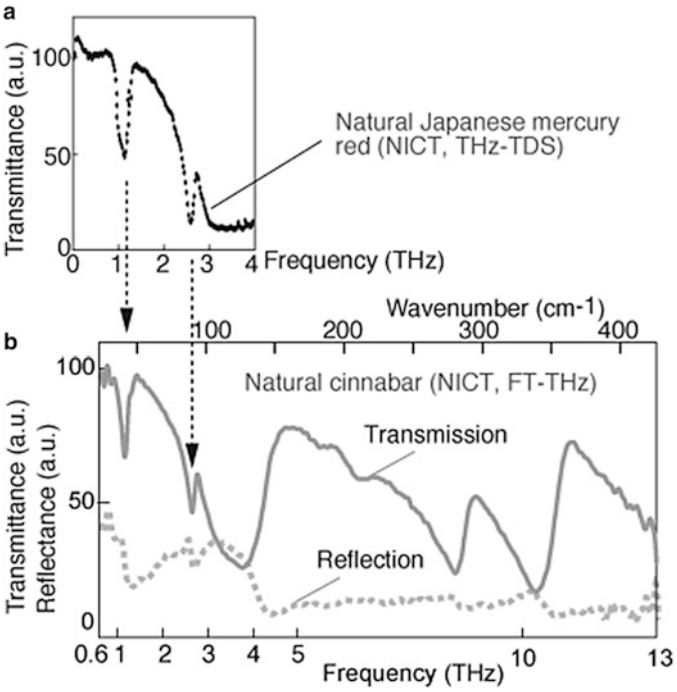

Fig. 14.2 Comparison of cinnabar spectra obtained by using (**a**) time-domain terahertz spectroscopy (TDS) and (**b**) Fourier transform infrared spectroscopy (FTIR)

4.5 THz make FTIR preferable. As a matter of fact, FTIR systems allow a broadband spectroscopy, being able to cover the range from 0.5 to 20 THz.

Figure 14.2 also shows that the spectrum of the cinnabar obtained in reflection mode is not clear enough to make possible its identification. In this framework, it is worth noting that THz reflection spectroscopy needs a well-calibrated setup, because the measurement is inherently relative and sensitive to the phase. Therefore, it is more challenging than the transmission aspect, although it is often preferable because it does not constrain object size, location, opacity, etc. On the other hand, when possible, both transmission and reflection measurements should be performed to gather as much information as possible and have a complete understanding of the spectral behavior of the material under test.

14.3 Time-of-Flight THz Imaging

THz imaging has experienced a rapid expansion in the past 20 years, and several imaging methodologies have been developed, among which time-of-flight approaches, THz false color images, and techniques based on pixel-by-pixel representation of (a) the amplitude of a pulse peak or of the spectrum at a specific frequency or (b) the amplitude or power integration over a specific time window or over a certain frequency range (Herrmann et al. 2000).

This section is focused on the time-of-flight THz imaging because it provides a broad characterization of the investigated objects, allowing a three-dimensional (3D) representation of their internal structure.

Time-of-flight THz imaging is performed by adopting a reflection measurement configuration, and its working principle is quite simple (Axel Zeitler 2013; Saeedkia 2013; Perenzoni and Paul 2014; Song and Nagatsuma 2015): an object, located at the focal distance from the emitter/receiver heads and probed by a THz signal, gives rise to a reflected waveform, which accounts for the object surface and (if the object is nonmetallic) for its inner electromagnetic features. In particular, as schematized in Fig. 14.3a, at each measurement point, the air–object interface as well as all the electromagnetic discontinuities possibly located inside the object (represented as interfaces A and B in Fig. 14.3a) generate reflections, which are recorded as a time-dependent waveform.

By collecting data along a line and integrating the gathered waveforms, a space–time image, referred as a THz radargram, is obtained as is sketched in Fig. 14.3b. This latter provides an example of generic time-dependent waveforms collected along a line a–a′ (left upper panel), a zoom of the signal gathered at a single point A (right upper panel), and the corresponding radargram (central bottom panel).

In a radargram the horizontal axis is the space axis and represents the measurement line; the vertical axis is the time axis and represents the time of flight, that is, the time T that the waveform employs to propagate from the emitter to an electromagnetic discontinuity and to go back to the receiver.

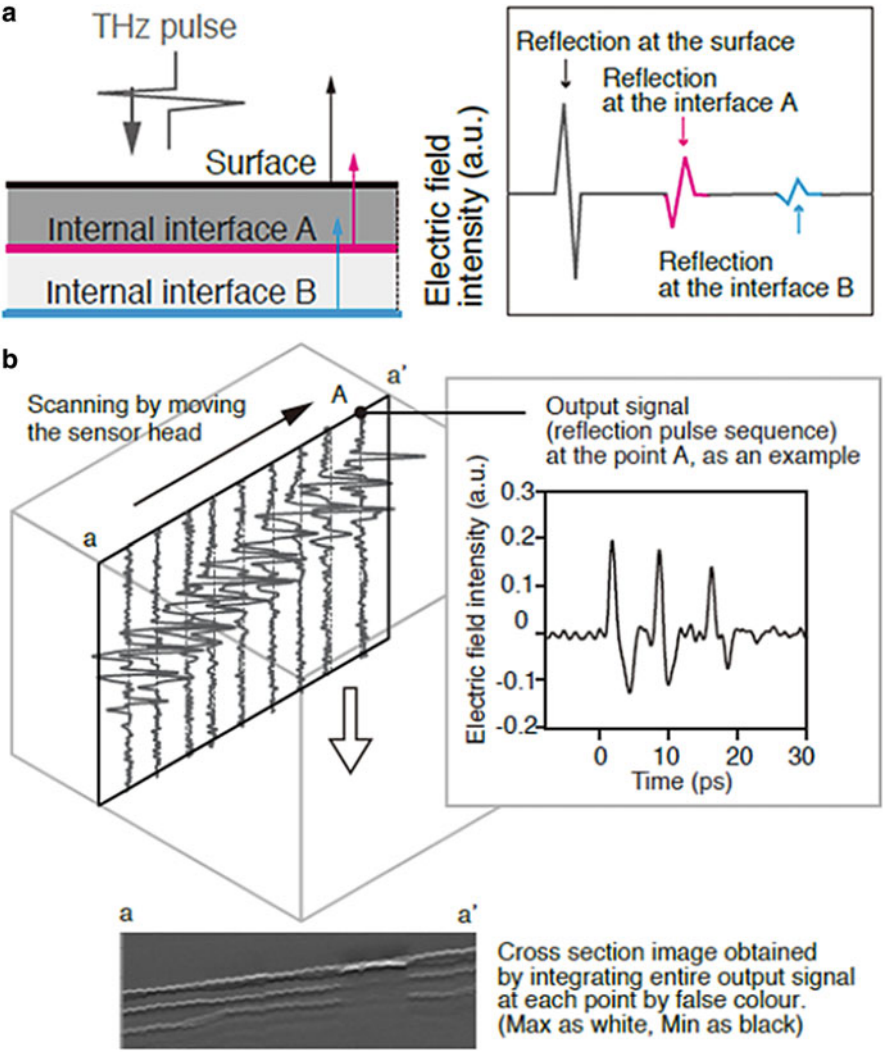

Fig. 14.3 Time-of-flight imaging principle: (**a**) single point measurement; (**b**) acquisition of a THz radargram

The time of flight T is related to the distance d between the THz probes and the detected discontinuities by $d = v\ T/2$, v being the wave propagation velocity into the encountered media. Therefore, a THz radargram provides a cross-sectional representation of the inner structure of the investigated object, which gives information on the position and thickness of possible inner layers. Moreover, by integrating data collected along parallel lines it is possible to obtain a 3D characterization of the investigated object. However, because a 3D view could make

the representation of the inner features not easy, two-dimensional (2D) images showing the surveyed scenario at different constant depths are commonly provided.

Finally, it is worth recalling that, when time-of-flight imaging is performed, noise filtering and deconvolution procedures are commonly applied to improve the image quality (Axel Zeitler 2013; Saeedkia 2013; Perenzoni and Paul 2014; Song and Nagatsuma 2015). Moreover, advanced data processing approaches, such as optical coherence tomography, Kirchhoff migration, and model-based procedures exploiting approximate models of the wave propagation phenomenon, have been proposed and successfully applied (Axel Zeitler 2013; Chan et al. 2007).

14.4 THz Imaging Examples

To assess the potentialities offered by THz imaging, two test cases concerning laboratory-prepared objects are herein presented.

The first example concerns an egg-tempera mock-up panel painting. This test panel was prepared following traditional medieval recipes for the execution of panel paintings (Gettens and Stout 1966), and its structure over the wood panel consisted of a gypsum (*gesso grosso*) and animal glue (rabbit skin glue) layer, a modern industrial linen canvas, and a final layer of gypsum (*gesso fine*) and animal glue (rabbit skin glue). The last layer was flattened with very thin sandpaper to give it a perfectly smooth surface. The final egg-tempera medium paint layers were made with six different pigments: yellow ochre α-FeO(OH); cinnabar HgS; green earth $K[(Al, Fe^{III}), (Fe^{II}, Mg)], (AlSi_3, Si_4)O_{10}(OH)_2$; verdigris $2Cu(CH_3COO)_2{\cdot}CuO{\cdot}6H_2O$; azurite $2\ CuCO_3{\cdot}Cu(OH)_2$; and ivory black $Ca_5(OH)(PO_4)_3$ with the addition of carbon black, in three different thicknesses (Fig. 14.4a).

The time-domain graph of the propagation of the THz radiation into the structure of the test panel and the reconstruction of the noninvasive cross section of a linear section of the test panel are shown in Fig. 14.4b, c. Looking at these graphs, the position of different refractive index discontinuities, versus time of acquisition of the THz signal through the depth of the panel structure, is evident. Obviously, the refractive index discontinuities are caused by the presence of the diverse materials. In particular, the presence of the linen canvas is revealed by the reconstructed THz image at around 170–175 ps of delay of the THz radiation (Fig. 14.4d).

The second example concerns a 50 mm × 50 mm × 4 mm dry wood object, whose upper face has been covered by a 1-mm-thick plaster layer, decorated by geometric shapes, which have been drawn by using a common HB pencil, and finally covered by a thin layer of black tempera paint. The images of the object during its preparation stage are shown in Fig. 14.5a.

This object has been scanned by using the Z-Omega fiber-coupled terahertz time domain (FiCO) system equipped with an automatic *x*-*y* positioning module, which enables us to scan, under a normal reflection measurement configuration, an area 150 mm × 150 mm with the smallest spatial offset along both *x* and *y* directions,

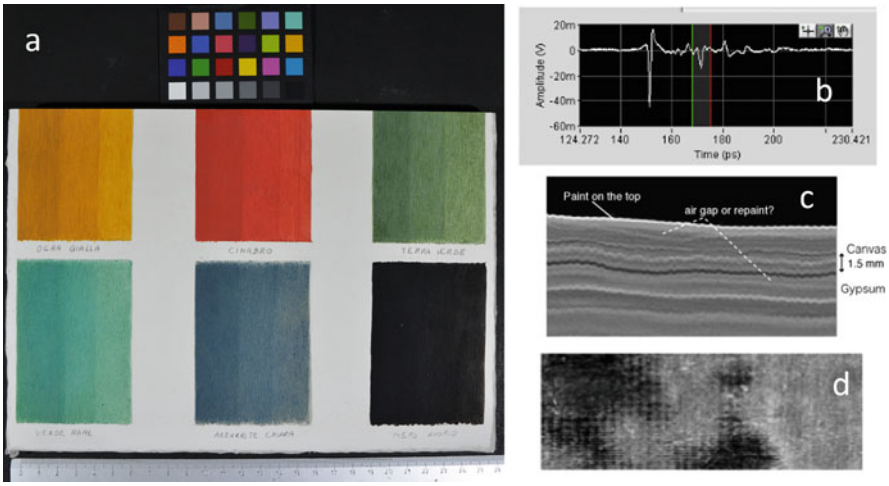

Fig. 14.4 (**a**) Egg-tempera mock-up panel painting. (**b**) Time-domain THz graph. (**c**) Noninvasive cross-section image of a linear section of the test panel. (**d**) Reconstructed image at about 175 ps delay showing the presence of the linen canvas

equal to 12 μm. The data have been collected on a 45 mm × 39 mm surface parallel to the upper face of the object with a 0.25-mm spatial step along both the *x*- and *y*-axes.

Figure 14.5b shows the radargrams gathered along the a–a′ measurement line and processed by means of a noise filtering procedure based on the concept of the actual frequency bandwidth of the data (Catapano and Soldovieri 2015). This radargram provides an image not only of the air–object interface but also of the inner plaster–wood interface. Moreover, the presence of the covered penciled square shape appears as an increased reflectivity occurring at the air–object interface.

The depth slices obtained by applying a topography correction approach (Catapano and Soldovieri 2015) to the filtered data are shown in Fig.14.5c and state the ability to detect material layers characterizing the object under test as well as the ability to discover and clearly image hidden penciled objects.

14.5 Conclusions and Open Issues

A brief overview assessing the potentialities offered in the frame of cultural heritage by spectroscopic and imaging devices working in the THz range has been provided here. The presented results encourage a widespread use of THz techniques, which is also supported by the technological advancements that are currently supporting the development of user-friendly systems, suitable for onsite noninvasive diagnostic analysis.

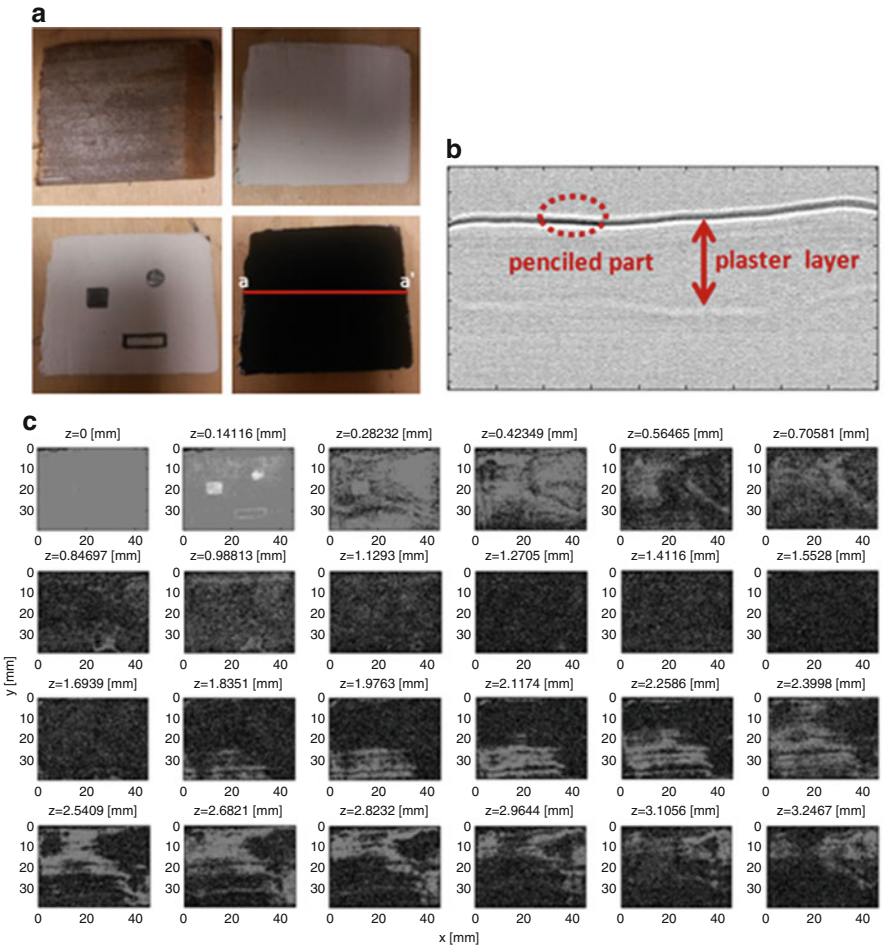

Fig. 14.5 THz imaging of a laboratory-prepared wood object: preparation steps (**a**); radargram along the red measurement line a–a′ (**b**); depth slices (**c**)

On the other hand, there are still several open challenges to be faced. In particular, as far as THz spectroscopy is concerned, the development of a global reliable and standardized database of material fingerprinting is desirable to make possible quantitative analysis and an effective material identification.

Conversely, in the frame of THz imaging, the development of advanced data processing procedures and their integration in standardized processing chains are worth being pursued to improve the ability to discriminate different material layers and provide accurate images of the inner features of the investigated artworks.

A further open challenge concerns the need of a systematic comparison among THz results and those provided by gold standard techniques for artworks surveys,

such as X-ray radiography and infrared imaging, to state the advantages and limits of THz technology. In this respect, some results concerning paintings are available at this moment, but a large amount of work is still required especially when other kinds of artwork are considered.

References

Catapano I, Soldovieri F (2015) THz imaging and spectroscopy: first experiments and preliminary results. In: Proceedings of 8th International Workshop on Advanced Ground Penetrating Radar (IWAGPR), 7–10 July 2015, 4 pp

Chan WL, Deibel J, Mittleman DM (2007) Imaging with terahertz radiation. Rep Prog Phys 70:1325–1379

Fukunaga K (2008) Terahertz spectral database: construction of open terahertz spectral database. J Nat Inst Inf Commun Technol 55:61–66

Fukunaga K, Hosako I (2010) Innovative non-invasive analysis techniques for cultural heritage using terahertz technology. C R Phys 11:519–526

Fukunaga K, Picollo M (2010) Terahertz spectroscopy applied to the analysis of artists' materials. Appl Phys A Mater Sci Process 100:591–597

Gettens RJ, Stout GL (1966) Painting materials, a short encyclopedia. Dover Publication Inc., New York

Gowen AA, O'Sullivan C, O'Donnell CP (2012) Terahertz time domain spectroscopy and imaging: emerging techniques for food process and quality control. Trends Food Sci Technol 25:40–46

Herrmann M, Tani M, Sakai K (2000) Display modes in time-resolved terahertz imaging. Jpn J Appl Phys 39:6254–6258

Hu BB, Nuss MC (1995) Imaging with THz waves. Opt Lett 20:1716–1719

Jackson JB, Bowen J, Walker G, Labaune J, Mourou G, Menu M, Fukunaga K (2011) A survey of terahertz applications in cultural heritage conservation science. IEEE Trans Terahertz Sci Technol 1:220–231

Jepsen PU, Cooke DG, Koch M (2011) Terahertz spectroscopy and imaging – modern techniques and applications. Laser Photonics Rev 5:124–166

Joseph CS, Patel R, Neel VA, Giles RH, Yaroslavsky AN (2014) Imaging of ex vivo nonmelanoma skin cancers in the optical and terahertz spectral regions. J Biophotonics 7:295–303

Karr C Jr, Kovach JJ (1969) Far-infrared spectroscopy of minerals and inorganics. Appl Spectrosc 23:219–223

Kawase K, Ogawa Y, Watanabe Y (2003) Non-destructive terahertz imaging of illicit drugs using spectral fingerprints. Opt Express 11:2549–2554

Nuss MC, Orenstein J (1997) Terahertz Time-Domain spectroscopy (THz-TDS). In: Gruener G (ed) Millimeter-wave spectroscopy of solids. Springer-Verlag, Heidelberg

Peiponen K-E, Kuwata-Gonokami M, Axel Zeitler J (eds) (2013) Terahertz spectroscopy and imaging. Springer-Verlag, Berlin/Heidelberg, pp 451–489

Perenzoni M, Paul DJ (2014) Physics and applications of Terahertz radiation, Springer Series in Optical Sciences, vol 173. Springer, Dordrecht

Picollo M, Fukunaga K, Labaune J (2015) Obtaining noninvasive stratigraphic details of panel paintings using terahertz time domain spectroscopy imaging system. J Cult Herit 16:73–80

Qin J, Ying Y, Xie L (2013) The detection of agricultural products and food using terahertz spectroscopy: a review. Appl Spectrosc Rev 48:439–457

Rutz F, Koch M, Khare S, Moneke M, Richter H, Ewert U (2006) Terahertz quality control of polymeric products. Int J Infrared Millimeter Waves 27:547–556

Saeedkia D (ed) (2013) Handbook of Terahertz technology for imaging, sensing and communications. Woodhead Publishing, Oxford

Shen YC, Lo T, Taday PF, Cole BE, Tribe WR, Kemp MC (2005) Detection and identification of explosives using terahertz pulsed spectroscopic imaging. Appl Phys Lett 86:3pp

Song H-J, Nagatsuma T (eds) (2015) Handbook of Terahertz technologies; devices and applications. Pan Stanford, Singapore

Tonouchi M (2009) Galore new applications of terahertz science and technology. Terahertz Sci Technol 2:90–101

van Exter M, Fattinger C, Grischkowsky D (1989) Terahertz time-domain spectroscopy of water vapour. Opt Lett 14:1128–1130

Yasui T, Yasuda T, Sawanaka K, Araki T (2005) Terahertz paintmeter for noncontact monitoring of thickness and drying progress in paint film. Appl Opt 44:6849–6856

Yu C, Fan S, Sun Y, Pickwell-MacPherson E (2012) The potential of terahertz imaging for cancer diagnosis: a review of investigations to date. Quant Imaging Med Surg 2:33–45

Chapter 15
FF-XRF, XRD, and PIXE for the Nondestructive Investigation of Archaeological Pigments

Francesco Paolo Romano, Lighea Pappalardo, Giacomo Biondi, Claudia Caliri, Nicola Masini, Francesca Rizzo, and Hellen Cristine Santos

Abstract This chapter discusses the integration of particle-induced X-ray emission (PIXE), full-field X-ray fluorescence (FF-XRF), and X-ray diffraction (XRD) for the analysis of archaeological pigments. It summarizes the research activity performed for developing these innovative, custom-built, and portable instruments. A novel analytical protocol has been developed by combining these techniques with the aim of performing an in situ quantitative characterization of painted materials. The potentiality of using this approach is demonstrated for manganese black used in archaeological pottery manufactured over time by different cultures.

Keywords Cultural heritage • Pigments • FF-XRD • PIXE • XRD

15.1 Introduction

During the past decade, a broad innovation process has been undertaken in the development of techniques to be applied in the study, restoration, and conservation of works of art in the cultural heritage field (Pollard and Heron 2008).

The new instruments and methodologies belong to different scientific fields and fulfill several requirements that can be considered optimal for the investigation of archaeological and artistic objects. In general, they are nondestructive (or microdestructive) and sensible to the physicochemical nature of the materials. Moreover, they are fast, allowing the systematic analysis of many objects in a short time, and they can be arranged in a compact and portable setup.

F.P. Romano (✉) • L. Pappalardo • G. Biondi
IBAM-CNR, Via della Biblioteca 4, 95124, Catania, Italy
e-mail: romanop@lns.infn.it

C. Caliri • F. Rizzo • H.C. Santos
LNS-INFN, Via S. Sofia 62, 95123, Catania, Italy

N. Masini
CNR-IBAM Institute for Archaeological and Monumental Heritage,
C. da Santa Loja, 85050, Tito Scalo, Potenza, Italy

N. Masini, F. Soldovieri (eds.), *Sensing the Past*, Geotechnologies and the Environment 16, DOI 10.1007/978-3-319-50518-3_15

In this framework, ion beam analysis and X-ray spectroscopy gained popularity among scholars operating in archaeological sciences. Their capability in the analysis of a wide variety of materials, and in the determination of both average composition (bulk analysis) and local composition (microanalysis), has been demonstrated (Pappalardo et al. 2003; Romano et al. 2005, 2011).

A challenging scientific case concerns the analysis of pigments used in antiquity. The analytical approach for characterizing painted artwork offers the opportunity to obtain new insights into ancient painting techniques, the nature and provenance of raw materials, and technological and artistic evolution over time. In addition, analytical results help to evidence the presence of degradation and then to elaborate a conservation policy.

However, painted surfaces exhibit a complex three-dimensional structure and a heterogeneous chemical composition. Consequently, the necessity of developing analytical protocols based on the integrated use of different analytical techniques (even portable and nondestructive) specifically developed for the investigation of painted artworks appears evident.

In the past decade, the research group operating at the LANDIS laboratory of the LNS-INFN and IBAM-CNR in Catania (Italy) dedicated many efforts in developing and integrating portable techniques for in situ quantitative investigations of materials of interest in the cultural heritage field (Pappalardo et al. 2003, 2007; Romano et al. 2005).

In this chapter, the combined use of full-field X-ray fluorescence (FF-XRF) imaging, particle-induced X-ray emission (PIXE), and X-ray diffraction (XRD) is discussed for applications concerning the compositional investigation of pigments. These techniques are particularly suited for pigment characterization. In fact, they allow two-dimensional elemental imaging (FF-XRF) for obtaining composition and chemical associations at different scales of length; mineralogical investigation (XRD) for determining the nature of different pigments, even in the presence of the same chemical elements in the pictorial layer; and quantitative analysis (PIXE) of the pictorial layer. Section 15.2 describes the portable PIXE, FF-XRF, and XRD instruments developed in recent years at the LANDIS laboratory. A brief technical description of the portable spectrometers and main analytical capabilities of the techniques is detailed as well.

In Sect. 15.3, the potentiality of these techniques for the compositional investigation of pigments in archaeological material is presented and discussed. As a case study is discussed the manganese black technique in fired pottery dated back to the Neolithic (pottery of Castelluccio, Sicily) (Pappalardo 1999) and to the more recent polychrome pottery in the Nasca culture in Southern Peru (Picciome et al. 2011; Silverman and Proulx 2002, Lasaponara, Masini Orefici 2016).

Section 15.4 reports a brief summary concerning incomes and novelty in the use of the techniques presented in the chapter.

15.2 Experimental Methods

15.2.1 The Portable PIXE-Alpha System

Particle-induced X-ray emission (PIXE) is an analytical method particularly suited to performing nondestructive compositional analysis of surface layers in cultural objects (Dran et al. 2004; Mandò 2005; Romano et al. 2011).

The technique is based on the irradiation of materials under investigation by means of a charged particle beam (protons or alpha particles) of a few MeV of energy. The primary beam induces the atoms composing the sample under analysis to emit characteristic X-ray fluorescence. The detection of these X-rays allows identifying the elements composing the sample and, under specific conditions, to perform a quantitative analysis of the raw data (Johansson et al. 1995; Verma 2007).

The sharp absorption of the incoming charged particles in the matter cause the PIXE investigation to be confined in a limited range. For these aspects, PIXE is particularly suited for the study of surface layers in works of art. Additionally, the PIXE technique presents a high-ionization cross section for low Z elements and a high chemical sensitivity for the light matrices. However, a limit of the PIXE technique is the need of using accelerators for the measurements, which makes the technique unsuitable for unmovable artworks.

In 1996, the LANDIS group started the development of a portable PIXE system (Pappalardo et al. 1996). The system, known as PIXE-alpha, was realized by using a low-activity (37 MBq) polonium (^{210}Po) source emitting alpha particles of 5 MeV energy as primary beam. Over time, different versions of the PIXE-alpha system have been developed (Romano et al. 2012; Pappalardo et al. 2013).

The ^{210}Po source presents a large compact annular geometry. The alpha particles emitted by the active annulus irradiate the samples with average incident angles of about 45° and a 5-mm path. The spot size of the primary alpha beam is 18 mm when it is not collimated. The induced X-ray fluorescence is detected by a silicon drift detector (SDD) at 180° (backward direction), through the central hole of the annular source. The distance between the sample and the detector is limited to 6–7 mm. The final version of the PIXE-alpha system is equipped with an SDD with 124 eV energy resolution at 5.9 keV. During measurements, helium is fluxed to minimize the absorption effects of air for both the incident alpha particles and the fluorescence X-rays coming from the sample. The minimum Z detected in this experimental setup is that of sodium (Na). Figure 15.1 shows the spectrometer during the analysis of the black gloss in an Attic pottery.

The system is suited to perform quantitative analysis by a proper calibration with reference standards. The reproducibility is better than 5%, including statistical effects. Quantitative analysis and minimum detection limit (MDL) of a reference SCo-1 geological standard (Govindaraju 1994) are summarized in Table 15.1.

Fig. 15.1 Particle-induced X-ray emission (PIXE)-alpha spectrum during the analysis of Attic Black Gloss (Pappalardo et al. 2015, 2016a)

Table 15.1 Minimum detection limit (MDL) values (in ppm) of the PIXE-alpha source

	Na_2O	MgO	Al_2O_3	SiO_2	K_2O	CaO	TiO_2	Fe_2O_3
Measured values (%)	1.0 ± 0.2	3.0 ± 0.2	17.0 ± 1.0	66.5 ± 1.3	3.0 ± 0.2	2.9 ± 0.2	0.7 ± 0.1	4.6 ± 0.9
Reference values (%)	0.97	2.9	14.8	67.8	2.9	2.88	0.68	5.54
MDL (%)	0.3	0.08	0.04	0.07	0.05	0.08	0.06	0.3

Maniatis et al. (1993)

15.2.2 The Portable XRD System

X-ray diffraction (XRD) allows the mineralogical characterization of materials (Jenkins et al. 1996). The technique is based on the detection of X-rays diffracted by the regular atomic structure in crystalline samples. The XRD pattern is the fingerprint of the arrangement of atoms and thus it enables discriminating the mineralogical phases even for samples presenting the same chemical composition.

In many cases, cultural heritages are composed of materials with a polycrystalline nature and, consequently, they can be successfully characterized by XRD. In addition, XRD can be used to determine signs and causes of degradation and thus can be helpful to establish a proper conservation procedure.

Despite the powerful information that can be obtained by performing XRD analysis, the necessity of a careful alignment, the low intensities of the diffracted beams, and the long measurement time have rather limited the development of portable XRD instruments in the past (Uda et al. 2005; Gianoncelli et al. 2008; Romano et al. 2006).

In 2006, the LANDIS group presented a first version of a portable XRD system based on the use of microfocus X-ray sources and polycapillary semi-lens (Romano et al. 2006). This experimental setup improved the foregoing limits and enabled the possibility of performing XRD with a high angular resolution and a low measurement time (typically 1 h) directly in the field.

This section presents a new modular version of the portable XRD system based on a low-weight setup. The instrument is based on a goniometric geometry. Source and detector are placed in a theta-theta geometry and the sample is positioned outside the goniometer. This setup opens the possibility to investigate unmovable objects (i.e., large paintings or wall paintings) in a nondestructive way.

Microfocus X-ray tubes (with Fe and Cr targets) and polycapillary optics (with spot size of 0.6 mm and 7 mm, respectively) are used as the X-ray source. They are fully interchangeable to optimize performance depending on the analytical application.

The goniometric mechanics allows measurements starting from low angles (i.e., 3–4°), necessary for investigating samples with a large *d*-spacing. The largest value of the planar distance that can be investigated by the system is equal to 21.9 angstroms.

The portable XRD system is shown in Fig. 15.2.

The system is equipped with a 25 mm^2 active surface Si-PIN detector. A custom-programmed electronics and acquisition allows a digital selection of the Fe-K (or Cr-K) energy for performing the diffraction. In Fig. 15.3 are shown a calcite reference pattern obtained by using the Fe target tube and a 6-mm semi-lens polycapillary, respectively.

Fig. 15.2 The portable X-ray diffraction (XRD) spectrometer during the analysis of a Hellenistic sculpture at the Paolo Orsi Archeological Museum in Syracuse (Italy)

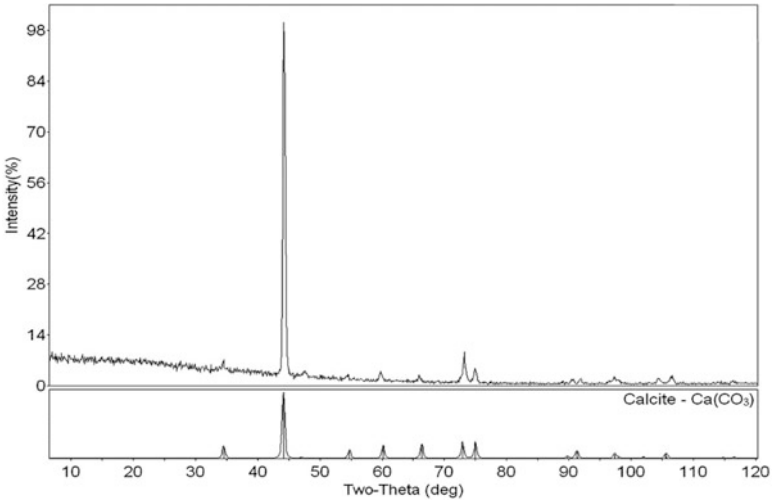

Fig. 15.3 Reference diffraction patterns taken at 0.05° angle step and 5-s acquisition time/step. Angular resolution is about 0.12°

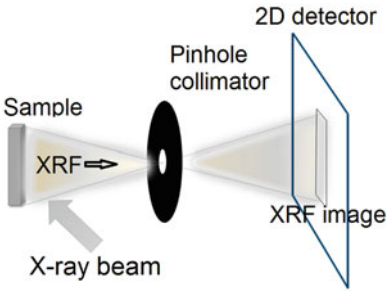

Fig. 15.4 Schematic illustration of the working principle of a full-field X-ray fluorescence (FF-XRF) device

15.2.3 Full-Field X-Ray Fluorescence

Interest in the nondestructive elemental mapping of materials has grown rapidly in a number of scientific disciplines. Scanning X-ray fluorescence is a nondestructive method suited to obtain this information. Measurements are performed by scanning the sample surface through a series of local measurements by a primary X-ray beam of small spot size (a few tens of micrometers). The induced X-ray fluorescence is detected at each of the irradiated position of the sample under investigation.

A different approach is used in the FF-XRF, in which the entire sample is excited by using a broad X-ray beam; an energy- and position-sensitive detector detects the characteristic fluorescence induced on the sample by a pinhole collimator of small dimensions. Sample, pinhole-collimator, detector, and source remain in fixed position during the measurement, and the need for scanning is avoided. A typical setup for a FF-XRF is shown in Fig. 15.4.

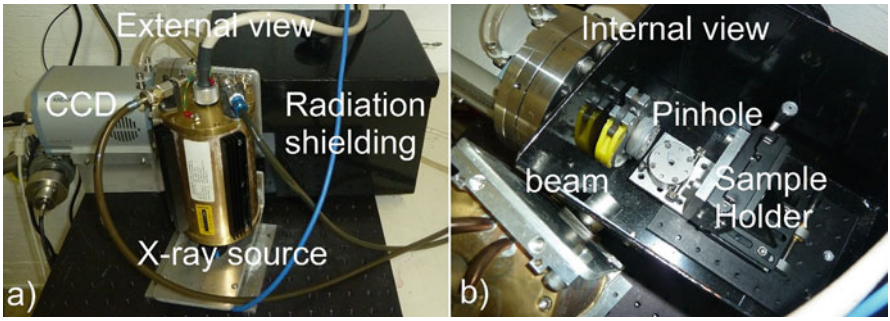

Fig. 15.5 FF-XRF device (*left*) and a detailed view of the measurement setup (*right*)

In this section, a new full-field X-ray camera developed at the LANDIS laboratory is described (Romano et al. 2013, 2014). A CCD camera is used as position- and energy-sensitive detector for X-rays in the range between 2 and 30 keV. A 70-μm pinhole-collimator is placed between the sample and the CCD, allowing performing the XRF imaging.

Samples are irradiated by using a medium-power X-ray tube emitting a large divergence beam. Its spot dimension on the samples is about 10 cm. The X-ray fluorescence, induced on the samples by the primary radiation, is detected through the pinhole collimator on the CCD detector. A multi-frames acquisition in single-photon counting and a proper post-processing of the data allow obtaining the X-ray fluorescence spectra and, consequently, performing the two-dimensional elemental mapping of the investigated materials. The energy resolution of the full-field X-ray camera is 133 eV at the Fe–Kα line. The spatial resolution was measured at different magnifications (obtained by moving the pinhole from/to the detector in the sample direction). A value as low as 20 μm was obtained at a 6× magnification. The full-field X-ray camera installed at the LANDIS laboratory is shown in Fig. 15.5.

15.3 Combined Use of FF-XRF, XRD, and PIXE for the Analysis of Pigments

This section discusses the potentiality of combining FF-XRF, XRD, and PIXE-alpha for the nondestructive chemical analyses of archaeological pigments. It should be noted that these techniques are developed in a mobile setup. Consequently, they can be applied for both laboratory routine analyses and applications in the field.

FF-XRF is a method suited to determine the two-dimensional elemental maps. With the possibility to work with different magnifications, elemental images can be obtained at different scales of length. In particular, FF-XRF allows both the macroanalysis (at a 0.3× magnification) of an area of 5 × 5 cm^2 with a spatial resolution of about 150 μm and the microanalysis (at a 6× magnification) of an area

of 2×2 mm^2 with a spatial resolution of 20 μm. Thus, both the global elemental composition (at the macrolevel) and the chemical association (at the microlevel) among elements can be evidenced in the images. However, the technique is penetrating the pictorial layer and it is not quantitative.

In most of the cases, ancient pigments present a mineral nature and can be successfully analyzed by XRD. The use of elemental information obtained by a preliminary FF-XRF can be used as chemical filter in the search/match procedure of XRD, limiting the search to a reduced number of phases and improving the accuracy of the mineral phase identification.

PIXE technique presents a limited and well-defined analytical depth. It is not penetrating and is thus suited for the analysis of surfaces. In the case of pigments, the analysis is usually limited to the pictorial layer, and the contribution in the experimental spectra coming from the substratum layer of paints is minimal. However, quantitative analysis of the PIXE data is possible only when the light matrix composition of the samples is known. This value was obtained by the previous XRD measurement and it can be used for quantitative calculation by using a conventional fundamental parameter approach.

The final result of this protocol is the quantitative analysis of the mineral pigment. A drawback consists in the necessity to investigate the same position in the sample by XRD and PIXE. In addition, FF-XRF gives a global result in a single measurement whereas PIXE and XRD should be executed in different points to cover the different shades of color identified by FF-XRF.

The analytical approach can be summarized as in the following. (i) First, a FF-XRF measurement allows identifying (qualitatively) the elements composing the sample. (ii) A subsequent XRD measurement is performed on the sample; the analysis of the diffraction pattern is carried out by limiting the search/match procedure only to the mineralogical phases that contains the elements already measured in the initial FF-XRF. (iii) Finally, those minerals identified by the XRD are used to define the matrix composition of the sample and to operate the quantitative calculation of the PIXE spectrum performed on the same position of the XRD.

15.4 A Case Study: The Manganese Black Technique in Different Cultures

The Manganese Black technique has been used for decorating artifacts in different historical periods and cultures. However, raw materials and firing processes have changed over time. This black pigment differs significantly in its chemical composition and manufacturing technology from the fired black obtained by the well-known iron reduction technique.

The main constituents of this pigment are manganese and iron oxides (Schweizer and Rinuy 1982). Manganese black occurs during the firing of manganese- and iron-rich clay slips. The raw material consists of pyrolusite (MnO_2) and hematite (Fe_2O_3) in a proportion that changes depending on the manufacturing receipt. Under oxidation conditions and at temperature of about 450 °C, MnO_2 undergoes a phase transformation to Mn_2O_3 (bixbyite), whereas at higher temperature (950–1100 °C) the Mn(III) of bixbyite can combine with iron oxides, forming the complex $MnFe_2O_3$ (jacobsite).

The first evidence of the use of a manganese-based pigment in pottery decoration is dated back to the Neolithic (Pappalardo 1999). The pottery of Castelluccio (Sicily), characterized by black-on-light geometric decorations, is one such evidence. During the Bronze Age, technological changes in the manufacture and in the raw materials occurred, as testified by the manganese black investigation from different areas of Mainland Greece. However, manganese black technology changed over a long period of time and was developed independently in different geographic areas. An additional interesting case is related to the decorations of the Nasca pottery, in Southern Peru (Vaughn et al. 2005, Pappalardo et al. 2016b).

The analytical protocol based on the combined use of FF-XRF, XRD, and PIXE allows a nondestructive investigation of the manganese black. Figure 15.6 shows the FF-XRF elemental maps of Fe and Mn in a pottery fragment from Castelluccio.

It is evident that the black decoration in the pottery is composed of a manganese black. Iron characterizes the red slip of the pottery. These elemental images give some important insights into the manganese black firing technology used in Sicily during the Neolithic. There is no chemical (spatial) correlation between Mn and Fe. Jacobsite was not formed in the firing process, suggesting a low temperature process.

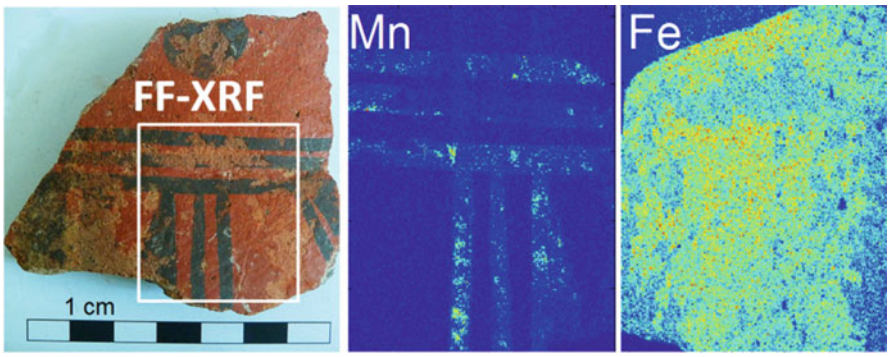

Fig. 15.6 The two-dimensional distribution of Mn and Fe obtained from the macro-FF-XRF measurement of a Neolithic fragment from Castelluccio (Sicily)

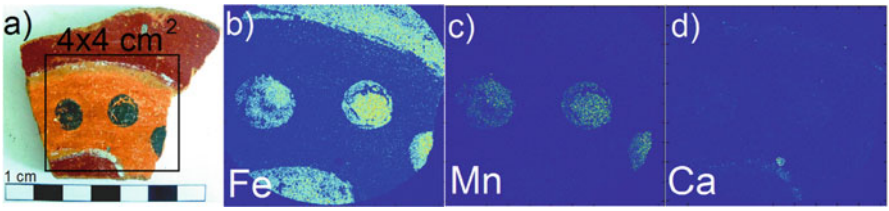

Fig. 15.7 The two-dimensional distribution of Mn and Fe obtained from the macro-FF-XRF measurement of a pottery fragment from the Nasca site of Cahuachi

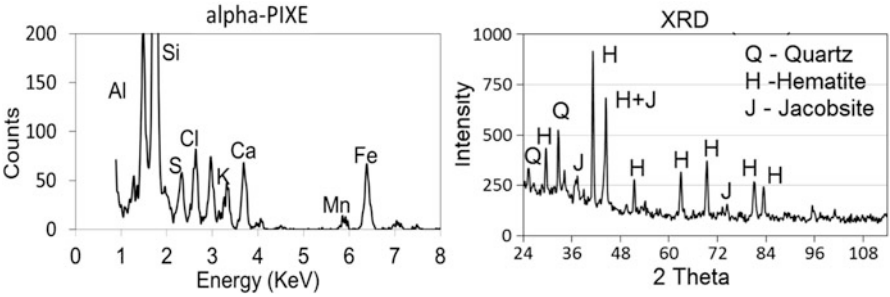

Fig. 15.8 XRD (*left*) and alpha-PIXE (*right*) on the black pigment of the Nasca fragment

A different result is obtained by FF-XRF investigations of Nasca pottery. Figure 15.7 shows the FF-XRF elemental maps of Fe and Mn in the case of a black decoration. Iron and manganese are spatially correlated as an indication of the presence of jacobsite formed by the iron- and manganese-slips transformation at high temperature.

However, FF-XRF is an elemental technique. To demonstrate the presence of jacobsite and to quantify the pigment, XRD and PIXE have to be performed as indicated in the previous section.

Figure 15.8 shows the XRD and PIXE data obtained on the black pigment. The search/match analysis of the diffraction pattern was determined by using the elemental data of FF-XRF. The presence of jacobsite is evident together with other main phases of quartz and hematite.

Finally, the minerals determined by XRD are used to define the light matrix in the PIXE quantitative calculation. Compositional results were 28.5% SiO_2, 35.5% Fe_2O_3, 4.3% $MnFe_2O_3$, and 20.3% other oxides. Error of the applied procedure is about 10%.

15.5 Summary and Conclusions

FF-XRF, PIXE, and XRD techniques allow development of a protocol for the quantitative analysis of archaeological pigments. FF-XRF imaging is a novel methodology for determining the elemental distribution in samples with high spatial resolution. It allows both the macro- and microanalysis of the samples. The global elemental composition and the chemical associations among elements can be evidenced in the images allowing new insights into the nature of pigments, production technology, and conservation state. Ancient pigments often present a mineral nature. The use of elemental information obtained by a preliminary FF-XRF can be used as chemical filter in a search/match procedure of XRD, limiting the search to a reduced number of phases and improving the accuracy of the mineral phase identification.

The PIXE technique presents a limited and well-defined analytical depth. It is not penetrating and is thus suited for analysis of the pictorial layer. Quantitative analysis of the PIXE data is possible using a conventional fundamental parameter approach by defining the light matrix composition with the mineral phases obtained by XRD.

FF-XRF, XRD, and alpha-PIXE, as discussed in the text, are portable methods and can be used in the field even for the investigation of unmovable cultural objects.

As an application of the analytical protocol based on these foregoing techniques, the manganese black case study has been discussed in pottery manufactured over time (starting from prehistory) and by different cultures in Sicily and Latin America.

References

Dran JC, Salomon J, Calligaro T, Walter P (2004) Ion beam analysis of art works: 14 years of use in the Louvre. Nucl Instrum Methods Phys Res Sect B 219–220:7–15

Gianoncelli A, Castaing J, Ortega L, Dooryhe E, Salomon J, Walter P, Hodeau JL, Bordet P (2008) A portable instrument for in situ determination of the chemical and phase compositions of cultural heritage objects. X-Ray Spectrom 37:418–423

Govindaraju K (1994) Compilation of working values and description for 383 geostandards. Geostand Newslett 18:1–158

Jenkins R, Snyder R, John Wiley & Sons (eds) (1996) Introduction to X-Ray powder diffractometry. John Wiley & Sons, New York

Johansson SAE, Campbell JL, Malmqvist KG (1995) Particle-induced X-Ray emission spectrometry (PIXE). 133 in chemical analysis: a series of monographs on analytical chemistry and its applications (JD Winefordner, Series Editor). Wiley, New York

Lasaponara R, Masini N, Orefici G (Eds) (2016) The ancient Nasca world: new insights from science and archaeology, Springer International Publishing

Mandò PA (2005) Nuclear physics and archaeometry. Nucl Phys A 751:393–408

Maniatis Y, Aloupi E, Stalios AD (1993) New evidence for the nature of the attic black gloss. Archaeometry 35:23–24

Pappalardo G, de Sanoit J, Musumarra A, Calvi G, Marchetta C (1996) Feasibility study of a portable PIXE system using a ^{210}Po alpha source. Nucl Instrum Methods Phys Res Sect B 109–110:214–217

Pappalardo L (1999) A portable PIXE system for the in situ characterisation of black and red pigments in neolithic, copper age and bronge age pottery. Nucl Instr Methods Phys Res Sect B 109–110:214–217

Pappalardo L, Romano FP, Garraffo S, de Sanoit J, Marchetta C, Pappalardo G (2003) The improved LNS PIXE-alpha portable system: archaeometric applications. Archaeometry 45:333–339

Pappalardo L, de Sanoit J, Marchetta C, Pappalardo G, Romano FP, Rizzo F (2007) A portable spectrometer for simultaneous PIXE and XRF analysis. X-Ray Spectrom 36:310–315

Pappalardo L, Alberti R, Calì C, Garraffo S, Litrico P, Pappalardo G, Rizzo F, Romano FP (2013) The new PIXE-alpha spectrometer for the analysis of Roman nummi surface. X-Ray Spectrom 42(1):33–37

Pappalardo L, La Rosa V, Rizzo F, Romano FP (2015) Non destructive PIXE-alpha characterization of pigments in Kamares pottery (1850–1700 B. C.) from Phaistos (Crete). X-Ray Spectrom 44(4):276–281

Pappalardo L, Barresi S, Biondi G, Caliri C, Caruso F, Catalano R, Lamagna G, Manenti GA, Monterosso G, Orlando A, Rizzo F, Romano FP, Santos HC (2016a) PIXE-alpha non-destructive and in situ compositional investigation of black gloss on ancient pottery. X-Ray Spectrom 45:258. doi:10.1002/xrs.2696

Pappalardo L, Masini N, Rizzo F, Romano FP (2016b) The polychromy of Nasca pottery: a nondestructive analytical approach for compositional and mineralogical investigation of pigments. In: Lasaponara R, Masini N, Orefici G (eds) The ancient Nasca world: new insights from science and archaeology. Springer International Publishing, pp 593–603. doi:10.1007/978-3-319-47052-8_24

Picciome P, Copat V, Costa A (2011) Castelluccio painted pottery. Traces in Times 1:1–18

Pollard MA, Heron C (eds) (2008) Archeological chemistry. RSC Publishing, Cambridge

Romano FP, Calvi G, Furia E, Garraffo S, Marchetta C, Pappalardo G (2005) A new portable XRF spectrometer with beam stability control. X-Ray Spectrom 34:135–139

Romano FP, Pappalardo G, Pappalardo L, Rizzo F (2006) The new version of the portable XRD system of the LANDIS laboratory and its application for the non destructive characterisation of pigments in ancient Roman frescoes. Il Nuovo Cimento B 121:881

Romano FP, Pappalardo L, Masini N, Pappalardo G, Rizzo F (2011) The compositional and mineralogical analysis of fired pigments in Nasca pottery from Cahuachi (Peru) by the combined use of the portable PIXE-alpha and portable XRD techniques. Microchem J 99: 449–453

Romano FP, Pappalardo L, Calvi G, Costa E, Marchetta C, Pappalardo G, Rizzo F, Russo S (2012) A new version of a portable polonium source for the non-destructive PIXE (particle induced X-ray emission) analysis in the cultural heritage field. Microchem J 101:95–98

Romano F, Altana C, Cosentino L, Celona L, Gammino S, Mascali D (2013) A new x-ray pinhole camera for energy dispersive x-ray fluorescence imaging with high-energy and high-spatial resolution. Spectrochim Acta B 86:60–65

Romano FP, Caliri C, Cosentino L, Gammino S, Giuntini L, Mascali D, Neri L, Pappalardo L, Rizzo F, Taccetti F (2014) Macro and micro full field X-Ray fluorescence with an X-Ray pinhole camera presenting high energy and high spatial resolution. Anal Chem 86:10892–10899

Schweizer F, Rinuy A (1982) Manganese black as an etruscan pigment. Stud Conserv 27:118–123

Silverman H, Proulx DA (eds) (2002) The Nasca. Blackwell, London

Uda M, Ishizaki A, Satoh R, Okada K, Nakajima Y, Yamashita D, Ohashi K, Sakuraba Y, Shimono A, Kojima D (2005) Portable X-ray diffractometer equipped with XRF for archaeometry. Nucl Inst Methods Phys Res B 239:77

Vaughn K, Conlee C, Neff H, Schreiber K (2005) A compositional analysis of Nasca pigments: implications for craft production on the prehispanic South Coast of Peru. In: Speakman RJ, Neff H (eds) Laser Ablation ICP-MS: a new frontier in archaeological characterization studies, pp 139–153

Verma HR (ed) (2007) X-ray fluorescence (XRF) and particle-induced X-ray emission (PIXE): atomic and nuclear analytical methods. Springer, New York

Part III
Information and Communications Technology and Sensing Technologies for Cultural Heritage

Chapter 16
Wireless Communication Platforms for Built and Natural Heritage Monitoring

María Inmaculada Martínez-Garrido and Rafael Fort González

Abstract This chapter reviews the use of wireless sensor networks in cultural and natural heritage monitoring and describes the platforms presently available on the market. The main characteristics of this technology are discussed in the context of demanding long-term monitoring. The issues addressed include the RF bands, transceiver models, and network topologies most often used, power source and consumption options, and the possible applications of the hardware/software developments for the platforms analyzed. The monitoring capabilities and versatility of each platform are investigated with respect to the sensors that can be installed to track the parameters of interest in heritage studies. End-user network configuration and the research opportunities afforded by this technology in the areas concerned are also highlighted.

16.1 Introduction

Many areas of research and technological development use monitoring techniques to track one or more parameters with a view to detecting and controlling anomalies. Wireless sensor networks are among the most promising technologies for these purposes, given the versatility of their application, low cost, low power demand, easiness of deployment, and flexible configuration.

M.I. Martínez-Garrido (✉)
Instituto de Geociencias (CSIC-UCM) and Departamento de Ingeniería Telemática y Electrónica (ETSIST, UPM), CEI Campus Moncloa (CSIC, UPM-UCM), C/José Antonio Nováis, 12, 28040, Madrid, Spain
e-mail: mi.martinez.garrido@csic.es

R. Fort González
Instituto de Geociencias (CSIC, UCM), CEI Campus Moncloa (CSIC,UPM,UCM), C/José Antonio Nováis, 12, 28040, Madrid, Spain
e-mail: rafael.fort@csic.es

N. Masini, F. Soldovieri (eds.), *Sensing the Past*, Geotechnologies and the Environment 16, DOI 10.1007/978-3-319-50518-3_16

These types of instruments are used, for instance, in building surveillance and automation (Spadacini et al. 2014), road safety and vehicle traffic (Daponte et al. 2014), intelligent farming (Aqeel-ur-Rehman et al. 2014), telemedicine (Paoli et al. 2012), and structural monitoring (Yildirim et al. 2013).

In heritage studies, node or monitoring point miniaturization and efficient energy management make this technology a powerful tool for minimally invasive, long-term monitoring. This type of monitoring is particularly useful for the preventive conservation of heritage assets (Bencini et al. 2008; Rodriguez-Sanchez et al. 2011) and is able to deliver information on the causes of decay by logging data on many environmental, microclimatic, or material parameters. Preventive action can therefore be taken before the damage occurs, and alarms or actuators can be built into the system to maintain the conditions required for satisfactory conservation.

16.2 Wireless Monitoring Techniques: Evolution and Characteristics

This section discusses the evolution of wireless monitoring in heritage environments, from conventional data loggers to today's wireless sensor networks. The most common and optimal networking configurations are also discussed.

The earliest wireless monitoring techniques were based on conventional data loggers, devices first applied for scientific purposes in the mid-1960s. As these instruments are usually small and with limited memory capability, the data acquisition rate and the maximum duration of a monitoring campaign are highly interdependent. Data loggers are consequently recommended for short- or medium-term monitoring over large areas where a substantial number of monitoring points are needed (Varas-Muriel et al. 2014; Varas-Muriel et al. 2014; Martínez Garrido 2015). Although the information collected with this technology may be well suited to research objectives, these devices cannot be configured nor can the data be downloaded remotely, a significant drawback where accessibility to the scenarios studied is inconvenient.

The cost of data loggers has declined over the years, although as they call for no additional hardware/software development and factory settings are hardwired into the devices for greater end-user convenience, they are still relatively expensive.

Radio loggers were the next family of monitoring techniques to be developed. These devices use radio communication for data transmission but are limited by the manufacturer with respect to the software and hardware supported to design intelligent processing tools or network additional sensors. This technology is characterized by configurational simplicity for the end-user and features remote data access, but it is not cheap.

Table 16.1 Functional and communication characteristics of data loggers, radio loggers, and wireless sensor networks

Technology	One down-load	Remote access	Smart data process	Long-term monitor	Multiparam. (>2)	Alerts	Low cost
Data loggers	No	No	No	Yes	No	No	No
Radio loggers	Yes	No	No	Yes	No	No	No
WSN	Yes	Yes	Yes	Yes	Yes	Yes	Yes

The limitations of the aforementioned technologies, which rule out long-term, low-cost monitoring with efficient information processing, led to the advent of wireless sensor networks (WSNs). In these systems the hardware/software configuration depends largely on user needs and therefore can be readily adapted to the end use. In addition, this technology is less costly than data or radio loggers, and a significant number of sensors can be networked for multiparametric processing (Martínez Garrido 2015).

Table 16.1 summarizes the general features associated with each technology. "Yes" under the "One download" column means that the data only needs to be downloaded once per period, and "No" means that because of insufficient device memory, downloads must be performed at given intervals to prevent overwrites. "Yes" under the "Remote access" column means that the data can be accessed remotely, and "No" that they cannot. "Yes" under the "Smart data process." column means that data are processed further to sensor behavior and seasonal tendencies, and "No" that they are not. "Yes" under "Long-term monitor" means that monitoring periods of more than 1 year are accommodated; "No" means that monitoring periods must be shorter or the data must be downloaded more frequently. "No" under the "Multi-param. (>2)" column means that devices are generally fitted with a single sensor and a maximum of two parameters (e.g., T and RH), and "Yes" that many sensors measuring different parameters can be installed. "Yes" under "Alerts" means that the system can be programmed to set off alerts when user-defined thresholds are exceeded, and "No" that it cannot. Low-cost technologies bear a "Yes" under that column, and technologies with a high initial cost bear a "No." Price is impacted by instrument configurability and the post-purchase development effort to be made by the end-user.

Many research projects and institutions involved in heritage monitoring deploy wireless sensor networks to record environmental data, study materials, or assess structural stability. Examples are to be found in the work conducted under SMOOHS (Smart Monitoring of Historic Structures), a European Union 7th Framework Programme for Research project that led to the creation of the Smartmote platform (Lehmann et al. 2011; Lehmann and Krüger 2011; Lehmann et al. 2013;

Smartmote Monitoring and Testing 2015); the low-cost sensor network monitoring performed by the Istituto per i Beni Archeologici e Monumentali (IBAM)–Italian Research Council (CNR) (Sileo et al. 2014), the Institut français des sciences et technologies des transports, de l'aménagement et des réseaux (IFSTTAR) (Le Cam et al. 2013), and the Spanish Instituto de Geociencias (IGEO, CSIC-UCM); the Monitoring Heritage System (MHS) project implemented by the Spanish Fundación Santa María la Real–Centro de Estudios del Románico (Chiriac et al. 2013); and the studies conducted by London University College's Centre for Sustainable Heritage (Agbota et al. 2014).

16.3 WSN: Frequency Bands and Network Topologies

Today's WSNs use the Zigbee-enhanced IEEE 802.15.4 protocol, but with a lower baud rate: these generally operate at frequencies of 902–928 MHz (USA), 868–870 MHz (Europe) 433.05–434.79 MHz (USA and Europe), 314–316 MHz (Japan), or 2.400–2.4835 GHz (universal).

Although any number of wireless communications network topologies are possible, the two most frequently used are the cluster-tree (Fig. 16.1a), favored for its low power demand, and the mesh array (Fig. 16.1b), for its high reliability (Martínez Garrido 2015).

In cluster-tree topology, communication is not interrupted if one of the end nodes fails, whereas a bridge node outage would shut down communication in all its associated nodes. In mesh topology, because every node is connected to all the others and data can consequently be routed along numerous pathways, communication is never interrupted.

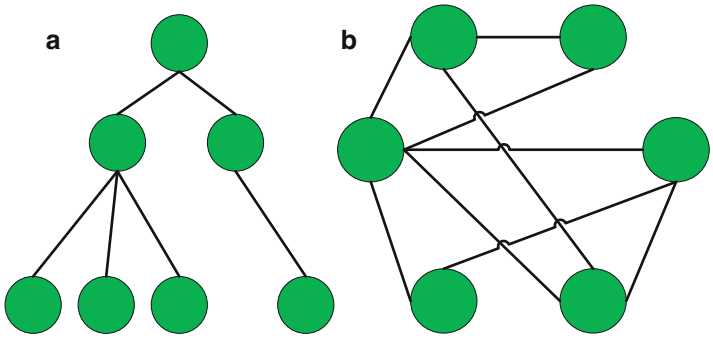

Fig. 16.1 (**a**) Cluster-tree topology; (**b**) mesh topology

16.4 Wireless Platforms

The earliest sensor networks were devised by the US Defense Advanced Research Projects Agency's (DARPA) Distributed Sensor Networks (DSN) project for military purposes. The first mote or densor node (WeC), designed at the University of California at Berkeley, was created in 1999. In the interim many platforms have been developed by research institutes, universities, and private companies. The turn of the century brought motes such as Rene (2000), Dot (2001), Mica (2002), Mica2 (2003), Telos and Cricket (2004), Startgate (2005), Sun Spot (2006), Iris (2007), and V-Link (2008). Waspmote (2009) was among the last devices to come to market in the first decade of this century (Kompis and Sureka 2010).

These systems afford a variety of opportunities for heritage work. The wireless platforms most widely used in this area are discussed next.

16.4.1 Arduino

Arduino hardware is an open source electronic platform based on ATmel ATmega8 and ATmega168 microcontrollers. The Arduino boards are the lowest cost boards on the market and the company's firmware runs on Windows, Macintosh OSX, and Linux operating systems. As its programming environment (open source software, C/C++ language) is simple and intuitive, it is one of the platforms most readily accessible for people with no prior electronic or programming training. These platforms offer an extensive range of possibilities for development and monitoring applications (Silva et al. 2012; Ferdoush and Li 2014; Sileo et al. 2014). The platform supports IEEE 802.15.4-compliant radio transceivers at frequencies of 2.405–2.48 GHz such as MRF24J40MA (Silva et al. 2012) or MaxStream's XBee modules (IEEE® 802.15.4 OEM RF Modules by MaxStream 2007).

Arduino board wireless communication is controlled by one of two modules, the Wireless Pro Shield or the Wireless SD shield. Although based on Digi's Xbee modules, they support any other device with the same footprint. Their line-of-sight range is 30 m indoors and 100 m outdoors. They can be used as serial-to-USB converters or set to command mode and configured for a variety of propagation and mesh networking options. These wireless modules communicate with the USB-to-serial converter or the microcontroller via an on-board switch. One of the differences between the two modules is that the Wireless SD shield is fitted with an SD card slot and the Wireless Pro Shield is not (Arduino 2015a, b).

As in all low-cost platforms, the lifetime of these devices is an essential parameter (Solahuddin and Ismail 2014). Arduino Uno boards (Fig. 16.2) can operate with an external power supply at a voltage of 6–20 V, with a recommended range of 7–12 V. These boards have 5- and 3.3-V power pins, and board-specific products (Solar Charger Shield) are available to use solar power with a backup

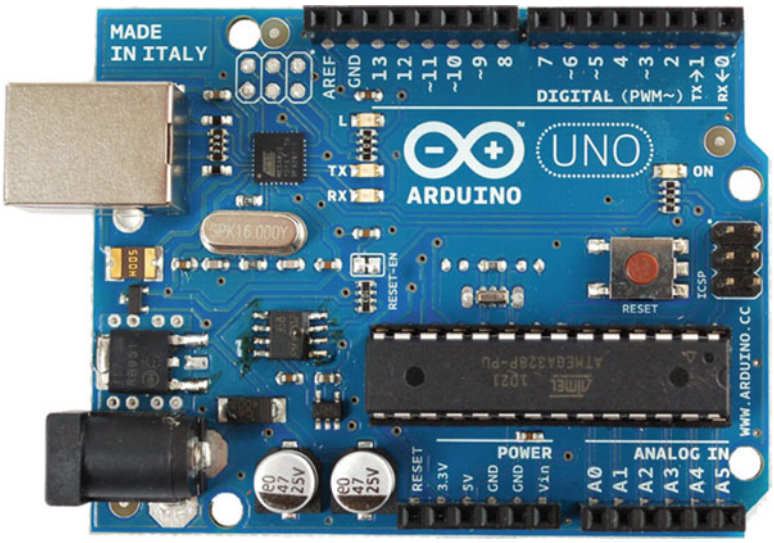

Fig. 16.2 Arduino Uno board

battery and supply the Arduino board with power at a regulated voltage of 5 V. Arduino Uno is fitted with 14 input–output pins, 6 of which can be used as PWM outputs, as well as 6 analogue inputs, a 16-MHz ceramic resonator, a USB connection, a powerjack, an ICSP header and a reset button (Arduino 2015c).

16.4.2 Libelium

Libelium's (Libelium Comunicaciones Distribuidas S.L. 2015) motes go by the trade name Waspmote (Fig. 16.3). They consist of a 14.7456-MHz ATmega1281 processor (Agbota et al. 2014) with 8 kB of RAM and a 128-kB flash memory. They are fitted with an SD card slot and measure 73.50 mm wide by 51.00 mm high by 13.00 mm deep, with a weight of 20 g. They can operate at a temperature range from −10 ° to +65 °C. A 32-Hz real-time clock is built into each Waspmote.

The motes also have seven analogue inputs, eight digital input/outputs, one PWM output, two UART ports, one synchronous communication I2C bus, one USB port, and one SPI bus. Temperature sensors operating at −40 ° to +85 °C with a precision of 0.25 °C as well as a ± 2 g/± 4 g/± 8 g accelerometer are standard items on Waspmote boards.

Waspmotes feature eight wireless interfaces [two long-range (3G/GPRS), three medium-range (802.15.4, ZigBee, WiFi), and three short-range (Bluetooth, RFID, NFC)]. ZigBee-based medium-range interfaces are widely used with Digi modules, as shown in Table 16.2.

Fig. 16.3 Libelium Waspmote

Table 16.2 Waspmote (Libelium Comunicaciones Distribuidas S.L. 2015) radiofrequency modules

Model	Standard	Frequency	Tx current (mW)	Sensitivity ((dBm)	Range[a]
XBee-802.15.4	802.15.4	2.4 GHz	1	−92	500 m
XBee-802.15.4-Pro	802.15.4	2.4 GHz	100	−100	7000 m
XBee-ZB	Zigbee-Pro	2.4 GHz	2	−96	500 m
XBee-ZB-Pro	Zigbee-Pro	2.4 GHz	50	−102	7000 m
XBee-868	RF	868 MHz	315	−112	12 km
XBee-900	RF	900 MHz	50	−100	10 km

[a]Line-of-sight, assuming free space in the Fresnel zone and a 5-dBi dipole antenna

The XBee-802.15.4-Pro operates in the 2.4-GHz ISM band widely used in recent cultural heritage applications (Rodriguez-Sanchez et al. 2011; Martinez-Garrido et al. 2013; Agbota et al. 2014; Mecocci and Abrardo 2014; Martínez-Garrido et al. 2014a, b). This frequency band has been intensely researched with experimental and radio propagation models (Turner et al. 2013; Kochlan and Micek 2014). Some of these studies showed that although the effect of indoor multipath propagation is a decisive design factor in wireless sensor networks, no material attenuation occurs when the motes are positioned at different heights. Human presence is not regarded as a significant problem in these propagation environments (Amzucu et al. 2014). The firmware for these modules can be updated with X-CTU software to support Digimesh protocol mesh topology.

The platform, called Waspmote-IDE, is based on and follows the same library and operating style as the Arduino open source platform (Severance 2014). The company has developed an application programming interface (API) that makes

Table 16.3 Memsic Inc. wireless sensor networks

	Application	Processor	Speed (MHz)	RAM (kbytes)	Radiofrequency range
Mica2	Wireless sensor networks, environmental monitoring, security and surveillance, distributed systems	Atmel ATMega 128 L, 8 bit	8–16	4	315 MHz, 433 MHz, 868 MHz–916 MHz
MicaZ	Indoor building monitoring and security, acoustic, video and vibration data	Atmel ATMega 128L, 8bit	8–16	4	2.4 GHz–2.48 GHz
Lotus	Industrial monitoring and analysis, seismic and vibration monitoring	Cortex M3 LPC 17 xx 32 bit	10–100	64	2.4 GHZ ISM
TelosB	Research and development	TI MSP 430 16 bit RISK	8	10	2.4 GHz–2.48 GHz ISM
Iris	Indoor building monitoring and security; acoustic, video, and vibration data	Atmel ATMega 1281	8	8	2.4 GHZ ISM
Cricket	Indoor location system, ultrasound location research, asset and people tracking	Atmel ATMega 128 L, 8 bit	8	4	433 MHz

Waspmote one of the most user-intuitive programmable motes on the market. This API, written in C/C++, includes Waspmote modules as well as sleep, deep sleep, and hibernate modes.

With a variety of models of sensor boards (for gas, agriculture, water quality), Waspmote-IDE features greater ease of use than other types of platforms. These boards are particularly suitable for monitoring multiple parameters within a given category, such as the concentration of carbon monoxide (CO), carbon dioxide (CO_2), or ozone (O_3) to determine air quality (gas board); or temperature (T), relative humidity (RH), rainfall, and air velocity, direction, and pressure for climatological assessments (agricultural board).

16.4.3 Memsic

Memsic, Inc. also manufactures a monitoring platform with an open software/hardware design.Memsic motes are programmed in nesC (Gay et al. 2014) programming language and run on the TinyOS operating system.

Of the various models of Memsic motes listed in Table 16.3, the Mica2 and IRIS families are of particular interest, given their applicability to environmental

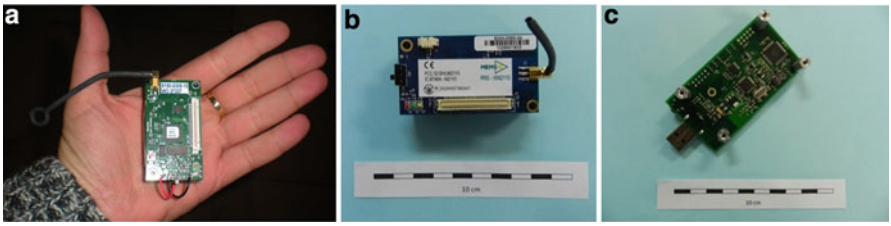

Fig. 16.4 Mica2 mote (**a**); Memsic IRIS mote (**b**); MIB520-CB board (**c**)

and indoor monitoring, respectively. The latter has a radio range threefold greater than the previous MICA mote and double the working memory of the earlier version (MEMSIC Inc. 2015a, b).

Mica2 MPR400 motes (RF band 868–916 MHz) (Fig. 16.4a) are fitted with a Chipcon CC1000 radio transceiver (Ilyas and Mahgoub 2004) that transmits at maximum current and an Atmel Atmega128L microcontroller: these feature a data rate of 38.4 kbps.

IRIS XM2110CB motes (Fig. 16.4b) use an IEEE 802.15.4-compliant Atmel AT86RF230 radio transceiver (Webster and Eren 2014) in the frequency band 2.4–2.48 GHz. They are fitted with an Atmel Atmega 1281 microcontroller; the data rate for these motes is 250 kbps (Martínez Garrido 2015).

Both motes feature a 51-pin expansion connector for sensor and data acquisition boards that supports analogue inputs, digital input/outputs, and I2C, SPI, and UART interfaces. The mote is powered by two AA (1.5-V) batteries or an external power source at a voltage of 2.7–3.3 V. These motes are 58 mm wide by 32 mm high and 7 mm deep, excluding the battery pack. The MIB520-CB board (Fig. 16.4c) features USB connectivity to the base station PC.

16.4.4 Smartmote

Other types of motes available on the market have been used in research, such as the SmartmoteWS platform (Smartmote 2015), designed with low-power modes that lengthen battery life.

Smartmote node sensors (Fig. 16.5) are fitted with a low-power microcontroller, a radio receiver, primary batteries, and a sensor board. The enclosure affords ANSI/IEC 60529 2004 IP65 protection against dust and pressurized water and can operate in a temperature range of $-25 + 85$ °C. The various models have different I/O configurations able to support UART or I2C ports. Two 8.5-Ah, 2.6-V lithium batteries with a service life of approximately 2 years can be connected to each mote.

Fig. 16.5 Smartmote platform sensor node

All nodes feature standard functions such as communications and data processing, which are built into the processor board. The node is based on a Texas Instruments MSP430F5437 microcontroller with two external power connectors of 3.3–3.6 V welded on one side.

For 2.4-GHz ISM band communication, an integrated Texas Instruments CC2520 radio transceiver (Texas Instruments Incorporated 2007) is used. The memory can be supplemented with an optional SD memory card, and they are fitted with a built-in 32.768-kHz crystal clock.

The base station runs on the Linux operating system (Debian distribution) and contains an SQL database to store network node data. It can also be connected to a data server or WLAN with a USB or LAN adapter (10/100 Mbit). It is fitted with a 700-MHz Broadcom BCM2835 CPU ARM1176JZF-S processor with a 512-MB RAM for applications and (maximum) 500-mA USB connectivity, among others (Broadcom Corporation 2015; ARM Ltd. 2015). It uses 5 voltage and has an SMA antenna connector for 2.4-GHz communications, web-based time synchronization, and a condensation-free operating range from −25 ° to +70 °C.

Its omnidirectional dipole antennas have a 2-dBi vertical linear polarization gain, a radio frequency of 2.4–2.5 GHz, a standing wave ratio of ≦1.5:1, and 50-Ω impedance; they measure 105 mm high by 10 mm wide and 120 mm deep and are fitted with an SMA connector for an extension cord to meet monitoring site needs.

Smartmote motes support a variety of sensors, making them a highly versatile platform for heritage monitoring (Martínez-Garrido and Fort 2016a): an SSE Sensing Ltd. CO2S-A device (SST Sensing Ltd. 2015) for CO_2, a Thies Clima anemometer (Thies Clima 2015), an Apogee Instruments Inc., SP-110 pyrometer (Apogee Instruments Inc. 2014), and a Sensirion SHT25 temperature and relative humidity sensor (Sensirion 2014).

16.5 Decay Detected with Wireless Sensor Networks

Wireless sensor networking is a technology suitable for monitoring many forms of decay in the cultural and natural heritage. Optimal node networking calls for a preliminary study with other noninvasive techniques (Martínez-Garrido and Fort 2014a), such as infrared thermography, contact hygrometry, electrical resistivity tomography, or ground-penetrating radar. These techniques deliver initial information on the areas most affected by sources of heat, human presence, dampness, or ventilation. Once the areas at highest risk are identified, long-term wireless sensor network tracking can be implemented for preventive conservation.

Wireless sensor network-based research addresses the factors to be analyzed in the cultural heritage, ranging from indoor or museified microclimatic conditions (Martínez-Garrido and Fort 2014b, 2016b) to the conditions affecting walls or specific materials.

As a tool for microclimatic characterization, WSNs are used to assess, track, and control air quality in monitored cultural heritage assets. They are extremely useful for assessing the effects of human presence or HVAC system operation on the microclimate (Martínez-Garrido and Fort 2014a).

When used for instrument materials, crack behavior over time (Mecocci and Abrardo 2014), the effect of vibrations and structural risk (Abruzzese et al. 2009), or the impact of solar radiation on the inner areas of walls can be monitored. These systems can also be deployed to characterize the thermal lag between the maximum outdoor temperature and the inside temperature materials, taking into account factors such as façade orientation, rainfall, and wind direction (Martínez-Garrido et al. 2014a, b).

An understanding of thermal and humidity gradients inside materials is useful for determining the behavior of walls in built heritage assets, but its utility is not confined to those assets. It is also a very suitable method for monitoring the natural heritage, for instance, where such gradients are affected by the presence or absence of solar radiation, which induces thermal expansion with implications for the conservation of materials exposed to the elements (Freire-Lista et al. 2014).

WSNs can also be used to monitor moisture and hence the salt content inside construction materials (Lehmann and Krüger 2011, Lehmann et al. 2013), capillary absorption-induced increases in damp levels inside walls or floors (Martínez Garrido et al. 2014a, b; Martínez-Garrido et al. 2014), or factors such as tidal movements in natural heritage enclaves (Martínez Garrido and Fort 2017).

16.6 Conclusions

In light of their versatility, wireless sensor networks are particularly suitable for the long-term monitoring of parameters that induce decay in natural and cultural heritage assets. Mote miniaturization reduces the aesthetic impact on the areas

studied, ensuring minimal invasiveness. Moreover, increasingly effective market solutions (low power, solar power) are in place to lengthen platform lifetime, lower the cost, enhance their data processing capabilities, and broaden the range of sensors that can be supported.

Arduino and Memsic are open design software/hardware platforms with a very low initial price tag. That is offset, however, by their higher development costs, which render platforms such as Libelium and Smartmote, characterized by greater ease of integration and development, more competitive.

Any decay detected with this type of devices can be addressed in the initial stages, and guidelines can be established for the preventive conservation of cultural and natural heritage assets.

Acknowledgments The present study was funded under GEOMATERIALES 2 (S2013/MIT-2914), CGL-2011-27902, and BIA2014- 53911-R projects and by the Complutense University of Madrid's research group on Heritage Stone Material Alteration and Conservation. M.I. Martínez-Garrido participated with the support of the Moncloa Campus of International Excellence (UCM-UPM). The manuscript was edited by Margaret Clark, professional translator and English language science editor.

References

Abruzzese D, Angelaccio M, Giuliano R, Miccoli L, Vari A (2009) Monitoring and vibration risk assessment in cultural heritage via wireless sensors network

Agbota H, Mitchell JE, Odlyha M, Strlic M (2014) Remote assessment of cultural heritage environments with wireless sensor array networks. Sensors 14(5):8779–8793

Amzucu DM, Li H, Fledderus E (2014) Indoor radio propagation and interference in 2.4 Ghz wireless sensor networks: measurements and analysis. Wirel Pers Commun 76(2):245–269

ANSI/IEC 60529 (2004) Degrees of protection provided by enclosures (IP code) (Identical National Adoption). National Electrical Manufacturers Association, Rosslyn

Apogee Instruments Inc (2014), Owner's manual pyranometer model Sp-110 and Sp-230. Available: http://www.apogeeinstruments.com/content/SP-110manual.docx [01/15, 2015]

Aqeel-Ur-Rehman, Abbasi AZ, Islam N, Shaikh ZA (2014) A review of wireless sensors and networks' applications in agriculture. Comput Stand Interfaces 36(2):263–270

Arduino (2015a) Wireless proto shield. Available: http://www.arduino.cc/en/Main/ArduinoWirelessProtoshield [22/06/2015]

Arduino (2015b) Wireless SD shield. Available: http://www.arduino.cc/en/Main/ArduinoWirelessShield [06/22, 2015]

Arduino (2015c) Arduino Uno. Available: http://www.arduino.cc/en/Main/ArduinoBoardUno [06/22, 2015]

Arm Ltd (2015) Arm1176 processor. Available: http://www.arm.com/products/processors/classic/arm11/arm1176.php [22/06/2015]

Bencini L, Collodi G, Di Palma D, Manes G, Manes A (2008) An embedded wireless sensor network system for cultural heritage monitoring. 2010 Fourth International Conference on Sensor Technologies and Applications (Sensorcomm) 185–190

Broadcom Corporation (2015) Bcm2835 processor. Available: http://www.broadcom.com/products/BCM2835 [22/06/2015]

Chiriac M, Basulto D, Lopez E, Prieto JC, Castillo J, Collado A (2013) The MHS system as an active tool for the preventive conservation of cultural heritage

Daponte P, De Vito L, Picariello F, Rapuano S, Tudosa I (2014) Prototype design and experimental evaluation of wireless measurement nodes for road safety. Measurement 57:1–14

Ferdoush S, Li X (2014) Wireless sensor network system design using raspberry Pi and Arduino for environmental monitoring applications. 9th International Conference on Future Networks and Communications (Fnc'14)/The 11th International Conference on Mobile Systems and Pervasive Computing (Mobispc'14)/Affiliated Workshops, 34, pp 103–110

Freire-Lista DM, Martínez-Garrido M, Fort R (2014) Monitoring techniques for microclimatic analysis in cultural and natural heritage for decay evaluation. 11th International Conference on Non-Destructive Investigations and Microanalymicroanalysis for the Diagnostics and Conservation of Cultural and Environmental Heritage Art'14, Madrid, Spain, Isbn: 978–84–697-0522-3. pp Ind 114

Gay D, Levis P, Von Behren R, Welsh M, Brewer E, Culler D (2014) The nesC language: a holistic approach to networked embedded systems. ACM SIGPLAN Not 49(4):41–51

IEEE® 802.15.4 OEM RF Modules By Maxstream (2007) Product manual V1.Xax – 802.15.4 Protocol For OEM RF Module Part Numbers: Xb24-...-001, Xbp24-...-001. Available: https://www.sparkfun.com/datasheets/Wireless/Zigbee/Xbee-Manual.Pdf [06/22, 2015]

Ilyas M, Mahgoub I (2004) In: Ilyas M, Mahgoub I (eds) Handbook of sensor networks: compact wireless and wired sensing systems. Crc Press, Boca Raton

Kochlan M, Micek J (2014). Indoor propagation of 2.4GHz radio signal propagation models and experimental results. 2014 10th International Conference on Digital Technologies (Dt), 125–129

Kompis C, Sureka P (2010) In: Kompis C, Sureka P (eds) Power management technologies to enable remote and wireless sensing

Le Cam, V., Lossec, M., Le Maulf, R., Lemarchand, L., Martin, W. And Le Pen, M., 2013. Towards autonomous wireless sensors systems in civil engineering: paving the way to an "energy oriented design method". Structural health monitoring 2011: Condition-based maintenance and intelligent structures, vol 2. pp 1780–1787

Lehmann F, Krüger M (2011) Wireless impedance measurements to monitor moisture and salt migration in natural stone. Proceedings of the European Workshop on Cultural Heritage Preservation, Berlin, Germany, September 26–28, pp 224–231

Lehmann F, Frick J, Krüger M, Menzel K (2011) Wireless monitoring of moisture content in mineral materials by electrical impedance measurements. In: Büyüköztürk O, Güneş O, Ali Taşdemir M, Akkaya Y (eds) Nondestructive testing of materials and structures: Proceedings of NDTMS-2011, Istambul, Turkey, May 15–18, 2011, Part I. Springer, Istambul, pp 1165–1173

Lehmann F, Martínez Garrido MI, Krüger M (2013) On the Advance of Impedance Measurements for Monitoring Moisture in Sandstone. In: Troi A, Lucci E (eds) Cultural heritage preservation, 3rd European workshop on cultural heritage preservation. Bozen, pp 259–264

Libelium Comunicaciones Distribuidas S.L. (2015) Waspmote datasheet. Available: http://www.libelium.com/es/ [01/12, 2015]

Martínez Garrido MI (2015) Aportación de la monitorización mediante redes de sensores y técnicas no invasivas para la conservación preventiva del Patrimonio [PhD. Thesis], School of Telecommunications Engineering (ETSIST), Technical University Of Madrid, Spain, 440pp

Martínez-Garrido MI, Fort R (2014a) Sensing technologies for monitoring and conservation of cultural heritage: wireless detection of decay factors. In: Rogerio-Candeleda MA (ed) Science, technology and cultural heritage. CRC Press, Balkema, pp 495–501

Martínez-Garrido MI, Fort R (2014b) Wireless sensor networks for a conservation monitoring in archaeological sites. In: Macchia A, Prestileo F, Cagno S (eds) Yococu 2014: professionals' experiences in cultural heritage conservation in America, Europe, and Asia. Cambridge Scholars Publishing Publicado, pp 256–268. isbn:9781443889766

Martínez Garrido MI, Fort R (2016a) Wireless monitoring for decay factors' detection in cultural and natural heritage scenarios In Spain. Sensing the past: geoscience and sensing technologies for cultural heritage. Chapter 27, Springer

Martínez-Garrido MI, Fort R (2016b) Experimental assessment of a wireless communications platform for the built and natural heritage. Measurement 82:188–201

Martinez-Garrido MI, Aparicio S, Fort R, Izquierdo MAG, Anaya JJ (2013) Decay assessment through wireless sensor networks implementation for architectural heritage conservation. In: Rogeriocandelera, Ma Lazzari, M Cano E (eds) Science, technology and cultural heritage. 6000 Broken Sound Parkway Nw, Ste 300, Boca Raton, Fl 33487–2742 USA: CRC Press, pp 71–74

Martínez-Garrido MI, Aparicio S, Fort R, Anaya JJ, Izquierdo MAG (2014a) Effect of solar radiation and humidity on the inner core of walls in historic buildings. Constr Build Mater 51(51):383–394

Martínez Garrido MI, Gómez Heras M, Fort R, Varas Muriel MJ (2014b) Monitoring moisture distribution on stone and masonry walls. In: Rogerio-Candeleda MA (ed) Science, technology and cultural hetitage for the conservation of cultural heritage. CRC Press, Balkema, pp 35–40

Martínez-Garrido MI, Fort R (2017) Wireless monitoring to detect decay factors in natural heritage scenarios in Spain: a case study at Lanzarote. In: Masini N, Soldovieri F (eds) Sensing the past. Geotechnol Environ 16. doi:10.1007/978-3-319-50518-3_24

Mecocci A, Abrardo A (2014) Monitoring architectural heritage by wireless sensors networks: san gimignano – a case study. Sensors 14(1):770–778

Memsic Inc. (2015a) Document part number: 6020-0124-01 Rev B. Available: http://www.memsic.com/userfiles/files/Datasheets/WSN/6020-0124-01_B_IRIS.pdf [06/22, 2015]

Memsic Inc. (2015b) Memsic wireless sensor nodes. Available: http://www.memsic.com/wireless-sensor-networks/ [23/06/2015]

Paoli R, Fernandez-Luque FJ, Domenech G, Martinez F, Zapata J, Ruiz R (2012) A system for ubiquitous fall monitoring at home via a wireless sensor network and a wearable mote. Expert Syst Appl 39(5):5566–5575

Rodriguez-Sanchez MC, Borromeo S, Hernandez-Tamames JA (2011) Wireless sensor networks for conservation and monitoring cultural assets. IEEE Sensors J 11(6):1382–1389

Sensirion (2014) Datasheet SHT25. Humidity and temperature sensor. Sensirion. Version 3. Available: https://www.sensirion.com/fileadmin/user_upload/customers/sensirion/Dokumente/2_Humidity_Sensors/Sensirion_Humidity_Sensors_SHT25_Datasheet_V3.pdf [26/01/2017]

Severance C (2014) Massimo Banzi: building arduino. Computer 47(1):11–12

Sileo M, Biscione M, Gizzi FT, Masini N, Martinez-Garrido MI (2014) Low cost strategies for the environmental monitoring of cultural heritage: preliminary data from the Crypt of St. Francesco D'assisi, Irsina (Basilicata, Southern Italy). In: Rogerio-Candeleda MA (ed) Science, technology and cultural heritage. CRC Press, Balkema, pp 27–34

Silva JFMC, Gomes RC, Nascimento AOF, Menezes JWM, Silva FD, Alves LEB (2012) Building a node for wireless sensor network based on open source plataform arduino. 2012 Brazilian Symposium On Computing System Engineering (Sbesc 2012), pp 224–224

Smartmote Monitoring And Testing (2015) www.smartmote.de [06/22, 2015]

Solahuddin YF, Ismail W (2014) Data fusion for reducing power consumption in Arduino-Xbee wireless sensor network platform. 2014 International Conference on Computer and Information Sciences (Iccoins)

Spadacini M, Savazzi S, Nicoli M (2014) Wireless home automation networks for indoor surveillance: technologies and experiments. EURASIP J Wirel Commun Netw 6:1–17

SST Sensing Ltd (2015) CO2S-A ambient range CO_2 sensor. Available: http://www.sstsensing.com/catalogue/co2-sensors [05/21, 2015]

Texas Instruments Incorporated, 02/10/2014 Rev. Diciembre 2007, 2007-Last Update, CC2520 Datasheet 2.4 GHZ IEEE 802.15.4/Zigbee RF transceiver. Available: http://www.ti.com/lit/ds/symlink/cc2520.pdf [01/15, 2015]

Thies Clima (2015) Anemometer. Available: http://www.thiesclima.com/wind.html [01/15, 2015]

Turner JSC, Ramli MF, Kamarudin LM, Zakaria A, Shakaff AYM, Ndzi DL, Nor CM, Hassan N, Mamduh SM (2013) The study of human movement effect on signal strength for indoor WSN deployment. 2013 IEEE Conference on Wireless Sensor (Icwise) 30–35

Varas-Muriel MJ, Fort R, Martínez-Garrido MI, Zornoza-Indart A, López-Arce P (2014a) Fluctuations in the indoor environment in Spanish rural churches and their effects on heritage conservation: hygro-thermal and co2 conditions monitoring. Build Environ 82:97–109

Varas-Muriel MJ, Martínez-Garrido MI, Fort R (2014b) Monitoring the thermal–hygrometric conditions induced by traditional heating systems in a historic Spanish church (12th–16th C). Energ Buildings 75:119–132

Webster JG, Eren H (2014) In: Webster JG, Eren H (eds) Measurement, instrumentation, and sensors handbook, second edition: electromagnetic, optical, radiation, chemical, and biomedical measurement. CRC Press, Boca Raton

Yildirim U, Oguz O, Bogdanovic N (2013) A prediction-error-based method for data transmission and damage detection in wireless sensor networks for structural health monitoring. J Vib Control 19(15):2244–2254

Chapter 17
Techniques for Seamless Color Registration and Mapping on Dense 3D Models

Ruggero Pintus, Enrico Gobbetti, Marco Callieri, and Matteo Dellepiane

Abstract Today's most widely used 3D digitization approach is a combination of active geometric sensing, mainly using laser scanning, with active or passive color sensing, mostly using digital photography. Producing a seamless colored object, starting from a geometric representation and a set of photographs, is a data fusion problem requiring effective solutions for image-to-geometry registration, and color mapping and blending. This chapter provides a brief survey of the state-of-the-art solutions, ranging from manual approaches to fully scalable automated methods.

Keywords Image-to-geometry registration • Color mapping • Color blending • 3D reconstruction

17.1 Introduction

In the cultural heritage (CH) domain, digital technologies are transforming the way researchers, archaeologists, and curators work. It is now widely acknowledged that accurate 3D digital models of cultural artifacts built from objective measures are becoming central to CH research, conservation, display, and dissemination of knowledge, and have many applications ranging from virtual restoration to visual communication.

A large variety of active and passive noninvasive systems exists for acquiring, at reasonable costs, a very dense and accurate sampling of both geometric and optical surface properties of real objects. However, today the most widely used 3D digitization approach is a combination of an active scanning device (e.g., laser triangulation, structured light, time-of-flight, interference) and digital photography. By using computational techniques, digital surfaces are reconstructed from the

R. Pintus • E. Gobbetti (✉)
CRS4, Visual Computing Group, Cagliari, Italy
e-mail: ruggero.pintus@crs4.it; enrico.gobbetti@crs4.it

M. Callieri • M. Dellepiane
ISTI-CNR, Visual Computing Group, Pisa, Italy
e-mail: marco.callieri@isti.cnr.it; matteo.dellepiane@isti.cnr.it

N. Masini, F. Soldovieri (eds.), *Sensing the Past*, Geotechnologies and the Environment 16, DOI 10.1007/978-3-319-50518-3_17

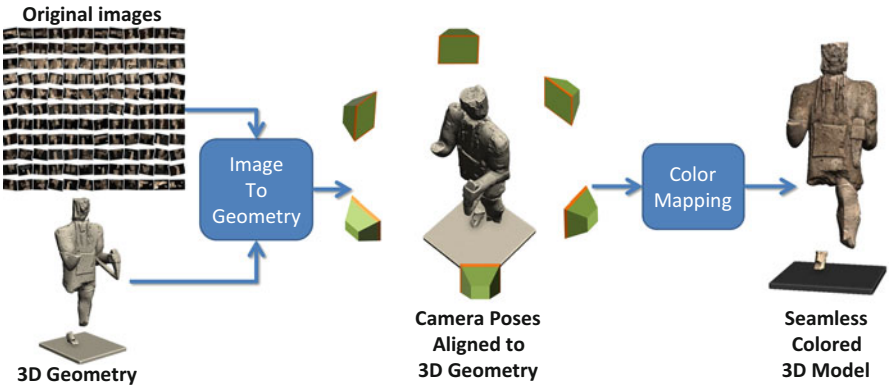

Fig. 17.1 Pipeline overview. The input data are a 3D geometry and a set of photos of the real object. First, an image-to-geometry alignment step registers the images to the 3D model, by producing a set of corresponding camera poses. By exploiting the resulting link between 3D points and pixels, a color mapping procedure produces a seamless color signal across the surface

scanner-generated range maps, and the color (or material) value sampled in digital photos is transferred onto the surface by registering the photos with respect to the 3D model, and projecting pixel values to the 3D surface using the recovered inverse projections (see Fig. 17.1). Since early demonstrations of the complete modeling pipeline (e.g., Bernardini and Rushmeier 2002; Levoy et al. 2000), this approach has proven to be particularly well suited to CH digitization, because 3D scanning and photographic acquisition campaigns can be performed quickly and easily, without the need to move objects to specialized acquisition labs. Even though passive purely image-based methods have recently affirmed themselves as a viable (and low-cost) 3D reconstruction technology (Remondino 2011), the pipeline based on active geometric scanning sensors and separate color acquisition still remains a widely used general-purpose approach, mainly because of the higher flexibility and reliability for a wider variety of settings (e.g., featureless surfaces) (Remondino 2011; Koutsoudis et al. 2014).

As exemplified in Fig. 17.1, producing seamless colored objects, starting from a geometric representation and a set of photographs, is a *data fusion* operation that requires the solution of two main problems. First, the color data must be *registered* with the geometric data, in order to establish the mapping between appearance information and the 3D surface with which it must be associated. Then, once this registration is known, the appearance, possibly coming from different sources (images), must be *mapped* to the surface to produce a seamless color signal, where each surface point has the single associated color (or material) that best approximates the original one.

In this chapter, we provide a brief overview of the many solutions that have been proposed for effectively solving these two steps of the coloring problem. We show that, although early works can deal only with small and medium datasets, and are

often limited to specific object classes, recent approaches are scalable in terms of the image and geometry side, and are mostly (and often completely) automatic, opening the way to interesting innovative applications.

17.2 Image-to-Geometry Registration

Image-to-geometry registration takes as input a dense 3D model, representing the shape of the imaged artifact, and a set of N photographs. Depending on the setting, the photographic dataset can cover the complete surface of the 3D object, only a part of it, or a larger area. The goal of registration is to find the intrinsic and extrinsic parameters of the imaging cameras in the reference frame of the 3D object. These parameters are required by the mapping step (see Sect. 17.3) to transfer color information from the images to the 3D model.

The most straightforward way to get 2D image data mapped to a geometry is to fix a calibrated camera rigidly to an acquisition device. *Fixed-relative* (or *colocated*) methods (Pulli et al. 1998; Fruh and Zakhor 2001, 2003) assume that the pose of the camera is already known and relative to the position of the range scanner (or other source of geometric data). Hence, they have the color intrinsically calibrated with the 3D just after the acquisition, avoiding an explicit image-to-geometry registration task.

On one hand, studies such as Yang et al. (2007) show that this kind of approach, in a hybrid framework that exploits other methods (e.g., *color-based*, see Sect. 17.2.3), can be applied in a number of interesting applications, because the color obtained in the acquisition phase can be used to map other photos with different appearances. Moreover, some range scanners also acquire color information at a quality that might be high enough compared to the application needs. However, even if there are hardware solutions able to sample geometry and color altogether, the color quality and resolution of integrated solutions are often insufficient for CH (e.g., low resolution, poor sensitivity), and rigidly mounting off-axis high-quality cameras often leads to visibility problems. Moreover, in many cases, it is not possible to acquire the 3D and the images at the same time. Sometimes the light condition needed for the photographic dataset must be different from that used during the 3D scanning. For instance, some sites of CH interest can be captured only at night (e.g., Piazza della Signoria in Florence (Corsini et al. 2013)). There is often an interest in mapping multiple image datasets acquired in different moments to the same geometry, such as the two image sets acquired by a professional photographer before and after the restoration of Michelangelo's statue of David (Dellepiane et al. 2008). Moreover, the different parallax of the camera and the range sensor in *fixed-relative* setups possibly results in the presence of occlusions; the color will thus be missed in some surface regions. Finally, although a *colocated* camera might help in aligning additional color images, it will not work with a general 2D signal. In the last decade a vast number of applications in CH use

multispectral (MS) acquisitions (e.g., far ultraviolet, far infrared thermal images). In contrast to a reflectance signal, which is typically from a visible wavelength, these signals might have really different appearance features; this inconsistency depends on variations of transmittance and absorption across the spectrum. The resulting images must be aligned to the geometry without exploiting the presence of the *colocated* camera.

All these reasons lead to a broad range of techniques to enable registration of independently acquired image and 3D datasets. The available solutions include manual registration methods (Sect. 17.2.1), feature-based approaches that match geometric and image features (Sect. 17.2.2), color-based techniques that exploit additional color signals from the 3D scanning device (Sect. 17.2.3), statistical approaches that rely on mutual information (Sect. 17.2.4), as well as general techniques that convert the hard to solve 2D/3D registration task to a 2D/2D registration obtained via structure-from-motion (SfM) followed by a more viable 3D/3D alignment problem (Sect. 17.2.5).

17.2.1 Manual Methods

The most common pipeline for mapping photos onto a 3D geometry consists of asking the user to select correspondences manually between pixels in the 2D domain and points in 3D. Hence, the initial step will be a sequence of point-and-clicks with which the user feeds the algorithm. Then, an automatic process will take the burden of refining the initial, manual, rough alignment via an error minimization strategy, and it will finally estimate the camera's intrinsic and/or extrinsic parameters. Initially, the solutions proposed focus on the definition of the most usable user interfaces to facilitate this labor-intensive task (Dellepiane et al. 2008; Fruh and Zakhor 2003). Later, there was a focus on speeding up and reducing manual operations. Borgeat et al. (2009) developed an interface where possible feature matches were highlighted. Another more efficient strategy is to include not only 2D/3D pairs, but also links between pixels in different images (Franken et al. 2005). Moreover, in particular settings, careful planning of image capture might be a solution to speed up or mostly automate the registration (Matsushita and Kaneko 1999). In any case, although these semi-automatic methods are robust due to continuous support and check by humans on the registration process, they are hardly applicable if the image set starts to expand over a certain moderate cardinality (e.g., tens or hundreds of photographs).

17.2.2 Feature-Based Methods

Feature-based techniques extract visual descriptors from the 3D model and the photographs, and solve the image-to-geometry problem by finding correspondences between them. Although among this class of methods a number of completely

automatic frameworks exist, this task is generally very complex because the pure geometry and the object, which is a mix of shape and texture, have very different appearances. For this reason, the works in this area are typically tailored to models with specific geometric characteristics, such as points, lines, circles (Stamos et al. 2008), rectangles (Liu and Stamos 2005), edge intensities (Neugebauer and Klein 1999), or viewpoint-invariant patches (Wu et al. 2008). Their performances are mostly reliable with 3D models of buildings, which show very sharp edges that can be easily extracted by a geometric operator applied to the 3D data, and are a very clear gradient signal in the 2D images. Another class of approaches (Kaminsky et al. 2009; Stamos and Alien 2001) focuses on the alignment of maps and/or floor plans (which contain a number of straight lines) with both indoor and outdoor environments acquired with 3D LIDAR scanners, which exhibit several linear edges and planes. Also the relationship between these features could help in finding a good set of camera poses. Liu et al. (2006) rely on the presence of clusters of vertical and horizontal lines, and they exploit the orthogonality constraints to drive the registration algorithm. They process the geometry to extract parallelepipeds, and they find correspondences between them and rectangles in the photographs. This method results in being very suitable for complex urban scenes.

A strong and robust feature that can be efficiently employed to find matches between images and shapes is the silhouette. A number of methods successfully use it to undertake image-to-geometry alignment (Lowe 1991; Brunie et al. 1992). The key idea is that silhouette contours are very fast and simple to extract both in the image and in the rendered input 3D model, and their appearance is very similar and independent of object texture. Lensch et al. (2000) present an efficient, hardware-accelerated implementation of such algorithms, and propose a robust similarity function. They also do not need any manual intervention.

Unfortunately, these techniques require the whole object to be visible in all input photographs. In addition, they moderately depend on the accuracy of the algorithm for background and foreground separation, which sometimes is refined manually by the user. This latter element might pose some restrictions on the acquisition setup and size of the framed object (e.g., a severe limitation for a large-scale target), reducing the spectrum of possible applications.

17.2.3 Color-Based Methods

Whereas *feature-based* methods try to extract a visual cue from the geometry comparable to the intensity or color signal in the photographs, *color-based* techniques exploit appearance data provided by the acquisition device and, hence, already attached to the geometric primitives (e.g., intensity, color, laser reflectance). In this scenario, the comparison of image descriptors and the computation of matches is naturally more efficient and reliable. The methods of Ikeuchi et al. (2007) and Sequeira and Gonçalves (2002) rely on the extraction of edges in the reflectance information. These data show characteristics similar to color images, because these edges come from the discontinuities in the materials across the surface, and they

are likely to produce gradients in the same regions both in the color and reflectance signals. Yang et al. (2007) use a colocated setup that produces a set of colored range maps. Then they extract image descriptors from the color captured by the scanner and by a handheld camera. The correspondences between these two sources are employed to compute the extrinsic and intrinsic parameters of the handheld camera, solving the 2D/3D registration.Wu et al. (2008) present a novel feature called VIP (viewpoint invariant patch), and apply it to both the image-to-geometry problem and to the registration of two shapes. They normalize the local orientation and viewpoint by performing local texture rectification, and by computing a dominant image gradient. Their method is a robust alignment strategy of images and scenes, even if they are seen from very different viewpoints or they have a little overlap. This framework is particularly suitable for large-scale and complex scenes when a lot of 2D/3D or 3D/3D registrations have to be undertaken.

17.2.4 Statistical Methods

Statistical image registration methods based on mutual information (MI) are extensively used in many applications. In the field of image-to-geometry registration, MI is capable of analyzing nonlinear correlations and photoconsistency between the intensity signal in the image and some measure present in the target surface, avoiding 3D descriptor extraction. The seminal work of Viola and Wells (1997) correlates the image gradient with a particular rendering of the surface normals. Cleju and Saupe (2007) improve this work by a global approach based on a stochastic mathematical framework for joint optimization of multiple image-to-geometry registrations.

When available, an important signal for MI computation is the intensity of the reflected laser beam. Williams et al. (2004) present an automatic registration that uses intensity comparisons between color images and geometry texture mapped with laser reflectance. They employ a gradient descent optimization to find the best solution that minimizes the alignment cost function. However, Hantak and Lastra (2006) show how in some cases the metric used in this approach produces multiple minima within the search space, dropping down the confidence in spotting the right minimum. Hence, they explore different information metrics applied to different environments. This leads them to the conclusion that coupling these metrics with global minimization techniques produce in general better results at the cost of higher computational time. The method of Mastin et al. (2009) exploits the statistical dependency that in urban scenes correlates the LIDAR elevation with the optical appearance. They measure MI between LIDAR and the optical signal, and apply downhill simplex optimization to find camera poses. They initialize each camera pose from GPS data, and harness the power of graphics hardware to reduce registration times dramatically. In the field of CH, Corsini et al. (2009) take Viola and Wells's idea of generating an intensity signal from normals, and extend that by including additional surface properties, such as ambient occlusion and reflection

directions. The hybrid method of Zheng et al. (2010) strives to integrate, instead, the advantages of *statistical* and *feature-based* registration (Zheng et al. 2010) by projecting the 3D surface onto 2D normal images. This enables the extraction of local geodesic descriptors, which can be used to perform an initial image-to-image and image-to-geometry registration, which is then refined by using MI and global stochastic optimization. Recently, Dellepiane and Scopigno (2013) proposed a MI framework that focuses on registration refinement; they globally tune the camera poses by fitting the original color signal with the color mapping result, thus removing artifacts produced by small image misalignments (see also Sect. 17.3.2).

Unfortunately, all these methods are robust only if they are given a good enough initial camera pose(s) in advance. Otherwise, it is likely they will not converge to a right solution. Moreover, signals used for correlation are not always available as geometric attributes.

17.2.5 Multiview Methods

In previous sections the vast majority of the approaches already mentioned aim at mapping one single image at a time; conversely, *multiview* techniques exploit the intrinsic grouping nature of the input images and the relations among them. The fundamental insight that underlies the class of *multiview*- based methods is to transform the original image-to-geometry registration problem into an image-to-image registration step, followed by an alignment between two 3D shapes. In particular, recasting the 2D/3D matching problem into a 3D/3D alignment is made possible by using available and mature structure-from-motion approaches, which take an image set and robustly generate a sparse point cloud of the framed object together with a structure of images aligned to it. Hence, registering the original dense geometry with the one resulting from the SfM step will implicitly solve the image-to-geometry mapping. Methods in this class are more generally applicable, inasmuch as they do not require such strict constraints as others do. Compared to *feature-based* methods (Sect. 17.2.2) they do not rely on specific features such as circles, lines, or orthogonal planes. Furthermore, they do not try to find correspondences between images and geometry, but they first find matches between images (SfM step), which is a much faster and simpler task, and then solve a pairwise geometry alignment, which is a well-studied problem too. Apart from the completely automatic *multiview* solutions, compared to *statistical* approaches (Sect. 17.2.4), the *multiview* methods reduce manual intervention and completely avoid the use of any additional attributes of the geometrical primitives, which are not always accessible, such as reflectance, color from the acquisition device, LIDAR elevation, or probability of detection (see Sects. 17.2.3 and 17.2.4). The techniques in the *multiview* class just need a moderate presence of any type of texture and/or geometrical features, which is a normal nonlimiting requirement of the classical SfM algorithm.

One of the earliest works in this field was due to Zhao et al. (2005), which presented a way to register a video onto a point cloud. By using motion stereo, they computed a point cloud and a set of relative camera positions from a continuous (oblique) video. After the alignment of just two frames with a dense point cloud directly obtained from a range sensor, they employed an ICP-based procedure to refine the registration between the sparse geometry and the target 3D models. This framework proved to be very efficient for coloring large-scale digital models in urban scenes. Unfortunately, it is limited to a dense and ordered (video) sequence of highly overlapping images. After this seminal contribution, some past methods have been updated in a hybrid framework that includes some advantages of a *multiview* processing step. For instance, Liu et al. (2006) extended their previous work on a *feature-based* 2D/3D mapping (Liu and Stamos 2005), by integrating a SfM geometry and an automatic 3D registration. They used a number of 3D scans to build a dense point cloud; in this step they inherited the *feature-based* approach of the previous work to find correspondences between 3D lines in the range images. Then, they computed a sparse geometry from the sequence of the input 2D photographs. They found the rotation, scale, and translation that minimized the distance between the two 3D shapes. Stamos et al. (2008) relaxed the line-based orthogonality constraint in order to apply the algorithm not only in urban scenes, but also in complex indoor architectures. Unfortunately, the limit of these hybrid systems to align only 3D models of architectural items remains, so that the spirit of *multiview* has not been completely exploited to solve a more general problem.

Inasmuch as relying on ordered sets of images is a too limiting constraint, such as in Zhao et al. (2005), a number of methods naturally arose that tried to deal with unordered sets of sufficiently overlapping photos. Moreover, acquisition of complex geometrical shapes inevitably leads to nonuniform image sampling; the capture must be performed adaptively, and the number and density of 2D frames per region depends on the presence and nature of surface occlusions. This kind of acquisition strategy eventually produces an unordered image set as input for the registration pipeline.

Li and Low (2009) register unordered image sequences from untracked and uncalibrated cameras onto 3D geometry. Their method is pure *multiview*. However, they make use of projectors to illuminate the scene of indoor environments with a special light pattern in order to increase the algorithm robustness in regions with a low presence of image features. They manually define a rough registration between the model from SfM and the detailed one. In the refinement stage, they exploit plane segmentation of the input geometry, and employ a cost function that is a mix of object-space error (point-to-plane distance), and image-based reprojection error. A further manual tuning of a heuristic parameter is required to weight these two error terms properly. Similar semi-automatic approaches have been proposed by Banno and Ikeuchi (2010) and Pintus et al. (2011c). The first presents an accurate texturing method that estimates camera extrinsic parameters by computing a sparse geometry from a spherical image stereo dataset. They measure the distance between the sparse and dense geometry (from a range sensor) by taking into account the uncertainty distribution of 3D in the stereo data. After the rough manual alignment of a few

images to the dense geometry, Pintus et al. (2011c) propose an image-to-geometry optimization that in a nonrigid manner independently deforms the sparse 3D points together with the poses of each camera. The error metric relies only on image-based reprojection error. On the other hand, their method is only applicable to uniformly sampled 3D models.

Due to the well-known problem that SfM techniques reconstruct a sparse 3D point cloud up to a scale factor, aligning it with the geometry from the range sensor requires an affine transformation. All the previous methods require minimal user intervention to define an approximate registration, which is the initial affine mapping condition for the final algorithm to converge. The lack of a completely automatic pipeline is the main drawback of these otherwise very robust techniques. To overcome this issue, recently, two completely automatic and orthogonal approaches have been presented that are capable of dealing with large input datasets and need neither an object-dependent parameter setting, nor, of course, a manual intervention.

Corsini et al. (2013) propose a novel multistage framework for a fully automatic 2D/3D global registration, shown in Fig. 17.2. After the SfM procedure, carried

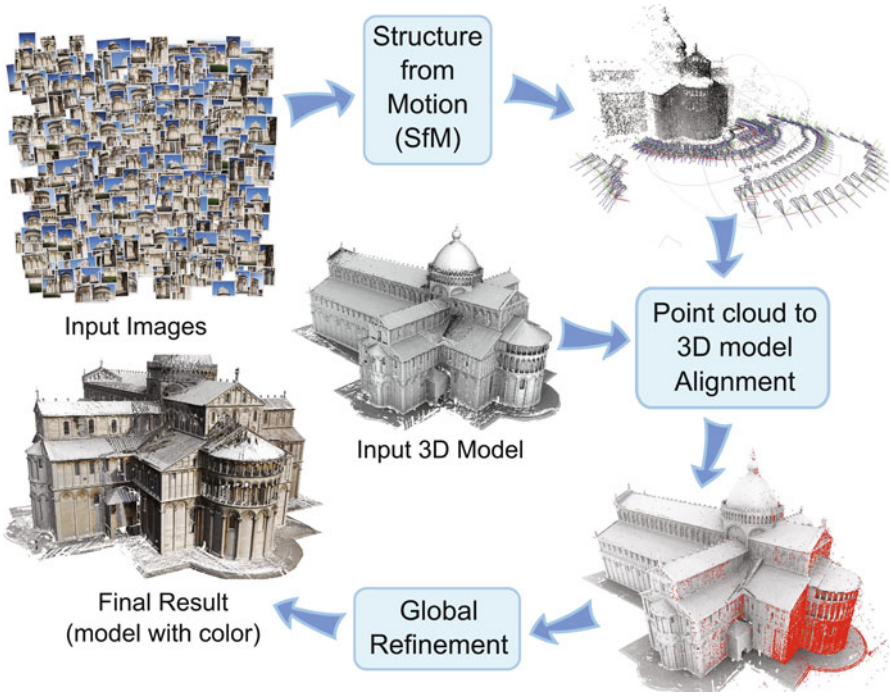

Fig. 17.2 The multi-image alignment proposed by Corsini et al. (2013), which uses an approach similar to Pintus et al. (2011c, 2015): The images are used to compute a sparse point cloud using SfM, and the cloud is then aligned to the target geometry, thus obtaining an initial camera orientation that will then be refined using mutual information (Reprinted from Corsini et al. 2013 with kind permission from Springer Science+Business Media)

out similarly to Pintus et al. (2011c), the generated sparse point cloud is aligned with the dense model by using a modified version of the four-point congruent set (4PCS) (Aiger et al. 2008) algorithm. The 4PCS deals with rigid motion, however, they extend it to cope with both different scales and an unknown amount of overlapping regions. Finally, a global refinement strategy is used based on mutual information, which minimizes the color reprojection error of the images onto the geometry. The method of Pintus et al. (2015) is another completely automatic solution that performs a coarse image-to-geometry alignment by using a GPU-based global stochastic registration approach to find the optimal affine transformation between the sparse SfM 3D and the dense, original point cloud (Agus et al. 2014). They propose a robust statistics to manage outliers, and a strategy to estimate automatically a local adaptive tolerance to deal with nonuniformly sampled 3D geometry. As in Pintus et al. (2011c), they refine intrinsic and extrinsic parameters of each camera in a nonrigid manner, by employing a specialized sparse bundle adjustment (SBA) step and an image-based error metric. Compared to Corsini et al. (2013), they do not require heavy preprocessing to make the SfM sparse point cloud dense, because the global registration method employed in the coarse alignment step recovers the globally optimal scale, rotation, and translation alignment parameters using a stochastic algorithm for pairwise affine registration of the coarse point cloud coming from SfM with the fine point cloud representing the geometric model (Agus et al. 2014).

These approaches based on fully automatic 2D/3D registration are more generally applicable and robust. Their main advantage is that they do not make any assumption tailored to the geometry type, size, or sampling, and are suitable to be applied to small, medium, and large objects of different natures. Because they are scalable, they remain suitable even if the image set size grows, opening possibilities for new scenarios and more interesting applications of unattended image-to-geometry alignment and mapping (e.g., automatic Web-based services). The most costly and difficult step is the automatic global registration, which can eventually be replaced, in difficult cases, by a simple manual initialization based on a few hand-picked correspondences between image and geometry, followed by local refinement.

17.3 Mapping Color to 3D Geometries

In all the described cases, the result of the image registration algorithms is the calibration and orientation of one or more photos in the reference space of a 3D geometry. Although there are many direct uses of a set of calibrated and oriented images, in most cases, the image alignment is used to map the color information onto the 3D geometry, thus obtaining a colored 3D model.

The recovered camera alignment data are, basically, a perspective projection matrix. By using this perspective projection, it is easy to establish the inverse

correlation between the color information on the photos and the 3D geometry. Using this inverse projection, the color can be mapped onto the 3D geometry: this principle is the basis for all the mapping methods.

The case of a single registered image is, then, trivial, because a simple inverse perspective projection will be enough to map the color onto the 3D geometry. The visibility problem determines what part of the surface is directly visible by the camera (and thus can be mapped from that specific photo) and can be solved numerically (precise but computationally cumbersome) or by exploiting the GPU, using the well-known shadow mapping algorithm or other specialized shaders. The visibility problem is more complex in the case of point clouds; inasmuch as direct shadow mapping would not work, Pintus et al. (2011a) use GPU accelerated screen-space operators, able to fill the sparse depth-map produced from the point cloud.

The problems arise when there is more than one photo that has to be mapped on the 3D surface. The basic inverse projection is still used to map color from the photos to the surface, however, the issue is now what happens when more than one input photo maps onto the same area of the 3D surface. It is necessary to determine, among the available registered photos mapping in a specific area of the 3D surface, which is the correct color information that has to be projected and/or to solve the "blending problem," that is, combine the available contribution to have a more continuous color mapping. This topic is covered in Sect. 17.3.1.

A common problem of the color mapping process is the fact that, no matter how precise the image-to-geometry alignment, it will never be perfect, or perfectly coherent between images. By applying local or local-global optimization of the cameras and projected color information it is possible to overcome the classical artifacts of ghosting and blurring. These methods are covered in Sect. 17.3.2.

Finally, another problem in the color projection from multiple registered cameras is the presence of lighting and photometric incoherence between the input photos, or the presence of view-dependent artifacts (e.g., highlights) that change their relative position from one photo to another. Although some of these issues can be reduced or removed by the blending process, there are specific methods in the literature that can be applied to solve these situations (see Sect. 17.3.3).

17.3.1 Projecting and Blending

An issue that is orthogonal to the mapping method is where to store the mapped color: a family of solutions uses (or creates) a surface parameterization and stores the mapped color in the texture map; a different approach is to encode color per vertex; finally, some algorithms may work regardless of the final color encoding.

The earliest works dealing with the mapping and blending problem tried to avoid entirely the computation of a static color mapping, but opted for a view-dependent texture mapping, dynamically creating a color mapping as the object was rendered. This was done, for example, by using a per-triangle computation of the best photo,

and perspective mapping directly on the graphics hardware, such as in Debevec et al. (1998); or by selecting the relevant images for a specific view, and then mixing multiple images using a weighting scheme (Pulli et al. 1998), blending the different contributions in a continuous mapped image.

Although it is able to provide good results, view-dependent texture mapping is not used much anymore, and the more modern color mapping methods all rely on the creation of a static mapping.

In these early examples, however, it is already possible to see the two opposite strategies that can be used when multiple photos are projecting on the same element of the 3D geometry that has to be mapped (a triangle, in texture mapping, or a vertex for per-vertex color mapping or in point clouds):

- Among the available contributions, the "best" photo for that specific element will be chosen, according to some criteria, and mapped on the surface.
- All the available contributions will be blended, using some form of weighting, and the interpolated result will be mapped on the surface.

The advantage of the first strategy is that the detail of the mapping remains at the same level of the input photos, but there will be discontinuities (color shift and detail misalignments) in the borders between areas assigned to different input photos. On the other hand, the color mapped using the blending strategy will produce a much smoother result, without discontinuities, but at the price of a less sharp appearance, and the presence of ghosting and blurring if the input photos are not perfectly aligned to the 3D geometry. The various methods available in the literature try to cover the spectrum between these two extremes, providing a solution that combines these two basic strategies.

The "best" contribution is one of the oldest strategies in color mapping; it is still used a lot in both open and commercial tools (Walkowski et al. 2008), especially when the final result of the mapping has to be a texture map. As the registered photos define a perspective projection, in most cases the projective transformations from the 3D surface to the input photos result in a natural and usable parameterization. Some mapping methods (Lensch et al. 2001; Rocchini et al. 2002; Callieri et al. 2002) build a parameterization for the 3D surface by dividing the triangulated mesh in patches, each one assigned to the "best" input image, parameterized using the perspective projection of that input image and packed in a texture map. Lensch et al. (2001) and Rocchini et al. (2002) filter the border between adjacent patches to reduce the discontinuity, whereas (Callieri et al. 2002) apply a texture-wide color/luminance correction to make the color uniform across the different photos.

Instead of using a simple "best contribution" criterion, but still wanting to use fragments of the original images directly, it is also possible to rely on existing image mosaicing and stitching optimization techniques, derived from the research on 2D image processing. Sinha et al. (2008) use a graph-cut optimization using a Markov random field (MRF) minimization framework to define, at a per-texel level, the most suitable photographic source to minimize incoherence, and then apply a Poisson blending to clear the remaining discontinuities. Lempitsky and Ivanov (2007) also

use this kind of MRF minimization, but at a per-triangle level, and Gal et al. (2010) also introduce a parameterization shifting order to correct image registration errors.

A different strategy may be to separate the high and low frequencies of the input images, and use different strategies to combine different bands to obtain a smooth mapping simultaneously, but with sharp details. Baumberg (2002) separates the input images in two bands: in every given area of the 3D model all the low-frequency components are blended using weights, but only the "best" high-frequency details are mapped. This solution is also used by Allène et al. (2008) and by Pintus et al. (2011a) on point clouds.

Among the methods blending all available contributions, performing a weighted sum is the most common way to combine contributions (Pulli et al. 1998; Bernardini et al. 2001; Callieri et al. 2008; Pintus et al. 2011a,b; Bettio et al. 2015). All these researchers use weighted blending. The weights used in these and other works are many, and are related to different aspects of the dataset. They may be related to geometry (depth discontinuities), camera (image sharpness, low quality on borders, image discontinuities), or geometry-camera relationship (orthogonality of the photo with respect to the surface, distance from the object). A useful feature of weighting schemes is that it is easy to add new metrics that are specific for a given dataset or acquisition/reconstruction technology.

In order to combine the different contributions in a single mapping, blending is simple and effective, but prone to blurring. To obtain a more continuous but sharp mapping, it is possible to solve a Poisson equation over the 3D surface (Chuang et al. 2009), taking into account the input image gradients, building a continuous yet nonblurred color field. Another interesting method is to use a super-resolution approach over the texture space (Goldluecke and Cremers 2009), resulting in a texture of the input photos that is more detailed.

Even though point clouds are widely used directly, without converting them to a triangulated surface, there are not many color mapping methods suitable for these kinds of data. Pintus et al. (2011a,b) work directly on the point clouds, mapping color to each vertex, using a weighted blending two-band strategy, able to work on very large datasets. Conversely, Arikan et al. (2014) use the point clouds to create a series of local meshes, defined by the areas framed by the registered photos, which are then properly stitched during rendering.

Many of the discussed techniques assume that both geometry and images fit in memory, which severely limits the scalability of the methods. Some methods assume, instead, that the 3D model is very small and fits in memory, and the image and mask dataset are stored in an out-of-core structure (e.g., Xu et al. 2010; Callieri et al. 2008). The approaches that scale to large amounts of color and geometric data are typically based on some variation of the weighted blending approaches. Callieri et al. (2008) and Bettio et al. (2013, 2015) deal with massive models by using two out-of-core structures, one for the model and one for images and masks. By contrast, Pintus et al. (2011b; 2011a) use a streaming framework for efficiently blending images on massive point clouds in a low memory setting and through memory-coherent operations, providing unprecedented performance (Fig. 17.3). In

Fig. 17.3 *First row*: Image blending on massive point clouds, the case of Michelangelo's David statue (0.25 mm dataset). It is a 470 million point 3D model with color coming from a 548 Mpixel dataset (67 photos). *Second row*: The effect of the image-based adaptive point cloud refinement on the final color signal; we present two images of the final colored model, and a comparison between the image blending on the original point cloud and the image blending on the adaptively refined geometry (With kind permission from Eurographics Association: Pintus et al. 2011b, Figs. 7, 8 and 9; Scopigno, R., Fig. 1)

addition, the latter approach supports adaptive geometry refinement as a function of image content, which is achieved during the blending phase by selectively refining the point cloud in areas with high-frequency image contents (Fig. 17.3, second row).

17.3.2 Fixing Misalignments

Color projection on 3D models is a straightforward and convenient way to obtain a visually pleasing result starting from a simple input. Nevertheless, annoying artifacts may appear on the model, regardless of the mapping strategy chosen.

One of major issues is due to the misalignments of images that have to be projected: this leads to the aliasing/blurring of fine details of models, because the images are simply projecting the same data on slightly different positions of the surface. Misalignments are less visible in the case of methods where a single image is chosen for projection: misalignments may be visible in the borders between adjacent patches. Unfortunately, the selection of a single image for each portion of a surface usually works well on simple cases, but when the number of images rises, it leads to very fragmented color, where artifacts are visible again.

The misalignment issues are only partially inherent to the registration and projection methods. They usually come from the quality of the input data, in particular:

- The camera parameters: It's important to stress that image registration is obtained by applying a camera model to fit real cameras. This means that in particular cases there will be no possibility of achieving a perfect alignment, because the model is not able to describe the camera perfectly.
- The 3D model quality: If the geometric representation of the object is not accurate, a perfect alignment will not be possible.
- The quality of images: Similarly as above, if the quality of 2D data is low, even semi-automatic methods may fail. Moreover, low- quality images may strongly concur in blurred and aliased details.

Given that the input data are not perfect, fixing the misalignments may not be an issue related to a better estimation of camera parameters. Some methods take this into account to get the best color: for example, Lempitsky and Ivanov (2007) inserted a term in their minimization function that should reduce misalignment artifacts. All these methods are based on a quite strong assumption: that the 3D model is accurate enough to allow an accurate color projection.

More recently, Dellepiane and Scopigno (2013) proposed a global refinement method to reduce misalignments. The result of any image-to-geometry registration method can be the input of this approach. The method is based on mutual information. The camera parameters of each image are refined by trying to fit the color projected by all the other images on the 3D model. In this way the error is globally distributed, and fine details are better preserved. This works regardless of the quality of the 3D model, and only camera parameters are changed.

The main way to achieve an optimized alignment, though, is to be able to modify all the elements of the projection dataset. In the following, we review the recently proposed methods.

The quality of color projection can be improved by modifying all the elements of the projection set: camera parameters, geometry, images. Recently the problem came out after the rise of multiview stereo matching techniques. In this case, similarly to the work by Gal et al. (2010), the big advantage comes from the fact that geometry and color are produced starting from the same input: the images. Given this, the geometry can be modified to better fit the images. Alternatively, taking into account the matching among images enables us to preserve detail. The work by Waechter et al. (2014) shows that this can be used to obtain large- scale 3D texturing.

In a more general case, geometry and images are acquired at a different moment, thus it could be harder to handle them. Pintus et al. (2011a) used a frequency analysis and the increase in data density to improve the projection on point clouds. In the case of triangulated surfaces, a possibility is to warp images so that they will project the same color information in the same part of the surface. Eisemann et al. (2008)

used it to fit textures to body models. They proposed a GPU implementation of the method that reaches real-time performances. Hence the algorithm can be employed not only in offline image-to-geometry registration frameworks, but also in image-based visualizations.

Dellepiane et al. (2012) extended the concept to more complex cases: for each portion of the surface, an image is chosen as the "leading" one. All the other images are warped using optical flow in order to project the same color detail as the leading one. The border between adjacent parts is handled by mixing the warping in order to avoid discontinuities. This approach is able to put together the advantages of the "best photo" approach (high- quality fine details) with the advantages of blending approaches (coherent color, no discontinuities).

More recently, Zhou and Koltun (2014) proposed a method to map color on data coming from depth cameras. The method put together the camera parameters' refinement and the flow-based approach in a unique system to be optimized. Given the complexity of the problem, the system was solved in an iterative way (by refining cameras and flow one at a time), and the results were more than satisfying.

17.3.3 Fixing Color and Lighting Issues

The other issue when dealing with color mapping from images is that the color is projected "as it is", without any previous knowledge of illumination conditions. This leads to the fact that illumination artifacts (highlights, shadows) are projected on the model.

The proper way to be able to remove artifacts would be to acquire the color under controlled light conditions (i.e., by knowing the position and intensity of the main sources of light in the scene). This is quite impractical during an onsite acquisition, or when working outdoors.

A possible approach is to analyze the images to detect and remove artifacts, but the purely image-based approaches are prone to errors and false positives (Xu et al. 2005; Guo et al. 2011). Another possible approach is to take advantage of the fact that more than one image will cover each part of the surface. In this case, some artifacts can be detected as outliers, and removed. These methods work reliably only when several images of the same portion are available (Frahm et al. 2010). This is not always possible, especially when high-quality images are needed. Hence, an alternative way is to have better knowledge of the lighting environment.

That being said, except for laboratory conditions and objects of small size, it's rarely possible to set up a controlled light environment. Alternatively, it's possible to try to estimate it: once the 3D model, the camera parameters, and the light positions are known, the lighting artifacts can be easily detected and removed. The lighting environment can be acquired using ad hoc devices (Corsini et al. 2008). An alternative solution can be to use the object itself as a light probe. The analysis of the behavior of artifacts (i.e., the change in position of highlights) can be used

to estimate the position of the main light sources in the scene. Palma et al. (2012) used video sequences to estimate the illumination environment, and also extracted a simplified description of the material of an object.

Another source of light that could be possibly estimated is the sky. Haber et al. (2009) analyzed the sky and the appearance of an object to estimate the skydome environment and relight images. Dellepiane et al. (2010a) estimated the sun's position (in an automatic or semi-automatic way) to remove hard shadows.

Finally, an interesting example of a controlled but easy to use light setup is FlISS (Dellepiane et al. 2010b), where the integrated flash device of the digital camera is used. This type of light has the advantage of being always at the same position w.r.t. the camera, and to provide dominant lighting in the scene. Hence, it is easy to detect and remove artifacts, and it is possible to obtain a partially calibrated color after a calibration step is performed once in a lifetime. Starting from the consideration that medium- to high-end single-lens reflex (SLR) cameras support fairly uniform flash illumination and RAW data acquisition modes that produce images where each pixel value is proportional to incoming radiance (Kim et al. 2012; Bettio et al. 2013, 2015) take the simpler approach of using constant color balance correction for the entire set of photographs and apply a per-pixel intensity correction based on geometric principles, taking into account distance and surface orientation.

17.4 Conclusions

We have provided an overview of many different approaches that have been proposed for effectively solving image-to-geometry registration and color mapping and blending. Despite the fact that in recent years many powerful pure vision-based methods have been developed and widely used to reconstruct both geometry and color, the interest in aligning 2D maps onto 3D surfaces remains very high. This is because different types of signals, or data acquired at different times, still need to be registered. Effectively solving 2D to 3D mapping and fusion is therefore of high importance for many application domains, including cultural heritage.

Although the various methods can be mixed and matched to create a pipeline for aligning and a separate one for producing seamless colored objects after alignment, we have seen that solutions of these two problems are often intertwined. In particular, a recent trend has been to perform fine registration steps during the color blending passes to produce seamless models. Moreover, whereas early techniques were mostly manual, most modern methods tend towards semi-automatic or automatic behaviors.

In CH practice it is, however, still common to introduce a human into the loop in order to control the fine behavior of algorithms. However, as data size is increasing, because acquisition is becoming fast and inexpensive, this fine control is increasingly becoming impractical, and we expect that automated methods will

increasingly become standard even in this application field. The increasing size of datasets is also forcing algorithm development to tackle scalability issues using specialized techniques. For this reason, although early methods, especially for the mapping step, required global operation with all data loaded into memory, modern methods strive to schedule localized operations, so as to minimize peak memory needs and I/O bandwidth.

The availability of modern fully scalable and mostly automatic techniques opens the door to innovative applications. In particular, cloud solutions based on Web services are emerging for performing heavy operations, with lean user interfaces often working on mobile graphics devices.

Although in this work we have focused mostly on the registration of color images onto the geometry, the techniques presented here are the basis for managing a number of multimodal fusion operations. Recent trends highlight in particular the need of enhancing geometric scans not only with the local body color of an object, but also with a detailed representation of the material and the appearance properties. In many cases, the rationale of the techniques reviewed here is still valid to deal with these more complex data, with limited modifications to implement the mapping and fusion (e.g., different descriptors for automatic alignment). On the other hand, sometimes microscale data acquired as 2D maps also provide information at the geometric level. For instance, reflectance transformation imaging acquisitions (Malzbender et al. 2001) make it possible to compute high-resolution normal maps, which, once registered, can be employed to refine the initial geometry (Nehab et al. 2005; Berkiten et al. 2014). This is usually done in a post-pass, however, a stronger coupling of the various phases of registration, mapping, and enhancement could lead to better and faster results, especially when dealing with massive amounts of data. An interesting avenue of future work would thus be to exploit the power of both approaches into a common scalable framework, in order to create highly detailed objects with higher resolution geometries combined with detailed digital models of materials.

Acknowledgements This work is partially supported by the EU H2020 Program under the Scan4Reco project (665091) funded under H2020-EU.3.6.3. We also acknowledge the contribution of Sardinian Regional authorities for Visual Computing activities (projects VIGEC and HELIOS).

References

Agus M, Gobbetti E, Villanueva AJ, Mura C, Pajarola R (2014) SOAR: Stochastic optimization for affine global point set registration. In: Proceedings of the 19th international workshop on vision, modeling and visualization (VMV), Oct 2014, Darmstadt, pp 103–110

Aiger D, Mitra NJ, Cohen-Or D (2008) 4-points congruent sets for robust pairwise surface registration. ACM Trans Graph (TOG) 27:85

Allène C, Philippe Pons J, Keriven R (2008) Seamless image-based texture atlases using multi-band blending. In: Proceeding of the ICPR. IEEE, pp 1–4

Arikan M, Preiner R, Scheiblauer C, Jeschke S, Wimmer M (2014) Large-scale point-cloud visualization through localized textured surface reconstruction. IEEE Trans Vis Comput Graph 20(9):1280–1292

Banno A, Ikeuchi K (2010) Omnidirectional texturing based on robust 3D registration through Euclidean reconstruction from two spherical images. Comput Vis Image Underst 114(4):491–499

Baumberg A (2002) Blending images for texturing 3D models. In: Proceeding of the BMVC, Citeseer, vol 3, p 5

Berkiten S, Fan X, Rusinkiewicz S (2014) Merge2-3D: combining multiple normal maps with 3D surfaces. In: 2nd international conference on 3D vision, Dec 2014, vol 1. IEEE, Los Alamitos/Washington/Tokyo, pp 440–447

Bettio F, Gobbetti E, Merella E, Pintus R (2013) Improving the digitization of shape and color of 3D artworks in a cluttered environment. In: Proceedings of the digital heritage, Oct 2013. IEEE, Piscataway, pp 23–30. Best Paper Award

Bettio F, Villanueva AJ, Merella E, Marton F, Gobbetti E, Pintus R (2015) Mont'e Scan: effective shape and color digitization of cluttered 3D artworks. J Comput Cult Herit (JOCCH) 8(1):4:1–4:23

Bernardini F, Martin IM, Rushmeier H (2001) High-quality texture reconstruction from multiple scans. IEEE Trans Vis Comput Graph 7(4):318–332

Bernardini F, Rushmeier H (2002) The 3D model acquisition pipeline. Comput Gr Forum 21:149–172

Borgeat L, Poirier G, Beraldin A, Godin G, Massicotte P, Picard M (2009) A framework for the registration of color images with 3D models. In: Proceedings of the 16th international conference on image processing (ICIP'09), IEEE Press, Piscataway, NJ, USA, pp 69–72

Brunie L, Lavallée S, Szeliski R (1992) Using force fields derived from 3D distance maps for inferring the attitude of a 3D rigid object. In: Computer Vision ECCV'92. Springer, pp 670–675

Callieri M, Cignoni P, Corsini M, Scopigno R (2008) Masked photo blending: mapping dense photographic data set on high-resolution sampled 3D models. Comput Graph 32(4):464–473

Callieri M, Cignoni P, Scopigno R (2002) Reconstructing textured meshes from multiple range RGB maps. In: VMV, Erlangen, pp 419–426

Chuang M, Luo L, Brown BJ, Rusinkiewicz S, Kazhdan M (2009) Estimating the laplace-beltrami operator by restricting 3D functions. Comput Gr Forum 28:1475–1484. Wiley Online Library

Cleju I, Saupe D (2007) Stochastic optimization of multiple texture registration using mutual information. Springer, Konstanz

Corsini M, Callieri M, Cignoni P (2008) Stereo light probe. Comput Gr Forum 27:291–300. Wiley Online Library

Corsini M, Dellepiane M, Ganovelli F, Gherardi R, Fusiello A, Scopigno R (2013) Fully automatic registration of image sets on approximate geometry. Int J Comput Vis 102(1–3):91–111

Corsini M, Dellepiane M, Ponchio F, Scopigno R (2009) Image-to-geometry registration: a mutual information method exploiting illumination-related geometric properties. Comput Gr Forum 28:1755–1764. Wiley Online Library

Debevec P, Yizhou Yu, Borshukov G (1998) Efficient view-dependent image-based rendering with projective texture-mapping. Springer, Berkeley

Dellepiane M, Benedetti L, Scopigno R (2010) Removing shadows for color projection using sun position estimation. In: Proceedings of the 11th international conference on virtual reality, archaeology and cultural heritage. Eurographics Association, pp 55–62

Dellepiane M, Callieri M, Corsini M, Cignoni P, Scopigno R (2010) Improved color acquisition and mapping on 3D models via flash-based photography. J Comput Cult Herit (JOCCH) 2(4):9

Dellepiane M, Callieri M, Ponchio F, Scopigno R (2008) Mapping highly detailed colour information on extremely dense 3D models: the case of David's restoration. Comput Gr Forum 27:2178–2187. Wiley Online Library

Dellepiane M, Marroquim R, Callieri M, Cignoni P, Scopigno R (2012) Flow-based local optimization for image-to-geometry projection. IEEE Trans Vis Comput Graph 18(3):463–474
Dellepiane M, Scopigno R (2013) Global refinement of image-to-geometry registration for color projection on 3D models. In: Digital heritage international congress. The Eurographics Association, pp 39–46
Eisemann M, De Decker B, Magnor M, Bekaert P, De Aguiar E, Ahmed N, Theobalt C, Sellent A (2008) Floating textures. Comput Gr Forum 27:409–418. Wiley Online Library
Franken T, Dellepiane M, Ganovelli F, Cignoni P, Montani C, Scopigno R (2005) Minimizing user intervention in registering 2D images to 3D models. Vis Commun 21(8–10):619–628
Frahm JM, Fite-Georgel P, Gallup D, Johnson T, Raguram R, Wu C, Jen Y-H, Dunn E, Clipp B, Lazebnik S et al (2010) Building Rome on a cloudless day. In: Computer vision–ECCV 2010. Springer, pp 368–381
Fruh C, Zakhor A (2001) Fast 3D model generation in urban environments. In: Proceedings of the MFI. IEEE, pp 165–170
Fruh C, Zakhor A (2003) Constructing 3D city models by merging aerial and ground views. Comput Gr Appl IEEE 23(6):52–61
Gal R, Wexler Y, Ofek E, Hoppe H, Cohen-Or D (2010) Seamless montage for texturing models. Comput Gr Forum 29:479–486. Wiley Online Library
Goldluecke B, Cremers D (2009) Superresolution texture maps for multiview reconstruction. In: Proceedings of the ICCV. IEEE, pp 1677–1684
Guo R, Dai Q, Hoiem D (2011) Single-image shadow detection and removal using paired regions. In: Proceedings of the CVPR. IEEE, pp 2033–2040
Haber T, Fuchs C, Bekaer P, Seidel H-P, Goesele M, Lensch HP et al (2009) Relighting objects from image collections. In: Proceedings of the CVPR. IEEE, pp 627–634
Hantak C, Lastra A (2006) Metrics and optimization techniques for registration of color to laser range scans. In: International symposium on 3D data processing, visualization, and transmission, third. IEEE, pp 551–558
Ikeuchi K, Oishi T, Takamatsu J, Sagawa R, Nakazawa A, Kurazume R, Nishino K, Kamakura M, Okamoto Y (2007) The Great Buddha project: digitally archiving, restoring, and analyzing cultural heritage objects. Int J Comput Vis 75(1):189–208
Kaminsky RS, Snavely N, Seitz SM, Szeliski R (2009) Alignment of 3D point clouds to overhead images. In: Proceedings of the CVPR workshops. IEEE, pp 63–70
Koutsoudis A, Vidmar B, Ioannakis G, Arnaoutoglou F, Pavlidis G, Chamzas C (2014) Multi-image 3D reconstruction data evaluation. J Cult Herit 15(1):73–79
Kim SJ, Lin HT, Lu Z, Suesstrunk S, Lin S, Brown MS (2012) A new in-camera imaging model for color computer vision and its application. IEEE Trans PAMI 34(12):2289–2302
Lensch H, Heidrich W, Seidel H-P (2000) Automated texture registration and stitching for real world models. In: Proceedings of the pacific graphics. IEEE, pp 317–452
Lensch HPA, Heidrich W, Seidel H-P (2001) A silhouette-based algorithm for texture registration and stitching. Graph Model 63(4):245–262
Lempitsky V, Ivanov D (2007) Seamless Mosaicing of image-based texture maps. In: Proceedings of the CVPR. IEEE, pp 1–6
Levoy M, Pulli K, Curless B, Rusinkiewicz S, Koller D, Pereira L, Ginzton M, Anderson S, Davis J, Ginsberg J et al (2000) The digital michelangelo project: 3D scanning of large statues. In: Proceedings of the SIGGRAPH. ACM, New York, pp 131–144
Li Y, Low K-L (2009) Automatic registration of color images to 3D geometry. In: Proceedings of the CGI. CGS, pp 21–28
Liu L, Stamos I (2005) Automatic 3D to 2D registration for the photorealistic rendering of urban scenes. In: Proceedings of the CVPR. IEEE, vol 2, pp 137–143
Liu L, Stamos I, Gene Yu, Wolberg G, Zokai S (2006) Multiview geometry for texture mapping 2D images onto 3D range data. In: Proceedings of the CVPR. IEEE, vol 2, pp 2293–2300
Lowe DG (1991) Fitting parameterized three-dimensional models to images. IEEE Trans Pattern Anal Mach Intell 13(5):441–450

Malzbender T, Gelb D, Wolters H (2001) Polynomial texture maps. In: Proceedings of the 28th annual conference on computer graphics and interactive techniques. ACM, pp 519–528

Mastin A, Kepner J, Fisher J (2009) Automatic registration of LIDAR and optical images of urban scenes. In: Proceedings of the CVPR. IEEE, pp 2639–2646

Matsushita K, Kaneko T (1999) Efficient and handy texture mapping on 3D surfaces. Comput Gr Forum, Blackwell Publishers, Oxford, UK, vol 18, pp 349–358

Nehab D, Rusinkiewicz S, Davis J, Ramamoorthi R (2005) Efficiently combining positions and normals for precise 3D geometry. ACM Trans Graph (TOG) 24(3):536–543

Neugebauer PJ, Klein K (1999) Texturing 3D models of real world objects from multiple unregistered photographic views. Comput Gr Forum 18:245–256. Wiley Online Library

Palma G, Callieri M, Dellepiane M, Scopigno R (2012) A statistical method for SVBRDF approximation from video sequences in general lighting conditions. Comput Gr Forum 31:1491–1500. Wiley Online Library

Pintus R, Gobbetti E (2015) A fast and robust framework for semi-automatic and automatic registration of photographs to 3D geometry. J Comput Cult Herit (JOCCH) 7(4):23:1–23:23

Pintus R, Gobbetti E, Callieri M (2011a) Fast low-memory seamless photo blending on massive point clouds using a streaming framework. J Comput Cult Herit (JOCCH) 4(2):6

Pintus R, Gobbetti E, Callieri M (2011b) A streaming framework for seamless detailed photo blending on massive point clouds. In: Proceedings of the eurographics area papers. pp 25–32

Pintus R, Gobbetti E, Combet R (2011c) Fast and robust semi-automatic registration of photographs to 3D geometry. In: The 12th international symposium on virtual reality, archaeology and cultural heritage Oct 2011. Eurographics Association, pp 9–16

Pulli K, Abi-Rached H, Duchamp T, Shapiro LG, Stuetzle W (1998) Acquisition and visualization of colored 3D objects. In: Proceedings of the ICPR. IEEE, pp 11–15

Remondino F (2011) Heritage recording and 3D modeling with photogrammetry and 3D scanning. Remote Sens 3(6):1104–1138

Rocchini C, Cignoni P, Montani C, Scopigno R (2002) Acquiring, stitching and blending diffuse appearance attributes on 3D models. Vis Comput 18(3):186–204

Sequeira V, Gonçalves GMJ (2002) 3D reality modelling: photo-realistic 3D models of real world scenes. In: Proceedings of the 3DPVT. IEEE, pp 776–783

Sinha SN, Steedly D, Szeliski R, Agrawala M, Pollefeys M (2008) Interactive 3D architectural modeling from unordered photo collections. ACM Trans Gr (TOG) 27:159

Stamos I, Alien PK (2001) Automatic registration of 2-D with 3-D imagery in urban environments. In: Proceedings of the ICCV. IEEE, vol 2, pp 731–736

Stamos I, Liu L, Chen C, Wolberg G, Yu G, Zokai S (2008) Integrating automated range registration with multiview geometry for the photorealistic modeling of large-scale scenes. Int J Comput Vis 78(2–3):237–260

Viola P, Wells WM III (1997) Alignment by maximization of mutual information. Int J Comput Vis 24(2):137–154

Waechter M, Moehrle N, Goesele M (2014) Let there be color! large-scale texturing of 3D reconstructions. In: Computer vision–ECCV 2014. Springer, pp 836–850

Walkowski F, Johnston RA, Price NB (2008) Texture mapping for the Fastscan hand-held laser scanner. In: Proceedings of the IVCNZ. IEEE, pp 1–6

Williams N, Low K-L, Hantak C, Pollefeys M, Lastra A (2004) Automatic image alignment for 3D environment modeling. In: Proceedings of the computer graphics and image processing. IEEE, pp 388–395

Wu C, Clipp B, Xiaowei Li, Frahm J-M, Pollefeys M (2008) 3D model matching with viewpoint-invariant patches (VIP). In: Proceedings of the CVPR. IEEE, pp 1–8

Xu S-C, Ye X, Wu Y, Zhang S (2005) Highlight detection and removal based on chromaticity. In: Image analysis and recognition. Springer, pp 199–206

Xu L, Li E, Li J, Chen Y, Zhang Y (2010) A general texture mapping framework for image-based 3D modeling. In: Proceedings of the international conference on image processing, Hong kong, pp 2713–2716

Yang G, Becker J, Stewart CV (2007) Estimating the location of a camera with respect to a 3D model. In: Proceedings of the 3DIM. IEEE, pp 159–166

Zhao W, Nister D, Hsu S (2005) Alignment of continuous video onto 3D point clouds. IEEE Trans Pattern Anal Mach Intell 27(8):1305–1318

Zheng H, Cleju I, Saupe D (2010) Highly-automatic mi based multiple 2D/3D image registration using self-initialized geodesic feature correspondences. In: Computer vision–ACCV 2009. Springer, pp 426–435

Zhou Q-Y, Koltun V (2014) Color map optimization for 3D reconstruction with consumer depth cameras. ACM Trans Gr (TOG) 33(4):155

Chapter 18
Integration and Analysis of Sampled Data: Visualization Approaches and Platforms

Roberto Scopigno and Matteo Dellepiane

Abstract The evolution of digitization technologies (2D and 3D) and the consequent wide availability of digital representations of artworks has ignited a number of works aimed at providing tools and platforms for archival, visual presentation, and integration of all those media. This chapter reviews some available instruments, focusing first on the platforms that could support the CH/DH professional in the single or cross-analysis of multimedia representations. Then, we discuss the available approaches for structuring and integrating the available data, presenting both the GIS-based solutions and the more recent Web-based systems. Some discussion on open issues concludes the contribution.

Keywords 3D models • Cultural Heritage • Visualization • Data archival • Multimedia data • Web-based data visualization

18.1 Introduction

The technological progress of digital sampling instruments (2D and 3D) has been impressive in the last two decades. We have many different technologies for acquiring digital representations of an object of interest, which can produce either 3D data (3D scanning or photogrammetric solutions sample at high-resolution the external surfaces, whereas tomographic systems also produce data on the internal structures) or 2D samplings (high-resolution imaging, HDR, RTI, multispectral images, video, etc.). But acquiring visual representations is not the ultimate goal of scholars or practitioners in digital humanities, or of people working in museums or in conservation. Given the mature status of the acquisition technologies, the emphasis is now moving to the design of instruments able to make proficient use

R. Scopigno (✉) • M. Dellepiane
CNR-ISTI, Pisa, Italy
e-mail: r.scopigno@isti.cnr.it; matteo.dellepiane@isti.cnr.it

N. Masini, F. Soldovieri (eds.), *Sensing the Past*, Geotechnologies and the Environment 16, DOI 10.1007/978-3-319-50518-3_18

of those digital models, supporting inspection, insight, and sharing of knowledge (Scopigno et al. 2011; Pintus et al. 2015). A pioneering experience was done in the framework of the restoration of Michelangelo's David (Callieri et al. 2004), where a number of visualization and data presentation approaches have been experimented with on top of the digital 3D model produced by Stanford's Digital Michelangelo Project.

Visual data are only a subset, even if an important one, of the overall *data* DH professionals use to support or facilitate the analysis and insight processes. Moreover, we also need to consider the issues concerning the creation, archival, and access to *metadata*, that is, the information that describes the available data and enables integration and *discoverability* of CH data.

All those data have to be stored and made accessible to the community. Therefore, a large number of different approaches for 3D/2D data visualization and archival emerged out of the intense research and tool design of the last decade. Moreover, in many cases coping with just a single visual representation is not sufficient: especially in digital humanities applications, an artwork has to be studied by sampling it with multiple technologies, each one producing a single data stream. This originates the need of being able to browse and inspect multiple types of media at the same time, possibly using a common visual analysis tool/platform. Data integration is therefore needed, both to have better input (e.g., to produce a more complete set of visual media describing the conditions of the artwork under study) or a better output (e.g., to document the reasoning process used to produce a given hypothesis). The scope of Sect. 18.2 is to review the approaches proposed thus far for supporting data integration and the visual media inspection and analysis tasks.

But the work does not stop at the visual representation stage and the subsequent data analysis. Together with multiple visual representation modes, we also have a large number of different sources of data that we need to store, interlink, and access. Those types of data depend on the specific application domain; unfortunately, not all subdisciplines of the digital humanities domain have the same requirements in terms of supporting data.

CH restoration is a good example of a DH subdomain showing sophisticated data management needs, in as much as it requires the management of both many different types of visual representation media (standard 2D, multispectral, RTI, 3D, etc.) and a very wide number of different sources of information that contribute to the characterization of the artwork. An information system supporting CH restoration should enable the management of all the data acquired during the preliminary phase of the restoration process (i.e., the data related to the nature of the artwork and its state of conservation) as well as the information produced during the actual restoration work (cleaning tests, restoration materials and methods, final reports, etc.). All those data have to be linked and correlated.

Different approaches have been proposed to enable data linking, either based just on databases where the data are represented and stored, or adding georeferences

to each specific data token and adopting data management platforms that allow encoding the geolocalization in an explicit manner (this is the case of the GIS systems, described in Sect. 18.3) or, more recently, using Web approaches and the related HTML5 technologies to support sophisticated data linking and integration (described in Sect. 18.4).

Because the themes and the related technologies touched on in this work are a wide set, we have to be very synthetic in the description. For a more detailed presentation we suggest a number of bibliographic references.

18.2 Platforms to Support Cross-Analysis of Multimedia Assets

Visual representations can be easily acquired and constitute an excellent resource to document the status of an artwork and to support remote and cooperative study and analysis. For each single medium we need technologies granting efficient encoding and visualization and, possibly, the capability to present those data on the Web.

18.2.1 Tools for Single Medium Visualization

Efficient visualization means taking into account a number of technical issues (data simplification, multiresolution encoding, compression, progressive transmission, GPU-enabled rendering). All those themes have been subjects of intense research and nowadays we have an arsenal of efficient technical solutions that can be adopted for the implementation of efficient visualization tools. Therefore, for each single medium we have plenty of solutions supporting efficient visualization.

Most image types are visualized natively by most Web browsers. Specific image types, such as reflection transformation images (RTI) (Malzbender et al. 2001) or high dynamic range (HDR) images (Debevec and Malik 2008) still require specific browsers or tools.

3D models are rendered by many systems, either using an encoding based on triangulated surfaces or adopting a representation and rendering approach based on point clouds. MeshLab is an example of a mesh processing system that is also often used as a visualization platform (Cignoni et al. 2008). Listing or presenting even just a subset of the existing 3D viewers is far beyond the scope of this chapter. We mention a viewer designed for a specific narrow class of artworks (Pal et al. 2013). It is an example of a specialized tool providing enhanced visualization features for degraded *parchment manuscripts*. These manuscripts may present severe distortion of the surface and wrinkles that increase the complexity of reading and deciphering

the textual content, both on the original and on digitized replicas of the manuscript. This interactive viewer has been designed to enable on-the-fly counterdeformation on the specific (small) area analyzed by the scholar; it also applies a rotation to the same area to make the line of the writing as horizontal as possible. By means of those real-time local modifications of the geometry, the tool allows enhancing the visual analysis of the digital representation nicely.

Until very recently, 3D browsers were delivered as applications to be installed on our desktops or portable PCs. With the advent of HTML5 and WebGL, more and more media browsers are built as components of standard webpages, thus allowing us to inspect even very complex visual data using only standard Web browsers. An example of a recent work that follows this trend is the Visual Media Server recently implemented in the EC INFRA "ARIADNE" project (Scopigno et al. 2015), where browsers for very high-resolution images, RTI images, and 3D models have been implemented on top of WebGL (Marrin 2011). An added value of the work done in ARIADNE is the automatic service for: (a) converting any visual media files in a Web-compliant, multiresolution format; and (b) supporting automatic publication on the Web. A simple front end allows users (the ARIADNE focus is oriented to the archaeological community) to upload the media file on a Web server; this media file is automatically converted into an efficient Web-compliant format (e.g., in the case of a 3D model, it is converted into a multiresolution model, also incorporating data compression features) and the user receives the URL from where the model is now freely accessible (see Fig. 18.1).

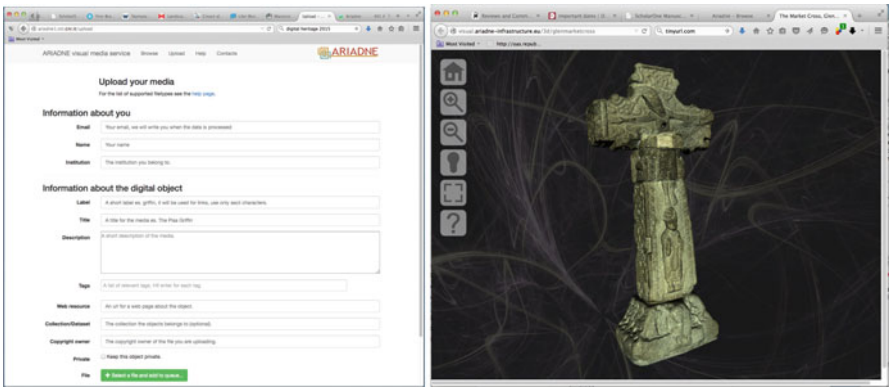

Fig. 18.1 The *ARIADNE* service for easy and automatic publication of visual models on the Web: The snapshot on the *left* presents the Web form for uploading the visual file; on the *right*, a snapshot of one of the 3D models contributed by users (See at: http://visual.ariadne-infrastructure.eu/), rendered inside a standard webpage

18.2.2 Tools for Cross-Media Visualization

An approach where each different medium has its own visualization tool severely impedes the analysis and study of a CH asset, because by definition no medium is better than the others and each one adds knowledge. Therefore, DH applications impel us to design technologies able to support the contemporary analysis of different media.

This requirement was at the basis of the design of the Cenobium system in 2006 (Corsini et al. 2010). This system was designed to support art scholars and students in the study of medieval sculptures (in this specific case, decorated capitals) by means of multiple representation media. From the very beginning, the Cenobium system was designed to provide what we called a *light table*, that is, a facility to support the side-by-side visual analysis of different media. The Cenobium system hosts many high-resolution images and 3D models for each capital; the user can select any image or 3D model (belonging to the same or to different capitals) and can selectively activate his or her visualization in a common interactive space (see Fig. 18.2).

A more comprehensive approach has been endorsed by Yale University while designing the Hyper3D system (Kim et al. 2014). Their starting point was that many different media types and formats are needed in CH and that most of them are

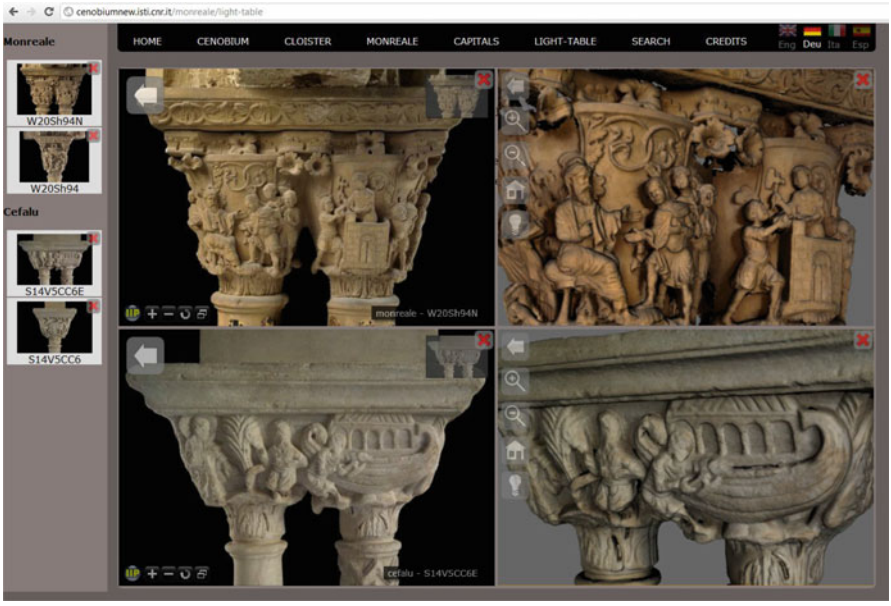

Fig. 18.2 The *light table* component of the Cenobum system, supporting side-by-side analysis of a selected group of 2D/3D representations

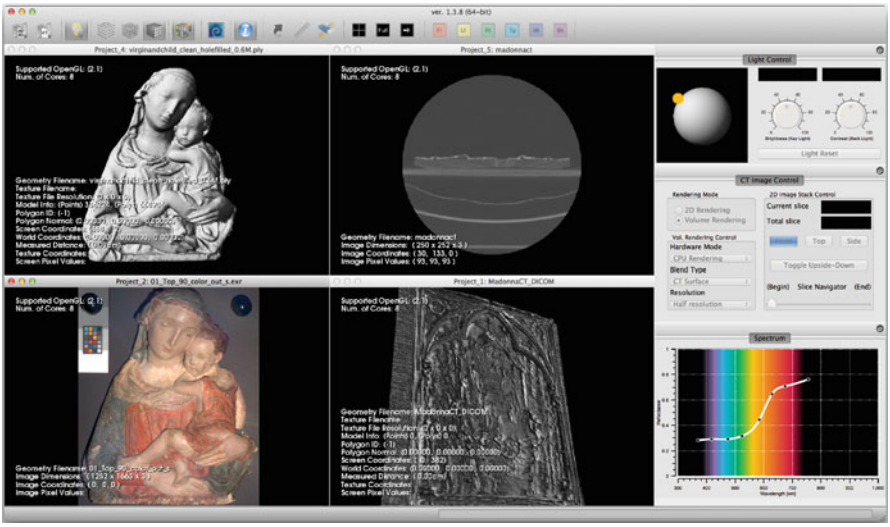

Fig. 18.3 A screenshot from the Hyper3D open source system developed by Yale University

available only inside specific tools, in most cases designed for non-CH communities (some clear examples are the medical or industrial tomographic devices/tools). The cost and complexity of use of many of those solutions originate a sustainability issue and this reduces the impact over the CH domain. Complexity of use also depends on the different terminologies and GUIs supported by the different tools (just a single example is the manipulation modality, implemented frequently in graphics systems with different interpretations of the trackball concept). Therefore, the Yale group has designed the Hyper3D system as an open source software tool, having a single intuitive interface consistent with conservators' needs. The system handles various types of 2D and 3D data and preserves user-generated metadata and annotations (see Fig. 18.3). According to our experience, this is the first complex open source tool focusing on data visualization of CH digital assets, rather than on geometry processing.

It provides tools for the integrated visualization of various types of visual data (2D images, hyperspectral images, volume data encoded using the DICOM standard, and triangulated 3D models, with or without textures). Among the peculiar features implemented are color conversion and visualization techniques to deal with hyperspectral and multispectral images. Visualization features are paired by coherent features for saving and retrieving user-generated metadata, for bookmarking specific visualization setups and procedures, and finally for creating annotations alongside the displayed images (implemented as hotspots laying over the image/3D model, with which text can be associated).

The system has been designed as a publicly accessible open source framework to enable extensive future modification; it is available under the GNU General Public License v3.0 via SourceForge at http://sourceforge.net/projects/hyper3d/. It is based on several other open source libraries: the Visualization Toolkit (VTK)

(Schroeder et al. 2006), the Insight Segmentation and Registration Toolkit (ITK) supporting volume rendering (Taka and Srinivasan 2011), QT for the design of the user interface (Dalheimer 2002), the Armadillo linear algebra API (Sanderson et al. 2010), and the OpenEXR API for HDR images (Digital 2009).

18.3 The GIS Approach to CH Documentation

Geographic information systems (GISs) have often been used to support documentation of CH assets, covering a wide spectrum ranging from the medium scale (a statue) to the large scale (an entire city or an archaeological site). GISs have been a major resource in archaeology for documenting the digging process and the findings (because in that case having a precise geolocation is of paramount importance). Many papers have been proposed in this specific subdomain. In as much as reviewing the use of GIS technology in archaeology is beyond the scope of this chapter, we cite here only a few papers that contain good lists of references (Chapman 2006; De Reu et al. 2013; Dell'Unto et al. 2015).

GIS solutions have also been proposed to encode knowledge and data concerning the state of conservation or to support restoration of artworks. In this case, the GIS approach is used to characterize the surface of the artwork, linking available knowledge (e.g., all the results of scientific investigation analysis) to specific regions defined over the artwork surface. An example of system following this approach is SICAR (Fig. 18.4).

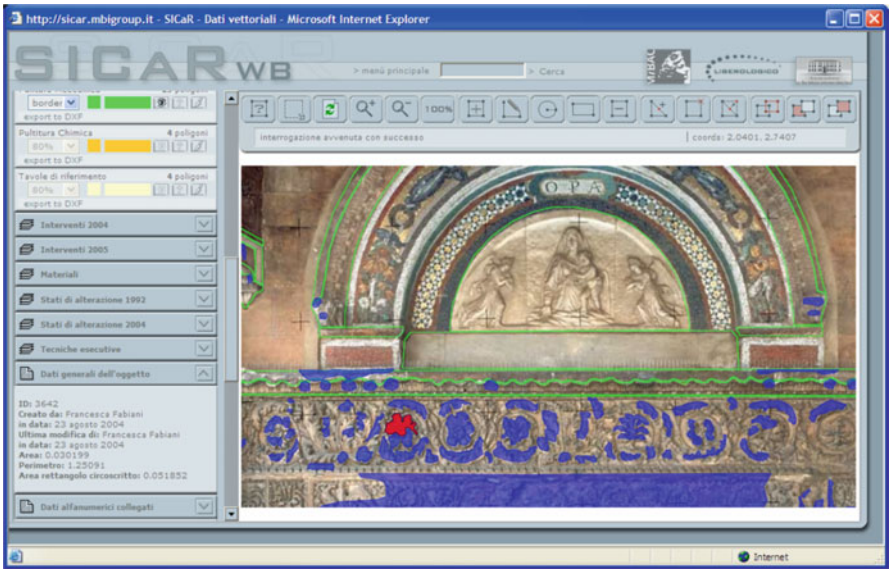

Fig. 18.4 The image presents the GUI of SICAR, showing the results of a surface characterization of the architrave of the S. Ranieri portal (Dome of Pisa, Italy)

18.3.1 SICAR Web: A GIS Approach to Support Documentation of Restoration Data

SICAR Web is a Web-based system for the management of information gathered during restoration analyses and intervention (either alphanumeric or raster data) that is mapped and georeferenced onto a 2D representation of the artwork (Baracchini et al. 2007, 2003; Fabiani et al. 2012; LiberoLogico 2015). It permits linkage to the digital representation of all data gathered during the analysis and intervention phases of the restoration process (e.g., raster images, documents in TXT format, hypertext (HTML), or semi-structured text (XML)). SICAR is based on a (raster) 2D representation of the artwork, on top of which the restorer can build any number of layers, each one containing regions drafted over the 2D raster representation and linked to specific data stored in the database. As with any other GIS platform, SICAR offers features to cross-compare different layers (overlay function) and to support the analysis of the data.

SICAR manages three classes of data, respectively related to: the artwork story (that includes two subcategories: historical documentation and constitutive materials and techniques), the artwork state of conservation (chemical, biological, or physical diagnosis of its decay, the detection of previous restorations, their nature, their location etc.), and, finally, data on the restoration in progress (materials used, techniques, and methods).

SICAR is configurable and accessible via the Web both for consultation and data entry. The application is designed to allow gathering and entering the documentation onsite and provides transversal access to all the data categories managed (geometric information, images, text documents, alphanumeric cards, etc.) ensuring crossed search between them and extreme ease of reference.

SICAR was adopted by the Italian Ministry of Cultural Heritage (MIBACT) in 2012 and is intended to be the infrastructure for encoding data on CH restoration produced by the restoration and conservation institutions belonging to the Italian Ministry of Cultural Heritage.

18.3.2 Pro and Cons of the GIS Approach

GISs have proved to be an extremely valuable resource in many DH applications. The use of this technology for data archival and management is extremely powerful because it allows us to support sophisticated data analysis features (cross-correlation of different types of data and production of new data layers as a computation/intersection of previous ones).

On the other hand, because by definition the GIS approach requires a precise characterization of the surface (i.e., precise definition of each specific parcel of the surface to which we want to assign a specific data value or interpretation), adopting a GIS approach requires the investment of considerable time in data input and some skills or extensive training of the operator.

The supporting space managed by GIS platforms was perceived as a limitation for some CH applications. GIS technology was originally developed to represent 2D 1/2 models (i.e., terrain models); it has been used both to represent 2D domains (e.g., painted surfaces, or facades of buildings projected on a plane, as in the case of the SICAR system) and terrain models. More recently, GIS systems have been extended by also supporting the direct representation of 3D domains (Dell'Unto et al. 2015). Again, this extends the capability of the system and its flexibility of use: we are no longer forced to work on projection planes, but can draw our regions directly over the 3D surface of the artwork. Unfortunately, moving to a full 3D space also requires increased expertise of the operator and a slightly more complex selection process of each single region over the represented 3D surface(s). The complexity of use and the time required to produce the documentation are the most critical limiting factors of the GIS-based approach.

18.4 Web-Based Platforms to Support Data Integration and Easy Accessibility

Several applications do not require the most important characteristic of the GIS approach (the layer concept and the possibility to cross-compare layers, using this feature as an analysis instrument) and thus impose much lighter requirements in the design of a data management approach. In many cases, the main feature required is just the possibility to create links interconnecting different data tokens, even in a georeferenced manner (i.e., linking a data token to a specific location/region of the surface of the artwork). In all those cases, we are not obliged to select a GIS platform, in as much as most of those features can also be implemented in a standard Web context. We can make proficient use of the hyperlink concept to implement systems that fulfill those categories of users.

We have already briefly mentioned in Sect. 18.2 that the progress of the Web platform (HTML5, WebGL) makes it possible to manage any visual medium in an efficient way, making it an integrated component of standard webpages and enabling visualized over standard Web browsers.

We have recently designed and implemented a software framework, called 3DHOP (3D Heritage Online Presenter) (Potenziani et al. 2015). 3DHOP has been designed to simplify the creation of interactive visualization webpages including high-resolution 3D models and other media and offering intuitive user interaction

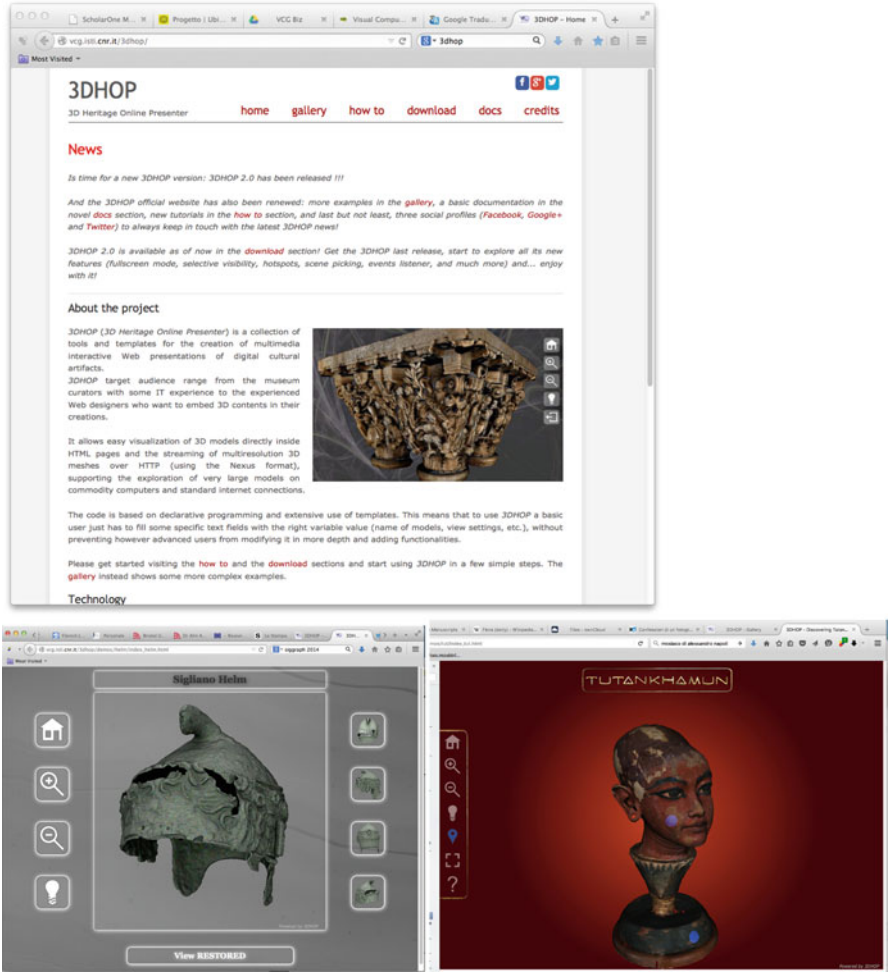

Fig. 18.5 3DHOP: The main webpage and snapshots from two 3DHOP instances

and manipulation features; moreover, these resources can be deeply and easily connected with the rest of the webpage elements (see Fig. 18.5). The most interesting characteristics of the 3DHOP framework are:

- The ability to work with extremely complex 3D meshes or point clouds (tens of millions of triangles/vertices), using a streaming-friendly multiresolution scheme.

- The easiness of use for developers, especially those with a background in Web programming, thanks to the use of declarative-style scene creation and exposed JavaScript functions used to control the interaction.
- The availability of a number of basic building blocks for creating interactive visualizations, each one configurable, but at the same time providing default behaviors and comprehensive documentation.

3DHOP was released as open source (GPL license) in April 2014. The downloadable package is available at the website: http://3dhop.net and it includes documentation, a series of tutorials (how-tos), and a gallery of examples.

3DHOP has been designed with the aim of being easy to use, especially for people having a background in Web development, thus without requiring solid knowledge of CG programming. 3DHOP is not a "silver bullet," able to support any possible application or visual communication project, but a framework designed to deal with specific needs. It is an ideal tool to visualize high-resolution single objects, especially with dense models coming from 3D scanning or collections composed of a few models. Conversely, 3DHOP is not suited to manage complex scenes made of low-poly objects (this is a common case when working with CAD, or procedural or hand-modeled geometries).

3DHOP makes possible a fast deployment process when dealing with simple interaction mechanisms, making it a good choice for quickly creating interactive visualization for a collection of models. Additionally, 3DHOP integrates extremely well with the rest of the webpage, thanks to its exposed JavaScript functions. The ideal situation is having the logic of the visualization scheme in the page scripts, and using 3DHOP for the 3D visualization. The 3DHOP tool has been designed with different levels of entry, to be as straightforward as possible for the simpler cases but, at the same time, able to provide enough configurable features to support the huge variability of cultural heritage artworks and applications.

The 3DHOP platform has been used recently to design a new instance in the overall 3DHOP family, aimed at presenting a single artwork (in this case, the Roman Annona sarcophagus, from the last third of third century AD, Museo Nazionale Romano and Palazzo Massimo, Rome, Italy) and a corpus of related data (Siotto et al. 2015). This artwork has been studied, subject to several different scientific investigation protocols, analyzed, and finally some hypotheses on its original polychrome decoration have been proposed. All this work and the related data have been stored in this specific 3DHOP installation. Therefore, we provide Web access to the high-res 3D model, with visual indication of the regions where scientific analyses have been done; users can open the related images or textual description of their results. Finally, two alternative preliminary reconstruction hypotheses of the original polychrome decoration have been encoded on the 3D model and are shown in Fig. 18.6.

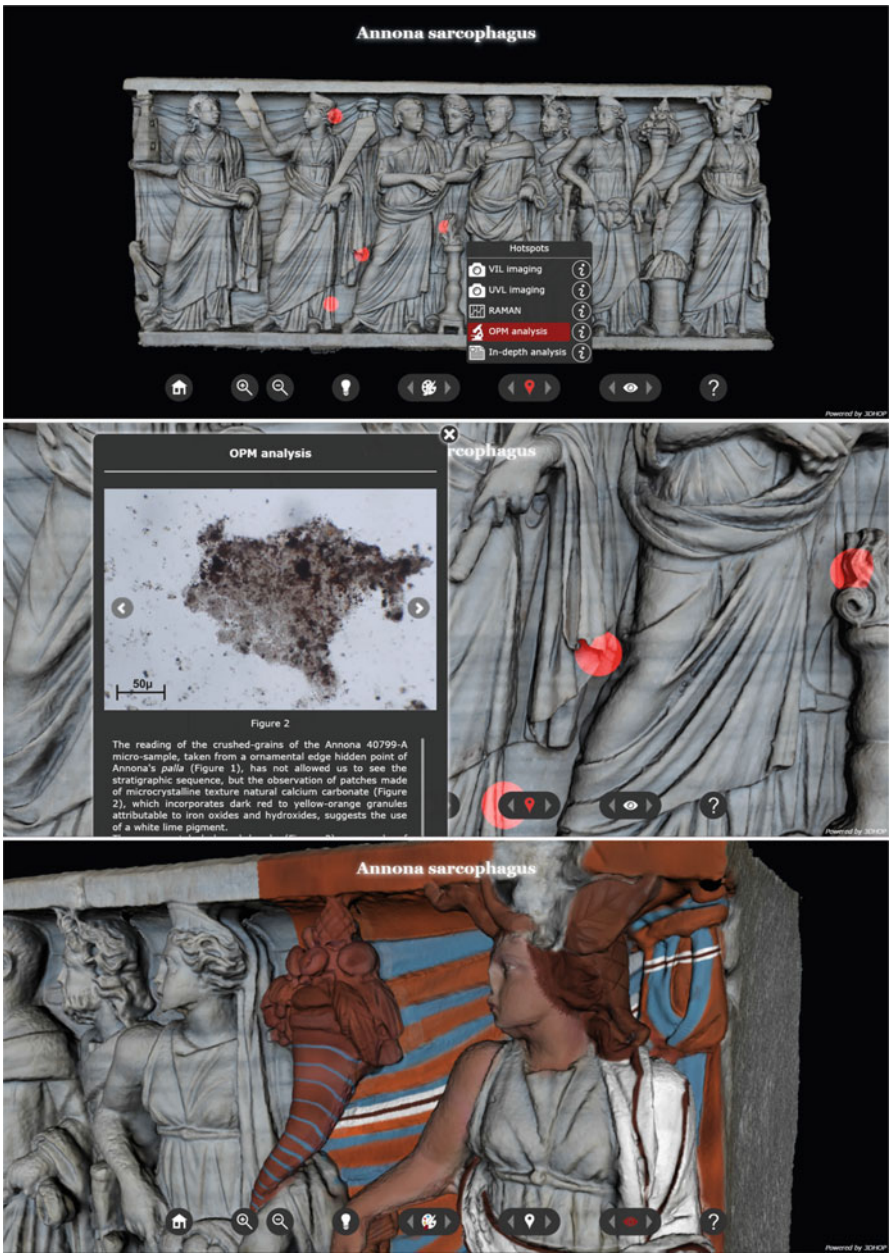

Fig. 18.6 Three snapshots from a 3DHOP instance designed to store and present all the data gathered in the study of a Roman sarcophagus (including results of scientific investigations)

This is an example of the potential of a Web-based platform to present artworks and the documentation corpus that describes our knowledge of the same asset. 3DHOP is just an example of what can be done with Web-based technology. The work on the Annona sarcophagus has only been started. The documentation material has been mapped over the 3D models and the corresponding 3DHOP instance can be accessed at http://vcg.isti.cnr.it//roman-sarcophagi/annona-sarcophagus/index.html (which also includes a grabbed video: http://vcg.isti.cnr.it//roman-sarcophagi/annona-sarcophagus/img/video-ISTI-CNR.mp4).

The second phase of this work is under construction: creating the 3DHOP documentation to allow other colleagues to understand the structure of the sarcophagus setup and to support them in the design of similar installations on the basis of the provided sarcophagus sample.

Similar systems for 3D visualization and integration of other types of data exist: one of the most interesting examples is represented by the Smithsonian Museum X3D visualizer http://3d.si.edu/, where several examples of acquired and modeled 3D objects can be visualized. X3D enabled the attachment of additional information to the models, to follow a "tour" of the objects by moving among the various hotspots on it, and also to have tours covering several objects that were grouped following a common concept. Additional tools for advanced visualization (e.g., measurement and cross-section) are already available. Although really efficient and visually pleasing, the viewer is currently owned by the museum, so its use cannot be extended to other use cases for now.

Although 3DHOP has been designed by focusing first on how to support the presentation of sophisticated visual media over the Web, another interesting Web platform has been designed following the inverse path, that is, thinking first about how to support structuring and interlinking CH documentation.

Modus Operandi is a documentation system developed by an Italian company, Culturanuova s.r.l., in collaboration with a primary restoration institution (Opificio delle Pietre Dure-OPD, Florence, Italy) (Chimenti 2010; Culturanuova 2015). Data are organized on the basis of standardized procedures and guidelines defined by major restoration and documentation institutions, such as OPD and the Istituto Centrale per il Catalogo e la Documentazione (ICCD), Rome, Italy. The system allows us easily to produce a structured report of all the data gathered in a restoration project; it also supports publishing and consultation of the data on the Web. Some examples of its use are available on the Web at http://www.modusweb.net/ (see also Fig. 18.7).

According to some feedback received from OPD colleagues, the system is easy to use and extremely effective as far as concerns the provided functionalities.

A peculiar characteristic of Modus Operandi is the automatic production of a formatted report (in MS Word format) that is returned to the user after completion of a documentation project and that can be used in all those cases where a formatted and printable document is needed.

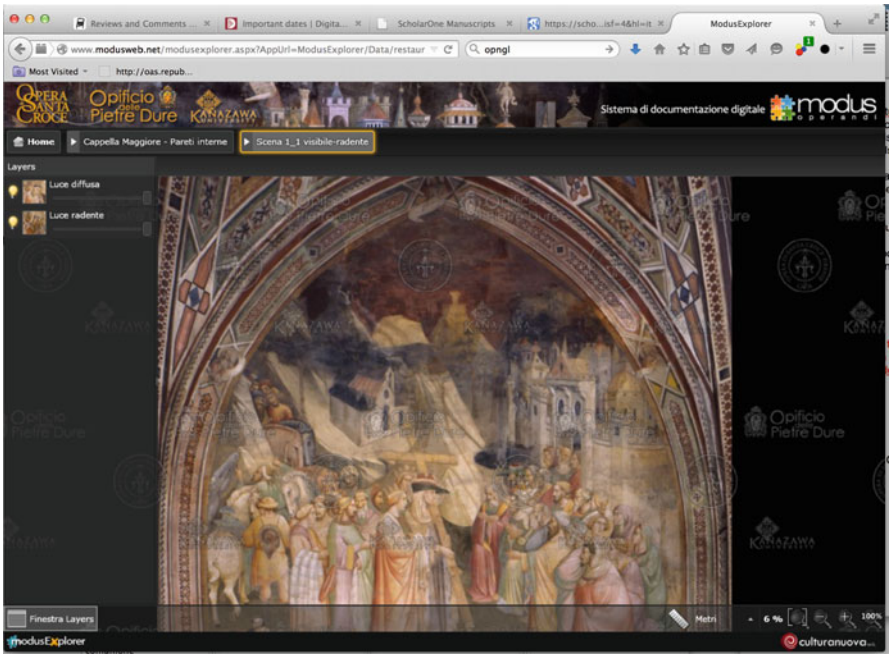

Fig. 18.7 A snapshot of one of the documentation systems implemented with the Modus Operandi platform (http://www.modusweb.net/)

The Scuola Normale Superiore (Pisa, Italy) has also developed an information system oriented to documentation of CH, called SIAS (System to Integrate Art and Science). It has been designed as a collaborative Web 2.0 system, supporting archival and access to the data produced in the study or restoration of an artwork (Barone et al. 2012, 2015).

18.5 Conclusion: Towards an Infrastructure for Multimedia CH Data?

The DH domain is extremely rich and complex, both in terms of types of visual media used in the study/analysis process and in terms of different types of knowledge/data that have to be linked to the virtual clone. The usual paper-based linear approach to present knowledge on a CH artwork shows all its limitations. We need systems able to break the linear approach, supporting sophisticated capabilities for integrating and creating correlations between different media. We have seen that at least two different approaches are possible to try to advance on this path:

1. Systems oriented to the *analysis* and *investigation* phase, that allow us to work with many different media types in a single context and enabling the use of a unified and common interface (e.g., Kim et al. 2014). Those media should support encoding and preservation of the reasoning path (annotation, bookmarks), to support scholars in preserving the *provenance* data that describe the analysis and comprehension process.
2. Systems oriented to *documentation* and *dissemination*, which by definition should work on the Web, to provide easy and ubiquitous access to the data (e.g., Culturanuova 2015). Again, the capability to browse over different media with a common interface has to be provided. But here an important focus is also to provide easy tools to create the links interconnecting the different information tokens with one or multiple digital representations of the artwork.

The Web is nowadays perceived as the main channel of publication and dissemination of knowledge. It could also become the container where programs are running, thus also allowing the design of systems of type 1 defined above as applications directly accessible from a webpage, thus removing the need of installing and updating applications on users' computers.

The Getty Conservation Institute has recently organized an experts' meeting to discuss the themes related to the integration of imaging and analytical technologies for conservation practice (held on September 10–12, 2013). The report produced as a followup of this meeting (Schmidt Patterson and Trentelman 2014) presents a comprehensive list of requirements and suggestions that we briefly enumerate here:

- Development of standards for more successful integration of data coming from different institutions and experiences (this includes work on metadata, ontologies and vocabularies, and policies for data sharing).
- Implementation of pilot studies/projects, which should have a short duration in time and should be instrumental in assessing the available data organization, archival, and presentation policies. Results from these pilots should be fed back to the design and standardization activities. The report suggests a set of criteria for the selection of those pilot projects.
- Consolidate a community of users and developers that is instrumental in gathering a solid view of user requirements and in establishing common and widely accepted good practices. This requirement is definitely concordant with the current policies of the EC, which has issued several calls aimed at consolidating DH communities and providing them with common e-infrastructures.
- Finally, an increased effort of funding agencies to issue calls on those themes, to support interdisciplinary projects aimed at designing and implementing a common infrastructure and tools.

The Getty report concludes by addressing the need for a new paradigm for data collection, archival, access, sharing, analysis, and interpretation; it stresses the need for a more cooperative approach to CH study. Visual media can become

the instrument to support cooperation and encoding of partial results; this vision requires the design of a specific platform or infrastructure.

Let us add a last comment concerning sustainability issues. Due to the still-limited economic impact of DH/CH applications, development is still mostly on the shoulders of academic/research partners, with only a few companies struggling with a market characterized by fast technical evolution and limited financial resources. Open source could be an important asset to stimulate development and further exploitation. Public funds invested in infrastructure projects shall also play a highly beneficial role, aiming to join forces between academia and industry.

Acknowledgements The research leading to these results has received funding from the European Union Seventh Framework Programme (FP7/2007-2013) under grant agreement n. 313193 (EC INFRA "ARIADNE" project) and H2020 Programme under grant agreement no. 654119 (EC "PARTHENOS" project).

References

Baracchini C, Fabiani F, Ponticelli P, Vecchi A (2007) Verso un sistema unico di riferimento per la documentazione di restauro: storia e sviluppi di sicar w/b (in italian). In: Proc. eARCOM 2007 – Sistemi informativi per l'architettura, Alinea Editrice, p 6

Baracchini C, Lanari P, Scopigno R, Tecchia F, Vecchi A (2003) SICAR: geographic information system for the documentation of restoration analyses and intervention. In: Proceedings of SPIE 5146, Optical metrology for arts and multimedia. SPIE, Bellingham, p 12. doi: 10.1117/12.501505

Barone V, Licari D, Nardini FM (2012, in press) RICH: research and innovation for cultural heritage. Conserv Sci Cult Herit 12:109–133

Barone V, Licari D, Nardini FM (2015) SIAS: a system to integrate art and science. More info on: http://sias.sns.it

Callieri M, Cignoni P, Ganovelli F, Impoco G, Montani C, Pingi P, Ponchio F, Scopigno R (2004) Visualization and 3D data processing in the David restoration. IEEE Comput Graph Appl 24(2):16–21

Chapman H (2006) Landscape archaeology and GIS. Tempus Pub Limited, Stroud

Chimenti M (2010) Modus Operandi – Documentazione informatica delle attività di conservazione e restauro (in Italian). Archeomatica 2:26–27

Cignoni P, Callieri M, Corsini M, Dellepiane M, Ganovelli F, Ranzuglia G (2008) MeshLab: an open-source mesh processing tool. In: Sixth eurographics Italian chapter conference, Salerno. pp 129–136. Eurographics

Corsini M, Dellepiane M, Dercks U, Ponchio F, Keultjes D, Marinello A, Sigismondi R, Scopigno R, Wolf G (2010) CENOBIUM – putting together the romanesque cloister capitals of the mediterranean region. Br Archaeol Rep Int Ser 2118:189–194

Culturanuova (2015) Culturanuova s.r.l. – modus operandi, http://www.culturanuova.com/. More info on: http://www.modusweb.net/

Dalheimer M (2002) Programming with QT: writing portable GUI applications on Unix and Win32. " O'Reilly Media, Inc."

De Reu J, Plets G, Verhoeven G, De Smedt P, Bats M, Cherretté B, De Maeyer W, Deconynck J, Herremans D, Laloo P, et al (2013) Towards a three-dimensional cost-effective registration of the archaeological heritage. J Archaeol Sci 40(2):1108–1121

Debevec PE, Malik J (2008) Recovering high dynamic range radiance maps from photographs. In: ACM SIGGRAPH 2008 classes. ACM, New York, p 31

Dell'Unto N, Landeschi G, Leander Touati AM, Dellepiane M, Callieri M, Ferdani D (2015) Experiencing ancient buildings from a 3D GIS perspective: a case drawn from the Swedish Pompeii Project. J Archaeol Method Theory 1–22. doi: 10.1007/s10816-014-9226-7.

Digital L (2009) Lucas digital ltd. openexr. More info on: http://www.openexr.com/

Fabiani F, Vecchi A, Siano S (2012) SIConArt sistema informativo per la conservazione (in Italian). In: Siano S (ed) Archeometria e restauro. L'innovazione tecnologica. Nardini Editore, pp 181–198

Kim MH, Rushmeier H, Ffrench J, Passeri I, Tidmarsh D (2014) Hyper3D: 3D graphics software for examining cultural artifacts. J Comput Cult Herit 7(3):14:1–14:19. doi: 10.1145/2567652. http://doi.acm.org/10.1145/2567652

LiberoLogico (2015) SICAR: a web GIS for restoration projects. More info on: http://www.liberologico.com/en/default/567/SICaR.html

Malzbender T, Gelb D, Wolters H (2001) Polynomial texture maps. In: Proceedings of the 28th ACM SIGGRAPH Conference, pp 519–528. ACM

Marrin C (2011) Webgl specification. Khronos WebGL Working Group

Pal K, Terras M, Weyrich T (2013) Interactive exploration and flattening of deformed historical documents. Comput Graph Forum 32(2):327–334. Proceedings of Eurographics

Pintus R, Pal K, Yang Y, Weyrich T, Gobbetti E, Rushmeier H (2015) A survey of geometric analysis in cultural heritage. Comput Graph Forum 35(1):4–31. doi: 10.1111/cgf.12668

Potenziani M, Callieri M, Dellepiane M, Ponchio F, Scopigno R (2015) 3DHOP: 3D Heritage online presenter. Comput Graph 52:129–141

Sanderson C (2010) Armadillo: an open source C++ linear algebra library for fast prototyping and computationally intensive experiments. NICTA Technical report

Schmidt Patterson C, Trentelman K (2014) Integrating imaging and analytical technologies for conservation practice – report of an experts meeting held 10–12 Sept 2013. The Getty Conservation Institute, http://www.getty.edu/conservation/our_projects/integrating_imaging.html

Schroeder W, Martin K, Lorensen B (2006) The visualization toolkit. Kitware, Clifton Park

Scopigno R, Callieri M, Cignoni P, Corsini M, Dellepiane M, Ponchio F, Ranzuglia G (2011) 3D models for cultural heritage: beyond plain visualization. Computer 44(7):48–55

Scopigno R, Ponchio F, Dellepiane M (2015) Visual Media Service, EC INFRA "ARIADNE" project (http://www.ariadne-infrastructure.eu/). More info on: http://visual.ariadne-infrastructure.eu/

Siotto E, Palma G, Potenziani M, Scopigno R (2015) Digital study and documentation of the colour and gilding on ancient marble artworks. In: Proceedings of Digital Heritage 2015, Granada. IEEE Press, p 8

Taka SJ, Srinivasan S (2011) NIRViz: 3D visualization software for multimodality optical imaging using Visualization Toolkit (VTK) and Insight Segmentation Toolkit (ITK). J Digit Imaging 24(6):1103–1111

Chapter 19
The Reconstruction of Archaeological Contexts: A Dialectical Relationship Between Historical-Aesthetic Values and Principles of Architecture

Francesco Gabellone

More we improve our tools, the further we can arrive to see, but not in the future, rather in the past"

(The Age of Adaline, Lee Toland Krieger, Eagle Pictures 2015)

Abstract The role of the virtual archaeology specialist is closely connected to the dialectic relationship between classical studies and the possibilities offered by these tools for three-dimensional (3D) modeling and simulation. Only through constant checks in 3D of the technical and construction, dimensional, and spatial aspects is it possible to validate the hypotheses that are formed from the philological study of the sources, archaeological data, and contemporary parallels. Through the presentation of some case studies, this chapter presents reflections on possible methodological approaches related to the problem of the reconstruction of archaeological context, from problems related to the transparency of information to the typological reconstruction or to reconstruction in the absence of sufficient data. Virtual archaeology is a promising sector in which to believe and invest, not only for those outcomes economically foreseen in terms of the capitalization of cultural assets, but also for the many expectations related to employment and the potential to use new, specialized figures. The archaeologist's and historian's contribution is decisive for being able to guarantee a certain scientific rigor for a virtual archaeology product, but also of contributions by sciences quite remote from the humanities, such as chemistry, physics, geology, and medicine, all disciplines that can find fertile connective tissue in this growing sector.

Keywords Virtual archaeology • 3D modeling • Virtual reconstruction • Building principles

F. Gabellone (✉)
CNR – IBAM (Istituto per i Beni Archeologici e Monumentali del Consiglio Nazionale delle Ricerche), via prov. le Monteroni, Lecce, 73100, Italy
e-mail: f.gabellone@ibam.cnr.it; www.itlab.ibam.cnr.it

N. Masini, F. Soldovieri (eds.), *Sensing the Past*, Geotechnologies and the Environment 16, DOI 10.1007/978-3-319-50518-3_19

19.1 Introduction

Every archaeological context constitutes a separate case, each presenting different questions and peculiarities that make the use of three-dimensional (3D) tools indispensable for detailed analysis of the architectural organism. In this process, the contribution of 3D modeling software is not limited to the pure generation and manipulation of the polygons in the space but is outstanding in its capacity to facilitate the interpretative processes. In the limited time available to many projects, it would certainly be impossible to examine the numerous considerations regarding equilibrium of the proportions, the juxtaposition of the volumes, or the application of the laws of statics, nor would it be easy to examine such questions on a vast scale using traditional drawing methods. It is therefore fundamental to recognize the substantial contribution of 3D modeling software to the study of ancient monuments. The greater three-dimensional awareness of an architectural organism provided by the modeling environment makes it possible to go into greater detail and have more control over the different reconstruction phases, with a notable increase in precision, productivity, and capability to respond to specific problems imposed by the observation and study of monuments within a space. It would be mistaken and restrictive to consider 3D modeling as merely one of the new representational tools that simply replace the drafting pen or pencil. The role of the virtual archaeology specialist is closely connected to the dialectic relationship between classical studies and the possibilities offered by these tools for 3D modeling and simulation. Only through constant checks in 3D of the technical and construction, dimensional, and spatial aspects is it possible to validate the hypotheses that are formed from the philological study of the sources, archaeological data, and contemporary parallels. Many original results achieved by mixed teams of classical scholars and specialists in virtual archaeology have been possible thanks to the verification and study of the monuments in the 3D environment, because only a minimal part of the proposed reconstruction is revealed to be plausible and compatible with the functional logic and construction and stylistic principles used by a particular civilization, in a precise historical period.

Then, we attempted to outline some methodological approaches to the reconstruction of ancient buildings, always trying to respect the scientific transparency principles, which may give recognition to the whole process of study that leads to the reconstruction.

19.2 Problems of Scientific Transparency in Virtual Archaeology Projects

Virtual archaeology aims to deliver, to the public, interpretative and reconstructive results on monuments and artworks whose figurativeness has been damaged or impaired. In this study process, all the information emerging from historical and

Fig. 19.1 Virtual reconstruction of the theater of Syracuse: evidence the maenads today are conserved and placed in their original position

archaeological research converges in digital models, which, represented in the form of an image, interactive application, or filmed segment, restore the heterogeneous results of a complex interdisciplinary investigation. Joined by the new digital languages in a number of possible forms, these results on their own summarize rigorous analytical and archaeometric data, which, along with the analysis methods, survey techniques, and interpretations, must by necessity be clear, comprehensible, and above all reusable. Only analysis of the preliminary data, shown in "transparent" form, will be able to validate the outcomes of a reconstructive study and guarantee, for new generations, a revision of the results without necessarily having to start the work again from the beginning. The scientific transparency of the basic information, and the very process that leads to formulating the reconstruction hypothesis, are thus the indispensable groundwork, providing a moment of verification that measures the quality level and the scientific rigor of every application and the study of virtual archaeology (Figs. 19.1 and 19.2).

All digital restoration or reconstructive archaeology projects always have a certain level of uncertainty, because one of the objectives of this discipline is precisely that of "proposing" plausible solutions. No reconstructive study would be at all reconstructive if all the original construction and decorative details were known: it would no longer be reconstruction, but restitution. To obtain high scientific rigor in virtual archaeology projects it is essential to gather the documentary bases and to transparently present the entire working process: objectives, methodology, reasoning, origins, and characteristics of the research sources, results, and conclusions (Fig. 19.3).

The recent expansion of virtual archaeology thus necessitates setting universally recognized standards, rules, and principles that make virtual reconstruction a rigor-

Fig. 19.2 Virtual reconstruction of the theater of Syracuse: virtual restoration of the maenads

ous practice based on the authenticity and accuracy of the simulated cultural content. As early as 2005, the joint efforts of many operators in the sector, such as research institutions, museums, associations, and foundations dedicated to protecting cultural heritage, produced what is known as the "London Charter." This "Magna Carta" of virtual heritage sanctioned the need to approach virtual reconstruction with scientific methodologies. It defines internationally shared standards establishing that the digital representation of cultural assets must be based on information and practices endorsed by those who make history or archaeology their life's work. The principles laid down in London established the obligation of a cultural communication that is clear in every phase and is comprehensible and assessable to its users. It thus becomes essential to indicate, within the 3D world itself, what techniques were employed in collecting the represented data, what methods were used to interpret them, and, of course, the level of truthfulness of the historical/cultural simulation based on them. More recently, in 2012, the Seville principles have the value of a charter defining not a system of laws and regulations, but the orientations of a vast scientific community that aims to give impetus to virtual archaeology as a mature discipline, one that lives with respect for these rules and is based on scientifically sound, widely shared methods. A full transparency of methods, techniques, and documentation accompanying a virtual archaeology project is necessary for the purposes of defining quality standards, raising the scientific value of a discipline that promises to inform, astound, and fascinate with ever greater effectiveness and rigor.

In particular, principle no. 7 of the Seville Charter stresses the need to prepare a comprehensive documentary base that regards the entire research process connected with creating digital content in virtual archaeology projects. The analysis methods,

Fig. 19.3 (**a**, **b**) Virtual reconstruction of the theatre of Syracuse: evidence of the telamons as conserved today and their virtual reconstruction

surveying techniques, and interpretations must all be declared, comprehensible, and reusable. Only analysis of the preliminary data will be able to validate the outcomes of a reconstructive study and guarantee for new generations a revision of the results without necessarily having to start the work again from the beginning. In this study process, the contribution made by 3D modeling software is not confined to merely generating and manipulating polygons in space but is highlighted in its ability to ease the interpretative processes. Many reflections on the balance of proportions, on the juxtaposition of volumes, on the application of the laws of statics, would

Fig. 19.4 Gorgoneion of the temple of Apollo in Siracusa: reconstructive drawing and rendering

certainly not be possible with the short time frames imposed by many projects, nor would it be a simple matter to handle these problems on a vast scale using traditional drafting methods. It is therefore essential to recognize the considerable contribution that 3D modeling software makes to the study of ancient monuments. The greater three-dimensional awareness of the architectural body that the modeling environment provides makes it possible to more deeply analyze and efficiently monitor the various reconstruction phases, with considerably greater accuracy, productivity, and ability to respond to specific problems imposed by the observation and study of monuments in space (Figs. 19.4 and 19.5).

It would be wrong and reductive to confine 3D modeling to being one of the new representation instruments that simply replace the drafting table or pencil. The specialist's role in virtual archaeology is closely connected with the dialectical relationship between humanistic knowledge and the possibilities these instruments offer for 3D simulation and modelling. Only a continuous 3D verification of the aspects of technique and construction, dimension, and space makes it possible to validate certain hypotheses that come to life from the philological study of the sources, from the archaeological data, and from contemporary comparisons. Many original results achieved by heterogeneous teams of humanists and specialists in virtual archaeology were made possible thanks to this moment of verification and study of the monuments in a 3D space, because only a minimum part of the reconstruction hypotheses is plausible and compatible with the functional logic and the constructive and stylistic principles in use by a given civilization.

Fig. 19.5 Temple of Apollo in Siracusa: hypothetical reconstruction of acroterion

19.3 Typological Reconstruction

In an overall setting dominated by the general need to have to establish quality standards and methods for the transparent reading of analytical and interpretative data, there is, however, a critical aspect that merits further discussion. As mentioned earlier, virtual reconstruction relies on the combined contribution of the results emerging from various disciplines, but what attitude is to be maintained in the presence of insufficient archaeological data? We often find ourselves concerned with sites that provide only fragmentary and patchy information that, although extremely important and precious on the scientific level, is often not enough to formulate realistic reconstruction hypotheses (Fig. 19.6).

To be sure, reconstruction must always grapple on various levels with missing data, because the rarest circumstance is precisely the one in which the available data are abundant and sufficient for defining with certainty a scientifically unassailable and unambiguous proposal. That said, there is no denying the charm of attempting to "imagine" possible solutions of use for nourishing a constructive debate on what buildings looked like in the past. The reconstructive study thus proceeds without sacrifices, pooling many data that although apparently negligible are indispensable when there are so few in number. The analysis continuously weighs them on the technological and functional level, making an effort to find a plausible reason for their existence. In the chronological phases closest to our own times, ruins provide data in greater numbers, and the most recurring question mark regards what elevations and surface finishing looked like (Fig. 19.7).

Fig. 19.6 Virtual reconstruction of the theatre of Syracuse. Despite the few archaeological data, we represent the "architectural typology" of a Greek theatre, with its canonical parts

In most Ancient Roman settings, buildings are reduced to pure structure, as Auguste Perret stated: "... *it is the ruin free of any superfluous definition that makes architecture – reduced to pure structure or to pure sign – beautiful*." Although one may agree with Perret's modernist enthusiasm and his preference for honest, unornamented forms, it must be recognized that this celebration of the bare structure has, in the popular imagination, led to major misunderstandings of the original appearance of ancient monuments. We all remember the similar purist positions of Johann Joachim Winckelmann, whose veneration for Greek statuary led him to stress their whiteness as one of the highest aesthetic expressions. Doubtlessly, then, given the communicative force and the plausibility of the computer-generated images, the effort to be made in proposing reconstructive solutions is perhaps more difficult than what took place in the past. Rendering represents reality as it has never been represented before today, and this is actually its real weakness. I still remember the comments – still as current as ever – of noted archaeologist Dinu Adamestesanu with regard to certain 3D reconstructions of the port area of Herakleia, made by Liliana Giardino and myself in the late 1990s. His only comment was "*they're too pretty*" – thereby underscoring an important problem linked to the restitution possibilities of rendering, which requires assigning a material and a shape to every element depicted. Indeed, the representation of a 3D model must resolve every detail realistically, also in this term's connotation associated with the possible and plausible, that is, with something that can indeed exist. By contrast, line drawing provides only information on shape, solely outlining the objects' contours. These contours may leave room for the interpretative imagination of those observing them, and take on connotations that differ from one another. Virtual reconstruction, then, with its ability to present photorealistic ancient settings, becomes "*too pretty*," perhaps

Fig. 19.7 (**a**, **b**) Virtual reconstruction of the theatre of Syracuse: in evidence of the deus ex machina

because it ventures beyond the possible, beyond those responses that scientific rigor requires us not to formulate. In truth, what is represented is reliable based on a percentage, and therefore, although the reconstruction of the structural apparatus might be plausible, the solution adopted for the facing and finishing might not be. Every proposed reconstruction should thus be accompanied by a "correspondence model," a graph showing the reconstruction's reliability percentage: this would make the representation honest, help remove misunderstandings, and above all allow scholars to refine their research on those elements that are still unclear.

19.3.1 An Example of Typological Reconstruction: The Sanctuary of Jupiter Anxur in Terracina

This work aims to offer a three-dimensional representation of the entire sanctuary. Three-dimensional (3D) graphics allows this representation to offer the visiting public images and animations that develop a greater awareness of its articulation in space and information on the intended and religious uses of the various monuments present within it. The Sanctuary of Jupiter Anxur in Terracina has unique historical and architectural features. Located on the peak of Monte S. Angelo, it is visible from afar, making it a reference point for the entire territory. At the same time, a large section of coastline can be dominated from the sacred complex (Figs. 19.8 and 19.9).

Fig. 19.8 The Sanctuary of Jupiter Anxur: typological reconstruction

Fig. 19.9 The Sanctuary of Jupiter Anxur: the entire complex

The sanctuary tells the city's story and enshrines it as a strategic location on the Appian Way, but also as an important port on the Mediterranean routes during those years of the Late Republic. However, as discussed earlier, its strongest feature is most certainly its monumental articulation, the relationship between the various buildings. Information on surface finishing is quite scanty: only for the portico behind the greater temple are fragments of color preserved. For these reasons, in the absence of certain and complete data on the buildings' original appearance, the decision was made to adopt rather customary facing materials widely used in the Republican Age, and reconstruction solutions derived from an approach we might define as both "logical" and "analogical." It is a reflection born from rules of composition lying outside the reconstruction process and more suited for the creative act, for building ex novo, for design. For Aldo Rossi, the term "analogical" is connected with typology, and becomes a mode of learning about and constructing the urban reality. Analogical, then, means based on analogy, on comparison with contemporary buildings, but also on indications connected with the canonical proportions of the classical orders as first described by Vitruvius. This attitude made it possible to formulate plausible reconstruction hypotheses, in which the archaeological information is safeguarded as an indispensable foundation of every proposed solution (Fig. 19.10).

Albeit at the typological (and that is to say, intentionally synthetic) level, this concept gives the visitor a clear idea of the three-dimensional impact of the site, which here, as in many Italian archaeological areas, is often extremely reduced or completely erased by the scarcity of remains visible on the ground.

Fig. 19.10 The Sanctuary of Jupiter Anxur: typological reconstruction of the stoa

Fig. 19.11 The Sanctuary of Jupiter Anxur: the oracle temple

The reconstruction of the layout restores the sense of space and of the architectural complexity of the various levels of elevation on which the original path of worship unwinds; it provides information on the dimensional relationship between the parts; it reveals its connection with the place. What emerges is nothing more than a concrete "idea" of a sanctuary, which, despite the various unique monumental elements, makes reference to a more general idea of organization of space, following rules imported from the Near East. The models of reference for these cultural complexes are to be sought in the late Hellenistic sanctuaries, such as those of Asclepius on Kos on the coast of Asia Minor, and Athena at Lindos, on the island of Rhodes, or the acropolis of Pergamon; on the other hand, the construction technique used, that of concrete with facing in opus incertum, with great plastic and tectonic possibility, was of the Italic tradition. But the architectural principles presiding over these complexes originated from the theories and works that spread from Hermogenes of Priene (a Greek/Asian architect who lived between the second half of the third and the first half of the second century BC) and were imported to Rome by Hermodorus of Salamis starting from 146 BC. The evident differences that exist between Latium's late Republican sanctuaries strengthen the idea of belonging to a typology rather than to a model (Fig. 19.11).

The term "type," in fact, represents not so much the image of a thing to be copied or imitated as the very idea of that thing. It is the very coding of a baggage of stylistic, formal, functional, and distributive characteristics. The reconstructive study of the larger temple began from the customary analysis of layouts, from descriptions, and from drawings of the finds. Of this temple, we have the drawings for the base and the capital of a Corinthian column. From these initial elements, an elevation hypothesis may be outlined, by obtaining the proportional relationships from the canonical measurements and comparing the results with some temples from the same period, in particular with the Temple of Antoninus and Faustina and

the Temple of Vic (Osona, Catalonia). A reading of Book IV of Vitruvius's *De Architectura* tells us that by measuring the column, one can obtain the size of the trabeation and of the individual architectural elements that make up the order. All this leads to a typologically consistent reconstruction, that is, referring to a Sullan Age temple of the Corinthian order, about which we know the layout, podium height, and column sizes. The same "logical and analogical" approach led to the reconstruction of the other buildings, of which drawings of trabeation fragments, column fragments, and above all the construction technique were published. We may therefore place this work in the context of "typological reconstruction," which is to say that although founded upon the scientific data emerging from the excavation and from the survey, it is developed in consideration of a technological and functional consistency related to the time of building and the rules of "sound construction," so to speak, which are valid at all times and in every part of the world. The most important aspect of this approach is to proceed with reliable elements and interpretations that, by chain reaction, might yield consequent effects and therefore deductions linked to a "logical and analogical" process. It is logical because it refers in fact to universal rules and principles of construction; it is analogical because it proceeds through comparison and analogy. It would have been highly interesting to propose an image of the sanctuary with a color hypothesis: archaeological research has been able to document its widespread and constant use in other settings. But this would certainly have led to a fanciful representation, in line with what is represented on some tables at École Nationale Supérieure des Beaux-Arts. These provide drawn depictions that, although taking the excavation documentation into account, often deviate from the scientific information to offer a neoclassical-style cross section of Roman architecture, with fanciful indications on the colors and a certain monumental emphasis of a vaguely eclectic taste. We thus find drawings of architectural fragments done by the researchers themselves, organized scrupulously on dimensioned, reliable, and realistic tables; but alongside them are reconstructions aimed more at communicating wonder than rigor.

19.3.2 Toward a Proposed Reconstruction of the Oikos in Piazza Duomo, Syracuse

Compared with the Sanctuary of Jupiter Anxur in Terracina just described, this case study presents even greater difficulties of interpretation, connected with an even greater and clearer scarcity of archaeological data. This structure may perhaps be deemed an extreme case, for which the scrupulous archaeologist should refrain from proposing any reconstruction hypothesis. Indeed, up to this point, we have stressed that in virtual reconstruction, the priority objective is to demonstrate the application of a rigorous method, which is to say highlighting and making transparent the path that runs from pure archaeological data to the specific contribution of 3D technologies in support of the interpretative processes. The second priority objective

is to demonstrate that there are conditions, which is to say the minimum data, for being able to advance hypotheses. Therefore, the archaeologist involved in the process of digitally visualizing an ancient setting must by necessity grapple with two opposing impulses. On the one hand, the prudential and hyperphilological approach typical of his or her training recommends limiting oneself solely to certain, conclusive data, preferably using a neutral language for the restitution of the parts for which no archaeological evidence survives; on the other hand, especially when working with archaeological evidence that, although extremely ephemeral or entirely absent, "must" be visualized either for their intrinsic importance or because it refers to realities clearly recorded in the literary sources, the attempt has been made to yield with excessive ease to the criterion of approximation and analogy. During the work performed with Fabio Caruso, an archaeologist at IBAM CNR in Catania regarding some major monuments in ancient Syracuse as part of the "Smart Cities" project, the need arose on a number of occasions to strike a balance between these opposing tendencies (Figs. 19.12 and 19.13).

We dwell here in particular on the *oikos* in Piazza Duomo and, later, on the scenic building of the Greek theatre in the Hellenistic Age. Precisely on the highest point of the island of Ortygia, the present-day Piazza Duomo, excavations during the 1990s brought to light traces of the foundation of an *oikos,* a single-celled building to be recognized as the colony's first place of worship: it may date as far back as the late eighth century BC. On the pavement of the present-day piazza, the layout of the *oikos* was traced out (along with that of the larger temple that was to incorporate the building at a later time), precisely to preserve the memory of what may be considered Greek Sicily's most ancient sacred building yet known. Despite the dearth of archaeological information, also because of the likely use of perishable materials both for the elevation and for the roof, we have attempted a reconstruction of the *oikos*. This attempt is not only because of its fundamental

Fig. 19.12 Decorative and figurative references for the hypothetical reconstruction of Oikos

Fig. 19.13 Proposed reconstruction of the Oikos

importance in the history of Syracuse in the Greek age, but also as a response to that reconstructive impulse that makes it possible to present a "plausible" version of the basic characteristics of a construction from the late geometric period. Indeed, there is no doubting the fact that the nonspecialist public, when the remains of a Greek sacred building are pointed out, is led to mentally reconstruct the forms of a classic temple, with a colonnade, a cella, and a roof built of durable materials. An augmented-reality representation of the *oikos* surrounded by the Baroque edifices of Piazza Duomo aims precisely at using this undeniable contrast to destroy this distorted perspective, while also offering, in a single overview, the precursors and the outcomes of the history of Western sacred architecture (Fig. 19.14).

The building's courageous reconstruction takes its inspiration from the votive home/temple scale models from the geometric and archaic period that have come down to us. In particular, account has been taken of the renowned small-scale model restored from the Heraion of Argos, not because it is one of the most complete, but because it seemed to be the most pertinent reference point: it has in fact become an accepted fact of archaeological research that the first generations of settlers in Syracuse were highly influenced by the Argos culture, as shown, for example, by some local figured kraters, modeled upon Argive prototypes used as cineraries in the burials of the city's most ancient elites. It is precisely from these vases that certain graphic elements for the decoration of the *oikos*'s elevation were obtained.

The usefulness of this operation is most certainly to be considered in the context of teaching aids for tourists, but also to the benefit of those scholars who, in this "reconstruction exercise," might find some elements for additional reconstruction hypotheses (Figs. 19.15 and 19.16).

Fig. 19.14 The reconstructed Oikos on actual Piazza Duomo. Screenshot of VR App

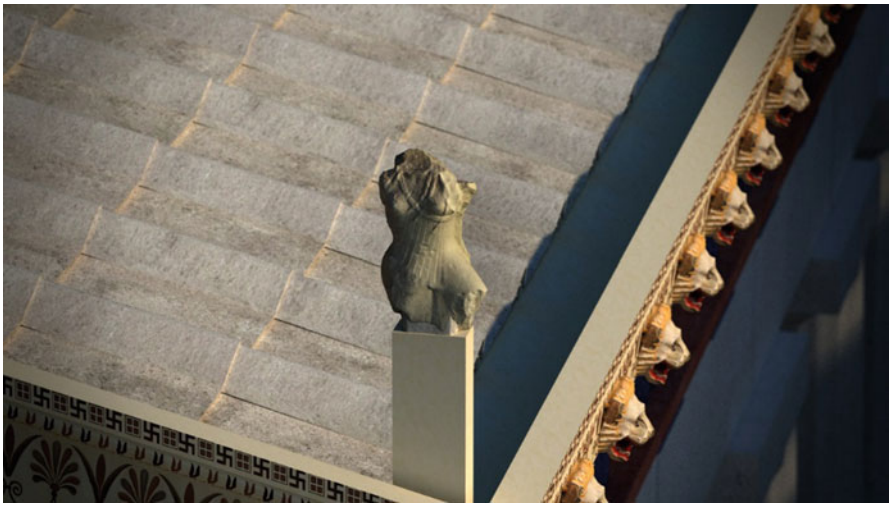

Fig. 19.15 Image-based model of Acroterion on Temple of Athena, in Siracusa

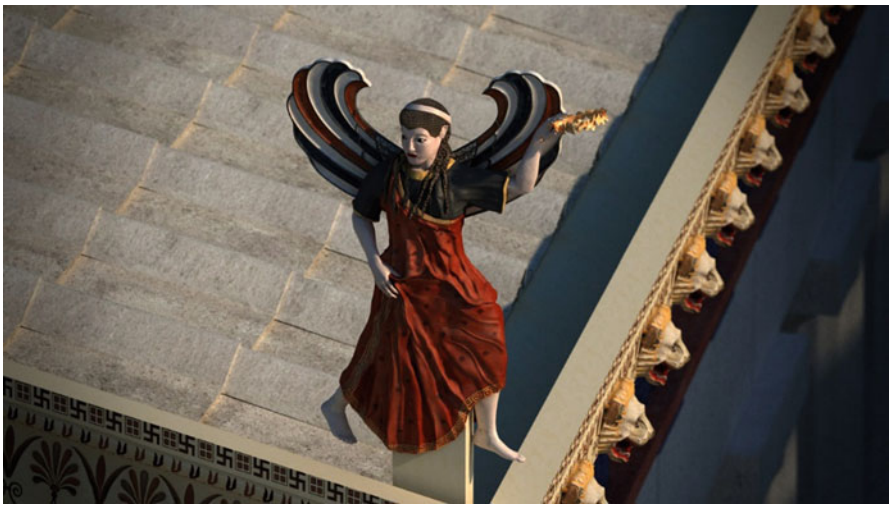

Fig. 19.16 Virtual reconstruction of Acroterion using sculpting and three-dimensional (3D) painting techniques

19.4 A Holistic Approach to the Reconstructive Study of Entire Cities

The example just described suggests how is difficult to propose reconstructions when we have only a few facts. This problem is more problematic if we try to reconstruct whole cities. In this regard, an holistic approach can be described here. In effect, there is an interesting point of view based on the idea that the properties of a system, from microscopic particles to the most complicated star systems, are to be considered as a whole: that is, they cannot be explained exclusively by their components. Patterned on this is the well-known philosophical position of Holism, which is of interest for certain implications connected with reconstructive archaeology. In fact, in recent times, the conviction has made inroads that not even the study of cultural heritage can any longer be perceived as a set of individual objects, preserved and catalogued in museums or collections with no links to the historical and social context. Ancient monuments are likened to complex, articulated units, such as tiles in a cultural heritage built by humankind by adding overlaid, connecting elements organized to give rise to genuine "architectural organisms" which, precisely as do organic forms, show this holistic vision. We are of course also speaking of cities, roads, monuments, homes, and aggregations of housing where the construction solutions are repeated and are recognizable as part of a "domain of

Fig. 19.17 Three-dimensional (3D) model of Pompeii using GIS automated features (Esri CityEngine)

belonging." The city is by all means the "domain" in which a holistic vision finds certain application: a building's construction determines unique conditions that influence adjacent and subsequent construction. The basic architectural elements – cornices, capitals, columns – themselves refer to an overall "idea of city" and of architecture (Fig. 19.17).

Therefore, the problem of reconstructing an ancient building must necessarily extend to the interpretation and study of the urban complex as a whole, to seeking and representing that "idea of city" in which the individual building is only a partial witness. Many buildings in a given city are in fact the expression of those formal, stylistic, and historical values in which it is possible to recognize, to describe, and thus also to reconstruct. However, the holistic approach, which is to say an approach based on comprehending the monuments with reference to the whole, does not preclude the possibility of using an inductive method, moving from the particular to the general, to find solutions to particular problems of interpretation. An interesting case in this regard, recently concluded in the laboratories of Lecce's IBAM ITLab, is provided by the generation of the 3D model of the city of Pompeii, developed thanks to assistance from Esri's CityEngine. The 3D model of the city was obtained by creating buildings with a typology referring to the Roman setting and to the building types documented for Pompeii. A database of typical elements is compared with the map data, and with such basic geometric entities as roads, walls, and houses, to generate a possible representation of the city that is certainly compatible with the map data and the reference models used to populate the blocks. The overall vision shifts the center of attention to the settlement models, to the placement of public areas, and to the extension of the sanctuaries, but also to the overall housing

Fig. 19.18 3D model of Pompeii using GIS automated features and manual modeling

Fig. 19.19 3D reconstruction of ancient Metapontum

density. This is a tool of undoubted usefulness for transmitting complex information simply and briefly, but also a convincing example of a holistic approach, in which the overall view, referring to a precise *modus costruendi* and thus to an "idea of architecture," was often a decisive factor in certain reconstructions of entire cities, which we discuss in these pages (Figs. 19.18, 19.19, and 19.20).

Fig. 19.20 3D reconstruction of ancient Lupiae (actual Lecce, Italy)

19.5 The Role of Virtual Archaeology in the Cultural Asset Knowledge Processes

An intense period of experimentation and research has led virtual archaeology to take on an increasingly prominent role in the processes of the exploitation, knowledge, and enhancement of cultural assets, plotting the outlines of a discipline that is now mature, credible, but above all potentially profitable. This aspect becomes quite clear when carefully analyzing the content of the numerous public and private initiatives in support of processes for capitalizing on cultural assets using digital technologies, in which digital heritage is taken as a driving element capable of attracting and at the same time simplifying the very modes of transmission of the cultural message (Fig. 19.21).

The central role of virtual archaeology is in some way clear, as a promising sector in which to believe and invest, not only for those outcomes economically foreseen in terms of the capitalization of cultural assets, but also for the many expectations related to employment and the potential to use new, specialized figures. Although this sector admittedly invests in and is fed by the various fields of research, from hard sciences to digital humanities, one may think of a more dynamic, modern, and interdisciplinary role for figures traditionally linked to sectoral studies conducted mostly in isolation. I am thinking of the archaeologist's and historian's contribution, which is decisive for being able to guarantee a certain scientific rigor for a virtual archaeology product, but also of contributions by sciences quite remote from the humanities, such as chemistry, physics, geology, and medicine, all disciplines that can find fertile connections in this growing sector. Virtual archaeology may perhaps today be deemed the discipline that more than all the others requires the

Fig. 19.21 (**a**, **b**) 3D reconstruction of the temple of Apollo in Siracusa. The section is useful for educational purposes and to understand well the ancient construction techniques (screenshot of VR App)

contribution of different areas of knowledge, because it is from the combination of different points of view that it is possible to attain results of absolute scientific rigor. Without interdisciplinary knowledge of the asset, there can be no credible virtual archaeology product that can also yield its results on the level of capitalization of the asset to be promoted, as alluded to earlier. The ineffectiveness of many digital products intended for museum communication is derived from the imbalance between the various components that come into play in determining the aspects characterizing a virtual archaeology project. Many products have their center of interest revolve around technological innovation, at the expense of the correctness of the content and, often, of the graphic rendering: this is often justified by the need

to offer innovative solutions that contain some advance ahead of the state of the art. It is an attitude in line only with the expectations of research, entirely extraneous to the logic of communicative effectiveness of a "product" to be used, whose value will have to come to terms with the public's final level of satisfaction. Yet it is precisely on this crucial aspect, connected to the quality of the rendering, to the quality of the scientific data, to the communicative effectiveness of the transmitted data, that a valid virtual archaeology "product" can be conceived. As something that can transcend pure technicalities and that aims straight for quality, even when this means using the metaphors of videogames and the magic of the visual effects employed in modern film-making, to represent – with a language that is simple and immediate, yet also spectacular – rigorous scientific information.

19.6 Conclusions

This chapter has highlighted the considerable potential of virtual reconstructions in terms of knowledge, communication, and the enhancement of cultural heritage. The ability to maintain a reliable virtual archaeology as a mature and promising discipline is linked to research of high scientific rigor. For this reason, it is important to assume a transparent approach and, above all, a clever use of 3D software, which does not simply replace the old drawing techniques but proposes a new way to solve old representation problems. Reconstruction is a synthesis of morphological, functional, aesthetic, and historical values. Only through the integration of 3D studies and the contribution of different disciplines can we provide valuable answers and the highest scientific rigor. Even when the data are scarce or insufficient, a reconstructive proposal may provide interesting didactic answers, proposing typological models in which the functional, stylistic, and constructive logics are correctly related to the studied period.

Acknowledgments We express our sincere thanks to Francesco Giuri and Ivan Ferrari from IBAM ITLab for having believed in the potential of this project and for their great 3D work.

References

Barletta BA (2001) The origins of the Greek architectural orders. Cambridge University Press, Cambridge

Caruso F, Gabellone F, Ferrari I, Giuri F (2015) Nuove proposte ricostruttive per una rilettura critica della documentazione archeologica su Siracusa in età greca. In: Arqueològica 2.0, International Congress of Archaeology and Computer Graphics, Heritage and Innovation, Ciudad Real, 15–17 Ottobre 2014

Courtois C (1989) Le bâtiment de scène des théâtres d'Italie et de Sicile. Étude chronologique et typologique. Louvain-la-Neuve, Providence (Rhode Island)

Diodato R (2005) Estetica del virtuale. Bruno Mondadori Editore, Milano

Gabellone F (n.d.) Il Santuario di Jupiter Anxur a Terracina, studio ricostruttivo tipolo-gico come ausilio per la visita in situ. In: Arqueológica 2.0, IV Congreso Internacional de Arqueología e Informática Gráfica, Patrimonio e Innovación, Sevilla, 20–22 Junio 2012 (Congress CD-Rom proceedings)

Gabellone F (2009) Ancient contexts and virtual reality: from reconstructive study to the construction of knowledge models. J Cult Herit 10S:e112–e117

Gabellone F (2012) La trasparenza scientifica in archeologia virtuale. Una lettura critica al Principio N.7 della Carta di Siviglia. In: SCIRES-IT, SCIentific RESearch and Information Technology, CASPUR CIBER. doi:10.2423/i22394303v2n2p99. http://caspur-ciberpublishing.it/index.php/scires-it/issue/current

Gargiani R (1993) Auguste Perret (1874–1954). Teoria e opera. Electa Mondadori, Milano

Rossi A (1978) L'architettura della Città. Marsilio Editori, Padova

Smuts JC (1926) Holism and evolution. Macmillan, London

Van Compernolle R (1966) Syracuse, colonie d'Argos? Kokalos 12:75–101

Voza G (1999) Lo scavo archeologico di Piazza Duomo, Siracusa

Chapter 20
Technologies for Visual Localization and Augmented Reality in Smart Cities

Giuseppe Amato, Franco Alberto Cardillo, and Fabrizio Falchi

Abstract The widespread diffusion of smart devices, such as smartphones and tablets, and the new emerging trend of wearable devices, such as smart glasses and smart watches, has pushed forward the development of applications where the user can interact relying on his or her position and field of view. In this way, users can also receive additional information in augmented reality, that is, seeing the information through the smart device, overlaid on top of the real scene. The GPS or the compass can be used to localize the user when augmented reality has to be provided with scenes of large size, for instance, squares or large buildings. However, when augmented reality has to be offered for enriching the view of small objects or small details of larger objects, for instance, statues, paintings, or epigraphs, a more precise positioning is needed. Visual object recognition and tracking technologies offer very detailed and fine-grained positioning capabilities. This chapter discusses the techniques enabling a precise positioning of the user and the subsequent experience in augmented reality, focusing on algorithms for image matching and homography estimation between the images seen by smart devices and images representing objects of interest.

Keywords Localization • Augmented reality • Deep learning • Smart cities • Landmark recognition

20.1 Introduction

The widespread diffusion of smart devices, such as smartphones and tablets, and the new emerging trend of wearable devices, such as smart glasses and smart watches, has pushed forward the development of applications where the user can interact relying on his or her position and field of view. In this way, users can also receive the needed information in augmented reality, that is, seeing the information through the smart device, overlaid on top of the real scene.

G. Amato (✉) • F.A. Cardillo • F. Falchi
CNR-ISTI, Pisa, Italy
e-mail: giuseppe.amato@isti.cnr.it; franco.alberto.cardillo@isti.cnr.it; fabrizio.falchi@isti.cnr.it

N. Masini, F. Soldovieri (eds.), *Sensing the Past*, Geotechnologies and the Environment 16, DOI 10.1007/978-3-319-50518-3_20

For instance, users can have information on monuments, shops, hotels, or restaurants with their smartphones by simply pointing toward the subject of their interest. The relevant information is displayed aligned with the real scene observed.

Some existing augmented reality systems use a GPS and a compass to determine the position and field of view of users to align reality and synthetic images correctly. These systems can be used, to some extent, outdoors with large-scale landmarks such as squares and archaeological sites, provided the user is located close to a precise preplanned position. In fact, these techniques suffer from high imprecision that is not generally noticed by users if they are located in approximately the right position. For instance, it is possible to have augmented reality of the Coliseum, showing how it looked before it was damaged, provided the user is located in the right position. However, these techniques cannot be used to offer augmented reality when users are located in arbitrary positions with respect to the subject of interest, because of the possible misalignment between reality and artificial scenes, due to the imprecision of the localization. The problem is even worse when dealing with objects of smaller dimensions, such as statues or paintings. In those cases, localization with a GPS and a compass cannot be used reliably.

Recently, techniques to determine precisely the position of the user and of the smart device were defined, which leverage on content-based image retrieval (Datta et al. 2005) and object recognition. The point of view of the user with respect to the observed object can be determined precisely by matching the observed scene with a set of prealigned images. By using this information, it is possible to place the virtual scene (images, videos, 3D model, animations, etc.) according to the correct perspective and position on top of the real scene. To execute these tasks we need to recognize what the user is looking at, determining the relative position of the user (Amato et al. 2011a), tracking the user movement, and finally rendering the virtual scene with the correct perspective. These operations are executed in real-time, with fluidity and precision, to improve user experience.

The use of visual analysis for determining the position of the user has the advantage that user localization can be executed in places where GPS cannot be used, such as indoor areas, and is able to provide much finer precision, which other techniques cannot provide. This is particularity true in the presence of an object of small size, or in the case where users want to have specific information of small details of larger objects (for instance, an epigraph on a wall of a building). On the other hand, visual recognition and tracking require that automatic visual recognizers for the elements to be identified and tracked should be built.

Even relatively small areas might possibly contain hundreds of details of interest that should be “active” and should trigger an augmented reality experience when observed. Consider, for example, a square in an historical city. It might include several buildings, various statues, various frescoes, and various details that can be of interest to cultural tourists and that should be recognized and tracked by the smart devices to provide users with an augmented reality experience. Even if the computing power of smart devices is quickly improving, the resources required to

perform real-time recognition and tracking of a large amount of subjects of interest are still a challenge. In this respect, techniques able to deal with large-scale archives of images to be recognized, and that can analyze images even with low-resource devices have been developed.

During the last few years, local descriptors, for instance, SIFT (Lowe 1999) and SURF (Bay et al. 2006), to cite two, have been widely used to support effective object recognition and visual tracking tasks. A local descriptor is generally an histogram representing statistics of the pixels in the neighborhood of an interest point (automatically) chosen in an image.

Executing object recognition tasks, relying on local features, is generally resource demanding. Each digital image, both queries sent by smart devices and images in the image libraries, are typically described by thousands of local descriptors. In order to decide that two images match because they contain the same object, local descriptors in the two images need to be pairwise compared, in order to identify matching patterns.

To reduce the cost of extracting, representing, and matching local visual descriptors, researchers have investigated the use of binary local descriptors, for example, BRISK (Leutenegger et al. 2011) or ORB (Rublee et al. 2011). With binary descriptors, each bin of the vector, representing the local descriptor, just contains 0 or 1. Binary descriptors are much faster to be extracted, are obviously more compact than nonbinary ones, and can also be matched faster by using the Hamming distance rather than the Euclidian distance. This allows their use on devices with low resources, such as smartphones, or when response time must be very short even in the presence of image libraries.

Reduction of the cost of image matching on a very large scale has been addressed by defining methods for quantizing and/or aggregating local features. Quantization methods, such as the bag of feature approach (BoF) (Sivic and Zisserman 2003), define a finite vocabulary of local descriptors, that is, a finite set of local descriptors to be used as representative. On the other hand, aggregation methods, such as Fisher vectors (FV) (Perronnin and Dance 2007) or vectors of locally aggregated descriptors (VLAD) (Jégou et al. 2010), analyze the local descriptors contained in an image to create statistical summaries that still preserve the effectiveness power of local descriptors and allow treating them as global descriptors.

Once an object has been recognized, local descriptors can also be used to compute an homography that maps the image seen by the smart device with the target image representing the recognized object. The computed homography embeds the needed information to estimate the relative position of the smart device precisely with respect to the object of interest. This allows a 3D rendering engine to be used to overlay the information associated with the object on top of the real scene with a precise alignment, continuously adapting to the movement of the device itself.

This chapter is organized as follows: In Sect. 20.2, we discuss the state-of-the-art technologies for automatic visual localization. Augmented reality goals, issues, and solutions are presented in Sect. 20.3.

20.2 Visual Localization

In this section, we consider the problem of automatically understanding the user information needs given a photo taken by the user with a mobile phone.

In this context, the computer vision literature focuses on answering three major questions:

- Where was the picture taken?
- What is in the photo?
- Where are the objects in the photo located?

For each question, a specific task has been defined:

Mobile visual localization aims at identifying the location in which a picture was taken. The visual approach has been proposed to overcome limitations of GPS-based approaches such as indoor environments, latency, and multipath effects (Schroth et al. 2011).

Visual landmark recognition is the task of identifying a building or monument in photos (Weyand and Leibe 2015). Essentially, it is a specification of the more general object recognition task which is central in computer vision.

Visual photo mapping considers the problem of placing photos on a map for organizing large datasets (Crandall et al. 2009). In this scenario, a photo taken from a long distance of an object (e.g., the Eiffel Tower) could be placed on the actual location of the object itself in order to improve user experience in browsing through the collection.

Coming back to the objective of this section, that is, understanding the user information needs, we believe that landmark recognition is the primary task. In fact, the most important question we have to answer is, "What is in the photo?" As an example, a tourist on top of the Eiffel Tower can take photos of many different tourist landmarks in Paris. If the visual query represents, for instance, Montmartre, the actual position of the tourist is not relevant as well as a precise localization of the landmark. Thus, even the localization of both the user and the landmark could be useful, however, the primary task is identifying the objects in the photo.

The minimum knowledge base for recognizing landmarks consists of a set of photos of each object that should be recognized. In the case where this set is either not available or not sufficient, public photos can be used. Many approaches have been proposed to leverage on Internet photo collections such as Flickr or Panoramio. In some particular cases, even the landmarks are automatically identified (Weyand and Leibe 2015) in public collections.

20.2.1 Object Recognition

Object recognition is essentially a classification task where the label to be assigned to a photo is the ID of the object. However, for both efficiency and scalability with

respect to the number of objects to be recognized, most of the approaches perform content-based image retrieval (CBIR) in the dataset applying a *k*-nearest neighbor classifier on the results set. In other words, a landmark is recognized in a query image if similar images, containing the same object, are found in the knowledge base.

20.2.1.1 Local Features-Based Approaches

In the last decade, the research on object recognition has focused on describing and matching local features, including SIFT (Lowe 1999) and SURF (Bay et al. 2006), extracted from interest points. Both the interest points and the description of the region around them should be robust to illumination variations and affine transformations. Given images described in terms of their local descriptors (thousands per image), comparing any two images results in comparing their local descriptors or aggregated information obtained by considering all the local descriptors in each image. In fact, direct comparison of local features is not only computationally expensive, but it also does not scale. For image registration and pose estimation, local features matching is mandatory in order to understand the geometric relationships between the images. For higher-level tasks such as retrieval and classification, research has focused on aggregating the information related to each local pattern in the same image.

In 2007, the bag-of-(visual) words model was proposed in order to improve scalability of object recognition (Perronnin and Dance 2007). It consists in replacing original local descriptors with the *ID* of the most similar descriptor in a predefined vocabulary. Following the BoW approach, an image is described as a histogram of the occurrence of (hundreds of thousands) visual words over the global vocabulary. The BoW is then the result of the aggregation of the information contained in the local descriptors. However, as mentioned before, it also performs a quantization of the information reducing each local description to an ID of a visual word. In Jegou et al. (2008) the matching, based on visual words, was refined in order to improve effectiveness of the BoW approach in reducing the quantization. A survey of BoW approaches for landmark recognition has been given in Bhattacharya and Gavrilova (2013).

With the goal of improving both effectiveness and efficiency, two aggregation approaches have recently been proposed: vector of locally aggregated descriptors (VLAD) (Jégou et al. 2010) and Fisher vectors (FV) (Perronnin and Dance 2007). The FV characterizes how a sample of descriptors deviates from an average distribution that is modeled by the Gaussian mixture model (GMM) estimated on a training set. This model can be seen as a probabilistic visual vocabulary. VLAD, instead, accumulates, for each image, the difference between the visual words from a vocabulary (hundreds) and the associated descriptors. Thus it can be seen both as an extension of the BoW and a simplified nonprobabilistic version of FV. Typically FVs achieve better results, however, many recent VLAD extensions (e.g., Delhumeau et al. 2013) have obtained very good results on largely used public datasets such as INRIA Holidays and Oxford Buildings.

Aggregation techniques describe the whole image. However, sometimes the relevant landmark only appears in a small portion of the picture. In Lazebnik et al. (2006), BoW was extended by partitioning the image into increasingly fine subregions aggregating features inside each subregion.

A promising extension of the aggregation techniques is embedding geometric information related to the region of interest from which the local descriptors were extracted (Tolias et al. 2015). By comparing two descriptions obtained aggregating both the local features and the geometric information, weak geometric matching can be performed resulting in more robust recognition.

Given the global fixed length description obtained with these techniques various access methods can be used as Euclidean locality-sensing hashing (Datar et al. 2004) and surrogate text representation (Amato et al. 2013). A trade-off between quality and efficiency/scalability can also be applied by varying the parameters of these approximate indexing techniques.

To improve the effectiveness of the large-scale approaches there are two largely used techniques: query expansion and reranking. Reranking considers the results set obtained with a CBIR system as a new dataset that is compared, typically sequentially, with the query image in order to apply a more effective similarity measure, generally exploiting geometrical information (Philbin et al. 2007). To this aim, a number of highly ranked and geometrically verified images are used to expand the original query with the goal of improving retrieval effectiveness (Chum et al. 2007; Amato et al. 2011b).

Recently, approaches based on classification of the local descriptors have been proposed for both landmarks (Amato et al. 2015) and websites (Akusok et al. 2015). The intuition is that the whole query image classification can leverage on the classification of each query descriptor.

Binary local descriptors (e.g., BRIEF, BRISK, and ORB (Heinly et al. 2012)) have also been proposed that allow more efficient extraction and matching with respect to traditional SIFT and SURF features. They all share the idea of comparing the luminance of a pair of pixels of the region to be described. The resulting binary description can be compared using the Hamming distance. Their aggregation is typically less effective and thus they are mainly used on mobile devices when local features matching is requested for pose estimation, image registration, or augmented reality.

20.2.1.2 Deep Learning

In Razavian et al. (2014) deep learning techniques, and in particular convolutional neural networks, have been tested on visual recognition tasks. Basically, the activation values of the neuron of a certain layer of the network are used as a global description of the image. The resulting feature is a fixed-length floating point vector (typically 4.096) that is used in very similar ways as the aggregation of local features. In fact, these activation features are a sort of aggregated hierarchical feature. Please note that local feature aggregations are shallow and not deep

because they do not create feature hierarchies (i.e., features defined combining other features). The results show that off-the-shelf neural networks can compete with state-of-the-art local descriptor aggregation techniques in image retrieval staff. At the moment, local features and their aggregations are still largely used, but we can expect the CBIR part of the overall landmark recognition pipeline to change significantly as a consequence of the adoption of convolutional neural networks-based features. Recently, efficient index approaches (Novak and Zezula 2014) have been successfully applied to activation features (Novak et al. to appear).

20.3 Augmented Reality

In an early review on the state of the art of augmented reality (Azuma et al. 1997), Azuma defines AR systems as:

Systems that have the following three characteristics:

- Combines real and virtual
- Interactive in real time
- Registered in 3-D.

The previous definition points to applications providing a view of the external (physical) world augmented with additional information. As a consequence, an AR application must:

- Determine the state of both the physical world and the virtual world.
- Augment the view of the external world with digital information that needs to be perfectly aligned with the 3D space.

The key to a successful AR app stays mostly in the quality of the alignment: if such an alignment is precise and computed in real-time, the users will get a new experience of the world, where digital information is seamlessly integrated with the real view.

In the context of mobile AR apps for smart cities, the previous considerations led to the so-called "video-see-through" apps: mobile applications that in real-time overlay information on top of the live videostream acquired by the device camera. The first (and basic) mobile AR apps used only the data coming from two sensors of the devices: the GPS receiver, for the location, and the digital compass, for the direction. However, this approach only allows us to estimate a global position of the device in an outdoor environment. Indeed, the high-quality cameras and fast CPUs/GPUs[1] equipping current mobile devices enable the development of AR apps based on computer vision: by "understanding" the current scene facing the camera; apps are able to estimate the relative position of the user with respect to specific points of interest and overlay digital information on the details of the scene. This

[1]CPU: central processing unit; GPU: graphics processing unit.

approach, commonly called natural feature learning and natural feature tracking, can be used in the implementation of both indoor and outdoor AR apps.

The rest of this section describes the basics of mobile AR app development based on computer vision algorithms. These apps usually require the following components.

- A module for scene understanding that estimates the relative position of the device with respect to a known scene. This module uses algorithms and techniques borrowed from the image matching and object recognition fields. More precisely, the module estimates where the user is located with respect to one out of a set of objects, called targets.
- A module for object tracking. The algorithms for image matching and object recognition, discussed in Sect. 20.2.1 are computationally expensive. When the app is first inspecting the scene looking for a target, the full computational power of the mobile device can be allocated to this task. However, once a target has been detected, the app must continuously update the device location and direction with respect to the detected target, while at the same time aligning and displaying the digital information. Tracking algorithms are able to "follow" an image area using techniques that are simpler and faster than those used for object recognition, freeing up resources for the other tasks.
- A module for displaying virtual information. There are no constraints on the type of information that can be displayed. They can be as simple as text strings and icons, describing, for example, the details of the scene, or as complex as 3D models, which require specialized hardware and sophisticated algorithms from computer graphics. In order to offer a smooth user experience, sophisticated AR apps try to eliminate the shaking affecting the information displayed in overlay, which is caused by the very small differences in the estimated user position and direction. This is usually achieved borrowing methods from the signal theory field, for example, a Kalman filter.

In the following we describe each component in a specific use case: the recognition of a 2D image (the target) that triggers an augmentation with a 3D model that is placed on top of the target. The 3D model is a reconstruction of the Roman amphitheatre in Lecce. The target, shown in Fig. 20.2, is an overlay of two images: three quarters of it contains a textured top view of the 3D model, and the upper left quarter contains a symbolic 2D map of the same amphitheater.

Target Images. Target images can be either synthetic or natural. Synthetic images (also known as fiducial markers) are usually composed of black and white dots, as shown in Fig. 20.1. They have high contrast, are asymmetric, and can be easily detected and tracked in almost any scene as long as they are fully visible. However, such markers come with some limitations: they are not aesthetically pleasing, especially if printed at larger sizes, and they cannot be used in AR contexts where the aim is to augment the view of large outdoor scenes. Fiducial markers are best used on printed materials, where their presence communicates the availability of additional virtual context. Current research on the recognition of fiducial markers

Fig. 20.1 From *left to right*. First two pictures: Examples of synthetic images used as fiducial markers for AR applications. They are very similar to 2D QR codes, shown in the third picture, that can be used as target images as well

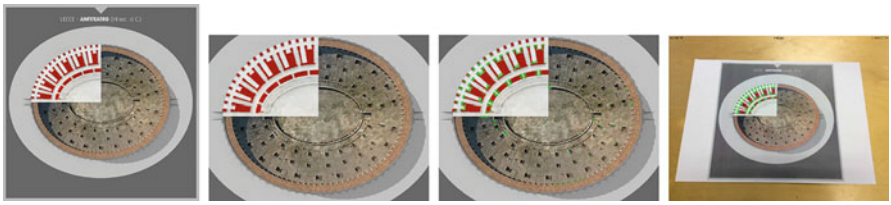

Fig. 20.2 From *left to right*: The print, placed in the physical world, whose recognition triggers the AR visualization; the target image, which is actually a crop of the first image; 500 ORB keypoints drawn on the target image; 500 ORB keypoints drawn on the video frame

focuses on improving the robustness toward occlusions (Bergamasco et al. 2011). Natural images, such as photographs or photorealistic pictures, are much harder to process and recognize. In our context, it means executing an object recognition algorithm on each video frame captured by the camera.

Target Placement. Section 20.2.1 presented some techniques for executing object recognition tasks. As already anticipated, one of the most successful approaches for recognizing targets in the AR domain uses sparse image representations based on local features, that is, visual properties extracted from neighborhoods of salient image points. Given the target image T and the video frame F, in order to establish whether T is in F, both the target and the frame are represented by a set of keypoints and related visual descriptors, also called feature vectors. A visual keypoint is a location in the image, identified by its coordinates (x, y), whose local visual properties are stable with respect to some geometrical transformations, such as rotation and scaling. The feature vector associated with a keypoint contains statistics about the color or the intensity values in an image patch surrounding the keypoint location (x, y), encoded as real-valued or binary numbers. There are several algorithms for the extraction of visual keypoints, each offering a different degree of invariance to affine or projective transformations and a different computational cost. In recent years there has been an increasing interest in proposing new keypoints and descriptors that enable fast extraction and matching procedures and that require a small memory footprint (Bay et al. 2006; Leutenegger et al. 2011; Lowe 1999; Rublee et al. 2011). A recent review and comparison can be found in Yang and Cheng (2014). Figure 20.2 shows the keypoints extracted by the oriented FAST and rotated brief (ORB) algorithm (Rublee et al. 2011) from the target image and a video

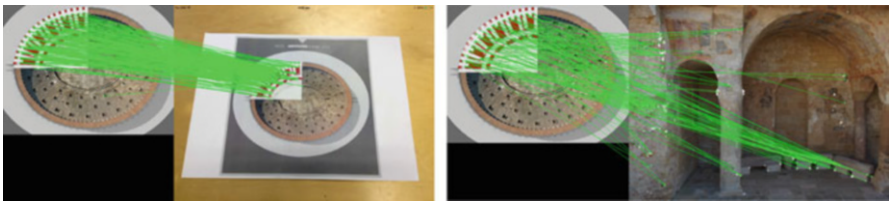

Fig. 20.3 Matching keypoints between the two images. Each *green line* connects a keypoint in the target image to the keypoint in the second image. These two images clearly show that the set of matches does not provide any information about the presence of the target in a scene. In order to establish whether the target is in the scene and where it is located, we need to perform a geometric verification of the matches

frame. The ORB features are well suited for mobile apps mainly due to their binary descriptors that have low memory requirements and allow fast comparison. Given the two sets of keypoints extracted from the target T and the video frame F (with the related descriptors), the matching procedure computes an initial set of matches M by associating each target descriptor with the closest frame descriptor according to a given distance function that depends on the type of the descriptors, whether real-valued or binary. However, M contains only couples of points whose descriptors are similar: the number of matches does not provide any real information about the presence of the target. The left image in Fig. 20.3 shows the matching ORB keypoints between the target and a video frame containing the target. The right image in Fig. 20.3 shows the matches between the target and a random photograph: even if the two images are very different, the number of matching keypoints is quite high. In order to establish whether the target T is present in the frame F, the app needs to verify that the relative positions of the matching keypoints in the two images are compatible with plausible geometric transformations of the target image. Before performing this geometric verification, it is worth reducing the number of matches by applying one or more heuristics, as discussed, for example, in the seminal paper by Lowe (1999). The images in Fig. 20.3 show only the matches that passed a filtering step using several heuristics; as the images show, there are false matches even after such an aggressive filtering. Because the target image is a planar object, the most likely transformation affecting its view in the frame is projective: the app needs to verify whether an homography H mapping T onto F exists (Amato et al. 2011a). It is likely that some of the matches in M are not compatible with a projective transformation whereas others are: the app accepts an homography H if the number of compatible matches (inliers) is high and the number of incompatible matches (outliers) is low. A very common approach for estimating H is the iterative random sample consensus (RANSAC) algorithm (Fischler and Bolles 1981). An homography corresponds to a 3×3 matrix, with eight degrees of freedom: in order to compute its parameters we need four point correspondences. First, RANSAC chooses four random matches, assumes that they are inliers, then uses them to compute the parameters of an homography $\hat{H}$. This estimate is then applied to all the other matches: the keypoints in the target are projected using $\hat{H}$ and are counted

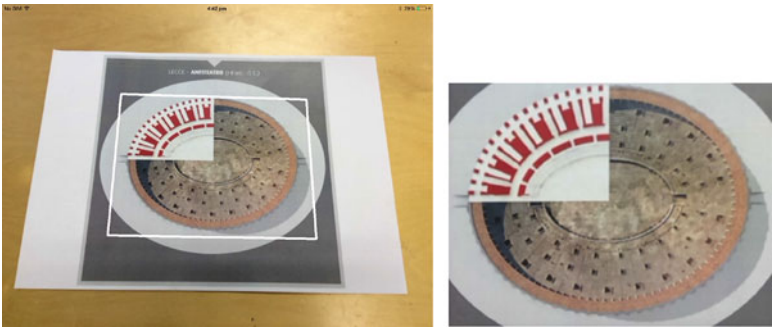

Fig. 20.4 *Left*: The *white box* shows the location of the target in the video frame, according to the homography $\hat{H}$ estimated using RANSAC. Its localization can be refined by performing a second iteration of the RANSAC algorithm. *Right*: Image obtained by projecting the video frame using the homography $\hat{H}^{-1}$. It is out of focus because it is part of the original input frame

as inliers only if their projection falls within a small radius of the corresponding keypoint in the video frame . After this estimation is repeated M times, RANSAC returns the estimate $\hat{H}$ with the largest number of inliers. RANSAC can return a wrong estimate $\hat{H}$ thus it is worth applying some heuristics to detect and reject the estimates that are likely incorrect (Kumar and Jawahar 2006). Heuristics that are commonly used concern the study of the determinant of the matrix, and the size and convexity of the projected region.

In order to locate more precisely the target image in the video frame, it is possible to refine the initial estimate $\hat{H}$ by applying its inverse matrix $\hat{H}^{-1}$, as shown in Fig. 20.4, to the video frame and computing a second homography between the projected frame and the target image T. The final homography matrix is the composition of the two homographies and is used to start the tracking of the target image. In fact, this homography embeds all the information needed to determine the relative position of the smart device facing the scene with respect to the recognized object or target.

Image Tracking. Once the target is localized, the app needs to stop extracting the visual features for object recognition and start tracking the region of the frame occupied by the target. Many tracking algorithms rely on the computation of the optical flow, defined as the apparent motion of the objects, surfaces, or edges in the image, between two consecutive video frames. When the aim is to track a target image in real-time on mobile devices, the choice is restricted to algorithms with a low computational cost. Many successful algorithms are based on the Lucas-Kanade transform (LKT) (Lucas et al. 1981). Given an initial set of locations (called tracks), LKT establishes how they moved by iteratively minimizing the squared differences between neighborhoods of the tracks. The success of the tracking also depends on the choice of the points to track: in the example of Fig. 20.5 the tracks have been extracted using the algorithm known as "Good Features to Track" (Shi and Tomasi 1994). Tracking an image for AR purposes is quite difficult: the tracks are usually

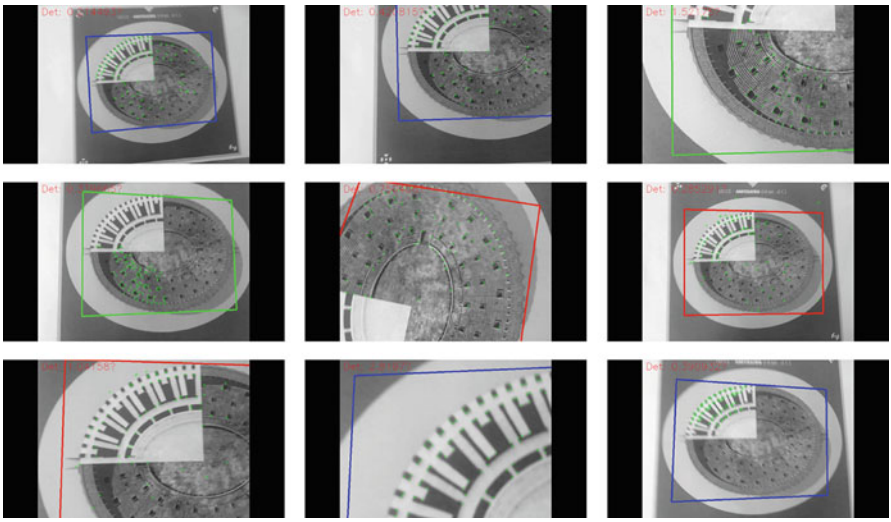

Fig. 20.5 Screenshots of an iPhone during tracking of the target. The sequence starts from the first image of the first row and proceeds *left to right*. The color of the bounding box around the location of the target image changes when the tracker reinitializes the set of tracks after losing too many of them. The last figure shows the estimated homography after many "zoom-in" and "zoom-out" movements of the device: the homography is not as accurate as the initial one, but still acceptable

lost by the tracker after some iterations (especially when the target is only partially contained in the video frame). The screenshots in Fig. 20.5 show an iPhone app tracking the target: the goal of the tracker is to maintain an accurate homography when the user moves the device closer to or farther from the target, while at the same time rotating it. As the images show, the tracker needs to reinitialize the tracks quite often, but it is able to maintain a good approximation of the initial homography, even if the target has been only partially visible for several times.

Aligning the Information. Once we know the location of the target we can display information in perfect alignment with the content of the scene. When the virtual information consists only of 2D data, the homography is enough for getting a good alignment. In the case of more complex visualizations, such as 3D models or interactive elements managed by complex window managers as in the iOS platform, we cannot simply use the homography returned by the tracker. We need to estimate the camera pose in a pinhole camera model (Hartley and Zisserman 2003). The procedure for computing the camera matrix used in the model, projecting 3D points on the 2D camera image, is not particularly complex, but it requires an intrinsics matrix that specifies the physical characteristics of the camera acquiring the videostream. The intrinsics can be computed using several camera calibration algorithms, among which the most used is Zhang (2000). Figure 20.6 shows the app running on an iPad rendering a very complex 3D model on top of the recognized target image.

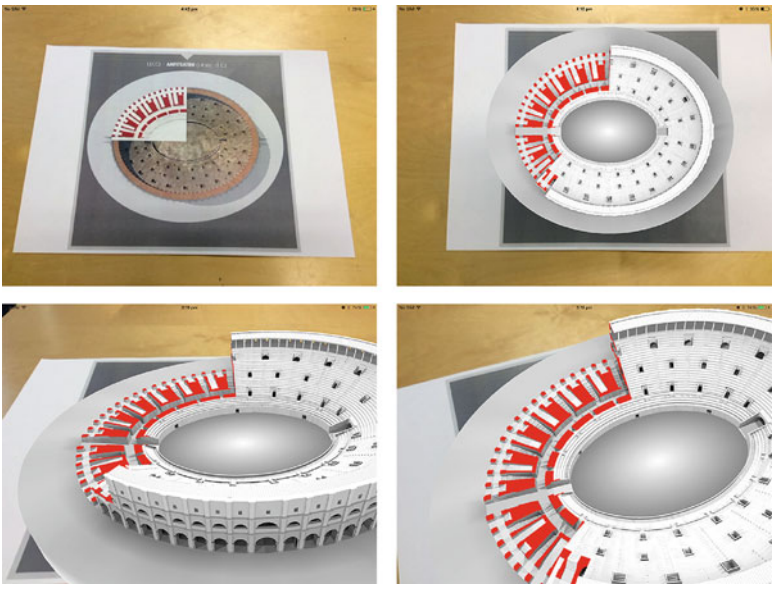

Fig. 20.6 Rendering of the 3D model on top of the target. The app is running on an iPad Air

Augmenting with Respect to the 3D Geometry of the World. The app discussed in this chapter is able to recognize a 2D image and overlay a 3D object (or other info) on top of it. The app can be easily extended to recognize a full scene in the videostream and overlay models on top of it, but it is restricted to projecting information on planar surfaces. More complex AR apps can align the virtual information with respect to the geometry of the external 3D world. This geometry needs to be computed as a point cloud. Point clouds of the 3D objects can be built via laser scanning or using a stucture-from-motion approach, in which the 3D geometry of an object is inferred from a set of photographs. For example, in Snavely et al. (2006) the authors present Bundler, an algorithm able to build a 3D model of a scene from a large collection of photographs. The alignment in 3D is performed by combining the algorithms and techniques described in Sect. 20.2 with a matching procedure similar to Bundler's.

Frameworks, Software, and Libraries. Nowadays several software tools and programming frameworks are available for the implementation of AR apps. A very good open-source multiplatform library is ARToolKit.[2] It offers both synthetic image and natural feature tracking, pose estimation, and 3D rendering via OpenSceneGraph[3] or Unity.[4] Commercial alternatives to ARToolKit are Qualcomm

[2] http://artoolkit.org/

[3] http://www.openscenegraph.org/

[4] https://unity3d.com/

Vuforia,[5] Total Immersion D'Fusion,[6] and Wikitude.[7] Complex 3D models can be rendered with the VCG library,[8] developed in the ISTI-CNR in Pisa, or with libGDX.[9] People with a basic knowledge of machine vision might want to use the OpenCV library,[10] that contains the implementation of many basic algorithms. All the images in this chapter were produced by proprietary source code that uses the OpenCV and VGC libraries. Point clouds can be built using, among others, Bundler[11] (Snavely et al. 2006) or Microsoft Photosynth.[12]

References

Akusok A, Miche Y, Karhunen J, Bjork KM, Nian R, Lendasse A (2015) Arbitrary category classification of websites based on image content. IEEE Comput Intell Mag 10(2):30–41. 10.1109/MCI.2015.2405317

Amato G, Bolettieri P, Falchi F, Gennaro C (2013) Large scale image retrieval using vector of locally aggregated descriptors. In: Similarity search and applications. Springer, Heidelberg, pp 245–256

Amato G, Falchi F, Claudio G (2015) Fast image classification for monument recognition. J Comput Cult Herit 8(4):18:1–18:25. http://dl.acm.org/citation.cfm?id=2724727

Amato G, Falchi F, Gennaro C (2011a) Geometric consistency checks for KNN based image classification relying on local features. In: Proceedings of the fourth international conference on SImilarity Search and APplications (SISAP'11). ACM, New York, pp 81–88. 10.1145/1995412.1995428. http://doi.acm.org/10.1145/1995412.1995428

Amato G, Falchi F, Gennaro C (2011b) Geometric consistency checks for KNN based image classification relying on local features. In: Proceedings of the fourth international conference on SImilarity Search and APplications. ACM, New York, pp 81–88

Azuma RT et al (1997) A survey of augmented reality. Presence 6(4):355–385

Bay H, Tuytelaars T, Van Gool L (2006) Surf: speeded up robust features. In: Leonardis A, Bischof H, Pinz A (eds) Computer vision – ECCV 2006. Lecture notes in computer science, vol 3951. Springer, Berlin/Heidelberg, pp 404–417

Bergamasco F, Albarelli A, Rodola E, Torsello A (2011) Rune-tag: a high accuracy fiducial marker with strong occlusion resilience. In: IEEE conference on computer vision and pattern recognition (CVPR 2011). IEEE, pp 113–120

Bhattacharya P, Gavrilova M (2013) A survey of landmark recognition using the bag-of-words framework. In: Intelligent computer graphics 2012. Springer, pp 243–263

Chum O, Philbin J, Sivic J, Isard M, Zisserman A (2007) Total recall: automatic query expansion with a generative feature model for object retrieval. In: IEEE 11th international conference on computer vision (ICCV 2007). IEEE, pp 1–8

[5] https://www.qualcomm.com/products/vuforia

[6] http://www.t-immersion.com/products/dfusion-suite

[7] http://www.wikitude.com/blog/dev2dev/

[8] http://vcg.isti.cnr.it/vcglib/

[9] https://libgdx.badlogicgames.com/

[10] http://opencv.org/

[11] http://www.cs.cornell.edu/~snavely/bundler/

[12] https://photosynth.net/

Crandall DJ, Backstrom L, Huttenlocher D, Kleinberg J (2009) Mapping the world's photos. In: Proceedings of the 18th international conference on world wide web. ACM, pp 761–770

Datar M, Immorlica N, Indyk P, Mirrokni VS (2004) Locality-sensitive hashing scheme based on p-stable distributions. In: Proceedings of the twentieth annual symposium on computational geometry. ACM, pp 253–262

Datta R, Li J, Wang JZ (2005) Content-based image retrieval: approaches and trends of the new age. In: Proceedings of the 7th ACM SIGMM international workshop on multimedia information retrieval (MIR'05). ACM, New York, pp 253–262

Delhumeau J, Gosselin PH, Jégou H, Pérez P (2013) Revisiting the VLAD image representation. In: Proceedings of the 21st ACM international conference on multimedia. ACM, pp 653–656

Fischler MA, Bolles RC (1981) Random sample consensus: a paradigm for model fitting with applications to image analysis and automated cartography. Commun ACM 24(6):381–395

Hartley R, Zisserman A (2003) Multiple view geometry in computer vision. Cambridge University Press, Cambridge/New York

Heinly J, Dunn E, Frahm JM (2012) Comparative evaluation of binary features. In: Computer vision–ECCV 2012. Springer, pp 759–773

Jegou H, Douze M, Schmid C (2008) Hamming embedding and weak geometric consistency for large scale image search. In: Computer vision–ECCV 2008. Springer, pp 304–317

Jégou H, Douze M, Schmid C, Pérez P (2010) Aggregating local descriptors into a compact image representation. In: IEEE conference on computer vision & pattern recognition, IEEE Computer Society, Washington DC, http://ieeexplore.ieee.org/document/5540039/

Kumar DS, Jawahar C (2006) Robust homography-based control for camera positioning in piecewise planar environments. In: Computer vision, graphics and image processing. Springer, pp 906–918

Lazebnik S, Schmid C, Ponce J (2006) Beyond bags of features: spatial pyramid matching for recognizing natural scene categories. In: IEEE computer society conference on computer vision and pattern recognition 2006, vol 2. IEEE, pp 2169–2178

Leutenegger S, Chli M, Siegwart R (2011) Brisk: binary robust invariant scalable keypoints. In: IEEE international conference on computer vision (ICCV 2011). IEEE, pp 2548–2555

Lowe D (1999) Object recognition from local scale-invariant features. In: The proceedings of the seventh IEEE international conference on computer vision 1999, vol 2. IEEE, pp 1150–1157

Lucas BD, Kanade T et al (1981) An iterative image registration technique with an application to stereo vision. In: IJCAI, IEEE Computer Society, Washington DC, vol 81. pp 674–679. http://ieeexplore.ieee.org/document/5540039/

Novak D, Batko M, Zezula P (to appear) Large-scale image retrieval using neural net descriptors. In: 38th ACM SIGIR international conference of research and development on information retrieval. Springer

Novak D, Zezula P (2014) Rank aggregation of candidate sets for efficient similarity search. In: Database and expert systems applications. Springer, pp 42–58

Perronnin F, Dance C (2007) Fisher kernels on visual vocabularies for image categorization. In: IEEE conference on computer vision and pattern recognition (CVPR'07). IEEE, pp 1–8

Philbin J, Chum O, Isard M, Sivic J, Zisserman A (2007) Object retrieval with large vocabularies and fast spatial matching. In: IEEE conference on computer vision and pattern recognition (CVPR'07). IEEE, pp 1–8

Razavian AS, Azizpour H, Sullivan J, Carlsson S (2014) CNN features off-the-shelf: an astounding baseline for recognition. In: IEEE conference on computer vision and pattern recognition workshops (CVPRW 2014). IEEE, pp 512–519

Rublee E, Rabaud V, Konolige K, Bradski G (2011) Orb: an efficient alternative to sift or surf. In: IEEE international conference on computer vision (ICCV 2011). IEEE, pp 2564–2571

Schroth G, Huitl R, Chen D, Abu-Alqumsan M, Al-Nuaimi A, Steinbach E (2011) Mobile visual location recognition. IEEE Signal Process Mag 28(4):77–89

Shi J, Tomasi C (1994) Good features to track. In: IEEE computer society conference on computer vision and pattern recognition (CVPR 1994). IEEE, pp 593–600

Sivic J, Zisserman A (2003) Video Google: a text retrieval approach to object matching in videos. In: Proceedings of the ninth IEEE international conference on computer vision (ICCV'03), vol 2, pp 1470. IEEE Computer Society, Washington, DC

Snavely N, Seitz SM, Szeliski R (2006) Photo tourism: exploring photo collections in 3D. In: ACM transactions on graphics (TOG), vol 25. ACM, pp 835–846

Tolias G, Bursuc A, Furon T, Jégou H (2015) Rotation and translation covariant match kernels for image retrieval. Comput Vis Image Underst 140:9–20

Weyand T, Leibe B (2015) Visual landmark recognition from internet photo collections: a large-scale evaluation. Comput Vis Image Underst 135:1–15

Yang X, Cheng KT (2014) Local difference binary for ultrafast and distinctive feature description. IEEE Trans Pattern Anal Mach Intell 36(1):188–194

Zhang Z (2000) A flexible new technique for camera calibration. IEEE Trans Pattern Anal Mach Intell 22(11):1330–1334

Chapter 21
RFID Sensors and Artifact Tracking

Marina Buzzi and Caterina Senette

Abstract As network bandwidth steadily increases and touchscreen mobile devices become ever more pervasive, objects achieve an electronic identity by actively building the "Internet of Things" (IoT). RFID technology as well as sensor networks (SN) are important elements in the creation of the IoT, with innovative customized apps designed around people. This chapter introduces basic features of RFID systems and discusses their potential in the field of cultural heritage protection and promotion. After a brief introduction, RFID is introduced, describing recent research improvements that integrate sensor ability in RFID (semi)passive tags. Next, we focus on its application in the field of cultural heritage, introducing related work and discussing possible scenarios of use. Finally, conclusions and future prospects end the chapter.

21.1 Introduction

The protection and preservation of cultural heritage is vital for our society. Cultural heritage contributes to education, empowering people with sensitivity to art and nature and facilitating learning in an informal setting. Moreover, knowledge of different cultures encourages respect and tolerance, helping create a social conscience. The United Nations Educational, Scientific and Cultural Organization (UNESCO) maintains a catalogue of World Heritage Sites whose cultural and physical significance are humanity's legacy. Legislation to protect monuments and works of art first appeared in Europe in the fifteenth century. Preservation of cultural heritage was first addressed in international law in 1907, and in the 1950s UNESCO and other intergovernmental organizations presented treaties for its protection in response to the destruction and looting of monuments and artwork during the Second World War (Blake 2000).

The current interest in cultural heritage preservation originates not only from simple protection of the historic, social, aesthetic, and scientific values of cultural assets but also from the economic returns that cultural heritage management can

M. Buzzi (✉) • C. Senette
Institute of Informatics and Telematics, National Research Council (IIT-CNR), Pisa, Italy
e-mail: marina.buzzi@iit.cnr.it; Caterina.Senette@iit.cnr.it

N. Masini, F. Soldovieri (eds.), *Sensing the Past*, Geotechnologies and the Environment 16, DOI 10.1007/978-3-319-50518-3_21

generate. Estimating the value of different artifacts or cultural aspects is a complex process and can be approached, economically speaking, by differentiating the intrinsic value of an opera, an art museum, or a well-preserved medieval city center from the positive economic impact on the local economy (jobs, revenues) derived from cultural investment (Bowitz and Ibenholt 2009).

Focusing our attention on tangible artifacts, people's attendance at museums, historical buildings, and other areas of interest is increasing. For instance, the Italian Ministry of Cultural Heritage and Activities and Tourism published statistics regarding the most visited cultural places in 2013 (museums, monuments, archaeological sites, and exhibitions in Italy), estimating that more than five million people visited the "Colosseum, Roman Forum and Palatine" archeological circuit, and more than two million explored the Pompeii excavation sites; further, 1,800,000 have accessed the "Galleria degli Uffizi" in Florence (more data are available at http://www.statistica.beniculturali.it/).

However, this increasing interest in exhibitions and auctions has encouraged the illicit trafficking of fakes and the theft of works of art. Investing in art is an attractive way for private individuals and companies to invest large amounts of money in small- or medium-size objects. With a business estimated at six billion US dollars per year (in 2002), the counterfeit and stolen artworks trade is considered the largest scale crime in the world after drug and gun trafficking (Jacob 2002). Counterfeiting and authentication of assets is so important that international investigative and police organizations are attempting to address it in different ways. Among possible solutions proposed in the literature for ensuring the protection of cultural assets in situ and during transportation, RFID systems could have an important role. This role could be exploited in particular during identification, transport, and authentication of works of art, although other technologies are the best choice in other phases, such as certification (e.g., carbon dating, statistical analysis of digital images), to verify the artwork's authenticity.

Preventing illicit trafficking in works of art, and thus combating the actions of criminal organizations, is the most important way to protect cultural heritage. Another aspect of the preservation of cultural assets is avoidance of accidental or malicious damage and prevention of wear caused by environmental variables (humidity, fire, etc.) or human intervention. As shown in recent studies (Bateman and Langford 1997; Tuan and Navrud 2008), the economic benefits accruing from the preservation of a cultural heritage site are enjoyed by both visitors and non-visitors. Visitors pay to access a site and benefit from the visit and non-visitors can still benefit from knowing that the cultural asset is being preserved. Another study by Ruijgrok et al. (2006), with an indicative cost–benefit analysis, shows that investment in conservation and in the development of security mechanisms for the most seriously threatened types of archaeological, geographic, and architectural heritage greatly outweigh the costs. Protecting a cultural asset means identifying it and monitoring its status over time in the environment where it is located, that is, knowing all the environmental variables that could endanger it. Moreover, the correct management of a cultural asset during transport from one site to another as well as the prevention of useless transfers or access to their box for inventory

and cataloguing purposes increase protection. Once again, the best candidate for this type of cultural asset management is RFID (radiofrequency identification) technology, which naturally provides identification and inventory functions without requiring a line of sight, as discussed in detail in the next section.

Tourists are increasingly demanding cultural experiences. In the past 20 years, museums have developed policies to share digital cultural resources using technology, starting with local indoor installations, moving to websites and social networks, and finally becoming mobile available via apps. This innovative communication policy blurs boundaries between an in situ physical museum and its associated digital resources (Dupuy et al. 2015). RFID has been successfully applied in creating personalized enriched experiences, enabling artifacts to be active elements in the user experience in a variety of ways, such as enriching their personal web pages as an accessible multimodal museum guide, or triggering other enriching functions depending on user actions. In this scenario of tracking and identification, security and privacy have a fundamental function.

21.2 RFID Systems

Since 1940, radiofrequency has been exploited for identification purposes, first in the military environment and later for civil applications, tracking or identifying objects, animals, and humans. An RFID (radiofrequency identification) system consists of a set of tags and readers, which enable the identification of tagged items, exploiting radio transmissions. Tags can be passive, active (battery-powered), or semi-passive. In passive tags, the communication exploits the energy induced by the reader. A passive tag is a radiofrequency transponder including a small integrated circuit (chip) with simple control logic and data storage functions. The chip is connected to an antenna and embedded in a paper label or wrapped into a package. These tags allow the transmission of data at short range without physical contact.

The reader consists of a transceiver controlled by a microprocessor able to communicate with the tag, retrieving all its information. Middleware software between the RFID system and the application configures and coordinates the hardware components, such as readers, printer-encoders, and motion sensors and processes and aggregates tag data, filtering out duplicate tag reads (O'Connor 2010).

Tags store information (including a factory-unique identifier) that can be accessed by readers. Because tags in the reader's read cone are activated simultaneously, the inventory is one fundamental feature provided by RFID, successfully applied in the transportation and logistics industry, where reducing cost and inefficiency are important targets. Moreover, the unique identification enables the tracking of tagged objects if an RFID infrastructure composed of multiple readers is available.

Readers and tags can operate in a range of frequencies (low, high, ultrahigh, microwave) offering different properties and limits, best matching different applications requirements. The reading distance depends on the frequency and on the size

Fig. 21.1 RFID readers and (semi)passive tags (Courtesy of CAEN RFID)

of the reader/tag antenna(s). Larger antennas increase the read distance. Small-sized handheld readers decrease the reading distance but by allowing easy interaction in the environment enhance the read chance (percentage of successful reads), because movement modifies the angle between the tag antennas and reader's read cone.

Tags form a kind of distributed memory that keeps the access keys to the network database, where additional information is stored. This infrastructure enables the creation of customized services to facilitate interaction and improve user experience. Passive tag's memories today extend up to 8 or more Kbytes (the second writable memory bank for Gen 2 ICs) (Dobkin 2007). An industry-driven standard distinguishes categories of products (Electronic Product Code EPCGlobal).

Enriching objects and the surrounding environment with tags and readers is possible to monitor an area of interest. Technically speaking, RFID transmission utilizes electromagnetic or electrostatic coupling in the range of the electromagnetic spectrum typical of radio waves. The unique identification enables operations such as selection, spatial localization, search, and tracking. The system's components communicate via radio signals and do not require physical contact or mutual visibility. This peculiarity distinguishes them from barcodes and QR codes (Fig. 21.1).

A variety of parameters depending on frequency and power need to be considered to optimally fit the needs of any specific application. Regarding power, we can distinguish between passive tags, semi-passive tags, and active tags:

- Passive tags: take advantage of the radio wave generated by the reader during the communication. Without an embedded transmitter they are smaller, and for this reason they can be inserted into cards and small objects.
- Semi-passive tags: equipped with a battery used to power the microchip or auxiliary devices (sensors), they have a great amount of rewritable memory. The transmission process works like that of passive tags.

– Active tags: equipped with batteries, they incorporate a receiver and a transmitter. Generally they are used in combination with environmental sensors and can trigger processes when environmental changes are detected.

Regarding frequency, each range exploits a specific technology and causes different system properties, as summarized in Table 21.1.

Communication modes of RFID systems are very heterogeneous. Some applications require reading passive tags from a distance of a few inches whereas others need to read active tags at a distance of several hundred meters. Every application has different requirements and constraints, so a feasibility field study must be performed in the actual environment to select the best frequency and tags.

In the field of cultural heritage, LF (low), HF (high), and UHF (ultrahigh) frequencies associated with passive tags have been widely adopted whereas active tags, more powerful but more costly, are usually exploited when small sets of expensive objects are tagged. Passive tags are especially convenient because they are small, cheap, and have a potentially infinite life.

Limits of RFID application are typical of the technology. Depending on the frequency reflection, shading and absorption phenomena can interfere with the reading process. For this reason, when RFID technology is applied, a feasibility study is necessary, involving the real objects and devices. Different frequencies have different issues. Tag reading can be challenging depending on the features of tagged items, that is, size, composition of materials, packaging, and tag placement. Three issues impact the reading: RF reflection caused by metals, shading from multiple antennas placed very close to one another, and absorption produced by liquids.

Furthermore, tag placement (i.e., its physical position in space) is crucial: in the worst case, if antenna and tag are perpendicular to one another, the reading may fail, whereas motion favors tag reading; that is, an operator with a handheld reader moves around tagged objects.

A wireless sensor is a device that can sense and communicate environmental variables (to catch their measurable changes) or detect environmental events producing an electrical or optical output. Wireless sensors can form a network (WSN) enabling the monitoring of different locations from one central station. RFID systems were created as a complementary technology with respect to the WSN. RFID readers and passive tags communicate their presence using minimal circuitry able to emit radio signals, which makes them low-cost, easy-to-use devices. The interoperability between RFID systems and wireless sensors opens the way to a wide range of applications needed to sense environmental conditions and receive information about neighboring objects, effectively extending the range of applicability of the RFID technology itself (Liu et al. 2007, 2008).

Today, new-generation semi-passive tags have the ability to sense several environmental parameters such as light, humidity, and temperature, becoming a key technology for “object-based” services. In the following, we report main research activities grounding and fueling these technological advances.

Several approaches combining an RFID tag with an energy-efficient and chip-embeddable sensor have been investigated (Duroc and Vera 2014). At present, only

Table 21.1 RFID technologies grouped by frequency

	Frequency range	Technology	Protocols	Reading distance	Features
LF	125/134 kHz	Passive tag	ISO 11784/5, 14,223	∼0.1 m	Low data rates
			ISO 18000–2 HiTag		
HF	13.56 MHz	Passive tags	MIFARE	∼1 m	High data rates/small size. Performs poorly in large groups.
			ISO 14443		
			ISO18000–3		
UHF	860–960 MHz	Passive tags	EPC class 0	∼2–7 m	High data rates/small size/high distance of reading. Ideal for large groups.
			EPC class 1		
			ISO 18000-6A, B, C		
		Semi-passive Tags	AAR S918, Intelliflex		
Microwave	2.4 GHz	Passive	ISO 18000–4 Intellitag/ μ-chip	10 m	Miniaturized tags/ frequency range shared with other technologies (WiFi, Bluetooth, ZigBee),
		Semi-passive	ISO 18000–4		
		Active	ISO 18000–4	30–50 m	

a few kinds of sensors satisfy such requirements: temperature, light, and pressure sensors are the most common (Vaz et al. 2010, Virtanen et al. 2010). Because sensor embedding increases both tag size and cost, an alternative solution is the functional integration of the antenna and the sensor component: the challenge is to transform the RFID tag antenna in a sensor. The antenna has three different sensitive regions: inductive region, near-field, and far-field, with different properties. The most interesting region is the near-field because any other element located in this region could be coupled with the antenna, interfering with the radiation pattern and changing the impedance of the antenna itself (Dobkin 2007). This effect has been exploited by Bhattacharya et al. (2009) to design a displacement sensor. The technology is currently oriented to creating cheap intelligent RFID tags that can combine sensing, computation, and communication in a single small device (Pesonen et al. 2009), integrating special materials in the tag antenna to sense environmental parameters. Capdevila et al. (2010) presented a passive multi-probe sensor using conventional UHF-RFID tags that implements impedance-based sensing with RFID probes able to detect those parameters that impact the dielectric permittivity and hence the tag antenna impedance.

Recently, Catarinucci et al. (2013) presented the Sensor-Tag (S-Tag) prototype and an augmented module for smart environmental sensing (RAMSES), which is a fully passive device with sensing and computation capabilities, showing the ability to harvest the RF energy emitted by an interrogator placed up to 10 m of distance and autonomously perform sensing, computation, and data communication (Catarinucci et al. 2013, De Donno et al. 2014).

Another type of sensing that could be useful in the context of protection of works of art is exploited with a prototype built by Todd et al. (2009), a battery-free threshold shock sensor with wireless readout via RFID circuitry, designed to provide low-cost sensors for monitoring shock loads in applications such as shipping.

Moving from simple passive tags to smart tags that can perform different functions thanks to integrated sensors and a microcontroller unit (MCU), we can extend the role of RFID systems in ubiquitous computing. An example has been developed (Yeager et al. 2008) in the form of a passive data logger (PDL) tag that records data over time or in relationship to location (wireless identification and sensing platform, WISP). However, being more expensive than passive RFID tags, it is not suitable for mass use.

Furthermore, a recent trend in logistics operations is to move the intelligence from tags to smart envelopes able to sense environmental variables as well as shock conditions for monitoring the integrity of their contents. In this way it is possible to reduce cost for various single items to an envelope containing several items.

21.3 Artifact Identification and Tracking via RFID

21.3.1 Management of Works of Art

The management of cultural assets involves two main scenarios: (1) monitoring during transport (moving objects) and (2) in situ control, to detect movement and possibly prevent theft or unauthorized handling (and possible damage). In the first scenario the work of art travels from its original location to an exhibition site or auction. Tracking the assets over an extended area involves geo-tracking monitoring and GPS systems. GPS calculates the user's three-dimensional (3D) position as well as other useful information such as speed, bearing, track, trip distance, distance to destination, and sunrise and sunset time (Bajaj et al. 2002). Because GPS is not designed for indoor use or in urban areas, wireless local area networks can substantially improve its performance in such environments (Bajaj et al. 2002). The association of the European Satellite Navigation infrastructure for civil use, GALILEO, can be exploited to overcome the limits of GPS technology when tracking cultural assets in "urban canyons" (Costantini et al. 2008; CUSPIS 2007).

In the context of secure transportation of cultural assets, RFID technology can be applied to prevent theft or damage of the assets, considering each truck as an indoor system to be controlled. Specialized transport companies guarantee protection during the journey using special packages, strongboxes, and security escorts. The Euridice EU project has investigated logistics and security aspects by dynamically combining the RFID-tagged cargo item, mobile users, and vehicle services. For example, a shipping container is under the range of sensors to monitor all its contents and its whereabouts, whereas a package is tagged with an RFID tag for logistics operations (inventory and destination). A protocol for secure transport of assets through a technological infrastructure for monitoring cargo has been proposed by Mostarda et al. (2010). Trusted experts insert in each package: (1) the set of cultural assets defined in the authorization certificate and equipped with an RFID passive tag; (2) temperature, light, and humidity sensors; (3) motion sensors for detecting movement inside the package; (4) sensors to measure the distance between two surfaces inside the package; and (5) an asset on board unit (ABU), a PDA governing all sensors. Last, a transport control unit (TCU) is installed on the roof of the truck to forward the position and time information provided by the positioning system. The reliability of package unwrapping detection depends on differences between inside and outside (package) values of temperature, humidity, and light that are vital in detecting unwrapping. When the differences are significant, an alarm is triggered. Differences in sensor readings can be achieved by isolating internal package conditions from the external ones. For instance, for light and humidity, packages composed of polystyrene and silicone can be used. Humidity depends on the artifact's material (e.g., wood, terracotta, or ceramic) and can be modified using dehumidification materials. For temperature, a small heater can be connected to a thermostat for constant values, which would ensure the integrity of the package during the journey (Mostarda et al. 2010).

The second scenario addresses the problem of monitoring assets in their location (such as a museum). Different tracking systems can be adopted depending on the site. If the cultural asset is located in an open area (i.e., an archaeological area) it can be tracked using the usual GPS system improved with the regional satellite-based augmentation system (EGNOS overlay).

If the cultural asset is located indoors (e.g., a museum), and its position cannot be determined using a GNSS (global navigation satellite system), RFID technology could offer an effective tracking solution. The cultural asset equipped with an RFID tag communicates its presence to an RFID reader that forwards it to control software. If this information does not reach the control center, an alarm/warning event is triggered. In addition, a position transmitter can be installed on the cultural asset so that if it leaves its standard position (for instance, because of theft) its movements can be tracked (Mostarda et al. 2010). These types of systems are mainly used for localization purposes. Another problem is RFID space coverage; to improve space coverage for localization purposes, Jinseok Lee et al. propose an object-tracking algorithm based on association with an RFID coverage scheme and a visual sensor. They first estimate the location of objects using multiple sensor nodes with an RFID virtual sensor, which is a combination of RFID readers having a reference point that represents the center of possible positions. The detection from readers with proximity to each object results in coarse localization. Image frames from two cameras improve the estimation, close to a real position based on a parallel projection model. The visual compensation sufficiently accomplishes the refined tracking, showing good localization performance (Lee et al. 2007).

Cultural asset management system services could enhance culture/art fruition and improve the security of cultural assets, adherence to international standards, and reduction of insurance costs, discouraging crime and possibly reducing theft risk.

21.3.2 Protection of Works of Art

Authentication has a fundamental role in many applications. Authentication guarantees that the artifact is original and not counterfeit. Cultural assets go through an authentication process performed by a qualified organization and managed by official departments. Sometimes, different authentication procedures are necessary for different parts of the same artifact to have a complete guarantee of the procedure's trustworthiness. This process generates a certificate vouching for the authenticity of the cultural asset. RFID systems can have a part in this scenario, storing certification codes associated with the tagged work of art. Using an additional security feature such as an RFID label to authenticate an asset requires definition of the conditions under which the authenticity of the security feature guarantees that the product itself is genuine (Lehtonen et al. 2008). Authenticating the tags is crucial for guaranteeing the originality of the cultural asset.

Compared to older authentication technologies, the advantages of RFID include non-line-of-sight reading, unique ID identification, availability of dynamic security features, and cryptographic resistance against cloning. The potential of RFID in anti-counterfeiting is further discussed by Staake et al. (2005).

RFID product authentication can be achieved by adding some security features to the transponder or using additional processing based on online product data. The main challenge for an RFID tag is to resist to cloning and forgery. The simplest cloning attack requires reading the tag serial number and programming the same number into another empty tag. To prevent this kind of attack, even the low-cost transponders (EPC Class-1 Generation-2) are equipped with a unique factory-programmed chip serial number, so to clone this number it is necessary to access hardware manufacturing data (EPC global 2005). The use of cryptographic challenge response protocols also provides significant improvement in a tag's cloning resistance, but they are vulnerable to data theft if the secret PIN codes or encryption schemes of valid products are stolen or sold to a third party to create faked tags. Nevertheless, as described in the literature there are several techniques for conducting a cloning attack against a single tag: side channel attack (RFID Journal 2006), reverse-engineering and cryptanalysis (Bono et al. 2006), brute-force attack (RFID Journal 2003), physical attacks (Weingart 2000), and different active attacks against the tag. Another attack against RFID systems that has important consequences for the overall process is denial of service (DoS); an example of DoS is desynchronizing tag and the database entry (Fu et al. 2010). Substantially, this type of attack can be carried out on basic RFID tags and must be addressed while maintaining the economical characteristics of the tag itself.

RFID tag memory can be exploited to provide authentication based on a biometry paradigm (analogue fingerprinting) on mobile devices (Schirripa et al. 2014). The proposed method uses an RFID tag, a 2D barcode, and an internet authentication archive. The authentication is based on a digital signature that combines the identification number and the product's unique random features. For a painting, these features could be the surface texture, or a high-resolution photograph of a detail of the painting, which presents intrinsic randomness because of its hand-made process.

Mostarda et al. (2007) describe the GTA (Geo-Time Authentication system) service for supporting archaeological discoveries and geo-referencing for mapping, identifying, and quickly positioning new cultural assets. Taking advantage of the GALILEO satellite to certify the origin and travels of the artwork, the system uses public key certificates and timing information to authenticate artifacts and to ensure security in their transport (Stalling 2006; Pozzobon et al. 2004). Geo-time authentication could be useful in art transport, inserting the destination coordinates in the certification phase. Identification, authentication, and secure transport supported by the satellite could be a deterrent to organized crime, thus making museums more confident about lending works of art. Smart RFID tags enriching security features are very useful when tagged objects have a relevant economic social and artistic value (Pateriya and Sharma 2011).

Concerning security, some kinds of advanced RFID devices implement basic access control mechanisms, cryptographic operations, cloning resistance, and one-time writing (Tuyls and Batina 2006; Juels and Weis 2005; Juels 2006). Of course, advanced active RFIDs still can be attacked; for example, they can be physically handled by an adversary, and they can be breached with appropriate technologies and be reused. In Lehtonen et al. (2007), counterfeiting of assets is opposed by means of a probabilistic-based approach for location-based authentication, using past location of products to detect counterfeit assets, as the history of a cultural asset is often used in authentication. However, because this past information is often unavailable it is easier to exploit information related to future locations rather than a previous one (Mostarda et al. 2007).

21.3.3 Smart Environments

Pervasive computing and localization technologies have been increasingly applied in the field of cultural heritage. Multimodal mobile devices have enabled a natural intuitive interaction, improving user experience. LF, HF, and UHF RFID have been increasingly exploited. Passive UHF tags offer a reading range that relaxes the proximity constraint of lower frequencies, enabling the reading from a distance of half a meter and more.

In near-field communication (NFC), for example, LF RFID technology is incorporated in modern smart phones such as Android and iOs devices, offering new interaction opportunities. Ceipidor et al. investigated the use of NFC to enhance user experience by retrieving additional content and accessing social activities using a smart phone (Ceipidor et al. 2013). Participatory design (PD) techniques are key factors in the design process because they enable the production of artifacts and services that are fully usable by users. Cober et al. (2012) applied PD techniques to simplify interaction for blind users and improve his or her experience in the museum.

Another branch of research focuses on enriching and adapting user experience, also benefiting from social activities. Karimi et al. (2012) investigated the recommender system for museums, by "sniffing" the surrounding environment using RFID technology. Similarly, Mody et al. (2009) exploited RFID and adapted recommender systems for personalizing platforms for the museum. However, observing user activities may pose privacy and security issues that must be carefully analyzed. Çayırezmez et al. (2013) investigates the use of RFID technology in the museum to overcome problems with inventories and security tracking, and to enable dynamism in artifact presentation, observing that this process requires adaptation to museum characteristics (needs, infrastructure, artifacts) and staff training.

Concerning social activities, sharing creates interest, attracts people to the exhibition, and allows people who miss the visit to still enjoy it. Kostoska et al. (2013) investigate sharing of memory data after a visit to a museum or exhibition

by performing surveys and trials showing that users can significantly enhance their experience when provided with simple and easy-to-use tools.

Detection of Indoor Mobile Objects with RFID Location-Based Service An emerging application of RFID is the indoor real-time localization system (RTLS) for supporting tasks including navigation, localization, mapping, and service applications based on people tracking and profiling. Tracking people inside the museum enables the creation of smart environments, providing personalized context-aware information based on a user's location. As already described, indoor environments are unsuitable for the GPS technique, Wireless Local Area Network (WLAN) devices are more expensive and larger than RFID tags, and Ultra Wide Band (UWB) systems can potentially interfere with some radar systems. Other non-RF-based techniques, such as ultrasonic, infrared (IR), and laser localization, are vulnerable to environmental impact and are restricted to line-of-sight (LOS) readability (Wu 2012). Several studies investigate the use of RFID for localization, aiming to decrease issues from the signal multi-path propagation and to support the greatest advantage(s) of (semi-)passive RFID tags: low price and ultra-small size (Wu 2012; Rahmati et al. 2007; Jingwangsa et al. 2010).

Location-based service (LBS) was investigated by Hahnel et al. (2004). To verify whether RFID technology can be used to improve the localization of RFID tags in movement, the authors used a robot equipped with a pair of RFID antennas. Making use of a previously created map and applying a probabilistic measurement model for RFID readers, the platform allows accurate localization of RFID tags in the environment. Considering that a location system requires a high positioning accuracy of about 1 m, and the traditional RFID systems can detect low-cost passive tags in the range of several meters, these improvements in the detection range of passive tags makes this technology more and more attractive.

Ambient Intelligence (AmI) In museums, location-based systems have additional challenging constraints: high accuracy is required because of the density of objects, and hardware components have to be invisible and noninvasive in regard to environments and artifacts. Until now, two types of technology have been widely experimented: infrared (IR)-based positioning and radiofrequency (RF)-based positioning. Currently, although many studies address the problem, there is still no universally valid and efficient solution; some systems need much equipment, whereas others are not very accurate or require user actions with poor usability and consequently bad user experiences (Kuflik et al. 2011). In the following, some attempts to address the problem are summarized.

Angelaccio et al. (2012) described an AmI-based information system, based on NFC technology, developed to access Cultural Heritage Areas in which different objects of artistic interest can be interfaced in a virtual way without affecting the historical environment. The goal is to apply noninvasive technology such as NFC to improve the system's context awareness, allowing users to receive customized information in a transparent way via mobile devices.

To achieve accurate localization information on a visitor or a group of visitors moving around a cultural heritage building, an effective low-cost system providing localization information is proposed by Mazzenga et al. (2010). It is based on the deployment of a very large number of passive RFID tags arranged inside the cultural area using adhesive tape. Because of the adoption of smart tagged RFID tapes, the setup and maintenance of the system are greatly simplified independently of the area (indoors or outdoors) where the localization system is deployed. Using the spatial map of recorded tag positions, the central systems that receive the radio signals from the excited tags can extract position information of the terminal by simply calculating the average of the coordinates of the detected tags. Results from a pilot study suggest that accuracy below 1 m can be theoretically achieved by properly selecting the density of RFID tags, for example, the number of smart tapes and the tags' distance on the tape.

Kuflik et al. (2011) proposed a solution that minimizes complexity while providing accuracy within 1.5–2 m from the object of interest. A museum is equipped with a radiofrequency (RF)-based positioning system relying on a wireless sensor network (WSN) composed of ad hoc RF devices. The WSN operates on the 2.4 GHz ISM band and is based on the 802.15.4 protocol, the underlying layer of the ZigBee protocol. The WSN is formed by three different kinds of objects: fixed RF tags (Beacons), small (matchbox size) mobile wearable RF tags (Blinds), and RF to TCP Gateways.

Kuo et al. (2009) introduced RFID for context-aware museum services in Korea (U-Museum applications): Temperature and Relative Humidity Monitoring System, Product and Asset Management System, Guide System. and Card System. In terms of preservation, the temperature and humidity monitoring system based on RFID sensors allows control over the environment, ensuring more precise protection of works of art, and is timesaving for operators. The U-Museum RFID Card provides integrated and personalized services such as self-directed tours while assuring efficient management of visitor flow.

21.4 Conclusions

After more than two decades, the visionary idea of Marc Weiser (1991) is still valid: user interfaces are disappearing in everyday objects with increasing functional capabilities. Indeed, the internet of objects is steadily pervading our life, and any current technological limits and constraints may soon be overcome. In the near future IoT main actors—RFID and sensors—could become more and more convergent, because miniaturizing and processing are rapidly progressing. In the field of art and culture this scenario would evolve quickly, creating new potential for the promotion and protection of cultural heritage.

The identification, tracking, and monitoring of cultural assets has several constraints including easy certification, effective authentication, and secure transport of artifacts. RFID in association with other technologies can increase the probability

of early detection of events, improving the overall level of protection of the cultural asset. Moreover, smart environments for smart customized services in the museum and other cultural areas can be created on an RFID infrastructure composed of tagged assets, readers, network connections, and middleware software. Intelligent RFID-based localization would offer user-centered access to works of art, increasing the number of users and enhancing their experience.

However, although RFID has been available for many years, it is still not pervading the cultural heritage field very quickly, possibly for two reasons: (1) some problems may arise when tagging several collections of heterogeneous artifacts depending on the frequency, and (2) the cost of an RFID infrastructure that needs to change the usual procedures, adapt the existing software, and integrate it with databases. Although a 100% reading accuracy remains a challenge from several physical conditions, the current level of accuracy could enhance management of cultural assets and it can rapidly compensate for the initial cost of infrastructure. In addition, it enables a set of value-added applications including augmented inventory efficiency, reducing errors and decreasing human effort, accurate identification, easy monitoring and tracking of artifacts, and improvement of (social) experience in cultural sites.

Probably one of the main challenges today remains the creation of a global RFID infrastructure that can be exploited by various actors and stakeholders to create a range of customized services and apps for simple interaction via touchscreen mobile devices, actively contributing to bringing the IoT to its full potential.

References

Angelaccio M, Basili A, Buttarazzi B, Liguori W (2012) Smart and mobile access to cultural heritage resources: a case study on Ancient Italian Renaissance Villas. In: IEEE 21st international workshop on enabling technologies: infrastructure for collaborative enterprises (WETICE), pp 310–314

Bajaj R, Ranaweera SL, Agrawal DP (2002) GPS: location-tracking technology. Computer 35(4):92–94

Bateman IJ, Langford IH (1997) Non-users' willingness to pay for a National Park: an application and critique of the contingent valuation method. Reg Stud 31(6):571–582

Bhattacharya R, Florkemeier C, Sarma S (2009) Towards tag antenna based sensing-An RFID displacement sensor. In: Proceedings of international conference on RFID, pp 95–102

Blake J (2000) On defining the cultural heritage. Int Comp Law Quart 49:61–85. doi:10.1017/S002058930006396X

Bono S, Green M, Stubblefield A, Juels A, Rubin A, Szydlo M (2006) Security analysis of a cryptographically enabled RFID device. Pre-print. Available at www.rfidanalysis.org

Bowitz E, Ibenholt K (2009) Economic impacts of cultural heritage–research and perspectives. J Cult Herit 10(1):1–8

Capdevila S, Jofre L, Bolomey JC, Romeu J (2010) RFID multi-probe impedance-based sensors. IEEE Trans Inst Measur 59(12):3093–3101

Catarinucci L, Colella R, Tarricone L (2013) Enhanced UHF RFID sensor-tag microwave and wireless components letters. IEEE 23(1):49–51

Çayırezmez NA, Aygün HM, Boz L (2013) Suggestion of RFID technology for tracking museum objects in Turkey. In: Digital heritage IEEE International Congress, vol 2, pp 315–318

Ceipidor UB, Medaglia CM, Volpi V, Moroni A, Sposato S, Carboni M, Caridi A (2013) NFC technology applied to touristic-cultural field: a case study on an Italian museum. In: The 5th international workshop on near field communication (NFC)

Cober R, Au O, Son JJ (2012) Using a participatory approach to design a technology-enhanced museum tour for visitors who are blind. In: Proceedings of the 2012 iConference ACM, New York, pp 592–594. doi:10.1145/2132176.2132301

Costantini S, Mostarda L, Tocchio A, Tsintza P (2008) DALICA: agent-based ambient intelligence for cultural-heritage scenarios. Intell Syst IEEE 23(2):34–41

Cultural Heritage Space Identification System (CUSPIS) (2007) European commission 6th framework program—2nd call Galileo joint undertaking http://www.gsa.europa.eu/fp6-cuspis-project

De Donno D, Catarinucci L, Tarricone L (2014) RAMSES: RFID augmented module for smart environmental sensing. IEEE Trans Instrum Meas 63(7):1701–1708

Dobkin DM (2007) The RF in RFID: passive UHF RFID in practice. Elsevier-Newnes, Amsterdam

Dupuy A, Juanals B, Minel, J-L (2015) Towards open museums: the interconnection of digital and physical spaces in open environments. MW2015: Museums and the Web 2105, Chicago, USA

Duroc Y, Vera GA (2014) Towards autonomous wireless sensors: RFID and energy harvesting solutions. In: Internet of Things. Springer International Publishing, pp 233–225

EGNOS (European Geostationary Navigation Overlay Service): www.esa.int/

EPC global standard powered by GS1: Object Naming Service (ONS) 5 Version 1.0 (2005)

EPCglobal (2005). Class-1 Generation-2 UHF RFID Conformance Requirements Specification v. 102 EPCglobal public document, February 2005

Fu Y, Zhang C, Wang J (2010) A research on Denial of Service attack in passive RFID system. In: International conference on anti-counterfeiting security and identification in communication (ASID). IEEE, pp 24–28

Hahnel D, Burgard W, Fox D, Fishkin K, Philipose M (2004) Mapping and localization with RFID technology. In: robotics and automation, ICRA '04.2004 IEEE international conference 1, pp 1015–1020

Jacob J (2002) Counterfeit art—how to keep it out of your collection. Chubb Collectors

Jingwangsa T, Soonjun S, Cherntanomwong P (2010) Comparison between innovative approaches of RFID based localization using fingerprinting techniques for outdoor and indoor environments. In: Advanced Communication Technology (ICACT), 2010 The 12th international conference on (vol. 2, pp 1511–1515). IEEE

Juels A (2006) Rfid security and privacy: a research survey. IEEE J Select Areas Commun

Juels A, Weis SA (2005) Authenticating pervasive devices with human protocols. In: Advances in cryptology–CRYPTO 2005. Springer, Berlin/Heidelberg, pp 293–308

Karimi R, Nanopoulos A, Schmidt-Thieme L (2012) RFID-enhanced museum for interactive experience. Springer Multimedia for Cultural Heritage Communications in Computer and Information Science 247:192–205

Kostoska G, Fezzi D, Valeri B, Baez M, Casati F, Caliari S, Tarter S (2013) Collecting memories of the museum experience. In: CHI '13 extended abstracts on human factors in computing systems (CHI EA '13). ACM, New York, pp 247–252

Kuflik T, Lanir J, Dim E, Wecker A, Corrá M, Zancanaro M, Stock O (2011) Indoor positioning: challenges and solutions for indoor cultural heritage sites. In: Proceedings of the 16th international conference on Intelligent user interfaces (IUI '11), pp 375–378

Kuo CW, Chiang JK, Lin QP (2009) The research on applying RFID information system architecture for museum service. In: Fourth international conference on computer sciences and convergence information technology, pp 218–222

Lee J, Park KS, Hong S, Cho WD (2007). Object tracking based on RFID coverage visual compensation in wireless sensor network. In: ISCAS 2007. IEEE international symposium on circuits and systems. IEEE, pp 1597–1600

Lehtonen M, Michahelles F, Fleisch E (2007) Probabilistic approach for location-based authentication. In: 1st international workshop on security for spontaneous interaction IWSSI 2007

Lehtonen M, Staake T, Michahelles F (2008) From identification to authentication–a review of RFID product authentication techniques. In: Networked RFID systems and lightweight cryptography. Springer, Berlin/Heidelberg, pp 169–187

Liu H, Bolic M, Nayak A, Stojmenovi I (2007) Integration of RFID and wireless sensor networks. In: Sense ID 2007 workshop at ACN SenSys, pp 6–9

Liu H, Bolic M, Nayak A, Stojmenovic I (2008) Taxonomy and challenges of the integration of RFID and wireless sensor networks. In: IEEE network, pp 26–32

Mazzenga F, Simonetta A, Giuliano R, Vari M (2010) Applications of smart tagged RFID tapes for localization services in historical and cultural heritage environments, 2010 19th IEEE international workshop on enabling technologies: infrastructures for collaborative enterprises WETICE, pp 186–191

Mody A, Akram M, Rony K Aman MS, Kamoua R (2009) Enhancing user experience at museums using smart phones with RFID. In: Proceedings of the systems, applications and technology conference. LISAT '09. IEEE Long Island, pp 1–5

Mostarda L, Tocchio A, Inverardi P, Costantini S (2007) A geo time authentication system. In: Trust management. Springer, New York, , pp 123–138

Mostarda L, Dong C, Dulay N (2010) Context-based authentication and transport of cultural assets. Pers Ubiquit Comput 14(4):321–334

O'Connor MC (2010) A guide to RFID middleware. RFID J

Pateriya RK, Sharma S (2011) The evolution of RFID security and privacy: a research survey. In: International conference on communication systems and network technologies (CSNT), pp 115–119. IEEE

Pesonen N, Jaakkola K, Lamy J, Nummila K, Marjonen J (2009). Smart RFID tags, development and implementation of RFID technology. In: Turcu C (ed). InTech. ISBN: 978–3–902613-54-7

Pozzobon O, WuUems C, Kubic K (2004) Secure tracking using trusted GNSS receivers and GALILEO authentication services. J Global Posit Syst

Rahmati A, Zhong L, Hiltunen M, Jana R (2007, June) Reliability techniques for RFID-based object tracking applications. In: Dependable systems and networks, 2007. DSN'07. 37th annual IEEE/IFIP international conference on IEEE, pp 113–118

RFID Journal (2003) RFID, privacy and corporate data. Feature Article, June 2, 2003. Available at http://www.rfidjournal.com on subscription basis

RFID Journal (2006) EPC tags subject to phone attacks. News Article, February 24. Available at http://www.rfidjournal.com/article/articleview/2167/1/1/ (4.5.2006)

Ruijgrok ECM (2006) The three economic values of cultural heritage: a case study in the Netherlands. J Cult Herit 7(3):206–213

Schirripa G, Cozzella L, Caciotta M, Colasanti R, Ferrari G (2014) Analogue fingerprinting for painting authentication 20th IMEKO TC4 international symposium and 18th international workshop on ADC modelling and testing research on electric and electronic measurement for the economic upturn Benevento, Italy, 15–17 September 2014

Staake T, Thiesse F, Fleisch E (2005) Extending the EPC network – the potential of RFID in anti-counterfeiting. In: Proceedings of the 2005 ACM symposium on applied computing. ACM Press, New York, pp 1607–1612

Stallings W (2006) Cryptography and network security: principles and practice, 4th ed. Prentice Hall

Todd B, Phillips M, Schultz SM, Hawkins AR, Jensen BD (2009) Low-cost RFID threshold shock sensors. IEEE Sensors J 9(4):464–469

Tuan TH, Navrud S (2008) Capturing the benefits of preserving cultural heritage. J Cult Herit 9(3):326–337

Tuyls P, Batina L (2006) RFID-tags for anti-counterfeiting. In: Topics in cryptology–CT-RSA 2006. Springer, Berlin/Heidelberg, pp 115–131

Vaz A, Ubarretxena A, Zalbide I, Pardo D, Solar H, Berenguer R (2010) Full passive UHF tag with a temperature sensor suitable for human body temperature monitoring. Circuits and systems II: express briefs, IEEE Transactions on, 57(2), 95–99

Virtanen J, Ukkonen L, Björninen T, Sydänheimo L (2010) Printed humidity sensor for UHF RFID systems. In: Sensors applications symposium (SAS), 2010 IEEE, pp 269–272

Weingart S (2000) Physical security devices for computer subsystems: a survey of attacks and defense. In: Cetin Kaya Koc, Christof Paar (eds) Proceedings of CHES'00, 1965 of lecture notes in Computer Science. Springer, pp 302–317

Weiser MD (1991) The computer for the 21st century. Scientific American Special Issue on Communications, Computers, and Networks, pp 66–75

Wu J (2012) Three-dimensional indoor RFID localization system. Ph.D. dissertation

Yeager DJ, Powledge PS, Prasad R, Wetherall D, Smith JR (2008, April) Wirelessly-charged UHF tags for sensor data collection. In: IEEE international conference on RFID, pp 320–327

Part IV
From Artifact to Historical Sites: Case Studies and Applications

Chapter 22
Detection of Maya Ruins by LiDAR: Applications, Case Study, and Issues

Arlen F. Chase and Diane Z. Chase

Abstract The study of ancient Mesoamerican landscapes and settlement has been significantly impacted in a positive way through the application of LiDAR (light detection and ranging). LiDAR has permitted the recovery of ground data from huge regional areas that are currently under a tropical canopy: the use of traditional methods of survey and mapping could never have resulted in the detailed data that are available through LiDAR. The analyses of LiDAR data are a conjunctive task that involves archaeologists with physicists and computer scientists. This interdisciplinary effort is producing new results and interpretations for all fields, but has also raised issues that need resolution, particularly involving data storage and distribution. LiDAR has already transformed the way in which Mesoamerican settlement survey is done, and future collection of LiDAR data will benefit Mesoamerica through helping to preserve a landscape of the past.

Keywords LiDAR • Settlement archaeology • Landscape archaeology • Maya • Mesoamerica

22.1 Introduction

For the ancient Maya area, LiDAR (light detection and ranging) has replaced all other remote sensing technologies as the most desirable tool for researching ancient settlement systems. In its ability to penetrate the tropical and subtropical canopy to reveal large areas of settlement, LiDAR is revolutionizing our understanding of the ancient Maya landscape and use of space (Chase et al. 2012). It is providing the means to study site size and population density, as well as large- and small-scale land modifications. Given the general absence of preexisting government or industry

A.F. Chase (✉)
Department of Anthropology, University of Nevada, Las Vegas, 4505 S. Maryland Parkway, Box 455003, Las Vegas, NV, 89154-5003, USA
e-mail: arlen.chase@unlv.edu

D.Z. Chase
Office of the Executive Vice President and Provost, University of Nevada, Las Vegas, 4505 S. Maryland Parkway, Box 451002, Las Vegas, NV, 89154-1002, USA

N. Masini, F. Soldovieri (eds.), *Sensing the Past*, Geotechnologies and the Environment 16, DOI 10.1007/978-3-319-50518-3_22

LiDAR surveys in Central America, archaeologists have served as the driving force for the procurement and expansion in the use of this technology in this part of the world, albeit with a reliance on individuals from other fields to help process the data. Similar to any new tool at an interface between disciplines, however, researchers are still learning how to use this new resource effectively.

LiDAR is not commonly used in Central America for environmental planning and construction projects to the same degree that it is in the United States and Europe, where the technology has a longer history of utilization for non-archaeological land management purposes (e.g., Johnson and Ouimet 2014: 11, on public database for New England states). Thus, in Central America LiDAR acquisition has usually been organized by independent archaeological researchers through grants or private funding; subcontracts are issued to undertake the LiDAR overflights that produce Log ASCII Standard (LAS) files. Different LiDAR companies, equipment, and strategies have been used to record the landscape, leading to some variability in the collection of point cloud data. Currently, although there is standardization for the LAS files and how the data are recorded, there is no official standardization for archaeological LiDAR processing or distribution anywhere in the world, and there are potential ethical concerns as well (discussed below). Yet, for the Maya area much of the collected point cloud data have become relatively standardized because the majority of overflights have been undertaken by the same entity, the National Center for Airborne Laser Mapping (NCALM) affiliated with the University of Houston and the U.S. National Science Foundation, leading to consistency in data presentation and post-processing.

With the exception of four reported LiDAR campaigns (Table 22.1), the archaeological LiDAR database for Mesoamerica has been largely produced by NCALM (Fernandez et al. 2014), although this may change in the near future as more archaeological projects procure LiDAR. The earliest LiDAR campaign in the Maya area was the one carried out at Caracol, Belize, in 2009 that established the value of this technology for large-scale settlement archaeology and landscape analysis, even in hilly and heavily forested areas (Chase et al. 2010, 2011a, b, 2012, 2013; Weishampel et al. 2010, 2013). The success of the Caracol LiDAR in documenting even slightly elevated archaeological remains spurred the use of this technology not only in Mesoamerica but also in other tropical areas, specifically at Angkor, Cambodia (Evans et al. 2013). Although the cost of LiDAR was initially of concern to many researchers (the 2009 LiDAR survey of 200 km^2 for Caracol cost US $171,000), archaeologists soon recognized that this technology was well worth the funds expended. Not only was more ground covered efficiently (traditional mapping methods would have required labor-intensive decades to do what was done in days), but the collected point cloud data were far more detailed than any survey data (providing elevation information and complete topographic data). Thus, each LiDAR campaign continues to establish the value of LiDAR data to Mesoamerican research agendas.

Following the collection of LiDAR data for Caracol by NCALM and with a recognition of its ability to successfully record ground data (Chase et al. 2010), there were other early LiDAR campaigns conducted in Mexico that did not use NCALM but also produced significant landscape data related to archaeological

Table 22.1 Spatial distribution of LiDAR (light detection and ranging) in Mesoamerica

Site/region	Year flown	Area covered (km^2)	Density (points/m^2)
Caracol, Belize	2009	200	20
Izapa, Mexico (Airborne 1)	2010	42.2	3.2
Angamuco, Mexico (not NCALM)	2011	9	15
Uxbenka, Belize	2011	103	12
El Pilar, Belize (Mayaniquel)	2012	20	20
Mosquita, Honduras	2012	122	15–25
El Tajin, Mexico (INAH/PEMEX)	2012	Unknown	Unknown
Western Belize	2013	1057	15
Mayapan, Mexico	2013	55	40–42
Tres Zapotes, Mexico	2014	72	12–13
Chichen Itza/Yaxuna, Mexico	2014	50	15
Cansahcab, Mexico	2014	26	15
Yaxnohcah, Mexico	2014	90	15
Izapa, Mexico (Airborne 1)	2014	47.5	3.1
El Ceibal, Guatemala	2015	400	15
Teotihuacan, Mexico	2015	120	20
Michoacan, Mexico	2015	40	20
Zacapu, Mexico	2015	40	20

ruins (Fisher et al. 2011; Rosenswig et al. 2013; Zatina Gutierrez 2014); the Izapa database was subsequently amplified (Rosenswig et al. 2014). In 2011 and 2012 NCALM engaged in LiDAR campaigns in southern Belize (Prufer et al. 2015; Prufer and Thompson 2016; Thompson and Prufer 2015) and in Honduras (Preston 2013). One other non-NCALM campaign in 2012 covered the Belize site of El Pilar (Ford 2014). The largest LiDAR campaign carried out to date in the Maya area was undertaken in 2013 by NCALM and covered 1057 km^2 of western Belize (Chase et al. 2014a, b; Chase and Weishampel 2016; Ebert et al. 2016b; Macrae and Iannone 2016; Moyes and Montgomery 2016; Yaeger et al. 2016). That same year, Mayapan was also overflown (Hare et al. 2014). In the summer of 2014, NCALM carried out a series of smaller campaigns in Mexico at Tres Zapotes, Chichen Itza/Yaxuna, Cansahcab, and Yaxnohcah. The results of these surveys are recorded by Hutson et al. (2016), Loughlin et al. (2016), Magnoni et al. (2016), and Reese-Taylor et al. (2016). In 2015, NCALM has flown LiDAR campaigns for El Ceibal, Guatemala (for Takeshi Inomata and Kazou Aoyama), for Teotihuacan (for Saburo Sugiyama), and for Michoacan (Christopher Fisher and Gregory Periera).

22.2 Case Study: Western Belize

Landscape and settlement archaeology in the Maya area came of age in 2009 with the original Caracol LiDAR survey of 200 km^2 at a density of 20 points/m^2 that immediately transformed Caracol from a 23 km^2 mapped site to one that filled

most of the digital elevation model (DEM) (A. Chase et al. 2010, 2011a, b, 2012, 2013; Weishampel et al. 2010, 2013). The survey undertaken by NCALM was very successful in gaining bare earth results that proved to be accurate when compared to existing maps or ground-truthing. Additionally, although not inexpensive, the cost of the survey was substantially less than an investment in on-the-ground time to cover the same area. The data showed a sprawling Maya city with dispersed public architecture connected dendritically by a road system to an epicenteral complex that once housed the ruling family and its administrative units (Chase and Chase 2001). LiDAR also proved to be exceedingly accurate at locating land modifications with low elevation, from house mounds to terracing; the DEM demonstrated the extent of the already known intensively modified landscape covered with agricultural terracing (Chase and Chase 1998) and thousands of residential groups (Chase and Chase 2004).

The Caracol LiDAR survey had profound effects on settlement pattern work within the Maya area. First, the effectiveness of LiDAR in recording ancient bare earth remains in the tropics was conclusively shown; the technology was particularly effective at Caracol because the overlying canopy had not been overly disturbed by modern activities. Second, it demonstrated that some Maya settlements could indeed be categorized as urban centers, more specifically "low density agricultural cities" (Fletcher 2009), and confirmed the large areas that some ancient Maya metropolitan areas occupied. Third, it definitively established the scale of ancient Maya terraced agriculture (at least for one site) and effectively showed a completely anthropogenic landscape. It also served to confirm the mapped settlement data that indicated that control of water was distributed among the residential groups (Chase 2012, 2016), contradicting previous assumptions that small constructed reservoirs could not sustain large populations through the dry season (e.g., Scarborough and Gallopin 1991 for Tikal) and that control of water was almost completely in the purview of the Classic Maya elite (Lucero 2006). The LiDAR data raised other questions about the size and scale of other Maya centers that lay beyond the surveyed area, as well as about the full extent of Caracol "the city" and Caracol "the polity."

In 2013, the Western Belize Archaeological Consortium worked together to obtain another 1057 km^2 of LiDAR data both east of and north of the original 2009 DEM. This new LiDAR permitted a better regional interpretation by revealing the eastern extent of the city of Caracol, as well as the extent of a series of sites in the Maya Mountains and the Belize Valley (Chase et al. 2014a, b). Before this point in time, the largest traditionally mapped settlement area was located at Calkmul, Mexico and covered some 30 km^2 (Chase and Chase 2003: 115). What these newer data demonstrated was the diversity in settlement patterns and strategies that existed within a contiguous part of the east-central Maya area. The LiDAR also showed that the Caracol settlement extended further to the east, revealing new road systems that permitted the city's easy access to key metamorphic resources that were needed elsewhere in the Maya lowlands (Chase et al. 2014a). The northern, eastern, and southern limits of the Caracol metropolitan area were identified, demonstrating that the city covered at least 200 km^2 and was fully integrated by means of a series of dendritic causeways that connected public administrative and market spaces to

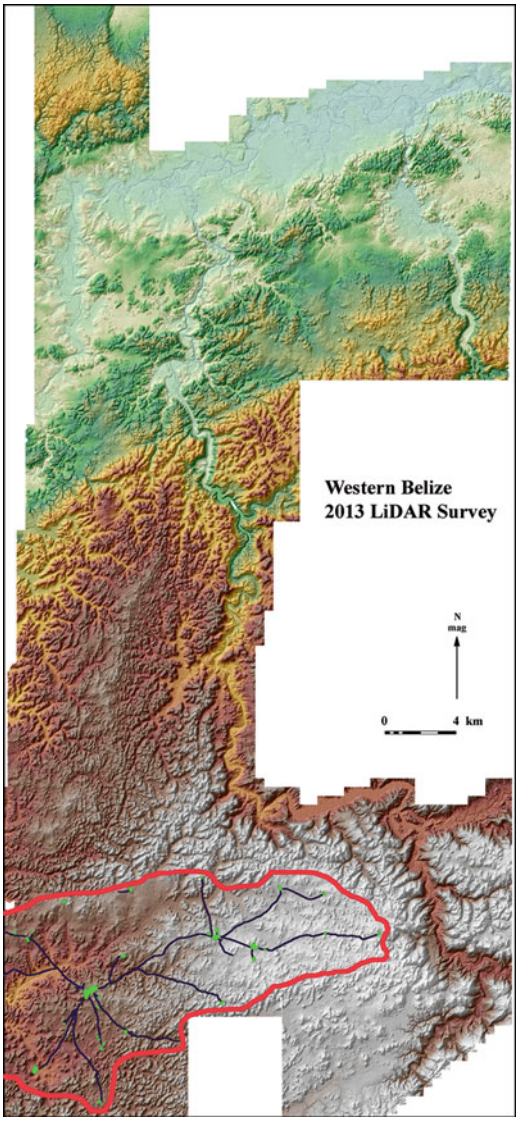

Fig. 22.1 The 2009 and 2013 digital elevation models (DEMs) combined to illustrate the area of western Belize that was covered and the approximate topography (*green* is low-lying land; *brown* and *white* are higher areas) and the extent of Caracol and its road system (outlined in *red* with roads in *blue* and public space in *green*)

the site epicenter (Fig. 22.1). There is no other settlement as large and as dense as Caracol within the area surveyed by LiDAR in 2013 (Figs. 22.2 and 22.3). Second-tier smaller settlements, covering a maximum spatial area of 1–5 km^2, are evident throughout the DEM and include the independent centers in the Belize Valley (Chase et al. 2014b: 8679). In general, however, the rest of the sites in the 2013 survey area are significantly smaller than Caracol.

Among the other intersite differences are the strategies that were utilized to produce the structural layout of the various centers and their agricultural adaptations.

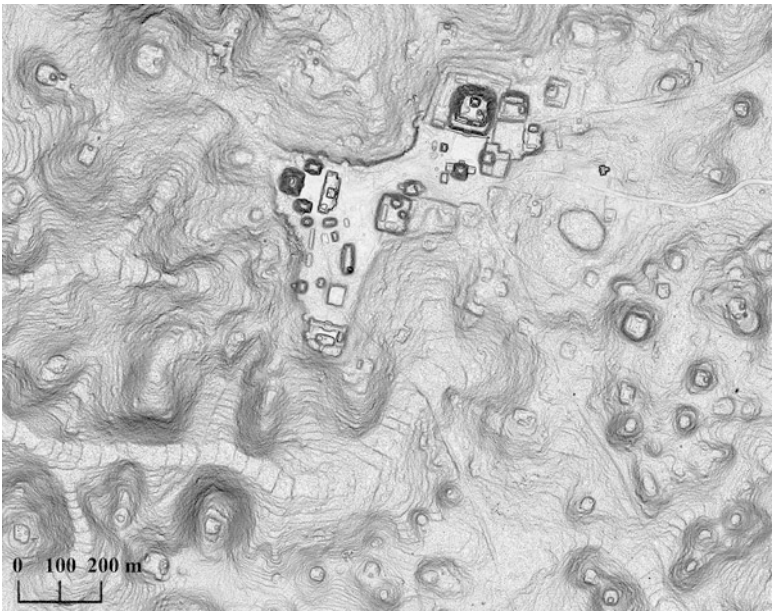

Fig. 22.2 The Caracol site epicenter, showing the public architecture, roads, residential settlement, and agricultural terracing. North is to top of page

The site of Caballo mimics Caracol's use of agricultural terraces and causeways, but at a smaller scale and without joining public architectural plazas together (Fig. 22.4). Minanha exhibits the use of terracing but does not use causeways (Iannone 2009). Yaxnoh uses causeways to connect small groups, but does not evince the agricultural terracing of Caracol (Chase et al. 2014b). In the Belize Valley, the site of Buena Vista does not employ agricultural terracing (Peuramaki-Brown 2014); Cahal Pech utilized a system of causeways to join outlying residential groups to the site epicenter (Cheetham 2004); and Baking Pot utilized internal causeways to unite its central public architecture (Chase et al. 2014b: 8682) and an agricultural strategy involving ditched fields that were effectively irrigated with water from the Belize River (Ebert et al. 2016a). The layouts of all these centers relative to their landscapes indicates that significant variability existed not only in site sizes and populations but also within the strategies employed among Classic Period Maya communities to produce livelihoods.

LiDAR and other remote sensing technologies do not directly provide time depth. The point cloud data give an accurate portrayal of the palimpsest of features that are evident on the ground surface at the time of collection, but not their dating, although sequential events can be derived from the remote sensing data when features overlie one another or other information is available. Because of the long history of archaeological research in western Belize, time depth can be ascribed to some of the architectural constructions that are visible in the archaeological

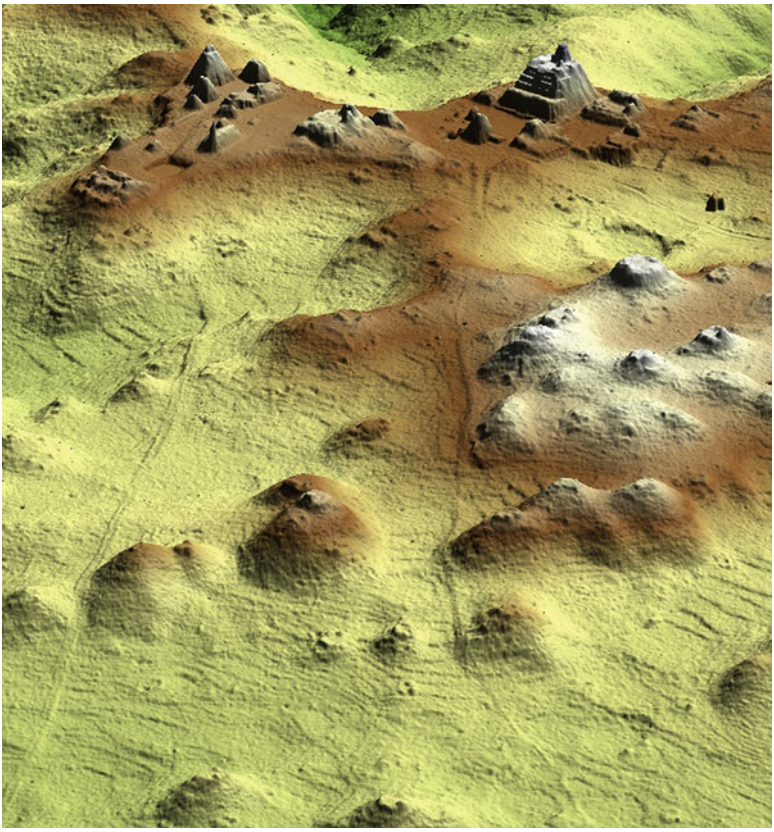

Fig. 22.3 A 2.5 D LiDAR image of the Caracol epicenter looking northwest; compare with Fig. 22.2

landscape. In particular, the architectural constructions constituting public space for initial Maya centers followed a stock plan, called an "E Group" (Freidel et al. 2017), consisting of a western pyramid and a long eastern platform usually associated with three buildings. This building assemblage is usually the initial public architecture constructed at a Maya site and remains largely unchanged through time at many centers because of ritual significance. However, far more of these E Groups were identified in the LiDAR than had been previously documented, providing clues as to the initial spacing of Maya centers in western Belize (Chase et al. 2014: 8685). Other nodes of public architecture are similarly visible in the LiDAR, and the archaeological work that has been done on many of these sites permits their constructions to be placed within a temporal framework (Garber 2004). The 2013 LiDAR campaign discerned defensive features only in two locations, at Xunantunich (Chase et al. 2014a: 216) and at El Pilar, which has now been dated to the Late Preclassic period before 250 AD (Ford 2016). Assuming a similar date for the Xunantunich feature, these data provide a glimpse into the hostile relationships

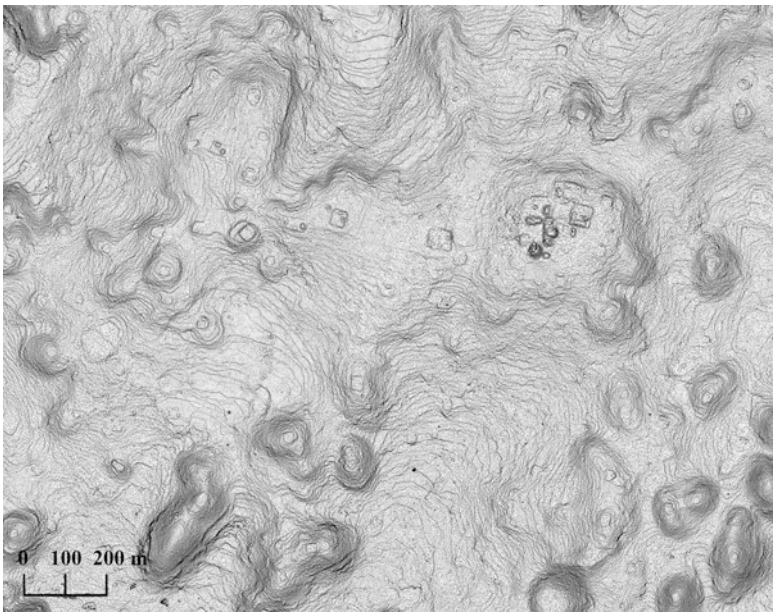

Fig. 22.4 The site of Caballo, Belize showing the public architecture and settlement enmeshed in an elaborate system of agricultural terracing. *Black dots* in mounds are looters' pits; north is to top of page

among sites at the onset of the Classic Period (ca. 250 AD) that may not have been gained otherwise. It is important to note, however, that dating the archaeological features seen in the LiDAR still must be deduced from the extant archaeological data.

22.3 Growing Pains: Issues to Be Resolved

The introduction of LiDAR to settlement archaeology and landscape studies in Mesoamerica has led to a series of methodological, technical, and institutional issues that need to be addressed (Chase et al. 2016). Perhaps the most difficult issue facing practitioners of LiDAR is the variation in ground cover that characterizes the Maya area (Chase et al. 2014). Vegetation differences caused by slash-and-burn or milpa agriculture and by hurricanes also means that traditional LiDAR vegetation removal algorithms may not be effective in generating bare earth points in certain environments (Crow et al. 2007), a problem that affects a significant part of Mesoamerica (Fernandez et al. 2014). This difficulty is particularly seen in areas of milpa regrowth, in areas of heavy scrub forest such as the Northern Maya lowlands, and in areas of grass regrowth as in the Belize Valley. This issue caught the attention of researchers at the site of Uxbenka in southern Belize, where Keith

Prufer and his colleagues (2015: 9) were able to demonstrate the devastating effects that slow regrowth after milpa farming and hurricanes had on the ability to detect ground features; the density of vegetation leads to a significant reduction in ground returns that can linger for more than a decade. LiDAR point clouds are quite clean beneath old growth forest, which is why the initial Caracol landscape recorded by LiDAR was so clear. However, in areas of clearing and regrowth, the point clouds are affected, making interpretation more difficult.

Archaeologists are generally not computer scientists and often cannot alter algorithms or reclassify the LAS point cloud data to make different interpretations. Thus, for Mesoamerican archaeology, the interpretation of LiDAR data is fed through off-the-shelf programs such as ARC-GIS and Surfer to generate digital elevation models (DEMs) that are used for analysis. Even the basic processing of point cloud data by entities such as NCALM uses off-the-shelf software to clean and assemble bare earth DEMs, although they also can make modifications to the programs being utilized. Collaboration between archaeologists and physicists/engineers means that a better product is achieved. For instance, when occupation at the site of Lower Dover, Belize could not be easily identified in the initial DEM produced for the 2013 Western Belize LiDAR Survey, the data were reclassified by NCALM in such a way as to more accurately remove the vegetation so that the mounded remains could be more easily discerned. In the northern lowlands, the topography is composed of natural hillocks that mimic constructed mounds; when combined with modern landscape disturbance and scrub vegetation, it can be very difficult to discern already mapped house mounds in some cases. Again, reworking the algorithms resolved much of this problem and brought the larger mounds into sharper relief. In some cases, however, identification of the less elevated smaller structures still remains problematic, but eventually technology and computer programs or algorithms will resolve their visualization as well.

Ultimately, we will benefit from best practices and standardization for the density and kinds of aerial LiDAR data produced, although at the same time realizing that this cannot be a strict end goal because "ALS observations can be highly customized to achieve specific levels of performance" (Fernandez-Diaz et al. 2014: 9995). Differences in how airborne LiDAR is collected (elevation, flight path, flight speed, pulse type, pulse wavelength, scan frequency, scan angle, etc.) have implications for the quality and kinds of point clouds that result (Fernandez-Diaz et al. 2014). Rosenswig and his colleagues (2014: 2) argue that the bare earth returns are what really count, and for archaeological uses, these returns are often the most essential. For the Izapa data, flown by an independent contractor, he argues that a density of 3.1 points/km^2 provides a similar density of ground points to Caracol's 20 points/km^2 in that both data sets are above 1 point/km^2; a subsequent publication argued that a ground point density of 0.7 (with a range from 0.0 to 6.9) provides a similar level of mound identification (Rosenswig et al. 2014: 7). Although both the vegetation present and the size of archaeological features of interest will ultimately determine both the spatial resolution of DEMs and number of ground points required to achieve that resolution, it should be kept in mind that any DEM cell lacking a ground return is often assigned one algorithmically through inverse

distance weighting, spline interpolation, or kriging (often the latter). Thus, these points have their values selected to mimic the surrounding ground returns. By their nature, built archaeological features often fail to mimic the underlying topography and, as such, any LiDAR campaign should endeavor to record sufficient points to minimize (and preferably eliminate) terrain cells with no ground returns. Essentially, all the mitigating factors involved in the collection and production of the LiDAR data must be considered (Fernandez-Diaz et al. 2014: 9962, 9967). As a final note, other uses of LiDAR data, in particular for three-dimensional (3D) modeling and algorithmic manipulation of raw LAS files, greatly benefit from higher densities of bare earth returns, so there may be no absolute answer to a minimum desired point density.

A final issue to be resolved is how LiDAR data should be stored and distributed. Funding agencies and some LiDAR providers have suggested that the collected data, or some portion of it, should be made publically available after a short period of time; however, this expectation may be at odds with countries in Mesoamerica that have experienced significant loss of cultural heritage from looting and site destruction. LiDAR can serve as a roadmap for many Maya sites, and the public posting of these maps with their geolocations could act to easily lead looters directly to their quarry. Thus, U.S. mandates regarding data management and accessibility may be seen as inappropriate for the countries that house Maya sites. Belize instituted a policy that prohibits raw LiDAR data from being publically distributed and asks that published LiDAR images not provide geo-coordinates (Chase et al. 2014: 218). Although discussions have taken place and concerns have been raised, neither Guatemala nor Mexico currently has policies in place regarding the accessibility and distribution of LiDAR data. As our technology improves and the cost decreases, all this may become moot. Google Earth already provides free satellite images for most of the world to most internet users. Eventually, higher-resolution data, and perhaps even LiDAR, will be collected from space, and it may be that the companies that own the satellites or requisition the surveys will also deem that they can distribute the data as they see fit, meaning that there will not even be a nominal role for nations in terms of regulating and approving their own landscape, let alone airspace. These are uncharted concerns that need to be addressed by the research communities and affected governments before better technology with more power and resolution becomes available.

22.4 Final Remarks

LiDAR has proven to be an extremely useful technology for detecting Maya ruins. It can recover information on a scale much larger than traditional survey (Chase et al. 2014a). As indicated by the work at Caracol, Belize, LiDAR is extremely effective

at revealing remains below heavy forest cover and can be used to differentiate human modifications on the landscape even in areas with extremely hilly terrain. By revealing remains at both a large scale and low elevation, it is possible to make interpretations about the ancient landscapes that might not otherwise have been possible. LiDAR is not inexpensive, but when contextualized in terms of the sizeable landscapes that are revealed and the time involved, the technology is cost efficient. However, on-the-ground mapping is still necessary for ground-truthing and for recording archaeological features with little or no elevation, and additional investigation is necessary to provide dates and functions for archaeological remains.

In some cases, LiDAR documents what had been expected but could not be proved with sampling, such as the extent of terracing at Caracol (Chase and Chase 1998, 2014; Chase et al. 2011b). LiDAR effectively shows how much of a landscape was modified, revealing not only the size of a settlement area but also its terraced agricultural fields and reservoirs. The scale of agricultural terracing and control of water flow over the landscape recorded in the Caracol LiDAR rivals the complexity of ancient agricultural features found in Southeast Asia, South America, and other parts of the world (Chase and Weishampel 2016; Chase et al. 2011). The 2013 campaign also revealed that there is substantial variation in the size of ancient Maya sites; they range in scale from small centers covering less than 1 km^2 (village) to massive cities covering more than 200 km^2. Although the size of ancient Maya sites could be only guessed at in the past, LiDAR provides a complete landscape that proves the scale and extent of these ancient settlements.

As more and more landscape areas are recorded with LiDAR in Mexico, Belize, Guatemala, Honduras, and El Salvador, researchers will continue to gain a much fuller understanding of and appreciation for the ancient peoples who once occupied these areas. The technology has resulted in the recognition that the ancient Maya had very large complex societies with the capacity for sustainability through the creation of completely anthropogenic environments. LiDAR is useful not only for recording ancient Maya cities and landscapes but also for helping to manage the cultural heritage and tourism of these locations. It is important that the recording of these landscapes with LiDAR continue and that we obtain as detailed and complete a record of the Maya area as is possible before modern encroachment destroys much of the ancient land use patterns that can still be seen in the recovered point clouds.

Acknowledgments The authors thank the National Center for Airborne Laser Mapping for working with us in the collection of quality LiDAR data, and particularly Juan Fernandez-Diaz. The original 2009 LiDAR was funded by a NASA Grant NNX08AM11G and the UCF-UF Space Research Initiative (John Weishampel, PI; Arlen and Diane Chase, Co-PIs). The 2013 LiDAR was collected as a result of a grant from the Alphawood Foundation channeled through the University of Central Florida for the Western Belize Archaeological Consortium (Arlen Chase, Diane Chase, Jaime Awe, John Weishampel, Gyles Iannone, Holley Moyes, Jason Yaeger, and M. Kathryn Brown). The Belize Institute of Archaeology was also particularly helpful in ensuring that the LiDAR campaigns were successful.

References

Chase ASZ (2012) Beyond elite control: Maya water management at the site of Caracol, Belize. Senior thesis, Departments of Archaeology and Computer Science, Harvard University, Cambridge. http://www.caracol.org/include/files/chase/asz12.pdf

Chase ASZ (2016) Beyond elite control: residential reservoirs at Caracol, Belize. WIREs Water 3:885–897

Chase AF, Chase DZ (1998) Scale and intensity in classic period Maya agriculture: terracing and settlement at the 'garden city' of Caracol, Belize. Cult Agric 20(2):60–77

Chase AF, Chase DZ (2001) Ancient Maya causeways and site organization at Caracol, Belize. Anc Mesoam 12(2):273–281

Chase AF, Chase DZ (2003) Minor centers, complexity, and scale in lowland Maya settlement archaeology. In: Iannone G, Connell S (eds) Perspectives on ancient Maya rural complexity. UCLA, Cotsen Institute of Archaeology, pp 108–118

Chase DZ, Chase AF (2004) Archaeological perspectives on classic Maya social organization from Caracol, Belize. Anc Mesoam 15:111–119

Chase DZ, Chase AF (2014) Path dependency in the rise and denouement of a classic Maya city: the case of Caracol, Belize. In: Chase AF, Scarborough VL (eds) The resilience and vulnerability of ancient landscapes: transforming Maya archaeology through IHOPE. American Anthropological Association, Arlington, pp 142–154

Chase ASZ, Weishampel JF (2016) Using LiDAR and GIS to investigate water and soil management in the agricultural terracing at Caracol, Belize. Adv Archaeol Pract 4:357–370

Chase AF, Chase DZ, Weishampel JF (2010) Lasers in the jungle: airborne sensors reveal a vast Maya landscape. Archaeology 63(4):27–29

Chase DZ, Chase AF, Awe JJ, Walker JH, Weishampel JF (2011a) Airborne LiDAR at Caracol, Belize and the interpretation of ancient Maya society and landscapes. Res Rep Belizean Archaeol 8:61–73

Chase AF, Chase DZ, Weishampel JF, Drake JB, Shrestha RL, Slatton KC, Awe JJ, Carter WE (2011b) Airborne LiDAR, archaeology, and the ancient Maya landscape at Caracol, Belize. J Archaeol Sci 38:387–398

Chase AF, Chase DZ, Fisher CT, Leisz SJ, Weishampel JF (2012) Geospatial revolution and remote sensing LiDAR in Mesoamerican archaeology. PNAS 109(32):12916–12921

Chase AF, Chase DZ, Weishampel JF (2013) The use of LiDAR at the Maya site of Caracol, Belize. In: Comer D, Harrower M (eds) Mapping archaeological landscapes from space. Springer, New York, pp 179–189

Chase AF, Lucero L, Scarborough VL, Chase DZ, Cobos R, Dunning N, Gunn J, Fedick S, Fialko V, Hegmon M, Iannone G, Lentz DL, Liendo R, Prufer K, Sabloff JA, Tainter J, Valdez F, van der Leeuw S (2014a) Topical landscapes and the ancient Maya: diversity in time and space. In: Chase AF, Scarborough VL (eds) The resilience and vulnerability of ancient landscapes: transforming Maya archaeology through IHOPE. American Anthropological Association, Arlington, pp 11–29

Chase AF, Chase DZ, Awe JJ, Weishampel JF, Iannone G, Moyes H, Yaeger J, Brown MK (2014b) The use of LiDAR in understanding the ancient Maya landscape: Caracol and western Belize. Adv Archaeol Pract 2:208–221

Chase AF, Chase DZ, Awe JJ, Weishampel JF, Iannone G, Moyes H, Yaeger J, Brown MK, Shrestha RL, Carter WE, Fernandez Diaz J (2014c) Ancient Maya regional settlement and inter-site analysis: the 2013 west-central Belize LiDAR survey. Remote Sens 6(9):8671–8695

Chase AF, Reese-Taylor K, Fernandez-Diaz JC, Chase DZ (2016) Belize. Progression and issues in the Mesoamerican geospatial revolution: an introduction. Adv Archaeol Pract 4:219–231

Cheetham D (2004) The role of "terminus groups" in lowland Maya site planning: an example from Cahal Pech. In: Garber J (ed) The ancient Maya of the Belize Valley. University Press of Florida, Gainesville, pp 125–148

Crow PS, Benham S, Devereux BJ, Amable G (2007) Woodland vegetation and its implications for archaeological survey using LiDAR. Forestry 80(3):241–252

Ebert CE, Hoggarth JA, Awe JJ (2015) Prehistoric water management in the Belize River Valley: LiDAR mapping and survey of the ditched field system of Baking Pot, Belize. In: Paper presented at the 13th annual Belize Archaeology and Anthropology Symposium, 2 July 2015, San Ignacio Cayo, Belize

Ebert CE, Hoggarth JA, Awe JJ (2016a) Classic period maya water management and ecological adaptation in the belize river valley. Res Rep Belizean Archaeol 13:109–120

Ebert CE, Hoggarth JA, Awe JJ (2016b) Integrating quantitative LiDAR analysis and settlement survey in the Belize river valley. Adv Archaeol Pract 4:284–300

Evans DH, Fletcher RJ, Pottier C, Chevance J-B, Sourtif D, Tan BS, Im S, Ea D, Tin T, Kim S, Cromarty C, De Greef S, Hanus K, Baty P, Kuszinger R, Shimoda I, Boornazian G (2013) Uncovering archaeological landscapes at Angkor using LiDAR. PNAS 110:12595–12600

Fernandez-Diaz JC, Carter WE, Shrestha RL, Glennie GL (2014) Now you see it... now you don't: understanding airborne mapping LiDAR collection and data product generation for archaeological research in Mesoamerica. Remote Sens 6:9951–10001

Fisher CT, Leisz S, Outlaw G (2011) LiDAR: a valuable tool uncovers an ancient city in Mexico. Photogramm Eng Remote Sens 77:962–967

Fletcher R (2009) Low-density, agrarian-based urbanism: a comparative view. Insight 2:2–19

Ford A (2014) Using cutting-edge LiDAR technology at El Pilar Belize-Guatemala in discovering ancient Maya sites—there is still a need for archaeologists! Res Rep Belizean Archaeol 12:271–280

Ford A (2015) Unexpected discovery with LiDAR: uncovering the citadel at El Pilar. Paper presented at the 13th annual Belize Archaeology and Anthropology symposium, 2 July 2015. San Ignacio Cayo, Belize

Ford A (2016) Unexpected discovery with LiDAR: uncovering the citadel at El Pilar in the context of the Maya Forest GIS. Res Rep Belizean Archaeol 13:87–98

Freidel DA, Chase AF, Dowd A, Murdock J (2017) Early Maya E groups, solar calendars, and the role of astronomy in the rise of lowland Maya urbanism. University Press of Florida, Gainesville. (in press)

Garber JF (ed) (2004) The ancient Maya of the Belize Valley. University Press of Florida, Gainesville

Hare T, Masson M, Russel B (2014) High-density LiDAR mapping of the ancient city of Mayapan. Remote Sens 6:9064–9085

Hutson S, Kidder B, Lamb C, Vallejo-Caliz D, Welch J (2016) Small buildings and small budgets: making LiDAR work in Northern Yucatan. Adv Archaeol Pract 4:268–283

Iannone G (2009) The jungle kings of Minanha: constellations of authority and the ancient Maya socio-political landscape. Res Rep Belizean Archaeol 6:33–41

Johnson KM, Ouimet WB (2014) Rediscovering the lost archaeological landscape of southern New England using airborne light detection and ranging (LiDAR). J Archaeol Sci 43:9–20

Loughlin MD, Pool CA, Shrestha R, Fernandz-Diaz JC (2016) Mapping the Tres Zapotes polity: the effectiveness of LiDAR in tropical alluvial settings. Adv Archaeol Pract 4:301–313

Lucero LJ (2006) Water and ritual: the rise and fall of Classic Maya rulers. University of Texas Press, Austin

Macrae S, Iannone G (2016) Understanding ancient Maya agricultural sytems through LiDAR and hydrological mapping. Adv Archaeol Pract 4:371–392

Magnoni A, Stanton TW, Wheeler JA, Osorio Leon JF, Perez Ruiz F, Barth N (2016) Assessing detection thresholds of archaeological features in airborne LiDAR data from Central Yucatan. Adv Archaeol Pract 4:232–248

Moyes H, Montgomery S (2016) Mapping ritual landscapes using Lidar: cave detection through local relief modeling. Adv Archaeol Pract 4:249–267

Peruramaki-Brown MM (2014) Neighbourhoods and dispersed/low-density urbanization at Buenavista del Cayo, Belize. Res Rep Belizean Archaeol 11:67–79

Preston D (2013) The El Dorado machine: a new scanner's rain-forest discoveries. The New Yorker, May 6, pp 34–40. http://www.newyorker.com/magazine/2013/05/06/the-el-dorado-machine

Prufer KM, Thompson AE (2016) LiDAR based analyses of anthropogenic landscape alterations as a component of the built environment. Adv Archaeol Practice:4:393–409

Prufer KM, Thompson AE, Kennett DJ (2015) Evaluating airborne LiDAR for detecting settlements and modified landscapes in disturbed tropical environments at Uxbenka, Belize. J Archaeol Sci 57:1–13

Reese-Taylor K, Atasta Flores FC, Anaya Hernandez A, Monteleone K, Uriarte A, Carr C, Peuramaki-Brown M (2016) Boots on the ground at Yaxnohcah: ground-truthing LiDAR in a complex tropical landscape. Adv Archaeol Pract 4:314–338

Rosenswig RM, Lopez-Torrijos R, Antonelli CE, Mendelsohn RR (2013) LiDAR mapping and surface survey of the Izapa state on the tropical piedmont of Chiapas, Mexico. J Archaeol Sci 40:1493–1507

Rosenswig RM, Lopez-Torrijos R, Antonelli CE (2014) LiDAR data and the Izapa polity: new results and methodological issues from tropical Mesoamerica. Archaeol Anthropol Sci 7:487–504

Scarborough VL, Gallopin GG (1991) A water storage adaptation in the Maya lowlands. Science 251:658–662

Thompson AE, Prufer KM (2015) Airborne LiDAR for detecting ancient settlements and landscape modifications at Uxbenka, Belize. Res Rep Belizean Archaeol 12:251–259

Weishampel JF, Chase AF, Chase DZ, Drake JB, Shrestha RL, Slatton KC, Awe JJ, Hightower J, Angelo J (2010) Remote sensing of ancient Maya land use features at Caracol, Belize related to tropical rainforest structure. In: Campna S, Forte M, Liuzz C (eds) Space, time, place: third international conference on remote sensing in archaeology. Archaeopress, Oxford, pp 42–52

Weishampel JF, Hightower JN, Chase AF, Chase DZ (2013) Remote sensing of below-canopy land use features from the Maya polity of Caracol. In: Djinjian F, Robert S (eds) Understanding landscapes: from discovery through land their spatial organization. Archaeopress, Oxford, pp 131–136

Yaeger J, Brown MK, Cap B (2016) Locating and dating sites using Lidar survey in a mosaic landscape in Western Belize. Adv Archaeol Pract 4:339–356

Zetina Gutierrez MG (2014) Prospeccion arqueologica basada en percepcion remota en la poligonal de proteccion de El Tajin, Veracruz. Las Memorias del VII Congreso Interno de Investigadores del INAH 2013 (in press). INAH, Mexico

Chapter 23
Ultrasonic Analysis of the Spanish Cultural Heritage: Six Case Studies

Monica Alvarez de Buergo and Rafael Fort Gonzalez

Abstract Nondestructive techniques (NDT) are particularly appropriate for the analysis of stone materials found in the built heritage. Moreover, portable NDTs can be used for onsite surveys of the object analyzed. Ultrasound propagation velocity (UPV) is one of the NDTs most commonly used in the diagnosis, conservation, and restoration of the cultural heritage. The technique consists in calculating the velocity from the time it takes an ultrasonic wave to travel across a known distance from an emitter to a receiver. The results provide useful information about the quality and degree of decay of building materials, which inhomogeneity must be factored into the calculations. The six examples of UPV surveys discussed here illustrate the utility of the technique in detecting areas of low velocity, which are normally indicative of decay. Combined with other NDTs and petrographic and petrophysical analyses, the findings afforded scientific and technical grounds for planning preventive, conservation, or restoration measures.

Keywords Stone • Nondestructive techniques • Building materials • Decay

23.1 Introduction

Nondestructive techniques (NDT) are highly useful for determining the quality of construction materials. They are particularly well suited for analyzing materials that form part of the cultural heritage as they are not invasive techniques, which means they will not change the physical, chemical, or mechanical properties or dimensions of these elements.

M. Alvarez de Buergo (✉) • R. Fort Gonzalez
Instituto de Geociencias IGEO (CSIC,UCM), C/José Antonio Nováis, 12, 28040, Madrid, Spain
e-mail: monica.alvarez@csic.es; rafael.fort@csic.es

N. Masini, F. Soldovieri (eds.), *Sensing the Past*, Geotechnologies and the Environment 16, DOI 10.1007/978-3-319-50518-3_23

Ultrasonic testing is one of the key NDTs for ascertaining the condition of many materials, being essential to acquire a greater practical knowledge of the results that can be achieved with this technique and the useful information it can provide for cultural heritage preservation strategies. In the 1920s, Sokolov proposed reflection measurements, in which a sound wave is pulsed from one side of the sample and transmitted to the other side, where it is reflected and returns to a receiver positioned at the point of emission. When the wave encounters a flaw or crack in the material, the signal is reflected and its traveling time altered. The recorded delay can be used to map flaw location and geometry. In the direct method, in which transmitter and receiver are located on opposite sides of the material, the same principle is involved: interruptions in the passage of the sound wave reveal the position and shape of flaws (Sokolov 1929, 1935a, b, 1941, 1946, 1948). Svahn (2006) contended that the use of ultrasound to characterize stone, which was not established until the 1950s, helps to evaluate stone condition, providing information about the result of consolidation treatments and detecting cracks and voids in the material. It also aids in the characterization of the mechanical properties of a material and hence its degradation.

Ultrasound is frequently used to diagnose the condition of metals, given their good response to the propagation of ultrasonic waves. Although the use of the technique to determine the quality of stone is much more recent, Bodare (1996) claimed that ultrasonic methods are now the NDT most commonly deployed to study stone of cultural interest. Many authors regard ultrasound propagation velocity (UPV) as a consolidated technique for stone conservation (Alonso and Suarez del Río 1985; Zezza 1990; Alvarez de Buergo and Gonzalez 1994; Benavente et al. 2006; Fort 2008; Fort et al. 2011, 2013a, b; Mamillan 1991; Marini et al. 2004; Montoto et al. 1994; Svahn 2006; Vasanelli et al. 2015; Weiss et al. 2002). In their review of the subject, Doehne and Price (2010) regarded ultrasound to be the predominant field method for stone conservation.

Nevertheless, its application to stone is more complex than that for other materials such as metals because stone is naturally inhomogeneous and exhibits substantial textural and mineralogical variations. It may contain natural discontinuities (stratification planes, schistosity, cracks) that affect wave propagation. A thorough understanding of the petrographic (texture, structure, mineralogy) and petrophysical (porosity, pore size, compactness, density) characteristics of the material analyzed is consequently a requisite to a correct interpretation of and an accurate diagnosis from UPV findings (Fort 2008).

The aim of this chapter is to show how the ultrasound technique allows determining the decay degree and the fissures and crack location in different materials of cultural and architectural heritage. For this purpose, six case studies are described. This information is very useful for defining intervention guidelines for the conservation and restoration of such heritage.

23.2 Brief Description of the Fundamentals of the Method: Methodology

23.2.1 Fundamentals

Ultrasounds are longitudinal elastic mechanical waves that propagate through solid, liquid, and gaseous media. As their frequency is more than 20 kHz, they are not perceptible to the human ear. High-frequency waves are useful for distinguishing and quantifying certain essential mechanical and structural properties of solids as well as their composition. Ultrasonic investigations are based on the observation and analysis of changes in wave characteristics induced by the medium through which it is propagated. Such changes, which are readily measured with appropriate instruments, can be related to the variations in the physical properties of the material resulting from inhomogeneities, discontinuities, cracks, and deterioration.

Sound waves can propagate across the surface of materials (surface waves, Rayleigh waves, Lamb waves). As their ability to penetrate solids is limited, however, their use in characterizing materials is likewise restricted.

Waves transmissible in depth are the ones normally used to study the physical-mechanical and structural properties of materials: these consist of longitudinal or primary (P) and transverse or secondary (S) waves. In longitudinal waves the particles in the medium vibrate parallel to the direction of the wave; that is, they oscillate back and forth, pressing together or spreading apart along the propagation axis. Transverse waves are transmitted perpendicularly to the direction of the ultrasonic beam and, in contrast to longitudinal waves, propagate across solid media only.

The kit that measures ultrasonic transmission consists essentially in an electrical pulse generator, transducers (ultrasound wave emitter and receiver), an amplifier, and an electronic synchronizing device to measure the time interval between pulse generation in the emitter and its detection by the receiver. The velocity is then calculated from distance and time.

The major advantages of this technique are its nondestructiveness and portability, the speed with which it takes and repeats measurements, and the affordability of the instruments required. Its main drawbacks are the difficulty encountered in inspecting elements with complex or irregular geometries; the need for calibration patterns; the necessity to take many measurements for thorough, representative analysis; the effect of material composition, texture, and structure on the results (grain size, type of material, anisotropy, etc.); its dependence upon environmental conditions (humidity); the need for a couplant; the sensitivity of measurements to the pressure exerted on the transducers; and the need for experienced technicians to interpret the results (Fort 2008).

Measurements can be taken in direct mode, in which the emitter and receiver are positioned on opposite, flat, and parallel surfaces of the material; in indirect mode, where both the transducers are on the same surface; or in semidirect or corner mode, with the transducers positioned on perpendicular planes (Mamillan 1991).

23.2.2 Methods

The UPV recordings were taken with a CNS Electronics PUNDIT kit, featuring a precision of ±0.1 μs. The 54-kHz and 1-MHz transducers used were fitted with a flat, round contact surface (50- and 11.82-mm diameter). A plasticine couplant was applied to enhance the contact and bond between stone surface and transducer. Most of the readings were taken in indirect mode, although in a few instances the direct method was used.

The UPV findings were supplemented with other techniques and tests, including surface hardness (PROCEQ original N-type Schmidt hammer), porosity accessible to water (RILEM 1980), mercury intrusion porosimetry (Micromeritics Autopore IV 9500, pore diameters 0.001–1000 mm, atmospheric pressure to 60,000 psi), and a (PROCEQ Profometer 4) magnetometer to detect metal elements.

23.3 Case Studies

The case studies discussed next illustrate the utility and reliability of UPV when assessing the degree of decay in heritage stone materials as a preliminary to planning and prioritizing conservation and restoration measures or designing relocation strategies for stone monuments.

These six real-life examples involved different environments (rural and urban), building materials (granite, sandstone, limestone), and forms of decay.

23.3.1 Case Study 1: 'Piedra Escrita' (Scripted Stone), Cenicientos, Madrid, Spain

This case study aimed primarily to assess the degree of stone decay as a preliminary to suitable intervention planning. The monument in question is a carved granite megalith nearly 5 m tall built by the Romans as a rural shrine to the goddess Diana (Fig. 23.1a) and dated by some authors in the second century BC (Cantó de Gregorio 2007). It is located at Cenicientos, a village 92 km west from the city of Madrid.

Although the stone is in generally good condition, it is moderately decayed to a degree that varies across the surface and with the orientation of each face of the monument. This variation is mirrored in the values of the physical, hydric, and mechanical properties observed. In other words, stone decay is highly dependent on orientation and morphology, as well as temperature and humidity, which determine the amount of rainwater runoff. That parameter, in turn, impacts the accumulation of moisture, water absorption by the stone materials, the chemical alteration–oxidation of iron minerals, and feldspar hydrolysis-mediated alteration of clay minerals. These processes are visible in changes not only in stone chemistry, but also in its physical

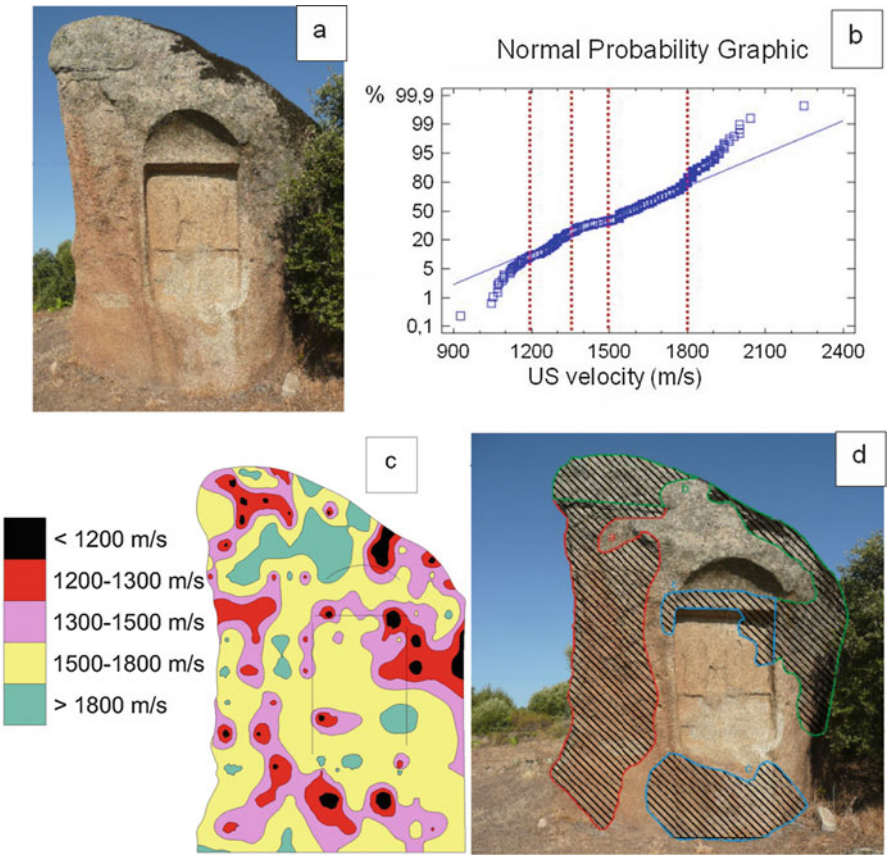

Fig. 23.1 Case Study 1: 'Piedra Escrita' (scripted stone), Cenicientos, Madrid, Spain. (**a**) Carved altar with a niche. (**b**) Probabilistic distribution curve of the ultrasound propagation velocity. (**c**) Five classes of distribution mapping of ultrasound velocity defining the most decayed areas (in *black* and *red*). (**d**) Interpretation of the results: the most decayed area is marked in a *red line*, *green* is decay induced by biological activity, and *blue* is area with fissures

characteristics and porosity. Decay is also conditioned and intensified by the cyclic nature of solar radiation, which is similarly dependent upon orientation.

The most prominent forms of decay in this biotitic monzogranite carved into a shrine by the Romans are fracturing, spalling, and grain disintegration. Its mean rebound hammer hardness is 30 (47 in healthy areas and 18 in decayed areas). Its porosity accessible to water is moderate, given the granitic nature of the rock (4.0%, ranging from 3.9 to 4.5%), with pore sizes of less than 5 μm accounting for 57% of the total (according to mercury intrusion porosimetry findings).

A total of 273 ultrasonic readings were taken on the surface of the element, using a 20 × 40-cm grid in the uncarved areas and a 20-cm-square grid in the rest. The mean value the ultrasound propagation velocity found was 1544 ± 267 m/s (with a

926-m/s minimum and a 2247-m/s maximum). The values were plotted on a normal probability graph (Fig. 23.1b), and the discontinuities observed on the resulting curve were used to establish five classes. Each class is assigned to a different decay condition for the same material: classes with the lowest velocity correspond to the most decayed material, and classes with the highest velocity to the best preserved one. The values were then mapped to generate Fig. 23.1c, which shows that the areas with the lowest velocities (black and red areas) appeared only sporadically, and most of the stone front exhibited moderate values (yellow).

Figure 23.1d combines the results of ultrasound velocities and visual inspection of the forms of decay on the surface of the material. The most severely decayed areas, at risk of medium-term detachment, are outlined in red, and the areas where grain disintegration is induced by biodeterioration are outlined in green. Blue outlining, in turn, indicates slight decay attributable to internal fissuring not visible on the surface.

The results were applied to ensure that, in the intervention planned for the near future, the most severely decayed areas of the monument will be prioritized.

23.3.2 Case Study 2: Kurutziaga Stone Cross, Durango, Vizcaya, Spain

Here, the study was conducted to assess decay before relocation of the monument.

This fifteenth-century Gothic sandstone cross is 4.3 m tall (Fig. 23.2a). Its base supports the shaft, prism, and crucifix, its three main elements, richly carved with Biblical scenes (Genesis, the apostolate, Calvary, and the Virgin Mary, all crowned by the sun and moon). After it was severely damaged in a terrorist attack, a hood (Fig. 23.2a) was installed to protect it from direct exposure to the elements during relocation planning. Today it is on display at the Kurutzesantu Museum, housed in Vera Cruz Chapel (likewise fifteenth-century).

The visual decay and its forms were mapped (Fig. 23.2b). Metal elements inside the stone, a possible source of weak points that could be damaged during relocation, were detected with a magnetometer (Fig. 23.2c).

Indirect UPV readings, 736 in all, were taken with 30-mm contact diameter, 0.5-MHz frequency transducers. A measurement grid consisting of 5-cm squares was used. The mean value of UPV found was 1852 m/s, with a range of <800 to >4200 m/s. The mean value observed in the crucifix was lower, at 1622 m/s. All the values were plotted on a normal probability graph (accumulated frequency versus velocity) from which six classes were defined (Fig. 23.2d). The threshold below which the material would be at risk during relocation was set at 1250 m/s. The UPV iso-areas mapped based on the six classes (Fig. 23.2e) identified five areas (red and black shading) with internal fissures and metal elements. That information proved to be very helpful when formulating the plan to dismantle, move, and reassemble this work of art.

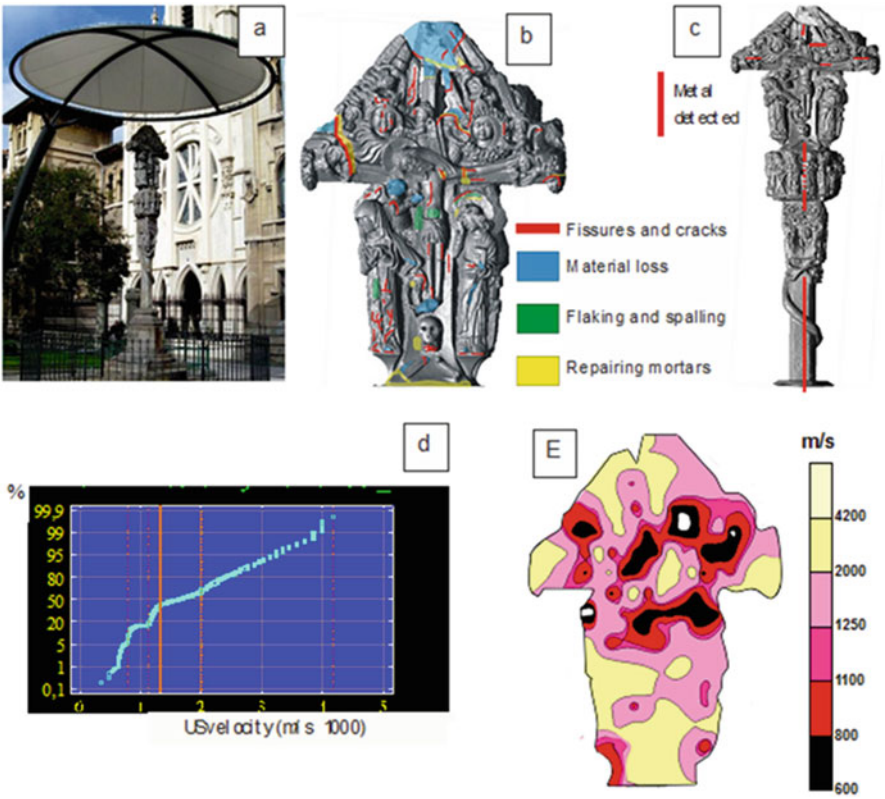

Fig. 23.2 Case Study 2: Kurutziaga stone cross, Durango, Vizcaya, Spain. (**a**) Location of the Kurutziaga stone. (**b**) Decay mapping by visual survey. (**c**) Metal element detection (for reassembly by pieces) by magnetometry. (**d**) Probabilistic distribution curve of ultrasound propagation velocity. (**e**) Mapping of ultrasound velocity iso-areas defining the most decayed areas (in *black* and *red*)

23.3.3 Case Study 3: The Royal Palace at Madrid, Spain

This study aimed to identify weak areas to prevent detachment of stone elements. The authors had previously acquired a good deal of research experience with the building in question (Perez-Monserrat 2013; Alvarez de Buergo and Fort 2014).

Madrid's eighteenth-century Royal Palace is a Baroque compound under the aegis of the Crown Heritage (Fig. 23.3a). Its main building materials are granite (Berroqueña monzogranite; Freire et al. 2015) and limestone (Colmenar biomicrite; Fort et al. 2013a, b, 2015). Granite was used for most of the flat façades and limestone for the ornamental elements. A few years ago, one of the limestone pieces on the architrave, weighing nearly 0.5 tonnes, toppled to the ground (Fig. 23.3b, c).

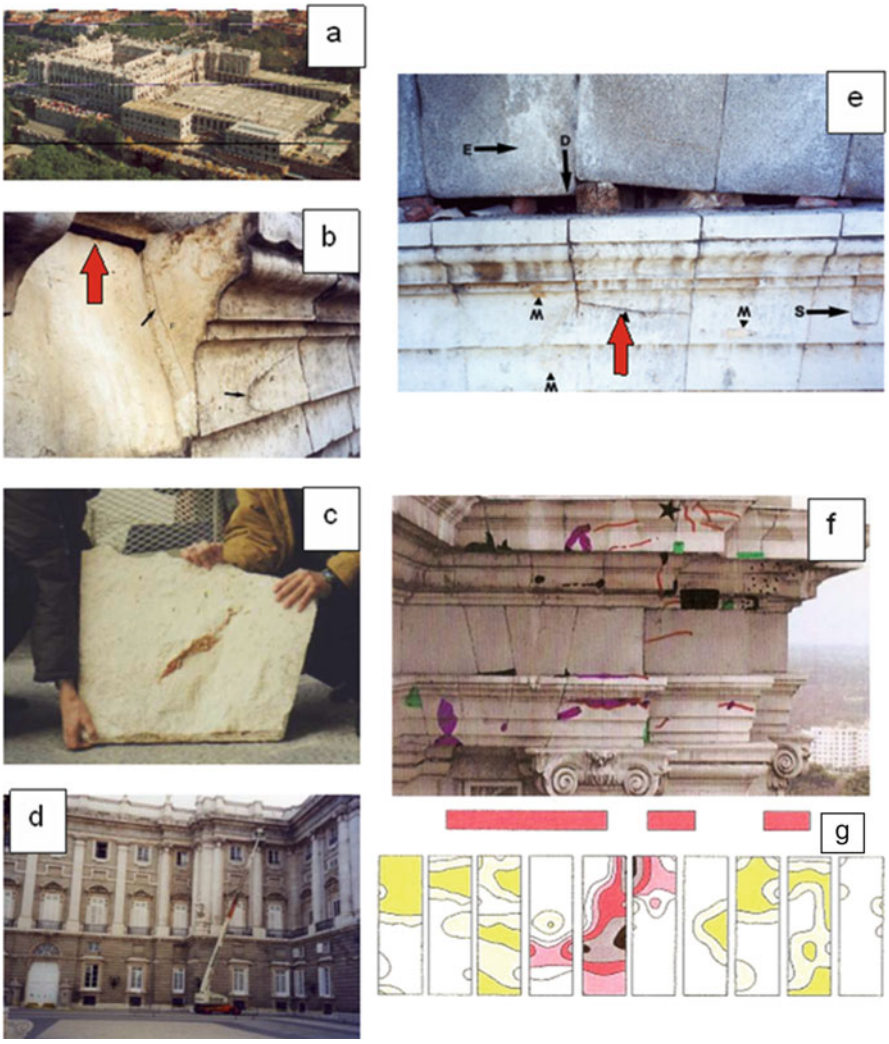

Fig. 23.3 Case Study 3: The Royal Palace at Madrid, Spain. (**a**) Aerial view of the Royal Palace, Madrid. (**b**) Hollow left by the fallen block, in which the *red arrow* points to the metallic tie element, and the small *black arrows* point to the cracks in the adjacent ashlar. (**c**) Detached ashlar. (**d**) The boom of the crane is located in the area of the detached ashlar (architrave). (**e**) Areas of detachment risk. The *red arrow* points to a crack similar to the one that caused the detaching and falling of the stone block. (**f**) Part of the architrave in which the visual stone decay was mapped: cracks (*red lines*), reintegration of stone loss with mortar (*purple*), stone fragment loss (*black*), and stone replacement (*green*). (**g**) Projection of the arhitrave ashlars shown in image (**f**) in which velocity iso-areas have been mapped: *red and black areas* show the lowest velocity and therefore the most decayed ashlars in risk of detachment. The *red rectangles* represent the location of metallic elements (anchorage, tying) detected by magnetometry

Research was conducted for nearly a full year to determine the causes of this collapse and prevent any further detachments with a view to employee and visitor safety, as well as to building conservation.

The cornices on all the building façades, and particularly the architrave, were thoroughly inspected over several months with the aid of a basket crane (Fig. 23.3d). The collapse was found to have been induced by oxidation of the iron bars anchoring the cornice stone. The concomitant increase in volume placed pressure on the stone, which ultimately cracked. One such iron element is visible in Fig. 23.3b (arrow). Fort et al. (2004), analyzing the iron elements and their by-products, found that the corrosion-mediated conversion of ferrite (iron oxide) into the polymorphs lepidocrocite and goethite (iron hydroxides) induced an 83% increase in volume (Fort et al. 2004), which translated into stress of the order of 150–200-MPa. As the compressive strength of the Colmenar limestone in which the iron elements are embedded is only 90–100 MPa, it cracked under the stress.

The inspection consisted primarily in indirect UPV and the use of a magnetometer to locate the iron anchor bars. Thanks to the thousands of readings recorded, a number of points at high risk of detachment were identified, such as shown in Fig. 23.3e.

The UPV map in Fig. 23.3g shows anomalously low values (black, gray, and red shading) for the fifth ashlar from the left (architrave). Iron bars (marked as red lines in Fig. 23.3f) similarly detected in this area could generate cracking such as illustrated in Fig. 23.3e and possible detachment of part of the ashlar in the short term.

This study proved to be particularly useful for the subsequent intervention on the building as a whole, in which priority could be given to the UPV- and magnetometer-determined high-risk areas.

23.3.4 Case Study 4: Nuestra Señora de la Asunción Church, Valdemorillo, Madrid, Spain

This study showed that UPV can be used to date stone structures. The church (Fig. 23.4a, b) combines a number of architectural styles (Fig. 23.4c), a reflection of its protracted construction during nearly ten centuries (from the eighth to the seventeenth). The primary building materials are homogeneous monzogranite, porphyritic granite, and porphyritic monzogranite, supplemented secondarily by gneiss, aplite, and leucogranite. All the stone was quarried in the vicinity of the village (Fort et al. 2010, 2013a, b).

Both UPV (Vp) and rebound hammer (Rn) measurements were taken on 200 façade ashlars. Ultrasonic readings were taken in reflection mode to the scheme depicted in Fig. 23.4d using 54-kHz transducers; 214 points were measured on the same materials in the source quarries.

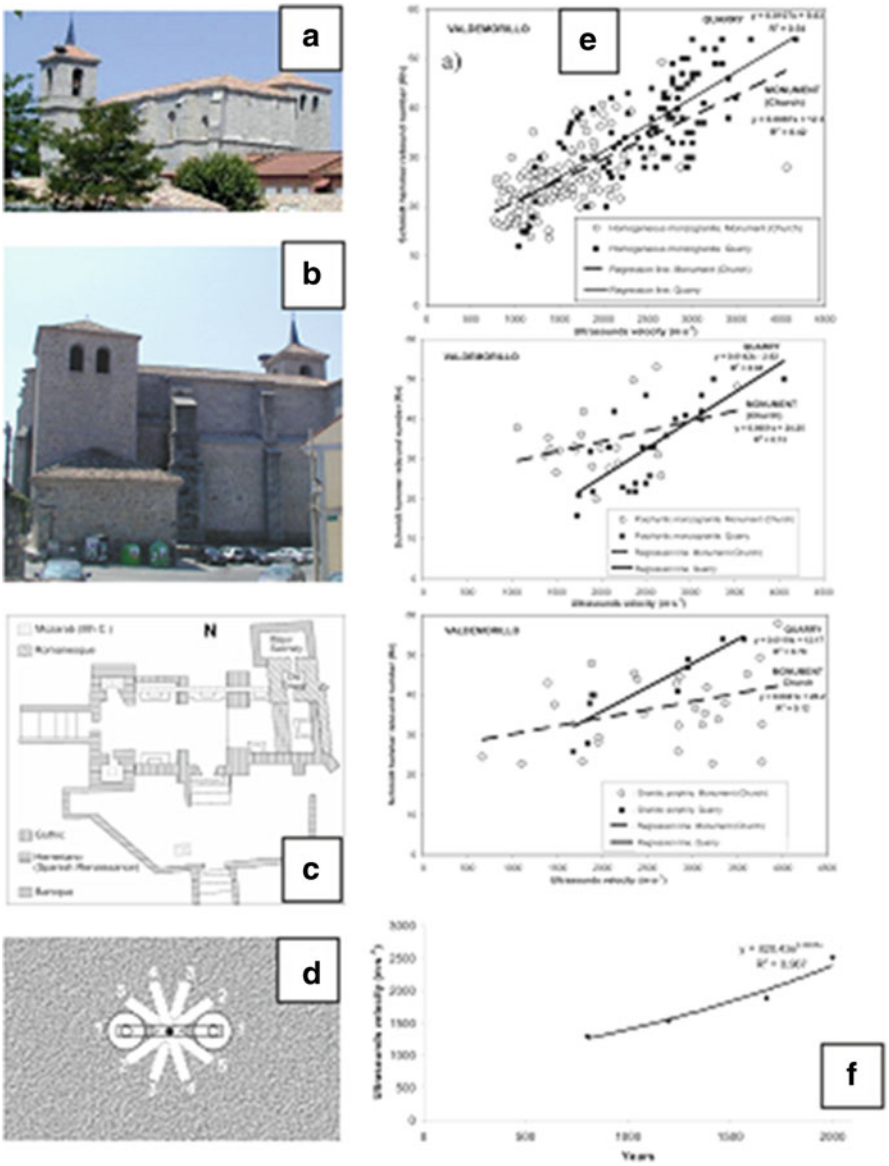

Fig. 23.4 Case Study 4: Nuestra Señora de la Asunción Church, Valdemorillo, Madrid, Spain. (**a**) South and east façades of the church. (**b**) North façade of the church. (**c**) Architectural styles: *yellow*, Mozarab (seventh century); *red*, Romanesque (twelfth century); *navy blue*, Gothic (fifteenth century), *green*, Herreriano (particular Spanish Renaissance style, Escorial type, sixteenth century); and *light blue*, Baroque (seventeenth century). (**d**) Arrangement of ultrasound measurements in each ashlar; transducers are separated by 20 cm. (**e**) Correlation between the ultrasound velocity of the church granitic ashlars and that of the granite provenance quarries. (**f**) Evolution of the ultrasound velocity values from monzogranite ashlars with respect to the epoch in which they were laid in the structure and from the present quarries

Figure 23.4e shows the Vp/Rn regression lines obtained for the granitic materials in the monument and its respective quarries. All the curves for the stone on the monument were similar to the findings for the quarry rock, although the systematically steeper slopes for the quarry than the monument materials denoted more intense alteration in the latter.

Last, the graph in Fig. 23.4f plots the average ultrasound velocities recorded on the surface of the monzogranite ashlars in the church and their variation against the period when the stone was laid. As the graph shows, the decline in mean Vp values with ashlar age was exponential. The periods of church construction are well defined and hence could be readily identified (Fig. 23.4c).

This exponential relationship may consequently be used as a dating criterion for building materials exposed to similar conditions (such as orientation and climate) as an initial approximation of the period when structures were erected.

The conclusion drawn is that the assessment of the condition of the stone in a building may provide a rough estimate of when it was built.

23.3.5 Case Study 5: The Stone Stela at Barros, Corrales de Buelna, Cantabria, Spain

Here, as in case study 2, the aim was to assess the degree of decay in the monument before its relocation.

This monolithic sandstone disk, measuring 165 cm in diameter and 34 cm thick (Fig. 23.5a), is a third-century stela associated with Sun worship. The survey focused on identifying cracks that could potentially cause damage during the relocation of the monument from a walkway alongside a heavily traveled road (Fig. 23.5b) to an indoor museum.

Hundreds of direct UPV readings (i.e., with the two transducers positioned on opposite sides of the disk) were recorded, using both a radial grid (Fig. 23.5c) and a quadrangular grid. The many cracks visible to the naked eye (Fig. 23.5d) were mapped (Fig. 23.5e). The UPV values for both sides of the stela, which ranged from 600 to >4000 m/s, were also mapped (Fig. 23.5f). Low-velocity values denoting weak areas were found to concur with cracks and stone decay. The UPV survey identified a crack 12 cm deep (solid black line in Fig. 23.5f) around which special precautions were adopted during relocation to prevent possible fracture.

The time versus distance curves in Fig. 23.5g (values measured across the dotted line shown in Fig. 23.5f) identified all the inner discontinuities.

With that information, the monument was successfully transported and arrived at its new location intact.

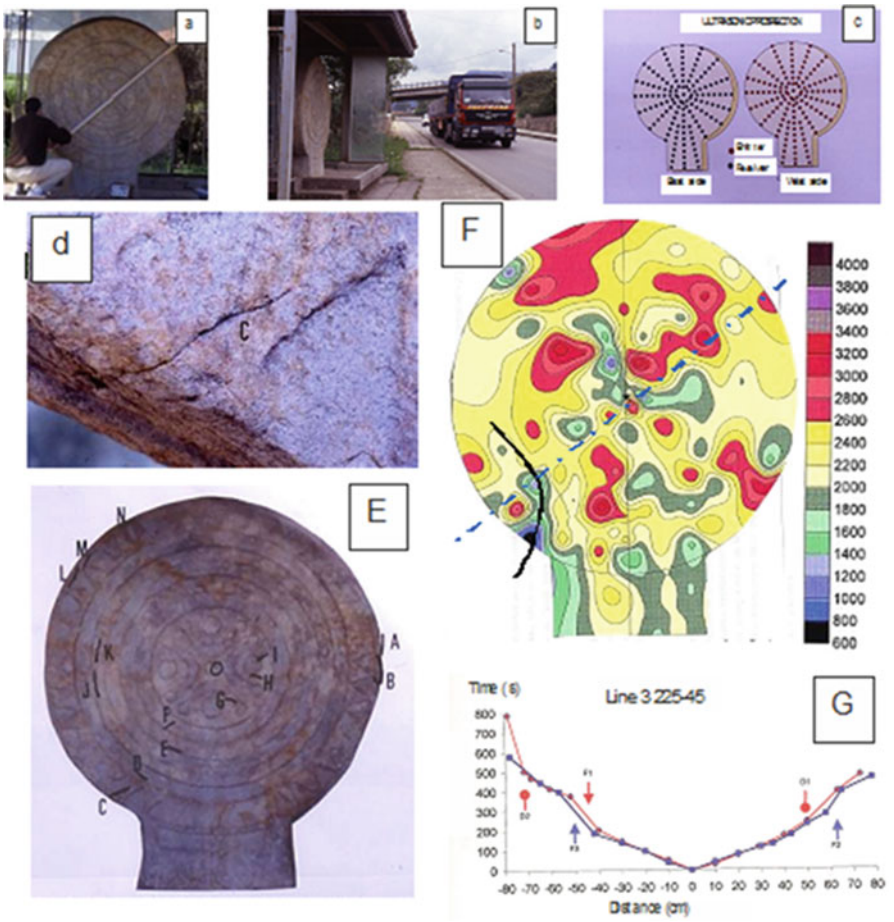

Fig. 23.5 Case Study 5: the stone stela at Barros, Corrales de Buelna, Cantabria, Spain. (**a**) Barros stone stela. (**b**) Position of the stela, a few meters away from the road. (**c**) Indirect mode measurements in both a radial and a rectangular arrangement of the transducers, and direct mode measurements with the transducers placed in both faces, front and back, as well as along its thickness. (**d**) Crack in the *bottom left-hand* corner of the sculpture. (**e**) Cracks visible to the unaided eye. (**f**) Ultrasound velocity distribution curve in which was detected the continuation of the crack toward the interior of the structure, which could result in its possible breaking during the moving process. (**g**) Variation in the receiving time of the ultrasound signal at different distances (one transducer is fixed and the other is moved), detecting anomalies

23.3.6 Case Study 6: The Real Alcázar (Royal Castle) at Seville, Spain

This study was conducted to determine the level of stone decay with a view to future intervention.

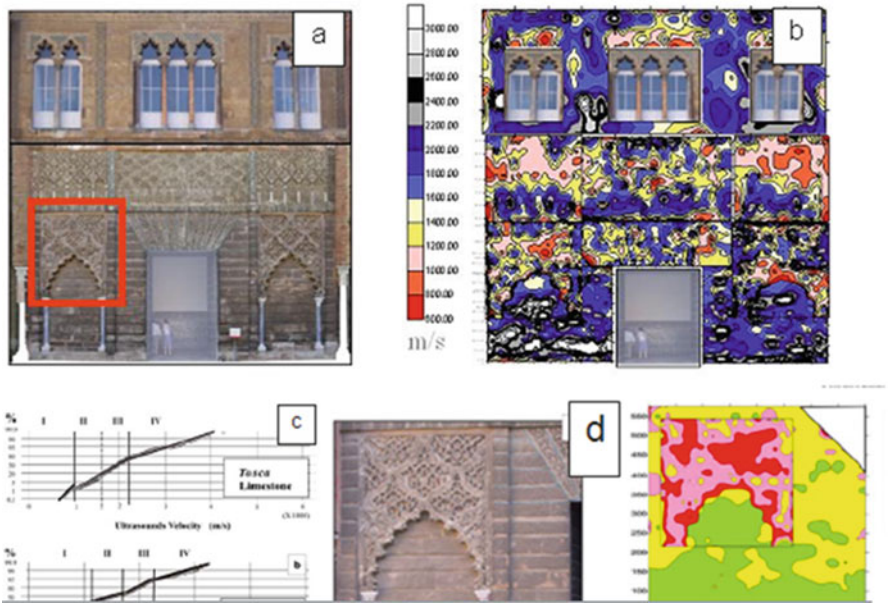

Fig. 23.6 Case Study 6: The Real Alcázar (royal castle) at Seville, Spain. (**a**) Don Pedro façade, Real Alcazar, Seville. (**b**) Ultrasound velocity survey. (**c**) Probabilistic distribution curve of ultrasound velocity for Tosca (TL) and Palomera (PL) limestones, distinguishing four classes. (**d**) Mapping of the altered areas built with Palomera limestone (the most decayed areas shown in *red*)

The Real Alcázar, a tenth-century castle, was built in Mudejar style. This study focused on its similarly Mudejar fourteenth-century "Don Pedro" façade (Fig. 23.6a). The wall, divided from top to bottom into three stories (upper, middle, lower) flanked on both sides by galleries, consists of ashlars and ornate arabesques. The materials primarily used for the dimension stones and ornamental elements were two types of limestone: Tosca (bioclastic limestone) was used on the lower story and both ashlars and arabesques on the middle and upper stories were made with Palomera (grain-supported limestone). The upper third of the facade has marble columns and elements made of other materials, such as ceramic tile, mortar, and brick (Vazquez et al. 2010).

A total of 4400 indirect UPV readings were taken on the façade (Fig. 23.6b) at a transducer frequency of 54 kHz. These transducers had a flat circular contact area 50 mm in diameter; the measurement grid consisted of 15-cm squares. Ultrasound velocity values were observed to differ depending on the variety of stone and its petrological properties. Within each variety, the lower the value, the more severe was the decay. Sclerometric surface hardness was also measured: the values shown for Palomera stone refer to the measurements for 23 ashlars and 20 uncarved areas at the rear of the arabesques, as the scant consistency of the carved stone precluded any such testing in those areas. The results showed that the Tosca ashlars had lower sclerometric indices (16) than the Palomera dimension stone (Vazquez et al. 2010).

The ultrasonic velocity values for the two stone varieties were grouped under four classes (Fig. 23.6c) and plotted on normal probability graphs. The lowest velocities, denoting the most severe decay, were grouped in class I and the highest values, indicating the slightest decay, in class IV. The maps obtained identified the weakest areas of the two varieties of stone (Fig. 23.6d). These findings can be used for planning interventions in the short term to ensure that the restoration and conservation of this monument are properly designed and engineered.

23.4 Conclusions

This review discusses six case studies in which the UPV analysis of building materials, mainly stone, proved highly useful for determining the degree of decay and planning preventive and remedial conservation. In the latter, intervention could be appropriately prioritized, determining the areas in need of urgent attention. Stone structure dating was also found to be possible with this technique, which was similarly instrumental as a preliminary to the relocation of stone elements.

Severely decayed areas can be rapidly visualized and located by mapping UPV findings. Moreover, normal probability plots of the results are a handy tool for determining different types of decay, in which the petrographic and petrophysical properties of the material should also be taken into account.

UPV analysis is a reliable, convenient, nondestructive, and portable technique for surveying whole elements or structures, characterized by its ability to deliver large amounts of data. This technique has become essential for characterizing materials of the cultural heritage, the hope being for its use in time, with new applications such as continuous monitoring in real time of accelerating aging processes of materials, as well as image processing that allows internal tomography of an element.

It should, however, be used in conjunction with petrographic and petrophysical as well as other nondestructive techniques.

Acknowledgments This study was funded by the Community of Madrid under the GEOMATERIALS 2 project (S2013/MIT-2914) and the Complutense University of Madrid's Research Group: "Alteración y Conservación de los Materiales Pétreos del Patrimonio" (ref. 921349).

References

Alonso FJ, Suárez del Río LM (1985) Velocidad de propagación de ondas en rocas carbonatadas. Trabajos de Geología 15:315–324

Alvarez de Buergo M, Fort R (2014) The Royal Palace of Madrid, Spain. Twenty years of stone conservation research. In: Brai M, Tranchina L, Alberghina M, Fontana D, Fernandez F (eds) Diagnostics for cultural heritage. Analytical approach for an effective conservation. UniNetLab, DiFC, Universita degli Studi di Palermo, Italia, pp 9–15. ISBN 978-88-907460-5-5

Álvarez de Buergo M, González T (1994) Estudio del método de la medida de la velocidad de propagación del sonido y su aplicación a edificios históricos. Ingeniería Civil 94:69–74

Benavente D, Martínez-Martínez J, Jáuregui P et al (2006) Assessment of the strength of building rocks using signal processing procedures. Constr Build Mater 20:562–568

Bodare A (1996) Non destructive test methods of cultural stone. Division of Soil and Rock Mechanics, Department of Civil and Environmental Engineering, Royal Institute of Technology, Stockholm

Cantó de Gregorio A M (2007) La 'Piedra Escrita' de Diana en Cenicientos (Madrid) y la frontera oriental de Lusitania. http://www.celtiberia.net/es/biblioteca/?id=1682&pagina. Last access 21 July 2015

Doehne E, Price CA (2010) Stone conservation: an overview of current research. 2nd edn. (Research in conservation). The getty conservation institute Los Angeles

Fort R (2008) Aplicación de la técnica de propagación de ondas ultrasónicas en el patrimonio pétreo. In: Actas de las III Jornadas Técnicas Durabilidad y conservación de materiales tradicionales naturales del patrimonio arquitectónico. Instituto Tecnológico de Rocas Ornamentales y Materiales de Construcción (INTROMAC). ISBN 978-84-691-5918-7

Fort R, Alvarez de Buergo M, Mingarro F, López de Azcona MC (2004) Stone decay in XVIII century monuments due to iron corrosion. The Royal Palace, Madrid (Spain). Build Environ 39:357–364

Fort R, Alvarez de Buergo M, Perez-Monserrat EM, Varas MJ (2010) Characterisation of monzogranitic batholiths as a supply source for heritage construction in the northwest of Madrid. Eng Geol 115:149–157

Fort R, Varas MJ, Álvarez de Buergo M, Freire D (2011) Determination of anisotropy to enhance the durability of natural stone. J Geophys Eng 8:S132–S144

Fort R, Alvarez de Buergo M, Perez-Monserrat EM et al (2013a) Evolution in the use of natural building stone in Madrid, Spain. The stone cycle and conservation of monuments. Q J Eng Geol Hydrogeol 46:421–428

Fort R, De Buergo MA, Perez-Monserrat EM (2013b) Non-destructive testing for the assessment of granite decay in heritage structures compared to quarry stone. Int J Rock Mech Min Sci 61:296–305

Fort R, Varas-Muriel MJ, Alvarez de Buergo M, Perez-Monserrat EM (2015) Colmenar limestone, Madrid, Spain: considerations for its nomination as a Global Heritage Stone Resource due to its long term durability. Geol Soc Lond Spec Publ 407:121–135

Freire-Lista D, Fort R, Varas-Muriel MJ (2015) Alpedrete granite (Spain). A nomination for the "Global Heritage Stone Resource" designation. Episodes 38:106–113

Mamillan M (1991) Methods for assessing the deterioration of stone monuments. In: Science, technology and the European Cultural Heritage. Butterworth-Heinemann, Bologna, pp 90–100

Marini P, Bellopede R, Manfredotti L (2004) About accuracy on ultrasonic measurements on stone. In: The 10th international congress on the deterioration and conservation of stone (ICOMOS). Stockholm, Sweden, pp 659–666

Montoto M, Valdeón L, Côtte P et al (1994) Non-destructive characterization of the state of deterioration of megaliths by ultrasonic tomography: a petrophysical interpretation. In: The 3rd international symposium on the conservation of monuments in the Mediterranean Basin, Venice, pp 3–9

Perez-Monserrat EM, Alvarez de Buergo M, Gomez-Heras M et al (2013) An urban geomonumental route focusingon the petrological and decay features of traditional building stones used in Madrid, Spain. Environ Earth Sci 69:1071–1084

RILEM (1980) Recommended tests to measure the deterioration of stone and to assess the effectiveness of treatment methods. Commission 25 PEM (Protection et erosion des monuments). Mater Struct 75:175–253

Sokolov SY (1929) On the problem of the propagation of ultrasonic oscillations in various bodies. Elek Nachr Tech 6:454–460

Sokolov SY (1935a) Ultrasonic oscillations and their applications. Tech Phys 2:1–23

Sokolov SY (1935b) Ultrasonic methods of detecting internal flaws in metal articles. Zavod Lab 4:1468–1473

Sokolov SY (1941) Ultrasonic methods of studying the properties of quenched steel and detecting internal flaws in metallic articles. Zh Tekh Fiz 11:160–169
Sokolov SY (1946) The use of ultrasonic oscillations for observing physico-chemical processes. Zh Tekh Fiz 16:784–790
Sokolov SY (1948) The use of ultrasonics in technology and physics. Zavod Lab 11:1328–1335
Svahn H (2006) Final report for the research and development project. Non-destructive field tests in stone conservation. Literature study. Rapport från Riksantikvarieämbetet 2006:3
Vasanelli E, Colangiuli D, Calia A et al (2015) Ultrasonic pulse velocity for the evaluation of physical and mechanical properties of a highly porous building limestone. Ultrasonics 60:33–40
Vazquez-Calvo C, Varas MJ, Alvarez de Buergo M, Fort R (2010) Limestone on the 'Don Pedro I' facade in the Real Alcázar compound, Seville, Spain. Geol Soc Lond Spec Publ 331:171–182
Weiss T, Rasolofosaon PNJ, Siegesmund S (2002) Ultrasonic wave velocities as a diagnostic tool for the quality assessment of marble. Geol Soc Lond Spec Publ 205:149–164
Zezza U (1990) Physical-mechanical properties of quarry and building stones. In: Veniale F, Zezza U (eds) Advanced workshop: analytical methodologies for the investigation of damaged stone. Pavia University, Pavia

Chapter 24
Wireless Monitoring to Detect Decay Factors in Natural Heritage Scenarios in Spain: A Case Study at Lanzarote

María Inmaculada Martínez-Garrido and Rafael Fort González

Abstract This chapter discusses a study conducted primarily to assess the quality of the communications delivered by a Smartmote wireless platform in the Jameos del Agua volcanic tunnel on the Spanish island of Lanzarote. The findings identified coverage needs and the position of tracking points required for a long-term monitoring campaign. The environmental conditions outside and the microclimate inside the tunnel were monitored with the wireless sensor network and backup data loggers to quantify conditions in the areas most heavily impacted by the major factors of decay: human presence and solar radiation. The thermal and relative humidity gradients inside the materials were also determined. In addition, the platform detected tidal-induced rises in humidity that affect the lake inside the volcanic tube.

24.1 Introduction

Jameos del Agua, similar to Cueva de los Verdes, is located inside the lava tube generated during the Corona eruption on Lanzarote, Canary Islands, Spain (29°90′27″ N; 213°25′52″ W). Jameos del Agua is sited in the section of tube closest to the coast. It owes its name (literally, "water hollows" in Spanish) to the existence of an interior lake, a singular geological formation. "Jameos" are large, naturally formed holes in a volcanic tube resulting from the partial collapse of its roof (Centros de Arte, Cultura y Turismo, EPEL del Cabildo de Lanzarote). The

M.I. Martínez-Garrido (✉)
Instituto de Geociencias (CSIC-UCM) and Departamento de Ingeniería Telemática y Electrónica (ETSIST, UPM), CEI Campus Moncloa (CSIC, UPM-UCM), C/José Antonio Nováis, 12, 28040, Madrid, Spain
e-mail: mi.martinez.garrido@csic.es

R. Fort González
Instituto de Geociencias (CSIC-UCM), CEI Campus Moncloa (CSIC, UPM, UCM), C/José Antonio Nováis, 12, 28040, Madrid, Spain
e-mail: rafael.fort@csic.es

N. Masini, F. Soldovieri (eds.), *Sensing the Past*, Geotechnologies and the Environment 16, DOI 10.1007/978-3-319-50518-3_24

tunnel now benefits from two types of environmental protection; it is located within the Malpaís de la Corona Natural Monument, and is listed as a scientific and cultural asset in the historic garden category (1999).

Many monitoring campaigns have been conducted on the Canary Islands, generally focusing on natural risk management with a view to creating volcanic risk alerts (Garcia et al. 2014). Synthetic aperture radar (SAR) interferometry is applied to determine the deformations induced by volcanic strain (Romero et al. 2003) and, in conjunction with the global positioning system (GPS), to ascertain variations in sea level (Fernandez et al. 2003). The concentration of CO_2 and SO_2 is monitored with GPS-assisted geodesic techniques (Marti et al. 2009). Tracking stations, in turn, record temperature (Borges et al. 2004), strain (Venedikov et al. 2006), or geomagnetic and gravimetric values (Lopez et al. 2012).

Despite the importance of monitoring the microclimate and material behavior in emblematic assets of geological, tourist, natural, or ecological interest such as Jameos del Agua, however, no active tracking campaigns have addressed these issues. The tourist appeal of this enclave, which has a restaurant in the tunnel itself and a museum ("The House of Volcanoes") in the same complex, generates heavy pedestrian traffic that may have an impact on its conservation.

In addition, the lake has considerable faunistic value, because it is home to a tiny (just 1 cm long) endemic blind albino crab, *Munidopsis polymorpha*. The existence of this crustacean creates a pressing need for monitoring, inasmuch as it is highly sensitive to changes in the physical properties and chemical composition of the seawater in the lake, as well as to visitor-related noise and light (Fig. 24.1).

This study aimed to assess the reliability of the communication afforded by a wireless sensor network before conducting a long-term monitoring campaign in the tunnel. Such preliminaries were designed to determine the monitoring points needed to cover the areas inside Jameos del Agua to track certain predefined parameters.

24.2 Geological Environment

The formation of this volcanic tube around 21 $\pm$ 6.5 thousand years ago concurred with a significant decline in sea level (Carracedo et al. 2003). When Corona erupted, it generated huge volumes of very fluid basaltic "pahoehoe" lava that flowed northwest–southeast from the volcanic cone to the southeast coast of Lanzarote, forming a winding, 25-m-diameter, 7600-m-long tunnel or tube. Its roof has collapsed in many places, resulting in what are known locally as "jameos" through which the tube can be accessed. The most prominent of these hollows have names: "Molino," "Puerta Falsa," "Cueva de los Verdes," and "Jameos del Agua." The latter two are open to the public. The lake inside Jameos del Agua is connected to the stretch of tube that runs into the sea for around 1600 m from the shore at a depth of 80 m (Mendo and Ortega 1988).

The walls and floor of the volcanic tube consist of alkaline basaltic coulees covered by subalkaline basaltic coulees with a higher idio-hypidiomorphic olivine

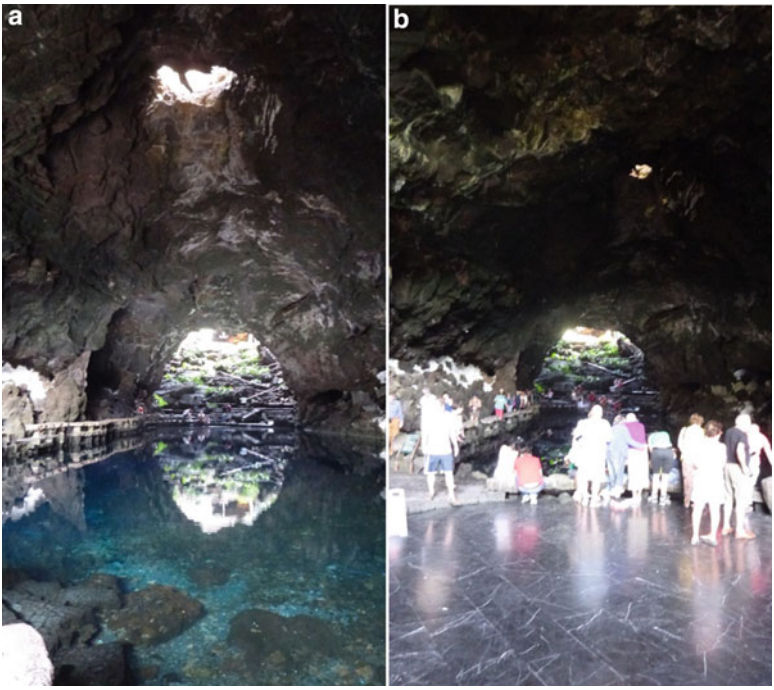

Fig. 24.1 Jameos del Agua, Lanzarote, Canary Islands, Spain: volcanic tube with interior lake (**a**); tourists visiting the tunnel (**b**)

phenocryst content in a plagioclase, olivine, and clinopyroxene microcrystalline matrix, altered by the presence of oxides. The basalt tunnel walls and floor are riddled with millimetric elongated pores formed by gas escaping from the molten lava. This basaltic lava with plagioclase and oxidized olivine crystals also contains zeolites, clinopyroxene, and iron oxides and sulfates (Carracedo et al. 2003).

Lanzarote forms part of Spain's Canary Island archipelago, located in the temperate zone of the Tropic of Cancer. It has a subtropical climate with a yearly mean temperature of 22 °C, wintertime lows normally not less than 14 °C, and summertime highs not more than 29 °C; yearly rainfall is less than 200 mm. The wind, especially the dust-laden type from the Sahara Desert, often blows in Lanzarote.

24.3 Methodology

By way of reference for the microclimate monitoring conducted in the Jameos del Agua tunnel, a formation on the Spanish island of Lanzarote (Fig. 24.2), the weather conditions prevailing outside this volcanic tube were also tracked. DS1923 i-button (Px) data loggers were positioned for that purpose at the House of Volcanoes museum (P1) and on the tunnel chimney (P2) (see Fig. 24.3, P1 and P2).

Fig. 24.2 Aerial view of the Jameos del Agua volcanic tunnel at Lanzarote, Canary Islands, Spain

Fig. 24.3 Data logger positions outside the Jameos del Agua volcanic tunnel at Lanzarote, Canary Islands, Spain: *P1*, House of Volcanoes; *P2*, tunnel chimney

The microclimatic conditions in the tube and inside the walls and floor were monitored with a Smartmote (Sx) (Smartmote 2015) wireless platform (Martínez Garrido and Fort 2017), as well as with four additional data loggers (P3–P6), as shown in Fig. 24.4.

The location of the monitoring points was determined in a preliminary study in which the factors considered included exposure to heavy pedestrian traffic or solar radiation and the existence of materials of interest inside the volcanic walls

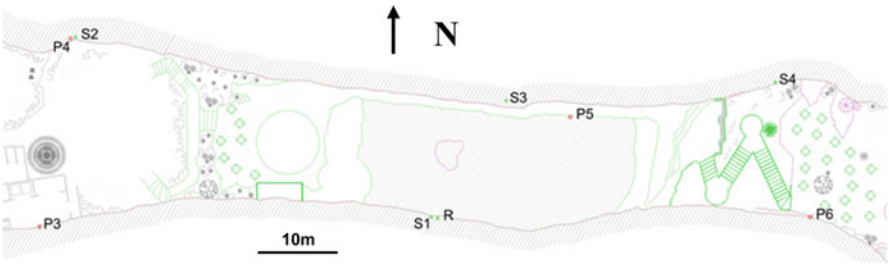

Fig. 24.4 Wireless sensor network nodes (*Sx*) and data loggers (*Px*) deployed at Jameos del Agua, Lanzarote, Canary Islands, Spain

and the floor close to the lake. The aim was to cover the entire scenario with the devices deployed.

For reasons of institutional organization, the monitoring period was divided into two stages: from 19 May to 14 June 2014 (27 days) and from 24 to 30 June 2014 (7 days). The mote sensors were numbered from X5 to X8 and positioned as described in Table 24.1, which summarizes the wireless technology used, the monitoring objectives, and the sensor positions.

24.3.1 Data Loggers DS1923

Maxim Integrated Products (2013) 16.3-mm-diameter, 5.9-mm-high DS1923 i-Button data loggers were used to measure temperature (T) and relative humidity (RH). These devices featured a resolution of 8 bits and operating ranges of −20 to +85 (with a precision of ±0.5 °C) for T and of 0–100% (with a precision of ±0.5%) for RH. OneWireViewer software was used to program the sensors and download the data. A constant 15-min sampling rate was established throughout.

The DS1923 model's 512-byte memory stored T/RH data and its 64-byte memory calibration data. When the memory was full, OneWireViewer overwrote all the data previously saved. (These devices can also be programmed for a measuring lag and separate sampling rates.)

24.3.2 Smartmote Wireless Sensor Network

SmartmoteWS hardware (release 3.21 with and without UART and release 3.23) was deployed and set to the low-power mode to lengthen battery lifetime. The platform was fitted with LEDs for integrated system control of data reception, power, and WiFi access.

Smartmote node sensors (Fig. 24.5) have a built-in low-power microcontroller, radio receiver, sensor board, and primary batteries. Model 3.21 motes, fitted with

Table 24.1 Monitoring network deployed at Jameos del Agua, Lanzarote, Canary Islands, Spain

	Type	Monitoring objective	Position
P1	Data logger DS1923	Outdoor conditions	Casa de los Volcanes
P2	Data logger DS1923	Outdoor conditions	Tunnel chimney
P3	Data logger DS1923	Conditions at tunnel SW entrance	Tunnel SW entrance
P4	Data logger DS1923	Conditions at tunnel NW entrance	Tunnel NW entrance
P5	Data logger DS1923	Interior conditions around lake	Tunnel interior, near lake
P6	Data logger DS1923	Conditions at tunnel SE entrance	Tunnel SE entrance
R	Smartmote WSN receiver base station	Data reception	Tunnel interior, central to platform
S1	Smartmote mote with four Sensirion SHT25 T/RH (temperature/relative humidity) sensors	Conditions inside tunnel/materials	X5: inside volcanic rock
			X6: inside volcanic floor
			X7: environmental, outside influence of volcanic wall
			X8: environmental, within influence of volcanic wall
S2	Smartmote mote with four Sensirion SHT25 T/RH sensors	Conditions inside tunnel/materials	X5: environmental
			X6: environmental, outward direction
			X7: (inside) crack
			X8: environmental, inward direction
S3	Smartmote mote with four Sensirion SHT25 T/RH sensors	Conditions inside tunnel/materials	X5: environmental
			X6: environmental, outward and eastward
			X7: environmental, outward and westward
			X8: inside volcanic rock
S4	Smartmote mote with four Sensirion SHT25 T/RH sensors	Conditions inside tunnel/materials	X5: environmental
			X6: environmental, exposed to solar radiation
			X7: environmental, inward
			X8: inside crack

I2C T/RH input pins, were used (Martínez Garrido and Fort 2017). Two 8.5-Ah, 2.6-V lithium batteries with a service life of approximately 2 years can be connected to each mote.

The (Sx) wireless network nodes sent information from their sensors to a receiver base station (R in Fig. 24.4) running on Linux (distributed by Debian) and fitted with a remotely accessible SQL database for data storage.

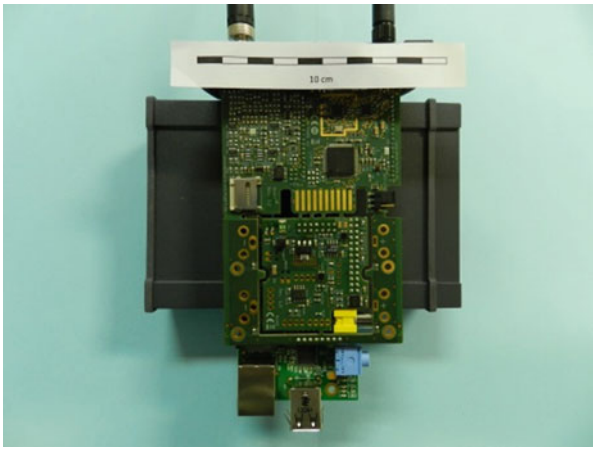

Fig. 24.5 Smartmote platform sensor node

A CC2520 radio transceiver, also built into the nodes, was used for 2.4-GHz ISM band communications; a 512-MB RAM, 700-MHz BCM2835 CPU ARM1176JZF-S processor was deployed. The devices were fitted with USB and SAM antenna connectivity and designed to run on 5 V power. Omnidirectional dipole antennas with a vertical linear polarization gain of 2 dBi were used, with an antenna extension for S4 (see Fig. 24.4) (Martínez-Garrido and Fort 2017).

The Sensirion T/RH sensors (Sensirion 2015) used for the Smartmote network, designed to operate at −25 °C to +85 °C, were set to a 1-min sampling rate for T/RH data. They were protected with E+E Elektronik EE00 enclosures, rugged Hygrosens/Sensirion high-density sintered polyethylene filters affording ANSI/IEC 60529 2004 IP65 protection against dust and pressurized water, which is especially suitable for volcanic environments. Because of this protection, the sensors were able to perform without electronic failure in very high humidity and reset speedily after recording conditions upward of 95% RH.

24.4 Results

The network communications findings and reading assessments follow.

24.4.1 Network Communications

Motes S2, S3, and S4 were positioned at 56.67, 18.33, and 50.00 m, respectively, from the base station (R) with no direct line of sight (Martínez-Garrido and Fort 2016a). The mean received signal strength indicator (RSSI) values were measured, as well as the correlation among the first bits in the frame received, which together denote signal quality. Battery consumption was practically imperceptible and 100%

of the messages emitted by motes S2 and S3 were received. The lowest RSSI value, −23.10 dBm, was observed for the mote with an antenna extension (S4; see Fig. 24.4), which exhibited a message success rate of 97.63%. Measured against Texas Instruments Incorporated (2007) radio transceiver specifications, quality was very close to excellence, with RSSI values of more than −40 dBm and correlations of upward of 104.5 in all cases (Martínez-Garrido and Fort 2014, 2016b).

24.4.2 Microclimatic Conditions in Jameos Del Agua as Recorded with Data Loggers

The device at point P1 logged the greatest variability in both T and RH. In the period monitored in June 2014, although the mean temperature exceeded 23 °C with highs of more than 30 °C every day (with a peak at 42.5 °C on 14 June 2014; see Fig. 24.6), the RH values were also very high, with a mean of 66.3% and peaks up to 95.6% (14 June 2014; see Fig. 24.6).

Another pertinent finding was the similarity in the P3 (SW entrance) and P6 (SE entrance) values for in-tunnel RH, in turn similar to the outside conditions, although the daily low RHs logged at P3 were closer to the outdoor conditions (P1) (Fig. 24.6; enlargement insert for early June on the lower right). Humidity varied less at P4 and P5, with higher values at P4 where routine watering of nearby plant life raised the RH recorded by the sensors. These readings not only failed to follow the same pattern as the other logs but were often completely reversed, delivering high readings when the other points recorded low values. In addition, thermal lags were observed between the outdoor and in-tunnel high temperatures, with maxima

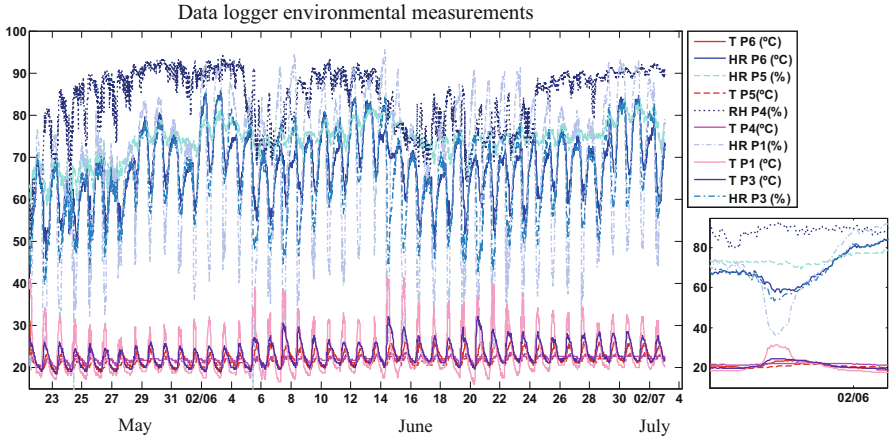

Fig. 24.6 Environmental conditions at Jameos del Agua, Lanzarote, Canary Islands, Spain, recorded with DS1923 i-button data loggers at monitoring points outside the tunnel, at the entrance to the tunnel, and deep within the tunnel

up to 5 h at P5 (the innermost logger), medium values of 2.5–3 h at P4, and minima of 1–2 h at P3 and P6.

The maximum Ts reached at the loggers with minimal lag relative to outdoor conditions were greater for west-facing P3 than for east-facing P6 because of the orientation of the sun's rays with respect to the positions of these points inside the tunnel (Fig. 24.6).

The outdoor high T and low RH values were recorded at around 1:00 PM in the interval between 22 May and 4 July and reflected first in west-facing P3, because at that time the effect of solar radiation was more significant than early in the morning when P6 was most exposed. The lines dividing successive dates in Fig. 24.6 refer to 12:00 midnight.

24.4.3 Microclimatic Conditions at Jameos Del Agua Recorded with the Wireless Sensor Network

24.4.3.1 In-Tunnel Environment

The data recorded by mote S2 and data loggers P4 and P3, positioned around the west exit (near the ponds) from Jameos del Agua, showed that the range of values was much wider in the southwest than in the northwest (Fig. 24.7). Sensors recorded environmental conditions at the mote (X5), 3.5 m to the left (X6), and 3.5 m to the right (X8) of the mote. The values were very similar, denoting no wide fluctuations in conditions in the area around the mote. Sensor X8 recorded two tiers of high temperatures: Ts climbed steadily until around 5:15 PM, and then declined slightly until around 7:00 PM, when they plateaued with minor fluctuations until midnight (on 31/05, 03/06, 07/06, and 11/06 2014; Fig. 24.7). This staggered decline mirrored the effect of human presence. The first downturn concurred with

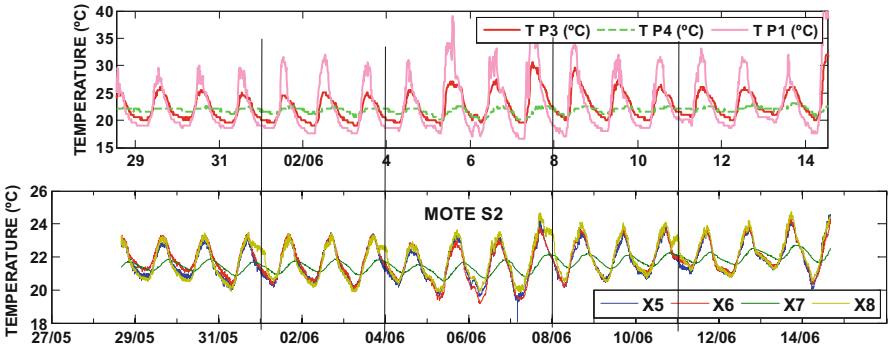

Fig. 24.7 Temperature recorded at mote S2 and points P1, P3, and P4 (see Figs. 24.3 and 24.4) at Jameos del Agua, Canary Islands, Spain

the general decrease in temperature and closure of the facility to the public, whereas the plateau from 7:00 PM to midnight concurred with pedestrian traffic to the restaurant area. Temperatures declined again thereafter in sensor X8 in mote S3 as well, which was also positioned in an area exposed to traffic. This pattern was not observed in any of the environmental sensors in motes S1 or S4 (Fig. 24.4), which were not as exposed. Sensor X7 in mote S2 (Fig. 24.4) was positioned in one of the cracks in the volcanic rock walls of the tunnel. Here the fluctuations were small (1.5–2.5 °C) and delayed by around 4 h relative to outdoor conditions (Martínez-Garrido 2015).

24.4.3.2 Effect of T/RH on Rock

Variability around mote S4 (Fig. 24.4), in contrast, was significant. Sensor X6, placed at the right of the mote and exposed directly to solar radiation, logged temperatures (T) upward of 36 °C. The area around mote S3 (Fig. 24.4) is roughcast to protect the rock from pedestrian traffic. Figure 24.8 compares the T/RH values recorded by environmental and inside-material sensors in the north-facing motes (S2, S3 and S4, Fig. 24.4). Note that the longest lag between the environmental temperature and the value inside the material was recorded by mote S2 (Fig. 24.8) followed by S3 and last by S4, that is, from west to east. The narrowest range of environmental T was observed for mote S3; the temperatures inside the rock fluctuated least in S4. Note the high humidity inside the volcanic rock at this latter mote, which while recording some of the highest temperatures caused by its exposure to solar radiation also logged the highest relative humidity (RH) (mean of 92.5% between 31/05/14 and 05/06/14). Humidity values inside the materials fluctuated least at mote S2 (with a mean of 74% for the period 31/05/14–05/06/14).

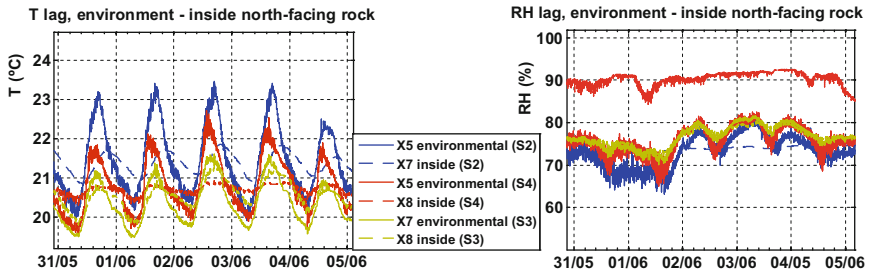

Fig. 24.8 Temperature (T) and relative humidity (RH) in the in-tunnel environment and inside the rock at motes S2, S3, and S4 (Fig. 24.4), Jameos del Agua, Canary Islands, Spain

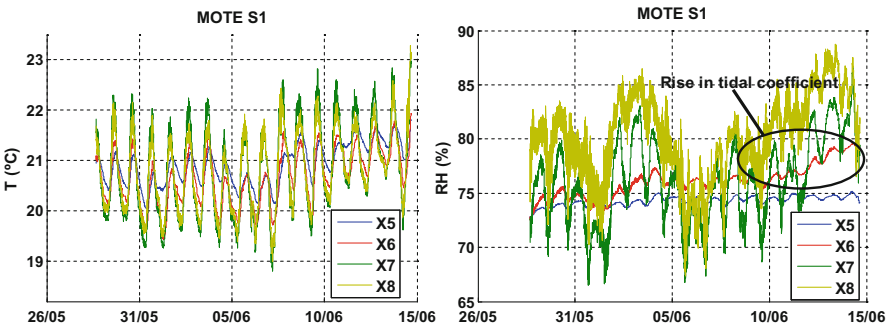

Fig. 24.9 T/RH conditions in the environment and inside the rock at mote S1 (Fig. 24.4) at Jameos del Agua, Canary Islands, Spain from 28/05/2014 to 04/06/2014

24.4.3.3 Effect of Tides

North-facing mote S1 (Fig. 24.9) proved to be of particular interest, as here conditions were analyzed inside the stone (X5), inside the volcanic floor (X6), and in the environment inside (X7) and outside (X8) the influence of the volcanic rock. The fluctuations in daily environmental conditions were most significant in X8, where the volcanic rock wall exerted a direct effect on the sensor; the temperature was highest, relative humidity lowest, and fluctuations narrowest at X7, which measured the environment free of that effect. The range of temperatures inside the rock in the walls was smaller than the values recorded inside the floor. In contrast, the range of RH variation for any given day (difference between daily high and daily low) was similar (slightly wider in the floor). A clear difference was observed between the two, however, in the pattern for the period as a whole (28/05/14–14/06/14; Fig. 24.9): the values inside the volcanic floor followed an upward trend after 10 June 2014, whereas inside the rock the values fluctuated scantily (difference between period high and low of 2.4%; Fig. 24.9) with a mean for the period of 74.3%.

The rise in humidity in mote 1, sensor X6, was of particular interest because it was correlated to tidal movements (see Table 24.2). The upper (high and very high) tidal coefficient values from 10 to 15 June 2014 (Fig. 24.9) concurred with rises in the humidity in the environment and in the floor, but not inside the rock. The tidal coefficient data, which provide a measure of the forecast tidal range (difference in height between consecutive high and low waters), were collected from Tablademareas (2014). On the days before the rise in the tidal coefficient (low and medium values, from 5 to 10 June 2014; Table 24.2), humidity was of the order of 76% but rose to 80% when the coefficient was high (14 June 2014; Table 24.2).

Sensor X8 (closer to the wall) recorded higher humidity than X7 (outside the influence of the wall) and narrower daily fluctuation, although the temperature patterns in the two sensors were very similar. The explanation might be found in

Table 24.2 Tidal table for 5–15 June 2014 at Arrecife, Lanzarote, Canary Islands, Spain

	Tide (HH:MM)				Tide height (m)				Tidal coefficient		
Date	1st low tide	1st high tide	2nd low tide	2nd high tide	1st low tide	1st high tide	2nd low tide	2nd high tide	12:00 midnight	12:00 noon	Category
05-Jun	1:21	7:33	13:33	19:58	−0.7	0.5	−0.5	0.7	44	44	Low
06-Jun	2:27	8:42	14:46	21:07	−0.6	0.5	−0.5	0.6	45	47	Low
07-Jun	3:35	9:51	15:57	22:13	−0.6	0.6	−0.5	0.7	50	54	Medium
08-Jun	4:35	10:51	16:59	23:10	−0.7	0.7	−0.6	0.8	58	63	Medium
09-Jun	5:27	11:41	17:50	–	−0.9	0.9	−0.8	–	67	72	Medium
10-Jun	6:12	0:00	6:12	12:25	−1.0	1.0	−1.0	1.1	77	82	High
11-Jun	6:54	0:45	19:19	13:08	−1.2	1.1	−1.2	1.3	85	90	High
12-Jun	7:35	1:29	20:02	13:50	−1.3	1.2	−1.3	1.4	92	96	Very high
13-Jun	8:17	2:13	20:45	14:33	−1.4	1.3	−1.5	1.5	98	99	Very high
14-Jun	9:00	2:59	21:31	15:18	−1.4	1.4	−1.5	1.6	98	95	Very high
15-Jun	9:45	3:46	22:19	16:05	−1.4	1.4	−1.5	1.6	94	92	Very high

Data taken from Tablademareas (2014)

the effect of possible air currents, which would raise the humidity recorded by X8. Because of its position near the wall, however, that sensor would record less daily fluctuation.

The environmental temperatures in the centrally located south-facing (S1; Fig. 24.4) and north-facing (S3; Fig. 24.4) motes were very similar, although the range of variation inside the rock was wider on the south side. The relative humidity findings followed much the same trend as temperature, with similar environmental values and values inside the rock on the north side. Here, however, the RH values inside the rock on the south were more stable.

24.5 Conclusions

The survey conducted at Jameos del Agua shows the effectiveness and utility of deploying wireless sensor networks to monitor microclimatic conditions as well as conditions inside volcanic materials (walls and floors). The parallel deployment of a series of data loggers is also very useful to characterize the outdoor environment and determine its differences with in-tunnel conditions with a view to saving on deployment costs.

The wireless platform studied delivered excellent communication quality. The entire scenario was monitored with just four sensor nodes that were able to cover areas characterized by pedestrian traffic or the presence of a lake, factors that could condition long-term campaigns to identify decay. The use of different types of sensors would enhance the geological, tourist, natural, and ecological benefits of such monitoring in pursuit of protection of the lake species and conservation of the asset as a whole, based on microclimatic parameters and their relationship to basaltic tubes.

Acknowledgments The authors thank the Casa de los Volcanes of Lanzarote Island Council, specially its director Jaime Arranz and Orlando Hernández for their help. The present study was funded under GEOMATERIALES 2 (S2013/MIT-2914) and CGL-2011-27902 projects and by the Complutense University of Madrid's research group on Heritage Stone Material Alteration and Conservation. M.I. Martínez-Garrido participated with the support of the Moncloa Campus of International Excellence (UCM-UPM). The manuscript was edited by Margaret Clark, professional translator and English language science editor.

References

ANSI/IEC 60529 (2004) Degrees of protection provided by enclosures (IP code) (identical national adoption). National Electrical Manufacturers Association, Rosslyn

Borges R, Hernandez-Guerra A, Nykjaer L (2004) Analysis of sea surface temperature time series of the south-eastern North Atlantic. Int J Remote Sens 25(5):869–891

Carracedo JC, Singer B, Jicha B, Guillou H, Rodríguez Badiola E, Meco J, Pérez Torrado FJ, Gimeno D, Socorro S, Láinez A (2003) La erupción y el tubo volcánico del volcán Corona (Lanzarote, Islas Canarias). Estud Geol 59(5-6):277–302

Centros de Arte, Cultura y Turismo, Epel del Cabildo de Lanzarote (1999) http://www.centrosturisticos.com/centros/CENTROS/published_es/DEFAULT/jameos_agua.html

Fernandez J, Yu TT, Rodriguez-Velasco G, Gonzalez-Matesanz J, Romero R, Rodriguez G, Quiros R, Dalda A, Aparicio A, Blanco MJ (2003) New geodetic monitoring system in the volcanic island of Tenerife, Canaries, Spain. Combination of InSAR and GPS techniques. J Volcanol Geotherm Res 124(3–4):241–253

Garcia A, Berrocoso M, Marrero JM, Fernandez-Ros A, Prates G, De La Cruz-Reyna S, Ortiz R (2014) Volcanic alert system (VAS) developed during the 2011–2014 El Hierro (Canary Islands) volcanic process. Bull Volcanol 76(6):825

Lopez C, Blanco MJ, Abella R, Brenes B, Cabrera Rodriguez VM, Casas B, Dominguez Cerdena I, Felpeto A, Fernandez de Villalta M, Del Fresno C, Garcia O, Garcia-Arias MJ, Garcia-Canada L, Gomis Moreno A, Gonzalez-Alonso E, Guzman Perez J, Iribarren I, Lopez-Diaz R, Luengo-Oroz N, Meletlidis S, Moreno M, Moure D, Pereda De Pablo J, Rodero C, Romero E, Sainz-Maza S, Sentre Domingo MA, Torres PA, Trigo P, Villasante-Marcos V (2012) Monitoring the volcanic unrest of El Hierro (Canary Islands) before the onset of the 2011–2012 submarine eruption. Geophys Res Lett 39:L13303

Marti J, Ortiz R, Gottsmann J, Garcia A, De La Cruz-Reyna S (2009) Characterising unrest during the reawakening of the central volcanic complex on Tenerife, Canary Islands, 2004–2005, and implications for assessing hazards and risk mitigation. J Volcanol Geotherm Res 182(1–2):23–33

Martínez Garrido MI (2015) Aportación de la monitorización mediante redes de sensores y técnicas no invasivas para la conservación preventiva del Patrimonio. Ph. D. thesis, School of Telecommunications Engineering (ETSIST), Technical University of Madrid, Spain

Martínez-Garrido MI, Fort R (2014) Sensing technologies for monitoring and conservation of cultural heritage: wireless detection of decay factors. In: Rogerio-Candeleda MA (ed) Science, technology and cultural heritage. CRC Press, Balkema, Leiden, pp 495–501

Martínez-Garrido MI, Fort R (2016a) Wireless communications platforms for built and natural heritage monitoring. In: In: Sensing the past: geoscience and sensing technologies for cultural heritage, Chapter 16. Springer, Cham

Martínez-Garrido MI, Fort R (2016b) Experimental assessment of a wireless communications platform for the built and natural heritage. Measurement 82:188–201

Martínez-Garrido MI, Fort R (2017) Wireless communication platforms for built and natural heritage monitoring. In: Masini N, Soldovieri F (eds) Sensing the past. Geotechnol Environ16. doi:10.1007/978-3-319-50518-3_24

Maxim Integrated Products, Inc. (2013) Last update, DS1923 Maxim Integrated. Available: http://datasheets.maximintegrated.com/en/ds/DS1923.pdf [01/15, 2015]

Mendo A, Ortega L (1988) El túnel de La Atlántida. Geo 14:9–25

Romero R, Carrasco D, Arana V, Fernandez J (2003) A new approach to the monitoring of deformation on Lanzarote (Canary Islands): an 8-year radar perspective. Bull Volcanol 65(1):1–7

Sensirion (06/06/2014, 2014) Last update, datasheet SHT25. Humidity and temperature sensor. Available: http://www.sensirion.com/fileadmin/user_upload/customers/sensirion/Dokumente/Humidity/Sensirion_Humidity_SHT25_Datasheet_V3.pdf [01/15, 2015]

Smartmote Monitoring and Testing (2015) www.smartmote.de [06/22, 2015]

Tablademareas (27/11/2014, 2014) Last update, Tabla de mareas en Arrecife, Lanzarote (Islas Canarias, España). [27/11, 2014]

Texas Instruments Inc. (02/10/2014) Rev. Diciembre 2007, 2007: Last update, CC2520 datasheet 2.4 GHZ IEEE 802.15.4/ZIGBEE RF transceiver. Available: http://www.ti.com/lit/ds/symlink/cc2520.pdf [01/15, 2015]

Venedikov AP, Arnoso J, Cai W, Vieira R, Tan S, Velez EJ (2006) Separation of the long-term thermal effects from the strain measurements in the Geodynamics Laboratory of Lanzarote. J Geodyn 41(1–3):213–220

Chapter 25
Integrated Monitoring at a Modern Architectural Masterpiece: The Case of Viaduct Basento in Potenza

Francesco Soldovieri and Jean Dumoulin

Abstract This chapter presents the interesting case study of the monitoring of the Viaduct Basento in Potenza (southern Italy). Two features make this case study fascinating. The first aspect is that Viaduct Basento is probably the most important and visionary architectural work of the famous structural engineer Sergio Musmeci. The second aspect concerns the application, almost unique in the scientific literature, of an integrated diagnosis approach combining a wide set of electromagnetic sensing technologies with advanced civil engineering analysis methodologies and tools.

25.1 Introduction

The integration of satellite, aerial remote sensing observations, and in situ sensing techniques is now recognized as the most suitable technological solution to monitor cultural heritage, infrastructures, and the surrounding territory. In fact, integration of the multi-observational platforms makes it possible to obtain a multiscale (spatial and temporal) vision of the site up to the diagnosis of the single artifact. In this way, it is possible to couple the capabilities of long-term monitoring with the early warning capabilities and high situational awareness during crisis events.

In recent years, research efforts have been carried out toward the development of integrated monitoring approaches. In this respect, it is worth noting how the "Integrated System for Transport Infrastructure Surveillance and Monitoring by

F. Soldovieri (✉)
Institute for Electromagnetic Sensing of the Environment (CNR-IREA),
Via Diocleziano 328, 80124, Napoli, Italy
e-mail: soldovieri.f@irea.cnr.it

J. Dumoulin
IFSTTAR, COSYS-SII, Route de Bouaye, CS4, Bouguenais, F-44344, France

Inria, I4S Team, Campus de Beaulieu, Rennes, F-35042, France
e-mail: jean.dumoulin@ifsttar.fr; jean.dumoulin@inria.fr

N. Masini, F. Soldovieri (eds.), *Sensing the Past*, Geotechnologies and the Environment 16, DOI 10.1007/978-3-319-50518-3_25

Electromagnetic Sensing (ISTIMES)" project (funded in the Joint Call FP7-ICT-SEC-2007 and ending on June 2012) was successful with the main aim of the design, assessment, and validation in preoperational phase of a system for the monitoring of critical transport infrastructures (Proto et al. 2010). The success of the project is testified by the fact that ISTIMES has been flagged as a "success/case story," a "high visibility/media attractive project," and as having a "substantial R&D breakthrough character" in the final review report by the European Commission.

The system exploits an information and communications technology (ICT) architecture able to supervise an integrated large network of in situ sensing techniques and space-based observation platforms; therefore, the ISTIMES approach is based on two main technological pillars.

The first one is an ICT system architecture exploiting web sensors and service-oriented technologies, which complies with specific end-user requirements, including interoperability, economical convenience, exportability, efficiency, and reliability (Soldovieri et al. 2014). In addition, the system is able to provide an easily accessible and transparent scheme for use by different (expert and not-expert) end-users and to integrate the monitoring indexes and images with other kind of information, such as GIS layers and historical datasets related to the monitored site.

The second pillar concerns the development, exploitation, and integration of a very wide range of heterogeneous electromagnetic sensors, static and mobile, capable of giving a minimally or noninvasive monitoring of the infrastructure, so not to affect the normal use or serviceability of the structure (Proto et al. 2010). In particular, the integration of state-of-the-art sensors enables a ground-based network, which is enhanced by satellite and airborne measurements. The project has exploited, assessed, and improved many different noninvasive electromagnetic sensing technologies, allowing both a global and a local vision of the infrastructure.

The effectiveness of the ISTIMES monitoring system has been finally demonstrated at the Viaduct Basento, in Potenza (Southern Italy). Viaduct Basento is the main road entrance to Potenza City and represents a significant example of modern architecture. The main outcome of the demonstration activity at Viaduct Basento was the feasibility proof of the flexibility and modularity of the ISTIMES system. All the ISTIMES sensing technologies were deployed to perform monitoring and diagnostics, and the results have been correlated and tested also by comparison with the sensors and techniques usually exploited by structural engineers, such as accelerometers and seismic ambient noise measurements. In addition, the modularity of the ISTIMES approach has permitted to extend it successfully to other kinds of infrastructure such as dams (Loperte et al. 2015) and a road network, both in the Basilicata (Southern Italy).

Therefore, the chapter is organized as follows. Section 25.2 is devoted to a brief description of the social importance and architectural value of the Viaduct Basento. Section 25.3 discusses the sensing technologies deployed at Viaduct Basento by focusing on the results achieved by ground-penetrating radar and infrared thermography. The conclusions end the chapter.

25.2 The Viaduct Basento

In the second half of the past century, several talented engineers were messengers of new concepts in structural designs and inspired future generations with their visionary innovations in civil engineering. One of the most representative figure is the Italian civil and aeronautical engineer Sergio Musmeci, whose best known masterpiece is the Viaduct Basento (1967–1976) (Giovannardi 2010).

Viaduct Basento crosses the river and is one of the main road entrances to the city of Potenza, which is the capital and the most important center of the Basilicata region, Italy (Figs. 25.1 and 25.2). The bridge is the main communication link between the industrial area and the residential area of the city.

One of the main ideas of Musmeci was the possibility of overcoming the concept that the relationship between mathematics and architecture is only theoretical. In fact, Musmeci reversed the usual point of view used in the structural design, where, after having fixed the structure geometry, the structural design issues are faced. In particular, Musmeci focused first to derive forms of the stresses incurred in different materials and structural systems, so that the final shape of the structure was mainly the result of an optimization, which ensured maximum efficiency in performance and minimal material usage.

Fig. 25.1 Location of Viaduct Basento and its aerial view (Source: figure in Bavusi et al. 2011)

Fig. 25.2 Basento Viaduct in Potenza, detail of a span (Source: figure in Bavusi et al. 2011)

The architectural solution on Viaduct Basento (Ponte sul Basento) is the result of this way of thinking; in fact, Musmeci's design was motivated by the need to produce shapes created by the forces and stress. Differing from the traditional approaches, wherein the shape of the structure is considered known, and the geometric variables are the unknowns to be determined, Musmeci designed Viaduct Basento by considering as key factors the maximum efficiency and driving forces through the chosen materials, constantly changing direction, if necessary. The main idea at the basis of the design was that all the structure would have been subjected to the same state of tension. As a result, Viaduct Basento is a piece of sculpture, of architecture, with a highly expressive form dynamically changing according to each observation point.

From a structural point of view, the deck of the Musmeci bridge constitutes a box section made of reinforced concrete, which is upheld every 17.30 m by a continuous reinforced concrete vault equivalent to four arches with wheelbases of 69.20 m and a free span among the supports of 58.80 m (Fig. 25.3). Thus, the bridge has an overall length of 69.20 m $\times$ 4 = 277 m. The road pavement is formed by 4 cm of binder and 3 cm of asphalt. The box section of the deck has longitudinal and transversal stiffening walls (internal sects), each 3.46 m long. The continuity of the deck is interrupted by a Gerber saddles system, which realizes simply laid beams (each 10.38 m) and other beams (each 24.22 m long) lying on supports 17.30 m distant and cantilevers of 3.46 m. The flat shape of the upper layer of the road is distorted by the lower part characterized by complex and fluid surfaces. These cavernous spaces can be exploited as a pedestrian walkway.

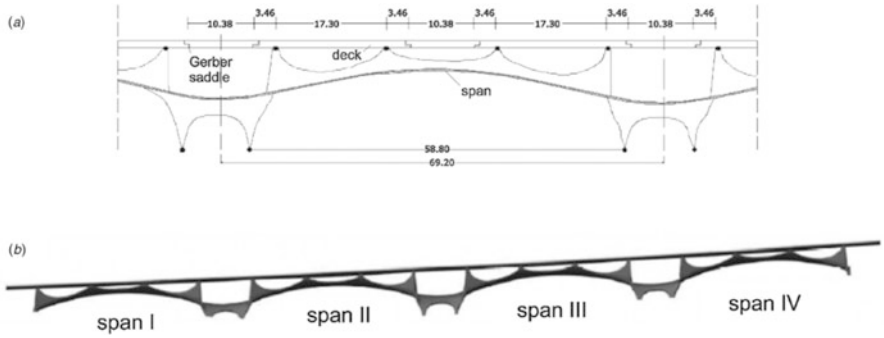

Fig. 25.3 The Musmeci bridge: longitudinal cross section of a span with the main elements of the span and deck (**a**); front figure of the whole bridge formed by four spans (**b**) (Source: figure in Bavusi et al. 2011)

This fascinating shape of the structure was first tested in a 1:10 scale model made of reinforced micro-concrete. The testing phase was carried out at the Institute of Modeling and Experimental Structures of Bergamo, and the main outcome was that the rupture was reached when the weight and overload increased to 100% of the original value. In particular, the design makes the viaduct particularly resistant against possible differential settlement or seismic vibrations, so common in the mountainous region of Potenza. In fact, the structure withstood the great earthquake in Irpinia in 1980, which reached 6.89 Mw on the Richter scale.

The resulting forms of calculations performed by Musmeci were too complicated to be carried out in industrialized repetitive modules, but nevertheless its realization did not greatly exceed the final cost with respect to a more conventional structure, where the reduction of the cost was pursued also by choosing a suitable structural concrete easily shaped.

25.3 Monitoring at Viaduct Basento

Observation and sensing capabilities in ISTIMES are ensured by a large suite of technologies able to provide minimally invasive or noninvasive monitoring and diagnostics. In particular, the following electromagnetic sensing techniques are deployed: synthetic aperture radar–satellite-based platform (SAR), hyperspectral spectroscopy (HYS), distributed optic fiber sensors (DOF), electrical resistivity tomography (ERT), ground-penetrating radar (GPR) systems, infrared thermography (IRT), ground-based systems for displacement monitoring as ground-based SAR (GBSAR), and optical displacement camera (ODM).

The integration of the aforementioned technologies allows a spatiotemporal monitoring of the structure at different scales, sampling periods, resolutions, and

depths of investigation. This approach also permits coupling the capabilities of long-term monitoring and quick damage assessment of the infrastructure during and just after crisis events. Therefore, the ISTIMES integrated observation strategy is able to comply with these requirements:

– *Global vision*: to perform wide areas of surveillance of the territory and of the embedded critical infrastructures. This vision is crucial to activate ground- and airborne-based techniques for a high-resolution investigation of the more critical areas.
– *Local scale*: to provide multi-sensed information about the status of the structure itself during normal service behavior and after a crisis event.

In this respect, the function of the space-based assets, and in particular the synthetic aperture radar satellite-based platform, is crucial for "global monitoring." In this frame, SAR observations can enhanced by the airborne platform surveys with hyperspectral and infrared sensors, so to gain information about the status of deterioration or damage of the surface of the infrastructure. The foregoing remote sensing observations are complementary to the "ground-based monitoring" (i.e., monitoring of the infrastructure itself), which is enabled by the sensing techniques both in situ and mobile. In this way, it is possible to gain other important information about the inner infrastructure and of the underground, with different degrees of depth investigation and spatial resolutions. Thus, detailed information can be obtained about all the main constructive elements of the transport infrastructure.

At Viaduct Basento, a large suite of ISTIMES sensing technologies were utilized for diagnostics and monitoring (Fig. 25.4): synthetic aperture radar (SAR) (Fornaro et al. 2013); distributed optical fiber sensor (DOF) (Minardo et al. 2012); infrared thermography using a cooled camera (COOLED IRT); hyperspectral spectroscopy; infrared thermography using an uncooled camera (UNCOOLED IRT); ground-penetrating radar using a mobile system (mobile GPR) or a manual system (manual GPR) (Bavusi et al. 2011); electrical resistivity tomography; optical displacement camera (ODM); ground-based SAR (GBSAR) (Stabile et al. 2013). In addition, measurements were performed with civil engineering techniques such as seismic ambient noise (SAN) and accelerometric noise measurements (ANM). In particular, ANM, in a suite of three tri-directional accelerometers, and SAN, consisting of a three-directional velocimeter, have been placed on the shell and on the deck to provide a reliable benchmark for other vibrational techniques such as ODM and GBSAR (Stabile et al. 2013). The overall arrangement of sensors allowed focusing observational efforts on the three main elements of the bridge: the shell, the deck, and the asphalt layer.

Figures 25.4 and 25.5 depict the richness of the sensing techniques exploited at Viaduct Basento, with several related diagnostic outcomes.

In this chapter, we focus on the main outcomes of two sensing technologies: ground-penetrating radar (GPR) and uncooled infrared thermography.

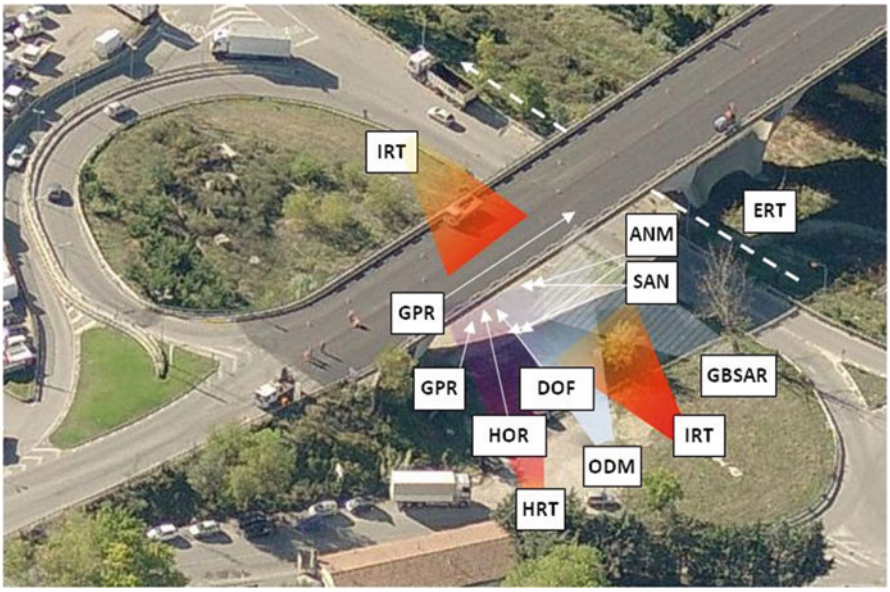

Fig. 25.4 Locations of ISTIMES sensors at Viaduct Basento

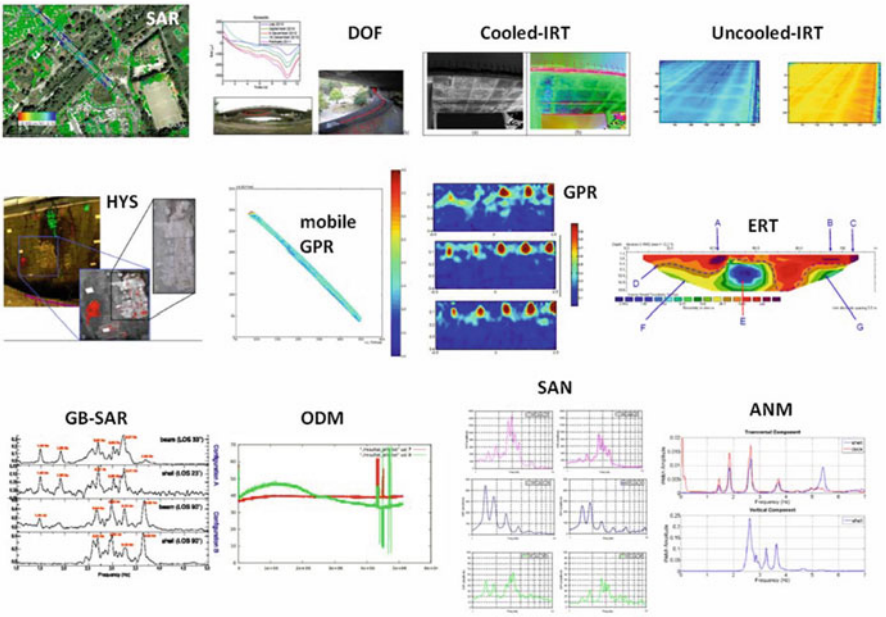

Fig. 25.5 Pictorial description of the results of ISTIMES sensing technologies at Viaduct Basento

25.3.1 GPR Surveys

Several GPR surveys were performed at Viaduct Basento with different aims, of which the details can be seen in Bavusi et al. (2011). Here, we present the representative case of the survey at the deck of the bridge, with the main aim being to retrieve information about the constructive features of the viaduct. A three-dimensional (3D) GPR survey for the bridge deck evaluation was carried out with an antenna working at a nominal frequency of 900 MHz. The details of the survey design are depicted in Fig. 25.6; in particular, 30 parallel GPR profiles 26 m long were collected, with spacing between the profiles equal to 0.1 m.

Figure 25.7 depicts one of the radargrams compared with its interpretation of the structural elements of the deck. The upper horizontal flat reflector at 2.0 ns can be associated with the reflection by the asphalt and upper concrete layer. In this level, the Gerber saddles appear absorptive because of rainwater infiltration, as suggested by the presence of concretions and corrosion of iron. Between 2.0 and 5.8 ns, there is a second medium layer containing stiffening walls forming the box structure depicted in Fig. 25.6. Other important features of this layer are the pillar support, similar to the stiffening walls but with greater thickness. Finally, a deep horizontal reflector is visible close to 6.0 ns that is representative of the lower concrete plate of the deck.

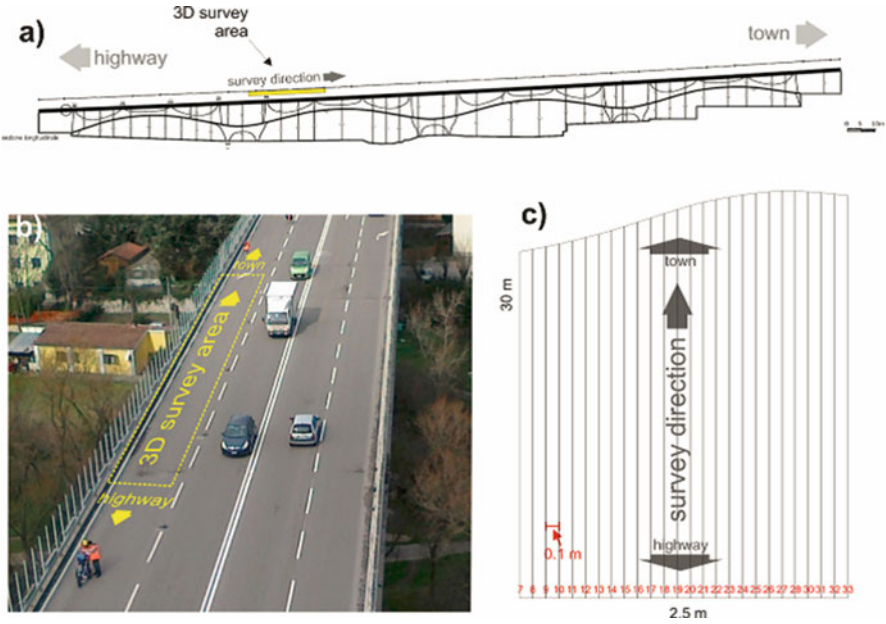

Fig. 25.6 GPR survey details (Source: figure in Bavusi et al. 2011)

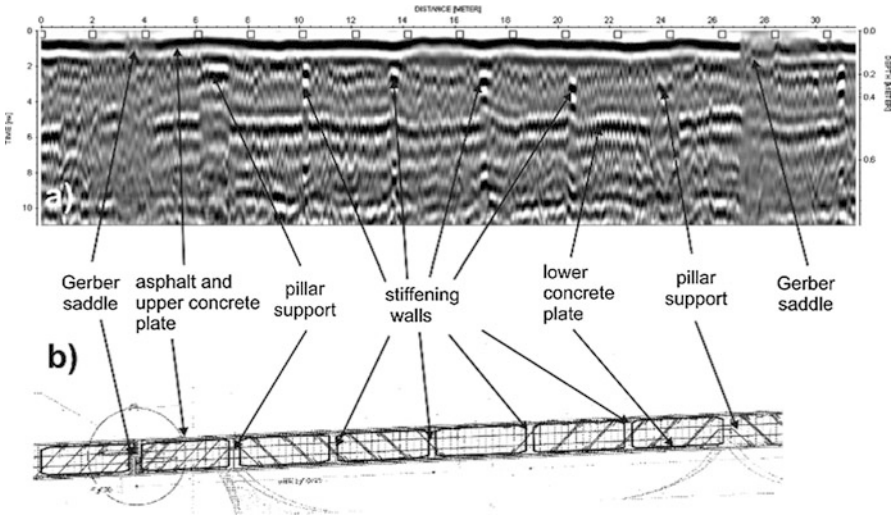

Fig. 25.7 Processed radargram (#19) (**a**) with the interpretation of its main reflectors on the bases of the original deck cross section (**b**) (Source*:* figure in Bavusi et al. 2011)

The data were also handled by means of advanced data processing based on the microwave tomographic approach (Leone and Soldovieri 2003; Soldovieri et al. 2007), wherein the main structural hidden features of the viaduct are identified as the areas characterized by significant amplitude of the electromagnetic contrast function (Soldovieri et al. 2007).

Figure 25.8 depicts the results achieved by the tomographic approach applied to radargram #19. The result is provided as the amplitude of the contrast function normalized with respect to the absolute maximum. The layered tomographic reconstruction allows us to detect the main structural features such as the upper and lower concrete plates, the stiffening walls, the pillar supports, and, finally, the Gerber saddles (Fig. 25.8b).

Figure 25.9 depicts three depth slices built by interpolating all the two-dimensional (2D) tomographic reconstructions. From top to bottom it is possible to observe several features: with reference to Fig. 25.9a, the Gerber saddles appear absorptive. Moreover, an important reflective feature appears at about 6 m along the *y*-axis and can be related to the presence of the pillar support. A less-defined reflection referable to the other pillar support appears at about 22 m along the *y*-axis.

Figure 25.9b shows a deeper layer (at 0.20 m) where reflections accounting for the stiffening walls appear very defined. Actually, the first one appears thicker than expected for the pillar support. Finally, at a depth of 0.40 m, a new longitudinal feature appears (Fig. 25.9c).

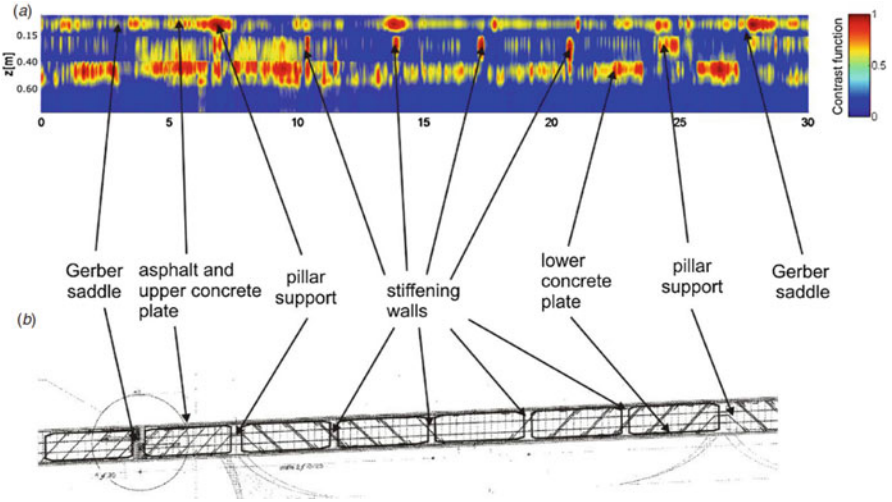

Fig. 25.8 Microwave tomography (MT)-based inversion of the radargram shown in Fig. 25.7. The result is provided in terms of contrast function normalized with respect to the absolute maximum (**a**), with the interpretation of its main reflectors on the basis of the original deck cross section (**b**) (Source: figure in Bavusi et al. 2011)

25.3.2 Infrared Thermography Using the Uncooled Camera (UNCOOLED IRT)

The uncooled infrared system (IRT) was deployed on a temporary mast at 6 m above the bridge desk during a 3-day period.

Figure 25.10 (upper left panel) shows an overview of the Viaduct Basento and the location of the span surveyed. Figure 25.10 (upper right panel) also shows a global view of the installation of the uncooled IRT system in a long-term monitoring configuration for demonstration purposes. The bottom left panel in Fig. 25.10 shows the implementation of the infrared camera, the weather station, and the GPS antenna on the mast. A specific mechanical mounting was designed and realized to fix the camera on top of the mast and also the wires fixed along the mast to reach the smart box (SensorBox). In the bottom right panel, Fig. 25.10 shows a view of the bridge deck surface taken at camera level; the red rectangle highlighted in the picture matches the area viewed by the infrared thermal camera.

The whole system was remotely controlled through a tablet PC used around the bridge via a wireless connection.

This survey provided the opportunity to demonstrate, on a bridge under traffic, that the prototype of a low-cost system using microbolometer FPA technology is operational by using standard protocols as much as possible. It was also a way to confirm experimentally, on a real structure, that the spectral bandwidth (LWIR) was well adapted to apparent temperature monitoring of infrastructures using infrared cameras of low measurement performance.

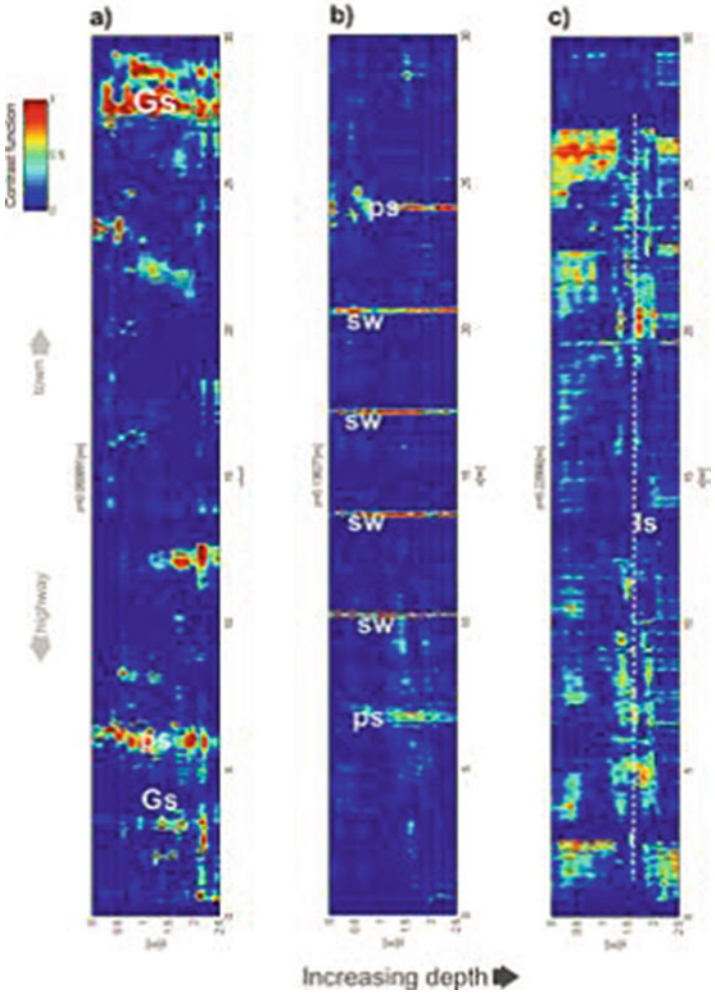

Fig. 25.9 Depth slices built starting from MT results: depth slices at 0.06 m (**a**); depth slices at 0.20 m (**b**); depth slices at 0.40 m (**c**). Results are shown in terms of contrast function normalized with respect to the absolute maximum (Source: figure in Bavusi et al. 2011)

After installation and preliminary tests, the long-term monitoring experiment was launched by using infrared image acquisition coupled with weather parameters for radiative corrections online. Data were continuously acquired for about 2.5 days.

Figure 25.11 shows two thermal image at two time steps (without averaging), which show that the bridge lanes were kept open to traffic during the whole experiment.

During these trials, weather parameters were acquired, but only outside temperature and relative humidity were stored. The sampling rate was fixed at 0.1 Hz by averaging 50 thermal images acquired at 5 Hz. For each 300 thermal images

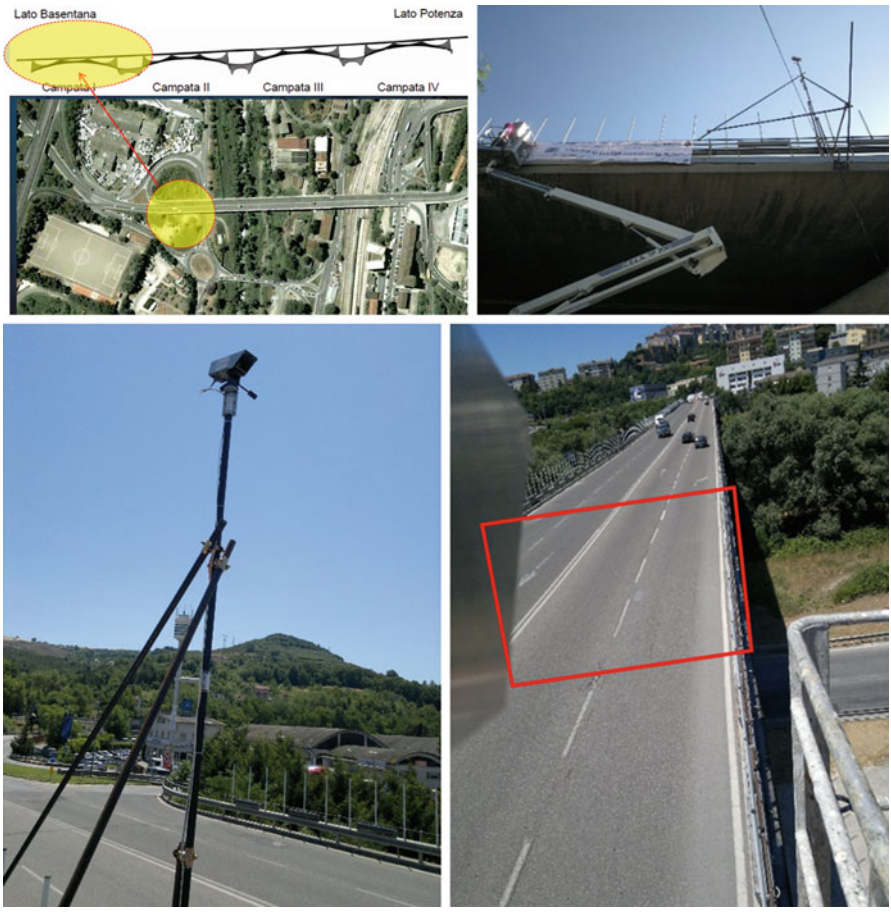

Fig. 25.10 *Upper left panel*: Global overview of the bridge and location of the installation of infrared thermography (IRT) system. *Upper right panel:* Bottom view of the mechanical mounting of the sensors. *Bottom left panel*: IR system installed on a mast. *Bottom right panel*: Schematic view of the area surveyed by the IR camera

acquired, an image sequence was stored in the internal hard drive of the SensorBox deployed on site. In the tested configuration, intermediate data transfer was carried out by using the remote control deployed on a tablet PC.

It has to be noted that the sun course was not parallel to the main direction of the bridge and induced a transversal thermal gradient at deck level for a finite period duration during thermal loading (morning) and relaxation (end of afternoon and evening). In particular, shadows of the protective railings could be observed at the beginning of deck surface thermal loading by direct sun (Fig. 25.12).

Figure 25.13 shows the apparent surface temperature evolution with time (thermogram) extracted at a fixed location of the deck surface and relative humidity

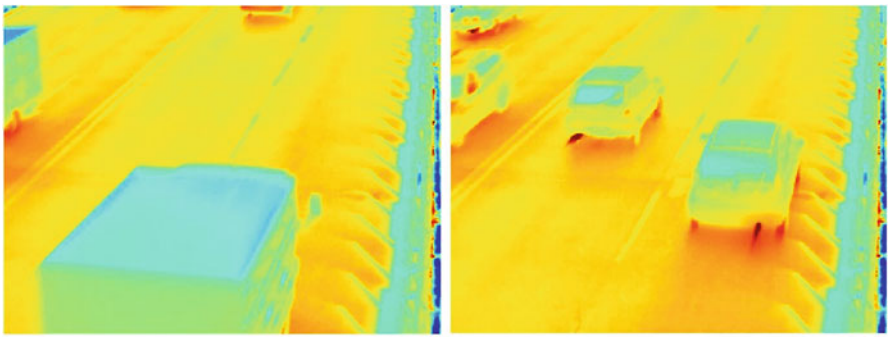

Fig. 25.11 Example of instantaneous thermal images showing the bridge is still open to traffic during the experiments

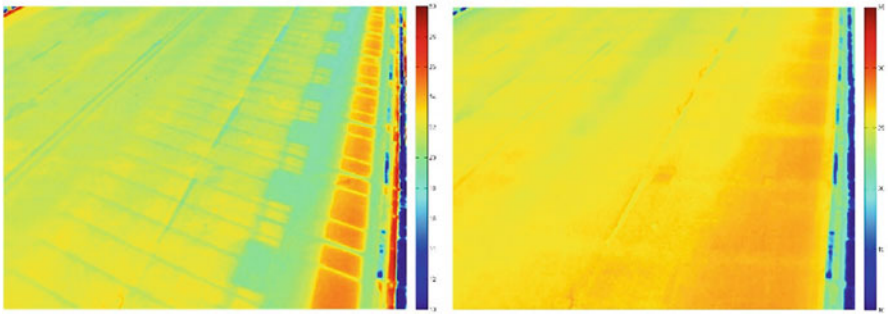

Fig. 25.12 Average thermal images during thermal loading (*left*) and thermal relaxation (*right*)

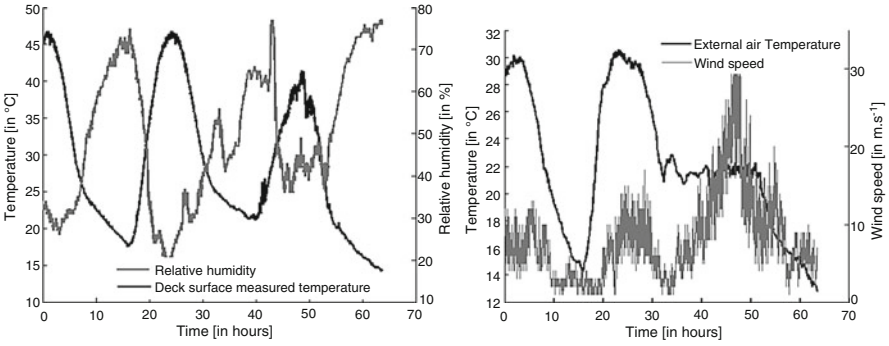

Fig. 25.13 Thermogram during 2.5 days and relative humidity evolution at bridge deck (*left*). Measured atmospheric temperature and wind speed evolution during the same period (*right*)

evolution in the same period. The third day was affected by intensive gusts, inducing a not negligible forced convection effect at the deck surface and also random sun shadowing by clouds. The two first days were in quite the same weather conditions (except for night).

The 0.1-Hz sampling rate chosen does not favor the discrimination between wind gust effect and direct solar heating shadowing, so that the signal is noisier for the third day. At least two cooling events can be observed on the third day, one at the beginning of the thermal loading and another one around noon. The measured relative humidity shows bursts of humidity increase, which match these sudden cooling events, although atmospheric temperature was quite constant because of the wind conditions.

The full thermal sequence analysis has been presented by Dumoulin et al. (2013). Because of the regularity of the weather conditions in the previous days of this experiment, it has to be noticed that the first period of the presented thermal evolution could be considered as representative of the thermal signature of the bridge deck in a quasi-established periodic regime. This approach was used by Dumoulin et al. (2013) to develop image processing and thermal analysis.

The stability of the previous environmental conditions also allowed us to carry out analysis on the night period (thermal relaxation part). Thus, fast Fourier transform (pulse phase thermography) and Singular Value Decomposition [principal component thermography (PCT)] analysis approaches were applied on the thermal relaxation part of the signal after the sun sets (night period) on the first day (see chapter IR).

Figure 25.14 depicts the amplitude and empirical orthogonal function (EOF) maps obtained after processing.

A regular grid is observed in both maps that could not be attributed either to traffic or to traffic lane painting at the bridge deck surface.

Figure 25.15 shows two 3D representations (left image) of the inner structure of the bridge deck and a 2D drawing of the inner box distribution. The box section of the deck has longitudinal and transversal stiffening walls (internal sects), each 3.46 m long (Fig. 25.15a). Its transversal cross section shows an ellipsoidal shape in the lower side with maximum thickness of 1.5 m and width of 16 m (Fig. 25.15b).

Finally, it can be stated that the inner structure mesh of the bridge deck can be retrieved on both computed maps. Nevertheless, the traffic signature induces blurring at the traffic lane level on the map.

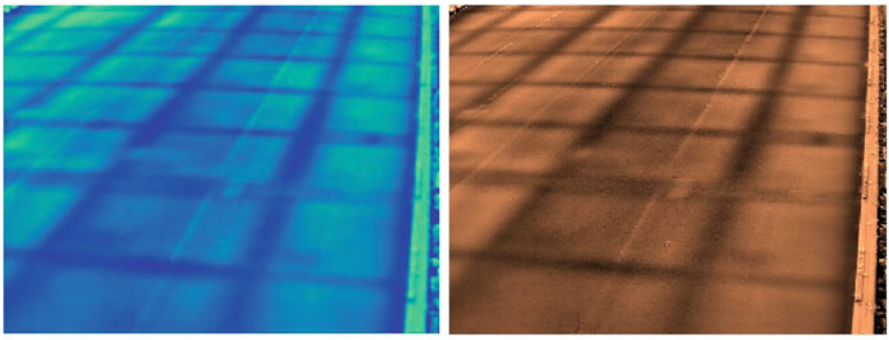

Fig. 25.14 Magnitude map (*left*); empirical orthogonal function (EOF) map (*right*)

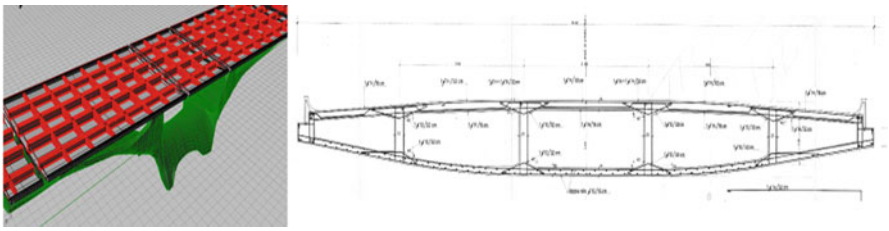

Fig. 25.15 Three-dimensional (3D) representation of the inner structure of deck (*left panel*) and two-dimensional (2D) view of the box repartition (*right panel*) (Source: figure in Bavusi et al. 2011)

25.4 Conclusions

This chapter has presented the validation of an integrated approach, based on the combination of electromagnetic sensing technologies with civil engineering analysis tools, for the monitoring of a modern architectural masterpiece such as the Viaduct Basento in Potenza. It has been demonstrated how the integration of sensing technologies permits a multiscale vision, wherein the wide area surveillance, ensured by the satellite and aerial technologies, is coupled to detailed diagnostics of the single structure made possible by the ground-based technologies.

In particular, we focused here on the deployment of ground-penetrating radar (GPR) and infrared thermography (IT) for investigation of the inside of the bridge, with particular attention to determining the hidden geometric features of the deck and to detecting possible deterioration situations. As conclusion and perspectives, we can say that results obtained on this real test site are promising. In particular, the coupling of GPR with IRT is a research field that should be investigated in depth in the future for such survey applications.

References

Bavusi M, Soldovieri F, Di Napoli R, Loperte A, Di Cesare A, Ponzo FC, Lapenna C (2011) Ground penetrating radar and microwave tomography 3D applications for the deck evaluation of the Musmeci bridge in Potenza, Italy. J Geophys Eng 8:S33–S46. doi:10.1088/1742-2132/8/3/S04. www.istimes.eu

Dumoulin J, Crinière A, Averty R (2013) Detection and thermal characterization of the inner structure of the "Musmeci" bridge deck by infrared thermography monitoring. J Geophys Eng 10(2):17 pages , IOP Science, doi:10.1088/1742–2132/10/6/064003.

Fornaro G, Reale D, Verde S (2013) Bridge thermal dilation monitoring with millimeter sensitivity via multidimensional SAR imaging. IEEE Geosci Remote Sens Lett 10(4):677–681. doi:10.1109/LGRS.2012.2218214

Giovannardi F (a cura di), Sergio Musmeci. Strutture fuori dal coro. Available at www.Giovannardierontini.it, 2010

Leone G, Soldovieri F (2003) Analysis of the distorted Born approximation for subsurface reconstruction: truncation and uncertainties effect. IEEE Trans Geosci Remote Sens 41(1): 66–74

Loperte A, Soldovieri F, Lapenna V (2015) Monte Cotugno Dam Monitoring by the Electrical Resistivity Tomography. IEEE J Sel Top Appl Earth Obs Remote Sens 8(11):5346–5351. doi:10.1109/JSTARS.2015.2476663

Minardo A, Persichetti G, Testa G, Zeni L, Bernini R (2012) Long term structural health monitoring by Brillouin fibre-optic sensing: a real case. J Geophys Eng 9:S64–S69

Proto M et al (2010) Transport Infrastructure surveillance and Monitoring by Electromagnetic Sensing: the ISTIMES project. Sensors 10(12):10620–10639

Soldovieri F, Hugenschmidt J, Persico R, Leone G (2007) A linear inverse scattering algorithm for realistic GPR applications. Near Surf Geophys 5(1):29–42

Soldovieri F, Dumoulin J, Ponzo F, Crinière A, Bourquin F, Cuomo V (2014) Association of sensing techniques with a designed ICT architecture in the ISTIMES project: application example with the monitoring of the Musmeci bridge. In: Proceedings of EWSHM – 7th European workshop on structural health monitoring, Nantes, France, July.

Stabile TA, Perrone A, Gallipoli MR, Ditommaso R, Ponzo FC (2013) Dynamic survey of the Musmeci bridge by joint application of ground-based microwave radar interferometry and ambient noise standard spectral ratio techniques. IEEE Geosci Remote Sens Lett 10(4): 870–874. doi:10.1109/LGRS.2012.2226428

Chapter 26
Case Studies Regarding the Application of THz Imaging to Cultural Heritages

Ilaria Catapano, Marcello Picollo, and Kaori Fukunaga

Abstract The ability of terahertz (THz) radiation to perform noninvasive investigations together with recent technological advances regarding the development of stable, flexible, and portable devices are motivating a widespread use of THz technology in the framework of cultural heritage. To provide practical examples of the potentialities offered by this emerging diagnostic tool, three case studies concerning the use of THz-pulsed TDI systems are briefly summarized here.

Keywords Cultural heritage diagnostic • Majolica surveys • Painting characterization • THz imaging

26.1 Introduction

In the past few years, terahertz (THz) imaging has become more and more common thanks to the development of a new generation of systems that allow onsite surveys without requiring large installations, thus keeping feasible the financial and logistical efforts. Accordingly, there are many examples, mainly referring to painting masterpieces (Seco et al. 2013; Koch-Dandolo et al. 2015; Picollo et al. 2015), that have allowed assessing the capability of THz waves to provide information useful to improve our knowledge of artworks. In particular, the results available in the pertaining literature have corroborated that THz investigation allows us to gather information about the technique used in the original artwork, and in any

I. Catapano (✉)
Institute for Electromagnetic Sensing of the Environment, National Research Council of Italy (IREA-CNR), Naples, Italy
e-mail: catapano.i@irea.cnr.it

M. Picollo
Nello Carrara Institute of Applied Physics, National Research Council of Italy (IFAC-CNR), Florence, Italy

K. Fukunaga
Applied Electromagnetic Research Center, National Institute of Information and Communications Technology, Tokyo, Japan

N. Masini, F. Soldovieri (eds.), *Sensing the Past*, Geotechnologies and the Environment 16, DOI 10.1007/978-3-319-50518-3_26

previous restoration treatments, to detect inner anomalies that are possibly affecting the structural integrity, as well as to discover hidden features.

It is worth noting that THz surveys can provide data that cannot be acquired using other nondestructive diagnostic tools such as infrared cameras and X-ray devices. In this framework, a significant example has been presented by Seco et al. (2013) concerning the fact that THz waves can reveal a feature that could correspond to the author's signature and which is not visible by means of optical and X-ray inspection. Such a result has been explained by assuming that the signature was written using a pencil (basically, carbon) and that the painting was covered by a top layer of finishing varnish which turned dark over time. As a consequence, the signature is optically obscured and cannot be detected by means of X-rays because the atomic weight of carbon (in the signature) and that of the surrounding canvas and paint are very similar. Conversely, the different reflectivity of carbon and of the surrounding canvas allowed the detection of the signature at THz frequencies.

Putting aside an overview of the available examples, which is outside the scope of this chapter, in the following we describe three case studies that are representative of the potentiality offered by THz imaging in the framework of artwork analysis. In particular, two of the presented case studies are concerned with painting masterpieces and one with a ceramic object.

26.2 THz Survey of an Oil-Canvas Painting

The first case study concerns the oil-on-canvas painting titled "Santa Cecilia (1626)" by Simon Vouet (Fukunaga 2012) (Fig. 26.1a). This painting was inspected by means of the Picometrix T-Ray 4000 system during its conservation process.

The main results concerning the square area and a rectangular one, both delimitated by white contours in Fig. 26.1a, are synthesized in Fig. 26.1b–f. In particular, the THz image and the X-ray image of the square area, which includes Santa Cecilia's face, are shown in Fig. 26.1b and 26.1c, respectively. These images reveal the presence of optically invisible lines that may be from an underpainting. The THz radargram and the depth slices shown in Fig. 26.1d–f are, instead, referred to measurement lines gathered in the rectangular area. This zone crosses the seam putting together the two canvas sheets used to create the support of the painting. This part had a defect in the form of a convex edge on the surface and was reformed toward the backside by using a suction table. The effectiveness of the conservator action is assessed by Fig. 26.1d, which provides a cross-sectional image wherein the two sewn canvas sheets appear. Moreover, Fig. 26.1e, f represent the surfaces of the two canvases and reveal that their cloth has almost the same mesh size but that the depth from the surface is slightly different. In particular, the canvas located in the bottom part of the painting is closer to the surface than the top one.

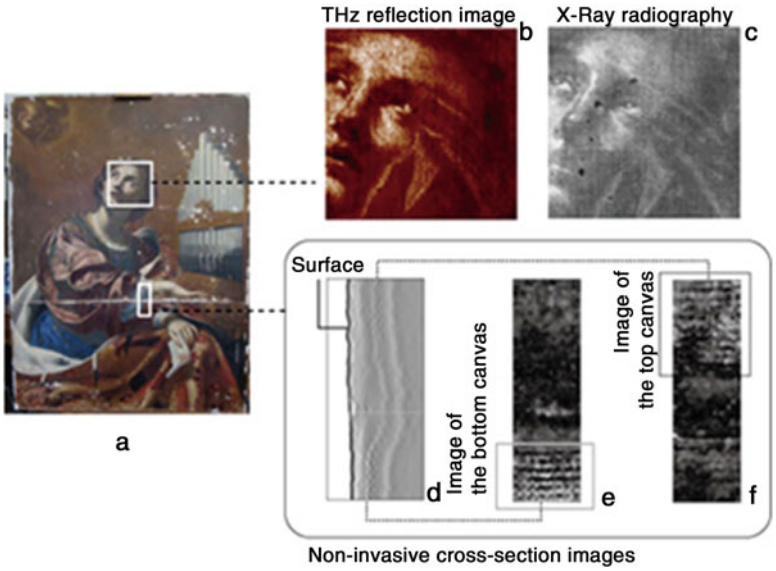

Fig. 26.1 Terahertz (THz) survey of the Santa Cecilia painting. (**a**) Picture of the painting. (**b**) THz image of the area around the face. (**c**) X-ray image of the area around the face. (**d**) THz radargram referring to a line crossing the part connecting the two canvas sheets. (**e**) Depth slice showing the bottom canvas. (**f**) Depth slice showing the top canvas

26.3 THz Survey of Tempera-Wood Panel Painting

The second case study regards the THz survey of the "Madonna with the Child" painting, which is a part of the "Polittico di Badia" masterpiece (c. 1300; 334 cm × 91 cm) by Giotto, from the permanent collection of the Uffizi Gallery in Florence, Italy (Koch-Dandolo et al. 2015; Tartuferi 2012) (Fig. 26.2a). This work of art is a tempera painting on wood and was investigated by using the Picometrix T-Ray 4000 system.

Figure 26.2 shows the THz radargram measured along the line a–a′ (see Fig. 26.2a) and reveals that, in contrast to modern tempera panel paintings, which use canvas or a mesh cloth applied directly on the panel, there are two gesso layers on this panel with the cloth placed between them. Therefore, this cross-sectional image proved that the artist followed a medieval procedure in making this panel painting. At the time of painting (around 1300 AD), flat wood panels were not commonly available, and a wood panel painting was simply part of the decorative area of a church. According to the conservators, this technique involves a gesso layer

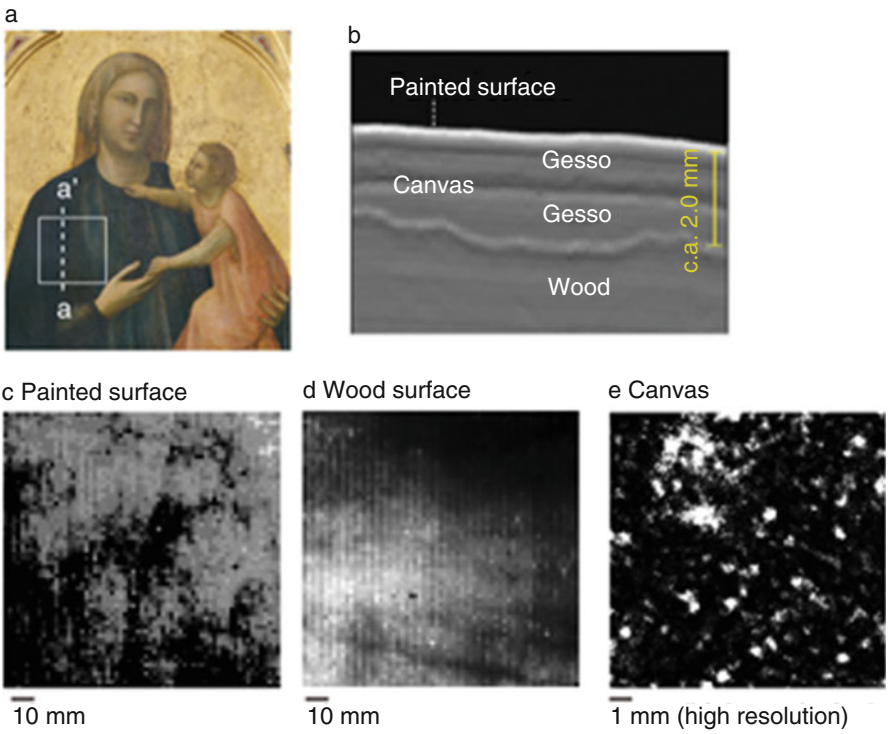

Fig. 26.2 THz survey of the Madonna with the Child. (**a**) Picture of the painting. (**b**) THz radargram gathered along the line a–a' in the picture of the painting. (**c**) THz image of the painted surface. (**d**) THz image of the wood panel surface. (**e**) THz image of the canvas/cloth in high resolution. The THz images refer to the area delimited by the white square in the picture of the painting

being spread directly on the carved wood base to obtain a reasonably flat surface. Then, a cloth was placed on top to ease the tension on the wood. Finally, another gesso layer was formed as a preparation layer for the painting.

The depth slices, referring to the white square in Fig. 26.2a and corresponding to the painted surface, the wood panel, and the canvas/cloth, are shown in Fig. 26.2c–e. These THz images reveal that the reflection image of the surface is affected by the pigments (see Fig. 26.2c), that the tool marks on the surface of the wood panel are visible (Fig. 26.2d), and a regular mesh pattern, which supports the conservator's description of the process adopted by the artist, appears in the high-resolution depth slice corresponding to the position of the cloth (Fig. 26.2e).

26.4 THz Survey of a Ceramic Object

The third case study considers majolica characterization and was performed by means of the Zomega fiber-coupled THz time domain system (Catapano et al. 2016).

The name majolica denotes tin-glazed pottery, that is, artworks such as crockery and tiles made by using earthenware ceramic coated with white tin-opacified glaze and decorated by using mineral pigments.

In Naples (Italy), the use of majolica tiles as decorative elements started around the eleventh to twelfth centuries and began recurring at the end of the fourteenth century, when majolica tiles were adopted to decorate churches and aristocratic houses. Moreover, owing to the reduction of the costs of production, majolica tiles were widely employed to cobble the residences of the middle class during the nineteenth century (Donatone 2001; Fiengo and Guerriero 2008). Therefore, today majolica tiles represent a widespread decorative element in a large number of historical buildings located in Naples, and their study deserves attention both to trace the historical evolution of the productive process and to help with preservation and restoration actions.

One of the nineteenth-century majolica tiles that was investigated is shown in Fig. 26.3a. The data were gathered with 1-mm spatial offset on a square surface with sides 150 mm long and centered on the majolica tile.

The radargrams referring to the continuous and dashed red lines in Fig. 26.3a are shown in Fig. 26.3b and 26.3c, respectively. These images reveal the presence of multiple close reflections occurring immediately beyond the first strong reflection, which are representative of different layers used to decorate the surface of the clay body. Moreover, a reflection appears about 9 ps below the first one and is interpretable as the glaze–clay interface.

The retrieved surface topography is shown in Fig. 26.3d and the depth slices are shown in Fig. 26.3e. Figure 26.3d shows clearly that, beyond several cracks, a depression affects the central portion of the surveyed region and allows the identification of the elevated decorative elements. These features, partially appreciable by means of a visual inspection, are the result of the handmade constructive process and are a proof of the fact that the nineteenth century majolica production was less refined than that of the eighteenth century and most ancient ones. This degeneration may have resulted from the abolition of the arts and crafts corporations and the necessity for reducing production costs.

The depth slices in Fig. 26.3e show that the brown and ochre-decorated parts appear clearly at $z = 0.06$ mm whereas the uniform white glaze layer starts at $z = 0.12$ mm. On the other hand, the glaze–clay interface is not imaged at a constant depth and, according to the information provided by the radargrams, it should be located between $z = 0.48$ mm and $z = 0.54$ mm. Below this latter depth, inhomogeneity affecting the inner clay structure, which appear as concentric fringes centered at the tile center, is imaged (see depth slices at $z > 0.54$ mm). Moreover, the depth slices provide information about the in-depth extension of the cracks affecting the majolica tile. As a final remark, we observe that comparison between the depth

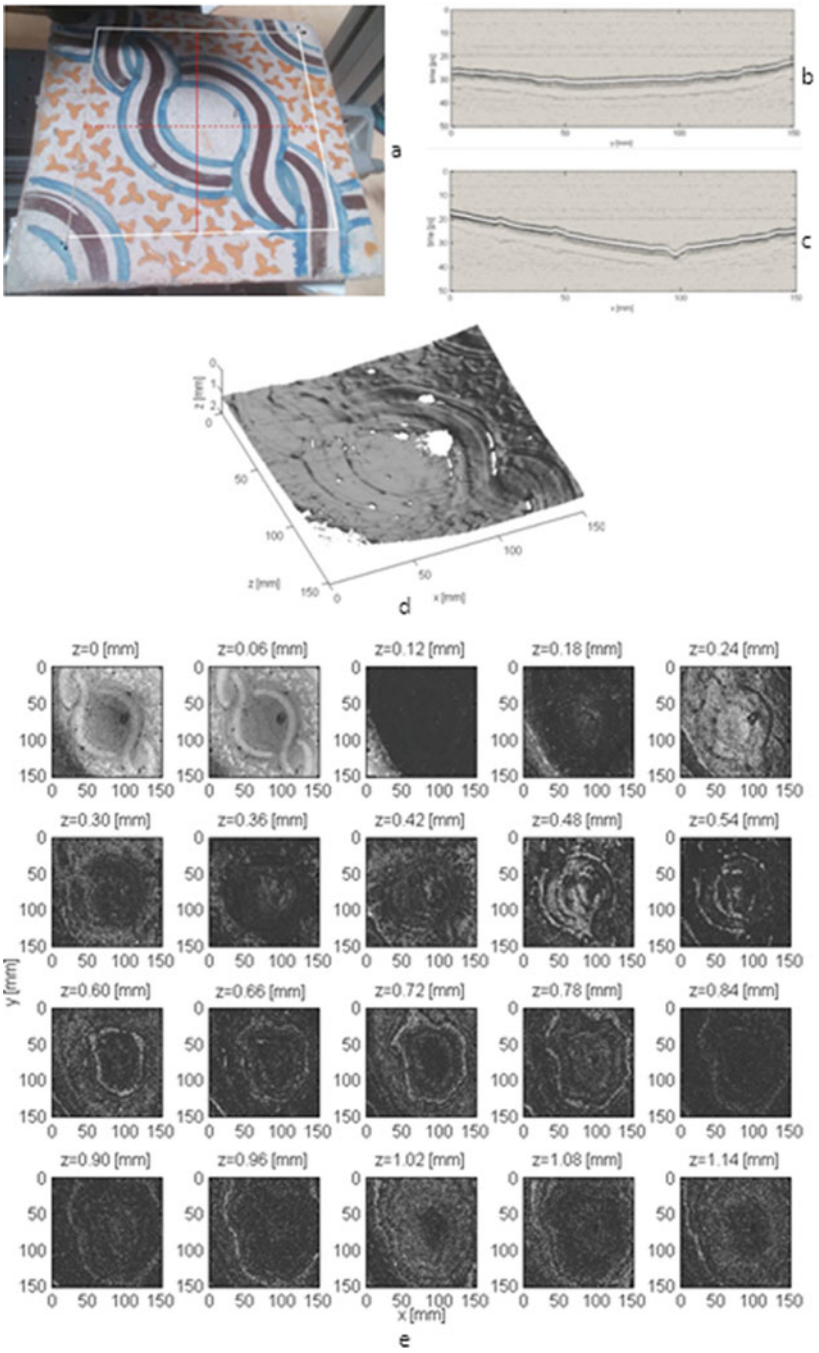

Fig. 26.3 Majolica tile surveyed by THz waves. (**a**) Picture of the majolica tile. (**b**) THz radargram is a continuous *red line*. (**c**) THz radargram is a continuous *dashed red line*. (**d**) THz image of majolica tile topography. (**e**) THz depth slices

slice at $z = 0.06$ mm and the majolica tile picture in Fig. 26.3a makes it evident that the blue part of the decoration is not imaged. This behavior could be related to the differences occurring among the electromagnetic features of the mineral pigments, but further investigations are needed to confirm or deny this hypothesis.

26.5 Conclusions

Three case studies concerning different kinds of works of art have been presented to corroborate the usefulness of time-of-flight THz imaging as a noninvasive and contactless diagnostic tool of artwork. The two examples referred to as paintings have been chosen because they are representative of THz potentialities and are considered relevant masterpieces. Conversely, the case study referring to the ceramic object is of relevant interest because it provides a first assessment of the potentialities offered by THz time-of-flight imaging with respect to majolica tile characterization.

References

Catapano I, Affinito A, Guerriero L, Bisceglia B, Soldovieri F (2016) Majolica imaging with THz waves: preliminary results. Appl Phys A 122(5):1–11

Donatone G (2001) La riggiola napoletana. Pavimenti e rivestimenti maiolicati dal Seicento all'Ottocento. Grimaldi, Napoli

Fiengo G, Guerriero L (2008) Atlante delle tecniche costruttive tradizionali. Napoli, Terra di Lavoro (XV–XIX). Arte Tipografica Editrice, Napoli

Fukunaga K (2012) THz technology applied to cultural heritage. In: 37th international conference on infrared, millimeter, and terahertz waves (IRMMW-THz), 23–28 Sept 2012

Picollo M, Fukunaga K, Labaune J (2015) Obtaining noninvasive stratigraphic details of panel paintings using terahertz time domain spectroscopy and imaging system. J Cult Herit 16:73–80

Seco C, Lopez V, Arauz G, Redo A, Palacios J, Tejada J (2013)) Goya's artwork imaging with teraherz waves. Opt Express 21:17800–17805

Tartuferi A (ed) (2012) Giotto, Il Restauro del Polittico di Badia. Mandoragora, Firenze

Chapter 27
A Case Study in Japan

Motoyuki Sato

Abstract In this section, we introduce case studies of archaeological surveys by ground-penetrating radar (GPR) carried out in Japan. Most of the archaeological sites in Japan are small and have uneven topography. We demonstrate that GPR surveys with advanced navigation systems can achieve very good GPR profiles. As an example, with these technologies inside "Kofun," which is a tumulus, several meters high, could be visualized by GPR. A GPR "Yakumo" could find detailed structure of buried stone structures. Borehole radar could be effectively used for a deep archaeological structure.

Keywords Archaeological survey • GPR • Multistatic radar • Yakumo • Navigation • GNSS • Total station • 3DGPR

27.1 GPR Survey for Archaeology in Japan

About 8000 archaeological surveys related to development are annually reported to the Japanese Agency for Cultural Affairs; roughly 500 additional surveys are done each year for academic research purposes. Most of the archaeological sites in Japan are located in conditions of quite complicated terrain, and many lie in areas that are highly developed, so ground-penetrating radar (GPR) surveys are rarely carried out in large flat areas.

Most of the archaeological surveys in Japan are prompted by the proposed development of roads and housing areas. In these cases, areas to be surveyed are narrow and in many cases the ground surface is not flat. Therefore, conventional GPR surveys cannot be easily accomplished. Burial mound structures, which are tumuli known as "kofun," are some of the most important archaeological targets in Japan. However, GPR has not been successfully used to survey tumulus sites to date,

M. Sato (✉)
Center for Northeast Asian Studies, Tohoku University, 41 Kawauchi, Sendai, 980-8576, Japan
e-mail: sato@cneas.tohoku.ac.jp

N. Masini, F. Soldovieri (eds.), *Sensing the Past*, Geotechnologies and the Environment 16, DOI 10.1007/978-3-319-50518-3_27

because carrying out a GPR survey is very difficult on a mound. In these cases, new technologies that use an additional antenna positioning system have proven to work quite well.

Although not numerous, there are some notable large-scale archaeological sites in Japan including Nara, the former capital of Japan in the eighth century AD, and Saitobaru, where we found many underground graves made in the fourth century AD. At these sites, effective GPR surveys using larger GPR systems have been carried out. In this section, we introduce some examples of unique archaeological surveys conducted in Japan.

27.2 Application of 3DGPR

27.2.1 3D GPR Imaging

In Japan, many kofun (tumuli) built mostly in the fourth to sixth centuries are present. A kofun (tumulus) is a small mound whose height is 3–10 m, and the stone grave room structure is normally located near the top of the tumulus. Many archaeologists and researchers have attempted to use GPR to survey tumulus sites, but most of such surveys have not been very successful. In Chap. 9 of this book, we demonstrated three-dimensional ground-penetrating radar (3DGPR) imaging by using a system that combines a GPR antenna with a high-precision location system. This method has the advantage of very precise 3D imaging but can also be adopted for surveys on ground surfaces that are not flat.

27.2.1.1 Sakitama Kofun

The Sakitama-kofun tumulus site, located about 50 km north of Tokyo, consists of several mounds. Since 2008 Tohoku University has carried out 3DGPR surveys in the Okunoyam-kofun tumulus (Fig. 27.1) and in Teppoyama-kofun tumuli at this site (Grasmueck and Viggiano 2007; Mahmoud et al. 2009). The transmitters of the iGPS system were set on the top of the mound (Fig. 27.2), and 3DGPR surveys were performed over an area roughly 10 m × 10 m on the top of the mound.

Figure 27.3 shows the horizontal slices obtained by the 3DGPR survey on the top of the mound of the Okuno-yama-kofun tumuli. To find the optimal GPR working frequency, three different antennas were used in this survey, with the center frequencies of 100 MHz, 250 MHz, and 500 MHz.

The 3DGPR system acquires very dense data sets, and the data can be used for precise subsurface imaging. In Fig. 27.3, we can clearly observe buried objects at depths of 2 m and 3 m by using the three different frequencies. In some cases, when we acquire GPR data from mounds, artifacts appear in the GPR profiles as a consequence of the surface topography. However, the three images in Fig. 27.3

Fig. 27.1 Okunyama-kofun tumuli, Sakitama-kofun tumulus site, Saitama, Japan

Fig. 27.2 Three-dimensional ground-penetrating radar (3DGPR) survey on Okunoyama-kofun tumulus at the Sakitama-kofun tumulus site, Japan

validate the existence of subsurface objects. Additionally, the images suggest a larger stone structure exists in this mound at about 3.5 m deep. In important archeological sites, which are registered by the Japanese government, we normally cannot get permission to excavate the sites. Therefore, GPR surveys can be the sole option to investigate the inner areas of important tombs.

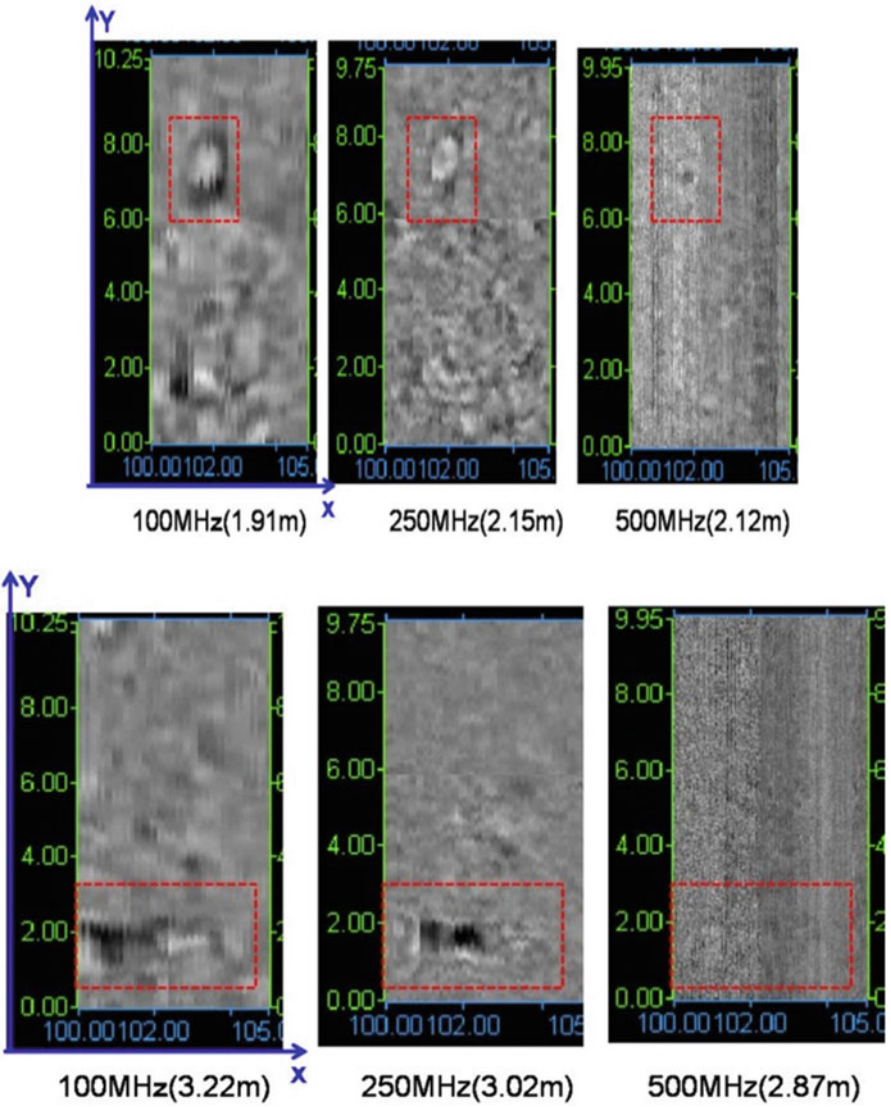

Fig. 27.3 Horizontal GPR slice imaged by 3DGPR system. Okunoyama-kofun tumulus, Japan

27.2.1.2 Kassenhara-Kofun Tumulus

The Kassenhara-kofun tumulus is located south of Sendai City, Japan. This is a relatively small mound, and the top of the tumulus is very narrow. In this site, a GPR system equipped with a reflection mirror and an automatic-tracking total station (Takahashi and Sato 2013) was used to track the position of the GPR antenna.

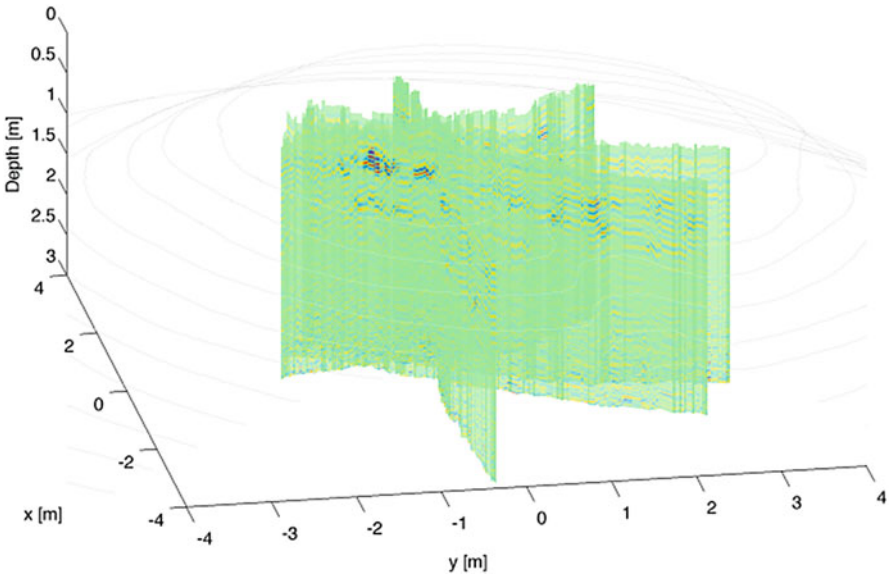

Fig. 27.4 3D GPR image of Kassenhara-kofun tumulus

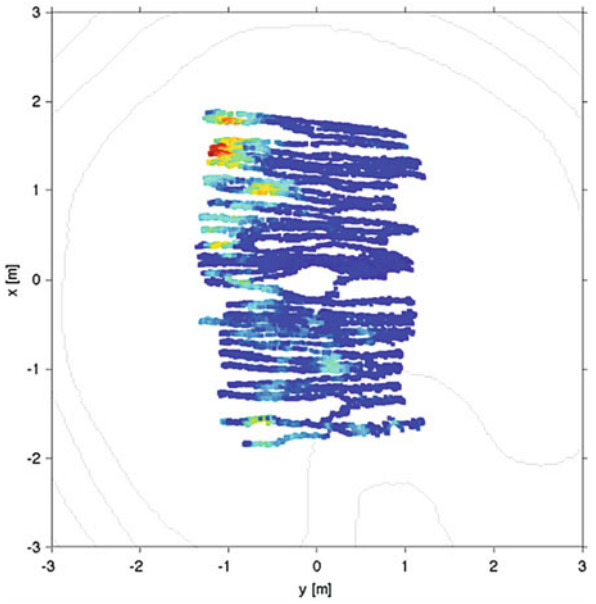

Fig. 27.5 GPR signal intensity plotted on three-dimensional topography on the top of the Kassenyama-kofun tumulus

This system is capable of high-precision measurement in uneven topographic areas. Figure 27.4 shows a three-dimensional display of the vertical profile of GPR data, and Fig. 27.5 shows a horizontal slice of the measured GPR signal around the top of the tumulus.

The GPR survey combined with an automatic-tracking total station cannot acquire very dense data sets. Therefore, the reconstructed image is not so accurate as that obtained by a 3DGPR system. However, thanks to the flexibility of the system and the measurement, we can detect an anomaly near the top of the mound.

27.3 Application of Yakumo

27.3.1 Nobiru Port Town

The first trial of the array GPR system "Yakumo", was conducted in February 2013 at Nobiru beach, which is located north of Sendai City, Japan (Sato et al. 2013; Chen et al. 2013). The Nobiru port was developed as an industrial port around 1880. However, the original plan of the port was abandoned after the harbor was seriously damaged by a typhoon. It was one of the first modern ports in Japan.

Figure 27.6 shows the original plan of Nobiru Town by the port. It was known that some archaeological structures remain preserved at this site. However, the 3.11 East

Fig. 27.6 Original plan of Nobiru Town, ca. 1880

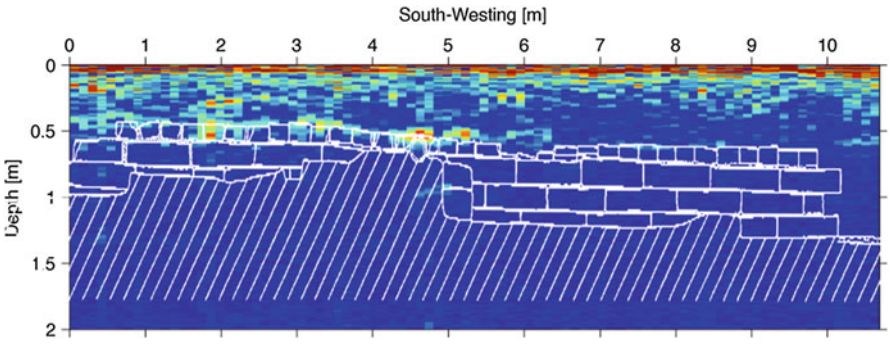

Fig. 27.7 GPR vertical profile section in Nobiru, showing the 10 m long and 60 cm × 60 cm cross section stone structure, part of a sewer system built about 100 years ago

Japan Great Earthquake and Tsunami struck this area in March 2011, and many of the archaeological specimens, such as bridge foundations, were seriously damaged or lost entirely.

One important archaeological artifact at this site is a sewer system made of stone plates, discovered about 10 years ago. It is 10 m long and 60 cm × 60 cm in cross-sectional area, buried at about 1 m depth. After the survey at that time, the structure was buried again in sand at the same location. However, the 2011 tsunami removed all the surface landmarks, and the original location of the buried structure was lost.

The survey area was covered by short grass on the site, but this presents no problem for the GPR survey. The soil in the area is soft sand and is relatively homogeneous. The survey was carried out in an area 20 m × 100 m, and the measurement took about 1 h, dramatically faster than a conventional GPR survey. By analyzing the acquired GPR data, we could find the buried structure. Figure 27.7 shows the vertical GPR profile, where the buried stone structure is evident. The size and the length of the detected object matches those measurements found in previous observations, and Fig. 27.8 shows the excavated structure.

27.4 Borehole Radar

The penetration of electromagnetic waves into soil is limited by the physical condition of the soil. However, if we can use drilled boreholes, radar antenna can be placed more closely to the deeply buried objects. Borehole radar is a special adaptation of GPR systems, in which the radar system is installed in a thin waterproof cylinder as shown in Fig. 27.9. The system can then be operated in boreholes. In a single-hole borehole radar setup, transmitter and receiver antennas are placed in a single down-hole sonde, and the operation of the radar is similar to that of a common GPR survey on the ground surface. If we have multiple boreholes near the targets, we can set transmitter and receiver antennas in separated

Fig. 27.8 The sewer system re-found by GPR survey

Fig. 27.9 Borehole radar

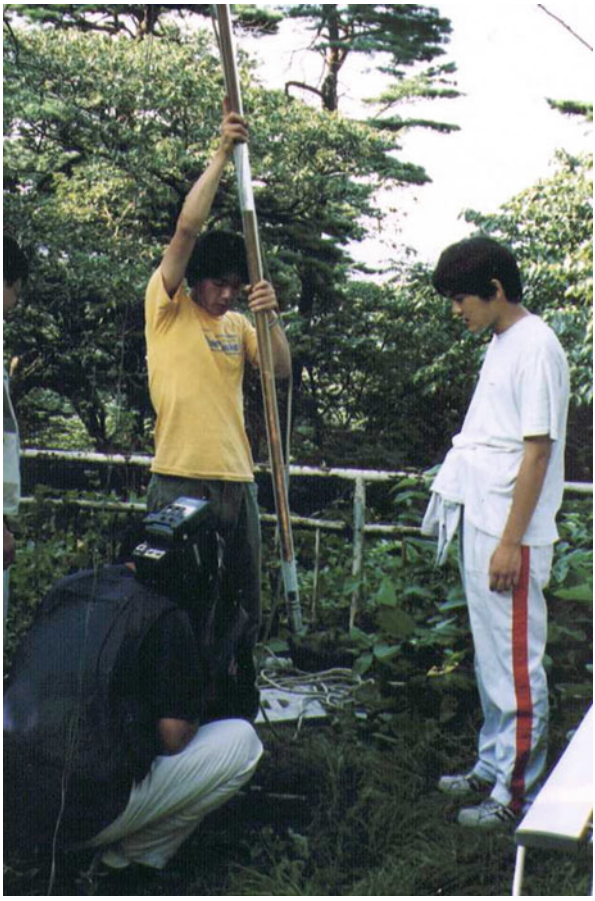

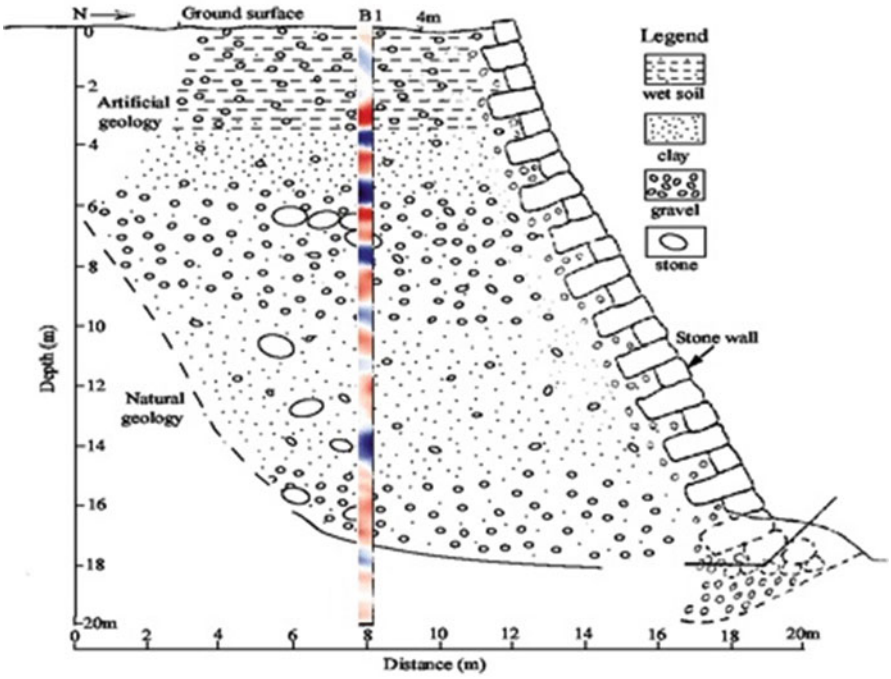

Fig. 27.10 Vertical profile of the inside structure of the stone wall of Sendai castle imaged by borehole–surface GPR (vertical radar profiling, *VRP*)

boreholes, and by measuring the transmission between antennas, we can image the area between the boreholes. A third configuration consists of setting one antenna in a borehole and the other on the ground surface. Using this layout, we can image the three-dimensional area around the borehole. This GPR survey configuration is called vertical radar profiling (VRP).

Figure 27.10 shows the visualized image inside the structure of a stone wall of Sendai castle, which was built around 1600. By using the VRP GPR measurement between the borehole and ground surface, we could detect stone structures at a depth of 8 m, which cannot be detected by a normal GPR survey conducted on the ground surface. The site was excavated, and the large stone structure shown in Fig. 27.11 was found.

27.5 Conclusions

In this chapter, we have demonstrated some advanced GPR survey techniques applied to archaeological surveys in Japan. After the East Japan great earthquake and tsunami struck in March 2011, we had many occasions to use GPR for recovery

Fig. 27.11 Excavated stone structure at Sendai castle

from the natural disaster. Our work has suggested that a better understanding of the structure of archaeological sites can be gained by nondestructive GPR surveys. Using GPR in archaeological survey work has the following important advantages:

1. GPR surveys reduce the risk of destruction of the archaeological sites by excavation.
2. GPR surveys allow estimation of the area of the archaeological structure for planning more detailed archaeological surveys and excavation.
3. GPR surveys enable the visualization of subsurface archaeological structures for academic research.

We believe the effective use of the GPR technique enhances the importance of an archaeological survey.

References

Chen J, Liu H, Takahashi K, Sato M (2013) Development of array GPR for archaeological survey and disaster mitigation. In: Proceedings of the near surface geophysics Asia Pacific conference, Beijing, July 2013

Grasmueck M, Viggiano DA (2007) Integration of ground-penetrating radar and laser position sensors for real-time 3D data fusion. IEEE Trans Geosci Remote Sens 45(1):130–137

Mahmoud G, Grasumeck M, Sato M (2009) Non-destructive 3D ground penetrating radar for imaging tree root architecture. Tech Rep IEICE SANE 109(219):67–72

Sato M, Doi K, Takahashi K (2013) Advanced GPR for archaeological survey. In: Proceedings IGARSS2013, Melbourne, July 2013

Takahashi K, Sato M (2013) 3D GPR survey of an ancient tomb using a self-tracking total station. In: Proceedings of the near surface geophysics Asia Pacific conference, Beijing, July 2013

Chapter 28
Investigating Luoyang by Remote Sensing: First Results

Fulong Chen, Nicola Masini, Enzo Rizzo, Ruixia Yang, Gerardo Romano, Antonio Pecci, and Rosa Lasaponara

Abstract Since the launch of the Silk Road Economic Belt (SREB) initiative in China, archaeological prospection has been increasingly emphasized by archaeologists, scientists, and government officials to uncover the civilization of the past and the evidence of the friendship between West and East. Compared with traditional field archaeology, remote sensing is an irreplaceable tool in archaeological investigations, taking advantage of large spatial coverage and high-spectral sensitivity to anomalies linking the occurrence of buried relics. In the framework of a Chinese–Italian bilateral project entitled "Smart Management of Cultural Heritage Sites in Italy and China: Earth Observation and Pilot Project," in 2014 we undertook preliminary investigations on some test sites in Han-Wei capital city and Dingding Gate in Luoyang City to assess the performance of remote sensing, including

F. Chen • R. Yang
Key Laboratory of Digital Earth Science, Institute of Remote Sensing and Digital Earth, Chinese Academy of Sciences, No. 9 Dengzhuang South Road, Haidian District, Beijing, 100094, China

International Centre on Space Technologies for Natural and Cultural Heritage Under the Auspices of UNESCO, Beijing, China

N. Masini
CNR-IBAM Institute for Archaeological and Monumental Heritage,
C. da Santa Loja, 85050, Tito Scalo, Potenza, Italy

E. Rizzo
Institute of Methodologies for Environmental Analysis, National Research Council,
C.da Santa Loja, 85050, Tito Scalo, Potenza, Italy

G. Romano
Institute of Methodologies for Environmental Analysis, National Research Council,
C.da Santa Loja, 85050, Tito Scalo, Potenza, Italy

University of Bari, C.da Santa Loja, 85050, Tito Scalo, Potenza, Italy

A. Pecci
Institute for Archaeological and Monumental Heritage, National Research Council,
C.da Santa Loja, 85050, Tito Scalo, Potenza, Italy

R. Lasaponara (✉)
CNR-IMAA, Institute of Methodologies for Environmental Analysis,
C. da S. Loya, 85050 Tito Scalo, Potenza, Italy
e-mail: rosa.lasaponara@imaa.cnr.it

N. Masini, F. Soldovieri (eds.), *Sensing the Past*, Geotechnologies and the Environment 16, DOI 10.1007/978-3-319-50518-3_28

space-borne synthetic aperture radar (SAR), unmanned aerial vehicles (UAV), and the surface geoelectrical method for the detection of archaeological features. The investigations have been planned considering that the characteristics of the expected archaeological features and the subsoil are not ideal for applications based on the use of remote sensing and geophysics. In fact, past archaeological excavations unearthed deep walls built in rammed earth with stone foundations covered by clayey soil. The aim of this preliminary investigation campaign has been to provide indications for a cost-efficient scientific mission to be conducted in the future on wider areas in Luoyang with the prospect of performing archaeological excavations.

Keywords SAR • ERT • UAV • Archaeological prospection • Luoyang • China

28.1 Introduction

"Silk Roads: The Routes Network of Chang'an-Tianshan Corridor," running across China, Kazakhstan, and Kyrgyzstan, was inscribed in the UNESCO World Heritage List in 2014. The Silk Road, a series of trade and cultural transmission routes connecting China to Europe, is witness to a civilizational friendship and harmony between the East and West dating back 2000 years that has left us with various relics to be uncovered and investigated (Chen et al. 2016). In the framework of the Chinese–Italian bilateral project "Smart Management of Cultural Heritage Sites in Italy and China: Earth Observation and Pilot Project," funded by the Italian of Ministry Affairs and launched in 2013, multidisciplinary researchers from China and Italy worked together for archaeological investigation as well as heritage conservation using Earth observation technologies focusing on well-known sites along the Silk Road, particularly for the ancient Luoyang city in China and that of Rome in Italy.

As the eastern starting point of the route, the ancient Luoyang city was once the capital of five dynasties from the twentieth century BC to the later Tang dynasty, including the Erlitou ruin (3900 BP; Xia Dynasty), Yanshi ruin (3600 BP; Shang Dynasty), Zhouwang City (2600 BP; Zhou Dynasty), Han-Wei capital city (1900–1500 BP; Eastern-Han to Wei Dynasties), and Sui-Tang capital city (1300–1100 BP; Sui to Tang Dynasties). It also has an important role for the Chinese civilization in the central plain of China. To understand the civilization procedure, social society in the past as well as palaeo-environmental evolution, archaeological prospecting was considered as an optimal solution by means of uncovering historical sites and reconstruction of surrounding palaeo-landscapes.

Taking advantage of large spatial coverage, high-spectral capabilities, and sensitivity to anomalies linked to subsurface relics, remote sensing is becoming a well-established tool for combining excavations in archaeological applications (Buck et al. 2003; Cavalli et al. 2007; Rowlands and Sarris 2007). More recently, very high resolution (VHR) remotely sensed images, for example, WorldView-1/2

of optical and TerraSAR/TanDEM-X of synthetic aperture radar (SAR) data, have been promoted for archaeological exploitation and excavation planning.

Although several well-known archaeological marks, including crop, soil, and shadow signs (Crawford 1929; Masini and Lasaponara 2007; Keay et al. 2014; Chen et al. 2015b), have been established through the joint efforts of archaeologists and scientists, remote sensing for archaeology is still at the early stage of development for the following reasons: (i) lack of a systematic methodology framework oriented for archaeological applications; (ii) the capability of SAR data for archaeology is not fully assessed; (iii) new methodologies need to be developed to go with the launch with new acquisitions; and (iv) the domain of remote sensing needs to be extended to include other remote sensing technologies, such as unmanned aerial vehicle (UAV) and geophysical investigations. Consequently, taking the Han-Wei capital city (Han and Wei Dynasty) and Dingding Gate (Sui-Tang Dynasty) in Luoyang as study sites, we conducted pilot investigations using a systematic space–air–ground observation solution; that is, satellite SAR remote sensing for both sites, and UAV prospections for three-dimensional (3D) modeling and geoelectrical measurements only in Dingding Gate. In the perspective of conducting the following extensive archaeo-geophysical campaign, the pilot investigations have been aimed at evaluating the most cost-effective approach for detecting archaeological features, considering that in both the two sites (i) the expected buried structures are deep (1–4 m) and are built with rammed earth with foundation made of stones; (ii) the subsoil is mostly clayey; and (iii) the surfaces of the areas, in particular that in Dingding Gate, are characterized by the presence of new structures and canopy. All these characteristics make this pilot project a challenge for remote sensing in archaeology.

28.2 Study Site and Joint Campaigns

28.2.1 Study Sites

Han-Wei capital city and Dingding Gate are two sites of the Silk Road Chang'an-Tianshan Corridor, located in the modern Luoyang city in Henan Province of China (see Fig. 28.1). Luoyang is one of the cradles of Chinese civilization situated on the central plain of China. It is influenced by a continental climate with four distinct seasons. The average annual temperature is 14 °C with sufficient rainfall mainly concentrated in summer season with an annual average of 540–550 mm. The geology is characterized by silt and clay. Winter wheat (growth cycle from later October to the middle of the next year) and corn (growth cycle from June to October) are two prevalent cultivated plants in agricultural areas.

The Han-Wei capital city dates back to 1900–500 BP. In 25 AD, Luoyang was declared the capital of the Eastern Han Dynasty by Emperor Guangwu of Han

Fig. 28.1 Study sites of Han-Wei capital city and Dingding Gate (marked by *pink rectangles*) located in the modern Luoyang City, Henan Province, China

and became the focal point of China. In the late second century, China again declined into anarchy and the Han capital of Luoyang was finally burned to ashes in 189 AD. In 493 AD, Emperor Xiaowen of the Northern Wei Dynasty moved the capital from Datong to Luoyang, and brought the ancient Luoyang city into a new period of prosperity reflected by the construction of the famous Longmen Grottoes (Chen et al. 2015b). Nowadays, the prosperity of the Han-Wei capital city has disappeared, leaving us with chronological documents as well as ancient buried remains. Figure 28.2 illustrates the reconstructed city based on chronological documents and field archaeological campaigns, particularly for the imperial palace (highlighted by the purple rectangle) comprising the Taji Hall Remains, Building Remains No. 3 and No. 2, and the Changhe Gate. It is clear that archaeological details are missing and thus further investigations are crucially required.

Dingding Gate (recognized as a World Heritage site along the Silk Road's Chang'an-Tianshan Corridor; Fig. 28.3a) was the main entrance to the outer-city wall and also the central axis of Luoyang City during the Sui and Tang Dynasties. Its name was changed from Jianguo Gate in the early days of Sui Dynasty. Emperor Yang of Sui, who moved to Luoyang and selected it as the capital city, was the first emperor to pass through the gate in history. Afterward, Dingding Gate was successively used as the main entrance to the outer city wall of Luoyang City for 530 years, becoming the entrance to a capital city with the longest time in Chinese history. Nowadays, only a section of city-wall foundation centered on the Dingding Gate has been excavated (covered by artificial structures; see Fig. 28.3b). Other archaeological relics, such as residential blocks, inner-city channels, and avenues, are still poorly understood, calling for future archaeological investigations.

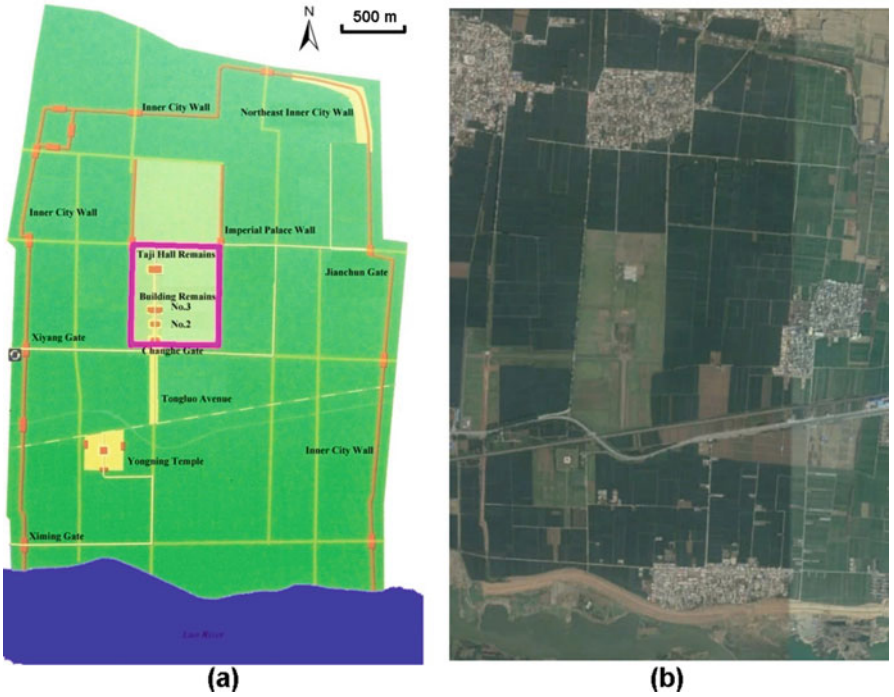

Fig. 28.2 Han-Wei capital city including the imperial palace (highlighted by *purple rectangle*), excavated in 2011–2013. (**a**) Reconstructed archaeological map based on chronological documents and field archaeological campaigns. (**b**) Optical remote sensing image from Google Earth

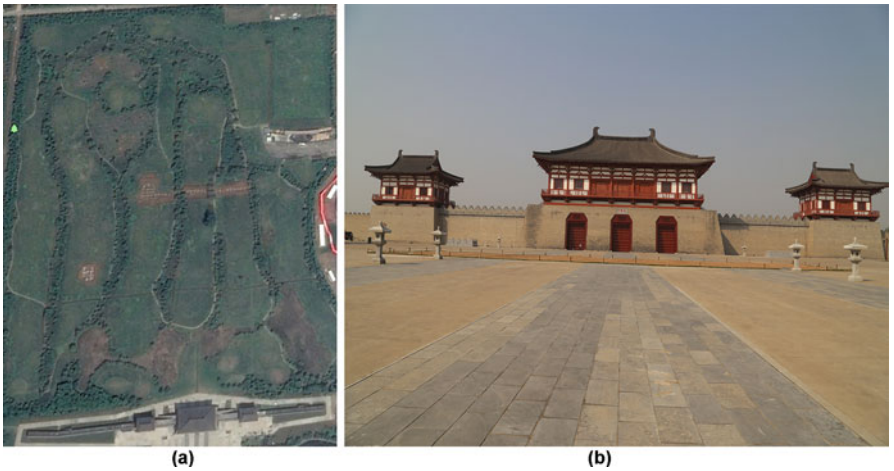

Fig. 28.3 Study site of Dingding Gate. (**a**) Optical remote sensing image from Google Earth. (**b**) Photograph of artificial structure covering the excavated city-wall foundation obtained in the field campaign in 2013

28.2.2 Joint Campaigns

In the framework of the Sino–Italian bilateral project, an international research team with approximately 15 fellows from Institute of Remote Sensing and Digital Earth, Chinese Academy of Science, Institute for Archaeological and Monumental Heritage, National Research Council of Italy, Institute of Methodologies for Environmental Analysis, National Research Council of Italy and Institute of Geographical Sciences, Henan Academy of Science, China, was established. Fellows with interdisciplinary expertise from archaeology, science, and engineering were important for project implementation (e.g., field archaeology planning, remote sensing data acquisition and processing, geophysical investigation, data mining and results interpretations, etc.).

In 2013–2014, two joint field campaigns were conducted (see Fig. 28.4). The aim of the first campaign was for preliminary understanding of the Han-Wei capital city and Dingding Gate. In October 2013, the joint research team visited the two study sites. The physical properties, including soil composition and moisture, land cover and land change, and the archaeological layout of sites, were obtained by

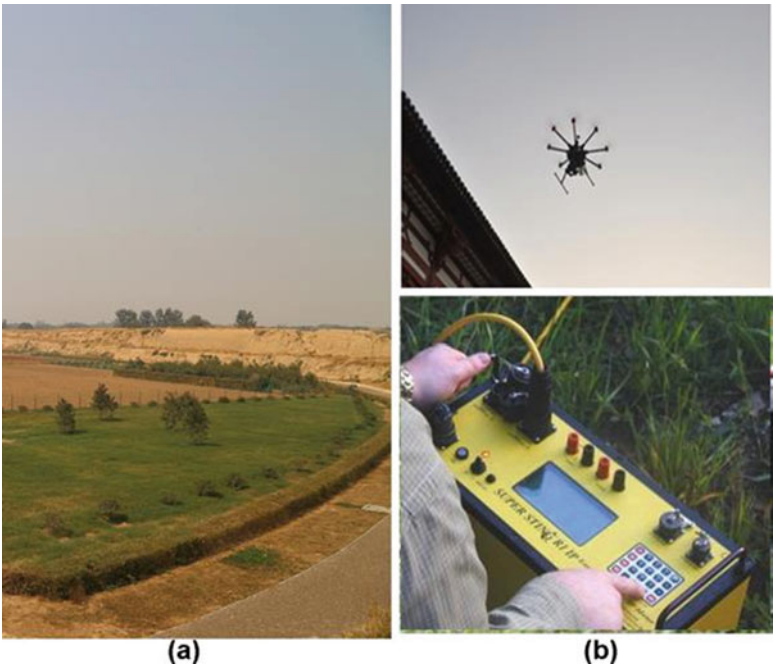

Fig. 28.4 Two joint field campaigns for the sites of Han-Wei capital city and Dingding Gate in 2013–2014. (**a**) Field surveying for the northwest inner-city wall of Han-Wei capital city in 2013. (**b**) Unmanned aerial vehicles (UAV) mission and geoelectrical measurements in Dingding Gate in 2014

field surveying and discussion with local administrations. In 2014, the second field campaign was focused on the geoelectrical measurements and UAV imaging for the Dingding Gate. Several preliminary results have been derived and are described in the following sections.

28.3 Rational Basis and Data Processing Methodology

28.3.1 SAR Remote Sensing for Archaeological Prospection

Past human occupation and activities have left traces and marks on the territory including landscape alterations and environmental changes that can be recognized even after centuries and millennia. All these marks can be detected from a space SAR system, because the alteration they produce can be revealed by radar return that is mainly dependent on the superficial roughness, structure (shape and orientation), type and status of material, and corresponding dielectric properties (about SAR for archaeology, see Lasaponara and Masini 2013; for applications in the field of landscape archaeology, see Chap. 5 by Tapete and Cigna 2016, this volume). Analogously to optical remote sensing, the shadow, vegetation, and soil and damp marks can also be observed in SAR images (Lasaponara and Masini 2013; Chen et al. 2015b).

The crop marks in SAR images are indicated by backscattering anomalies linked to the occurrence of buried archaeological structures. Either for the negative marks above wall foundations and positive marks above the damp or nutritious soil of buried pits and ditches, the crop mark is more evident in specific stage of plant growth, for example, the period from the crop's revival to the growth. The occurrence of archaeological remains can change soil types and contents (e.g., nutrients) as well as drainage capability, resulting in the well-known phenomenon of soil and damp marks. Soil and damp marks can be detected by exploiting backscattering anomalies induced by the variations in grain size, soil density, and soil texture as well as the soil's dielectric constant. (For more details, please see Chen et al. 2015a.) As for the shadow marks (optical shadow marks, not to be confused with radar shadows), they are the result of shading, in the presence of low sunlight, caused by relief. The latter, if illuminated by radar, produce a backscattering response, thus allowing us to observe the typical microtopography linked to the presence of shallow remains. As an example, the reader is referred to the case of Sabratha in Libya, which is well visible from Cosmo SkyMed X-band spotlight images published by Chen et al. (2015b), and the ruins of Niya in the Xinjiang region (China) visible from C-band Sentinel-1 data (Chen et al. 2016)

For enhancement of the archaeological marks as well as a quantitative analysis of the crop marks using multitemporal SAR data, we designed a data processing diagram (Fig. 28.5). (i) Feature detection by archaeological marks on SAR images: for the co-registered SAR image sets (N acquisitions), temporal stacking is helpful

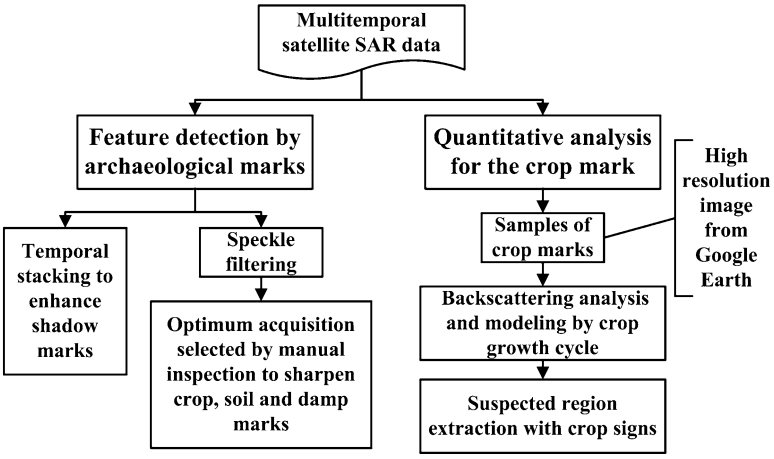

Fig. 28.5 Multitemporal synthetic aperture radar (SAR) data processing for sharpening archaeological marks and a quantitative analysis of the crop marks

to suppress speckle noise (an unfavorable noise occurs in SAR images because of the coherence nature of the system) by increasing the equivalent number of looks (ENL) with a factor of Sqrt (N). Thus, weak archaeological features can become prominent, particular for the shadow marks showing consistent phenomena in all acquisitions. Also, spatial filters (e.g., enhanced Lee approach, 1980) can be applied for speckle noise suppression, and then backscattering anomalies linking crop, soil, and damp marks can be identified by manual inspection. Once the optimal acquisition was determined, a Gaussian filter could be applied to the selected SAR imagery to further sharpen archaeological marks. (ii) Quantitative analysis for the crop marks: the presence of subsurface archaeological deposits influences surface vegetation patterns in response to the variations of water and other nutrients, demonstrating a growth cycle anomaly, particularly in the spring and autumn seasons. Those anomaly phenomena can sometimes be identified on high-resolution images on Google Earth, providing guidance for the sample collection of crop marks on SAR images once all data are geocoded with a uniform geocoordinate system. Then, the temporal variation of backscattering on crop marks can be modeled, acting as the training set for the suspected region extraction with crop signs on the entire landscape.

28.3.2 UAV 3D Modeling

High-resolution surveying was traditionally associated with quite expensive tools and facilities, ranging from data acquisition to the processing chains. One of the most important revolutions ongoing today is that several technologies are available

at different costs for different purposes and needs; thus, even with a small budget it is possible to implement very effective solutions. One of these technologies is based on the use of unmanned aerial vehicles (UAV), commonly known as drones, an aircraft that can be piloted remotely.

Compared to traditional aerial archaeology with aircraft flight, the UAVs offer several advantages, particularly as they are low in cost and require less time. A traditional aircraft must take off from an airport, sometimes far from the work area, whereas a drone, particularly one with a rotary wing, can be transported into the area of interest, take off directly from there in a few minutes, and has the ability to cover a large area in a short window of time.

There are currently a wide range of UAVs. A classification of diverse UAV systems based on size, weight, endurance, range, and flying altitude is given by Nex and Remondino (2013). A typical UAV platform for geomatics purposes has costs ranging from 1000 to 50,000 Euro, depending on (i) payload, (ii) instrumentation, (iii) degree of automation, and (iv) autonomy in battery characteristics.

The reasons for the success of UAVs are also the innovative vision, the very high resolution of the obtainable products (orthophotographs, digital elevations models), and the availability of easy tools of image processing based on structure from motion (SfM) (Neitzel and Klonowski 2011; Nex and Remondino 2013).

SfM is a range-imaging technique that allows obtaining the three-dimensional (3D) model of objects and landscapes from two-dimensional (2D) image sequences, coupled with local motion signals. To carry out scene triangulation and reconstruction, traditional photogrammetric methods require single stereo-pairs and the 3D location of ground control points. The SfM approach addresses this issue by using multiple partially overlapped images, namely, a highly redundant bundle adjustment based on matching features. For additional details see the comprehensive introduction to SfM technique in Westoby et al. (2012).

28.3.3 Geoelectrical Method for Underlying Archaeological Feature Detection

The geophysical methods that are most commonly used are electrical resistivity and magnetic and ground-probing radar. Although the geoelectrical results are usually combined with magnetic and electromagnetic data to highlight the buried archaeological structures (Rizzo et al. 2005; Chianese et al. 2010; Capozzoli et al. 2015), the geoelectrical technique is a useful method for archaeological investigation because it explores subsurface layers and objects in a relative short time and provides a more economical alternative to exploratory drilling and excavation. The electrical resistivity method is based essentially on the measurement of an electric field artificially created in the ground by two pairs of electrodes fixed in the ground and connected to a specific instrument (geo-resistivity meter): a pair constitutes the current injection circuit (A and B) and the other (M and N) measures the drop

of potential generated in the ground. The potential difference measured depends on the current applied, the electrical resistivity of the subsurface medium, and the geometric factor determined by the array configuration. Therefore, a single apparent resistivity value is obtained on each combination of source and receiver electrode positions (quadrupole). For many combinations of the survey configuration, a subsoil distribution of the apparent resistivity values is obtained (pseudo-section). The pseudo-section provides a smooth image of the 'true' resistivity structure with depth; therefore, dedicated software uses an inversion routine, which allows automatically determining a two-dimensional resistivity model of the subsurface starting from the data measured at the surface.

28.4 Experimental Results

28.4.1 SAR Remote Sensing for Han-Wei Capital City

28.4.1.1 Archaeological Marks on SAR Images

Considering the infancy stage of SAR remote sensing for archaeology (Lasaponara and Masini 2013; Chen et al. 2015a), a pioneering effort was made to assess the potential of satellite X-band SAR data in detecting archaeological marks (for more details, see Chen et al. 2015b). Forty scenes of COSMO-SkyMed X-band Stripmap data covering Luoyang City, Henan, China in the observation period of 27 February to 17 October 2013 were acquired. The SAR data, in ascending orbit with HH polarization, have an image pixel spacing of 2.264 and 0.769 m in azimuth and range direction, respectively. The calculated ground spatial resolution is approximately 3 m taking into account the 20° incidence angle.

Archaeological features (see Fig. 28.6) were detected using the multitemporal SAR data processing methodologies illustrated in Fig. 28.5, "Feature detection by archaeological marks." The reconnaissance of shadow marks was distinct in the temporal stacking imagery (see Fig. 28.6a) owing to the 6.3-fold enhancement of ENL in the derived temporal-averaged SAR imagery. Ground-truthing clarified that the shadow marks were related to rammed earth structures of the Northeast Inner City Wall (red arrows in Fig. 28.6a). For the crop marks, the acquisition of SAR imagery on 19 March 2013 shows the best performance for indicating crop marks (Fig. 28.6b).

After the Gaussian filter, the crop anomalies with two regular features linked to subsurface archaeological remains can be identified. Local archaeologists interpreted the positive mark to be a man-made pit with rich nutrients, and the other to be buried foundations of buildings. For the soil and damp marks, the flood on 22–24 July 2013 in Luoyang (caused by heavy rains; the accumulated precipitation record was 102 mm) provided an opportunity to sharpen soil moisture anomalies linked to the occurrence of buried archaeological structures. Manual inspection showed that the Gaussian-filtered SAR imagery acquired on 25 July 2013 (one day after the

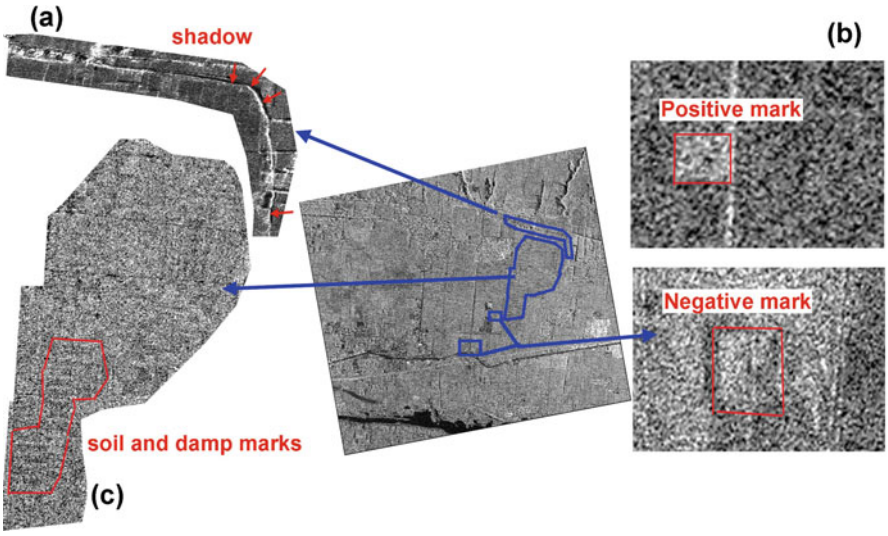

Fig. 28.6 Shadow, crop, soil, and damp archaeological marks observed on processed COSMO-SkyMed SAR imagery. (**a**) Shadow mark from archaeological evidence. (**b**) Crop marks. **c** Soil and damp marks

heavy rain) demonstrated the best performance in detecting soil and damp marks (Fig. 28.6c). Linear features highlighted by the red polygon were interpreted to be foundations of walls or buildings.

28.4.1.2 Quantitative Analysis of the Crop Mark

Using the 40 scenes of Cosmo-SkyMed images already mentioned, the crop sign on the site of Han-Wei capital city was further investigated (Fig. 28.7) by applying the "quantitative analysis for the crop mark" chain in Fig. 28.5. To mitigate the effect of anthropogenic activities, a core subarea centered on the Imperial Palace with a dimension of 3.34×4.74 km^2 was selected (Fig. 28.7a). The crop mark samples were extracted synergistically using the archaeological layer and anomalies on Google Earth images (highlighted in green). The Chinese Gaofen-1 optical imagery, including a panchromatic image and multispectral images at 2 m and 8 m of geometric resolution, respectively, were utilized for land-use and land cover classification. The methodology of Gram–Schmidt spectral sharpening was applied for the fusion of the Gaofen-1 image. Then, a classification map was derived with four categories including buildings, water, roads, and wheat farmland (Fig. 28.7b). Considering the occurrence of crop signs with the wheat farmland, this classification map applied to masking potential false alarms with no vegetation. Then, the temporal variations of SAR backscattering of crop mark samples and normal features were analyzed (Fig. 28.7c); it is clear that there is a remarkable

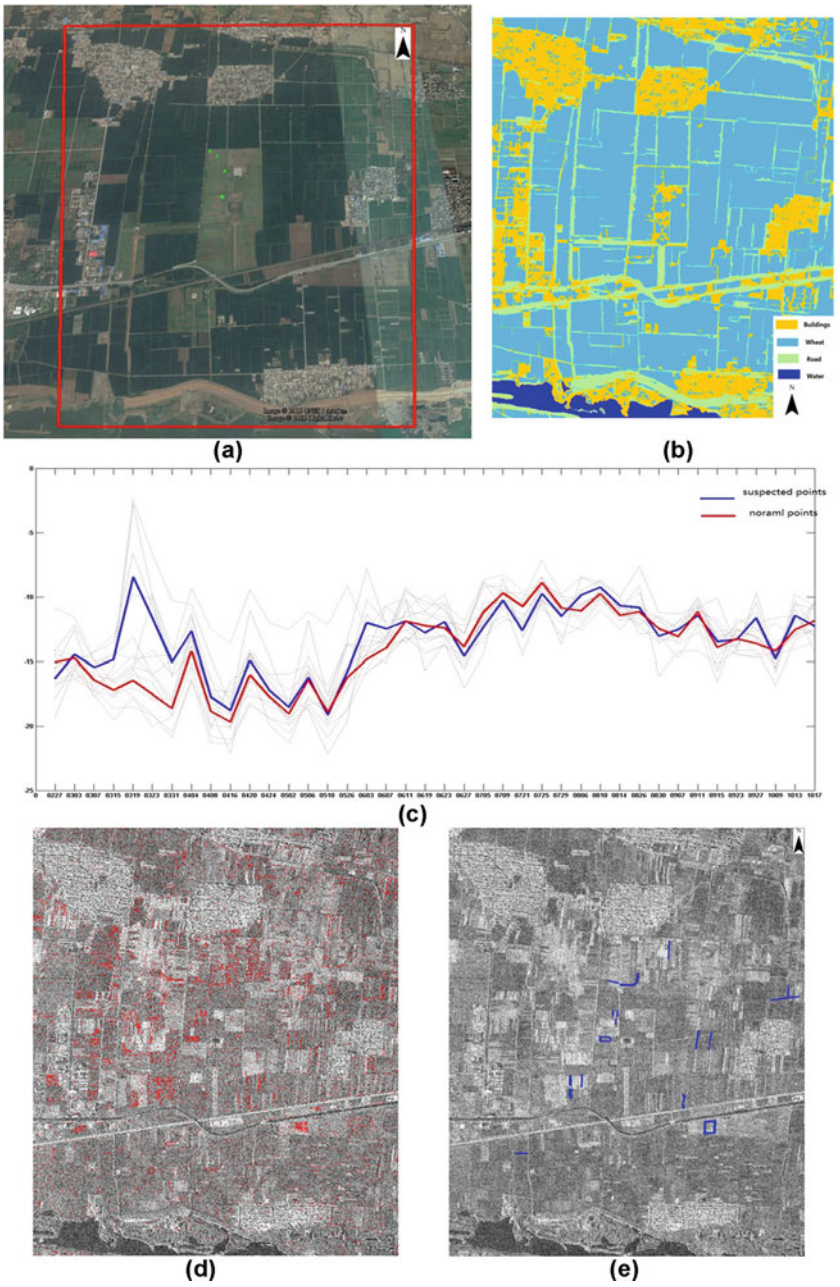

Fig. 28.7 Quantitative analysis of the crop marks. (**a**) Selected subzone of Han Wei capital city; samples of crop marks are highlighted by *green dots* or *rectangles*. (**b**) Classification map of Gaofen-1 optical imagery for masking. (**c**) Temporal variation of SAR backscattering of crop signs (highlighted in *blue*) and normal features (highlighted in *red*). (**d**) Suspected pixels or regions with crop signs by using the twofold classification method based on a decision tree. (**e**) Final suspected regions with crop signs by manual inspection

difference in the spring season, particularly for the period from 27 February to 31 March 2015, when the wheat revived and/or in the elongation phase. Based on the backscattering analysis, a twofold classification via the decision tree method was applied to extract suspected pixels and regions with crop signs (Fig. 28.7d). The classification rules via backscattering-variation slopes (BS) are summarized as follows:

Rule 1: BS in the period 7 March to 15 March 2015 > 0.5
Rule 2: BS in the period 15 March to 19 March 2015 > 6.0
Rule 3: BS in the period 19 March to 23 March 2015 < −3.0

The derived suspected spots overlapped on the SAR imagery, as illustrated in Fig. 28.7d. Because of the speckle noise of SAR images, the initial results were rather coarse. Taking into account the regular topology of underlying ancient remains (linear, rectangle, circle), final suspected regions with crop signs were further extracted (Fig. 28.7e) by manual inspection of initial spots (Fig. 28.7d). The proposed data processing chain as well as derived results will be validated by geophysical investigations or field excavations in the near future.

28.4.2 Integrated Remote Sensing Approach in Dingding Gate

28.4.2.1 SAR-Based Detection of Archaeological Traces

Because of the wide swath (40 km) of Stripmap Cosmo-SkyMed data, the site of Dingding gate can also be covered by the 40 multitemporal SAR data. The processing module of "Feature detection by archaeological marks" in Fig. 28.5 was used to enhance the archaeological traces. Speckle noise in the temporal-averaged SAR imagery in Dingding Gate (highlighted by the red polygon in Fig. 28.8) was significantly mitigated by the increased ENL with a factor of 6.3. However, no archaeological marks or signs can be observed on the SAR imagery, interpreted by the following two causes: (i) the upper-layer surface of the site changed grossly in the recent 10 years (e.g., the construction of a golf garden), destroying archaeological marks linked to the buried remains; and (ii) the depth of the archaeological features buried in the site was too deep (i.e., 2–3 m as recorded by the field excavation; Chen et al. 2004) to indicate backscattering anomalies in SAR images. Consequently, the UAV mission and geophysical investigations were further applied for the archaeological prospection in this site (for more details, please refer to Sects. 28.4.2.2 and 28.4.2.3).

28.4.2.2 UAV-Based Survey in Dingding Gate

In Dingding Gate, some surveys at different heights, with different temporal acquisition of images in oblique and nadiral mode, have been performed to obtain

Fig. 28.8 Temporal-averaged SAR imagery covering the site of Dingding Gate (highlighted by *red polygon*)

very detailed digital terrain models (DTM) and orthophotographs to use as a cartographic base for georeferencing geophysical results.

For the aerial survey we used a low-cost drone with 100,000 RMB. It has a structure in carbon fiber with a weight of 9.5 kg, a diameter of 1000 mm, and a payload of about 5 kg. Propulsion is provided by an electric motor powered by a battery that allows a flight range of 15 min in standard condition. The remote control operates up to a maximum distance of 1500 m, with the horizontal and vertical speed ranging from 2.5 to 12 m/s and 3 to 4 m/s, respectively; with a camera that can shoot video in full HD and take photographs in 14 megapixels. UAV surveys, performed in Dingding Gate, aimed at providing the digital surface model (DSM) of the area to observe and interpret further microrelief linked to potential shallow remains. The images were captured in manual, oblique, and nadiral mode, from a height of 80 m.

The processing of the images was performed by exploiting the capability of SfM algorithms of the software Photoscan (AgisoftPhotoScan User Manual 2014). The processing included the following phases: (i) selection of photographs taken with overlap requirement (75–85% of forward overlap and 50–50% of side overlap) to minimize blind zones; (ii) computation of camera position and orientation for each photograph; (iii) alignment of photographs and building of a sparse point cloud; (iv) generation of dense point cloud model; (v) building of 3D model polygonal mesh; and (vi) textured 3D modeling.

The highly detailed 3D model of the scene (Fig. 28.9) allowed us also to analyze the backscattering response of relief and microrelief of the scene in relationship to the geometric characteristics as already done in other applications (Lasaponara et al. 2016)

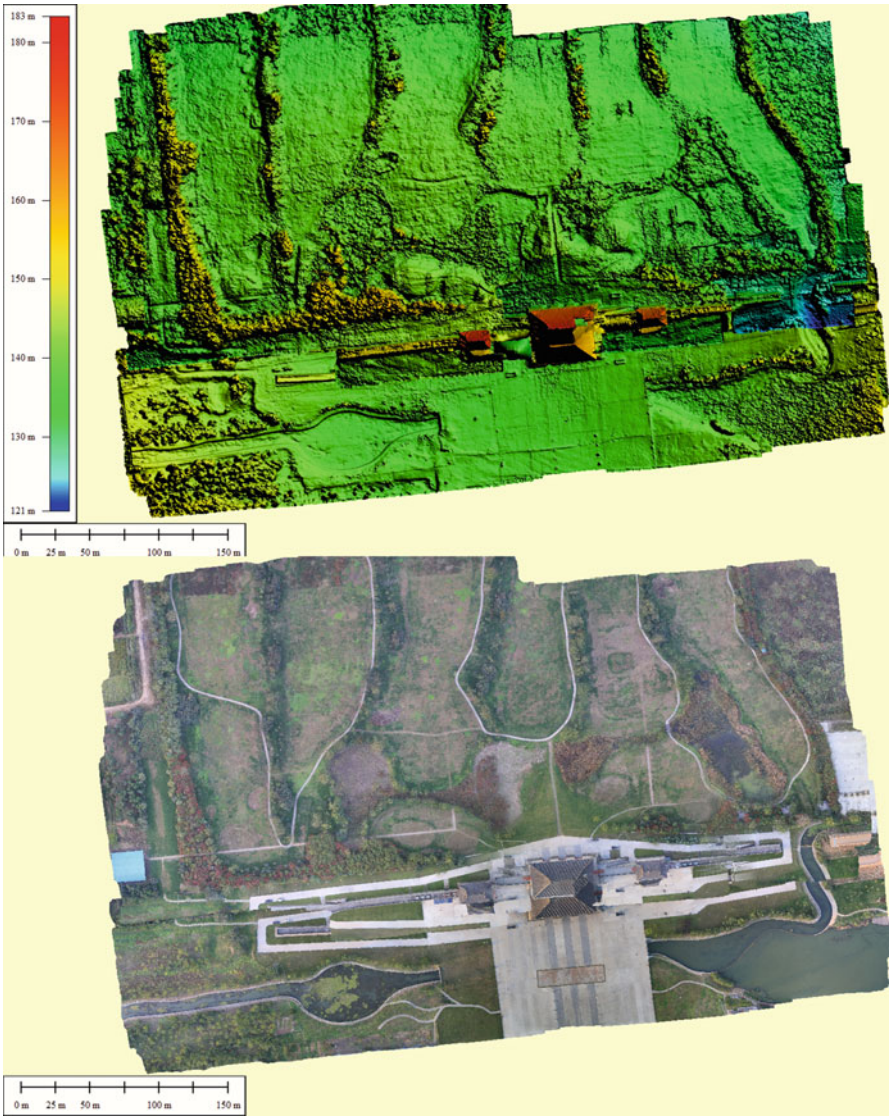

Fig. 28.9 UAV-based survey in Dingding Gate. *Upper:* digital elevation model obtained by using structure-from-motion applied to images taken from UAV; *bottom*: ortho-photograph

28.4.2.3 Geoelectrical Measurements for Dingding Gate

In Dingding Gate archaeological area, n. 6 electrical resistivity tomography (ERT) was carried out (Fig. 28.10) to obtain the resistivity distribution of the subsoil and to find a hypothetical correlation with archaeological features (main avenue and

Fig. 28.10 Locations of the six ERTs (superimposed on Google Earth image) in Dingding Gate

channels). Figure 28.11 shows the five ERTs carried out across the hypothetical location of the main avenue. Each ERT used 60 electrodes with an electrode spacing of 1 m, and for each profile more than 500 measurements of apparent resistivity have been computed according to the 2D pseudo-section scheme with Wenner array configuration. This configuration permits obtaining an investigation depth of about 6 m.

To obtain a 2D electrical model, all the acquired apparent resistivity data were inverted using the RES2Dinv software (Geotomo software). The inversion routine is based on the smoothness constrained least-squares inversion implemented by a quasi-Newton optimization technique. The subsurface is subdivided into blocks whose number is related to those of measuring points.

The optimization method adjusts the 2D resistivity model, trying to reduce iteratively the difference between the calculated and measured apparent resistivity values (RMS error). The acquired ERTs have a low RMS (<4%) and the inversion routine provided the topography effect. The resistivity distribution of the ERTs should be divided in two main electro layers: a shallow one with relative low resistivity value (<40 ohm*m) up to 2–3 m from the surface; and a deep one with a high relative resistivity layer (>100 ohm*m). The ERT images highlight some peculiarities that should be associated at the presence of an "old avenue" delimitated by a wall and/or channels. Table 28.1 describes the archaeological stratigraphy coming from a field excavation (Chen et al. 2004).

The archaeologists highlighted three distinct archaeological layers as much as 3 m deep during an excavation close to the south wall. Layer I has a depth range

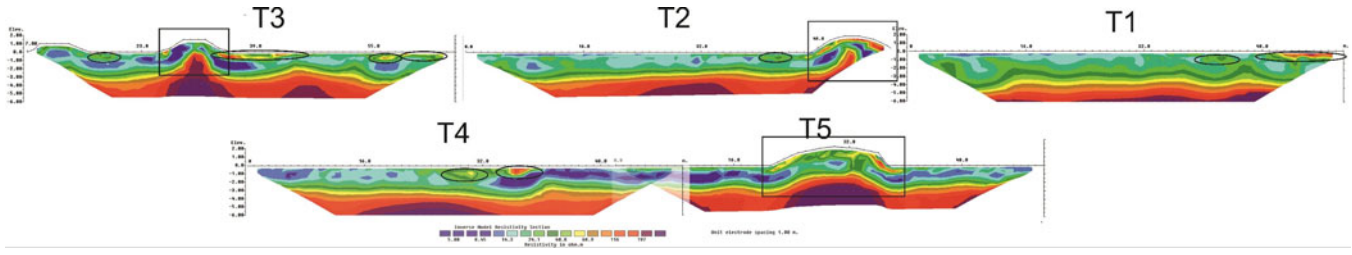

Fig. 28.11 ERTs carried out in Dingding Gate archaeological area. Archaeological remnants with resistivity anomalies are marked by *black squares* and *circles*

Table 28.1 Archaeological stratigraphy of Dingding Gate

Layer	Depth (cm)	Color, aspect	Cultural deposits (Chen et al. 2004)	Resistivity values
I	55–180	Brown and soft	From the Jin and Yuan Dynasties and continuing up to modern times	
II	40	Yellowish-brown, including large chunks of red clay	From the Song Dynasty. Porcelain shards as well as broken architectural fragments from the Tang and Song. At the bottom of this layer, archeologists discovered remains from the late Tang and Northern Song gates and road surfaces	< 40 ohm*m
III	50–65	Yellowish-brown and contains a fair amount of sand	Porcelain shards and architectural remnants dating from Tang Dynasty. At the bottom of the third layer, remains of the gate from the early and late middle Tang period along with traces of rammed earth from the late Sui and early Tang were found	

Chen et al. (2004)

of 5–180 cm (layer from 55-cm depth to the surface linked to the modern time deposit), with a cultural deposit from the Jin and Yuan Dynasties and continuing up to modern times. Layer II is deep around 40 cm. The archaeological reports said that soil in this layer is yellowish-brown together with large chunks of red clay, corresponding to cultural deposits from the Song Dynasty. Also at the bottom of this layer, archeologists discovered remains from the late Tang and Northern Song Dynasties. Layer III has a depth ranging from 50 to 65 cm. The soil in this layer is yellowish-brown and contains a fair amount of sand. The cultural deposits show porcelain shards and architectural remnants dating from the Tang Dynasty. At the bottom of layer III, remains of the gate from the early and late middle Tang period along with traces of rammed earth from the late Sui and early Tang Dynasties were found. The shallow resistivity layer incorporates the three archaeological levels. From a detailed analysis, the ERT images highlight some relative shallow resistive lens (black circles in Fig. 28.11) that should be associated to the remains of layer I. Moreover, a rounded protuberance is found in the deep relative high resistive layer inside the two small hills localized along the ERT T3, T2, and T5 (black square in Fig. 28.11). The shape of these structures led us to think about a lateral edge of the main road coming from the Dingding Gate to the south-central gate of the outer city wall of Luoyang.

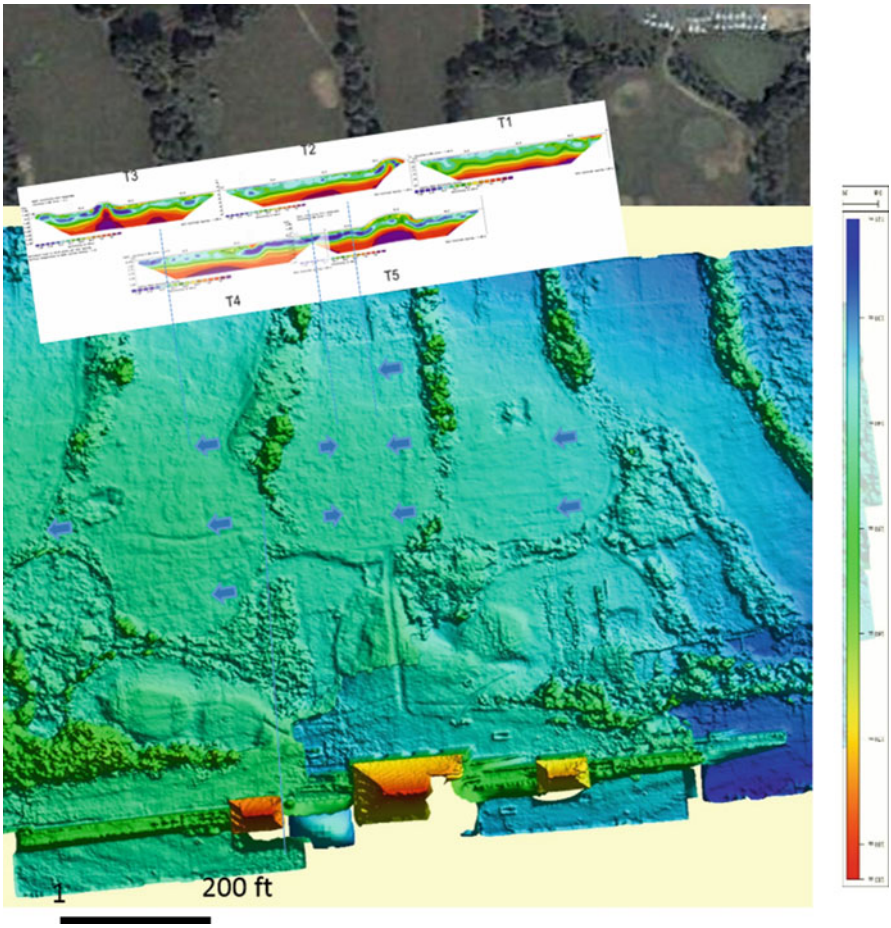

Fig. 28.12 ERTs overlain on the DEM derived for the SfM-based processing of aerial images taken from the drone. The DEM indicates some linear features (*arrows*) referable to possible roads that seem to be confirmed by the geoelectrical investigations

The hypothesis about the archaeological features seems to be confirmed by the UAV-based survey. The observation of the DEM derived from the processing of aerial images taken from the drone puts in evidence some linear features (denoted by arrows) referable to possible roads (Fig. 28.12).

28.5 Conclusions

In this study, extended remote sensing technologies, including satellite SAR, UAV, and geoelectrical investigations, for archaeological prospection were used on the two well-known World Heritage sites of Han-Wei capital city and Dingding Gate

in the framework of the China–Italian bilateral project. The investigations have been performed on two test areas to evaluate the capability of remote sensing for a more extensive archaeological prospecting campaign to conduct in the future, considering that the building materials of the potential cultural target to be detected, the characteristics of the subsoil, and the surface are not ideal for an application based on the use of earth observation technologies. In fact, past archaeological excavations revealed the presence of walls built with rammed earth, based on stone foundations, covered by a deep layer of earth that is predominantly clayey.

In both sites 40 multi-temporal SAR data of Stripmap Cosmo-SkyMed have been used to detect possible features of cultural interest. For the mitigation of speckle noise and the enhancement of possible archaeological marks, a multitemporal SAR data processing approach has been developed and used, thus allowing to identify a number of relief and crop marks referable to the presence of shallow and buried remains.

In Dingding Gate the results from SAR data processing were not equally good because the upper-layer surface of the site HAD changed in the most recent 10 years for the construction of a golf garden, destroying archaeological marks linked to buried remains, and modifying the depth of the expected remains (from 1 to 3 m). However, in Dingding gate UAV surveys and geoelectrical investigations were performed with promising results whose interpretation, exploiting ancillary data, would indicate the presence of a system of buried roads and channels typical of the Sui Tang urban planning and architecture.

The results obtained indicate the need to pursue the use of SAR imagery focusing on time-series backscattering anomalies related to the wheat growth cycle and other proxy indicators, results of the physical interaction between the archaeological deposits and the surrounding soil. These preliminary tests in Luoyang demonstrate the capability of geoelectrical prospection which in the future should be employed for validating results from SAR-based investigations along with other geophysical techniques, such as georadar with low- and medium-frequency antennae.

The analysis and interpretation of the features and cultural layers, discovered and identified by the use of diverse technologies, have a strategic importance for the preservation and conservation of archaeological relics as well as for the promotion of remote sensing as an operative tool in Chinese archaeology. Considering the proposed initiative of SREB, the approach herein proposed is a reference basis useful to plan more studies and investigations on a variety of archaeological sites. Finally, following the Copernicus approach, the use of ground truth for validating the results obtained from remote sensing along the Silk Road connecting China to Europe can also support and further extend development of remote sensing for archaeology.

Acknowledgments This work was supported by funding from the Hundred Talents Program of the Chinese Academy of Sciences (CAS) (Y5YR0300QM), Youth Director Fund Category-A of Institute of Remote Sensing and Digital Earth, CAS (Y5ZZ02101B), and the Italian Ministry of Foreign Affairs in the framework of the Great Relevance Project "Smart management of cultural heritage sites in Italy and China: Earth observation and pilot projects."

Author Contributions Fulong Chen, Nicola Masini, and Rosa Lasaponara did the SAR data processing and methodology development. Fulong Chen together with Nicola Masini designed the research. UAV surveys have been performed by Ruixia Yang and processed by Antonio Pecci. Geophysical data have been acquired and processed by Enzo Rizzo and Gerardo Romano. Fulong Chen, Nicola Masini, Rosa Lasaponara, and Enzo Rizzo have interpreted the results of remote sensing and geophysical investigations. Fulong Chen and Nicola Masini drafted the manuscript. All authors contributed to the field campaign as well as the finalization of this paper.

References

AgisoftPhotoScan User Manual (2014) Professional edition, version 1.1

Buck PE, Sabol DE, Alan R, Gillespie AR (2003) Sub-pixel artefact detection using remote sensing. J Archaeol Sci 30:973–989

Capozzoli L, Caputi A, De Martino G, Giampaolo V, Luongo R, Perciante F, Rizzo E (2015) Electrical and electromagnetic techniques applied to an archaeological framework reconstructed in laboratory, 8th International workshop on advanced ground penetrating Radar – IWAGPR 2015, Florence, Italy, 7–10 July, 2015.

Cavalli RM, Colosi F, Palombo A, Pignatti S, Poscolieri M (2007) Remote hyperspectral imagery as a support archaeological prospection. J Cult Herit 8:272–283

Chen L, Li Y, Shi Z, Xie X (2004) Excavation report on the dingding gate. Chinese Archaeol 6:87–94

Chen F, Lasaponara R, Masini N (2015a) An overview of satellite synthetic aperture radar remote sensing in archaeology: From site detection to monitoring. J Cult Herit http://dx.doi.org/10.1016/j.culher.2015.05.003

Chen F, Masini N, Yang R, Milillo P, Feng D, Lasaponara R (2015b) A space view of radar archaeological marks: first applications of COSMO-SkyMed X-band data. Remote Sens 7(1):24–50. doi:10.3390/rs70100024

Chen F, Masini N, Liu J, You J, Lasaponara R (2016) Multi-frequency satellite radar imaging of cultural heritage: the case studies of the Yumen Frontier Pass and Niya ruins in the Western regions of the silk road corridor. Int J Digit Earth. doi:10.1080/17538947.2016.1181213

Chianese D, Lapenna V, Di Salvia S, Perrone A, Rizzo E (2010) Joint geophysical measurements to investigate the Rossano of Vaglio archaeological site (Basilicata Region, Southern Italy). J Archaeol Sci 37:2237–2244

Crawford O G S (1929) Air photography for archaeologists. Ordnance survey professional papers, new series, 12. HMSO, Southampton

Keay SJ, Parcak SH, Strutt KD (2014) High resolution space and ground-based remote sensing and implications for landscape archaeology: the case from Portus, Italy. J Archaeol Sci 52:277–292

Lasaponara R, Masini N (2013) Satellite synthetic aperture radar in archaeology and cultural landscape: an overview. Archaeol Prospect 20:71–78. doi:10.1002/arp.1452

Lasaponara R, Masini N, Pecci A, Perciante F, Pozzi Escot D, Rizzo E, Scavone M, Sileo M (2016) Qualitative evaluation of COSMO SkyMed in the detection of earthen archaeological remains: The case of Pachamacac (Peru). J Cult Herit. doi:10.1016/j.culher.2015.12.010

Lee J-S (1980) Digital image enhancement and noise filtering by use of local statistics. IEEE Trans Pattern Anal Mach Intell 2:165–168

Masini N, Lasaponara R (2007) Investigating the spectral capability of QuickBird data to detect archaeological remains buried under vegetated and not vegetated areas. J Cult Herit 8:53–60

Neitzel F, Klonowski J (2011) Mobile 3D mapping with a low-cost UAV system. Int Arch Photogramm Remote Sens Spatial Inf Sci XXXVIII-1/C22:39–44

Nex F, Remondino F (2013) UAV for 3D mapping applications: a review. Appl Geomat 6:1–15

Rizzo E, Chianese D, Lapenna V (2005) Integration of magnetometric, GPR and geoelectric measurements applied to the archaeological site of Viggiano (Southern Italy, Agri Valley-Basilicata). Near Surface Geophys 3:13–19

Rowlands A, Sarris A (2007) Detection of exposed and subsurface archaeological remains using multi-sensor remote sensing. J Archaeol Sci 34:795–803

Tapete D, Cigna F (2016) Chapter 5: SAR for landscape archaeology. In: Masini N, Soldovieri F (eds) Sensing the past. Geoscience and sensing technologies for cultural heritage. Springer, Cham, pp 101–116, chapter 5

Westoby MJ, Brasington J, Glasser NF, Hambrey MJ, Reynolds JM (2012) 'Structure-from-Motion' photogrammetry: a low-cost, effective tool for geoscience applications. Geomorphology 179:300–314

Chapter 29
Integrated In Situ Investigations for the Restoration: The Case of *Regio* VIII in Pompeii

Nicola Masini, Maria Sileo, Giovanni Leucci, Francesco Soldovieri, Antonio D'Antonio, Lara de Giorgi, Antonio Pecci, and Manuela Scavone

Abstract This chapter presents the study case of the integration of noninvasive in situ investigation methods able to provide information useful to survey and characterize the state of decay of some masonry walls and frescoes in two blocks (*insulae*) of the *Regio* VIII in Pompeii. The integrated investigations demonstrated the complementarity of ground-penetrating radar (GPR), seismic tomography, and infrared thermography (IRT) for the diagnosis of the state of conservation and the restoration of structures and surfaces of archaeological monuments. The investigation was very useful in planning the restoration work.

Keywords Pompeii • Restoration • Non invasive in situ investigations • GPR • Infrared thermography • Seismic tomography

N. Masini (✉) • M. Sileo • A. D'Antonio • A. Pecci • M. Scavone
CNR-IBAM Institute for Archaeological and Monumental Heritage,
C. da Santa Loja, 85050, Tito Scalo, Potenza, Italy
e-mail: n.masini@ibam.cnr.it; m.sileo@ibam.cnr.it; a.dantonio@ibam.cnr.it; m.scavone@ibam.cnr.it

G. Leucci • L. de Giorgi
Institute of Archaeological and Monumental Heritage, CNR (National Research Council)-IBAM (Italy), Lecce, Italy
e-mail: g.leucci@ibam.cnr.it; l.degiorgi@ibam.cnr.it

F. Soldovieri
Institute for Electromagnetic Sensing of the Environment (CNR-IREA),
Via Diocleziano 328, 80124, Napoli, Italy
e-mail: soldovieri.f@irea.cnr.it

N. Masini, F. Soldovieri (eds.), *Sensing the Past*, Geotechnologies and the Environment 16, DOI 10.1007/978-3-319-50518-3_29

29.1 Introduction

Correct planning of the restoration interventions of architectural and archaeological monuments requires a detailed study of building techniques and materials, the mapping of decay patterns, the localization of damage, and the identification of their causes.

In particular, the detection and mapping of voids and cracks in the masonry structures and plaster detachments and alterations are crucial (1) to verify the stability of load-bearing structures and (2) to evaluate the state of conservation of architectural and painting surfaces, respectively.

In the past, such information was obtained by means of coring of samples and other destructive inspections. Nowadays, increased awareness of the historical and artistic value and brittleness of artifacts mandates the use of noninvasive investigations. This provision is in agreement with the first axiom of the Theory of Restoration of Cesari Brandi, which states that "only the material form of the work of art is restored". . . because "the material ensures the transmission of the image to the future" (Brandi 1963).

In the past two decades, development of the technologies associated with geophysical methods, improvement of performance and resolution of sensors and devices, and the increasing availability of user-friendly software for data analysis, processing, and interpretation have led to an increasing interest in the use of in situ nondestructive testing (NDT). In this way, it is possible to give an answer to the several issues related to the structural stability assessment and the analysis (qualitative and quantitative) of weathering of building materials, by respecting the value and fragility of the artifact. With particular reference to structural restoration, as declared by ICOMOS (2003) the investigations should be aimed not only to "safety evaluation" but also to "understanding of the significance of the structure."

The available NDT techniques are based on different working principles. Their choice for studying a particular conservation problem depends on the physical properties of the building materials. In particular, in the case of masonry structures, the choice of the method to be used depends on these factors:

1. The characteristics of the constituents of building materials such as bricks (fired or sun-dried), stone (sandstone, limestone, etc.), and mortar (gypsum, lime, pozzolanic, ordinary Portland cement)
2. The kind of decay to be identified and mapped (fractures, moisture content, plaster detachments)
3. The depth of investigation and the size (which dictates the spatial resolution) of the target (crack size, plaster/fresco thickness, air thickness between plaster and wall)

A few items of this information, such as those related to the material constituents, can be achieved by geochemical and petrographic analyses in the laboratory. Other information related to decay characterization can also be obtained by in situ investigation techniques, such as ground-penetrating radar (GPR), seismic

tomography, and infrared thermography (IRT), which prove to be effective and complementary for all the building elements of cultural interest (from the wall to plaster).

For sake of brevity, we only provide the main characteristics from the theoretical and application aspects of these methods, referring the reader, for a more comprehensive discussion, to the chapters in this volume by Persico and Sato (2016), Leucci (2016), and Dumoulin (2016), respectively.

29.1.1 Ground-Penetrating Radar

Ground-penetrating radar (GPR) exploits the capability of electromagnetic waves (EM) to propagate in a medium (such as masonry structures, concrete beams, fresco) with the aim to identify the inner reflections in correspondence of interfaces separating media with different electromagnetic properties (dielectric permittivity, electrical conductivity, and magnetic permeability) (Persico 2014). The GPR equipment exploits an antenna pair in which the transmitting antenna sends short EM pulses into the subsurface and the receiving antenna collects the backscattered radar echoes. The nominal frequency of the antenna is typically in the range of 800–2000 MHz for investigating media ranging from a wall 1 m thick to a plaster layer 5–10 cm thick.

To provide quantitative information on features of cultural interest (masonry or plaster thickness) and decay pathologies (void and crack size), the crucial step is the estimation of subsurface propagation velocity (Persico 2014). This estimated EM wave velocity permits the conversion of the time into depth along the radar profile.

The result of GPR data processing allows identifying interfaces between different constructive layers (which typically could be found in the ancient Roman walls in *opus coementicium*) or local reflectors referable to iron bars (which typically are inserted during consolidation interventions), voids, or fractures. In addition, the presence of moisture in the medium is detected by determining the increase of conductivity that causes a high absorption of the EM waves. To facilitate the interpretation of the reconstructed images compared to standard data processing, an effective approach is based on the use of microwave tomography able to obtain high-resolution images useful for the detection and the shape reconstruction of localized features both for archaeological prospection (Soldovieri and Orlando 2009) and for historical monument investigations (Leucci et al. 2011).

The various modalities of three-dimensional (3D) GPR result in visualization that can help us in interpreting those anomalies referring to strong reflectors (e.g., relating to the presence of large inhomogeneities and voids), but at the same time it is not possible to see 'subtle' anomalies attributable to weak reflectors, whose nature is more easily understood by looking at the radargrams. This behavior occurred during the GPR investigation of the columns of a Romanesque rose window in Apulia (Masini et al. 2007). The radargrams allowed us to understand how the columns were joined with the central oculus of the rose window: in some cases with iron belts

and molten lead, in other cases just inserting the columns inside hollow cylindrical elements. This information made possible to reconstruct the relative chronology of building phases and to suggest the most effective measure of reinforcement.

In the field of architectural heritage, GPR surveys have been performed for detecting the constructive characteristics of masonry structures (Maierhofer and Leipold 2001; Ranalli et al. 2004; Binda et al. 2005; Masini et al. 2010a) and for investigating the foundation subsoil and discovering archaeological remains, also in conjunction with other geophysical, physical, and biological techniques (Cardarelli et al. 2002; Cataldo et al. 2005; Nuzzo et al. 2007).

In particular, Ranalli et al. (2004) applied GPR for evaluating the state of conservation of the facade of a medieval church, estimating the thickness of its walls, and characterizing the forms and deterioration of masonry composed by external ashlars and the rubble core nucleus. Leucci et al. (2007) detected and assessed fractures in marble columns in the crypt of Otranto Cathedral by GPR in reflection mode. In Spain, Perez-Gracia et al. (2008) detected the point of contact between the Roman remains and the materials used in later restorations in the Theatre of Sagunto and Solla et al. by integrating GPR and simulation of FDTD (finite-difference time-domain) models achieved to identify the ancient profile of a Roman bridge.

29.1.2 Seismic Methods

The seismic method exploits seismic waves, created by a controlled source, that propagate through the subsurface. Seismic methods (sonic and ultrasonic) proved to be effective in providing information useful for the evaluation of the state of conservation of masonry structures, stone decorative elements, stuccoes, and plaster (Binda et al. 2003; Cosentino et al. 2009; Leucci et al. 2012; see also Chap. 8 by Leucci, this volume). The analysis of propagation characteristics of seismic waves, the measurement of the two travel times, and the computation of the two-dimensional (2D) or three-dimensional (3D) velocity distribution allow providing indirect information on the presence of inhomogeneities, cracks, and fractures.

Seismic waves are classified into two groups: surface waves and body waves. The first can propagate along the boundary of the solid. The second propagates through the volume of an elastic medium in two different ways: (i) by compression and dilatation uniaxial strains in the direction of wave travel (the so-called compressional waves or longitudinal or primary or P-waves); or (ii) by a pure shear strain in a direction perpendicular to the direction of wave travel (the so-called shear waves or transverse or secondary or S-waves). Seismic tomography proved to be the most effective way to provide information on constructive characteristics of buildings and artifacts from the elastic waves (sonic or ultrasonic) because it exploits data acquired not only in the direct mode but also along paths that are not perpendicular to the wall surfaces. The resolution achieved by seismic tomography depends on the wavelength. Layers or objects can be discerned when their thickness is less than one fourth the wavelength (λ). In many cases, it is still possible to discriminate two

targets also with thickness less than 1/4 λ, thus allowing us to investigate a large variety of decay patterns and constructive characteristics difficult to see from GPR. This was the case of Tricarico Cathedral where the integration of GPR and seismic tomography allowed evaluation of the size and severity of some fractures visible on the outer sides of the pillars as well as understanding that the pillars were affected by a crushing phenomenon (Leucci et al. 2011).

Finally, seismic tomography can be employed for applications more focused on the mechanical behavior analysis of historical masonry structures. This kind of application makes seismic tomography a routine technique in the field of restoration and retrofitting of monuments and built heritage, especially when it is used in a complementary way with in situ tests aimed at determining the stress, deformability, and resistance features of masonry. This application occurs in the integration of seismic tomography with the flat jack test, performed by making a cut to a uniform depth into the mortar courses and inserting the flat jack or a couple of jacks, which are pressurized to the desired level. In this context, the reader is referred to Binda et al. (2003), who investigated the pillars of the Cathedral of Noto using sonic tomography and the flat jack test, and to Saisi et al. (2015), who assessed the state of preservation of Gabbia Tower in Mantia after an earthquake by integrating sonic tomography with flat jack tests and ambient vibration tests.

29.1.3 Infrared Thermography

Infrared thermography (IRT) is a remote sensing technique capable of acquiring infrared radiation emitted by objects above 0 K. By means of the Stefan–Boltzmann law, the energy can be measured in terms of temperature by using a suitable IR device. The energy emitted by the surface depends on a large number of properties such as (1) the spectral property (emissivity, reflection), (2) the thermal property (conductivity, specific heat, diffusivity), and (3) other physical properties of the underlying material such as water content, porosity, and density (for additional detail on IRT in relationship to the thermo-optical properties of materials, see the chapter by Dumoulin (2016)in this volume). Accordingly, the interpretation of IR images is not an easy task. However, for the inspection and diagnosis of historic buildings IRT is generally used to map moisture, detect shallow subsurface voids and defects, and evaluate the conservation treatments in a qualitative way.

IRT surveys can be carried out in two ways depending on the source that creates the heat transfer process, which can be (1) passive, when the source of the thermal wave is natural, or (2) active, when an artificial source is used to create the thermal excitation of the object to be investigated. The active technique can be used in four ways: (i) graduated heating thermography; (ii) lock-in thermography; (iii) pulsed thermography (PT); or (iv) pulsed phase infrared thermography (PPT).

(i) In graduated heating thermography, surface temperature is measured during heating. (ii) Lock-in thermography, based on the concept of the thermal wave, consists of introducing periodically modulated heat into the specimen or object and monitoring the periodic temperature modulation phase, referred to the modulated

heat supply. (iii) PT consists of recording temperature decrease after the specimen is heated briefly. (iv) PPT, which is based on the Fourier transform, combines the advantages of both pulsed infrared thermography and lock-in thermography.

In the field of artistic and architectural restoration, the passive technique is mostly used for various purposes such as (i) the detection of shallow subsurface voids and defects of architectural surfaces (Inagaki et al. 1999; Maierhofer et al. 2003), (ii) to map moisture (Grinzato et al. 2002a), and (iii) to evaluate conservation treatments (Avdelidis and Moropoulou 2004). The integrated use of different active techniques with or without passive thermography is also applied for decay analysis of outdoor cultural heritage such as the murals of the monastery of Molybdoskepastos, whose decay has been evaluated by using graduated heating thermography, lock-in thermography, and PPT by Kordatos et al. (2013).

For operational use, the active approach is usually applied to small areas (e.g., mosaics, specimens in laboratory) when the controlled thermal excitation is feasible.

Passive thermography is mainly employed for large areas to be investigated (e.g., architectural surfaces, mural paintings). The limits in terms of discriminability of thermal anomalies generally make necessary the use of the following:

- Other noninvasive in situ investigations as done by Moropoulou et al. (2013) for monitoring cleaning interventions on architectural surfaces of medieval fortifications in Rhodes, and Nuzzo et al. (2010) for detecting cracks and conservation treatments in the Romanesque rose window of Troia (Southern Italy)
- Different thermographic equipment and spectral bands as done by Grinzato et al. (2002b) to identify hidden structures, evaluate the adhesion of frescoes, and map cracks in the Chapel of Scrovegni painted by Giotto between 1303 and 1305;
- New data processing approaches such as visual analytics to extract from multitemporal IRT data the decay patterns of the calcarenite architectural facade of the Cathedral of Matera (Danese et al. 2010).

29.1.4 Integration

The usefulness of the results achievable by GPR, seismic, and IRT methods for the knowledge and assessment of the state of conservation of cultural heritage depends on the quality of the feedback between scientists (experts in noninvasive diagnostics) and end-users (archaeologists, architects, conservators). The quality of this feedback entails the end-user capability of transforming the diagnostics outcomes into information easily interpretable for multiple purposes such as mapping, monitoring, and assessing decay pathologies, planning conservation, and retrofitting interventions.

From our experience (Masini et al. 2010b; Masini et al. 2013) in the field of cultural heritage and namely the conservation of monuments, we noted that there is a relevant gap in the information sharing/transfer between professionals (geophysicists/physicists/engineers) and end-users (conservators/historians/architects).

This gap is generally caused by the difficulty in interpreting the results obtained by noninvasive diagnostics in terms of information useful to characterize and monitor the state of conservation (e.g., detection of cracks in the masonry) as well as to improve the historical knowledge of monuments and artifacts (e.g., identification of ancient building elements and phases).

Several experiences suggest an integrated strategy aimed at improving the interpretation of diagnostics and remote sensing by means of the following steps:

(a) Integration and fusion of in situ noninvasive tests and geophysical methods
(b) Comparison between direct data (carrots, endoscopic tests, visual inspection) and results from noninvasive tests, including geophysics
(c) Use of specimens or test beds for the detection of archaeological features and monitoring of monuments and sites
(d) Augmented reality as a tool for facilitating the interpretation of noninvasive investigations

As examples of the approach (a), the reader is referred to Pérez-Gracia et al. (2013), wherein GPR and seismic tomography were integrated for the physical and geometrical characterization of structural elements of the Mallorca Cathedral. D'Aranno et al. (2015) investigated an ancient Roman wall through high-resolution geomatics, geophysical methods, and chemical analysis: laser scanner surveys allowed analyzing wall geometry and surface, chemical analyses were performed to identify the constitutive material, and GPR provided information on the inner core of the wall. Other examples are in found in Masini et al. (2007) and Moropoulou et al. (2013).

With respect to approach (b), we cite two case studies. One is related to the Cathedral of Matera, where investigations by GPR were aimed at characterizing the inner structure of two pillars by exploiting the available data provided by a coring (Masini et al. 2010a). The second application is related to the Cathedral of Tricarico where an integrated approach-based GPR and sonic prospecting was applied to detect cracks and inhomogeneities in the inner structure of masonry pillars (Leucci et al. 2011). For two pillars of the Tricarico Cathedral, the results have been compared with coring and endoscopy, thus facilitating the interpretation of GPR and sonic tomography on the other pillars of the church. The results of GPR and sonic tomography allowed discovery of the existence of a crushing phenomenon affecting the pillars of the cathedral, thus suggesting the most effective retrofitting solution.

The approach (c) is based on the use of specimens that allows developing reproducible and highly accurate diagnostics methods to be applied for on-site investigations. It could be used (i) for investigations strongly based on one diagnostic test, such as IRT for investigating architectural and painted surfaces or ultrasonic investigations, to evaluate and quantify superficial alterations of natural stone (Meier et al. 2016), or (ii) for applications based on the use of more noninvasive tests such as IRT and GPR for evaluating the state of conservation of frescoes as well of the underlying masonry structure (Carlomagno et al. 2011).

Finally, an example of the approach (d) is given by Gabellone et al. (2013), wherein experienced augmented reality improved the interpretation of GPR prospections carried on the floor and walls of the chapel of the Holy Spirit in Lecce.

In this work, we present the approach used and the obtained results in an investigation campaign in some *insulae* of Region VIII of the Roman town of Pompeii aimed at providing information for the safety and retrofitting of walls and frescoes. The scope of this investigation was the detection of cracks and the survey of the inner core of masonry walls and the identification of detachments of frescoes. For the first target, GPR and seismic tomographies have been employed; for the second one, we used GPR and IRT. For both the case studies, and in particular for the masonry, the study of the constructive characteristics, proved to be very important for the interpretation of results.

29.2 Pompeii: History, Conservation Issues, and the Study Area

29.2.1 Historical Setting

Pompeii is one of the largest archaeological areas and most visited cultural heritage sites in the world. Its peculiarity is given by the extraordinary state of integrity of the buildings, which make possible to have a clear vision about how common people lived in ancient times. This appearance is the heritage of the volcanic eruption of Mount Vesuvius, which if on one hand caused the end of Pompeii and the death of most of its inhabitants, on the other hand, thanks to the volcanic cover of ash and pumice, made possible the preservation of the city's structures.

The foundation of Pompeii dates back to the seventh to sixth century BCE. It came under the domination of Rome in the fourth century. With the expansion of the Roman republic, which ended with the Second Punic War (218–202 BC), begins the development of the Pompeii that we know, with its streets, public buildings, and houses discovered by the first archaeological excavations conducted under the reign of Charles of Bourbon in 1748 (Fiorelli 1875). The city of Pompeii was directly involved in the great changes caused by the Roman expansionist policy, projected toward the conquest of the entire Mediterranean basin. The city enjoyed a period of prosperity and wellness obscured, however, by the social wars that destabilized the whole region.

The event that inevitably links the history of Pompeii to historiography and the collective scenario is undoubtedly the eruption of Vesuvius in 79 AD. After the eruption, the Emperor Titus immediately organized emergency assistance to coordinate the necessary aid to the reconstruction of Pompeii. However, the thick layers of ash covering Pompeii did not allow its reconstruction and the return of the population.

The rediscovery of Pompeii happened in 1748 in the age of King Carlo of Borbone when a Spanish military engineer unearthed intact buildings and wall paintings, immediately arousing the interest of scholars and intellectuals all over Europe.

Since then Pompeii has had a long and intense history of studies, surveys, excavations, and discoveries, becoming an important place not only for knowledge of Roman culture but also for the development of modern archeology.

29.2.2 Pompeii: Toward a Systematic Approach to Its Conservation

The modern history of Pompeii has been also marked by damage and destruction caused by earthquakes and bombing during WW II (Garcia 2006). Recently, constant and frequent collapses have occurred as the outcome of the difficulty of coping with systematic maintenance with the problems of degradation of materials and structures caused by weathering affecting exposed archaeological structures, the poor compatibility and effectiveness of consolidation work based on concrete made in the twentieth century, and, finally, the impact of tourism.

Following approval by the European Commission of the Great Pompeii Project, the Italian Ministry of Heritage and Culture has developed a multi-annual action plan aimed at addressing in a systematic way the issues of preservation and enhancement of the archaeological area. The Great Pompeii Project primarily aims at solving in a systematic way the issue of conservation by adopting an approach based on (1) extensive and detailed knowledge of archaeological, historical, and structural data, aimed at timely identification of risk factors and (2) systematic planning of conservation interventions and the strengthening of management capacity and scheduled periodic intervention. In particular, the plan of knowledge, through a periodic monitoring of the state of conservation of archaeological structures, is conceived as a tool for support the planning, in an effective and timely manner, of conservation and retrofitting works necessary for the prevention of traumatic events, which can lead to irreversible loss of archaeological evidence.

To this aim it is fundamental to use in an operational way all the available technologies and procedures for the diagnosis of decay pathologies to support decision making for the design and execution of restoration work. This strategy is applied at Regio (Region) VIII, where an extensive investigation campaign has been conducted by using direct surveys, in situ noninvasive tests, and laboratory analyses.

Only a small part of this experience at Regio VIII is shown here. According to the theme discussed in the first paragraph, this chapter considers the approach based on noninvasive site investigation to detect and map nonvisible decay pathologies such as cracks and fractures inside masonry and the detachment of plaster and frescoes. For the sake of brevity, only the results of investigations performed on a wall of the Basilica and frescoes in the Gymnasium are shown and discussed.

29.2.3 Study Area: Regio VIII, Basilica, and Gymnasium

The urban fabric of Pompeii was divided into nine regions or *Regio* by the archaeologist Fiorelli in the 1860s (Fiorelli 1875). Each regio in its turn contains a number of blocks of buildings bounded by roads, named *insulae*. One of the largest regions (*regiones*) is Regio VIII, divided into seven insulae. It occupies the southwestern sector of the urban area and is bounded (on the south) by an irregular stretch of city walls between the two gates, Porta Stabia and Porta Marina (Fig. 29.1).

Regio VIII includes a number of (1) public palaces and spaces such as the Triangular Forum, Basilica, Comitium, the theatre, and the Odeon; (2) religious buildings such as the Sanctuary of Athena and Hercules, Sanctuary of Venus, and Temples of Aesculapius and Isis; and (3) significant private houses such as domus of Championnet, domus of the Geometric Mosaics, and the houses of the Cornelii.

The investigated monuments herein shown are in the Basilica and Sarno baths (Koloski Ostrow 1990; Ioppolo 1992) (Fig. 29.1)

The Basilica is dated back to 130–120 BC and is one of the oldest examples of Roman basilica. It is located in the southwest corner of the Foro and was used to carry out business and for the administration of justice. The Basilica has a rectangular plan with dimensions of about 67.50×25 m^2 and is divided into three naves by two rows of columns having Ionic capitals and presenting a brickwork trunk with grooves obtained by brick. The walls are made in *opus incertum* and plastered externally, whereas the inner walls were decorated in I Stile[1], with stucco in relief.

The Sarno baths consist of a block of four levels built in the second century BCE. Severely damaged by the earthquake of 62 AD, the thermal rooms were still being renovated at the time of the eruption. The most significant rooms are the *Frigidarium*, decorated by paintings representing the Sarno River (from which comes the name of Sarno Bath) and Nilotic landscapes, and the *gymnasium* (Fig. 29.1, bottom), which occupies most of the complex, with frescoes depicting athletes and fight scenes dated to 50 AD (Koloski Ostrow 1990).

[1]The evolution of Pompeian painting is distinguished in four periods, each one characterized by a distinct style by the German archaeologist August Mau (1900). The first style, known also as an encrustation or masonry style, dominated a period between 200 BC and 80 BC. It is characterized by the simulation of some materials such as marble and architectural elements such as wooden beams, white cornices and pillars, and the use of vivid colors. The second style, also referred to as illusionism or the architectural style, was most popular in the first century BCE. It is characterized by the use of trompe l'oeil compositions to create the optical illusion of three-dimensional objects, architectural elements, and landscapes. The third style, or ornate style, was popular in the last two decades of the first century BCE. It developed as a reaction against the austerity of the second style. Fourth-style paintings depict large-scale narrative scenes and panoramic views.

Fig. 29.1 Plan of Regio VIII (*top*), three-dimensional (3D) model of Basilica (*middle*), with indication of the investigated area: southern wall of Basilica (indicated with *dashed quadrangular light blue box*) and wall paintings in the Gymnasium in Sarno Baths (*red box*). *Bottom*: detail of the wall paintings

29.3 Investigations of Basilica Masonry Structures

29.3.1 Building, Materials and Techniques

Some walls in *opus incertum* on the southern side of the Basilica have been investigated by GPR and sonic tomography (Fig. 29.2, bottom left) with the aim to evaluate the state of conservation of the masonry, including the detection of possible cracks, fractures, and voids. Before carrying out the noninvasive investigations, several surveys have been conducted with the aim to provide the geometry of the walls, identify possible deformations, and to obtain detailed ortho photographs useful to study the building techniques. The 3D geometry of the walls has been obtained by processing and integrating terrestrial and aerial images taken from a drone by using structures from motion-based software. In this way, it has been possible to establish that the walls do not exhibit significant out-of-plane deformations.

Fig. 29.2 *Top:* Digital model of southern wall of the Basilica investigated by GPR and seismic tomography. The wall is interrupted by plastered fluted semicolums built with bricks. *Bottom left*: GPR data acquisition. *Bottom right*: Detail of the masonry composed of irregular stone elements of Peperino

The investigated wall, interrupted by plastered fluted semicolums, has a thickness of approximately 0.65 m and is partially plastered with mortar composed of pozzolana and sand (Fig. 29.2, upper). The wall is composed of three layers, among which the central one (about 30 cm thick) is sufficiently connected with two adjacent ones about 15 cm thick. The external layers are built by using irregularly shaped and randomly placed first-sized or uncut tuff blocks of dimensions ranging from 12 to 18 cm (Fig. 29.2, bottom right). The central nucleus is also composed by irregularly shaped and randomly placed uncut tuff blocks of dimensions ranging from 8 to 14 cm.

The volcanic tuff named Peperino has a trachytic composition consisting of black crushed and elongated slag, immersed in a grayish cineritic matrix. The mass is entirely lithified by welding and neoformation of feldspars. It presents very variable characteristics as a function of the amount of slag.

The petrographic study[2] allowed establishing that the mortars were prepared with air lime mixed with aggregate, including sand and gravel, of both volcanic and local origin, belonging to volcaniclastic deposits of the Somma-Vesuvio, probably reworked by streams (alluvial deposits). The main mineralogical constituents of the aggregate constituents are related to two types of lava (predominantly plagioclase or mostly leucite), along with glass and/or pumice and clino-pyroxene. Secondary mineralogical components are feldspar (plagioclase and sanidine) and leucite. Finally, accessory components are olivine, biotite, and carbonate clasts (spathic calcite and calcite micritic).

29.3.2 GPR Data Acquisition and Processing

The GPR survey was carried out with a georadar Ris-Hi-Mod equipped with the 2000-MHz (center frequency) antennae manufactured by Ingegneria dei Sistemi (IDS). The selection of the working frequency was carried out on the basis of the resolution and investigation depth required by survey objectives. The acquisition was performed as follows: 512 samples per scan for a recording time window of 30 ns with the application of a manual gain function. To obtain a 3D GPR pseudo-representation, GPR profiles were collected with 0.33-m spacing (Fig. 29.3, top).

The quality of the raw data was improved by means of appropriate processing. Processing steps can be summarized as follows: (i) horizontal scaling (80 scans/m) to allow data interpolation in the *X*-direction; (ii) amplitude normalization, consisting of the declipping of saturated traces using a polynomial interpolation procedure;

[2]The petrographic analyses have been conducted by Giovanni Quarta and Davide Melica of CNR-IBAM.

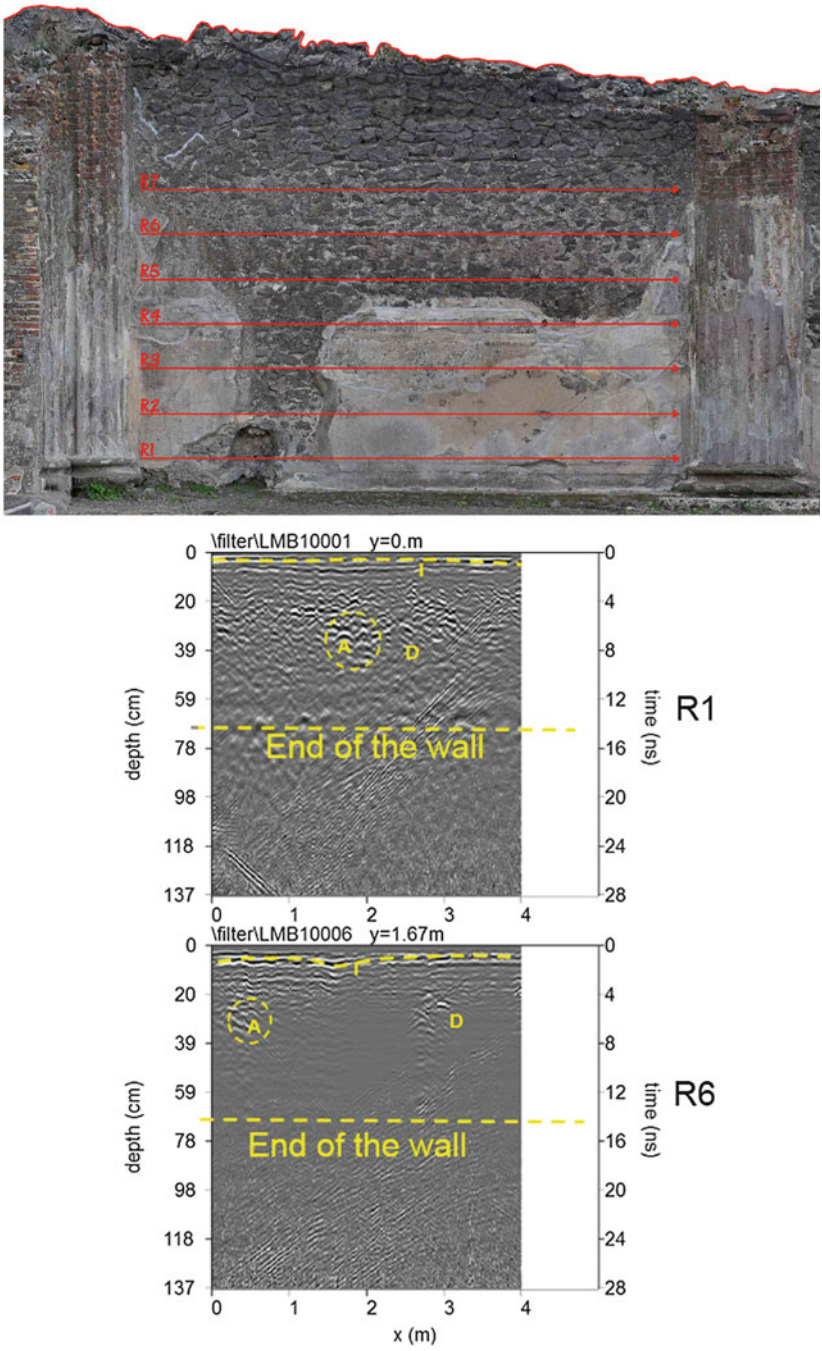

Fig. 29.3 *Top:* Wall of Basilica: location of GPR profiles. *Middle* and *bottom:* Processed radar sections related to the profiles *R1* and *R6*

(iii) Kirchhoff 2D-velocity migration performed on the basis of a 2D-velocity distribution. The goal of the migration is to trace back the reflection and diffraction energy to their "source."[3]

A good penetration of the electromagnetic energy was observed because of the low resistivity of volcanic material (Russell and Stasiuk 1997) used to build the masonry. In fact, at about 15 ns (corresponding to a thickness of about 0.65 m when the mean velocity value of 0.086 m/ns is used) it is possible to detect the end of the wall (Fig. 29.3, middle and bottom).

For sake of brevity, only the results obtained on 4 m of the southern wall of Basilica are shown (see Fig. 29.3, middle and bottom). The observation of radargrams points out the presence of reflectors for all the 15 ns corresponding to the thickness of the investigated wall. In particular, in radargrams R1 and R6 a slightly undulating reflection is present (labeled *I* in Fig. 29.3, middle) and clearly identifiable at time ranging from about 0.5 to 1.0 ns (0.02 m–0.05 m thick). Because of its high amplitude, denoting a strong electromagnetic contrast, this reflection has been interpreted as resulting from a more compact layer associated with the plaster contact.

At about 4–5 ns, corresponding to 15–20 cm, horizontal/slightly undulated reflections result from the interface between the external masonry layer (of about 15 cm) and the central layer. The undulating pattern of the reflecting surface is caused by the morphological characteristics of the masonry composed of irregularly shaped tuff and randomly placed on mortar beds.

Hyperbolic reflections (labeled A in Fig. 29.3) are associated to voids present inside the wall. They are located in several positions along the *x*-axis but seem to have the same depth (about 0.25 m) in the wall. This interpretation was related to the fact that is clearly evident a polarity change in the single radar trace. The anomalies labeled "D" indicate possible discontinuities. These anomalies confirm an irregular pattern most likely associated with the internal arrangement of uncut or first-sized tuff block.

Figure 29.4 shows three other radargrams with an interpretation of the reflections. The reflectors are referable to three different causes: detachment of plaster (labeled with a), voids and discontinuities between the two constructive layers (labeled with b) and cracks (labeled with c) in the central layer.

A way to obtain easily interpretable maps for understanding the plan distribution of reflection amplitudes is the creation of horizontal time slices (Conyers and Goodman 1997). This data representation is important in GPR investigations as it allows an easier correlation of the most important anomalies found in the area at the same depth (Conyers 2012). Because of possible velocity changes across the

[3]The Kirchhoff two-dimensional (2D)–velocity migration is done in the *x*–*t* range, which means that a weighted summation for each point of the profile over a calculated hyperbola of preset bandwidth is performed. The GPR data processing was performed used GPR-slice software (Goodman 2013).

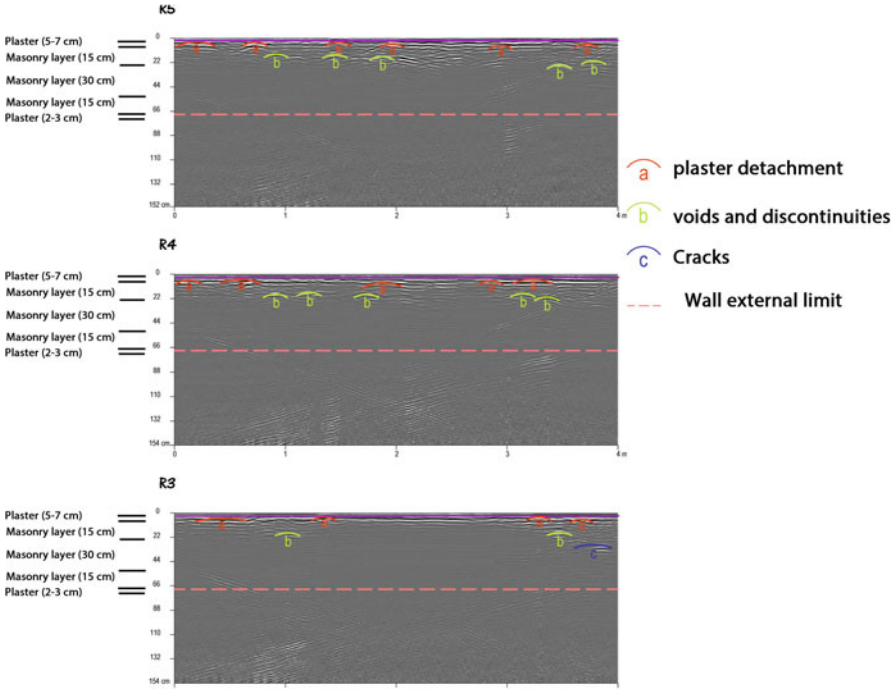

Fig. 29.4 Radargrams R3–R5 with interpretation of the results. Letters *a*, *b* and *c* denote reflections associated with plaster detachment, voids, and discontinuities and cracks, respectively. *Dashed pink line* indicates the wall external limit

investigated area and with depth, horizontal time slices can be considered only approximate depth slices. As underlined by several authors (e.g., Conyers and Goodman 1997), ideally the datasets for time slices should be derived from parallel profiles with a minimum spacing. Transect spacing should be less than one half the wavelength of possible reflections returned from the smallest target to be mapped: the transect spacing was 0.15 m. Assuming a 2000-MHz central frequency, the criterion of half the wavelength implies a transect spacing of 0.021 m. In theory, this should preclude the use of time slicing on these data. The effective target area is measured by the radius of the Fresnel zone.

For the surveyed area in a medium of dielectric permittivity of 12 and at depth of 0.65 m, this gives the theoretical target areas of about 0.24 m. As the anomalies lie within 0.65 m of the wall surface, the resolution of time slices constructed from profiles taken at 0.15-m intervals will be near the optimum. Time slice maps are built averaging the amplitude (or the square amplitude) of the radar signal within consecutive time windows of width Δt. In the investigated walls of the Basilica in Pompeii, the time slice technique has been used to display the amplitude variations

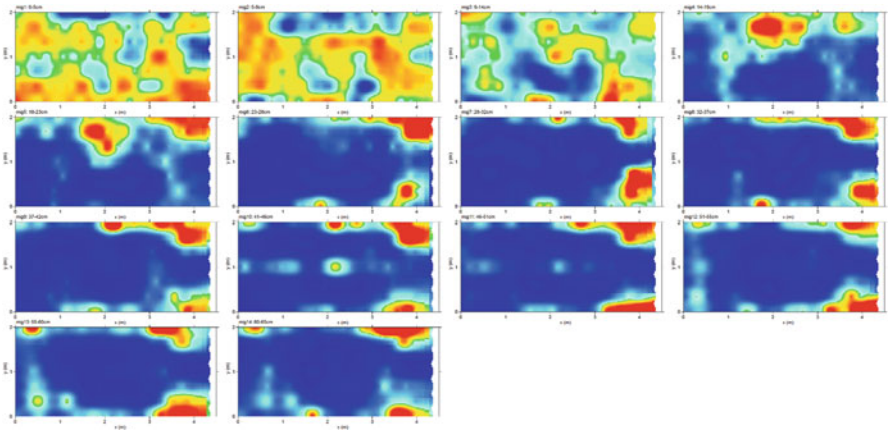

Fig. 29.5 The Basilica walls: depth slices

within overlay time windows of width $\Delta t = 1$ ns. The selected two-way time interval corresponds to a wall layer, approximately 0.04 m thick, and the time slices are located between 0 and 0.65 m in depth. The slices shown in Fig. 29.5 were obtained using the processed data. Several events are visible as high-amplitude anomalies. All anomalies are discontinuous and related to the presence of cracks and voids.

Figure 29.6 shows two time slices selected at the depths of 18–23 and 46–51 cm, both of them close to the interface between the wall central layer and the external layer. Comparing the two time slices with the radargrams in Fig. 29.4, it is possible to establish that the high-amplitude anomalies are associated to local discontinuities, which do not ensure an effective connection between the three masonry layers.

Another approach for visualizing 3D radar data has been proposed by Conyers (2004, 2012). In this case, after an appropriate processing of radar data, a 3D image of the diffracting or reflecting object can be easily obtained by (i) extraction of a particular complex signal attribute (trace envelope), the grid data are converted to the reflection strength or amplitude envelope thanks to a Hilbert transformation; and (ii) thresholding (a threshold value must be entered). Hence all amplitudes greater/equal than the threshold value are considered per definition; (iii) 3D contouring by means of iso-amplitude surface. As pointed out by Conyers (2004), in this case the choice of the threshold is a crucial task. Figure 29.7 depicts the same data set with iso-amplitude surfaces using a threshold value of 60% of the maximum complex trace amplitude. Obviously, lowering the threshold value, increases the visibility of the main anomaly and smaller objects, but also heterogeneity noise. A relatively strong continuous reflection is visible on the threshold volumes (between 0.02 and 0.65 m). This visualization technique points out better the damaged zone.

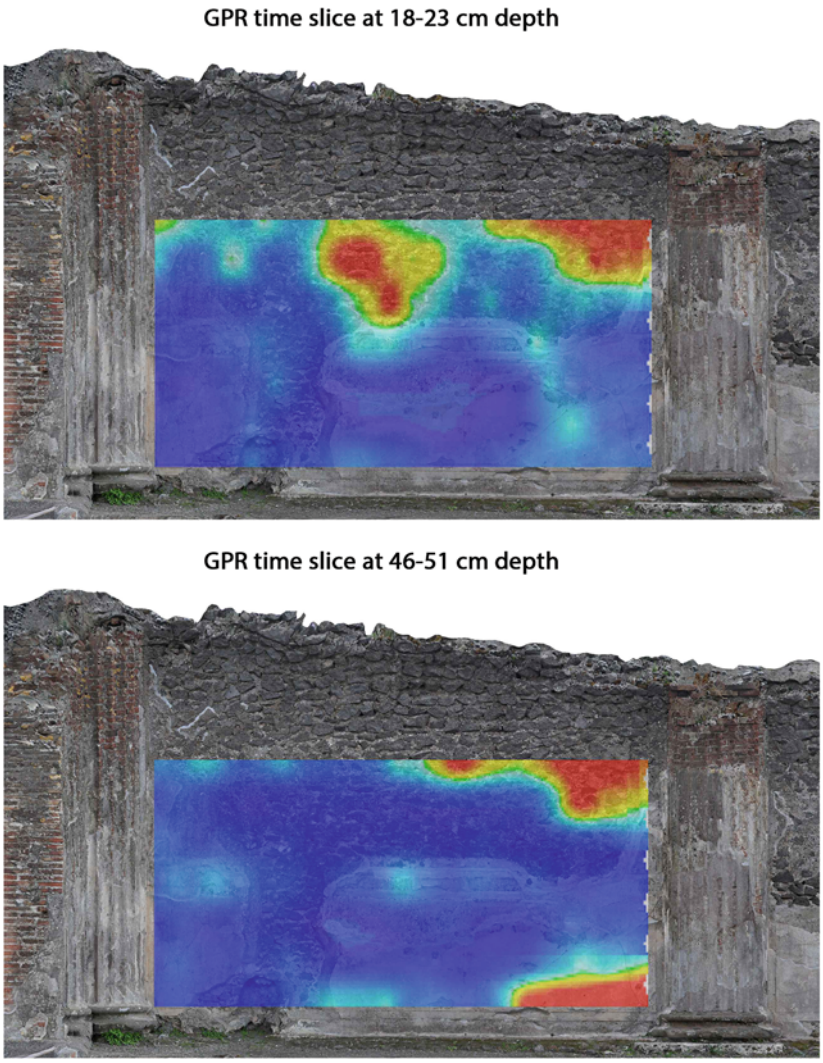

Fig. 29.6 GPR time slices at depths of 18–23 cm and 46–51 cm

29.3.3 Seismic Tomography Data Acquisition and Analysis of the Basilica Walls

Seismic tomography of the Basilica walls consisted of 3D reconstruction based on the travel-refracted wave amplitude. Images were obtained from the first arrival of the waves. Data were acquired obtained along the 4 m × 2 m area (Fig. 29.8a).

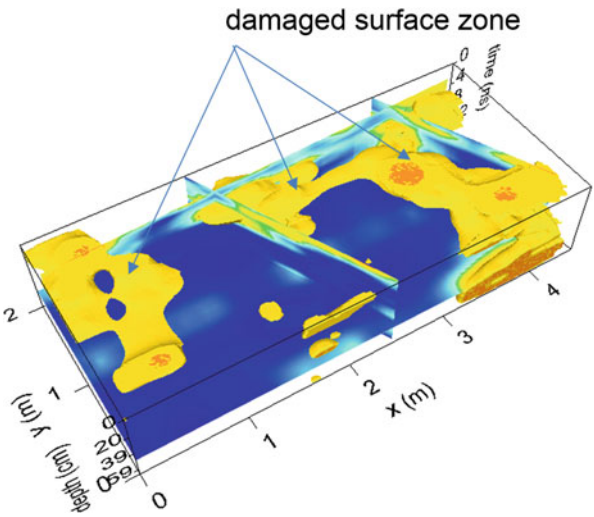

Fig. 29.7 The Basilica walls: iso-amplitude surfaces using a threshold value of 60%

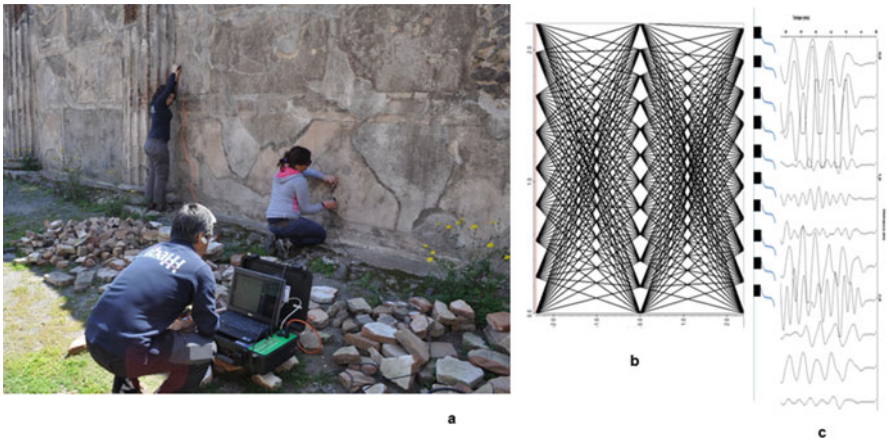

Fig. 29.8 The Basilica walls: seismic tomography. (**a**) Position of the accelerometers on the wall. (**b**) Ray paths in a hypothetic homogeneous wall. (**c**) Seismogram

A piezoelectric pulse at 55 KHz was used as the seismic source. Data were acquired with a high-frequency sensitivity accelerometer (55 KHz).

To cover the whole space, the medium has been divided into cells or elements, and the results are obtained as the sum of the values in each of the cells. In the case of nonhomogeneous media, the seismic wave is refracted because of changes in the wave velocity associated with adjacent cells, and the tomography equations are solved in an iterative computational process until a reliable and accurate solution is attained. The computational process, the simultaneous interactive reconstruction

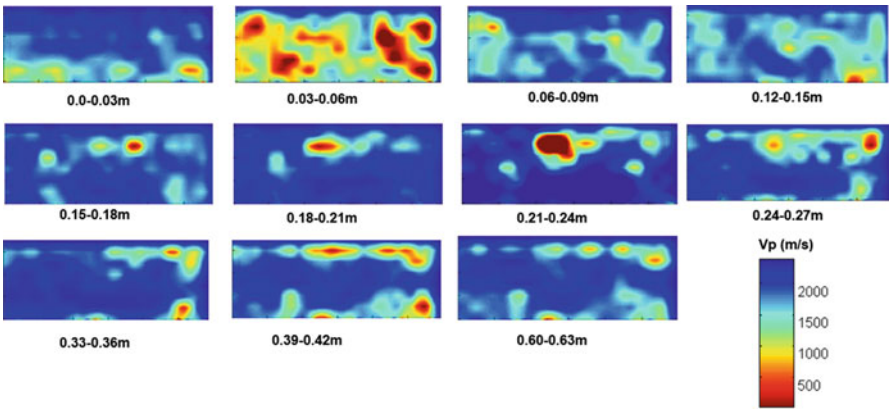

Fig. 29.9 The Basilica walls: P-wave velocity distribution at several depths in the wall

technique (SIRT), contemplates ray curvature as a consequence of internal refractions. The characteristics of each cell are defined in the case that at least one ray path crosses the cell (Fig. 29.8b, c). The Reflex software was used for the inversion of the seismic data.

Seismic tomography seems to confirm the existence of discontinuities and voids. Several zones of the depth slices presenting lower velocities (400–500 m/s) could be associated with cracks or more damaged parts of the wall (Fig. 29.9). These low-velocity zones are usually located close to the wall surface or in the shallowest part of the wall. The depth of 0.21–0.24 m, in correspondence with the interface between external and central masonry layers, is characterized by the lowest P-wave velocity values (about 250–350 m/s); this indicates the probable presence of voids and consequently the lack of connection between the two wall layers. Such a hypothesis is confirmed by a GPR time slice at 0.18–0.23 cm: in fact, the areas of the wall exhibiting low P-wave velocity values are also characterized by high-amplitude GPR (see Fig. 29.10). This behavior can be observed at the top center and upper right of the wall (Fig. 29.10).

Irregular and small changes on the velocity are most likely caused by the irregular arrangement of materials inside the structure. However, it is noticeable that the wall exhibits high inhomogeneity. Low P-wave velocity values are also found at depths of 0.39–0.42 m (see Fig. 29.11, top), also corresponding, in this case, to high-amplitude GPR (Fig. 29.11, bottom), and consequently referable to voids and discontinuities between wall layers.

The case study just discussed demonstrates the importance of integrating different diagnostic techniques, such as GPR and seismic tomography, to infer reliable information about the presence of degradation pathologies.

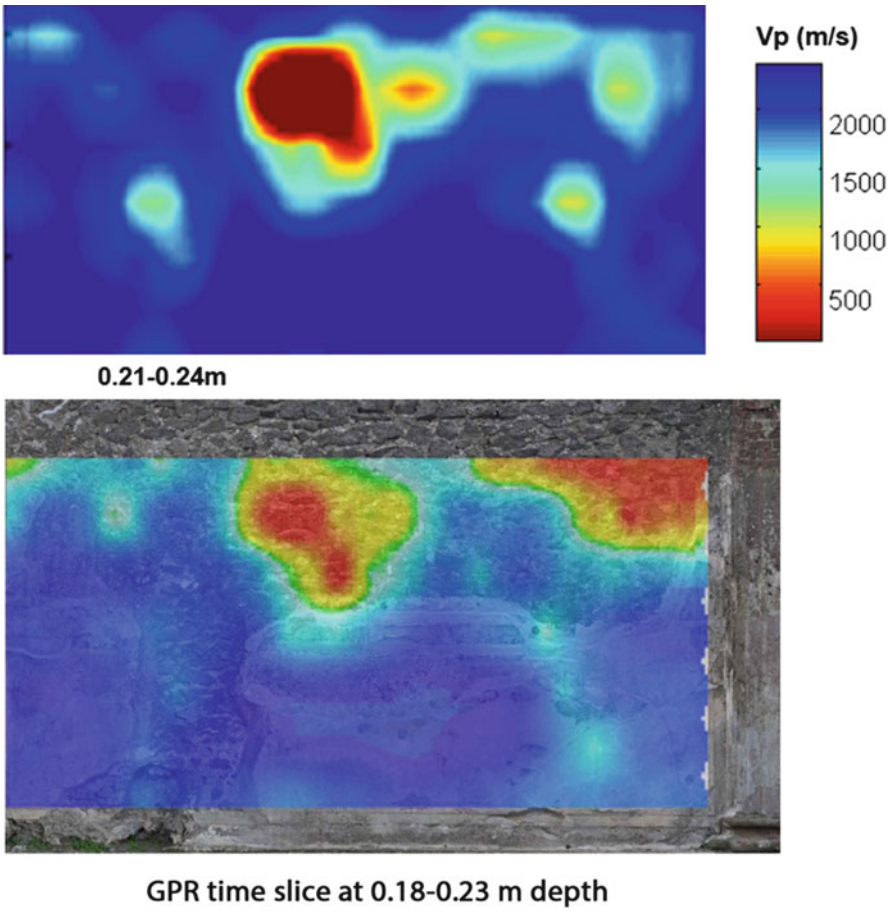

Fig. 29.10 Comparison between P-wave velocity distribution at depths of 0.21–0.24 m (*upper*) and GPR time slice at depths of 0.18–0.23 m (*bottom*). The high-amplitude GPR corresponds to low velocity values, confirming the presence of voids and discontinuities between the central nucleus and the external layer of the wall

29.4 Conservation Assessment of the Fresco of Sarno Baths by GPR and IRT

29.4.1 Introduction

The knowledge of Roman painting is mainly derived from the unique conditions of preservation of Pompeii and the other Vesuvian cities of Herculaneum and Stabia,

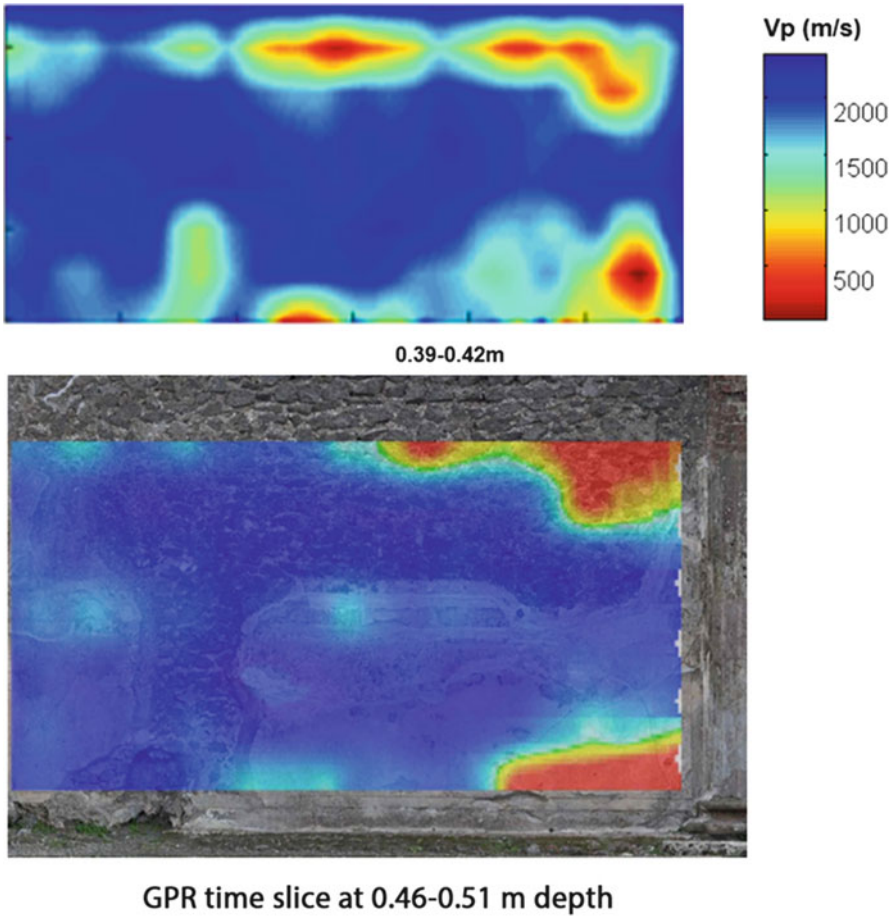

Fig. 29.11 Comparison between P-wave velocity distribution at 0.39–0.42 m depth (*up*) and GPR time slice at 0.46–0.51 m depth (*bottom*)

where huge quantities of wall paintings have been discovered. Pompeian paintings are dated between the second century BC and 79 AD, the eruption date.

Pompeian wall paintings were done in fresco, tempera, and encaustic. The frescoes were done on plaster of fresh lime with ground pigments diluted in water. Tempera painting was performed by diluting the colors with sticky and gummy solvents, such as egg yolk, and the wax. Finally, the encaustic painting was achieved with colors mixed with wax.

Although 80% of the wall paintings in Pompeii have been detached, applied to a new support, and conserved in museums, there are still several paintings in the ruins

of Pompeii and most of them need conservation treatment and restoration, because these are affected by delamination (or detachment), flaking, disruption, cracks and hatching, and mechanical damage.

Delamination is the most common cause of deterioration of frescoes because such works of art were originally created using a complex construction technique based on different plastering sequences. In addition, the 'original' heterogeneity is worsened by the differential nature of the materials used in restoration.

On the basis of the direct observation of investigated frescoes and from the scientific literature, the plaster stratigraphy of wall painting in Sarno Baths seems to be composed of three layers.

The deepest plaster is the so-called arriccio, 3–4 cm thick, the function of which is to cling to the wall and provide a good moisture reserve for the overlying layers. The second layer (1–1.5 cm thick) is composed of gray-colored sublayers (inserted 'wet to wet') made up of a lime binder with an aggregate containing black volcanic sand and lumps of calcareous material. The under sublayer of plaster is slightly coarser than the upper layer. Finally, there is the 'intonachino,' which is a thin white plaster layer consisting of a lime binder with crystalline calcite as one of the aggregates.

29.4.2 Noninvasive Investigations on Frescoes by GPR and IRT

Two walls of the Gymnasium of the Sarno Baths (located in Insula 2 of Regio VIII) have been investigated by using GPR and IRT with the aim to evaluate the state of adherence of plaster layers and other possible features referable to decay pathologies of wall painting.

Before GPR and IRT prospections, an architectural survey was performed by structure-from-motion photogrammetry, by processing multiple photographs with a large overlap. In this way, orthophotographs and digital models of the wall paintings were achieved whose details allowed us to map decay pathologies of paintings. Figure 29.12 shows the 3D visualization of the two wall paintings located at South and East, respectively. The 3D mesh and textured models (Fig. 29.12: upper and bottom, respectively) indicate the lack of the external layer of fresco as well as other decay pathologies such as deposits, biological patina, and efflorescence (salt coating).

For sake of brevity we discuss only the results obtained from GPR and IRT investigations on one of the two investigated wall paintings, in particular, the largest one (south wall), shown in Fig. 29.13.

The GPR survey was performed with the Hi-Mod GPR of IDS using the antenna at 2-GHz frequency. The GPR antenna was moved on the painted surface by using a plastic panel against the wall. GPR data were collected with 512 samples per scan for a recording time window of 30 ns and a manual gain function. The survey was carried out in continuous mode along 0.2-m spaced parallel profiles in the part of

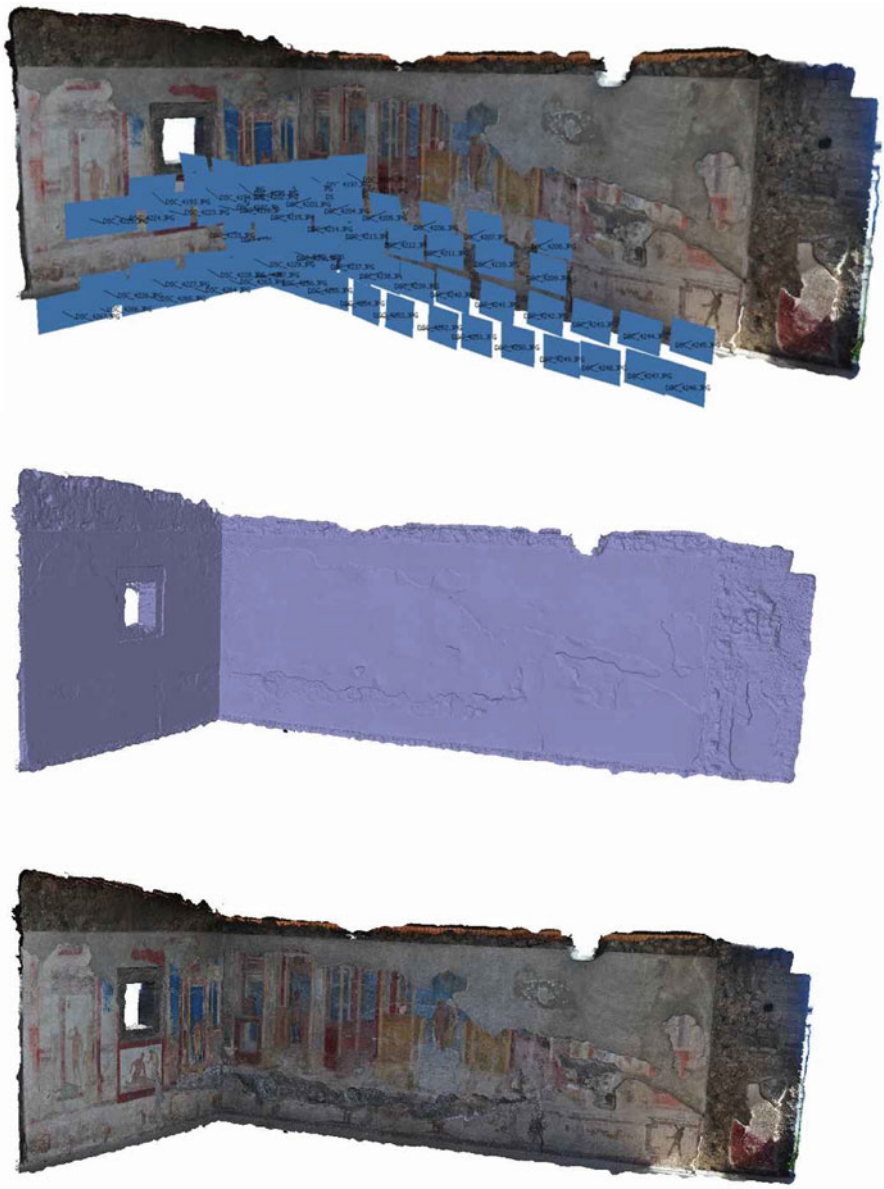

Fig. 29.12 3D mesh and textured model of the wall paintings in the Gymnasium

the fresco less damaged (dimensions of the surveyed area, 1 m × 5 m from 1 m in height above the floor), which allowed an optimal contact of the georadar with the wall painting. The velocity value for the electromagnetic wave was estimated as equal to 0.10 m/ns.

Fig. 29.13 The Gymnasium: Orthophotograph of the south wall painting. The *black rectangular box* denotes the area of fresco investigated by GPR

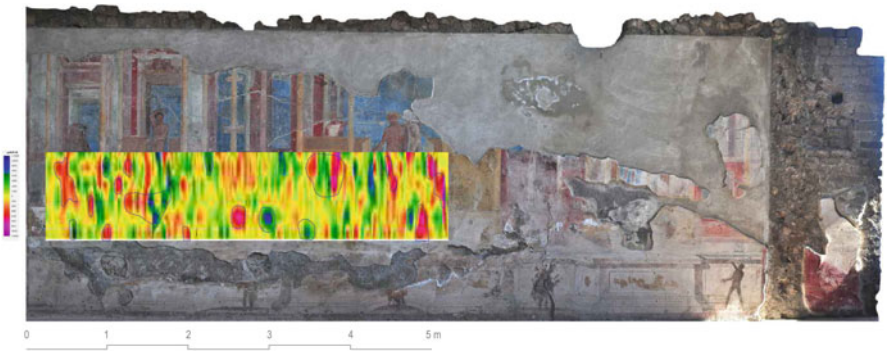

Fig. 29.14 The Gymnasium: Detail of the wall painting with GPR time slice at 4.7 cm depth. *Light blue lines* border areas characterized by high amplitude

To obtain further information on the presence of discontinuity, appropriate processing has been performed for easier interpretation. Processing steps can be summarized as follows:

- Background removal procedure (Persico and Soldovieri 2008) for the filtering of the wall interface response
- Declipping to eliminate local saturations in amplitude of the traces followed by an interpolation procedure for the reconstruction of the saturated waveforms
- Kirchhoff migration by adopting the velocity of EM wave equal to 0.10 m/ns
- Low-pass filtering that deletes high-frequency noise present in radar scans

GPR-processed data show few reflectors, likely associated with nonperfect adhesion of the plaster to the wall in a depth range 1–5 cm.

The highest values of radar amplitude are observed at the depth of 4.7 cm in correspondence to the interface between the plaster (the third layer, the deep arriccio) and the wall (see Fig. 29.14). Other significant values of radar amplitude

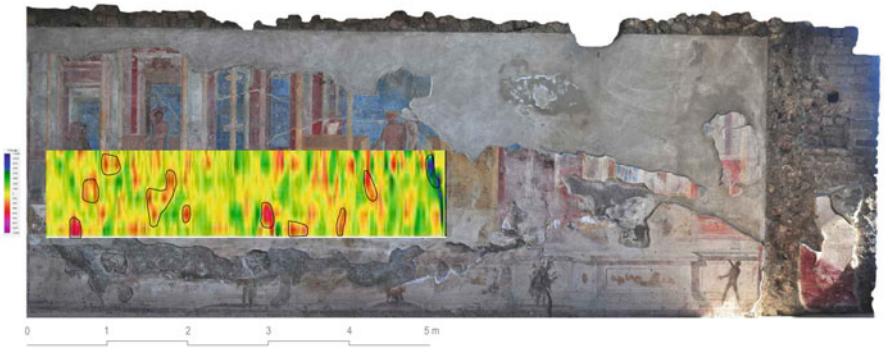

Fig. 29.15 The Gymnasium: Detail of the wall painting with GPR time slice at 3.5 cm depth. *Black lines* border areas characterized by high amplitude likely referable to detachment between two plaster layers (arriccio and deep arriccio)

are at a depth between 2 and 3 cm near to the interface between 'arriccio' and 'deep arriccio' (see Fig. 29.15).

The entire wall painting has been also investigated by IRT with the aim to provide complementary data for facilitating the interpretation of GPR results. In particular, the main interest has been that to verify the presence of thermal anomalies in correspondence with the GPR signal of high amplitude.

IRT prospections have been performed by using the passive method in an indoor environment. IRT images were collected with a FLIR SC660 sensor FPA (Focal Plane Array) uncooled microbolometer operating in the spectral range between 7.5 and 14 μm. The identification of thermal anomalies depends on the surface characteristics of emissivity and roughness and on the physical properties of the materials. In this way, information is gained about the thickness, type, and state of preservation of the plaster.

Despite the low natural heating, the thermal maps exhibit few spatial temperature changes, which can be associated with salt coating, patina, and deposits; other more significant thermal anomalies are referable to possible problems of detachment or sparse adherence between plaster layers (Fig. 29.16).

The integration and fusion of GPR and IRT methods (see Fig. 29.17) provided a map of possible areas of interest likely referable to decay pathologies or inhomogeneities in the multi-layered structure of the frescoes.

In particular, the matching between GPR reflectors and thermal anomalies could be reasonably considered an indicator of detachments or scarce adherence between plaster and wall or of problems of delamination between the plaster layers.

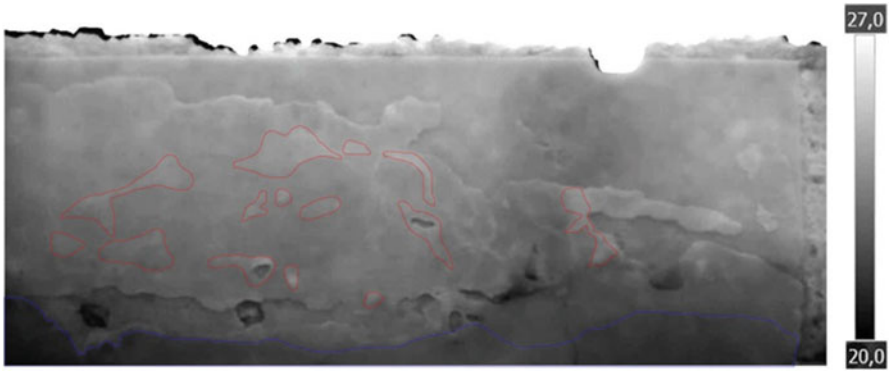

Fig. 29.16 The Gymnasium: Detail of IRT image of the wall painting. *Red lines* border areas characterized by thermal anomalies likely referable to detachment. *Blue lines* indicate areas affected by rising damp

Fig. 29.17 The Gymnasium: Detail of the wall painting. *Black* and *light blue lines* border areas characterized by high-amplitude GPR at 3.5 and 4.7 cm depth, respectively. *Red lines* border areas characterized by thermal anomalies. *Blue lines* indicate areas affected by rising. The images show that most of the thermal anomalies are characterized by GPR at high amplitude at 3.5-cm depth, likely resulting from the presence of detachment or scarce adherence between the plaster layers of the fresco

29.5 Conclusions

This chapter has presented two interesting cases of integration among noninvasive diagnostics techniques in the framework of work of restoration of the Regio VIII in the Pompeii.

The first study case is concerned with the detection of cracks and the collection of constructive features of masonry structures, whereas the second is related to the identification and survey of fresco detachment.

For the first study case, GPR and seismic tomographic methods were integrated for the diagnosis of walls in *opus incertum* on the southern side of the Basilica. The main outcome of this survey was the evaluation of the state of conservation of masonry, including the detection of possible cracks, fractures, and voids. Before carrying out the GPR and seismic investigations, several surveys were conducted to provide the geometry of the walls, identify possible deformations, and to obtain detailed orthophotographs useful to study the building techniques. The 3D geometry of the walls has been obtained by processing and integrating terrestrial and aerial images taken from a drone. In this way, it has been possible to establish that the walls present significant cracks and discontinuities in the masonry but do not exhibit out-of-plane deformations.

The second test case was concerned with fresco investigation at two walls of the Gymnasiun of Sarno Baths (located in insula 2 of Regio VIII). In this case, the joint use of GPR and IRT permitted gaining information about possible detachments or scanty adherence between plaster and wall or problems of delamination between the plaster layers. The integration was based on the spatial correlation of the GPR and thermal anomalies, and it was possible to obtain a map of areas affected by decay pathologies or inhomogeneities in the multi-layered structure of the frescoes.

Acknowledgements The present publication is based on the results of non invasive investigations performed in 2015 by CNR_IBAM, funded by Samoa srl, for the restoration of Regio VIII.

Author Contributions N. Masini conceived the study. N. Masini and M. Sileo wrote the paper, with the contribution of G. Leucci for paragraphs 29.3.2. 29.3.3 and 29.4.2, and A. D'Antonio for the study area (paragraph 29.2). F. Soldovieri reviewed the manuscript. GPR and seismic data have been acquired by G. Leucci, L. De Giorgi and M. Sileo. Leucci and Sileo processed GPR data. Seismic data have been processed by Leucci. Infrared data have been acquired and processed by M. Sileo. The terrestrial surveys has been performed by M. Scavone, A. Pecci and A. D'Antonio, the UAV-based surveys has been made by A. Pecci. The interpretation of data has been done by N. Masini, G. Leucci, M. Scavone, M. Sileo.

References

Avdelidis NP, Moropoulou A (2004) Applications of infrared thermography for the investigation of historic structures. J Cult Herit 5:119–127

Binda L, Saisi A, Zanzi L (2003) Sonic tomography and flat jack tests as complementary investigation procedures for the stone pillars of the temple of S.Nicolo' L'Arena (Italy). NDT & E Int 36:215–227

Binda L, Zanzi L, Lualdi M, Condoleo P (2005) The use of georadar to assess damage to a masonry Bell Tower in Cremona, Italy. NDT & E Int 38(3):171–179

Brandi C (1963) Teoria del restauro di Cesare Brandi. Edizioni di Storia e Letteratura, Rome

Cardarelli E, Godio A, Morelli G, Sambuelli L, Santarato G, Socco LV (2002) Integrated geophysical surveys to investigate the Scarsella vault of St. John's Baptistery in Florence. Lead Edge 67:467–470

Carlomagno GM, Di Maio R, Fedi M, Meola C (2011) Integration of infrared thermography and high-frequency electromagnetic methods in archaeological surveys. J. Geophys. Eng 8(2011):S93–S105

Cataldo R, De Donno A, De Nunzio G, Leucci G, Nuzzo L, Siviero S (2005) Integrated methods for analysis of deterioration of cultural heritage: the Crypt of "Cattedrale di Otranto". J Cult Herit 6:29–38

Conyers LB (2004) Ground-penetrating Radar for archaeology. AltaMira, Walnut Creek

Conyers LB (2012) Interpreting ground-penetrating Radar for archaeology. Left Coast Press, Walnut Creek

Conyers LB, Goodman D (1997) Ground-penetrating Radar: an introduction for archaeologists. AltaMira, Walnut Creek

Cosentino PL, Capizzi P, Fiandaca G, Martorana R, Messina P (2009) Advances in micro geophysics for engineering and cultural heritage. J Earth Sci 20:626–639

D'Aranno PJV et al (2015) High-resolution geomatic and geophysical techniques integrated with chemical analyses for the characterization of a Roman wall. J Cult Herit. doi:10.1016/j.culher.2015.06.005

Danese M, Demšar U, Masini N, Charlton M (2010) Investigating material decay of historic buildings using visual analytics with multi-temporal infrared thermographic data. Archaeometry 52(3):482–501

Dumoulin J (2016) Infrared thermography: from sensing principle to non destructive testing considerations. In: Masini N, Soldovieri F (eds) Sensing the past. Springer, Cham

Fiorelli G (1875) Descrizione di Pompei. Tipografia Italiana, Napoli

Gabellone F, Leucci G, Masini N, Persico R, Quarta G, Grasso F (2013) Non-destructive prospecting and virtual reconstruction of the chapel of the Holy Spirit in Lecce, Italy. Near Surf Geophys. doi:10.3997/1873-0604.2012030

Garcia L (2006) Danni di guerra a Pompei. Una dolorosa vicenda quasi dimenticata, Studi della Soprintendenza Archeologica di Pompei 15. "L'Erma" di Bretschneider, Roma

Goodman D (2013) GPR Slice Version 7.0 Manual. http://www.gpr-survey.com. Accessed 28 Jan 2017

Grinzato EP, Bison G, Marinetti S (2002a) Monitoring of ancient buildings by the thermal method. J Cult Herit 3(2002):21–29

Grinzato EP, Bressan C, Marinetti S, Bison PG, Bonacina C (2002b) Monitoring of the Scrovegni Chapel by IR thermography: Giotto at infrared. Infrared Phys Technol 43(3–5):165–169

ICOMOS (2003) ICOMOS Charter- principles for the analysis, conservation and structural restoration of architectural heritage. Ratified by the ICOMOS 14th General Assembly, in Victoria Falls, Zimbabwe, October 2003

Inagaki T, Ishii T, Iwamoto T (1999) On the NDT and E for the diagnosis of defects using infrared thermography. NDT&E Int 32:247–257

Ioppolo G (ed) (1992) Le Terme del Sarno a Pompei. Iter di un'analisi per la conoscenza, il restauro e la protezione sismica del monumento, Soprintendenza Archeologica di Pompei. Monografie 5. "L'Erma" di Bretschneider, Roma

Koloski Ostrow A (1990) The Sarno Bath Complex. "L'Erma" di Bretschneider, Roma

Kordatos EZ, Exharcos DA, Stavrakos C, Moropoulou A, Matikas TE (2013) Infrared thermographic inspection of murals and characterization of degradation in historic monuments. Constr Build Mater 48:1261–1265

Leucci G (2016) Seismic and Sonic Applications on artifacts and historical building. In: Masini N, Soldovieri F (eds) Sensing the past. Springer, Cham

Leucci G, Masini N, Persico R, Soldovieri F (2011) GPR and sonic tomography for structural restoration: the case of the cathedral of Tricarico. J Geophys Eng 8(3):76–92. doi:10.1088/1742-2132/8/3/S08

Leucci G, Masini N, Persico R, Quarta G, Dolce C (2012) A multidisciplinary analysis of the crypt of the holy spirit in monopoli (Southern Italy). Near Surf Geophys 10:1–8. doi:10.3997/1873-0604.2011032

Leucci G, Persico R, Soldovieri F (2007) Detection of fractures from GPR data: the case history of the Cathedral of Otranto. J Geophys Eng 4:452–461

Maierhofer C, Leipold S (2001) Radar investigation of masonry structures. NDT & E Int 34: 139–147

Maierhofer C et al (2003) Detection of shallow voids in concrete structures with impulse thermography and radar. NDT&E Int 36:257–263
Masini N, Nuzzo L, Rizzo E (2007) GPR investigations for the study and the restoration of the Rose Window of Troia Cathedral (Southern Italy). Near Surf Geophys 5:287–300
Masini N, Persico R, Rizzo E (2010a) Some examples of GPR prospecting for monitoring of the monumental heritage. J Geophys Eng 7:190–199. doi:10.1088/1742-2132/7/2/S05
Masini N, Persico R, Rizzo E, Calia A, Giannotta MT, Quarta G, Pagliuca A (2010b) Integrated techniques for analysis and monitoring of historical monuments: the case of S. Giovanni al Sepolcro in Brindisi (Southern Italy). Near Surf Geophys 8(5):423–432. doi:10.3997/1873-0604.2010012
Masini N, Gabellone F, Leucci G, Persico R, Soldovieri F (2013) Enhancement of the information content available from non invasive diagnostics for restoration and knowledge of architectural heritage. In: Proceedings of Built heritage 2013 monitoring conservation management, Milano, 18–20 Nov 2013, pp 824–828
Mau A (1900) Pompeji in Leben und Kunst. Engelmann, Leipzig
Meier T, Aura M, Fehr M, Köhn D, Cristiano L, Sobott R, Mosca I, Ettl H, Eckel F, Steinkraus T, Erkul E, Schulte-Kortnack D, Sigloch K, Bilgili F, Di Gioia E, Parisi Presicce C (2016) Chapter XX: Investigating surficial alterations of natural stone by ultrasonic surface measurements. In: Masini N, Soldovieri F (eds) Sensing the past. Geoscience and sensing technologies for cultural heritage. Springer, Cham
Moropoulou A, Labropoulos K, Delegou E, Bakolas A (2013) Non-destructive techniques as a tool for the protection of built cultural heritage. Constr Build Mater 48:1222–1239
Nuzzo L, Masini N, Rizzo E, Lasaponara R (2007) Integrated and multiscale NDT for the study of architectural heritage. In: Michel U, Civco DL, Ehlers M, Kaufmann HJ (eds) Proceedings of SPIE, remote sensing for environmental monitoring, GIS applications, and geology VIII, vol. 7110, p 711015
Nuzzo L, Calia A, Liberatore D, Masini N, Rizzo E (2010) Integration of ground-penetrating radar, ultrasonic tests and infrared thermography for the analysis of a precious medieval rose window. Adv Geosci 24:69–82
Pérez-Gracia V, Caselles JO, Clapés J, Martinez G, Osorio R (2013) Non-destructive analysis in cultural heritage buildings: evaluating the Mallorca cathedral supporting structures. NDT & E Int 59:40–47
Pérez-Gracia V, González-Drigo R, Di Capua D (2008) Horizontal resolution in a non-destructive shallow GPR survey: an experimental evaluation. NDT&E Int 41:611–620
Persico R (2014) Introduction to ground penetrating radar: inverse scattering and data processing. Wiley, Hoboken. ISBN:9781118305003
Persico R, Sato M (2016) Ground penetrating radar: technologies and data processing issue for applications in the field of cultural heritage. In: Masini N, Soldovieri F (eds) Sensing the past. Springer, Cham
Persico R, Soldovieri F (2008) Effects of the background removal in linear inverse scattering. IEEE Trans Geosci Remote Sens 46(4):1104–1114
Ranalli D, Scozzafava M, Tallini M (2004) Ground penetrating radar investigations for the restoration of historic buildings: the case study of the Collemaggio Basilica (L'Aquila, Italy). J Cult Herit 5:91–99
Russell JK, Stasiuk MV (1997) Characterization of volcanic deposits with ground-penetrating radar. Bull Volcanol 58(7):515–527
Saisi A, Gentile C, Guidobaldi M (2015) Post-earthquake continuos dynamic monitoring of the Gabbia Tower in Mantua, Italy. Constr Build Mater 81:101–112
Soldovieri F, Orlando L (2009) Novel tomographic based approach and processing strategies for GPR measurements using multifrequency antennas. J Cult Herit 10:e83–e92

Erratum to: Investigating Surficial Alterations of Natural Stone by Ultrasonic Surface Measurements

Thomas Meier, Michael Auras, Moritz Fehr, Daniel Köhn, Luigia Cristiano, Robert Sobott, Ilaria Mosca, Hans Ettl, Felix Eckel, Tim Steinkraus, Ercan Erkul, Detlef Schulte-Kortnack, Karin Sigloch, Filiz Bilgili, Elena Di Gioia, and Claudio Parisi Presicce

Erratum to:
Chapter 12 in: N. Masini, F. Soldovieri (eds.),
***Sensing the Past*, Geotechnologies and the Environment 16,**
https://doi.org/10.1007/978-3-319-50518-3_12

The original version of Chapter 12 was inadvertently published with incorrect author name "Michal Auras" instead of "Michael Auras". The chapter has been updated.

The updated original online version of this chapter can be found at
https://doi.org/10.1007/978-3-319-50518-3_12

N. Masini, F. Soldovieri (eds.), *Sensing the Past*, Geotechnologies and the Environment 16, DOI 10.1007/978-3-319-50518-3_30

Index

N. Masini, F. Soldovieri (eds.), *Sensing the Past*, Geotechnologies and the Environment 16, DOI 10.1007/978-3-319-50518-3